Springer Series in Geomechanics and Geoengineering

Alessio Ferrari
Lyesse Laloui *Editors*

Advances in Laboratory Testing and Modelling of Soils and Shales (ATMSS)

Springer

Springer Series in Geomechanics and Geoengineering

Series editor

Wei Wu, Universität für Bodenkultur, Vienna, Austria
e-mail: wei.wu@boku.ac.at

About this Series

Geomechanics deals with the application of the principle of mechanics to geomaterials including experimental, analytical and numerical investigations into the mechanical, physical, hydraulic and thermal properties of geomaterials as multiphase media. Geoengineering covers a wide range of engineering disciplines related to geomaterials from traditional to emerging areas.

The objective of the book series is to publish monographs, handbooks, workshop proceedings and textbooks. The book series is intended to cover both the state-of-the-art and the recent developments in geomechanics and geoengineering. Besides researchers, the series provides valuable references for engineering practitioners and graduate students.

More information about this series at http://www.springer.com/series/8069

Alessio Ferrari · Lyesse Laloui
Editors

Advances in Laboratory Testing and Modelling of Soils and Shales (ATMSS)

Springer

Editors
Alessio Ferrari
École Polytechnique Fédérale de Lausanne
Lausanne
Switzerland

and

Unviversità degli Studi di Palermo
Palermo
Italy

Lyesse Laloui
École Polytechnique Fédérale de Lausanne
Lausanne
Switzerland

ISSN 1866-8755 ISSN 1866-8763 (electronic)
Springer Series in Geomechanics and Geoengineering
ISBN 978-3-319-52772-7 ISBN 978-3-319-52773-4 (eBook)
DOI 10.1007/978-3-319-52773-4

Library of Congress Control Number: 2017930200

Printed on acid-free paper

This Springer imprint is published by Springer Nature
The registered company is Springer International Publishing AG
The registered company address is: Gewerbestrasse 11, 6330 Cham, Switzerland

Preface

Soils and shales are receiving increasing attention as rarely in the past decades. Indeed, many of the scientific and technological challenges of this century involve such materials. The development of engineering solutions to the energy quest and to minimize the impacts on climate requires in fact a deep understanding of the geomechanical behaviour of soils and shales. Applications such as geo-energy exploitation and underground energy storage, CO_2 geological sequestration, nuclear waste disposals, enhanced geothermal system—to mention a few—can be carried out only if reliable predictions can be made on the actual behaviour and long-term performance of such systems. The understanding and the capability to perform predictions of the behaviour of these systems can be gained only through advanced theoretical and experimental research on the involved geomaterials. Moreover, there is a strong need for shared knowledge among the different researchers and practitioners working for these challenging applications.

In this spirit, the ATMSS International Workshop "Advances in Laboratory Testing & Modelling of Soils and Shales" (Villars-sur-Ollon, Switzerland; 18–20 January 2017) has been organized to promote the exchange of ideas, experience and the state of the art among major experts active in the field of experimental testing and modelling of soils and shales. The workshop has been organized under the auspices of the Technical Committees TC-101 "Laboratory Testing", TC-106 "Unsaturated Soils" and TC-308 "Energy Geotechnics" of the International Society of Soil Mechanics and Geotechnical Engineering.

This volume contains the invited keynote and feature lectures, as well as the papers that have been presented at the workshop. The topics of the lectures and papers cover a wide range of theoretical and experimental research, including unsaturated behaviour of soils and shales, multiphysical testing of geomaterials, hydromechanical behaviour of shales and stiff clays, the geomechanical behaviour of the Opalinus Clay shale, advanced laboratory testing for site characterization and in situ applications, and soil–structure interactions.

We would like to express our thanks to all the authors for their outstanding contributions. We are especially grateful to Valentina Favero, for the assistance with the preparation of this book.

Alessio Ferrari
Lyesse Laloui

Contents

Advanced Laboratory Testing for Site Characterization and In – situ Application Studies

Soil-Structure Interactions

Constitutive and Numerical Modelling of Soils and Shales

Keynote Lectures

Hydro-mechanical Behaviour of Unsaturated Argillaceous Rocks

Bernardo Caicedo[1(✉)], Jairo Martin Espitia[1,2], and Luis Vallejo[3]

[1] Department of Civil Engineering, Universidad de Los Andes, Bogotá, Colombia
bcaicedo@uniandes.edu.co
[2] Mining Engineering Department, UPTC, Sogamoso, Colombia
[3] Department of Civil and Environmental Engineering, University of Pittsburgh, Pittsburgh, USA

Abstract. The paper studies the hydromechanical behaviour of an argillaceous rock from the Colombian Andes. The influence of total suction on some physical/mechanical properties is analyzed on an argillaceous rock from the Colombian Andes. A wetting path was applied to the rocks using the vapor transfer technique. Uniaxial compression tests were conducted on specimens at different levels of suction. Also, microstructural observations are carried out using a Mercury Intrusion Porosimeter Apparatus. Results from the laboratory tests indicate that anisotropic deformations took place during the wetting path. Also, total suction contributed to a considerable and non-linear reduction in the peak compressive stress, elastic modulus and stress thresholds of the tested samples. Microstructural analysis indicated the influence of suction on the dominant pores.

Introduction

A substantial portion of rocks forming part of the earth's crust are of argillaceous nature and are usually present in many mining and infrastructure projects (Pineda et al. 2014). For example, in Colombia a significant part of the population, infrastructure and mining projects are located in the eastern Andes mountain range. In this area, some argillaceous rocks outcrop causing significant challenges for the stability of rock excavations. Indeed, the mineralogical composition of this material makes it sensitive to environmental conditions, such as variation in water content (Corkum and Martin 2007). Furthermore, its mechanical behaviour is the result of the combination of sedimentation, gravitational compaction (consolidation), uplift/unloading (overconsolidation) and cementation/bonding (Gens 2013).

The hydro-mechanical behaviour of argillaceous rocks has been studied recently using the vapor transfer technique (Pham et al. 2007; Valès et al. 2004; Yang et al. 2012). Some features of the behavior of this material in unsaturated conditions can be highlighted as follows: (I) during the application of hydric cycles (without mechanical loading) it is observed hysteresis in the water retention curve, anisotropic deformations and permanent volumetric strains in the material; (II) elastic properties and strength are controlled by the hydric state and the hydric history of the material; (III) the material is degraded as a consequence of hydric cycles.

A. Ferrari and L. Laloui (eds.), *Advances in Laboratory Testing and Modelling of Soils and Shales (ATMSS)*, Springer Series in Geomechanics and Geoengineering,
DOI 10.1007/978-3-319-52773-4_1

These studies have focused on evaluating the hydro-mechanical behavior of rocks from geologic formations of Europe. Nonetheless, only few experimental studies have been performed on South American argillaceous rocks.

Thus, the aim of this paper is to study the hydro-mechanical behaviour of an argillaceous rock from the eastern Andes mountain range in Colombia in an attempt to establish relations between total suction and some mechanical properties of the material.

Material and Methods

Material

The material studied is an indurated Cretacic-aged argillite from the Belencito formation. In Colombia, this material has occasioned stability problems in both surface and underground rock excavations, especially in some areas of the eastern Andes mountain range. Commonly, this argillaceous rock contains on average 53.2% of clay minerals (kaolinite and illite), 29.0% of calcite, 11.0% of quartz, and less than 6.0% of other minerals (e.g. opaque minerals and Muscovite). Some index properties at the initial state are provided in Table 1.

Table 1. Index properties of the argillaceous rock.

Property	Value
Bulk density	2570 (kg/m^3)
Specific gravity	2.76 (-)
Water content	1.50 (%)
Liquid limit	25 (%)
Plastic limit	15 (%)

Irregular rock block samples were collected from a limestone quarry of the Holcim Company located in Nobsa (Colombia). A detailed description of handling and specimen preparation is described in (Espitia and Caicedo 2014). 15 cylindrical samples, of 20 mm in diameter and 40 mm in height perpendicular to bedding plane, were bored with air pressure to minimize alteration caused by liquid water. The tested specimens were obtained from three rock blocks (rock block 1-B1, rock block 10-B10 and rock block 17-B17).

Suction Control

Suction was applied using vapor equilibrium technique. This technique is implemented by controlling the relative humidity in a sealed system (Delage et al. 2008). The experimental program consisted of the application of a wetting path to the rock specimens. For this, the cylindrical specimens were set in an airtight acrylic container in which saturated saline solutions imposed relative humidity (RH). We select five

Table 2. Saline solutions used.

Saline solution	Relative humidity (%)	Suction (MPa)
$CaCl_2.6H_2O$	33	151
$K_2CO_3.2H_2O$	47	102
$NaBr.2H_2O$	57	78
NaCl	72	46
K_2SO_4	95	7

saline solutions to cover a range of relative humidity between 33% and 95%. The values of relative humidity and their corresponding suction are given in Table 2. During the measuring period, the temperature stayed approximately constant at 22.9 ± 1.0°C.

The wetting path was imposed on a group of 15 specimens from B1, B10 and B17 rock blocks. The moisture equilibrium of the rock samples in the controlled humidity atmosphere was assumed when weight and strains were stabilized. For this, one sample was instrumented to measure axial and radial strains during conditioning (see Fig. 1). Also, five specimens were used to track the evolution of mass in a different container. Once specimens attained equilibrium, mechanical tests were performed on three samples (see Fig. 2).

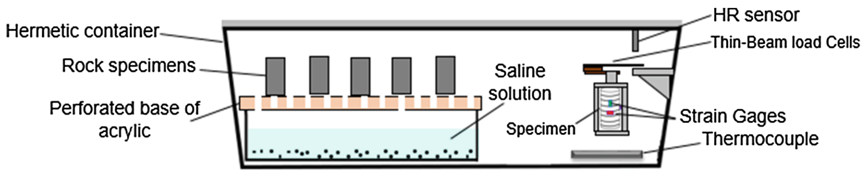

Fig. 1. Experimental setup for suction control.

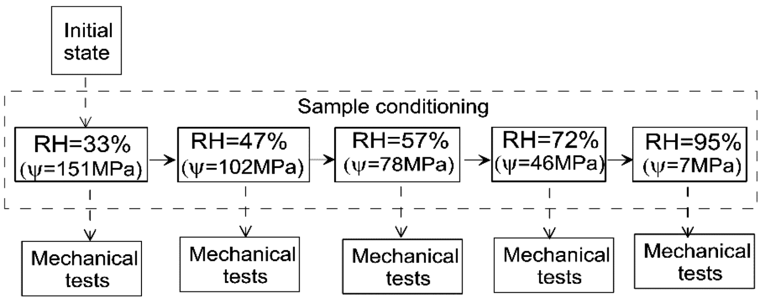

Fig. 2. Illustration of the wetting path.

Mechanical Test

Uniaxial compression tests were conducted on conditioned specimens in a controlled displacement load frame. The axial displacement rate was 0.1 mm/min. Two strain gauges were fixed in each direction (axial and radial). Also, during the mechanical tests, Acoustic Emission (AE) activity was monitored to track the process of failure of the specimens. The rock moisture was assumed to remain constant during the test due to their short duration (20 min). The experimental setup is shown in Fig. 3.

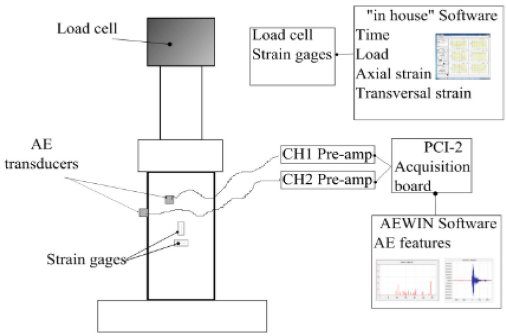

Fig. 3. Experimental setup for mechanical tests.

Experimental Results

The water retention curve (WRC) under unconfined conditions was determined using a chilled-mirror dewpoint psychrometer (Decagon-Devices 2007). For this, a cylindrical specimen was cored from rock block 10 of 33 mm in diameter and 50 mm in height, then some slices of 4 mm in height were cut with a cutoff saw machine. The obtained samples fitted in the plastic capsule used in the WP4 occupying less than the half in height. Three samples were used to measure the initial suction after trimming resulting in an average of 102.25 MPa and a water content of 1.50%. First, the specimen was brought to a dry state, then a wetting path and after a drying path was imposed.

The drying path was obtained by setting the rock specimen in a desiccator containing silica gel for an amount of time needed to attain the desired water content. Afterwards, the specimen was placed in the plastic capsule, covered with stretch film and stored in a Styrofoam box to let the internal distribution of moisture until the measurement of the total suction. Once the specimen achieved the dry state, then the wetting path was imposed. For this, vapor transfer technique using distilled water was applied for obtaining the wetting path. The specimen was exposed to the humid environment for enough time to achieve a higher water content. The same procedure was used to allow the internal distribution of moisture. Figure 4 shows the WRC along a wetting-drying cycle of the undisturbed rock (the path to achieve the dry state is shown with square symbols).

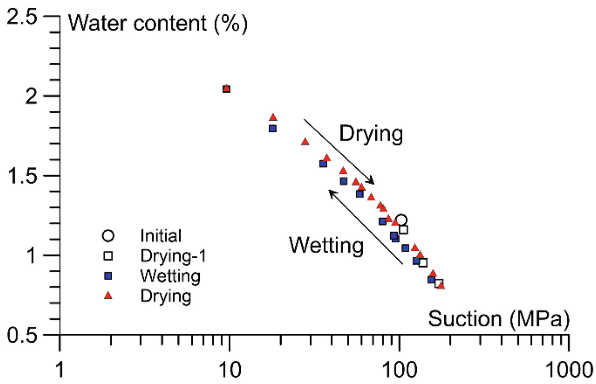

Fig. 4. Water retention curve.

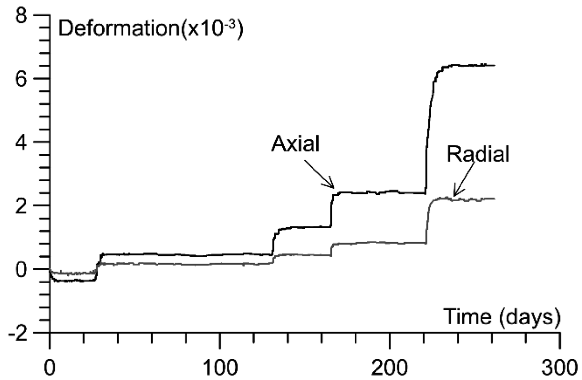

Fig. 5. Axial and radial strains during the wetting path.

Regarding deformations due to swelling, Fig. 5 indicates anisotropy strains in the material. Also, it can be noticed that the main strains variations occurred in the last hydric state (from 46 MPa to 7 MPa of total suction). Thus, it is reasonable to suppose that the principal changes will occur at this hydric stage. An analysis of Fig. 5 shows that the ratio between axial and radial strains ranges from 2.7 to 3.

Effect of Suction on the Mechanical Behaviour

The results correspond to specimens with bedding plane normal to the direction of load application. Figure 6 presents for different values of suction the Stress-Axial Strain curves of rock block B1 specimens under uniaxial compression. From these data, we obtained the peak stress and the elastic modulus.

Figure 7 contains the peak stress versus suction for all of the tested specimens. A significant reduction in the peak stress can be identified. Comparing the peak stress for the higher (151 MPa) and lower suction (7 MPa), reductions of 61%, 58%, and

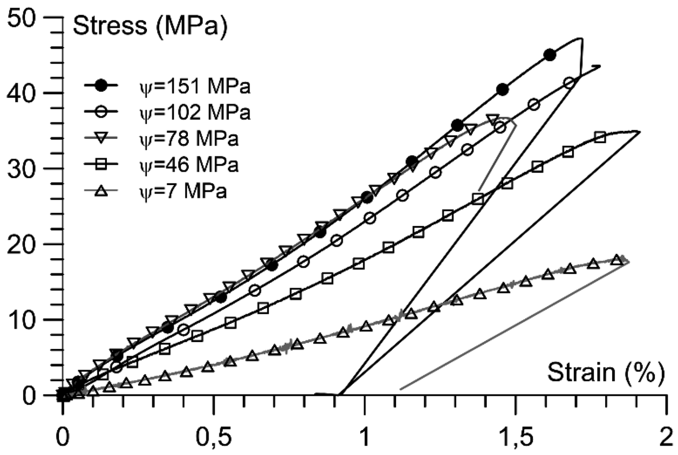

Fig. 6. Plots of stress against axial and radial strains for B1 specimens.

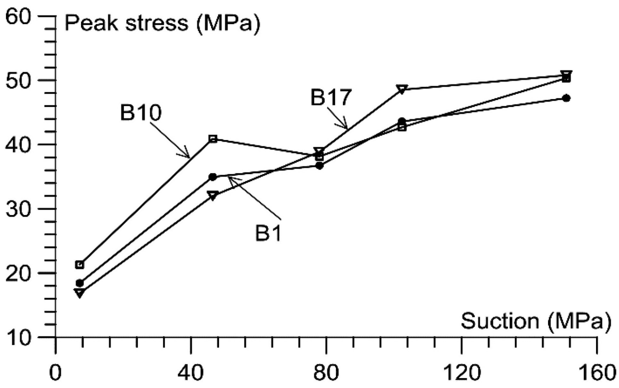

Fig. 7. Plots of peak stress against suction for B1, B10, B17 specimens.

67% are obtained for B1, B10 and B17 respectively. It is important to notice that this reduction occurs with a small variation in the water content of the material, from 1% for the driest condition to 2.3% for the wettest condition. Therefore, in the context of rock excavations in this material, the considerations of this features are essential to conceive safer designs. Besides, more than 70% of the uniaxial compressive strength reduction is observed for the last hydric state as expected. An additional observation is a non-linear relation between peak stress and suction.

We use the moving point regression technique to improve the analysis of strain gage data. This technique uses a "sliding window" approach to move through an x, y data set, fitting a straight line over a user-defined interval. The slope at each point is calculated over the interval and recorded, the process being repeated at successive points (Eberhardt et al. 1998).

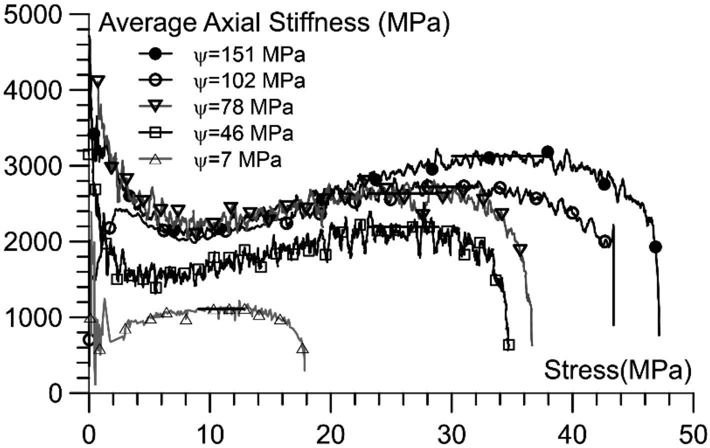

Fig. 8. Plots of axial stiffness against stress for B1 specimens.

The Axial Stiffness-Stress curves for B1 specimens are shown in Fig. 8. These curves provide a moving point average of the changes in the Young´s modulus throughout loading (Eberhardt et al. 1998). In general, it is noticed an increment in the Axial Stiffness as suction rise. Also, Fig. 8 depicts a non-linear behavior of the Axial Stiffness against stress for the values of suction considered in this study.

From Fig. 8 for each suction curve, the elastic modulus was estimated as the average of the axial stiffness along the quasi-linear condition (from 61 ± 6% to 77 ± 5% of the peak stress). This procedure was performed for the B10 and B17 rock block specimens. Accordingly, Fig. 9 summarizes the values of elastic modulus versus suction. Some data dispersion could be noticed from this Figure for suction values of 102 MPa. Despite this, a general non-linear decrease in the elastic modulus can be observed. For the extreme conditions of suction, elastic modulus decreases 65%, 58%

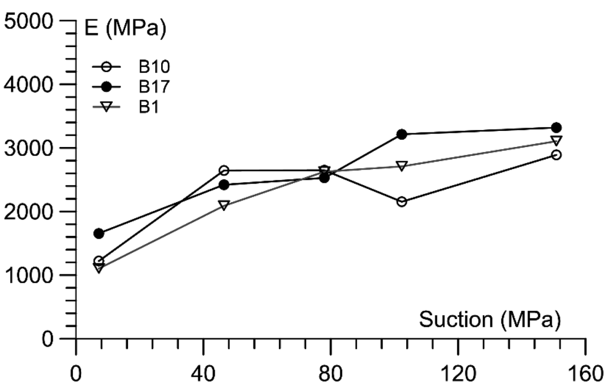

Fig. 9. Plots of elastic modulus versus suction.

and 50% for B1, B10 and B17 rock blocks. Further, more than 63% of the elastic modulus reduction occurs for the last hydric state as expected.

Microstructural Observations

At the end of each hydric state, a freeze-dried specimen was used to perform a microstructural analysis. The aim was to evaluate variations in the pore size distribution of the material. To do this, we use an ‘AutoPore IV 9500-Micrometrics Instrument Corp.’ porosimeter.

Figure 10 plots pore size distribution (PSD) curves for specimens at different hydric states. The dominant pore for the undisturbed material is about 40 nm and exhibits some macropores. PSD curve for the higher suction (ψ = 151 MPa) indicates a dominant pore of approximately 34 nm while a considerable increase in the dominant pore of the PSD curve for the lower suction (7 MPa) is observed (180 nm). These features are in agreement with the swelling that was detected in the material (see Fig. 5). In general, for this wetting path applied are not identifying substantial changes in the macroporosity of the material. Therefore, the main observations in its behavior may be attributed to variations in its microporosity and mesoporosity.

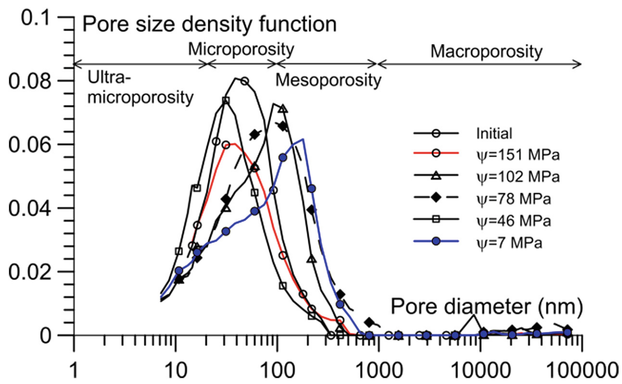

Fig. 10. Variation of pore size distribution versus suction.

Acoustic Emission Activity

The Monitoring of Acoustic Emission (AE) has been proven as a powerful tool to track the process of failure of materials subjected to mechanical load (Tang and Hudson 2010). It was considered to study some features of the brittle behavior of the material. Specifically, we use the cumulative hits to identify the crack initiation stress threshold (σ_{CI}) and crack stress damage threshold (σ_{CD}). For this, Diederichs et al. (2004) state that these stresses can be determined from cumulative hits versus axial stress log-log plots. σ_{CI} is the first point where the rate of crack emissions suddenly increases with a small change in load. Besides, σ_{CD} is where the second sudden increase in the slope of

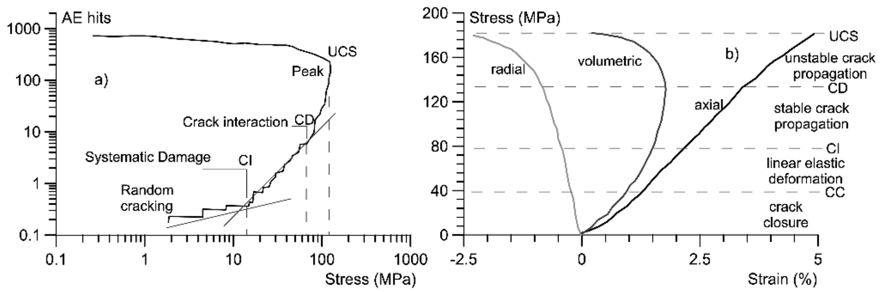

Fig. 11. Identification of stress thresholds (a) from AE hits (b) from volumetric strains modified from Diederichs et al. (2004).

the AE curve occurs (Fig. 11a). On the other hand, σ_{CI} and σ_{CD} can also be obtained from the axial stress versus volumetric strain plot. Bieniawski (1967) defines σ_{CI} as the stress level that limits the linear axial stress versus volumetric strain behavior and σ_{CD} as the stress level where the volumetric strain is reversed (Fig. 11b).

Figure 12 presents the identification of the stress thresholds according to the methodology described in Fig. 11 from one sample conditioned at RH = 33%. Figure 13 reports values of crack initiation threshold (σ_{CI}) and crack damage threshold (σ_{CD}) determined from volumetric strains and cumulative AE activity for different suction values. As illustrated in Fig. 13, stress thresholds increase with suction and present a satisfactory fit (Fig. 13a). Normalized data with the peak stress of each specimen are presented in Fig. 13b. For the different hydric states, σ_{CI} appears approximately at 20% of peak stress while σ_{CD} shows large variability and occur between 60% and 80% of the rupture stress (Fig. 13b).

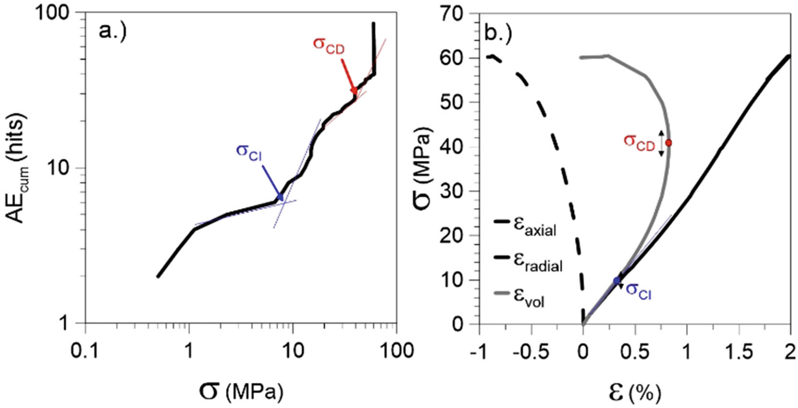

Fig. 12. Identification of stress thresholds (a) from AE hits (b) from volumetric strains.

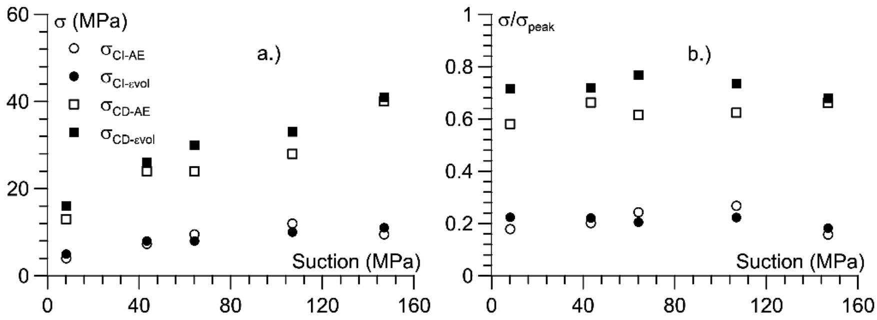

Fig. 13. Crack initiation threshold (σ_{CI}) and crack damage threshold (σ_{CD}) for different values of suction.

Conclusions

The mechanical properties of argillaceous rocks from the Colombian Andes Mountains are influenced by their moisture content which is the result of its high clay content (53%).

As reported for other argillaceous rocks, the water retention curve represented a hysteresis loop. Dimensions of the specimens tested (20 mm in diameter and 40 mm in height) helped to reduce the time to obtain moisture equilibrium for each hydric state. Axial and radial strains due to the wetting path imposed without mechanical load were found to be clearly anisotropic with a ratio between 2.7 and 3.

Elastic properties of the rock are dependent on the hydric state and exhibit a non-linear relation with suction. Peak stress displays a decrease of at least 58%, while the reduction in elastic modulus is at least 50%. It is important to mention that these changes result from small variations in the water content.

The Average Axial Stiffness showed a non-linear behaviour in most of the loading process. Only, in an interval that varies between 61 ± 6% and 77 ± 5% of the peak stress were identified a quasi-linear trend. Also, the Average Axial Stiffness evidenced an increment as suction increased.

Acoustic emission activity is used to identify the crack initiation and the stress damage thresholds. Despite the limited results, this feature is of great interest for linking the influence of rock moisture on the mechanical properties of argillaceous rocks and their process of failure. However, further tests are needed to confirm the influence of suction on the pattern of acoustic emission.

References

Bieniawski ZT (1967) Mechanism of brittle rock fracture. Part I. Theory of the fracture process. Int J Rock Mech Min Sci Geomech Abs 4:395–406

Corkum AG, Martin CD (2007) The mechanical behaviour of weak mudstone (Opalinus Clay) at low stresses. Int J Rock Mech Min Sci 44:196–209. doi:10.1016/j.ijrmms.2006.06.004

Decagon-Devices I (2007) WP4 Dewpoint PotentiaMeter for models WP4 and WP4-T Operator’s Manual Version 5
Delage P, Romero E, Tarantino A (2008) Recent developments in the techniques of controlling and measuring suction in unsaturated soils. In: Paper presented at the 1st European conference on unsaturated soils, Durham, United Kingdom
Diederichs MS, Kaiser PK, Eberhardt E (2004) Damage initiation and propagation in hard rock tunnelling and the influence of near-face stress rotation. Int J Rock Mech Min Sci 41:785–812
Eberhardt E, Stead D, Stimpson B, Read RS (1998) Identifying crack initiation and propagation thresholds in brittle rock. Can Geotech J 35:222–233
Espitia J, Caicedo B (2014) Mechanical behavior of unsaturated argillaceous rocks under uniaxial compression through acoustic emission. In: Khalili RKE (ed) Sixth international conference on unsaturated soils, UNSAT 2014, Sydney, Australia, pp 1597–1603
Gens A (2013) On the hydromechanical behaviour of argillaceous hard soils-weak rocks. In: Paper presented at the 15th European conference on soil mechanics and geotechnical engineering, Athens, Greece
Pham QT, Vales F, Malinsky L, Nguyen Minh D, Gharbi H (2007) Effects of desaturation–resaturation on mudstone. Phys Chem Earth Parts A/B/C 32:646–655
Pineda JA, Alonso EE, Romero E (2014) Environmental degradation of claystones. Géotechnique 64:64–82
Tang CA, Hudson JA (2010) Rock failure mechanisms: illustrated and explained. CRC Press, New York
Valès F, Nguyen Minh D, Gharbi H, Rejeb A (2004) Experimental study of the influence of the degree of saturation on physical and mechanical properties in Tournemire shale (France). Appl Clay Sci 26:197–207
Yang DS, Bornert M, Chanchole S, Gharbi H, Valli P, Gatmiri B (2012) Dependence of elastic properties of argillaceous rocks on moisture content investigated with optical full-field strain measurement techniques. Int J Rock Mech Min Sci 53:45–55

Plastic Deformations of Unsaturated Fine-Grained Soils Under Cyclic Thermo-Mechanical Loads

C.W.W. Ng(✉) and C. Zhou

The Hong Kong University of Science and Technology, Kowloon, Hong Kong
cecwwng@ust.hk

Abstract. Plastic deformation of unsaturated soils under cyclic thermo-mechanical loads is important to the serviceability of many earth structures, such as the high-speed railway embankment and energy pile. In this keynote, experimental and theoretical studies of cyclic thermo-mechanical behaviour of unsaturated fine-grained soils are presented. Particular attentions are given to cyclic shear behaviour of unsaturated soil at various suctions and temperatures, as well as soil volume changes under heating and cooling at different suctions.

Introduction

Soils in many earth structures such as high-speed railway embankment and energy pile are often subjected to cyclic thermo-mechanical loads, which may induce volume changes and hence settlements. Figure 1 shows the volume change behaviour of two saturated fine-grained soils, remolded clay tested in triaxial and intact silty clay in oedometer, under cyclic heating and cooling (Campanella and Mitchell 1968; Di Donna and Laloui 2015). It is clear that with an increasing number of thermal cycles, the cumulative plastic contraction of the two soils accumulated, albeit at a decreasing rate. During the cooling phase, however, it appears that there were two opposite responses. Remolded clay expanded but intact silt contracted. No existing constitutive soil model can capture the observed cyclic behaviour of soils reported in the figure well.

In this keynote, constitutive modelling and experimental study of cyclic thermo-mechanical behaviour of two unsaturated fine-grained soils are briefly described. Particular attentions are paid to (a) plastic soil deformation induced by cyclic mechanical shearing at various suctions and temperatures; (b) soil volume changes under heating and cooling cycles. Measured results are compared with theoretical model predictions. It should be noted that some contents of this keynote are based on and extracted from Ng et al. (2016), Zhou and Ng (2016a) and Zhou and Ng (2016b).

A. Ferrari and L. Laloui (eds.), *Advances in Laboratory Testing and Modelling of Soils and Shales (ATMSS)*, Springer Series in Geomechanics and Geoengineering,
DOI 10.1007/978-3-319-52773-4_2

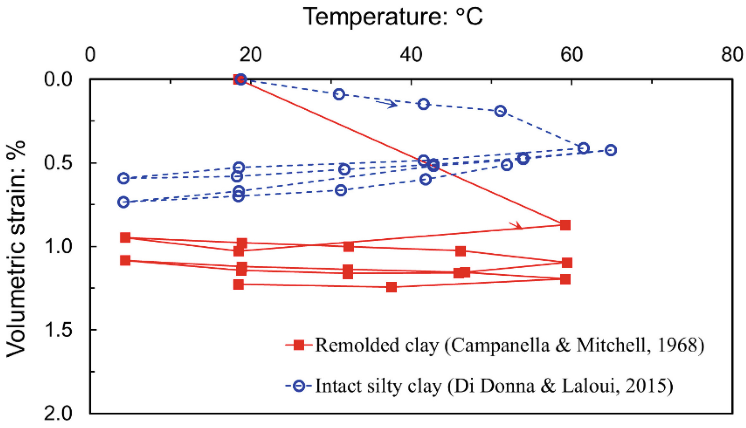

Fig. 1. Measured volume changes of saturated fine-grained soils under thermal cycles.

A Cyclic Thermo-Mechanical Model for Unsaturated Soil

Constitutive Variables

In order to analyse soil behaviour under cyclic thermo-mechanical loading at various suctions, a new constitutive soil model is formulated in the triaxial space (Zhou and Ng 2016a). Three variables are used to define the stress state of soil specimen, including mean Bishop's stress (p^*), deviator stress (q) and suction (s). Two volumetric variables, i.e., specific volume (υ) and degree of saturation (S_r), are chosen to define the relative proportions of solids, water and air within an unsaturated soil element. Moreover, the temperature (T) is included to model thermal effects on soil behaviour. Apart from the above six variables, two state parameters (ξ and ψ) are adopted:

$$\xi = f(s)(1 - S_r) \tag{1}$$

$$\psi = e - e_c \tag{2}$$

where e and e_c are the current and the critical state void ratios corresponding to the current stress in the υ-lnp^* plane. The state parameter ξ, which was introduced by Gallipoli et al. (2003), is used to describe the stabilisation effects on soil skeleton arising from water meniscus between soil particles approximately. According to Eq. (1), the value of ξ depends on two terms: $f(s)$ and $(1-S_r)$. The first term $f(s)$ represents the stabilizing normal force exerted by a single water meniscus, while the second term (1-S_r) implicitly accounts for the number of water meniscus per unit soil volume. The other state parameter ψ, which was proposed by Been and Jefferies (1985), is used to describe how far the soil state is from the critical state in terms of void ratio. According to the definition in Eq. (2), positive and negative values of ψ denote soil states on the wet side and the dry side of the critical state line (CSL), respectively,

The Three Bounding Surfaces

The bounding surface plasticity theory of Dafalias (1986) is adopted in the development of the proposed model, with three bounding surfaces (F_c, F_s and F_h) constructed. The first one F_c is defined to describe elastoplastic behaviour during compression. It is well-known as loading collapse (LC) surface in the $p^*-q-\xi$ space and shown in Fig. 2. F_c can be described as:

$$F_c = p^* - p_0(T,\ \xi) \tag{3}$$

where $p_0(T,\xi)$ is the preconsolidation pressure,

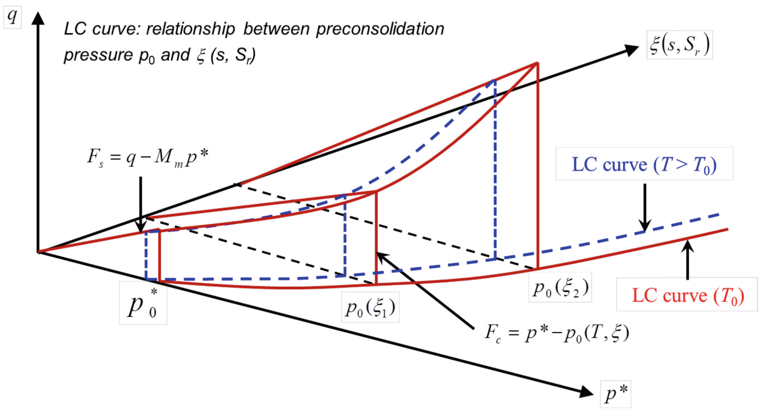

Fig. 2. Bounding surfaces Fs and Fc in the p* − q − ξ space with thermal effects.

Furthermore, $p_0(T,\xi)$ is related to normal compression lines (NCLs) and isotropic unloading-reloading lines at various conditions of T and ξ:

$$\frac{p_0(T,\xi)}{p_{atm}} = \exp\left(\frac{N(T,\xi) - \upsilon - \kappa \ln\left(\frac{p^*}{p_{atm}}\right)}{\lambda(\xi) - \kappa}\right) \tag{4}$$

where the atmospheric pressure p_{atm} (101 kPa) is included as a reference pressure; $\lambda(\xi)$ and κ are slopes of NCL and unloading and reloading line (URL) in the υ-lnp^* plane, respectively; and $N(T,\xi)$ is the intercept of NCL (specific volume at the reference pressure), described by the following equation:

$$N(T,\xi) = [N_0 - r_N(T - T_0)]\,[1 - a\,(1 - \exp(b\,\xi))] \tag{5}$$

where N_0 is the value of $N(T,\xi)$ at zero suction and at a reference temperature; r_N, a and b are soil parameters describing suction and thermal effects on NCL. According to Eq. (5), the value of $N(T,\xi)$ decreases with an increasing temperature but with a decreasing suction. This relationship is supported by the experimental results reported by (Zhou and Ng 2016a). Consequently, the effects of s, T and S_r on $p_0(T,\xi)$ are included through the term $N(T,\xi)$.

The other two surfaces F_s and F_h are relevant to elastoplastic behaviour during shearing and suction change, respectively. Details of these two boundary surfaces were reported by Zhou and Ng (2016a).

Elasto-Plasticity

For each loading process, both elastic and plastic strains can occur. Elastic and plastic strains are calculated using the following two equations:

$$\begin{cases} d\varepsilon_v^e = \dfrac{dp^*}{K} - \dfrac{\alpha_{sk}}{1+e}dT \\ d\varepsilon_q^e = \dfrac{dq}{3G_0} \\ dS_r^e = \dfrac{ds}{K_w} \end{cases} \tag{6}$$

$$\begin{cases} d\varepsilon_v^p = \Lambda_{(c)} + D_{v(s)}\Lambda_{(s)} + D_{v(h)}\Lambda_{(h)} \\ d\varepsilon_q^p = D_{q(c)}\Lambda_{(c)} + \Lambda_{(s)} + D_{q(h)}\Lambda_{(h)} \\ dS_r^p = D_{w(c)}\Lambda_{(c)} + D_{w(s)}\Lambda_{(s)} + \Lambda_{(h)} \end{cases} \tag{7}$$

where $d\varepsilon_v^e$ and $d\varepsilon_v^p$ are the elastic and plastic volumetric strains respectively; $d\varepsilon_q^e$ and $d\varepsilon_q^p$ are the elastic and plastic shear strains respectively; dS_r^e and dS_r^p are the elastic and plastic increments of S_r respectively; K is the elastic bulk modulus for soil skeleton; G_0 is the very small strain shear modulus; K_w is the ratio of incremental suction to elastic decrement of degree of saturation; and α_{sk} is isotropic thermal expansion coefficients for soil skeleton; $\Lambda_{(c)}$, $\Lambda_{(s)}$ and $\Lambda_{(h)}$ are the loading indices for compression, shearing and suction change mechanism respectively; $D_{q(c)}$, $D_{w(c)}$, $D_{v(s)}$, $D_{w(s)}$, $D_{v(h)}$ and $D_{q(h)}$ are the dilatancy factors. Experimental results in the literature generally seem to suggest that soil response upon cooling may be idealized as elastic and reversible (Hong et al. 2013). For simplicity, the same assumption is adopted in this current study. More discussion is given in the section of "Interpretations of measured and computed results".

Equation (7) does not explicitly consider thermally induced plastic increments of strain and degree of saturation. Any phenomenon of thermo-plasticity is implicitly taken into account. This is because normal compression line, critical state line in the υ-lnp^* plane and water retention curve in the current model are all temperature-dependent. A change of temperature would alter the location of bounding surfaces for the plastic mechanism of shearing, compression and suction change. The loading indices $\Lambda_{(c)}$, $\Lambda_{(s)}$ and $\Lambda_{(h)}$ in Eq. (7) are therefore all dependent on temperature, determined through hardening law and condition of consistency. From the bounding surface F_s, $\Lambda_{(s)}$ is calculated using the following equations:

$$\Lambda_{(s)} = \frac{1}{K_s^p}(dq - M_m dp^*) \tag{8}$$

$$K_s^p = \frac{G_0 h}{M_m}\left(M \exp(-n_b\psi)\left(\frac{\bar{\rho}_s}{\rho_s}\right) - M_m\right) \tag{9}$$

where h and n_b are soil parameters; ρ_s and $\bar{\rho}_s$ are Euclidian distances with respective to shearing, depending on the last loading reversal, current and maximum stress ratios. The value of $\rho_s/\bar{\rho}_s$ is zero when there is a 180° reversal in the stress path and approaches 1 as soil stress state moves towards F_s. It can be deduced from Eq. (9) that plastic modulus K_s^p decrease as the ratio $\rho_s/\bar{\rho}_s$ increases. This is consistent with experimental observation that larger plastic strain would be induced as stress state approaches bounding surface. This is one of the key features of the proposed model different from other conventional elastoplastic models for unsaturated soils (e.g., Alonso et al. (1990) and Chiu and Ng (2003)). In these previous models, soil response is assumed to be purely elastic when soil state is inside bounding (yield) surface. In addition, $\Lambda_{(c)}$ and $\Lambda_{(h)}$ in Eq. (7) can be determined based on the condition of consistency for bounding surfaces F_c and F_h, respectively. More details of the proposed cyclic thermo-mechanical model is given by Zhou and Ng (2016a).

Test Apparatuses

To test unsaturated soil at various temperatures, a suction-controlled triaxial apparatus was developed to allow for independent control of suction and temperature. To apply thermal loads, a heating system was installed. The system adopted the axis-translation technique to control matric suction. In order to avoid possible compliance errors by using externally mounted LVDT, internal Hall-effect transducers were adopted to measure local strains at centre portion of each soil specimen. The accuracy is about 3 μm, corresponding to vertical strains of about 0.003%. Careful calibration tests show that the suction probe and Hall effect transducer are both sufficiently temperature compensated in the temperature range from 20 to 60 °C. Details of the cyclic triaxial system and measuring devices were reported by Ng and Zhou (2014).

To investigate soil behaviour under heating and cooling cycles, a double cell triaxial system (Ng and Menzies 2007) was modified by installing a temperature control system. Figure 3 shows a schematic diagram of the modified double cell triaxial system. Compared to the cyclic triaxial system above, the double cell triaxial system is able to apply not only heating but also for cooling soil specimen incrementally. Furthermore, a much smaller specimen height of 20 mm can be used in this apparatus to reduce suction equalisation time. Soil temperature can reach the target temperature within six hours. Similar to the cyclic triaxial system, the axis translation technique is used to control the matric suction of soil specimen. After calibration, the accuracy of volumetric strain measurement is 0.03%. Details of the temperature-controlled double cell system and calibration methods were reported by Ng et al. (2016).

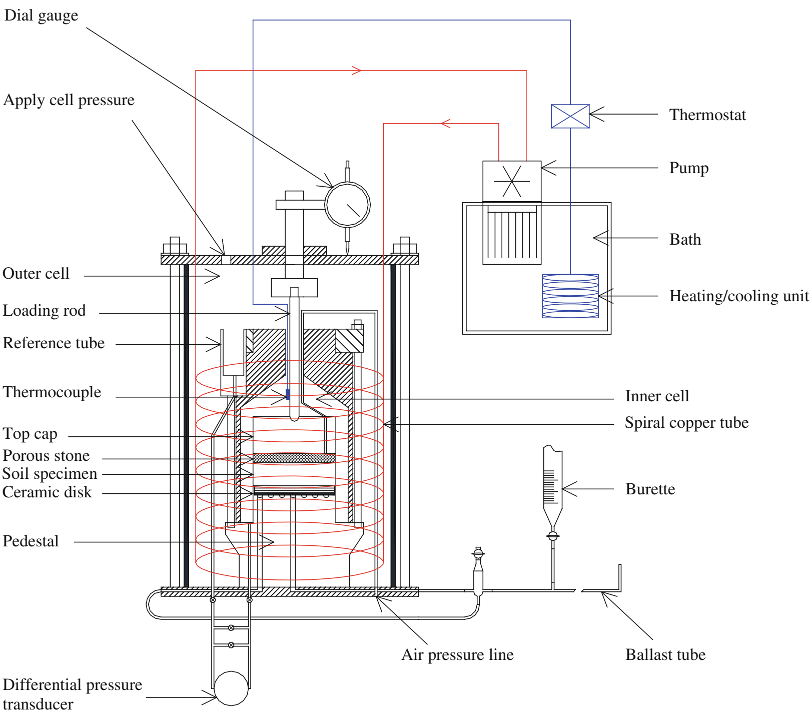

Fig. 3. Schematic diagram of suction- and temperature-controlled double cell triaxial system (Ng et al. 2016).

Test Soils and Specimen Preparation

Two fine-grained soils tested are reported in this study: recompacted silt and intact and recompacted clay. The silt tested is a yellowish-brown completely decomposed coarse ash tuff (CDT), commonly found in Hong Kong and often used as construction material. Following the Unified Soil Classification System (ASTM 2011), CDT is classified as silt (ML). Each triaxial specimen, 76 mm in diameter and 152 mm in height, was compacted in 10 layers at optimum water content of about 16.3% and dry density of about 1760 kg/m^3. The initial suction after compaction is 95 ± 2 kPa as measured by a high capacity suction probe.

The clay tested is a loess soil taken from Shaanxi Province, China. It is an aeolian sediment. According to the Unified Soil Classification System (ASTM 2011), the loess is classified as a clay of low plasticity (CL). Following the sampling procedures specified by GEO (2000), intact block loess samples were manually extracted. In the laboratory, a cutter ring with 76 mm diameter and 20 mm height was used to obtain the intact specimens. The initial void ratio was about 1.17 and the initial suction was 200 ± 20 kPa. For recompacted specimens, static compaction was adopted. Each specimen, 76 mm in diameter and 20 mm in height, was statically compacted in 2 layers. The compaction water content and void ratio were 10.9% and 1.17, respectively.

These properties were controlled to be the same as the initial state of the intact specimens for later comparison.

Test Program and Procedures

Series A: Mechanical Cyclic Shear Tests on CDT at Various Suctions and Temperatures

To investigate thermal effects on mechanical cyclic behaviour of unsaturated CDT, nine triaxial tests were carried out at three temperatures (i.e., 20, 40 and 60 °C). Three levels of soil suction (i.e., 0, 30 and 60 kPa) were considered and used at each temperature. There were four stages in each temperature- and suction-controlled cyclic triaxial test, including isotropic consolidation, suction equalisation, thermal equalisation and cyclic loading-unloading. Figure 4 shows the thermo-hydro-mechanical path of each test in the first three stages. These three stages are designed to control soil specimen to the target stress, suction and temperature, respectively. At the last stage of each test, soil specimen was subjected to cyclic shearing. Cyclic deviator stress in the haversine form was applied while net confining pressure was maintained at 30 kPa. The difference between maximum and minimum applied deviator stresses is defined as cyclic deviator stress q_{cyc}. Four levels of cyclic stress (30, 40, 55 and 70 kPa) were applied to each specimen in succession. At each level of q_{cyc}, 100 cycles were applied at a frequency of 1 Hz. More details of this series of tests were given by Ng and Zhou (2014).

Series B: Heating and Cooling Cyclic Tests on Loess

Four heating and cooling cyclic tests were carried out at different suctions and temperatures. Two of them (R0 and R100) were carried out on recompacted loess specimens but at different suctions (0 and 100 kPa). The other two (I0 and I100) were carried out on intact loess specimens at suctions of 0 and 100 kPa. Figure 5 shows the

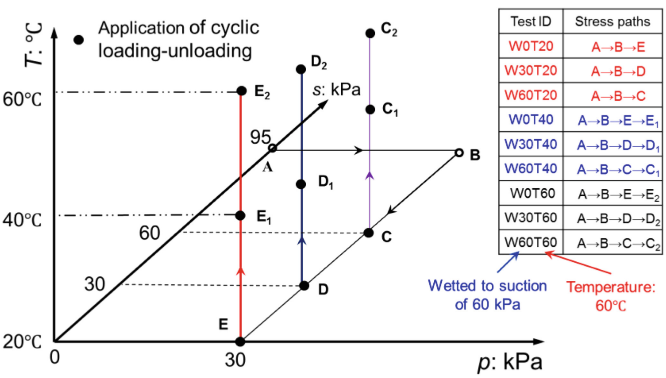

Fig. 4. Stress path of suction and temperature controlled cyclic shear tests (Series A).

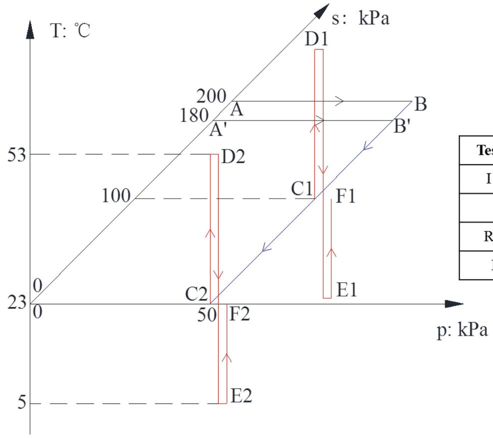

Test ID	Stress paths
I100	A→B→C1→D1→E1→F1
I0	A→B→C2→D2→E2→F2
R100	A'→B'→C1→D1→E1→F1
R0	A'→B'→C2→D2→E2→F2

Fig. 5. Stress path of cyclic heating and cooling tests (Series B).

thermo-mechanical loading paths of the loess specimens. Each test consisted of three stages: isotropic compression, wetting and thermal cycle. More details of this series of tests were given by Ng et al. (2016).

Comparisons of Measured and Computed Results

Cyclic Stress-Strain Relations at Various Suctions and Temperatures

Figure 6 compares the measured and computed cyclic stress-strain relations of recompacted CDT specimens at zero suction but at different temperatures (20 and 60 °C) (refer to tests W0T20 and W0T60 in Fig. 4). At each temperature, there was an increase in the measured accumulation of plastic strain with the number of cycles. It is evident that the measured behaviour such as the non-linearity and hysteresis of stress-strain relations during unloading and reloading cycles can be captured by the new constitutive model presented in previous section reasonably well. This is mainly because the proposed model incorporates effects of stress reversal and strain on soil behaviour. When the loading direction changes (180° reversal in the stress path), the value of $\rho_s/\bar{\rho}_s$ becomes zero and therefore the value of Kp s becomes very large (see Eq. (9)). Soil response is essentially elastic at the beginning of each loading or unloading process. During subsequent shearing with an increasing strain, the value of $\rho_s/\bar{\rho}_s$ continues to increases. Hence, the plastic modulus becomes smaller and larger plastic strain would be predicted.

As shown in the figure, the cyclic stress-strain relations follow the same trend at zero suction but at different temperatures. Furthermore, the measured accumulation of plastic strains increased with an increase in temperature. The observed thermal effects on the accumulated plastic strains can be theoretically explained by thermal softening. According to Eqs. (3), (4) and (5), the preconsolidation pressure $p_0(T,\xi)$ is smaller at a higher temperature. With a smaller preconsolidation pressure and hence a lower OCR, soil specimen behaves softer.

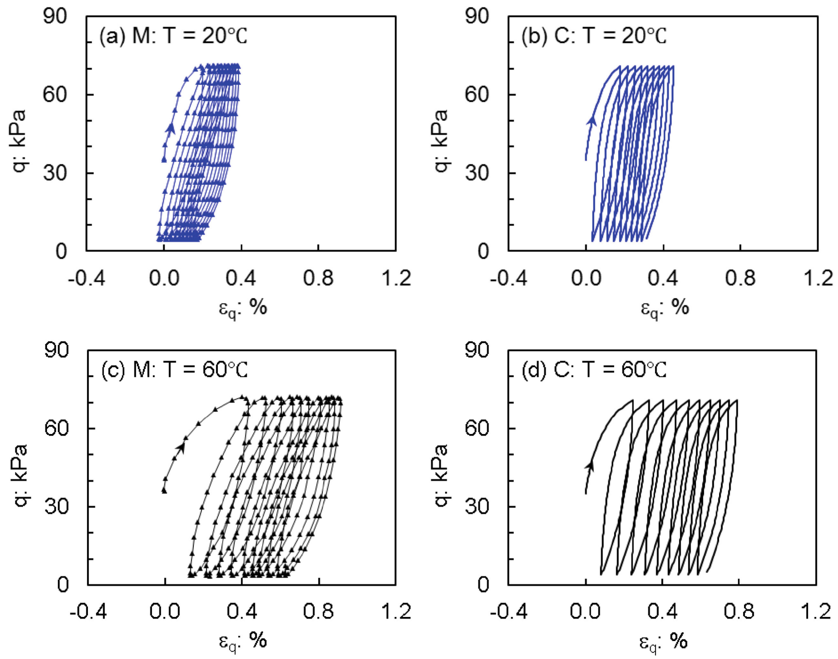

Fig. 6. Measured (M) and computed (C) cyclic stress-strain relations at different temperatures and at zero suction of CDT.

Effects of Number of Mechanical Load Cycles on Plastic Strain Accumulation at Various Suctions and Temperatures

Figure 7 shows the influence of suction and temperature on the relationship between $\varepsilon_{ap(100)}/\varepsilon_{ap(1)}$ and q_{cyc}, where $\varepsilon_{ap(1)}$ and $\varepsilon_{ap(100)}$ are plastic strains induced by the first cycle and 100 cycles, respectively. At three different suctions (0, 30 and 60 kPa) and at 20 °C (i.e., tests W0T20, W30T20 and W60T20), all three measured relationships between $\varepsilon_{ap(100)}/\varepsilon_{ap(1)}$ and q_{cyc} were similar, when applied q_{cyc} was between 30 and 40 kPa. When q_{cyc} was increased from 40 kPa to 70 kPa, however, the ratio of $\varepsilon_{ap(100)}/\varepsilon_{ap(1)}$ increased significantly by about 40% at zero suction. On the contrary, the ratios of $\varepsilon_{ap(100)}/\varepsilon_{ap(1)}$ appeared to be independent of q_{cyc} at suctions of 30 and 60 kPa. These observations can be explained by the existence of threshold q_{cyc} values at various suctions. As observed by Zhou and Ng (2016b), the threshold q_{cyc} at zero suction is below 70 kPa. With a significant increase in preconsolidation pressure with increasing suction (illustrated by the LC curve in Fig. 2 conceptually), the threshold q_{cyc} is larger than 70 kPa at suctions of 30 and 60 kPa (Zhou and Ng 2016b). Consequently, at q_{cyc} of 30 and 40 kPa, which are lower than threshold q_{cyc} at all $u_a - u_w$, the ratio $\varepsilon_{ap(100)}/\varepsilon_{ap(1)}$ is almost independent of $u_a - u_w$. At q_{cyc} of 70 kPa, which is higher than the threshold stress at zero suction but lower than the threshold stress at $u_a - u_w$ of 30 and 60 kPa, $\varepsilon_{ap(100)}/\varepsilon_{ap(1)}$ decreases with an increase in $u_a - u_w$. The existence of a threshold q_{cyc} should be considered in the geotechnical designs. To minimize plastic

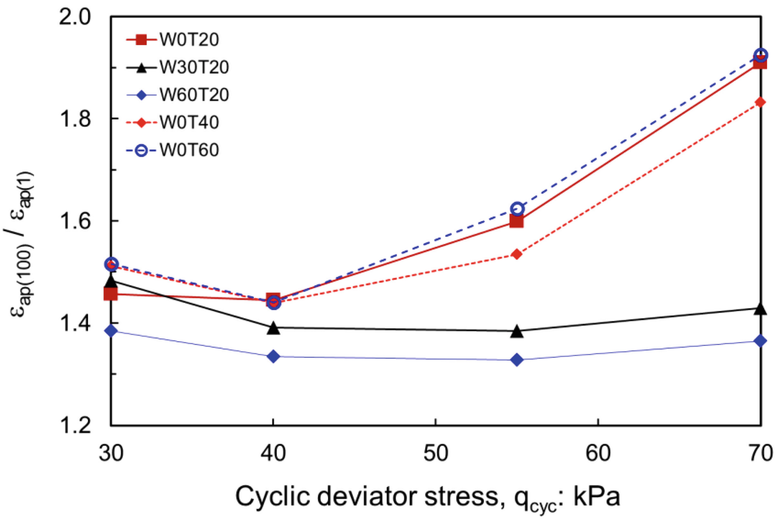

Fig. 7. Influence of number of cycles on plastic strain accumulation at different suctions and temperatures of CDT.

strain accumulation of soils and to improve long-term performance of earth structures, the design cyclic loads should be kept lower than the threshold value.

It can be also seen from Fig. 7 the measured ratio of $\varepsilon_{ap(100)}/\varepsilon_{ap(1)}$ decreased slightly from when q_{cyc} was increased from 30 to 40 kPa, at zero suction and at three different temperatures (i.e., tests W0T20, W0T40 and W0T60). Beyond 40 kPa, the ratio increased with an increase in $q_{cyc.}$ It is evident that the relationship between $\varepsilon_{ap(100)}/\varepsilon_{ap(1)}$ and q_{cyc} is almost independent of temperature. Temperature-induced differences in $\varepsilon_{ap(100)}/\varepsilon_{ap(1)}$ are all less than 10% at the three temperatures. The negligible difference in $\varepsilon_{ap(100)}/\varepsilon_{ap(1)}$ at various temperatures is likely because in the temperature range of 20 to 60 °C, thermal effects on the threshold q_{cyc} is very minor (Zhou and Ng 2016b).

Influence of Temperature on Plastic Strain Accumulation

Figure 8 shows the effects of temperature on $\varepsilon_{ap(100)}$ at two different suctions (0, and 60 kPa) of CDT. It is clear that the influence of temperature on $\varepsilon_{ap(100)}$ are qualitatively similar at different suctions. At a given suction, $\varepsilon_{ap(100)}$ increases consistently with an increase in temperature at q_{cyc} of 30, 40, 55 and 70 kPa. The measured $\varepsilon_{ap(100)}$ at 60 °C is about two times of that at 20 °C. For the recompacted CDT specimens, the preconsolidation pressure is beyond 100 kPa, which is much larger than the net confining stress of 30 kPa. It is therefore that soil stress state was inside bounding surface during the heating process. According to the thermo-mechanical model illustrated in Fig. 2,

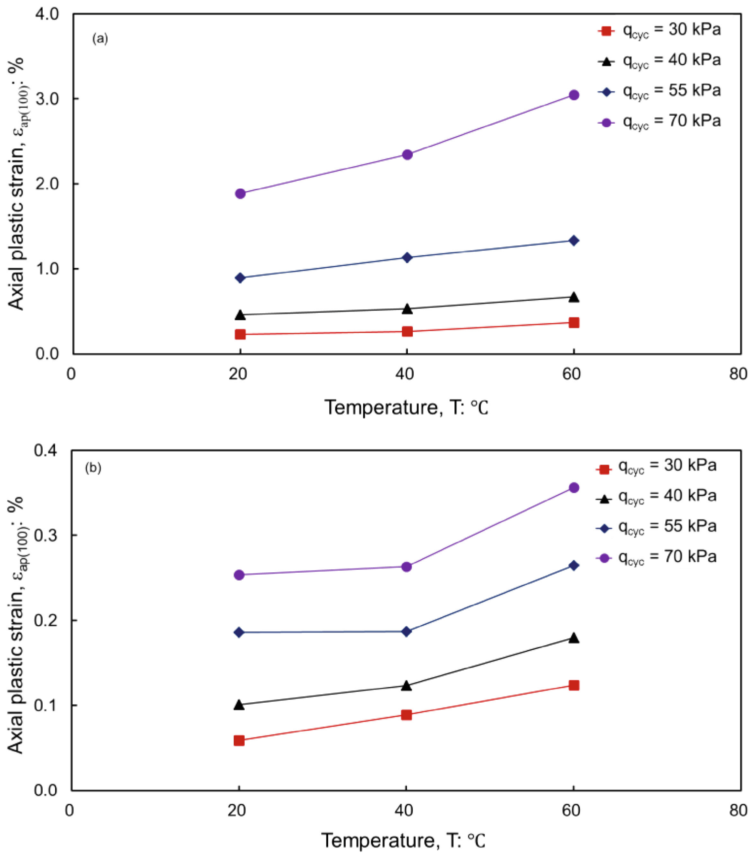

Fig. 8. Thermal effects on plastic strain accumulation of CDT at (a) s = 0 kPa and (b) s = 60 kPa.

the preconsolidation pressure should decrease with an increase in temperature. For example, as temperature increases from 20 to 40 °C, the OCR decreases by about 10% and the axial plastic strain increases by about 30%. Given a smaller overconsolidation ratio, it is expected that a larger axial plastic strain should be induced in the heated specimen during the subsequent stage of cyclic loading-unloading.

As far as the authors are aware, the current geotechnical design guides (for instance, design methods for railway embankments and pavements) generally do not consider thermal effects on soil behaviour since soil specimen is only required to be tested at room temperature (AASHTO 2008). When the in-situ temperature is significantly higher than room temperature, ignoring thermal effects may underestimate the irreversible ground settlement induced by cyclic loads significantly.

Influence of Suction on Plastic Strain Accumulation of CDT

It is clearly revealed in Fig. 8 that at a given temperature and q_{cyc}, $\varepsilon_{ap(100)}$ decreases significantly with increasing suction. For example, at q_{cyc} of 70 kPa and 20 °C, $\varepsilon_{ap(100)}$ decreases from about 2% to 0.25% as $u_a - u_w$ increases from 0 to 60 kPa. The percentage of reduction is up to about 90%. The decrease in $\varepsilon_{ap(100)}$ with an increase in suction is mainly because as suction increases, the preconsolidation pressure of soil specimen increases, as illustrated in Fig. 2. Given a larger preconsolidation pressure and hence a higher OCR, soil specimen behaves stiffer, as described by Eq. (9).

Some current geotechnical design guides have considered effects of soil moisture on soil behaviour using empirical methods. For example, AASHTO (2008) for pavement design suggests that soil specimen is prepared and tested at a reference moisture condition. Variations in soil behaviour with soil moisture are then estimated using some empirical models. Since the relationship between axial plastic strain and suction depends on temperature, as illustrated in Fig. 8, regression parameters in these empirical models should be a function of temperature.

Volume Change Behaviour of Loess During Thermal Cycles

Figure 9 shows the observed volumetric behaviour of recompacted and intact loess specimens during heating and cooling cycles at two different suctions, i.e., 0 and 100 kPa, obtained from tests in Series B. During the heating process, the measured contractive volumetric strain increased with increasing temperature and at an increasing rate. The observed heating-induced soil contraction can be explained using the proposed bounding surface model. According to Eqs. (3) through (5), the pre-consolidation pressure decreases as temperature increases. During the heating process, soil state approaches F_c surface, resulting in plastic contraction.

When temperature decreases from 53 to 13 °C, the measured contractive volumetric strain of intact and recompacted specimens increased, but at a much slower rate of around 2×10^{-3}%/°C (close to thermal expansion coefficient of clay (about 2.9×10^{-3}%/°C)). This process may be considered as that the soil state is within the bounding surface, meaning that it is an essentially elastic deformation due to thermal contraction of soil particles. When temperature keeps decreasing, from 13 to 5 °C, a plastic contractive volumetric strain at a larger rate of 2.5×10^{-2}%/°C can be observed, suggesting that plastic strain is induced by cooling to 5 °C, which is close to the critical temperature (i.e., 4 °C) of water at which water should have the largest density. This may imply that a volume reduction of water would be expected for a given mass of water, leading to an extra plastic deformation of water and re-arrangement of soil structure.

It should be pointed out that cooling-induced plastic strain is different from previous studies on saturated soils. As discussed in the introduction, Campanella and Mitchell (1968) and Di Donna and Laloui (2015) measured volume changes of saturated remolded illite and natural silty clay during cooling from 60 to 5 °C. For both soils, only elastic contraction and slight expansion were observed during cooling. The discrepancy between the current study and the two previous studies may be because the

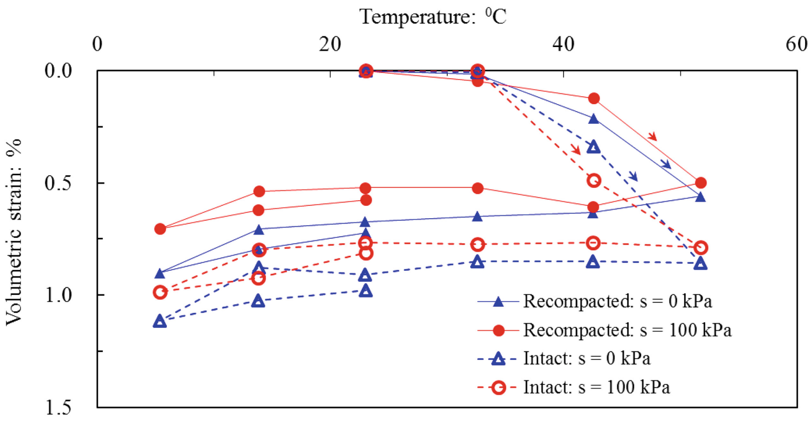

Fig. 9. Measured volume changes of intact and recompacted loess under thermal loads.

void ratio of loess specimen (at both intact and recompacted states) is about 20% and 60% larger than those of the remolded illite and natural silty clay specimens, respectively. Given a much larger void ratio, some large voids of loess are unstable (Sun et al. 2007) and can be destroyed by cooling-induced particle contraction. Consequently, cooling may induce particle re-arrangement and plastic contraction in the loess specimen.

The observed plastic contraction of intact and recompacted specimens during cooling from 15 °C to 5 °C cannot be predicted by any existing elasto-plastic theory, which generally predicts elastic contraction during cooling. A new 'temperature decrease, TD' bounding surface may be introduced in existing elastoplastic thermo-mechanical models to simulate the observed elasto-plastic behaviour during cooling, as shown in Fig. 10. When temperature is high than the critical value (1 → 2)

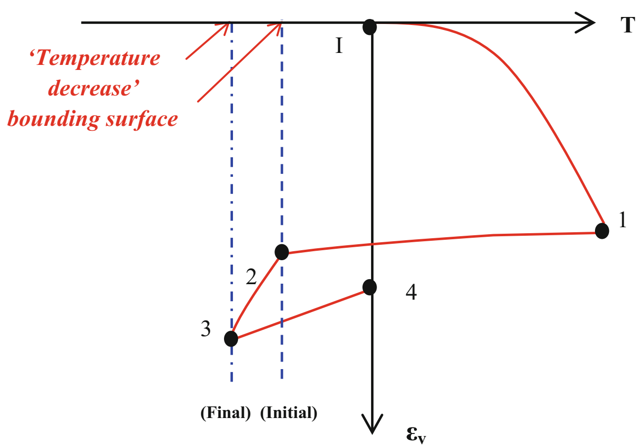

Fig. 10. Proposed temperature decrease (TD) bounding surface.

corresponding to the TD bounding surface, soil response may be assumed to be elastic. When soil state reaches the TD bounding surface, soil response under continuous cooling is regarded as elastoplastic (2 → 3).

Summary and Conclusions

Based on measured and computed results, key conclusions are summarized as follows:

(1) During cyclic mechanical shearing, measured plastic deformation of completely decomposed silt (CDT) increases continuously with an increase in q_{cyc} at a given suction and temperature. The rate of increase is almost constant at q_{cyc} lower than a threshold value, but increases significantly at q_{cyc} higher than the threshold value. The existence of a threshold q_{cyc} implies that the applied cyclic loads should be lower than this threshold value in order to minimize plastic strain accumulation of soils and to improve long-term performance of earth structures.

(2) Measured plastic deformation of unsaturated CDT increases significantly with decreasing suction and increasing temperature. The observed effects of suction and temperature can be explained by the fact that preconsolidation pressure of the unsaturated soil increases with increasing suction (suction hardening), but decreases with increasing temperature (thermal softening). Since the current geotechnical designs of railway embankments and subgrade soils of pavement generally use soil parameters determined at room temperature only, soil deformation induced by cyclic mechanical loads may be significantly underestimated.

(3) As temperature increases from 23 to 53 °C incrementally, contractive volumetric strain of both intact and recompacted loess specimens increases. During the cooling process from 53 to 13 °C, contractive volumetric strain (essentially elastic) keeps increasing at a much reduced rate. When temperature further decreases from 13 to 5 °C, a plastic volume contraction at a much higher rate is observed. To simulate the observed plastic response during cooling, a new 'temperature decrease, TD' bounding surface may be introduced in existing models.

Acknowledgements. The authors would like to acknowledge the contributions from research grant 51509041 provided by the National Science Foundation of China and also the grants 16209415, 16216116, 617213 and HKUST6/CRF/12R supported by the Research Grants Council (RGC) of the HKSAR.

References

AASHTO (2008) Mechanical empirical pavement design guide: a manual of practice. American Association of State Highway and State Highway Officials, Washington, DC

Alonso EE, Gens A, Josa A (1990) Constitutive model for partially saturated soils. Géotechnique 40(3):405–430

ASTM (2011) Standard practice for classification of soils for engineering purposes (unified soil classification system). American Society of Testing and Materials, West Conshohocken

Been K, Jefferies MG (1985) A state parameter for sands. Géotechnique 35(2):99–112

Campanella RG, Mitchell JK (1968) Influence of temperature variations on soil behavior. J Soil Mech Found Div 94(3):709–734
Chiu CF, Ng CWW (2003) A state-dependent elasto-plastic model for saturated and unsaturated soils. Géotechnique 53(9):809–830
Dafalias YF (1986) Bounding surface plasticity. I: mathematical foundation and hypoplasticity. J Eng Mech 112(9):966–987
Di Donna A, Laloui L (2015) Response of soil subjected to thermal cyclic loading: experimental and constitutive study. Eng Geol 190:65–76
Gallipoli D, Gens A, Sharma R, Vaunat J (2003) An elasto-plastic model for unsaturated soil incorporating the effects of suction and degree of saturation on mechanical behaviour. Géotechnique 53(1):123–135
GEO (2000) Geoguide 2: guide to site investigation. Geotechnical Engineering Office of Hong Kong government
Hong PY, Pereira JM, Tang AM, Cui YJ (2013) On some advanced thermo-mechanical models for saturated clays. Int J Numer Anal Meth Geomech 37(17):2952–2971
Ng CWW, Cheng Q, Zhou C, Alonso EE (2016) Volume changes of an unsaturated clay during heating and cooling. Géotechnique Lett 6(3):192–198
Ng CWW, Menzies B (2007) Advanced unsaturated soil mechanics and engineering. Taylor & Francis, London
Ng CWW, Zhou C (2014) Cyclic behaviour of an unsaturated silt at various suctions and temperatures. Géotechnique 64(9):709–720
Sun DA, Sheng DC, Xu Y (2007) Collapse behaviour of unsaturated compacted soil with different initial densities. Can Geotechnical J 44(6):673–686
Zhou C, Ng CWW (2016a) Simulating the cyclic behaviour of unsaturated soil at various temperatures using a bounding surface model. Géotechnique 66(4):344–350
Zhou C, Ng CWW (2016b) Effects of temperature and suction on plastic deformation of unsaturated silt under cyclic loads. J Mater Civil Eng 28(12):04016170. ASCE

Shale Capillarity, Osmotic Suction and Permeability, and Solutions to Practical Testing Issues

Russell T. Ewy(✉)

Chevron Energy Technology Co., San Ramon, USA
RussEwy@chevron.com

Abstract. For typical shales (void ratio 0.15 to 0.42), modal pore throat sizes range from a few nm to a few tens of nm. Unstressed shales, even when fully saturated, have negative pore water pressure (capillary tension). However, the total suction is often greater than this, especially for highly-compacted shales with extremely small pore size. The additional suction is due to effects associated with clay surfaces. Osmotic pressures can be directly measured, and they can easily be several MPa, a combination of solute suction and clay-related effects. The small pore sizes in shales also result in extremely low values of permeability and of consolidation coefficient. All these characteristics directly impact testing protocols. The first step in any test should be to apply sufficient confining stress to raise the pore pressure up to a positive, measured value. Undrained consolidation, combined with undrained triaxial compression and with small sample sizes (and drainage screens when necessary), results in acceptable test durations. A range of effective consolidation stress values is attained by first equilibrating shale samples in varying amounts of suction, to vary the water content. Non-aqueous fluids are required when sampling, to avoid swelling, and are often necessary for pore lines if osmotic pressures are to be avoided.

Capillary Suction (Pore Water Tension) and Total Suction

The pore sizes in shales and claystones are extremely small, leading to strong capillary effects. While the clay interlayer space is too small to be accessed even by high-pressure mercury, the pore structure that exists external to the clay grains is mostly accessible, and this represents the majority of the total pore space in a typical shale. Figure 1 shows wetting-phase saturation vs. capillary pressure for five example shales. These are predicted air-brine capillary pressure curves generated by transforming measurements of mercury saturation vs. mercury pressure. These five shales have the following natural void ratio values: A 0.42, B 0.40, F 0.27, G 0.225, H 0.15. Complete descriptions of these shales can be found in Ewy (2014). Ewy (2015) contains additional information, including normalized pore size distribution curves. The modal pore throat sizes span about one order of magnitude, from $\sim$3 nm to $\sim$30 nm equivalent radius, and are smaller for lower void ratio. Thus, in-situ compaction due to burial results in both smaller pore size and lower porosity.

A. Ferrari and L. Laloui (eds.), *Advances in Laboratory Testing and Modelling of Soils and Shales (ATMSS)*, Springer Series in Geomechanics and Geoengineering,
DOI 10.1007/978-3-319-52773-4_3

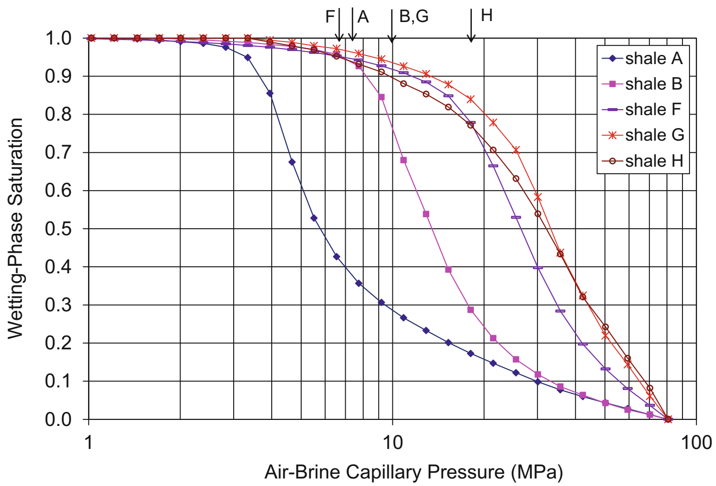

Fig. 1. Saturation vs. capillary pressure, converted from mercury injection data. Arrows show separately predicted capillary pressure (pore water tension) due to core retrieval.

Added to the figure with arrows are values of expected pore water tension (capillary suction), for the unstressed shales, estimated using Eq. 1 (Ewy 2014):

$$p_w = (1 - B)\sigma_m - \sigma'_m \tag{1}$$

where p_w = pore water pressure after unloading due to core retrieval (suction is negative), B = Skempton's B parameter, σ_m = in situ mean total stress and σ'_m = in situ mean effective stress.

Figure 2 shows the actual measured water retention behavior (water saturation vs. total suction) obtained through laboratory measurements. Each data point is a separate sample, which results in some scatter. Values of total suction were applied using vacuum desiccators containing saturated salt solutions (Ewy 2014). Added to the figure with arrows are the values of 'native-state' total suction for each shale. Native-state suction is the value measured on a completely preserved sample which has neither gained nor lost any water compared to its in-situ condition, but which is now at zero total stress.

While the arrows in Fig. 1 are estimated (not measured) values of capillary suction, the arrows in Fig. 2 are measured values of total suction. Shales A and B have native-state total suction smaller (closer to zero) than the estimated capillary suction. Total suction is expected to be equal to or greater than capillary suction; probably the two are actually close and the estimated capillary suction is in error. It is reasonable that in high-porosity shales such as these, total suction is dominated by capillary suction because much of the pore water is 'free' water as opposed to near-clay water. These two shales, and a similar shale (Shale C in Ewy 2014) all have native-state total suction less than 6 MPa, void ratio from 0.37 to 0.42, and modal pore size greater than 10 nm. For Shale C the estimated capillary suction is equal to the measured native-state suction (Ewy 2014).

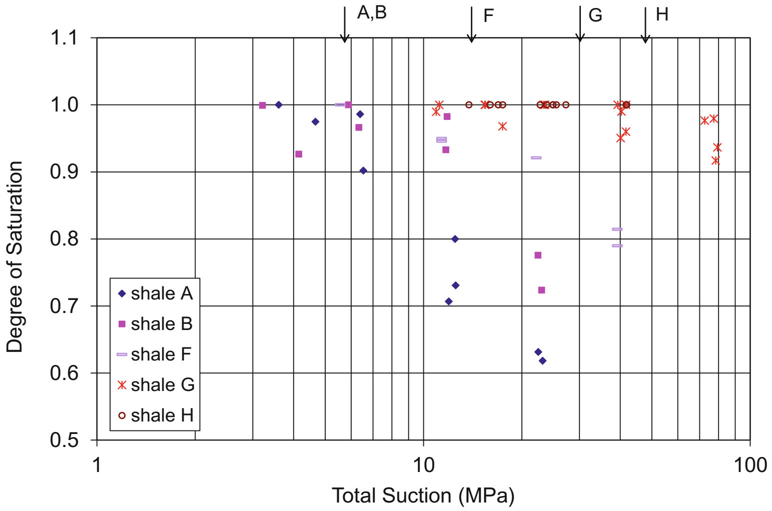

Fig. 2. Measured saturation vs. total suction (each data point is a separate sample). Arrows show measured values of native-state (fully-preserved) total suction for each shale.

For the more highly-compacted shales (F, G & H), which have lower void ratio and smaller modal pore size, the measured native-state total suction is significantly greater than the estimated capillary suction. In these shales a more significant portion of the water is near-clay water and is directly affected by the clay surfaces; thus, total suction is not dominated by capillary suction (pore water tension), as it includes these additional effects.

The actual measured saturation values for native-state (Fig. 2) are .98–1.0 for H, .95–1.0 for A, B & G, and .94–.95 for F. All five shales are at or close to full saturation, even though the pore water has gone into tension due to unloading and, in some cases, is quite highly negative. Using the estimated capillary suction values (arrows, Fig. 1) and the air-brine saturation curves from MICP (Fig. 1), the predicted values of saturation are generally lower than measured (Fig. 2). For shales A, B & H the predicted values are significantly lower than actually measured on the samples, for shale G it is slightly low, while for F it is quite similar.

As a general rule, shales retain water more strongly than predicted by air-brine capillary pressure curves obtained from MICP. They can remain highly-saturated even at high values of capillary suction (and total suction); this effect is most prominent for lower-porosity shales which have modal pore size smaller than 10 nm. Such shales also have total suction values significantly greater than capillary suction. While the curves in Fig. 1 have not been corrected for small pores uninvaded by mercury, nor for sample shrinkage that occurs due to vacuum drying prior to MICP, such corrections are not expected to alter the overall conclusions.

Osmotic Suction

Total suction in shales is comprised of several components: capillary suction, solute suction, clay-related osmotic suction and clay-related electrostatic. For shales containing only their native pore water, solute suction is at most a few MPa. However, total osmotic suction can be significant (clay-related electrostatic mechanisms, and solute suction, likely appear combined with clay-related osmotic mechanisms in the lab). Osmotic pressure can be directly measured in the lab by placing a brine of known water activity against one end of a sample (of known pore water activity) and measuring the pore pressure within the sample (Ewy and Stankovic 2010). As long as all pore water tension has been removed prior to brine exposure, the difference between the two pressures is the osmotic pressure.

Figure 3 shows measured values of osmotic pressure on an example shale (Shale D from Ewy 2014, similar to Shale F). A positive pressure value means the shale pore pressure was less than the applied brine pressure. Freshwater (activity = 1.0) resulted in a shale pore pressure greater than the applied water pressure (a negative osmotic pressure), because the shale was osmotically 'pulling' additional water into the shale. For strong brines (water activity 0.9 and lower) the opposite effect occurred.

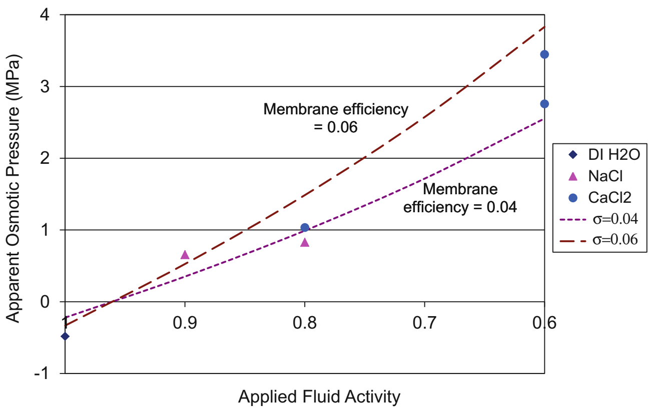

Fig. 3. Measured osmotic pressure using deionized water and various brines, Shale D (similar to Shale F). Certain other shales show higher membrane efficiency.

The curves in the figure are computed using Eq. 2 (Ewy 2015):

$$\Delta P = \sigma (RT/V) \ln \left(a_{ws}/a_{wf} \right) \tag{2}$$

where ΔP is the osmotic pressure, σ is the membrane efficiency, R is the gas constant, T is absolute temperature, V is the partial molar volume of water, a_{ws} is the water activity of the shale, and a_{wf} is the water activity of the fluid in contact with the shale. The shale activity is set to 0.96, as the samples were equilibrated to this value (which is lower suction than native-state) in order to reduce the pore water tension. The samples were also put under stress prior to fluid exposure in order to ensure complete saturation and near-zero pore water tension.

Although the exact value of sample pore water activity with the sample under stress is not certain, the main finding is that, for this shale, membrane efficiency is only on the order of 5%. Osmotic pressures occur, but are generally low unless the fluid activity is significantly different than the pore water activity.

However, more highly compacted (lower porosity) shales have higher membrane efficiencies and higher values of osmotic pressure. For example, on Shale I (low porosity, similar to shale H) equilibrated to 0.92 activity and then put under stress, we measured osmotic pressures of 5 to 14 MPa with fluids of 0.8 activity, corresponding to membrane efficiencies of 25% to 70%. Using freshwater on several different shales of medium porosity to low porosity (0.22 down to .11 void ratio) we measured osmotic pressures of −2.5 to −5.5 MPa, indicating significant osmotic forces pulling water into the shales.

Osmotic pressure effects can only be eliminated if the water activity of the fluid in contact with the shale is equal to the activity of the pore water within the shale. The pore water activity is, generally, reflected by the total suction measured on the shale. However, total suction goes down (becomes smaller) when shales are put under stress, because the capillary suction (pore water tension) is reduced.

Significant sample swelling can occur even when the fluid activity matches the pore water total activity, if the samples are not under stress (Ewy 2014). For most shales, ~4 MPa stress is sufficient to limit swelling to less than 1% (Ewy 2015).

Permeability and Pressure Diffusivity

Shales have quite low values of permeability, and of pressure diffusivity (consolidation coefficient, c_v), mainly governed by the pore size. Table 1 lists values of these two parameters for some example shales. Pressure diffusivity was measured using a liquid pressure-pulse technique with one boundary being an absolute no-flow boundary (zero volume), as described in Ewy and Stankovic (2000). It is seen that going from a void ratio of 0.40 down to 0.15 results in two orders of magnitude decrease in permeability and pressure diffusivity. It is not so much the change in void ratio that causes this, but the change in pore throat size.

Table 1. Coefficient of consolidation, and permeability, for some example shales. Shales D and E are roughly similar to Shale F – see Ewy (2014).

Shale	B	D	E	G	H
void ratio	0.40	0.29	0.28	0.22	0.15
c_v (mm^2/hr)	65	26	6.5	4.5	0.6
k (10^{-21} m^2)	5–10	~2	~0.5	~0.3	~0.03

Consolidation Stage and Triaxial Loading Stage

Because unstressed shales, even if fully saturated, have negative pore water pressure, the first step in any test should be to apply sufficient stress to negate this tension and bring the pore pressure up to a positive and measurable value. If this is not done, then it is not known what the pore pressure is inside the shale. It will be some negative value, but an unknown value. If a test starts in this state, any load put on the shale might change the pore pressure, but by an unknown amount.

The procedure we have adopted (Steiger and Leung 1991) is to perform undrained hydrostatic consolidation as the first step for triaxial compression. This is followed by undrained triaxial compression. An example for Shale G is shown in Fig. 4. In this example, the first confining stress level was sufficient to bring the pore pressure up to a positive, but too low, value. The confining stress was raised in order to confirm positive pore pressure and full saturation (note this also provides a measurement of Skempton's B parameter). This was then followed by undrained triaxial compression at an axial strain rate of 5E−08/sec, with the sample fitted with side drains.

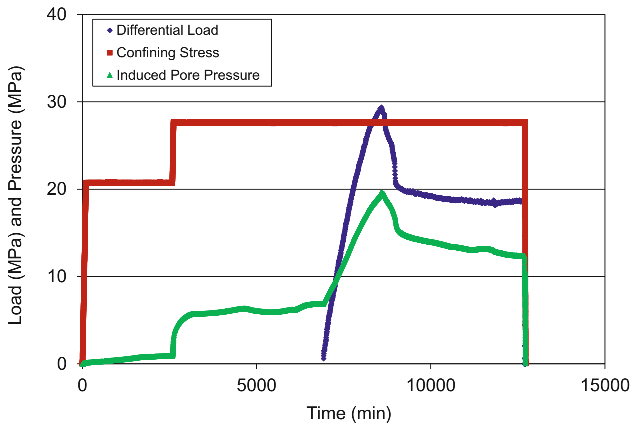

Fig. 4. Example sequence for undrained consolidation followed by undrained triaxial.

The allowable strain rate is computed using equations in Head (1998), based on the consolidation coefficient, the sample size, drainage conditions, and estimated strain at failure. For this shale the allowable strain rate for undrained triaxial compression is ∼2E−08/sec without side drainage and ∼4E−07/sec with side drainage. Since our screen strips are vertical and contact the circumference only on two opposite sides, the strain rate was set to 5E−08 rather than 4E−07.

To keep strain rates manageable we use small samples (D = 19 mm, L = 38 mm). Even so, drained triaxial compression is usually not feasible. For this shale the allowable strain rate for drained triaxial compression is between 1E−09/sec and 4E−08/sec, depending on drainage conditions. For higher permeability shales, drained triaxial compression is sometimes feasible. Undrained consolidation followed by undrained triaxial compression always leads to the shortest overall test time. The test in Fig. 4 was completed in less than 9 days, and some tests can be completed even more quickly, especially for shales of higher permeability.

If the pore pressure attained during undrained consolidation is greater than desired, excess pressure can be drained out of the sample. An example is shown in Fig. 5, for Shale E. This was a drainage phase inserted into the consolidation stage. Even though the time needed for this is controlled by pressure diffusion, it does still add significant time to a test due to pore volume storage. This drainage took more than 10 days, and the entire test with triaxial ended up taking 27 days.

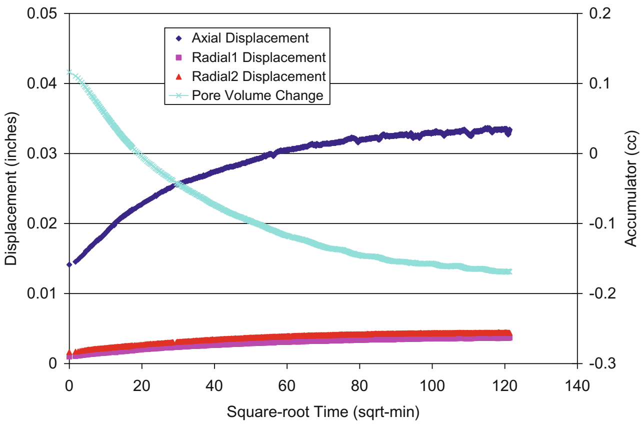

Fig. 5. Example drained consolidation phase, with measured strains and expelled fluid.

An easier method for attaining higher effective confining stress (lower pore pressure) during consolidation is to equilibrate the sample at higher suction prior to testing. Generally, samples are placed in vacuum desiccators of four to five different suction values, to prepare them for testing. Sample water content is a direct function of the imposed total suction. The samples with higher water content (lower suction) will generate more pore pressure and settle at a low effective confining stress during consolidation, while samples with lower water content will generate less pore pressure and settle at higher effective confining stress.

In the event that pore pressure does need to be adjusted during the consolidation stage, draining fluid (reducing pressure) is usually less problem-prone than pushing fluid into the sample (raising pressure). If a sample does not generate positive pore pressure, the best course of action is to keep increasing the confining stress until positive pore pressure is attained, or remove the sample. Attempting to saturate the pore space by pushing in brine or water can add many weeks to a test. The reason is that the time is no longer controlled by the pressure diffusivity but is now controlled by permeability. If there is any air in the pore space, the sample can reach saturation only by physically moving fluid from the ends of the sample to the interior of the sample. This takes place orders of magnitude more slowly than movement of a pressure wave.

Other Testing and Sample Handling Considerations

Ewy (2015) provides several recommendations on core preservation, sample handling and testing. Some key points are summarized here:

Inert or non-aqueous fluids (e.g. oil) in the pore lines have the advantage that they will not create osmotic pressures; they have the disadvantage that pore fluid can only be squeezed out of the sample and not pushed into the sample, and that certain conditions could result in capillary pressure altering the measured pore pressure. Use of brine in the pore lines ensures no capillary pressure and allows fluid movement in both directions; the disadvantage is that the measured pore pressure could be different than the sample internal pore pressure due to osmotic pressure.

Samples should be cut with hydrocarbon and stored in sealed containers of hydrocarbon, or in small airtight containers, or in vacuum desiccators of controlled suction. The latter allows evaporation of hydrocarbon residue from the samples, which is advisable. Samples stored in brine will swell, even if the brine activity matches the shale pore water activity. Use of air as a cutting fluid will dry out shales unless it is humidified; however, this may be the best option for shales of low saturation, to avoid hydrocarbon penetration into the pore space. Shales that have lost too much moisture should not be used for testing; neither should shales that have been contacted by brine or water when not under stress. Shale core material should always be kept completely sealed, and air exposure must be minimized, to avoid moisture loss and reduction of water content.

References

Ewy RT, Stankovich RJ (2000) Pore pressure change due to shale-fluid interactions: Measurements under simulated wellbore conditions. In: Pacific Rocks 2000, 4th North American rock mechanical symposium, Seattle, USA, 31 July–3 August. Balkema, Rotterdam, pp 147–154

Ewy RT, Stankovic RJ (2010) Shale swelling, osmosis, and acoustic changes measured under simulated downhole conditions. SPE Drilling & Completion, SPE 78160, pp 177–186, June

Ewy RT (2014) Shale swelling/shrinkage and water content change due to imposed suction and due to direct brine contact. Acta Geotech 9:869–886

Ewy RT (2015) Shale/claystone response to air and liquid exposure, and implications for handling, sampling and testing. Int J Rock Mech Min Sci 80:388–401

Head KH (1998) Manual of soil laboratory testing: Effective stress tests, vol 3. Wiley, Chichester

Steiger RP, Leung PK (1991) Consolidated undrained triaxial test procedure for shales. In: Proceedings of 32nd U.S. rock mechanical symposium, Norman, OK, USA, pp 637–646. Balkema, Rotterdam

Modelling the Mechanical Behaviour of Callovo-Oxfordian Argillite. Formulation and Application

A. Gens(✉), M. Mánica, J. Vaunat, and D.F. Ruiz

Division of Geotechnical Engineering and Geosciences,
Department of Civil and Environmental Engineering,
Universitat Politècnica de Catalunya, Barcelona Tech, Barcelona, Spain
Antonio.gens@upc.edu

Abstract. The paper presents a constitutive model for argillaceous rocks, developed within the framework of elastoplasticity, that includes a number of features that are relevant for a satisfactory description of their hydromechanical behaviour: anisotropy of strength and stiffness, nonlinear behaviour and occurrence of plastic strains prior to peak strength, significant softening after peak, time-dependent creep deformations and permeability increase due to damage. Both saturated and unsaturated conditions are envisaged. The constitutive model is then applied to the simulation of triaxial and creep tests on Callovo-Oxfordian (COx) claystone and to the analysis of the excavation of a drift in the Meuse/Haute-Marne Underground Research Laboratory. The pattern of observed pore water pressures and convergences during excavation are generally satisfactorily reproduced. The effect of incorporating creep is also demonstrated.

Introduction

Argillaceous soils and rocks are very widespread in nature; it has been estimated that they constitute as much as half of the global sedimentary rock mass and that they outcrop in about one third of the emerged earth surface. In consequence, they are frequently encountered in many civil engineering works. A good constitutive description of their hydromechanical behaviour is therefore required in order to predict their behaviour in a consistent and rational manner. In addition, argillaceous rocks are now of special interest in areas of energy geotechnics and environmental engineering. For instance, in petroleum engineering, argillaceous rocks not only play the customary role of caprock in an oil/gas reservoir but they are now also the source medium of hydrocarbons extracted by unconventional means often involving hydraulic fracture. Also, they are one of the preferred geological settings for the disposal of high-level radioactive waste because of their low permeability, significant retardation properties for radionuclide migration, lack of economic value (with the exception of gas or oil shales) and their significant capacity for hydraulic self-sealing of fractures. The work presented in this paper has been in fact developed in the context of studies for nuclear waste disposal.

A. Ferrari and L. Laloui (eds.), *Advances in Laboratory Testing and Modelling of Soils and Shales (ATMSS)*, Springer Series in Geomechanics and Geoengineering,
DOI 10.1007/978-3-319-52773-4_4

The behaviour of this type of rock can be, given the diversity of geological histories, quite variable but there are quite a few common features that can be identified: anisotropy, some degree of softening, time-dependent behaviour and variation of permeability with damage (Gens 2013, Jardine et al. 2015). To focus the work, however, the study has been developed in the context of the activities being carried out in the Meuse/Haute-Marne (MHM) Underground Research Laboratory (URL), located in Eastern France, near the town of Bure, constructed and operated by the French national radioactive waste management agency (ANDRA). The host rock of the laboratory is Callovo-Oxfordian clay.

The paper presents a constitutive model that attempts to incorporate a number of features of behaviour of argillaceous rocks including strength and stiffness anisotropy, nonlinear isotropic hardening to account for plastic deformations prior peak strength, softening behaviour after peak, a non-associated flow rule, time-dependent deformations and dependency of permeability on irreversible strains. The constitutive model is then checked against laboratory tests performed on Callovo-Oxfordian clay. Afterwards, in order to demonstrate the performance of the model developed, a coupled hydromechanical analysis of a drift excavation in the MHM laboratory is described.

Formulation of the Constitutive Model

The description of the mechanical model is divided in two parts: (i) instantaneous response and (ii) time-dependent response. The instantaneous response corresponds to the strains that occur immediately in response to changes in effective stress whereas the time-dependent response relates to the strains that develop in time under constant effective stresses. The effective stresses are defined as:

$$\boldsymbol{\sigma}' = \boldsymbol{\sigma} + S_e s\, B\, \mathbf{I}$$

where $\boldsymbol{\sigma}'$ is the effective stress tensor, $\boldsymbol{\sigma}$ is the total stress tensor, S_e is the equivalent degree of saturation, s is either suction or pore water pressure (with a negative sign), B is Biot's coefficient and $\mathbf{I}$ is the identity tensor. It should be noted that this definition incorporates the possibility of taking into account unsaturated states. It is also important to note that the term instantaneous response does not preclude the occurrence of deformations developing in time that are associated with effective stress changes caused by the progressive dissipation of excess pore water pressures.

Instantaneous Response

The instantaneous response is formulated within the framework of classical elasto-plasticity. The following Mohr-Coulomb expression is adopted to define both yield and failure surfaces:

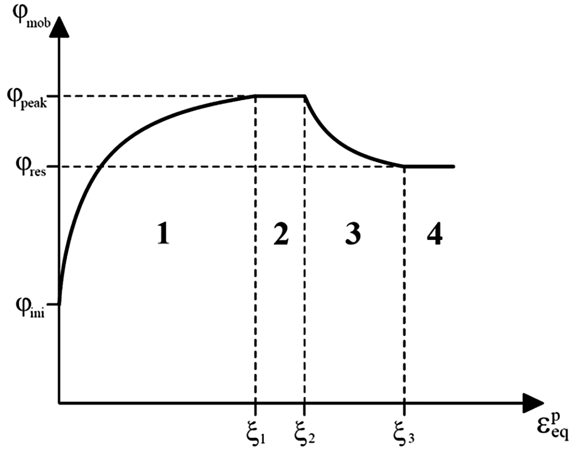

Fig. 1. Evolution of friction angle in hardening and softening.

$$f = \left(\cos\theta + \frac{1}{\sqrt{3}}\sin\theta\sin\varphi\right)J - \sin\varphi(c\cot\varphi + p') = 0$$

where p' is the mean effective stress, J is the second invariant of the deviatoric stress tensor, θ is Lode's angle, c is the cohesion and φ is the friction angle. Corners have been smoothed using Sloan and Booker (1986) procedure. The evolution of the yield surface is specified by the variation of the friction angle in the piecewise manner defined in Fig. 1 for friction angle. Cohesion varies in a parallel way in accordance with:

$$c_{mob} = c_{peak}\cot\varphi_{ini}\tan\varphi_{mob}$$

The state variable controlling the variation is:

$$\varepsilon^p_{eq} = \left(\frac{2}{3}\boldsymbol{\varepsilon}^p : \boldsymbol{\varepsilon}^p\right)^{1/2}$$

where $\boldsymbol{\varepsilon}^p$ is the plastic strain tensor.

To prevent excessive dilatancy, a non-associated flow rule is adopted, controlled by the parameter, ω ($\omega = 1$ implies associativity):

$$\frac{\partial g}{\partial \boldsymbol{\sigma}'} = \omega\frac{\partial f}{\partial p}\frac{\partial p}{\partial \boldsymbol{\sigma}'} + \frac{\partial f}{\partial J}\frac{\partial J}{\partial \boldsymbol{\sigma}'} + \frac{\partial f}{\partial \theta}\frac{\partial \theta}{\partial \boldsymbol{\sigma}'}$$

Anisotropy is introduced via a non-uniform scaling of the stress tensor as described in Manica et al. (2016). To preserve the axisymmetric nature of the anisotropy, the following scaling is used:

$$\boldsymbol{\sigma}'^{ani} = \begin{bmatrix} \frac{\sigma'^r_{11}}{c_N} & c_S\sigma^r_{12} & \sigma^r_{13} \\ c_S\sigma^r_{12} & c_N\sigma'^r_{22} & c_S\sigma^r_{23} \\ \sigma^r_{13} & c_S\sigma^r_{23} & \frac{\sigma'^r_{33}}{c_N} \end{bmatrix}$$

Time-Dependent Response

The additional viscoplastic strains due to the time-dependent component (creep) of the model are computed from a modified form of Lemaitre's law. It is assumed that the time-dependent deformations are mainly caused by deviatoric stresses. Thus the viscoplastic strain rate, $\dot{\boldsymbol{\varepsilon}}^{vp}$, is given by:

$$\dot{\boldsymbol{\varepsilon}}^{vp} = \frac{2}{3}\frac{\dot{\varepsilon}^{vp}}{q}\mathbf{s};\, q = \left(\frac{3}{2}\mathbf{s}:\mathbf{s}\right)^{1/2};\, \dot{\varepsilon}^{vp} = \gamma\langle q - \sigma_s\rangle^n \left(1 - \varepsilon^{vp}_{eq}\right)^m$$

where γ is a viscosity parameter, σ_s is a threshold from which viscoplastic strain are activated, n and m are material constants and the state variable of the time-dependent response is given by

$$\varepsilon^{vp}_{eq} = \int_o^t \left(\frac{2}{3}\dot{\boldsymbol{\varepsilon}}^{vp}:\dot{\boldsymbol{\varepsilon}}^{vp}\right)^{1/2} dt$$

Permeability

To achieve a good representation of the coupled hydro-mechanical behaviour, it is necessary to incorporate the increase of permeability associated with rock damage. In the framework of the constitutive law described, it is assumed that there is a dependency of permeability, $\mathbf{k}$, on the magnitude of the plastic strains, as indicated by the plastic multiplier, λ^p:

$$\mathbf{k} = \mathbf{k}_0 e^{\eta\lambda^p}$$

where $\mathbf{k}_0$ is the intrinsic permeability of the intact rock and η is a constant that controls the rate of change. In addition, laws for relative permeability and the retention curve are also required when dealing with unsaturated states.

Comparison with Experimental Results

For space reasons, comparison of the model predictions with experimental results is limited. For the instantaneous response, to triaxial tests performed under two different confining pressures are used (Fig. 2). The time-dependent component is checked with reference to three creep tests performed under different values of deviatoric stresses (Fig. 3). It can be observed that a good agreement is achieved. It should be noted that

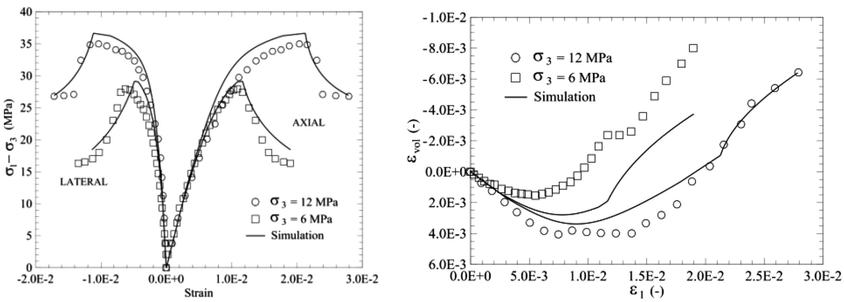

a) b)

Fig. 2. Observations (Armand et al. 2016) vs. constitutive law results. Triaxial tests (a) Axial and lateral strains, (b) volumetric strains.

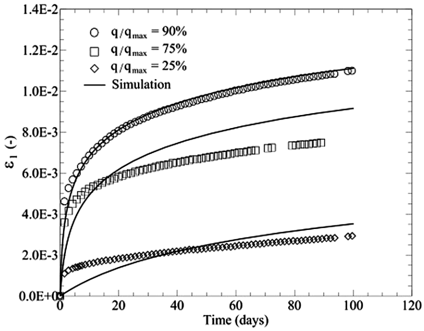

Fig. 3. Observations (Armand et al. 2016) vs. constitutive law results. Creep tests

the initially unsaturated state of the specimens has been taken into account in the model calculations.

Coupled Hydromechanical Analysis of a C Excavation

A simplified analysis of the excavation of a drift in the MHM URL is presented in this section. The drift has a 2.6 m diameter circular section and has been excavated with a road header at the −490 m level. The drift alignment was parallel to the major horizontal principal stress. As a result, the state of stress perpendicular to the axis of the drift was practically isotropic with $\boldsymbol{\sigma}_v = 12.7$ and $\boldsymbol{\sigma}_h = 12.4$ MPa. The *in situ* pore water pressure at that level in zones not affected by excavations is 4.7 MPa. The plane-strain mesh used in the analysis and the main boundary conditions adopted are indicated in Fig. 4a. The excavation was simulated using the deconfinement curve shown in Fig. 4b. The same Figure also shows the pore pressure applied to the boundary as a function of the distance to the front.

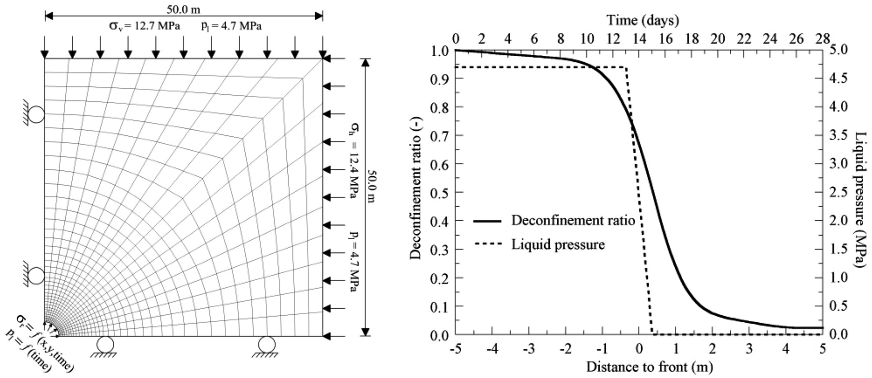

Fig. 4. (a) Mesh and general boundary conditions used in the analysis, (b) Boundary conditions on the excavation wall.

As an example of the results, Fig. 5 shows the observed and computed pore pressure values measured in borehole OHZ1521 where a good match can be noted. The rapid reduction of the water pressures in PRE_02 and PRE_03 can only be obtained only if the increase of permeability due to damage is considered. The model also accounts for the pore pressure increase in PRE_04 when excavation approaches as well as for the observed evolution of the PRE_05 pressure. This good agreement has been achieved in spite of the fact that the 2D representation of the real excavation can only be very approximate.

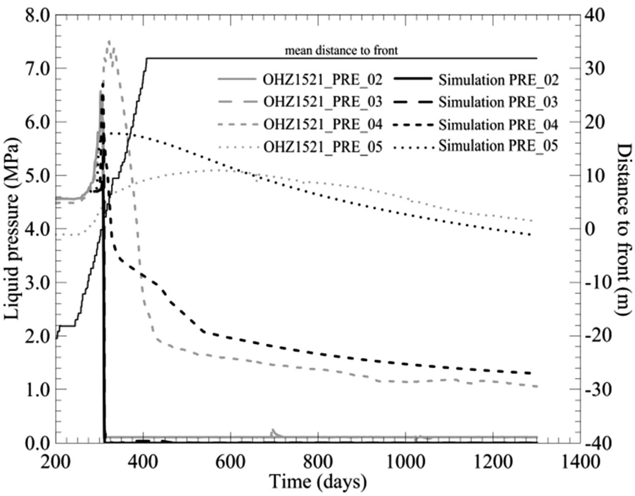

Fig. 5. Observed (Seyedi et al. 2016) and computed pore pressures in borehole OHZ1521.

Finally to check the effects of creep in the model predictions, the evolution of horizontal and vertical convergences computed with and without the time – dependent component are presented in Fig. 6. It can be observed that when creep is incorporated, an adequate agreement with observations is obtained although the model significantly underestimates the observed anisotropy of convergences. When creep is omitted, the long term behaviour of the excavation is completely missed.

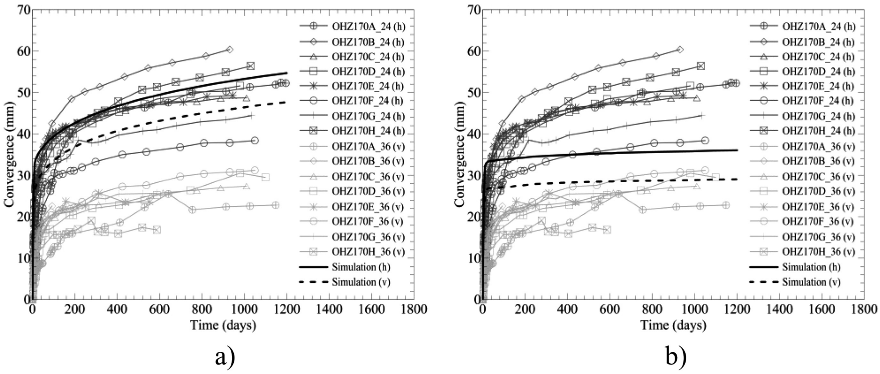

Fig. 6. Observed (Seyedi et al. 2016) and computed horizontal and vertical convergences (a) Time-dependent strains considered, (b) Time-dependent strains omitted.

Concluding Remarks

A constitutive model for argillaceous rocks has been presented that incorporates a significant number of the characteristic features of behaviour for this type of material. The model has been successfully applied to the simulation of laboratory tests and of a deep excavation of a drift in the MHM underground laboratory.

Acknowledgements. The financial and technical assistance of ANDRA to the work presented is gratefully acknowledged. The first author has been supported by a Conacyt scholarship (Reg. No. 270190).

References

Armand G, Conil N, Talandier J, Seyedi D (2016) Fundamental aspects of the hydromechanical behavior of the Callovo-Oxfordian claystone – from experimental investigations toward a modelling perspective. Comput Geotech (in press)

Gens A (2013) On the hydromechanical behaviour of argillaceous hard soils-weak rocks. In: Anagnostopoulos A et al. (eds) Proceedings of 15th European Conference on Soil Mechanics and Geotechnical Engineering (Part 4). IOS Press, Amsterdam, pp 71–118

Jardine RJ, Brosse A, Coop MR, Hosseini KR (2015) Shear strength and stiffness anisotropy of geologically aged stiff clays. In: Rinaldi VA et al (eds) Deformation Characteristics of Geomaterials. IOS Press, Amsterdam, pp 156–191

Manica M, Gens A, Vaunat J, Ruiz DF (2016) A cross-anisotropic formulation for elasto-plastic models. Geotech. Lett. 6:156–162

Seyedi D, Armand G, Noiret A (2016) "Transverse Action". A model benchmark exercise for numerical analysis of the Callovo-Oxfordian claystone hydromechanical response to excavation operations. Comput Geotech (in press)

Sloan SW, Booker JR (1986) Removal of singularities in Tresca and Mohr-Coulomb yield functions. Commun Appl Numer Meth 2(2):173–179

Intrinsic and State Parameters Governing the Efficiency of Bentonite Barriers for Contaminant Control

Andrea Dominijanni[1], Mario Manassero[1(✉)], Giacomo Boffa[1], and Sara Puma[2]

[1] Politecnico Di Torino, c.so Duca Degli Abruzzi 24, 10129 Turin, Italy
mario.manassero@polito.it
[2] Geotechnical Engineering, c.s. Duca Degli Abruzzi 42, 10129 Turin, Italy

Abstract. The osmotic, hydraulic and self-healing efficiency of bentonite based barriers (e.g. geosynthetic clay liners) for containment of polluting solutes are governed by both the chemico-physical intrinsic parameters of the bentonite, i.e. the solid density (ρ_{sk}), the total specific surface (S), the fixed negative electric surface charge (σ), the Stern fraction (f_{Stern}), and by the chemico-mechanical state parameters able to quantify the solid skeleton density and fabric, i.e. the total (e) and nano (e_n) void ratio, the average number of platelets per tactoid ($N_{l,AV}$), and the effective electric fixed-charge concentration ($\bar{c}_{sk,0}$). In turn, looking at saturated active clays only, the state parameters seem to be controlled by the effective stress history (SH), ionic valence (v_i) and related exposure sequence of salt concentrations in the pore solution (c_s). A theoretical framework, able to describe chemical, hydraulic and mechanical behaviors of bentonites in the case of one-dimensional strain and flow fields, has been set up. In particular, the relationships, linking the aforementioned state and intrinsic parameters of a given bentonite with its hydraulic conductivity (k), effective diffusion coefficient (D_s^*), osmotic coefficient (ω) and swelling pressure (u_{sw}) under different stress-histories and solute concentration sequences, are presented. The validity of the proposed theoretical hydro-chemico-mechanical framework has been tested by comparison of its predictions with some of the available experimental results on bentonites (i.e. hydraulic conductivity tests, swelling pressure tests and osmotic efficiency tests).

Bentonite Structure

Bentonite is a clay soil that usually contains a significant percentage (e.g., $\geq$ 70%) of the three-layered (2:1) clay mineral montmorillonite. Isomorphic substitution in montmorillonite usually results in the replacement of a portion of tetravalent silicon (Si^{4+}) and trivalent aluminium (Al^{3+}) in the crystalline structure with a divalent metal, such as magnesium (Mg^{2+}), and this leads to a negative surface charge. The ideal unit cell formula of montmorillonite is: $\{(OH)_4Si_8Al_{3.44}Mg_{0.66}O_{20}\cdot nH_2O^{0.66-}\}$, with an average surface charge of 0.66 equivalent per unit cell. Montmorillonite crystals consist of parallel-aligned, alumino-silicate lamellae, which are approximately 1 nm thick and 100–200 nm in the lateral extent. The unit cell parameters are 0.517 nm and 0.895 nm,

A. Ferrari and L. Laloui (eds.), *Advances in Laboratory Testing and Modelling of Soils and Shales (ATMSS)*, Springer Series in Geomechanics and Geoengineering,
DOI 10.1007/978-3-319-52773-4_5

which correspond to a unit cell area of 0.925 nm^2, or one unit charge per 1.4 nm^2. The corresponding surface charge, σ, is equal to 0.114 $C \cdot m^{-2}$. The total specific surface of a single platelet, S, available for water adsorption is approximately equal to 760 $m^2 \cdot g^{-1}$, assuming a solid density, ρ_{sk}, of 2.65 $Mg \cdot m^{-3}$ or a specific gravity, G_s, of 2.65 (-).

Montmorillonite particles can be represented as infinitely extended platy particles, also called platelets or lamellae. The half distance, b, between the montmorillonite particles can be estimated from the void ratio, e. Norrish (1954) showed that bentonite can have a dispersed structure or fabric in which clay particles are present as well separated units, or an aggregated structure that consists of packets of particles, or tactoids, within which several clay platelets are in a parallel array, with a characteristic interparticle distance of 0.9 nm.

The formation of tactoids has the net result of reducing the surface area of the montmorillonite, which then behaves like a much larger particle with the diffuse double layer only fully manifesting itself on the outside surfaces. The formation of tactoids is due to internal flocculation of the clay platelets, and mainly depends on the concentration and the valence of the ions in the soil solution and, to a lesser extent, on the effective isotropic stress history or, in turn, on the total void ratio, e_{tot}. The average number of clay platelets or lamellae forming tactoids, $N_{l,AV}$, increases with an increase in the ion concentration and valence of cations in the soil solution, whereas there is not apparent unique trend in $N_{l,AV}$ versus the total void ratio e_{tot} for a given concentration. Unfortunately, the number of platelets in a tactoid cannot be predicted and must be estimated from macroscopic measurements of the transport parameters (e.g. hydraulic conductivity). A complicating factor is the non-uniform distribution of ions in mixed systems. For instance, in Na^+-Ca^{2+} systems, the distribution of the ions is not random, but the charges within the tactoids are mainly neutralized by Ca^{2+}, whereas those on the outer surfaces are substantially enriched in Na^+ over Ca^{2+}.

The average half spacing, b, in perfectly dispersed clays may be estimated, assuming a uniform distribution of the clay platelets in a parallel orientation (Dominijanni and Manassero 2012b) from the relation:

$$b = \frac{e}{\rho_{sk} S} \tag{1}$$

If the clay has an aggregated structure, only the external surface of the tactoids is in contact with the mobile fluid, therefore the void space within the platelets in the tactoids should be subtracted from the total void space to obtain the micro-void space, e_m, with reference to the conducting pores (Dominijanni and Manassero 2012b). If $N_{l,AV}$ is the average number of platelets per tactoid and d_d is the thickness of the diffuse double layer wrapping the external surface of the tactoid divided by the average spacing between the platelets in the tactoid ($2b_n$), the external or effective specific surface, S_{eff}, and the internal specific surface, S_n, are given by:

$$S_{eff} = \frac{S}{N_{l,AV}} \tag{2a}$$

$$S_n = \frac{(N_{l,AV} + d_d - 1)}{N_{l,AV}} S \tag{2b}$$

The average half spacing between the platelets in the tactoid, b_n, as determined by means of X-ray measurements, can vary between 0.2 nm and 0.5 nm (Shainberg et al. 1971). The total void ratio, e_{tot}, of the bentonite is given by the sum of the void ratio inside the tactoid representing the nano or non-conductive pores (nm size), e_n, and the void ratio representing the micro or conductive pores (μm size), e_m. The water inside the tactoids can be considered part of the solid particles and is excluded from the transport mechanisms.

The void ratio associated with the internal surfaces of the tactoid, e_n, can be estimated as follows:

$$e_n = b_n \rho_{sk} S_n \tag{3}$$

where ρ_{sk} = density of the solid particles. The corrected half spacing, b_m, between the tactoids, in the case of an aggregate microstructure of bentonite, can be estimated from an equation similar to Eq. 1, or

$$b_m = \frac{e_m}{\rho_{sk} S_{eff}} \tag{4}$$

where $e_m = e_{tot} - e_n$ = void ratio representing the void space between the tactoids.

When the number, $N_{l,AV}$, of clay platelets in the tactoids increases, the external specific surface decreases and the half spacing, b_m, between the tactoids increases, even though the total void ratio remains constant and the void ratio representing the pore volume available for the transport decreases.

Guyonnet et al. (2005), through a comparison of the results of hydraulic conductivity tests and microscopic analyses of bentonite structure based on small angle X-ray scattering and transmission electron microscopy, showed that high values of the hydraulic conductivity are related to an aggregated fabric (also called the hydrated-solid phase), while low values of the hydraulic conductivity are related to a dispersed fabric (also called the gel phase). These experimental results can be explained by the increase in the average micro-pore size, due to tactoid formation.

State Parameters

Referring to the conceptual scheme and the possible evolutions of the bentonite fabric previously described, other state parameters can be derived from the basic average number of platelets per tactoid, $N_{l,AV}$. Equation (2a) gives the effective specific surface, S_{eff}, based on the single platelet specific surface, S (= 760 $m^2 \cdot g^{-1}$), and the basic state parameter $N_{l,AV}$. Moreover, another useful state parameter can be directly derived from the latter through the following equation (see also Dominijanni et al. 2013):

$$\bar{c}_{sk,0} = \frac{(1 - f_{Stern}) \cdot \sigma}{F} \cdot \rho_{sk} \cdot S_{eff} \tag{5}$$

where: $\bar{c}_{sk,0}$ = effective fixed charge concentration of the solid skeleton relative to the solid volume (mol·m^{-3}); f_{Stern} = fraction of electric charge compensated by the cations specifically adsorbed in the Stern layer ranging between 0.70 and 0.95 (-), and F = Faraday's constant (= 96,485 C·mol^{-1}). The proposed state parameters can be influenced primarily by the concentrations of ions, c_s, in the pore solution and by the void ratio related in turn to the effective isotropic component of the stress history of the considered bentonite.

Table 1. Intrinsic and state parameters for mechanical and chemical models.

Fields	Actions	Intrinsic parameters	State parameters
Mechanical	Shear stress: τ	ρ_{sk}, φ_{cv}	e, p', ψ
Chemical	Ion concentration: c_s	S, σ, f_{Stern}	$N_{l,AV}$, S_{eff}, $\bar{c}_{sk,0}$

Notes: p' = isotropic effective stress component; ψ = dilatancy angle; φ_{cv} = friction angle at the critical state.

Once the family of chemical state parameters describing the bentonite fabric at the nano and micro scale have been defined, a parallel development can be drawn with some aspects of the well known elasto-plastic-work-hardening models within the traditional soil mechanics (e.g. the Cam Clay model) able to describe the mechanical behavior of the particulate media on the basis of a series of intrinsic and state parameters as reported in Table 1.

As shown in Dominijanni and Manassero (2012a,b), the framework that includes the aforementioned chemical parameters is able to link the coupled transport phenomena of water and ions by imposing the chemical equilibrium between the bulk electrolyte solutions and the internal micro-pore solution at the macroscopic scale level, through the Donnan, Navier-Stokes and Nernst-Planck equations. Moreover, also some specific aspects of the mechanical behavior can be modelled and coupled with the chemical and transport behavior by taking into account the different types of intergranular actions, beyond the solid contact stress and the bulk pore pressure (Terzaghi 1943), such as electro-magnetic attraction/repulsion and osmotic swelling/suction forces (Mitchell and Soga 2005).

In principle, and similar to the evolution of the basic Cam Clay model by Alonso et al. (1990) through the UPC model for unsaturated soil, the intrinsic and state parameters listed in Table 1 and the related framework can extend the basic theoretical approaches to include the mechanical behavior that is related to the fabric of the active fine grained soils under fully saturated conditions, taking into account not only actions such as the stress history and the related void ratio, but also the ion species and the concentration changes in the pore fluids.

In the following discussion, the developed framework is applied to interpret some experimental results from the literature and from the authors' own laboratory testing, showing how the framework provides insight into the physico-chemico mechanisms that determine the observed macro-scale behavior of active clays.

Validation of the Solute Transport and Swelling Model

In order to obtain an extended validation of the proposed theoretical framework, Dominijanni and Manassero (2005), Dominijanni et al. (2006), and Manassero and Dominijanni (2010) proposed a model obtained by upscaling the modified Navier-Stokes equation and the Nerst-Plank equations and using the Donnan equations to impose the chemical equilibrium between the bulk electrolyte solutions and the internal micro-pore solution. The proposed model provided a satisfactory interpretation of the experimental results of Malusis and Shackelford (2002a,b), Malusis et al. (2013) and Dominijanni et al. (2013) in terms of osmotic efficiency, ω, of two bentonites (see Tables 2 and 3 and Fig. 1) tested with solutions characterized by salt (KCl, NaCl) concentrations up to a maximum of c_s = 100 mM. The experimental data are in good agreement with the linear relationship, predicted by the theoretical model, relating the restrictive tortuosity factor, τ_r, to the osmotic efficiency coefficient, ω, as follows:

$$\tau_r = 1 - \omega \tag{6}$$

Table 2. Physical and chemical intrinsic properties of the considered bentonites.

Type	Dominijanni et al. (2013), Puma et al. (2015) and Boffa et al. (2016)	Malusis and Shackelford (2002a,b)	Seiphoori (2014) and Manca (2015)	Mazzieri et al. (2011, 2013)	Di Emidio (2010)
Liquid Limit, *LL* (%)	525	478	420	530	650
Plasticity Index, *PI* (%)	–	439	355	480	600
Specific Gravity, G_s (-)	2.65	2.43	2.74	2.65	2.66
Principal Minerals (%):					
montmorillonite mixed-layer	98	71	85	90	95
illite/smectite	-	7	-	-	-
quartz	-	15	4	-	-
other	-	7	11	-	-
Cation Exchange Capacity, *CEC* (meq/100 g)	105	47.7	74.0	94.5	44.5

Table 3. Range of physical and state parameters of the bentonites in contact with deionized water and NaCl, KCl and $CaCl_2$ solutions.

	Dominijanni et al. (2013) Puma et al. (2015) and Boffa et al. (2016)	Malusis and Shackelford (2002a,b)	Seiphoori (2014)	Manca (2015)	Mazzieri et al. (2011, 2013)	Di Emidio (2010)
Hydraulic Conductivity, k (m/s)	$6.00 \cdot 10^{-12}$ $1.20 \cdot 10^{-10}$	$1.63 \cdot 10^{-11}$	$1.0 \cdot 10^{-14}$ $1.0 \cdot 10^{-13}$	$1.6 \cdot 10^{-11}$ $2.2 \cdot 10^{-8}$	$6.5 \cdot 10^{-11}$	$6.42 \cdot 10^{-12}$
Steric Tortuosity Factor, τ_m (–)	0.30 0.36	0.14	0.20	0.30 0.50	0.35	0.35
Total Void Ratio, e_{tot} (–)	0.60 4.50	3.76	0.53 1.20	2.15 5.40	5.13	2.55
Micro-Void Ratio, e_m (–)	0.10 2.99	2.56	0.05 0.38	1.23 4.35	3.6	1.13
Effective Diffusion Coefficient, D_s^* (m^2/s)	$5.0 \cdot 10^{-10}$	$2.7 \cdot 10^{-10}$	–	–	–	–
Osmotic Efficiency, ω (–)	0.00 0.68	0.35	–	–	–	–
Effective Specific Surface, S_{eff} (m^2/kg)	24.14 216.71	164.40	36.18 92.15	6.09 121.81	159.65	129.94
Average Number of Platelets per Tactoid, $N_{l,AV}$ (–)	3.5 31.5	3.6	5.7 14.5	4.3 85.9	5.0	6.2
Stern Coefficient, f_{Stern} (–)	0.80 0.90	0.90	0.70	0.85	0.80	0,9
Fixed charge concentration, $\bar{c}_{sk,0}$ (M)	0.008 0.076	0.046	0.035 0.089	0.003 0.059	0.100	0.041

where τ_r represents the ratio between the osmotic effective diffusion coefficient, D_ω^*, that is measured in an osmotic test (Malusis et al. 2001; Malusis and Shackelford 2002b; Dominijanni et al. 2013) and the effective salt diffusion coefficient, D_s^*, that is obtained by extrapolating the value of D_ω^* at $\omega = 0$. Also, the evaluation of the osmotic swelling pressure theoretically calculated on these samples by the use of the same input

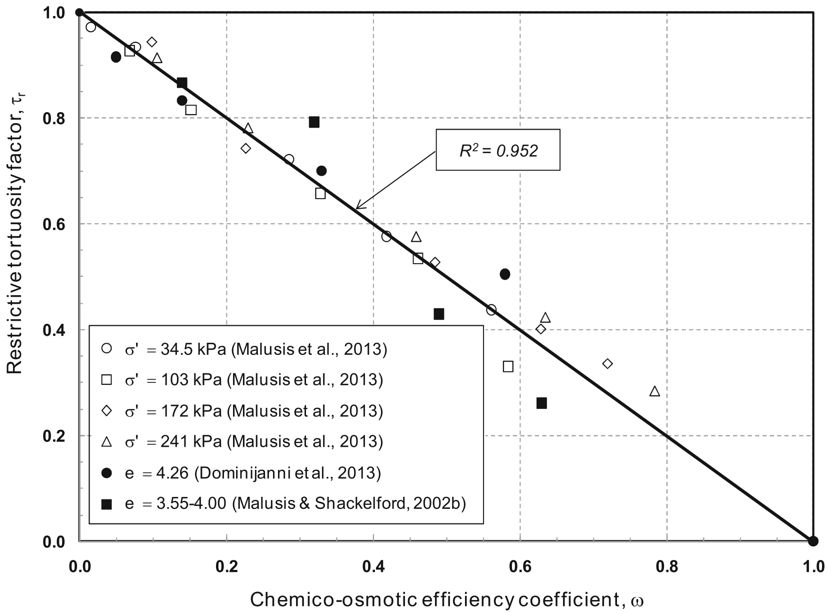

Fig. 1. Restrictive tortuosity factor versus chemo-osmotic efficiency coefficient with the theoretical linear relation.

parameters referring in particular to $N_{l,AV}$, S_{eff}, $\bar{c}_{sk,0}$, was in very good agreement with the related experimental results (see Manassero et al. 2014). However, the range of salt concentrations, c_s, investigated within the experimental tests previously noted, was not sufficient to induce any significant variation in bentonite fabric and, therefore, the values of the defined fabric state parameters ($N_{l,AV}$, S_{eff} and $\bar{c}_{sk,0}$).

For this reason, a more general and reliable validation of the proposed theoretical framework for modelling the bentonite hydro-chemico-mechanical behavior requires consideration of other experimental results, such as both the hydraulic conductivity and the swelling pressure, using ion concentrations higher than 200 mM and, possibly, $\geq$ 1000 mM. In the case of the higher ion concentrations, the fabric of the bentonites undergoes major changes due to flocculation phenomenon under low confining stress (high void ratio) resulting in a significant increase in the average number of platelets per tactoid and a correspondent decrease in the effective specific surface and fixed charge concentration of the solid skeleton as summarized in Table 4.

A series of hydraulic conductivity, swelling and oedometer tests performed on different bentonites by different authors (see Table 2 and 3) have been analysed to validate the proposed general framework.

The comparison of experimental and theoretical results consists of the following steps:

– Referring to a first series of hydraulic conductivity tests on different bentonites and permeant solutions, an assessment of the effective specific surface, S_{eff}, has been

Table 4. Ranges of variation of monovalent ion equivalent concentrations that influence the main performance parameters of bentonites.

Main performance parameters of bentonite barriers	Ranges of monovalent ion concentration, c_s [mM]	Notes
Osmotic efficiency, ω	0–100	No fabric variation. For c_s higher than 100 mM $\omega = 0$
Swelling pressure, u_{sw}	0–200	Small fabric variation. For c_s around 200 mM $u_{sw} = 0$
Hydraulic conductivity, k	200–5000	Significant fabric variation and significant k increments
Steric tortuosity factor, τ_m	200–5000	Significant fabric variation and significant τ_m increments

performed using the following equation (Kozeny 1927; Carman 1956; Dominijanni et al. 2013).

$$k = \frac{\tau_m}{3} \frac{e_m^3}{(1 + e_m) \cdot (\mu_w + \mu_{ev})} \frac{\gamma_w}{(\rho_{sk} S_{eff})^2} \tag{7}$$

Neglecting as a first approximation the electro-viscosity coefficient, μ_{ev}, the definitions of the remaining undefined terms are: τ_m = matrix or steric tortuosity factor (≤ 1), that takes into account the tortuous nature of the actual permeant pathways through the porous medium due to the geometry of the interconnected pores, μ_w = water viscosity coefficient, and γ_w = water unit weight.

– Evaluation of the average number of platelets per tactoid, $N_{l,AV}$, and $\bar{c}_{sk,0}$ via Eqs. 2a and 5, respectively, and assessment of the theoretical results in terms of swelling pressure, u_{sw}, as follows (from Dominijanni et al. 2013):

$$u_{sw} = 2RTc_s \left[\sqrt{\left(\frac{\bar{c}_{sk,0}}{2 \cdot e_m \cdot c_s} \right)^2 + 1} - 1 \right] \tag{8}$$

where R is the ideal gas constant and T is the absolute temperature (K). The comparisons of the latter with the experimental swelling test results for the same bentonite samples are plotted in Fig. 2.

– An additional assessment of the reliability of the proposed theoretical model, with reference to Eq. 8, is shown in Fig. 3, where all the swelling and oedometer test results in terms of swelling pressure of the samples permeated or hydrated with

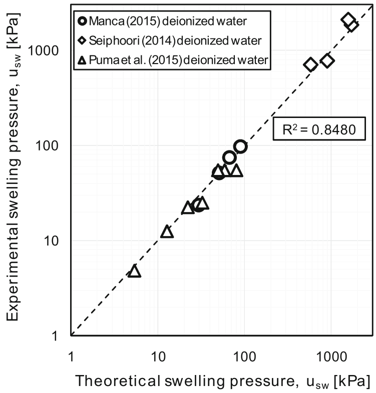

Fig. 2. Experimental versus theoretical swelling pressure using input state parameters from hydraulic conductivity tests.

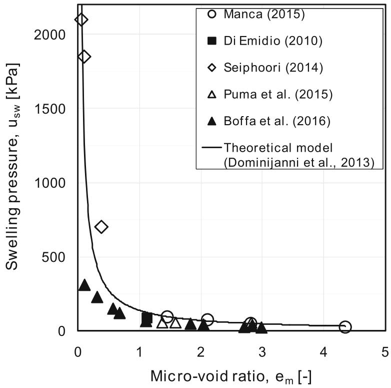

Fig. 3. Swelling pressure versus micro-void ratio for samples tested with deionized water and solutions with monovalent ion equivalent concentration cs $\leq$ 10 mM.

deionized water or low concentration solutions ($c_s \leq 10$ mM) are shown together with the obtained theoretical trend.

Finally, all the available bentonite samples, in contact with both deionized water and different chemical solutions, have been considered for the assessment of the basic state parameter, $N_{l,AV}$, throughout the experimental swelling pressure measurements (Eq. 8). This parameter is uniquely linked with the other two electro-fabric state parameters, (i.e. S_{eff}, $\bar{c}_{sk,0}$) and, moreover, provides, as previously illustrated, a satisfactory prediction of chemico-osmotic, hydraulic and, swelling/shrinking behaviors of bentonites. The obtained $N_{l,AV}$ values have been plotted versus the micro-void ratio, e_m, in Figs. 4 and 5, with Fig. 5 simply being the enlargement of the vertical axis close to the origin of Fig. 4. After an initial decrease up to minimum value, the values of $N_{l,AV}$ show, for any given electrolyte concentration (apart from the unique case of deionized water), a continuous increasing trend when the micro-void ratio increases.

In order to relate $N_{l,AV}$ to e_m and c_s, the following equation has been proposed:

$$N_{l,AV} = N_{l,AV0} + \frac{\alpha}{e_m} \cdot \left(\frac{c_s}{c_0} + 1\right) + \beta \cdot e_m \cdot \left[1 - \exp\left(-\frac{c_s}{c_0}\right)\right] \tag{9}$$

where c_0 represents the reference concentration (= 1 mol/l), $N_{l,AV0}$ is the ideal average minimum number of lamellae per tactoid when $c_s = 0$ and $e_m \rightarrow \infty$; $\alpha = e_m \cdot \left(N_{l,AV} - N_{l,AV0}\right)$ for $c_s = 0$ is a coefficient relating $N_{l,\mathrm{AV}}$ and e_m when $c_s = 0$ and β is a constriction degree coefficient of the platelets. The parameters $N_{l,AV}$ and β are both depending on bentonite type, pre-treatments (e.g. removal of soluble salts, consolidation), hydration and chemicals exposure sequence.

The available experimental data have been fitted by imposing $N_{l,AV0} = 4.79$, $\alpha = 0.91$ and $\beta = 42.45$ (coefficient of determination, $R^2 = 0.89$).

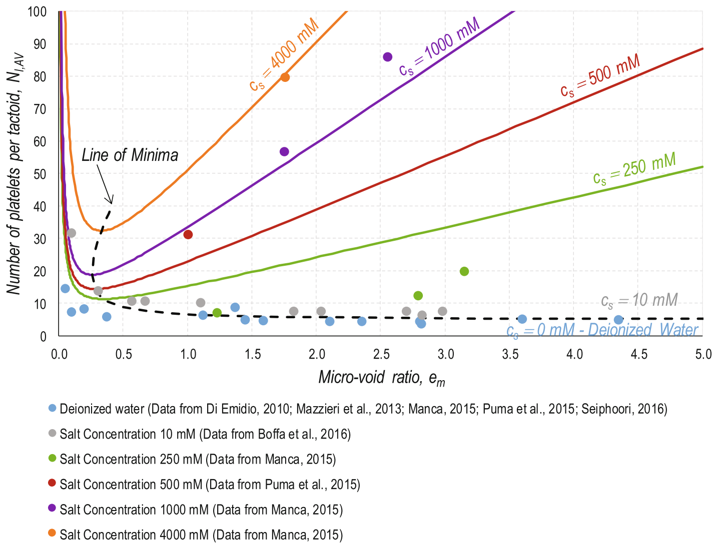

Fig. 4. Average number of platelets per tactoid ($N_{l,AV}$) versus micro void ratio (e_m) based on values from the interpretation of hydraulic conductivity, osmotic and swelling tests (Fitting parameters: $N_{l,AV0}$ = 4.79, α = 0.91, β = 42.45; coefficient of determination, R^2 = 0.89).

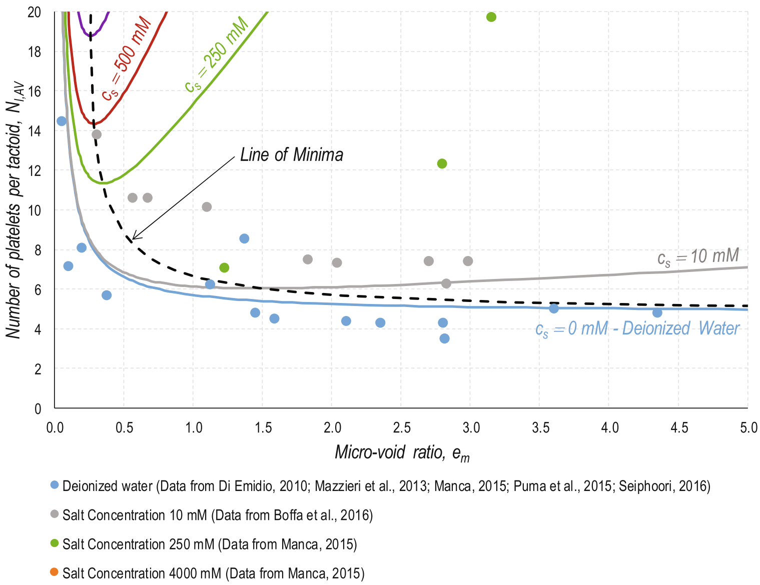

Fig. 5. Enlargement of Fig. 4 for the range $0 < N_{l,AV} < 20$.

Some Preliminary Comments

A series of chemico-fabric state parameters (i.e. effective specific surface, S_{eff}, average number of platelets per tactoid, $N_{l,AV}$, and solid skeleton electric fixed charge concentration, $\bar{c}_{sk,0}$) were defined to predict the chemico-osmotic, hydraulic, and swelling behavior of bentonites. Moreover, a theoretical model was presented, based on the state parameters listed over, and its capability to predict some experimental results (from the literature and from this research programme) was assessed. The comparison of the theoretical results versus the experimental results was good.

Moreover, plotting the average number of platelets per tactoid, $N_{l,AV}$, versus the micro-void ratio, e_m (i.e. the pore volume of the inter-tactoids), for different ion concentrations of the pore solutions, an interesting trend was observed. In fact, for any given ion concentration for the solution in contact with the bentonite (apart from deionized water), the value of $N_{l,AV}$, after an initial decrease and a minimum value, shows a continuous increasing trend with increase in the micro-void ratio.

A preliminary theoretical function has been proposed to relate the number of lamellae per tactoid with the micro-void ratio and the salt concentration. This function represents the state boundary surface of the chemical-mechanical coupled model. The ideal line, that represents the minimum loci of the aforementioned function at the different ion concentrations, c_s, of the solutions in contact with the bentonite versus e_m may represent a separation line between swelling and shrinking behaviors of the considered bentonites, similar to the case of unsaturated soils where the expanding and collapsible behaviors are dependent on the degree of saturation or suction versus the confining stress and/or void ratio (see Alonso et al. 1990).

However, further experimental studies must be implemented in order to corroborate the aforementioned theoretical framework, but some very interesting and useful knowledge can already be theoretically modeled and practically exploited for prediction and assessment of the performance of bentonite barriers for subsurface pollutant containment.

References

Alonso E, Gens A, Josa A (1990) A constitutive model for partially saturated soils. Géotechnique 40(3):405–430

Boffa G, Dominijanni A, Manassero M, Marangon M, Zaninetta L (2016) Mechanical and swelling behavior of sodium bentonites in equilibrium with low molarity NaCl solutions under oedometric conditions. Acta Geotechnica (under review)

Carman PC (1956) Flow of gases through porous media. Butterworths, London

Di Emidio G (2010) Hydraulic and chemico-osmotic performance of polymer treated clays. Ph. D. Thesis. Ghent University, Ghent

Dominijanni A, Manassero M (2005) Modelling osmosis and solute transport through clay membrane barriers. In: Alshawabkleh A, et al (eds) Waste Containment and Remediation (ASCE Geotechnical Special Publication No. 47). ASCE, Reston/VA

Dominijanni A, Manassero M (2012a) Modelling the swelling and osmotic properties of clay soils. part I: the phenomenological approach. Int J Eng Sci 51:32–50

Dominijanni A, Manassero M (2012b) Modelling the swelling and osmotic properties of clay soils. part II: the physical approach. Int J Eng Sci 51:51–73

Dominijanni A, Manassero M, Puma S (2013) Coupled chemical-hydraulic-mechanical behavior of bentonites. Géotechnique 63(3):191–205

Dominijanni A, Manassero M, Vanni D (2006) Micro/macro modeling of electrolyte transport through semipermeable bentonite layers. In: Thomas HR, (ed) Proceedings of the 5th international congress on environmental geotechnics, 26–30 June, 2006, Cardiff, Wales, UK, vol II. Thomas Telford, London, pp 1123–1130

Guyonnet D, Gaucher E, Gaboriau H, Pons CH, Clinard C, Norotte V, Didier G (2005) Geosynthetic clay liner interaction with leachate: correlation between permeability, microstructure and surface chemistry. J Geotech Geoenviron Eng 131(6):740–749

Kozeny J (1927) Ueber kapillare Leitung des Wassers im Boden. Sitzungsber Akad Wiss, Wien 136(2a):271–306

Malusis MA, Shackelford CD, Olsen HW (2001) A laboratory apparatus to measure chemico-osmotic efficiency coefficients for clay soils. Geotech Test J 24(3):229–242

Malusis M, Kang J, Shackelford CD (2013) Influence of membrane behavior on solute diffusion through GCLs. In: Proceedings of the international symposium on coupled phenomena in environmental geotechnics (CPEG), ISSMGE TC, Torino (Italy) 1–3 July 2013, vol 215. CRC Press, Taylor & Francis Group, London, pp 267–274

Malusis MA, Shackelford CD (2002a) Chemico-osmotic efficiency of a geosynthetic clay liner. J Geotech Geoenviron Eng 128(2):97–106

Malusis MA, Shackelford CD (2002b) Coupling effects during steady-state solute diffusion through a semipermeable clay membrane. Environ Sci Technol 36(6):1312–1319

Manassero M, Dominijanni A (2010) Coupled modelling of swelling properties and electrolyte transport through geosynthetic clay liner, Key-note Lecture. In: Proceedings of the sixth international congress on environmental geotechnics (6ICEG), New Delhi, India, 8–12 November 2010, vol 1. Tata McGraw Hill, New Delhi, pp. 260–271

Manassero M, Dominijanni A, Musso G, Puma S (2014) Coupled phenomena in contaminant transport. Theme Lecture. In: Proceedings of the 7th international congress on environmental geotechnics. lessons, learnings & challenges, engineers Australia (EA) (AUS), 7th international congress on environmental geotechnics, Melbourne (Australia), 10–14 November 2014, pp. 144–169

Manca D (2015) Hydro-chemo-mechanical characterization of sand/bentonite mixtures, with focus on their water and gas transport properties. Ph.D. Thesis. EPFL, Lausanne, Switzerland

Mazzieri F, Di Emidio G (2011) Caratteristiche e prestazione di geocompositi bentonitici preidratati. In: Proceeding 24th italian geotechnical conference, Napoli, June 2011. AGI, Rome, 735–742 (in italian)

Mazzieri F, Di Emidio G, Fratalocchi E, Di Sante M, Pasqualini E (2013) Permeation of two GCLs with an acidic metal-rich synthetic leachate. Geotext Geomembr 40(10):1–11

Mitchell JK, Soga K (2005) Fundamentals of soil behavior. John Wiley and Sons, New York

Norrish K (1954) The swelling of montmorillonite. Discuss Faraday Soc 18:120–134

Puma S, Dominijanni A, Manassero M, Zaninetta L (2015) The role of physical pretreatments on the hydraulic conductivity of natural sodium bentonites. Geotext Geomembr 43:263–271

Seiphoori A (2014) Thermo-hydro-mechanical characterization and modelling of MX-80 granular bentonite. Ph.D. Thesis no 6159. EPFL, Lausanne, Switzerland

Shainberg I, Bresler E, Klausner Y (1971) Studies on Na/Ca montmorillonite systems. 1. The swelling pressure. Soil Sci 111(4):214–219

Terzaghi K (1943) Theoretical soil mechanics. John Wiley and Sons, New York

Multiscale Approach to Micro-Poro-Mechanical Modelling of Unsaturated Shales

Richard Wan(✉) and Mahdad Eghbalian

Department of Civil Engineering, University of Calgary, Calgary, AB, Canada
wan@ucalgary.ca

Abstract. The paper outlines the multiscale mathematical formulation of clay-rich shales as a swelling capillary porous medium with a resolution as fine as the nanoscale. The starting point is the description of the physicochemical interactions between elementary crystalline units–the so-called clay sheets or platelets. By way of homogenization, the clay platelet physics is upscaled to represent a system of randomly dispersed shale particles at the microscale with the void spaces partially saturated with a liquid, i.e. water. The end result is the constitutive description of clay shales enriched with microstructural details down to the clay platelet level that can readily describe swelling or shrinkage in terms of physicochemical loading.

Introduction

The swelling and shrinkage of clay-rich geomaterials such as shales are of widespread relevance in Geomechanics with particular reference to geo-environmental and petroleum engineering applications. More specifically, the presence of kinematical constraints at the structural level causes such local deformational processes to result into intense fracturing within the material. Moreover, clay barriers in waste repositories present partially saturated conditions that introduce more complexities into the mathematical problem description due to the presence of three distinct phases, i.e. water, air, solid together with associated interfaces.

The expansive behaviour of porous media in both saturated and partially saturated cases has been studied by many researchers from the macroscopic point of view, within phenomenological approaches, Sridharan and Rao (1973), and thermodynamics framework, Sposito (1972), or mixture theory, Huyghe and Janssen (1997). However, with increasing material heterogeneities such as micro-cracks and the implication of several coupled physics, the above-mentioned approaches become less adequate. This is because in such approaches the interactions between the various physics involved are either mostly overlooked or wrongly applied. Such approaches attempt to study the interactions between the various physics at the macro-scale where they are tightly coupled. Hence, one cannot simply introduce new physics at that scale. It is recalled that the physics are only additive at the micro-level, and not at the macroscopic level.

Given the overall progress in the area of micromechanics and multiscale modelling, a renewed effort to describe clay-shale behaviour at the microstructural level is timely

A. Ferrari and L. Laloui (eds.), *Advances in Laboratory Testing and Modelling of Soils and Shales (ATMSS)*, Springer Series in Geomechanics and Geoengineering,
DOI 10.1007/978-3-319-52773-4_6

and appropriate. With this motivation, the current work develops the mathematical formulation of clay-shale constitutive behaviour across the scales via homogenization techniques, with emphasis on electro-chemical physics at the nanoscale and partially saturated conditions. The derivations that follow in this paper are quite comprehensive, but scarce in the main-stream geomechanics literature, except for the pioneering works of Dormieux et al. (2006a,b), Pichler and Dormieux (2009), Cariou et al. (2013), among others in micro-poro-mechanics.

Mathematical Model

Based on SEM images of clay-shale, we identify the macro-, micro- and nano-scales transcending lengths in the centimeters at the core sample level to the nanometer range at the clay sheet (platelet) level.

Multiscale Representation of Clay-Shale

The hierarchy of scales in clay-shale is herein idealized by introducing three levels to facilitate its mathematical formulation, see Fig. 1.

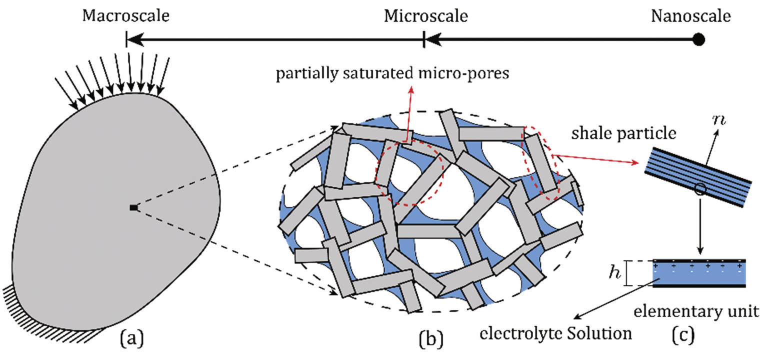

Fig. 1. Three-scale representation of the microstructure of clay-shale: (a) an engineering scale within a boundary value problem, (b) a micro-scale with randomly dispersed ensemble of shale particles, (c) nano-scale structure of a shale particle.

Starting from a boundary-value problem setting involving a clay-shale geostructure, a material point is hereby extracted that represents the so-called macro-scale (Fig. 1a) where all classic engineering measures such as stress, strains and pore fluid pressures operate. When enlarged, a given material point exposes an arrangement of randomly dispersed shale particle ensembles (aggregates), forming void spaces that are partially saturated (micro-scale), see Fig. 1b.

It is worth mentioning that such distribution of shale particles refers to remoulded samples of shale; whereas in compacted state, these particles are oriented in a preferential direction. The framework presented here can be easily modified to consider such a scenario. Also, shales usually comprise of a considerable amount of clay along with large inclusions of silt, quartz or feldspar. Another assumption used in this study is that no such inclusions are considered. However, these can be readily accommodated into our formulation by introducing a meso-scale in the multi-scale representation illustrated in Fig. 1. In fact, our ongoing work involves such inclusions together with unsaturated microcracks at the mesoscale. The reader can also refer to Cariou et al. (2013) for similar treatment.

Zooming further reveals the microstructure of each shale particle fully saturated with an aqueous electrolyte solution. This is referred to as the nanoscale which is illustrated in Fig. 1c. Each shale particle ensemble is in fact composed of an arrangement of elementary crystalline units formed by a pair of so-called clay sheets (platelets) surrounded by bound water and with an inter-layer of cations in between. The clay platelets can be constituted of minerals such as smectite, kaolinite and illite. Herein, it is assumed that smectite is the dominant constituent of shale particles with swelling characteristics.

A Template for Homogenization: From Basic Unit (Nanometer) to Stack of Platelets (Micrometer)

This stage of homogenization refers to the transfer from the basic clay platelet-pair unit in the nanometer scale to the platelet stack or cluster scale in the micrometer range. We investigate the poro-mechanical behaviour of the clay stack in which the clay platelets are flat with width to length ratio $w = h/\ell \ll 1$, and oriented with normal $\mathbf{n}$ in space. An idealization of this clay stack into a REV of volume V results into considering a solid matrix inside which are embedded oblate inclusions filled with fluid as shown in Fig. 2.

We assume an elastic solid phase (volume V^s) in this study such that the deformation of a shale particle is controlled mainly by the variation of inter-platelet spacing under the

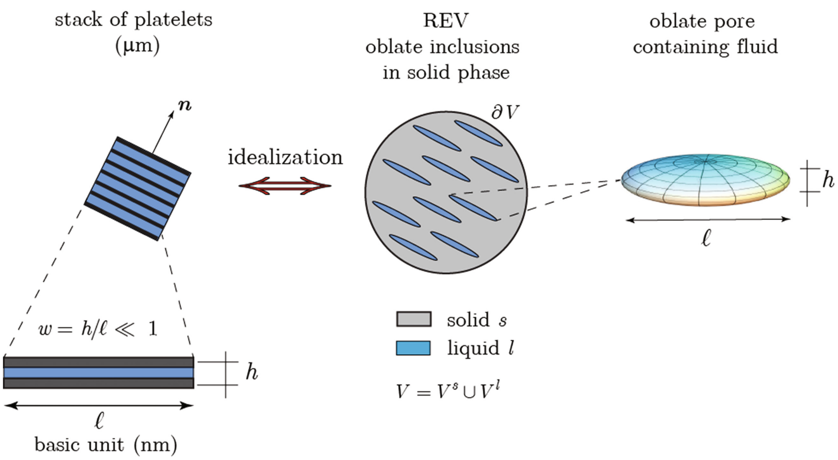

Fig. 2. Upscaling from basic unit to stacked or randomly distributed platelets.

action of electro-chemical forces. In fact, the platelets carry negative charges and interact with the cations and anions present in the inter-platelet fluid with a solute concentration n^s. Non-uniform and non-equal concentration of negative and positive charges result into an electrical field that causes a repulsive force arising from a pressure, π^s, between the platelets. The problem at hand is very complex and will be approximated so that this repulsive force can be determined as a function of the solute concentration n^s, and the distance, h, between platelets using the electric double layer theory and Poisson-Boltzmann equation (Dormieux et al. 2003; Moyne and Murad 2003).

The stress within the liquid (volume V^l) is thus given by the hydrostatic pressure p^l augmented with a contribution coming from the repulsive force, while the pressure at the exterior of the platelets is still at p^l. The dependency of the repulsive force produced by the electrical potential between the two platelets on the spacing can be seen analogously as springs with resultant restoring forces equal and opposite to the excessive repulsive force to hydrostatic pressure. The equilibrium spacing h is reached whenever the resultant of spring restoring forces together with the force exerted by the fluid pressure on the exterior faces of the top and bottom platelets are equal to the net force exerted by the inter-layer fluid; see Fig. 3. Thus, π^s is the so-called osmotic pressure

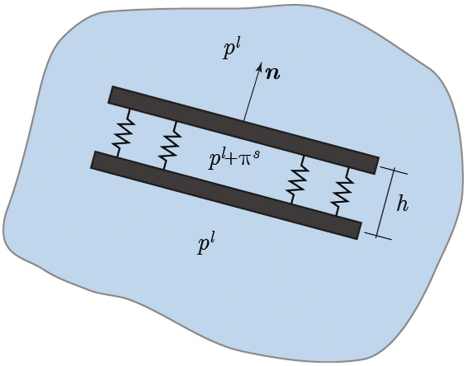

Fig. 3. Notion of osmotic pressure.

responsible for swelling in clay-rich shales.

Thus, the stress tensor for the fluid inside the inter-platelet layer is given by:

$$\sigma^l_{ij} = -p^l \delta_{ij} - \pi^s n_i n_j; \quad \pi^s = \pi^s_0 + h_0 \left.\frac{\partial \pi^s}{\partial h}\right|_{(h_0, n^s_0)} \varepsilon^l_{ij} n_i n_j \tag{1}$$

where $\mathbf{n}$ is the normal vector to the platelet. In the above, the expression of the osmotic pressure π^s has been expanded following a Taylor's series about an equilibrium reference state defined by π^s_0, h_0 and n^s_0 to reveal a so-called strain ε^l_{ij} in the inter-platelet fluid. Thus, the stress tensor in the fluid can be further written as:

$$\sigma^l_{ij} = \mathbb{C}^l_{ijkl}\,\varepsilon^l_{kl} + \sigma^p_{ij};\;\; \mathbb{C}^l_{ijkl} \; = -h_0 \frac{\partial \pi^s}{\partial h}\bigg|_{(h_0, n^s_0)} n_i n_j n_k n_l;\;\; \sigma^p_{ij} = -p^l \delta_{ij} - \pi^s_0\, n_i n_j \quad (2)$$

This fluid stress σ^l_{ij}, which is uniform throughout the fluid phase within volume V^l, consists of a contributional term arising from the osmotic pressure π^s with strains ε^l_{ij} and a pre-stress or eigenstress σ^p_{ij}. It is worth noting that unlike similar works such as in Dormieux et al. (2006b), the pre-stress here is not dependent on strain; thus resulting in a more relevant treatment of the problem which is achieved by defining rather a stiffness for the fluid phase at the platelet level.

On the other hand, the stress in the solid phase made up of platelets is uniform throughout V^s and is assumed to follow linear, isotropic elasticity, i.e.

$$\sigma^s_{ij} = \mathbb{C}^s_{ijkl}\,\varepsilon^s_{kl};\;\; \mathbb{C}^s_{ijkl} \; = k^s\,\delta_{ij}\delta_{kl} + 2\mu^s\left[\frac{1}{2}(\delta_{il}\delta_{kj} + \delta_{ik}\delta_{jl}) - \frac{1}{3}\delta_{ij}\delta_{kl}\right] \quad (3)$$

where k^s and μ^s are the bulk and shear moduli respectively.

We endeavour to calculate the average stress within the REV of volume V subjected to a uniform strain (eigenstrain) applied on its boundary ∂V. This REV comprises a solid matrix dispersed with a number of oblate inclusions filled with fluid such that $V = V^s \cup V^l$ as an idealization of a stack of clay platelets shown in Fig. 2. Thus, the stress at any point $\mathbf{x}$ inside the REV can be put in the following form using the generalized forms of stiffness tensor $\mathbb{C}_{ijkl}$ and pre-stress tensor σ^p_{ij}:

$$\sigma_{ij}(\mathbf{x}) = \left\{\begin{array}{l} \mathbb{C}^s_{ijkl} \\ \mathbb{C}^l_{ijkl} \end{array}\right. \varepsilon_{kl}(\mathbf{x}) + \left\{\begin{array}{ll} 0 & \text{in } V^s \\ \ominus - p^l\,\delta_{ij} - \pi^s_0\, n_i n_j & \text{in } V^l \end{array}\right. \quad (4)$$

This stress should satisfy equilibrium equations (ignoring body forces) in the REV, while displacements u_i compatible with a uniform strain E_{ij} are being applied on its boundary, i.e.

$$\frac{\partial \sigma_{ij}}{\partial x_j} = 0 \quad \text{in } V; \quad u_i = E_{ij} x_j \;\; \text{on } \partial V \quad (5)$$

Due to linearity, the solution of Problem $\mathbf{P}$ involving Eqs. (2) to (5) is obtained in two steps by superposing the solutions of two sub-problems $\mathbf{P}_1$ and $\mathbf{P}_2$. In the first step, in Problem $\mathbf{P}_1$, we consider a uniform strain ($\mathbf{E}$) boundary condition with pre-stress blocked and set to zero, i.e.

$$\frac{\partial \sigma^1_{ij}}{\partial x_j} = 0 \;\; \text{in } V; \quad u^1_i = E_{ij} x_j \;\; \text{on } \partial V; \;\; \text{with } \sigma^1_{ij} = \mathbb{C}_{ijkl}\,\varepsilon^1_{kl} \quad (6)$$

Based on the average strain theorem, i.e. the average strain within the REV must be equal to the constant strain applied on its boundaries, the microscopic strain simply relates linearly to the macroscopic one through some localization tensor A_{ijkl}, i.e.

$\varepsilon^1_{ij} = A_{ijkl}E_{kl}$. Then, calculating the volume average of the stress over the REV, and noting Eq. (4) with $\sigma^p_{ij} = 0$,

$$\begin{aligned} \textstyle\sum^1_{ij} &= \left\langle \sigma^1_{ij} \right\rangle^{rev} = \tfrac{1}{V}\int_{V^s} \mathbb{C}^s_{ijkl}\,\varepsilon^1_{kl}\,dV^s + \tfrac{1}{V}\int_{V^l} \mathbb{C}^l_{ijkl}\,\varepsilon^1_{kl}\,dV^l \\ \textstyle\sum^1_{ij} &= \bar{\mathbb{C}}_{ijmn}E_{mn};\;\; \bar{\mathbb{C}}_{ijmn} = (1-f)\,\mathbb{C}^s_{ijkl}\,\langle A_{klmn}\rangle^s + f\,\mathbb{C}^l_{ijkl}\,\langle A_{klmn}\rangle^l \end{aligned} \tag{7}$$

where $\langle\,.\,\rangle^\alpha$ is the $\alpha-$phase average over phase volume V^α, and $f = V^l/V$ is the microporosity.

Next, in Problem $\mathbf{P}_2$, the system is loaded by introducing the pre-stress, but with the strain set to zero this time, i.e.

$$\frac{\partial \sigma^2_{ij}}{\partial x_j} = 0 \quad \text{in } V; \quad u^2_i = 0 \;\text{ on } \partial V;\; \text{ with } \sigma^2_{ij} = \mathbb{C}_{ijkl}\,\varepsilon^2_{kl} + \sigma^p_{ij} \tag{8}$$

If the average stress is denoted by Σ^2_{ij}, we can conveniently apply Hill-Mandel lemma together with Maxwell-Betti reciprocal work theorem to fields ε^1_{ij} and σ^2_{ij} to get $\left\langle \sigma^2_{ij}\,\varepsilon^1_{ij}\right\rangle^{rev} = \left\langle \mathbb{C}_{ijkl}\,\varepsilon^2_{kl}\,\varepsilon^1_{ij}\right\rangle^{rev} + \left\langle \sigma^p_{ij}\,\varepsilon^1_{ij}\right\rangle^{rev} = \Sigma^2_{ij}\,E_{ij}$. Further applying Hill-Mandel lemma to ε^2_{ij} and σ^1_{ij} gives: $\left\langle \sigma^1_{ij}\,\varepsilon^2_{ij}\right\rangle^{rev} = \left\langle \mathbb{C}_{ijkl}\,\varepsilon^1_{kl}\,\varepsilon^2_{ij}\right\rangle^{rev} = \Sigma^1_{ij}\left\langle \varepsilon^2_{ij}\right\rangle^{rev} = 0$. Based on the above, $\left\langle \sigma^2_{ij}\,\varepsilon^1_{ij}\right\rangle^{rev} = \left\langle \sigma^p_{ij}\,\varepsilon^1_{ij}\right\rangle^{rev} = \Sigma^2_{ij}\,E_{ij}$ and since $\varepsilon^1_{ij} = A_{ijkl}E_{kl}$, we finally arrive in terms of microvariables that $\Sigma^2_{ij} = \left\langle \sigma^p_{kl}A_{klij}\right\rangle^{rev} = f\,\sigma^p_{kl}\langle A_{klij}\rangle^l$.

The macroscopic stress Σ_{ij} over the REV consisting of an assembly of clay platelets with the micro-void space fully saturated with fluid is found by superposition of the two solutions, i.e.

$$\Sigma_{ij} = \Sigma^1_{ij} + \Sigma^2_{ij} = \bar{\mathbb{C}}_{ijkl}\,E_{kl} + f\,\sigma^p_{kl}\,\langle A_{klij}\rangle^l \tag{9}$$

where $\bar{\mathbb{C}}_{ijkl}$ is the homogenized constitutive tensor in Eq. (7). The calculation of the average stress as carried out herein refers to Levin's theorem (Levin 1967).

The solid phase (clay platelets) is incompressible, and hence the fluid phase only contributes to volumetric strains. In other words, the net amount from fluid flux in/out of the REV gives rise to inviscid deformations. Applying the volume average operator to the REV to strains in each of the phases, we finally find that the localization term for the fluid leads to $f\,\delta_{ij}\,\langle A_{ijkl}\rangle^l = \delta_{kl}$ so that Eq. (9) then becomes:

$$\begin{aligned} \Sigma_{ij} &= \bar{\mathbb{C}}_{ijkl}\,E_{kl} - p^l\delta_{ij} - \pi^s_0\beta_{ij};\;\; \beta_{ij} = f\,n_k\,n_l\langle A_{klij}\rangle^l \\ \bar{\mathbb{C}}_{ijkl} &= \mathbb{D}_{ijkl} - f\,h_0\,\tfrac{\partial \pi^s}{\partial h}\,n_i\,n_j\,\beta_{kl};\;\; \mathbb{D}_{ijkl} = \mathbb{C}^s_{ijmn}(I_{mnkl} - f\langle A_{mnkl}\rangle^l) \end{aligned} \tag{10}$$

The only step that remains to be completed is to derive the proper expression for the localization tensor A_{ijkl} which describes the microstructural arrangement of the fluid filled oblate-shaped inclusions in the clay matrix (Fig. 2). This matrix-inclusion-type configuration is well adapted to the Mori-Tanaka scheme (Mori and Tanaka 1972) which gives a solution for A_{ijkl} in the case of elliptical pores embedded into an elastic matrix subjected to a uniform strain on the boundaries. The solution is expressed based on Eshelby tensor N^s_{ijkl} (Mura 1987) of the solid phase and as such the localization tensors for fluid and solid phases are:

$$\langle A_{ijkl}\rangle^l = \left[I_{ijkl} - (1-f)N^s_{ijkl}\right]^{-1}; \quad \langle A_{ijkl}\rangle^s = \left[(1-f)I_{ijkl} - f(I_{ijkl} - N^s_{ijkl})\right]^{-1} \tag{11}$$

If we consider the limit $w = h/\ell \to 0$ (hairline inclusions) together with an infinite number of cracks and $v^s = 0.5$ as Poisson's ratio of the solid phase, the expression for the homogenized stress in the clay platelet stack with orientation $\mathbf{n}$ and micro porosity f is recalled and completed with further details:

$$\begin{aligned}
&\Sigma_{ij} = \bar{\mathbb{C}}_{ijkl}\,E_{kl} - p^l\delta_{ij} - \pi^s_0\beta_{ij}; \quad \bar{\mathbb{C}}_{ijkl} = \mathbb{D}_{ijkl} - fh_0\,\tfrac{\partial\pi^s}{\partial h}\,n_i\,n_j\,\beta_{kl};\\
&\beta_{ij} = \delta_{ij} - f(\delta_{ij} - n_i n_j);\\
&\mathbb{D}_{1111} = 4\mu^s(1-f); \ \mathbb{D}_{1122} = 2\mu^s(1-f);\\
&\mathbb{D}_{1212} = \mu^s(1-f); \ \text{other components are zero.}
\end{aligned} \tag{12}$$

It is seen in the above that the homogenized constitutive tensor $\bar{\mathbb{C}}_{ijkl}$ for the clay platelet stack is transversely isotropic with the first term $\mathbb{D}_{ijkl}$ describing the elasticity of the clay platelets, and a second term relating the contribution of electrochemical interactions, i.e. microscopic repulsive electrostatic forces. This emerges as a result of the coupling between electrochemical stress and deformation in our formulation. The effect of van der Waals forces between platelets in addition to electrostatic double layer forces is considered in a separate study (Wan and Eghbalian 2016).

Upscaling from Micro- to Macro-level

The next step is to move up to the macro scale where the REV is comprised of an arrangement of individual expansive shale particles with the void space being partially occupied by the same electrolyte solution as in the nano-pores at the previous scale of investigation. This scale refers to a material point in a typical finite element computation of a boundary value problem. An isotropic distribution of shale particles forming the solid phase is assumed for simplicity which, as mentioned earlier, refers to the case of remoulded shale samples. As such, an idealization of the 3-phase system leads to an REV with a continuous solid phase within which are embedded spherical inclusions saturated by either gas or liquid, as illustrated in Fig. 4.

Because of partially saturated conditions, capillary stresses due to the difference between the gas and liquid phases enter the stress formulation. Also, since the pores are all connected and are under thermodynamic equilibrium, the gas, liquid and capillary pressures are the same throughout the REV. Surface tensions in solid-liquid (γ^{sl}) and solid-gas (γ^{sg}) interfaces are considered in addition to liquid and gas pressures p^l and p^g respectively (Chateau and Dormieux 2002; Dormieux et al. 2006a). Furthermore, the stress tensor within the membrane with normal n_i separating 2 phases α and β must be considered and is given as $\omega^{\alpha\beta}_{ij} = \gamma^{\alpha\beta}(\delta_{ij} - n_i n_j)$ along the formed interface $\Gamma^{\alpha\beta}$.

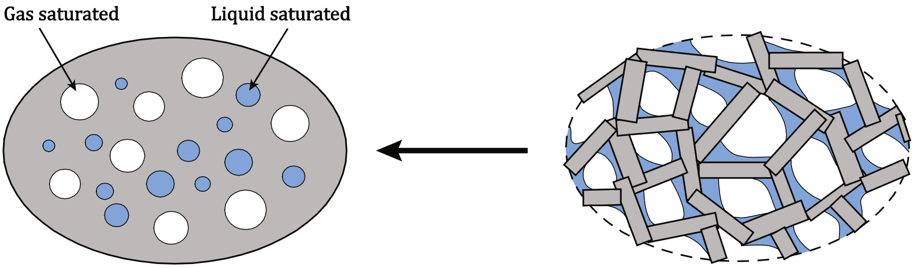

Fig. 4. Idealization of microscale into REV with spherical inclusions.

We will follow the template presented in the previous section to express the 'macroscopic' stress of the REV in terms of 'micro-constituents', i.e.

$$\sigma_{ij}(\mathbf{x}) = \left\{ \begin{array}{l} 0 \\ 0 \\ 0 \\ 0 \\ \bar{\mathbb{C}}_{ijkl} \end{array} \right. \varepsilon_{kl}(\mathbf{x}) \; + \left\{ \begin{array}{ll} -p^l\delta_{ij} & V^l \\ -p^g\delta_{ij} & V^g \\ \gamma^{sl}(\delta_{ij} - n_i n_j) & \Gamma^{sl} \\ \gamma^{sg}(\delta_{ij} - n_i n_j) & \Gamma^{sg} \\ -p^l\delta_{ij} - \pi_0^s\beta_{ij} & V^s \end{array} \right. \tag{13}$$

in the REV subjected to a uniform strain E_{ij} on its boundary.

In Eq. (13), the solid phase is described by the homogenized constitutive tensor and the pre-stress derived at the previous scale, i.e. Eq. (12). As before we derive the expression of the new homogenized stress Σ_{ij} in the REV at the macroscale (Fig. 4). Again, two sub-problems are examined: one in which pre-stresses are blocked with the application of uniform strains on the boundary, and the other where pre-stresses are introduced with zero strains on the boundary. The solutions of the two problems, found by applying Hill-Mandel condition as in the template, superimposed eventually lead to the following expression for the homogenized stress Σ_{ij} where surface tension forces have vanished since the interface between liquid and gas (Γ^{lg}) was ignored:

$$\begin{array}{l} \Sigma_{ij} = \bar{\mathbb{C}}^{sc}_{ijkl}E_{kl} - p^c(S^p - 1)B_{ij} - p^l\delta_{ij} - R_{ij}; \quad \bar{\mathbb{C}}^{sc}_{ijkl} = (1-\varphi^p)\left\langle \bar{\mathbb{C}}_{ijmn}A_{mnkl}\right\rangle^s \\ R_{ij} = (1-\varphi^p)\left\langle \beta_{kl}A_{klij}\right\rangle^s\pi_0^s; \quad B_{ij} = \varphi^p\left\langle A_{klij}\right\rangle^p\delta_{kl} \end{array} \tag{14}$$

where superscript 'p' refers to the pore space containing gas and liquid phases, $\varphi^p = (V^g + V^l)/V$ is the porosity, $p_c = p^g - p^l$ the matric suction, $S^p = V^l/V^p$ is the liquid degree of saturation, and finally B_{ij} is the tensorial form of Bishop's parameter. The contribution of surface tension forces is studied in the case of a cracked clay sample in Wan and Eghbalian (2016). Also, note that A_{ijkl} is the new localization tensor in this upscaling that can be estimated over the solid and fluid phases using this time the self-consistent scheme (Budiansky 1965; Hill 1965). This scheme is suitable for poly-crystalline structures, where neither of phases can be considered as matrix or inclusion, such as the one shown is Fig. 4. Finally, we get the following expression:

$$\begin{aligned}
&\bar{\mathbb{C}}^{sc}_{ijkl} = k^{sc}\,\delta_{ij}\delta_{kl} + 2\mu^{sc}\left[\tfrac{1}{2}(\delta_{il}\delta_{kj} + \delta_{ik}\delta_{jl}) - \tfrac{1}{3}\delta_{ij}\delta_{kl}\right] \\
&k^{sc} = -h_0 \frac{\partial \pi^s}{\partial h}\Big|_{(h_0, n_0^s)} \left[\frac{f\,(1-4\varphi^p)(\varphi^p+2)(7\varphi^p+2)}{12(2-3\varphi^p)(1+\varphi^p)\varphi^p}\right] \\
&\mu^{sc} = -h_0 \frac{\partial \pi^s}{\partial h}\Big|_{(h_0, n_0^s)} \left[\frac{f\,(\varphi^p+2)(1-4\varphi^p)}{16(1+\varphi^p)\varphi^p}\right] \\
&R_{ij} = \pi_0^s \frac{(\varphi^p+2)(1-4\varphi^p)}{(2-3\varphi^p)}\,\delta_{ij}; \quad B_{ij} = \pi_0^s \frac{4\varphi^p(1+\varphi^p)}{(2-3\varphi^p)}\,\delta_{ij}
\end{aligned} \tag{15}$$

while the capillary pressure is simply made to follow the degree of saturation based on van Genuchten equation (van Genuchten 1980) with p_0^c and λ as model parameters, i.e.

$$S^p = \left[1 + \left(\frac{p^c}{p_0^c}\right)^{\frac{1}{1-\lambda}}\right]^{-\lambda} \tag{16}$$

On an ending note, it should be mentioned that a different mathematical approach based on asymptotic expansion technique was presented in Murad and Moyne (2006a,b) and Mainka et al. (2013) to study the partially saturated conditions in swelling clays.

Concluding Remarks

This short paper outlines the main steps involved in the micro-poromechanical formulation of 'effective' stresses in clay-shale spanning the macro- and nano-scale with two levels of porosity and homogenization treatments. Details of the homogenization procedural calculations are presented for the transfer from nano-scale physics involving shale particles with saturated nano-pores to the micro-scale where micro-pores between an aggregate of shale particles are partially filled with water. The shale sample is assumed to consist only of clay with the smectite being the dominant mineral giving the system a swelling characteristics. In the end, a tensorial stress expression is obtained identifying the various contributions such as elasticity, capillary and swelling stresses. The latter is directly upscaled from electrostatic force computations at the clay platelet level by solving Poisson-Boltzmann equation. All poro-mechanical features of the system including elastic properties and a tensorial form of Bishop's coefficient (Eq. 14) are explicitly presented based on pertinent microscopic properties of the clay shale system. Thus, the model can readily simulate complex swelling and shrinkage of clay-shales using basic intrinsic parameters.

Acknowledgements. Financial support for this research was provided by the Natural Sciences and Engineering Research Council of Canada (NSERC) and Foundation CMG.

References

Budiansky B (1965) On the elastic moduli of some heterogeneous materials. J Mech Phys Solids 13:223–227

Cariou S, Dormieux L, Skoczylas F (2013) An original constitutive law for Callovo-Oxfordian argillite, a two-scale double-porosity material. Appl Clay Sci 80–81:18–30

Chateau X, Dormieux L (2002) Micromechanics of saturated and unsaturated porous media. Int J Numer Anal Methods Geomech 26(8):831–844

Dormieux L, Kondo D, Ulm F-J (2006a) Microporomechanics. Wiley, Chichester. doi:10.1002/0470032006

Dormieux L, Lemarchand E, Coussy O (2003) Macroscopic and micromechanical approaches to the modelling of the osmotic swelling in clays. Transp Porous Media 50(1–2):75–91

Dormieux L, Lemarchand E, Sanahuja J (2006b) Comportement macroscopique des mat´eriaux poreux `a microstructure en feuillets. Comptes Rendus - Mec 334(5):304–310

Hill R (1965) A self-consistent mechanics of composite materials. J Mech Phys Solids 13:213–222

Huyghe J, Janssen J (1997) Quadriphasic mechanics of swelling incompressible porous media. Int J Eng Sci 35(8):793–802. doi:10.1016/S0020-7225(96)00119-X

Levin V (1967) Thermal expansion coefficient of heterogeneous materials. Mekhanika Tverd Tela 2:83–94

Mainka J, Murad AM, Moyne C, Lima AS (2013) A modified form of Terzaghi's effective stress principle of unsaturated expansive clays derived from micromechanical analysis. In: Hellmich C, Pichler B, Adam D (eds) Fifth Biot Conf Poromechanics. American Society of Civil Engineers, Vienna, Austria, pp 1425–1434

Moyne C, Murad M (2003) Macroscopic behavior of swelling porous media derived from micromechanical analysis. Transp Porous Media 50(1–2):127–151

Moyne C, Murad MA (2006a) A two-scale model for coupled electro-chemo-mechanical phenomena and Onsager's reciprocity relations in expansive clays: I Homogenization Analysis. Transp Porous Media 62(1):333–380

Moyne C, Murad MA (2006b) A two-scale model for coupled electro-chemo-mechanical phenomena and Onsager's reciprocity relations in expansive clays: II computational validation. Transp Porous Media 63(1):13–56

Mura T (1987) Micromechanics of defects in solids. Mechanics of elastic and inelastic solids. vol 3, 2nd edn. Springer, Dordrecht. doi:10.1007/978-94-009-3489-4

Pichler B, Dormieux L (2009) Cracking risk of partially saturated porous media-part I: microporoelasticity model. Int J Numer Anal Methods Geomech 34:135–157

Sposito G (1972) Thermodynamics of swelling clay-water systems. Soil Sci 114(4)

Sridharan A, Rao GV (1973) Mechanisms controlling volume change of saturated clays and the role of the effective stress concept. Geotechnique 23(3):359–382. doi:10.1680/geot.1973.23.3.359

Tanaka K, Mori T (1972) Note on volume integrals of the elastic field around an ellipsoidal inclusion. J Elasticity 2:199–200

Van Genuchten MT (1980) A closed-form equation for predicting the hydraulic conductivity of unsaturated soils. Soil Sci Soc Am J 44(5):892–898

Wan RG, Eghbalian M (2016) Micromechanics approach to swelling behaviour of capillary-porous media with coupled physics. Submitted to Transport Porous Med

Feature Lectures

Measurement of Supercritical CO_2 Permeability in Porous Rock at Reservoir Conditions

F. Zhang[1,2(✉)], B. Ye[2], W.M. Ye[2], and L. Xua[2]

[1] Nagoya Institute of Technology, Nagoya, Japan
cho.ho@nitech.ac.jp
[2] Tongji University, Shanghai, China

Abstract. In CO_2 capture and storage (CCS) projects, measuring permeability of supercritical CO_2 in porous rock is a key important factor in predicting the migration and evaluating the long-term stability of injected CO_2. In this paper, a new device for measuring CO_2 permeability coefficient in porous rock at reservoir conditions is described, in which the pressure and temperature of injected CO_2 are usually at supercritical state. In the measurement, the supercritical CO_2 flowing through rock samples is depressurized to gaseous phase whose flow rate could be easily measured with normal gas meters. An average flow rate over a period of time is used to calculate the permeability of CO_2 in rock sample under supercritical state. An application example using a siltstone for testing proves that the device can measure the permeability of supercritical CO_2 in porous rock effectively.

Introduction

In CO_2 capture and storage projects (CCS), accurately measuring permeability of supercritical CO_2 in porous rocks is of great significance in predicting the migration and evaluating the long-term stability of injected CO_2. The injected CO_2 in CCS is usually under supercritical state, i.e., its pressure and temperature are beyond the critical point (7.38 MPa and 31.8 °C). The confining pressure for the reservoir rock is also high due to the thick overburden ground layers. Therefore, in order to measure the permeability of supercritical CO_2 in porous rock under reservoir conditions, the test device must be able to apply high confining pressure to the samples and inject CO_2 at high pressures at controlled temperature. Two kinds of flowing test of CO_2 in the laboratory are usually adopted, one is steady-state method and another is unsteady-state method. In unsteady-state method, the flow-rate and the pressure of CO_2 do not keep constant during test, and therefore the permeability can only be evaluated empirically based on a given mathematical model. While in steady-state method, the flow-rate and the pressures are in a steady state and is more suitable for measuring the permeability directly. Relatively few researches (Akbarabadi and Piri 2013; Zuo et al. 2012; Krevor et al. 2012; Perrin and Benson 2010; Perrin et al. 2009; Luquot and Gouze 2009) were reported with the steady-state method because the testis more time consuming and complicated.

A. Ferrari and L. Laloui (eds.), *Advances in Laboratory Testing and Modelling of Soils and Shales (ATMSS)*, Springer Series in Geomechanics and Geoengineering,
DOI 10.1007/978-3-319-52773-4_7

In this study, a new device based on steady-state method was developed to conduct supercritical CO_2 seepage tests at high confining and injection pressures under controllable temperature, satisfying the real situation in CCS. The device is very simple but effective and easy to be handled.

Description of Test Device

The newly-developed test device for supercritical CO_2 is shown in Photo 1. The device consists of a pressure cell, a syringe pump for CO_2, a pressure amplifier for confining pressure, a heating unit, and a measurement system. Figure 1 shows a schematic diagram of supercritical CO_2 measuring device. The pressure cell is used to provide a seepage chamber for the test. Figure 2 shows Sectional views of pressure cell. The shell of the cell body consists of a base plate and a top cover, as shown in Fig. 2(a). The base plate and top cover are made of stainless steel, and their minimum thickness is 15 mm in order to be able to withstand the high hydraulic pressure in the seepage chamber during the test. The top cover is fixed on the base plate by 12 screw bolts. In the seepage chamber, the rock sample is placed between two metal pedestals with a diameter of 50 mm. The two pedestals are linked by two springs to tightly clamp the sample. Both pedestals have a hole in the center. The lower pedestal connects with the CO_2 inlet pipe, and the upper pedestal connects with the CO_2 outlet pipe. During the test, CO_2 flows through the rock sample from the lower pedestal to the upper pedestal. Two porous metal plates are buried in the upper and lower pedestals to ensure an even flow of CO_2 within the sample. A heating pipe is set in the seepage chamber and by the side of the sample, which is connected to water bath pipe. A drainage valve is set on the top cover, which can be used to drain the water from the seepage chamber after testing. A safety valve that can release the cell pressure once it exceeds an alarm value is installed next to the drainage valve. As shown in Fig. 2(b), five valves are set around the base plate, which can control the inflows and outflows of CO_2, the water bath and confining pressure.

As shown in Fig. 1, a syringe pump is employed to pressurize the CO_2 from a gas cylinder to reach an expected pressure. Because the pump is hydraulic and can only work on liquid fluid, a freezer is used to first cool the gaseous CO_2 to the liquid state before it is sent to the syringe pump. The syringe pump can pressurize the liquid CO_2 up to 15 MPa.

The syringe pump is connected to two buffer tanks, i.e., the inlet buffer tank and the outlet buffer tank, with 1/8-inch stainless steel pipes. These two tanks are used to keep the inlet and outlet pressures of CO_2 steady during testing. Both tanks have a volume of 100 ml. The pressurized liquid CO_2 from the syringe pump is first stored in the inlet buffer tank and then flows to the seepage chamber. In the seepage chamber, it is heated by the heating unit and reaches the supercritical state. The CO_2 flowing out of the seepage chamber is first stored in the outlet buffer tank and then flows to the flow rate meter to measure its flow rate. During testing, the temperature of the seepage chamber should exceed 31.8 °C and the CO_2 pressure in the outlet buffer tank should exceed 7.38 MPa to guarantee that the CO_2 is in a supercritical state. Moreover, the pressure in the inlet buffer tank should always exceed the pressure in the outlet buffer tank so that the pressure difference can continuously drive the seepage process.

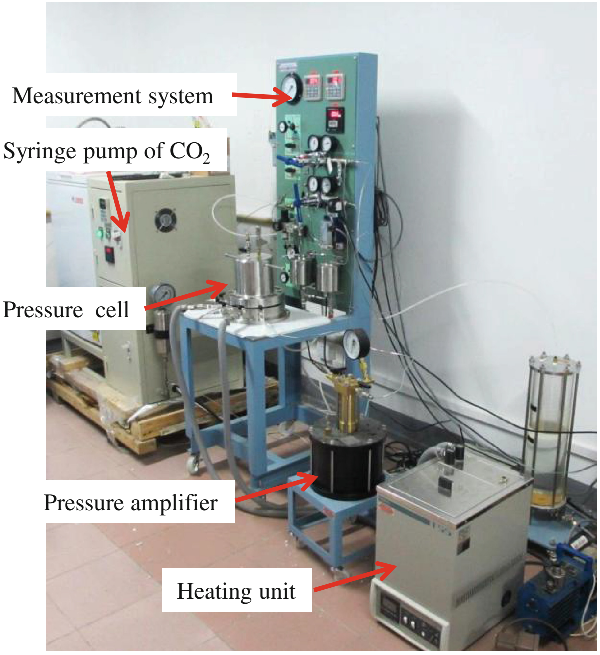

Photo 1: Newly-developed measuring device for supercritical CO2.

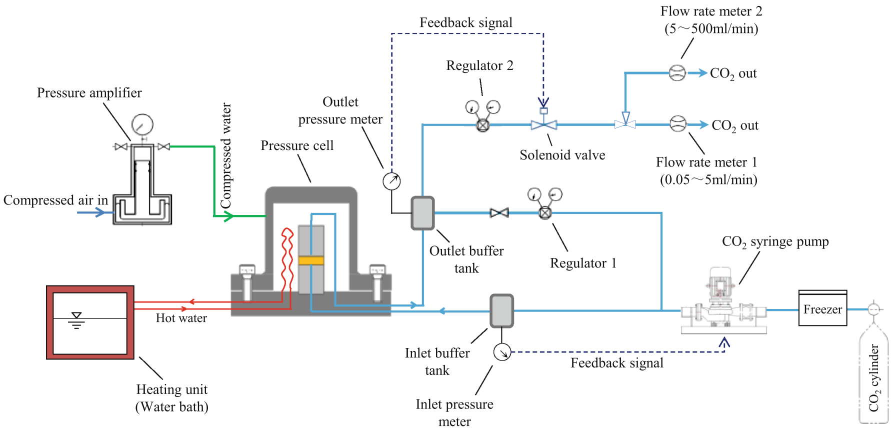

Fig. 1. Schematic diagram of newly-developed measuring device for supercritical CO_2.

Because the seepage rate of CO_2 in rock is slow, the process of accumulating pressure in the outlet buffer tank to the expected value from zero pressure is lengthy. Therefore, another pipeline is used to connect the syringe pump to the outlet buffer tank, as shown in Fig. 1. Before the seepage test starts, the syringe pump can directly inject CO_2 into the outlet buffer tank and allow the pressure in the outlet buffer tank to

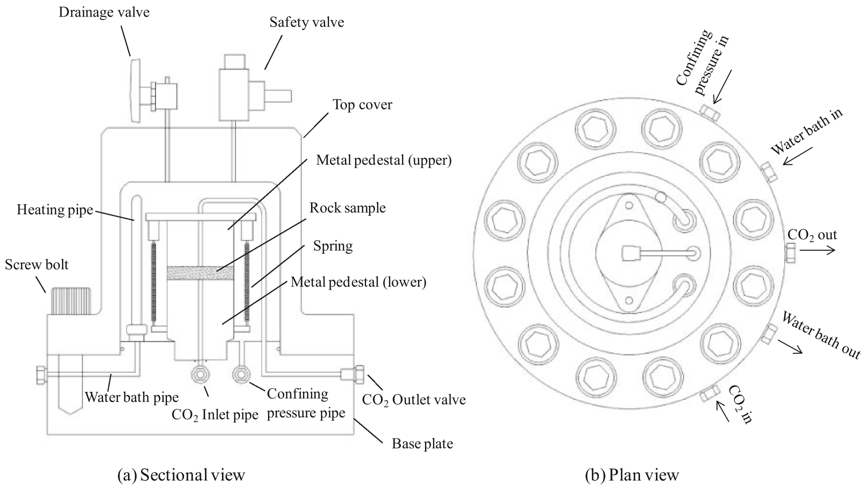

Fig. 2. Sectional views of pressure cell.

quickly reach the expected value. A regulator can adjust the pressure in the outlet buffer tank. When the seepage test begins, the pipeline that links the outlet buffer tank and the syringe pump will switch off.

The pressure amplifier is used to provide the required confining pressure to the rock sample by pressurizing water in the seepage chamber. The schematic diagram of pressure amplifier is shown in Fig. 3. It features two cylindrical pressure chambers with different diameters. The lower chamber is filled with air and has a larger diameter, whereas the upper one is filled with water and has a smaller diameter. A piston links these two pressure chambers. An air compressor is employed to pressurize the air in the air pressure chamber. The pressurized air pushes the piston upward and pressurizes the water in the water pressure chamber. Because the sectional area of the air pressure chamber is 30 times that of the water pressure chamber, the pressure in the air pressure chamber can be amplified to 30 times that of the water pressure chamber. The water pressure chamber is connected to the pressure cell by stainless steel pipelines. Thus, the amplified water pressure can be transferred to the water in the seepage chamber, which can provide the required confining pressure. A regulator is set at the air entrance of the pressure amplifier. The regulator can adjust the pressure in the air pressure chamber and thereby control the confining pressure in the seepage chamber.

The heating unit is a thermostatic water cycling device that can elevate and control the temperature of the seepage chamber by the water bath method. The unit contains a 10-liter thermostatic water tank. When the heating unit operates, an electric heater warms the water in the tank, and the water temperature is held constant during testing. The heated water is pumped into the pressure cell through a sealed spiral heating tube in the pressure cell to heat the surrounding water within the cell. Throughout the thermal circular system, the temperature of the pressure cell can be controlled to a prescribed value in a very high accuracy with an error less than ±0.1 °C.

A pressure meter measures the injection pressure of CO_2 at the inlet buffer tank. This pressure meter can send feedback signals to the CO_2 syringe pump. If the injection

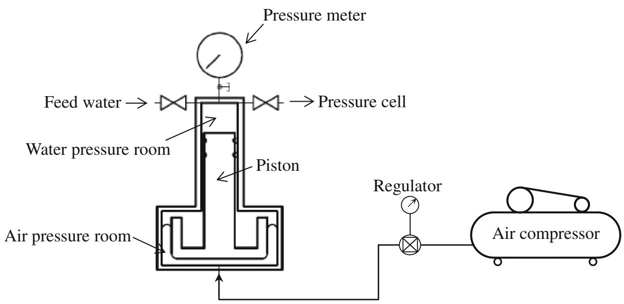

Fig. 3. Schematic diagram of pressure amplifier.

pressure falls below or exceeds the expected values, the syringe pump can start or stop automatically according to the feedback signals. The outlet pressure of CO_2 is measured at the outlet buffer tank by another pressure meter.

The flow rate of CO_2 is measured at the outlet pipe, which is connected to the outlet buffer tank. As discussed above, the pressure in the outlet buffer tank should exceed 7.38 MPa. However, commonly employed flow rate meters cannot operate at such high pressures. Therefore, a solenoid valve and a regulator are set between the outlet buffer tank and the flow meter. The solenoid valve is normally closed during testing. The CO_2 flowing through the sample will accumulate in the outlet buffer tank, and its pressure will slowly increase. When the cumulative pressure exceeds a preset upper limit, the pressure meter at the outlet buffer tank will send a feedback signal to the solenoid valve to open it. The CO_2 stored in the outlet buffer tank then flows to the regulator to reduce the CO_2 pressure to one atmosphere. During this depressurization process, the CO_2 transitions from the supercritical state to the gaseous state, and the flow rate meter can measure its flow rate at these reduced pressures. After the solenoid valve opens, the pressure in the outlet buffer tank will decrease due to the outflow of CO_2. Once the pressure in outlet buffer tank falls below a preset lower limit, the solenoid valve will close. The pressure in the buffer tank will accumulate until it exceeds the upper limit, and the solenoid valve will open again. In this way, even though the CO_2 outlet pressure cannot remain constant, it can be restricted between the preset upper and lower limits. The preset upper and lower pressure limits of the solenoid valve are determined according to the testing requirement. Generally, the upper limit can be set as the desired value of the outlet pressure, and the lower limit can be set a little less than the upper limit. Notably, the flow rate meter does not measure the continuous real-time flow rate of CO_2 that flows through the sample in this setup but an instantaneous flow rate when the solenoid valve opens. However, an average flow rate is easily obtained by integrating the volume of CO_2 that flows through the flow meter over a certain period. Due to the depressurization process, the CO_2 volume is measured in the gaseous state, and this volume should be converted to the supercritical state volume according to the density ratio under different conditions.

Because the permeability of different rocks varies greatly, two flow rate meters with different measurement ranges are prepared. One can measure the flow rate of gaseous CO_2 from 0.005 ml/min to 5 ml/min, and the other can measure larger flow rates ranging from 5 ml/min to 500 ml/min. These two meters can be switched over by a three-way valve. By combining these two flow rate meters, the device can measure the permeability within a range of approximately 10^{-14} m/s to 10^{-9} m/s.

Tests on Bentonite and Rock Samples

The rock sample used in this study was prepared to a diameter of 5 cm and height of 1 cm and placed between the two metal pedestals. The sample was sealed with a transparent Teflon thermoplastic tube to exclude the water used as the hydraulic confining pressure medium. Photo 2 shows the rock sample installed in pressure cell and the bentonite sample.

The test procedures are defined as follows:

(1) After the rock sample is installed, the top cover of the pressure cell is fixed on the base plate.
(2) The seepage chamber is filled with water, and the pressure amplifier applies a hydraulic confining pressure to the rock sample.
(3) The seepage chamber is heated with the heating unit to reach the desired temperature.
(4) The syringe pump is opened, and CO_2 is injected into the inlet and outlet buffer tanks. When the pressure in the outlet buffer tank reaches the expected value, it is disconnected from the syringe pump.
(5) The syringe pump continues to inject CO_2 into the inlet buffer tank until its pressure reaches the expected value, which should exceed the pressure in the outlet buffer tank.
(6) The inlet and outlet valves in the pressure cell body are opened, and the CO_2 is allowed flow through the samples for a given time to expel the air within the samples and pipes.
(7) The measurement system is opened, and the inlet pressure, outlet pressure, and flow rate of CO_2 are recorded.

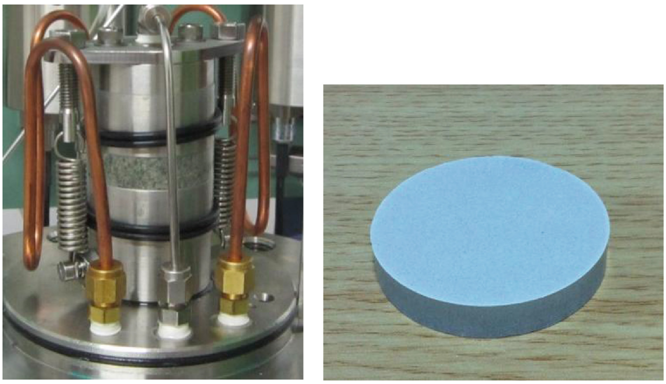

(a) Rock sample (b) Bentonite sample

Photo 2: Rock sample installed in pressure cell and bentonite sample.

Test using the new device was first carried out on a bentonite sample. The bentonite, called GMZ01, was obtained from Inner Mongolia, China. Before testing, the sample was compacted to a dry density of 1.90 g/cm^3 (with a void ratio of e = 0.40 and a natural moisture content of w = 10.56%).

The performance test was conducted according to the experimental protocol described in the previous section. The confining pressure was set to 15 MPa, and the temperature was set to 45 °C. The inlet pressure (injection pressure) of CO_2 was set to approximately 10 MPa, and the outlet pressure (back pressure) was set to approximately 9 MPa. Thus, CO_2 passed through the sample under a pressure difference of approximately 1 MPa. The seepage process only persisted for a short period of 582 s to demonstrate the detailed characteristics of the measured pressure and flow rate data.

Figure 4 displays the time history of pressure and flow rate for bentonite in supercritical CO2 seepage test. The two pressures were measured at the inlet and outlet buffer tanks. As shown in Fig. 4, the inlet pressure slowly decreased as the CO_2 flowed out of the inlet buffer tank after the start of the seepage test. When the inlet pressure decreased below the lower limit (Point A in Fig. 4), the syringe pump began to operate and injected CO_2 into the inlet buffer tank. The inlet pressure began to increase. When the inlet pressure exceeded the upper limit (Point B in Fig. 4), the syringe pump stopped, and the inlet pressure began to decrease again. Therefore, the inlet pressure fluctuated around 10 MPa. When the CO_2 accumulated in the outlet buffer tank, the outlet pressure slowly increased. Once the outlet pressure exceeded the upper limit (Point C in Fig. 4), the solenoid valve opened, and the CO_2 began to flow out of the outlet buffer tank. The outlet pressure soon fell to the lower limit (Point D in Fig. 4), and the solenoid valve closed. The CO_2 began to accumulate again. Therefore, the outlet pressure also fluctuated around 9 MPa. Moreover, the CO_2 flowing out of the outlet buffer tank was depressurized to a gaseous state and its flow rate was measured

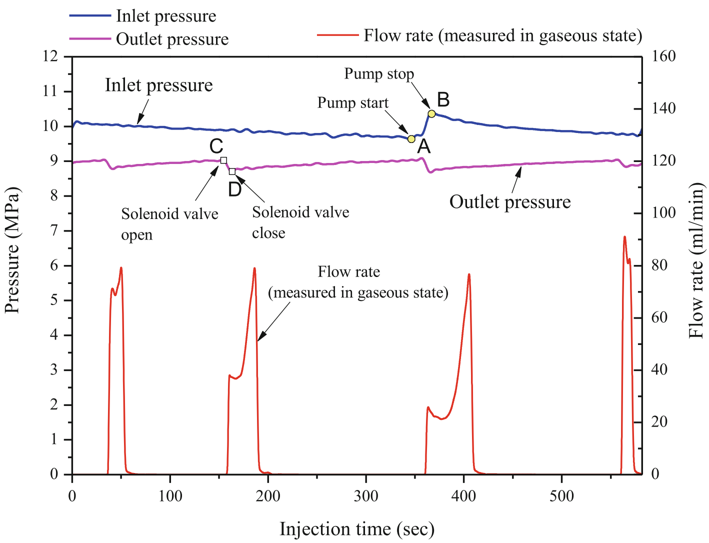

Fig. 4. Time history of pressure and flow rate of supercritical CO_2 for bentonite.

with the flow meter. As discussed above, this flow rate is measured in the gaseous state and is not the real-time value of the CO_2 that seeps through rock samples. Rather, it is an instantaneous value measured when the solenoid valve opened. Therefore, the measured flow rate curve exhibited a pulse profile.

Because the inlet and outlet pressures were not constant during the seepage process, an average value of the inlet and outlet pressures was used to calculate the CO_2 permeability. Similarly, an average flow rate over a certain period can also be easily obtained with simple calculation. Based on the assumption that the supercritical CO_2 flow still obeys the Darcy's law, the permeability of supercritical CO_2 in rock can then be easily obtained. The measured data for bentonite are shown in Table 1. It is clearly that the newly developed device can measure the permeability of supercritical CO_2 accurately under high pressure and controllable temperature.

Table 1. Measured data for bentonite.

Average inlet pressure, $\bar{p}_{in}$	9.91 MPa
Average outlet pressure, $\bar{p}_{out}$	8.92 MPa
Total volume of CO_2 in gaseous state	85.0 ml
Average flow rate, $\bar{q}_{gas}$ (in gaseous state)	8.73 ml/min
Average flow rate, $\bar{q}_{sc}$ (in supercritical state)	0.0444 ml/min
Permeability, k (in supercritical state)	3.73×10^{-11} m/s

As the second application, the seepage test was conducted on highly porous (44%) silt rock sampled from the Boso Peninsula, Japan. The testing conditions were the same as those of the performance test described in the previous section, i.e., the confining pressure, the temperature, the inlet pressure and the outlet pressure were set to 15 MPa, 45 °C, 10 MPa and 9 MPa, respectively.

Because the syringe pump started and stopped according to the preset lower and upper limits of the pressure in the inlet buffer tank, the inlet pressure fluctuated around 10 MPa. The solenoid valve controlled the outlet flow of CO_2; thus, the outlet pressure also fluctuated around 9 MPa. The integrated flow rate of CO_2 is measured at gaseous state on which flow rate of supercritical CO_2 is estimated. The integrated flow, Q_{gas}, is a nearly linear function of time, which indicates that the assumption that the flow of supercritical CO_2 in the rock obeys Darcy's law is reasonable. The results calculated for the silt rock are shown in Table 2. The permeability of supercritical CO_2 in the sample was determined to be 3.90×10^{-11} m/s.

Table 2. Measured data for silt rock.

Average inlet pressure, $\bar{p}_{in}$	9.92 MPa
Average outlet pressure, $\bar{p}_{out}$	8.90 MPa
Total volume of CO_2 in gaseous state	587.1 ml
Average flow rate, $\bar{q}_{gas}$ (in gaseous state)	9.78 ml/min
Average flow rate, $\bar{q}_{sc}$ (in supercritical state)	0.0480 ml/min
Permeability, k (in supercritical state)	3.90×10^{-11} m/s

Conclusions

A test device is newly designed to measure the permeability of supercritical CO_2 in porous rock, having the ability to apply a high confining pressure to rock samples and to inject CO_2 at high pressures and controllable temperatures. The main conclusions are as follows:

(1) Instead of measuring directly the flow rate of supercritical $CO_{2,}$ by some elaborately arrangement of reducing the pressure with buffer tanks and pressure-controllable solenoid valves and regulators, it is possible to measure the flow rate of depressurized gaseous CO_2, based on which the permeability of supercritical CO_2 can easily be evaluated.
(2) The proposed methodology can avoid using any expensive flow meters that are very expensive and could not be afford to buy in normal laboratory. And above all, the device is easy to handle.
(3) Performance tests on bentonite and rock samples proved that the newly developed device can provide satisfactory performance.

References

Akbarabadi M, Piri M (2013) Relative permeability hysteresis and capillary trapping characteristics of supercritical CO_2/brine system: an experiment study at reservoir conditions. Adv Water Resour 52:190–206

Krevor SCM, Pini R, Zuo L, Benson SM (2012) Relative permeability and trapping of CO2 and water in sandstone rocks at reservoir conditions. Water Resour Res 48(2):W02532

Luquot L, Gouze P (2009) Experimental determination of porosity and permeability changes induced by injection of CO_2 into carbonate rocks. Chem Geol 265:148–159

Perrin JC, Benson SM (2010) An experimental study on the influence of sub-core scale heterogeneities on CO_2 distribution in reservoir rocks. Transp Porous Med 82:93–109

Perrin JC, Krause M, Kuo CW, Milijkovic L, Charoba E, Benson SM (2009) Core-scale experimental study of relative permeability properties of CO_2 and brine in reservoir rocks. Energy Proc 1:3515–3522

Zuo L, Krevor S, Falta RW, Benson SM (2012) An experimental study of CO_2 exsolution and relative permeability measurements during CO_2 saturated water depressurization. Transp Porous Med 91:459–478

Measurement of Mechanical Properties of Thin Clay Films and Comparison with Molecular Simulations

Benoit Carrier[1], Matthieu Vandamme[1(✉)], Roland Pellenq[2,3,4], and Henri Van Damme[2,3,4]

[1] Laboratoire Navier (UMR 8205), CNRS, ENPC, IFSTTAR, Université Paris-Est, 77455, Marne-la-Vallée, France
matthieu.vandamme@enpc.fr

[2] Department of Civil and Environmental Engineering, Massachusetts Institute of Technology, 77 Massachusetts Avenue, Cambridge, MA 02139 USA

[3] Centre Interdisciplinaire des Nanosciences de Marseille, CNRS (UPR 7251), Campus de Luminy, 13288, Marseille Cedex 09, France

[4] ⟨MSE⟩2, UMI 3466, CNRS-MIT, 77 Massachusetts Avenue, Cambridge, MA 02139 USA

Abstract. Here, we focus on the hydromechanical behavior of self-standing clay films with a thickness of a few dozen microns. We measure their elastic and creep properties and how those properties depend on the interlayer cation and on the relative humidity (or water content). Those experimental results are compared with the elastic and creep behavior of nanometric clay particles, which we characterize by molecular simulations. Significant qualitative differences between the behavior of the clay films and that of the clay particles are observed, which suggests that the hydromechanical behavior of the clay films is significantly impacted by their mesostructure (i.e., by how the clay particles or tactoids are arranged in space). Upscaling the hydromechanical behavior of the clay films from that of the clay particles may be challenging.

Introduction

Understanding the hydromechanical behavior (i.e., the effect of water content or relative humidity on the mechanical behavior) of clay-rich soils or rocks is of importance for a variety of applications relevant for civil or petroleum engineering. For instance, clayey soils shrink or expand upon drying or wetting, which can significantly damage buildings built on them. Another example is that of boreholes drilled through shales, whose stability can be impaired when the drilling fluid diffuses through the shale and makes it swell. One more example is that of the disposal of long-lived and high-level nuclear waste in France, for which deep geological disposal has been selected. The storage site should be implemented in a Callovo-Oxfordian argillite (i.e., a clay-rich rock), which will serve as the geological barrier which ensures appropriate containment of radionuclides: to estimate the quality of this containment, the hydromechanical behavior of the argillite must be well characterized and modeled.

A. Ferrari and L. Laloui (eds.), *Advances in Laboratory Testing and Modelling of Soils and Shales (ATMSS)*, Springer Series in Geomechanics and Geoengineering,
DOI 10.1007/978-3-319-52773-4_8

The hydromechanical coupling observed at the scale of the engineer originates from the nanometric scale of the clay particles of which clay-based materials are constituted. Therefore, many scientists aim at predicting the macroscopic hydromechanical behavior of the material by upscaling the hydromechanical behavior of the clay particle. However, their effort is impeded by the complexity of the material, which is often heterogeneous (e.g., clay-rich rocks are often not made of clay only) and with a complex microstructure: the characteristic size of heterogeneities can span several orders of magnitude, so that several steps of upscaling are required to move from the nanometric scale up to the macroscopic one.

Here, we study self-standing clay films (Carrier et al., 2013) with a thickness of a few dozen microns (see Fig. 1 left) –an idea inspired from the work of Zabat (1996) and Zabat et al. (1997). The motivation for studying such films is the following: we aim at designing the simplest and smallest clay-based systems on which we can perform regular tensile macroscopic testing. In the spirit of bottom-up approaches, aiming at performing a first step of upscaling, we then want to understand whether the mechanical behavior of the clay films (and its dependence on relative humidity and/or water content) can be predicted from that of the clay particle. Such understanding is the topic of this manuscript.

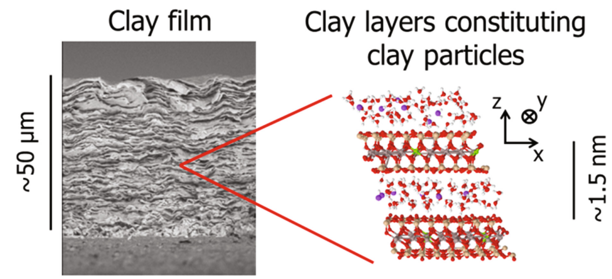

Fig. 1. Clay systems studied in this work: (left) self-standing clay films with a thickness of a few dozen microns, which we characterized experimentally, and (right) nanometer-thick clay layers, which we studied by molecular simulations.

To do so, here we study and compare two systems with different characteristic length scales (see Fig. 1): self-standing clay films with a thickness of a few dozen microns (see Fig. 1 left), and nanometer-thick clay layers of which clay particles are constituted (see Fig. 1 right). On both systems (i.e., at both scales), we study how elastic and creep properties depend on the interlayer cation, and on relative humidity or water content. The clay films are characterized experimentally, while the clay layers are studied by molecular simulations.

The manuscript is organized as follows. First, the materials and methods used to measure the elastic and creep properties of the self-standing clay films we manufactured are introduced. Then, the computational methods used to study the elastic and creep properties of the nanometric clay particles are described. Finally, the results of both studies are presented, compared, and discussed.

Materials and Experimental Methods for Characterization of Hydromechanical Behavior of Self-standing Clay Films

In this section, we present the materials and methods used for the measurement of the elastic and creep properties of our self-standing montmorillonite clay films with a thickness of about 50 μm. Details on how the samples were prepared can be found in (Carrier et al., 2013) and details on how their mechanical properties were measured can be found in (Carrier et al., 2016).

Manufacturing of Samples

The samples were made of the montmorillonite clay SWy-2. Three types of materials were used: the natural clay SWy-2 (which contains both Na^+ and Ca^{2+} interlayer cations, in approximate proportion of 2 to 1), the same clay homoionized with Na^+ cations, and the same clay but homoionized with Ca^{2+} cations.

The samples were manufactured with each of the 3 types of materials mentioned. Manufacturing consisted in preparing a slurry with the clay of interest, and in depositing the slurry on a polyethylene substrate. After evaporation, a clay film remained, with a diameter of several centimeters and a thickness of about 50 μm (see Fig. 1 left). This film could be peeled off from the substrate, so that the film was self-standing. For both experiments, samples were cut in those deposited films into rectangles of about 9.3 mm by 80 mm.

The order parameters, calculated from the analysis of rocking curves obtained by X-ray diffraction (Carrier et al., 2016), were at least equal to 0.66 for all films: the manufactured films were anisotropic, with the clay particles being preferentially oriented parallel to the substrate on which the film was deposited (see Fig. 1 left).

Measurement of Elastic and Creep Properties

The elastic and creep properties of the manufactured self-standing films were measured by tensile testing, in chambers in which both temperature and relative humidity were controlled. The temperature in the chambers was that of the room and was equal to about 25° C. The relative humidity in the chambers was controlled by circulating an air that was previously blown into a bottle containing a salt solution. Measurements were performed at various relative humidities, on a full cycle of drying and wetting. We also measured the water adsorption isotherms of the films (Carrier et al., 2013), so that results could be displayed as a function of relative humidity as well as water content.

The chambers were manufactured out of PMMA and hence were transparent, so that, upon testing, the samples could be imaged with a digital camera. By digital image correlation (Bornert et al., 2010), the strains of the samples were measured in a contactless manner.

Tensile experiments for the characterization of the elastic properties were performed with a tensile testing machine. From each experiment we obtained a stiffness, which was the slope of the linear portion of the measured stress-strain curve. We called this stiffness a 'normalized stiffness', because the stress was calculated by dividing the applied force by the cross-sectional area of the dry film and not by the true cross-sectional area of the film (since this latter depends on relative humidity). For what concerns the measurement of creep properties, we designed our own tensile apparatus: one extremity of the sample was kept immobile, while its other extremity was fixed to a mobile ball slide which could move linearly on a rail. This mobile ball slide was linked to a string to which a weight was attached, thus making it possible to apply a constant tensile load to the sample. We termed 'axial creep strain' the axial strain of the film measured in excess of the axial strain right after loading.

Details on the experimental protocol, together with pictures of the setups we used, can be found in (Carrier et al., 2016).

Computational Methods for Characterization of Elastic and Creep Properties of Clay Particles by Molecular Simulations

The elastic and creep properties of montmorillonite clay particles were characterized by molecular simulations (Carrier et al., 2014). The simulated system was made of 2 solid clay layers with water in the interlayer space. Both particles with Na^{+} and Ca^{2+} interlayer cations were modeled. Simulations were performed at various amounts of interlayer water, to characterize how mechanical properties depend on water content. We used the LAMMPS package.

To characterize the elastic properties of the clay particle, simulations were performed in the isothermal-isobaric ensemble, i.e., at fixed number of water molecules, fixed compressive stress (equal to the atmospheric pressure), and fixed temperature (equal to 27° C). Since the stress applied to the system was fixed, over the simulation run the simulation box would deform. With the help of the Parinello-Rahman fluctuation formula (Parinello and Rahman, 1982), the full stiffness tensor of the particle could be calculated from the fluctuations of the dimensions of the box. We repeated the simulations at various water contents.

The creep properties were characterized in the isothermal-isobaric ensemble as well, but the imposed stress was now a constant shear stress σ_{xz} (by using the coordinate system displayed in Fig. 1 right), which hence tended to make the two adjacent clay layers slide over each other. Simulations were repeated at various shear stresses up to about 50 MPa and 3 water contents corresponding to 1, 2, or 3 layers of interlayer water.

Results and Discussion

Elastic Properties of Clay Films and Clay Particles

Experimentally, we observed (see Fig. 2 left) that, independent of the interlayer cation, the (normalized) stiffness of the clay films decreased with relative humidity. Interestingly, over a full cycle of drying and wetting, the stiffness exhibited a hysteresis when

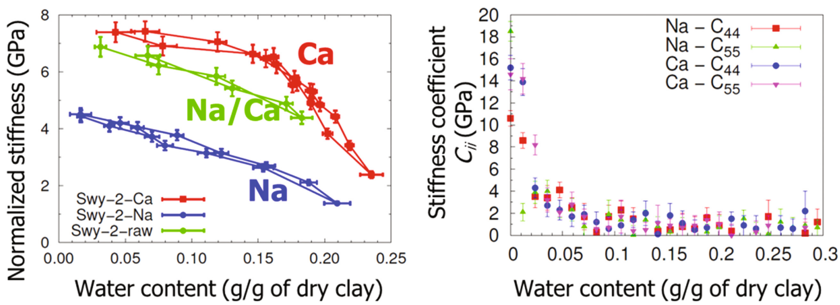

Fig. 2. (left) Normalized stiffness of clay films and (right) out-of-plane shear stiffness of clay particles. C_{44} and C_{55} correspond to stiffness coefficients C_{yzyz} and C_{xzxz}, respectively, when using the coordinate system displayed in Fig. 1.

plotted versus relative humidity, but exhibited no hysteresis when plotted versus water content (see Fig. 2 left). Also the stiffness of the films depended significantly on the interlayer cation.

For what concerns the elastic properties of the clay particles, two types of behavior were observed, depending on the stiffness coefficient of interest: in-plane stiffness coefficients were found to exhibit only a moderate dependence on water content, while out-of-plane coefficients were found to decrease very significantly as soon as some water was added to the interlayer (e.g., see Fig. 2 right). But, for all stiffness coefficients, almost no dependence of the stiffness coefficients on the interlayer cation was observed.

Therefore, comparing the elastic behavior of the clay films with that of the clay particles (see Fig. 2), a significant qualitative difference is observed: at given water content, the interlayer cation plays no role on the stiffness tensor of the clay particle, but plays a significant role on the stiffness of the clay film. A possible reason for this qualitative difference is that, experimentally, the stiffness of the film that was measured is the drained one (i.e., at fixed relative humidity and hence fixed chemical potential of the water), while the stiffness coefficients obtained by molecular simulations are undrained ones (since they were obtained with simulations performed at fixed amount of water content). But, another possible reason for this difference is the mesostructure of the films (i.e., how the clay particles or tactoids are arranged in space), which could strongly depend on the interlayer cation, and hence significantly influence how the behavior of the clay particle is being upscaled at the scale of the clay film.

Creep Properties of Clay Films and Clay Particles

For what concerns the creep experiments on the clay films, at all relative humidities, we observed that the axial creep strain increased logarithmically with time (see Fig. 3 left). From such observation, we introduced a creep coefficient $\alpha = d\varepsilon/d(\ln t)$, where ε is the strain and t is the time, and a creep compliance $\kappa = bd/F$, where F is the force applied by clay layer, b is the width of the sample, and d is the basal spacing of a dry clay layer

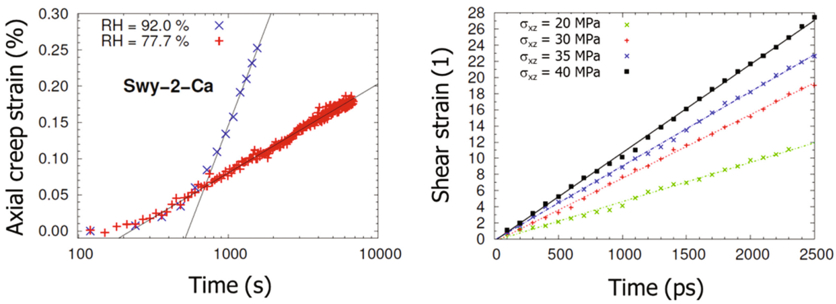

Fig. 3. Typical (left) axial creep strain of axially loaded film of SWy-2 clay homoionized with Ca^{2+} interlayer cations and (right) shear strain of sheared clay particle of montmorillonite with Na^{+} interlayer cations.

(i.e., 9.55 Å). At a given relative humidity, this creep compliance was 0.5 to 1 order of magnitude larger for samples with Na^{+} interlayer cations than for samples with Ca^{2+} interlayer cations. Also, for both types of samples, this creep compliance increased exponentially with water content.

For what concerns the molecular simulations of creep of the clay particles, we found that the relative displacement of the adjacent clay layers with respect to each other increased quite linearly with time, so that, at given shear stress, a shear strain rate could be calculated. At all water contents considered, we found that the viscous behavior of the clay particle was of the Bingham type: below a critical shear stress, the shear strain rate remained close to zero, while above this critical shear stress, the shear strain rate increased linearly with stress.

Comparing the creep behavior of the clay films with that of the clay particles, a significant qualitative difference is observed: creep strains increase linearly with time at the scale of the clay particle, but increase logarithmically with respect to time at the scale of the clay film. Here again, the mesostructure appears to significantly influence how the behavior of the clay particle is being upscaled at the scale of the clay film.

Conclusions

We studied the elastic and creep behavior of montmorillonite clay systems at two different scales: clay films with a thickness of a few dozen microns (characterized experimentally), and nanometer-thick clay layers constituting clay particles (studied by molecular simulations).

Both the stiffness and viscous behavior of the clay films at given water content depended significantly on the interlayer cation. In contrast, at given water content, the stiffness tensor of the clay layer was found to be almost independent of the interlayer cation. Experimentally, for given clay film, when increasing the water content, the stiffness of the films decreased with increasing water content, and their stiffness compliance increased exponentially with the water content. At all hydric states considered, creep strains increased logarithmically with respect to time at the scale of the clay film, but increased linearly with respect to time at the scale of the clay particle.

Therefore, significant qualitative differences were observed between the hydromechanical behavior of the clay particles and that of the clay films, in spite of the fact that our clay films are relatively simple clay systems: indeed, our clay films are homogeneous (i.e., contain only clay) and relatively well ordered (i.e., with clay particles preferentially ordered parallel to the plane of the film). However, even for such model systems, predicting their hydromechanical behavior from that of the clay particles with nanometric thickness of which they are constituted may already prove to be a challenge.

References

Bornert M, Valès F, Gharbi H, Nguyen Minh D (2010) Multiscale full-field strain measurements for micromechanical investigations of the hydromechanical behaviour of clayey rocks. Strain 46:33–46. doi:10.1111/j.1475-1305.2008.00590.x

Carrier B, Wang L, Vandamme M, Pellenq RJM, Bornert M, Tanguy A, Van Damme H (2013) ESEM study of the humidity-induced swelling of clay film. Langmuir 29:12823–12833. doi:10.1021/la402781p

Carrier B, Vandamme M, Pellenq RJM, Van Damme H (2014) Elastic properties of swelling clay particles at finite temperature upon hydration. J Phys Chem C 118:8933–8943. doi:10.1021/jp412160e

Carrier B, Vandamme M, Pellenq RJM, Bornert M, Ferrage E, Hubert F, Van Damme H (2016) Effect of water on elastic and creep properties of self-standing clay films. Langmuir 32:1370–1379. doi:10.1021/acs.langmuir.5b03431

Parrinello M, Rahman A (1982) Strain fluctuations and elastic constants. Strain 76:2662–2666. doi:10.1063/1.443248

Zabat M (1996) Microtexture et propriétés mécanique de films solides de particules colloidales. Ph.D. thesis, Université d'Orléans

Zabat M, Vayer-Besançon M, Harba R, Bonnamy S, Van Damme H (1997) Surface topography and mechanical properties of smectite films. Prog Colloid Polym Sci 105:96–102

Advanced Meso-Scale Modelling to Study the Effective Thermo-Mechanical Parameter in Solid Geomaterial

F. Wuttke(✉), A.S. Sattari, Z.H. Rizvi, and H.B. Motra

Institute of Geosciences, University of Kiel, Kiel, Germany
fw@gpi.uni-kiel.de

Abstract. The effects of coupled thermo-mechanical processes under consideration of micro-fracturing of the solid geomaterial on mechanical and thermal properties of geomaterials are investigated and subsequently simulated using advance Lattice Element Method (LEM). As a result of that extension, the alteration of effective parameter due to structural changes become numerically understandable. Hence, the simulation of the coupled processes on the meso-scale helps to develop and validate reliable identification method for real cases. The obtained results make it obvious that LEM has a large potential for fracture problems in geomaterials.

Introduction

The change of effective parameter in solid geomaterial is coupled with structural or multi-phase changes. Effective parameters represent the properties over a solid volume of a larger scale. Hence, the effective parameters are influenced by micro- and meso-scale structural or multi-field alterations and the change of coupled effective T-M parameter should be studied based on a micro or meso-based model. The thermo-mechanical alteration in solids are often linked with distributed small fracture networks. As the literatures suggest, the basic conductivity depends on the mineral phase, porosity and saturation in rocks. Alteration of this basic property happens under mechanical or thermal stresses. These stress fields cause “mechanical or thermal micro cracking”, either by differential expansion or shrinkage in solids (Clauser & Huenges 1995). Therefore, fracture discontinuities resulting from thermo-mechanical stresses have to be considered in modeling.

Failure of bounded and cemented geomaterials is complex and often stochastical in nature. Under thermo-mechanical loading the main cracks having various branches and numerous micro cracks occur. The mechanism of failure depends upon heterogeneity of geomaterials varying at many length scales e.g. clay or binders (nanoscale) to sand and gravel (centimetres). Lattice based approach, (Batchelor et al. 1977, Bahrami et al. 2004, Bahrami et al. 2006) to simulate the nucleation and propagation of cracks, inherits the material heterogeneity with domain meshing techniques (Voronoi and Denaluay triangulation) and simple failure laws based upon linear elastic fracture mechanics (LEFM) with step wise removal of elements exceeding the tensile strength. There exist various kinds of lattice models based upon the spring laws. The first and the

A. Ferrari and L. Laloui (eds.), *Advances in Laboratory Testing and Modelling of Soils and Shales (ATMSS)*, Springer Series in Geomechanics and Geoengineering,
DOI 10.1007/978-3-319-52773-4_9

simplest is based on Hookean spring to transmit normal forces (Zhang et al. 2011a,b) and after extended by (Zhou et al. 2012) in a 3D to model mode I fracture problems. Born spring model (Kuipers et al. 1992) with an additional degree of freedom in tangential direction is able to capture the shear behaviour of the sample. The third model termed as beam or granular model (Tsuji et al. 1993) takes into consideration of the displacement, rotation and moments, in addition to forces at the nodes. In studies related to mode I failure, rotational degree of freedom is neglected due to small rotational stiffness. For the generated lattice network in the above mentioned methods, displacement in the nodes are calculated either by enforcing equilibrium at each point with a set of linear algebraic equations (Kuipers et al. 1992), by iteratively energy minimizing (Cheng 1999) or dynamic relaxation (Yun et al. 2010). Thermal conduction in cemented and boned geomaterials are dominated by conduction. The thermal conductivity of constituting parts varies over a range of two orders of magnitude with solid grains thermal conductivity about 10 W/mK and air 0.01 W/mK. The thermal properties of soil mass are dominated by soil properties and boundary conditions like: grain size and shape, pore fluid characteristics, applied load, quality and quantity of contact, porosity, mineralogy and drainage conditions (Moukarzel et al. 1992, Woodside et al. 1961, Tavman et al. 1998, Weidefeld et al. 2002, Bahrami et al. 2006). The thermo-mechanical solver based on LEM is able to solve the nucleation and propagation of cracks in particulate matter effectively and efficiently requiring a few physical parameters (Rizvi et al. 2016).

Methodology and Mathematical Background

The lattice based method to model solid and cemented granular materials was first proposed to model elasticity problems. The fundamental work behind the method is that of the frameworks or spatial trusses. The shear failure mechanism under direct stresses (tension or compression), which is the cause of failure is inherited due to representation of the system by means of connecting members as a triangulated grid. The failure criteria of each element is calculated from the Linear Elastic Fracture Mechanics (LEFM). The discretization of continua are done using Voronoi cells. Each cell is seeded with one nucleus and Delaunay triangulation scheme is used to connect the neighboring nuclei. This generated network of connected nuclei or nodes serve as a discretization of solids.

Modeling of Fracture Simulation by LEM

The major advantages of LEM is the ease fracture simulation, even under complicated fracture network. Simple linear-elastic material is mostly assumed. The lattice elements carry the external or internal mechanical loads and can be modeled as: (1) springs, (2) truss or rods, and (3) beams. The basic idea for lattice models is based on the equivalence of strain energy stored in a unit cell of a lattice with its continuum counterpart under constant strains, $U_{cell} = U_{continuum}$. The detailed process has been presented by (Lawn 1993), in which the relationship between the triangular Timoshenko beam lattice and its micropolar continuum equivalent is obtained. The Young modulus of the lattice elements determines the stiffness of the continuum discretized with the lattice. In case of spring elements, the simplest elastic-brittle Hookean's spring is chosen as lattice element. Only two parameters, spring constant ks and failure force F_c are required to define a lattice. The scaling rule of k_s is provided by, $k_s = E_s A/L$, where, A is the cross section area represented by lattice, L is the lattice length and E_s is a proportionality constant related to Young's Modulus of geomaterial. It should be noted that E_s is not the macroscopic Young's modulus and needs to be calibrated prior to simulation. The relationship between the Young's modulus of the truss (E_t) and continuum (E), which is obtained by (Donze 1999), is, $E_t = \sqrt{3}LE/2A$. In the presented 2D approach, the material is considered as a bonded or congealed grain assembly represented by Voronoi cells and connected by elastic beams with three continuous degrees of freedom, normal and tangential translations and rotation. In 3D case, 6 degrees of freedom exist. The particles are assumed unbreakable, undeformable and can solely undergo translational and rotational displacements. The equivalent elastic behavior depends on contact stiffness. The 2D contact stiffness matrix, k_{Local}, in local coordinates $(x^{'}, y^{'})$ for Euler–Bernoulli beam elements is used. For the modeling of heterogeneities, different mechanical properties (E) are assigned to the lattice elements describing the different components (particles, voids, inclusion etc). Using stiffness method as given below, the displacements in each Voronoi cell can be obtained: $[\,F_{x1} \quad F_{y1} \quad M_1 \quad F_{x2} \quad F_{y2} \quad M_2\,]^T = k_{Global}[\,u_1 \quad v_1 \quad \phi_1 \quad u_2 \quad v_2 \quad \phi_2\,]^T$. The LEFM describes the failure of materials under the assumptions of linear elasticity. The failure criterion is the important factor in fracture simulation. The maximum circumferential stress (Caballero et al. 2006), the maximum elastic strain energy density (D'Addetta et al. 2002), the maximum normal principal stress (Lilliu et al. 2003), the maximum energy release rate (Wang et al. 2008, Nicolas et al. 2013) are examples of such failure criteria. In here, fracturing is modelled by simply removing lattice element exceeding a specified threshold related to the critical energy release rate of rock based on work of Wong et al. 2015. The lattice axial force threshold, F_c, is, $F_c = \sqrt{2G_{\mathrm{I}}k_s A} \Rightarrow \sigma_c = \sqrt{2G_{\mathrm{I}}E_b/L}$ where, G_{I} is energy release rate based on failure modeI, $G_{\mathrm{I}} = K_{\mathrm{I}}^2/E$, K_{I} is fracture toughness of the failure mode I. With lattice axial force calculation, $F_{x'1}$, the lattice elements exceeding the following fracture criteria are removed: $\left(F_{x'1}/A + \alpha \cdot \max(M_1, M_2)/W\right)/\sigma_c > 1$, where, α is equal to 0.005 and W is section modulus. The critical shear force value, τ_c, is defined based on Mohr-Coulomb equation, $\tau_c = \sigma_c tan\phi + C$, with C as cohesive strength and ϕ as fraction angle. When the following equation is satisfied, the lattice element breaks due to shear failure: $\left(F_{y'1}\Big/A\right)\Big/\tau_c > 1$. When an element exceeds its threshold, it will be crack, removed from the matrix and the process will be repeated. The above procedure and the strength criterion, prevents the consideration of any non-linearity's and fracturing in the model. Fig. 1 shows trivial benchmarks of a 2D plate with a central hole subjected to tensile or compression load.

The modes of failure are following the explanation described above. Compression loading produce critical stresses along the loading path while tension tries to split the granular assembly along the middle plane (Fig. 1).

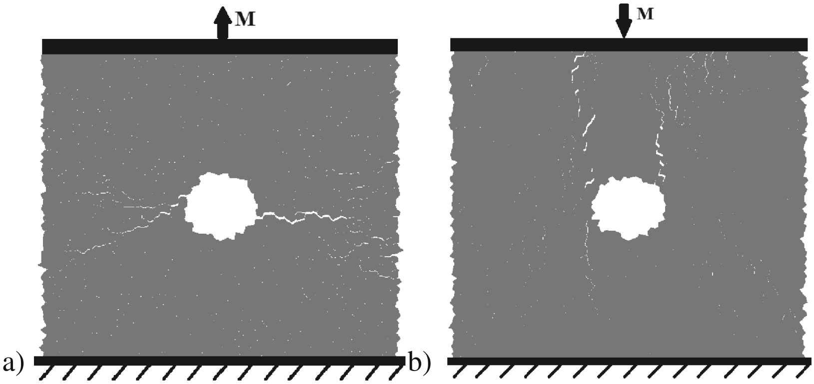

Fig. 1. A granular assembly subjected to (a) compressive and (b) tensile loading. The failure surface corresponds to that of generated with continuum based modelling.

Modelling of Steady Heat Transport by LEM

Heat transfer in granular material is complex in nature due to its dependence on many physical parameters, such as, grain contact points, porosity, mineralogy, shape and size of solid phase. The type and quality of contacts among grains play an important role in the transfer of heat due to conduction, which is the dominant mode of heat transfer in granular solids. The mathematical details and numerical scheme is given in our previous work (Rizvi et al. 2016). 1D truss elements are used to model heat transfer in vacuum. The method is able to model the temperature distribution among the individual grains.

Coupled Problem of Thermo-Mechanics by LEM

A sequential thermo-mechanical coupled scheme is adopted to model the failure of material based on lattice based model. The failure is defined when total strain energy stored in each element is exceeding the work of fracture. The thermal strain, ε_T, is calculated assuming a linear elastic expansion of each element due to temperature gradient: $\varepsilon_T = \alpha_L \triangle T$. Two different thermo-mechanical examples under mechanical compression, tension load and thermal gradient are presented in Fig. 2a and b. A distinct pattern appears as the material fails on one side and thermal conduction path among particles becomes increased due to the extra normal contact force arising from compressive stress. In opposite, because of tensile loading, generation of micro cracks achieve a reduction in normal contact forces among the particles and a reduction of the local conductance follows. Consequently, the method is able to calculate the change in effective parameters of thermo-mechanical loaded granular assembly and bonded geomaterial due to generation of micro fissures as rising in many engineering problem.

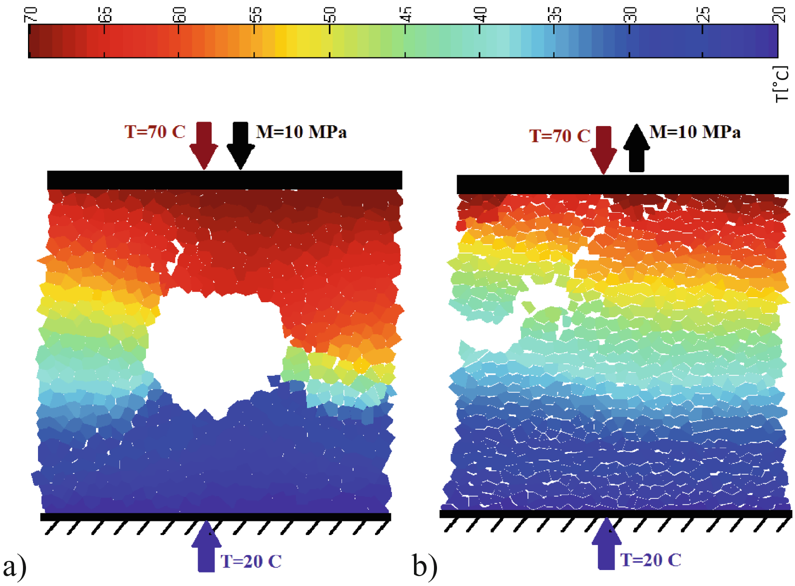

Fig. 2. (a) A granular assembly subjected to thermo-mechanical loading under compressive loading and (b) under tensile loading. The top surface is heated at 70°C and the bottom at 20°C.

Simulation and Validation

The foregoing developments where used to explain the change of thermal conductivity of rocks under temperature influence (Clausner et al. 1995). The authors postulate that change of porosity is the major influencing factor of the thermal conductivity of dense rocks without open pore systems. The numerical method was applied on rock samples from geothermal projects to study the influence of thermal load on thermal, geomechanical and geophysical rock. Figure 3 shows the micro sections of the analyzed rock material. It's obvious that the section with that different minerals contain lots of possible fracture point by different thermal expansion or compression behavior of the minerals.

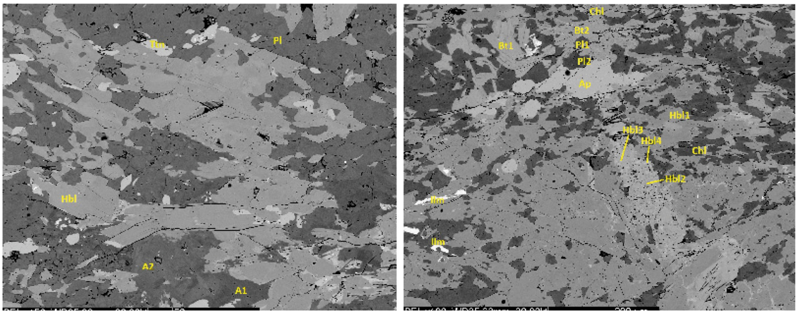

Fig. 3. Micro sections of rock samples with minerals and heterogeneities.

The properties of surrounding rocks in the vicinity of a geothermal source with very high fluid temperatures (>375° C) are strongly influenced by thermal load. To design the drilling and thermal production technologies correctly, all rock parameter and its variation under coupled T-H-M fields has be determined correctly. As fundamental questions related to this problem are:

(a) change of microstructural, textural characteristics under thermal loads (fabric, micro cracks),

(b) the role of existing stress field on micro fractures,

(c) the effect of structural changes on thermal, mechanical and geophysical material parameters.

Experimental Setup and Boundary Conditions

To study the rock material as given in Fig. 4, a true triaxial device for rock testing is used. This device is capable of applying confining pressure up to 600 [Mpa], arbitrary deviatoric stresses, isothermal loads between 20°C to 600°C and simultaneous measurement with ultrasonic P and polarized S waves in three orthogonal directions of the cubic sample. For this study, following thermal and mechanical loads are applied to the cubic sample: temperature rises in a steps from 20°C to 600°C, confining pressure is kept constant at two different pressures 100 and 150 MPa. The P- and polarized S- wave pulses are applied to determine the material changes.

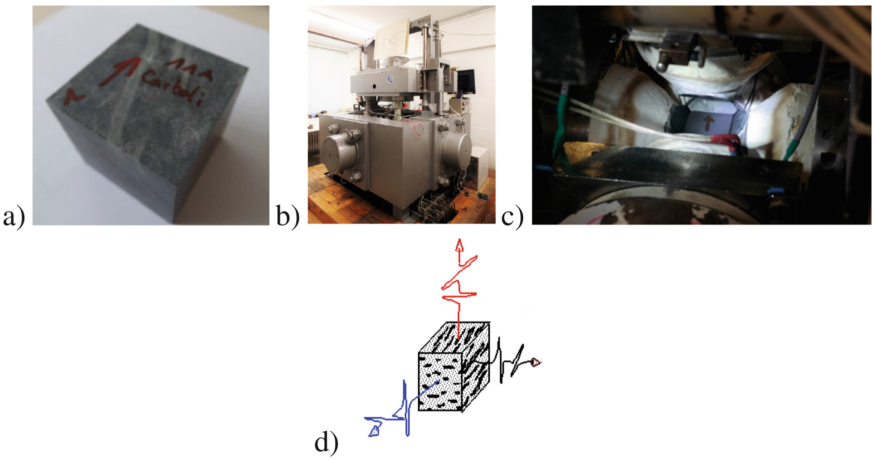

Fig. 4. Experimental true triaxial rock testing device: (a) rock sample, (b) true triaxial device for rock samples, (c) view of the 3D pistons, (d) schematics of the polarized wave propagation.

Simulation and Results

The experimental test results show, as expected, a strong dependency on the velocities corresponding to the confining pressure and thermal loads, Fig. 5.

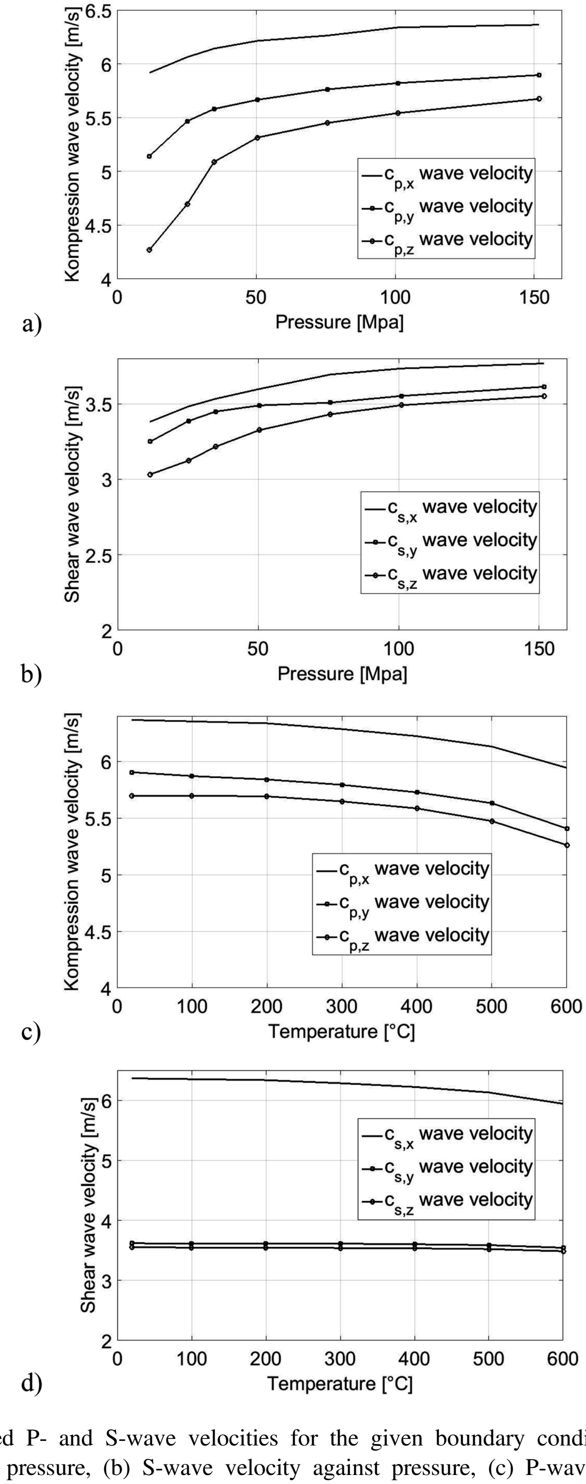

Fig. 5. Measured P- and S-wave velocities for the given boundary conditions: (a) P-wave velocity against pressure, (b) S-wave velocity against pressure, (c) P-wave velocity against temperature, (d) S-wave velocity against temperature.

Beside the stiffness under thermal loads, Fig. 6a, the thermal conductivity λ [$Wm^{-1}K^{-1}$] based on reported velocities relationships (Schön 2011, Gegenhuber 2012) and (Esteban et al. 2015) is determined with an empirical relation based on compression wave velocity c_p *[m/s]* and temperature T [°C], Fig. 6b. To understand the influence of thermal caused fissures on the effective thermal conductivity, the cubic rock sample (same size as testing sample 43x43 mm) analysed by the Lattice based approach under same given mechanical and thermal boundary conditions. A mesh dependence test was performed to find the suitable mesh size and a convergence limit of 0.1% is adopted. The material parameters (Elasticity, poission ratio, thermal expansion, thermal conductivity and work of fracture) used in the simulation are obtained from the experiment. These material parameters are assigned to the lattice elements connecting the nuclei of each cell. The simple 1D truss elements reduce the 3D problem by a dimensionality of two orders.

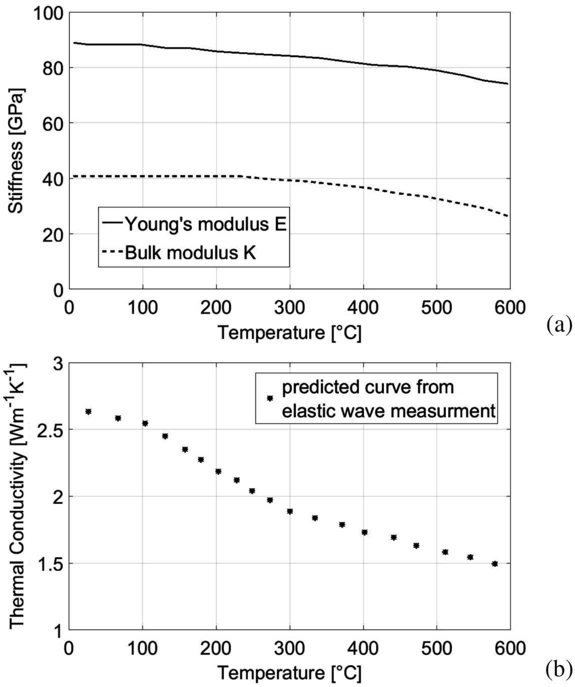

Fig. 6. (a) Determined stiffness evolution based on the measured stress-strain relation, (b) Predicted thermal conductivity evolution based on the measured wave velocities.

The failure fracture analysis, fracture toughness, mode I failure is considered as $K_{IC} = 1\,[MPa \cdot m^{0.5}]$. Failure of elements happen when the strain energy stored due to thermal expansion and mechanical stress exceeds the failure criteria defined by LEFM. After failure of the 1D element, the neighboring Voronoi cells are not linked together anymore and thus the heat conduction path is lost, resulting in with reduction of effective thermal conductivity of the sample. The broken connections are assigned for thermal property of air and a negligible mechanical stiffness. A zero stiffness is avoided not to result in non-convergence large matrix sets. During this study, temperature related mineralogical changes are neglected. The constituting minerals (especially metamorphic rocks) of the sample rock shows very little effect at those temperature ranges as considered in this study. During the coupled T-M simulation, Fig. 7, it becomes visible as the micro cracks start to originate and then branch and propagate, merging and splitting from the edges towards the center of the sample with increasing crack mesh density over time and thus causing reduction in thermal conduction path. The effective simulated thermal conductivity $\lambda_{eff,simul}$ is determined by calculating the heat flow Q in a unit time through an volume $\lambda_{eff} = \left(\dot{Q} \cdot l\right) / (A \cdot \Delta T)$, where Q is the heat flow, l is the length, A the area, and ΔT the temperature difference. With passage of time and stepwise elevation of temperature, the sample is pervaded with micro cracks, thus hindering the movement of energy in the form of heat. This nucleation of micro cracks is slowed down by application of confining pressure, which acts as a crack arresting measure. An argument could be made that the applied pressure also enhances the thermal conduction of the material, but the increase in negligible as the pressure is not sufficient to congeal and seal the pore inside the material. Figure 8 shows the

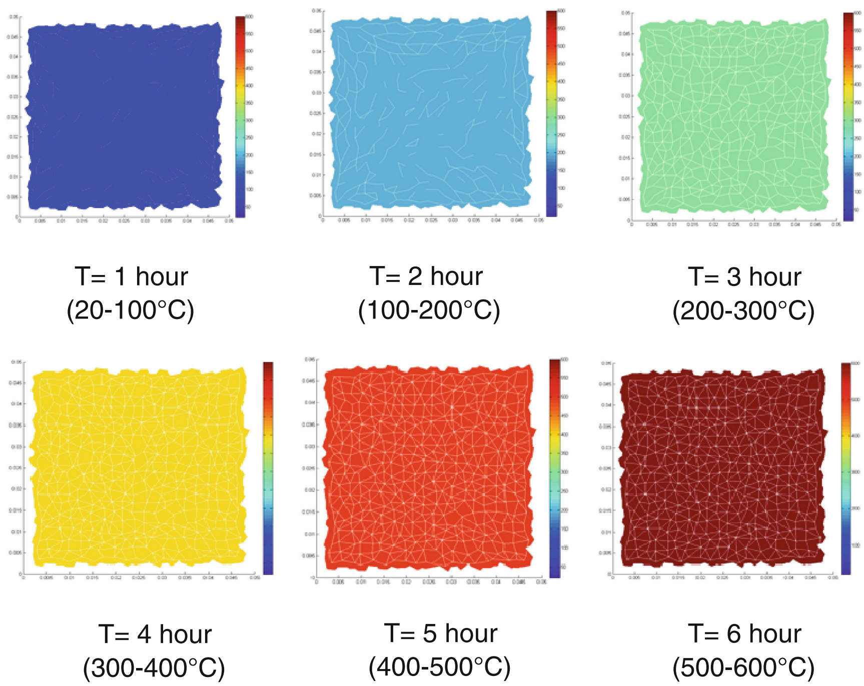

Fig. 7. Cross-section of the nucleation of micro cracks by coupled thermo-mechanical loading in the sample, with confinement pressure of 100 MPa and increasing thermal load from 20 up to 600°C.

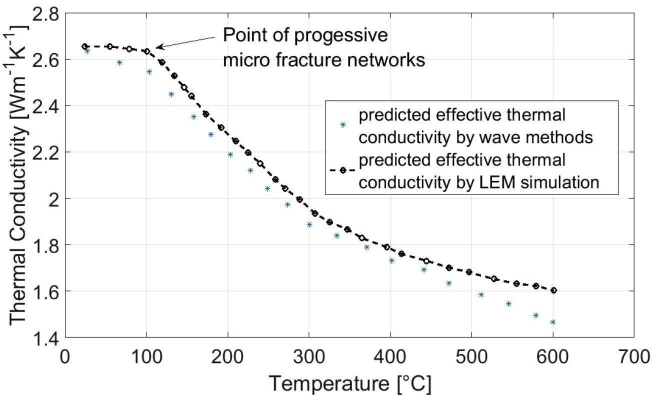

Fig. 8. Comparison of predicted effective thermal conductivity from the wave based measurements and the predicted effective thermal conductivity from the Lattice Element simulation.

change in effective thermal conductivity of the sample with thermal rise. The predicted effective thermal conductivity from the measurement is compared with the simulated effective thermal conductivity. The graph shows a good argument between the measured and simulated results using meso-scale modeling method. The numerical method confirm the statements of Clauser & Huenges (1995) who argued the dominant effects for thermal conductivity of rocks is generation of micro cracks.

Conclusion

The experimental measurements show that with increasing thermal load on the sample, the P and S-wave velocities are decreasing. The probable cause of this change is the formation and widening of the cracks in the sample. The measurements suggest that with temperature rise, a reduction in the elastic modulus and thermal conductivity value of the sample is observed. Lattice based method is able to predict the change in thermo-mechanical properties as measured during the experimental thermal conductivity tests.

Acknowledgment. This research project is financially supported by Federal state funding at Kiel University and research grant “DuoFill” provided by the Federal Ministry for Economic Affairs and Energy, Germany (BMWi/ZIM KF3067303KI3).

References

Bahrami M, Culham JR, Yovanovich MM, Schneider GE (2006a) Review of thermal joint resistance models for non-conforming rough surfaces in a vacuum. Appl Mech Rev 59:1–12
Bahrami M, Yovanovich MM, Culham JR (2004) Thermal joint resistances of non-conforming rough surfaces with gas-filled gaps. J Thermophys Heat Transf 18:326–332
Bahrami M, Yovanovich MM, Culham JR (2006b) Effective thermal conductivity of rough spherical packed beds. Int J Heat Mass Transf 49:3691–3701

Batchelor FGK, O'Brien RW (1977) Thermal or electrical conduction through a granular material. Proc Roy Soc Lond A 355:313–333
Caballero A, Carol I, Lopez CM (2006) New results in 3D meso mechanical analysis of concerete specimen using interface elements. In: Computational modelling of concrete structure, pp 43-52. Taylor and Francis, London
Cheng GJ, Yu AB, Zulli P (1999) Evaluation of effective thermal conductivity from the structure of a packed bed. Chem Eng Sci 54:4199–4209
Clauser C, Huenges E (1995) Thermal conductivity of rocks and minerals. In: Ahrens T.J. (ed.) Rock physics & phase relations: a handbook of physical constants. Americ. Geophysical Union
D'Addetta GA, Kun F, Ramm E (2002) On the application of a discrete model to the fracture process of cohesive granular materials. Gran Matter 4:77–90
Donze FV, Magnier SA, Daudeville L, Mariotti C (1999) Numerical study of compressive behaviour of concrete at high strain rates. J Eng Mech 125:1154–1163
Esteban L, Pimienta L, Sarout J, Piane CP, Haffen S, Geraud Y, Timms NE (2015) Study cases of thermal conductivity prediction from p-wave velocity and porosity. Geothermics 53:255–269
Gegenhuber N, Schön JH (2012) New approaches for the relationship between compressional wave velocity and thermal conductivity. J Appl Geophys 76:50–55
Kuipers J, van Duin K, van Beckum F, van Swaaij W (1992) A numerical model of gas-fluidized beds. Chem Eng Sci 47:1913–1924
Lawn BR (1993) Fracture of Brittle Solids, 2nd edn. Cambridge University Press, New York
Lilliu G, van Mier JGM (2003) 3D lattice type fracture model for concrete. Eng Fract Mech 70:927–941
Moukarzel C, Herrmann HJ (1992) A vectorizable random lattice. J Stat Phys 68:911–923
Rizvi ZH, Sattari AS, Wuttke F (2016) Numerical analysis of heat conduction in granular geomaterial using lattice elements. In: 1st international conference on energy geotechnics, Kiel, Germany
Schön JH (2011) Physical properties of rocks: a workbook. Elsevier publication, Oxford
Tavman S, Tavman IH (1998) Measurement of effective thermal conductivity of wheat as a function of moisture contact. Int Commun J HeatMass Transf 25:733–741
Tsuji Y, Kawaguchi T, Tanaka T (1993) Discrete particle simulation of 2D fluidized bed. Powder Technol 77:79–87
Woodside W, Messmer JH (1961) Thermal conductivity of porous media I unconsolidated sands. J Appl Phys 32:1688–1698
Wang YH, Leung SC (2008) A particulate scale investigation of cemented sand behaviour. Can Geotech 45:29–44
Wong JKW, Soga K, Xu X, Delenne JY (2015) Modelling fracturing process of geomaterial using Lattice Element Method. In: Geomechanics from micro to macro, pp. 417–422
Yun TS, Matthew Evans T (2010) Three-dimensional random network model for thermal conductivity in particulate materials. Comput Geotech 37:991–998
Zhang HW, Zhou Q, Zheng YG (2011a) A multi-scale method for thermal conduction simulation in granular materials. Comput Mat Sci 50:2750–2758
Zhang HW, Zhou Q, Xing HL, Muhlhaus H (2011b) A DEM study on the effective thermal conductivity of granular assemblies. Powder Technol 205:172–183
Zhou Q, Zhang HW, Zheng YG (2012) A homogenization technique is proposed to simulate the thermal conduction of periodic granular materials in vacuum. Adv Powder Technol 23:104–114

Identification of Local Mechanisms in Clays and Energy-Based Modelling

Mahdia Hattab[1(✉)], Jean-Marie Fleureau[2], and Ching-Shung Chang[3]

[1] Laboratoire d'Etude des Microstructures et de Mécanique Des Matériaux, Université de Lorraine, CNRS UMR, 7239 Metz, France
mahdia.hattab@univ-lorraine.fr
[2] Laboratoire de Mécanique Des Sols Structures et Matériaux, CentraleSupélec, CNRS UMR, 8579 Châtenay-Malabry, France
[3] Department of Civil Engineering, University of Massachusetts, Amherst, USA

Abstract. The paper addresses the issue of how physical-chemical aspects affect the mechanical behaviour of clays and how they could be integrated in the mechanical modelling. A significant influence of the high-plastic-clay fraction on the behaviour of clayey materials was experimentally highlighted, such as the compression index variation, or the strong and very marked decrease of friction angle. Microstructural investigation provides further understanding allowing to relate the observed phenomena to an activated mechanisms acting at the level of clay particles. A new approach using the Chang and Hicher micromechanical model was proposed, where physical-chemical effects, acting between clays clusters, are incorporated. Local mechanisms are introduced through repulsive and attractive forces obtained from the derivation of energy potentials.

Introduction

The mechanical behaviour of saturated clayey sediments appears very complex. One of the reasons of this complexity resides in their composition, which generally consists of large fractions of clayey minerals with different mineralogies, for which the mechanisms acting at the microscopic level during mechanical loading are not very well known. The aggregate structure of clayey sediment makes this medium a mechanically complex system.

Based on Chang and Hicher (2005) modelling, Chang et al. (2009) suggested that clay can be regarded as an assembly of clusters; this assumption appears experimentally quite realistic. In this model, the deformation of the assembly can be obtained by integrating the movement of the inter-cluster contacts in all orientations. The effect of the inter-cluster interaction was explicitly approached by a contact law. Nonetheless, these models do not consider the mechanisms related to physical-chemical interactions that we know significant when the clay is viewed in terms of its microstructure.

Two aspects discussing this issue are examined in the present paper.

The first part discusses experimental results combining triaxial tests (on isotropic and σ'_3 constant paths) and microstructural investigations of a Mix-Clay material. The clayey material is composed of kaolin clay (kaolin P300) and montmorillonite (Greek clay), whose mineralogies are quite different. The aim in this approach was to vary the

A. Ferrari and L. Laloui (eds.), *Advances in Laboratory Testing and Modelling of Soils and Shales (ATMSS)*, Springer Series in Geomechanics and Geoengineering,
DOI 10.1007/978-3-319-52773-4_10

physical-chemical properties of a clayey mixture material, and then to follow the variation of both mechanical properties and microstructure (Hattab et al. 2015).

The second part proposes a new modelling for the clay behaviour (Hattab and Chang 2015) by incorporating in the Chang and Hicher (2005) micromechanical approach attractive and repulsive forces, similar to van der Waals (1873) and double-layers forces (Gouy 1910; Chapman 1913; van Olphen 1977), but acting between clays clusters.

In this paper, the simulations concern the behaviour on isotropic loading.

Material and Experimental Method

The Kaolin/Montmorillonite mix is termed $M_x\%$, where x denotes the montmorillonite fraction (Fig. 1). The basic clays are Montmorillonite ($M_{100\%}$), characterized by a high plasticity, and the Kaolin P300 (K) by a low plasticity. In this way, Atterberg consistency limits variation in the mix-clay will suggest the change on the physical-chemical properties versus the Montmonrillonite fraction (Hattab et al. 2015).

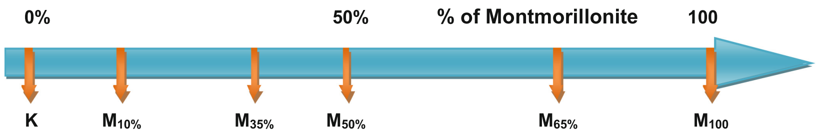

Fig. 1. The mix-clay and its montmorillonite fraction.

The mixtures were made by dry mixing of the basic clays, and then hydration of the powder. Triaxial tests were carried out under drained conditions on saturated, remoulded, and normally consolidated clay samples. The microstructure analyses were conducted using Scanning Electon Microscope (SEM) technique (Hattab and Fleureau 2010; Hattab et al. 2015).

Discussion Around the Experimental Results

Mix-Clay Behaviour at the Ultimate Critical State

Triaxial test under σ'_3 = 600 kPa, represented in Fig. 2a, show that the kaolin clay (K) presents the highest maximum strength q_{max}. Then, a slight increase in montmorillonite content noticeably decreases the q_{max} value. From around 35% of montmorillonite, the behaviour seems to remain unchanged and becomes completely similar to that of the $M_{100\%}$. Consequently, a small percentage of montmorillonite considerably lowers the internal friction angle showing the total control of the montmorillonite fraction over the behaviour of the mix-clay (Fig. 2b).

When the path approaches the ultimate critical state, microstructure observations show a material locally structured by bands of preferential direction (Fig. 3), in different zones, where slip mechanism can likely be activated. A remarkable feature is

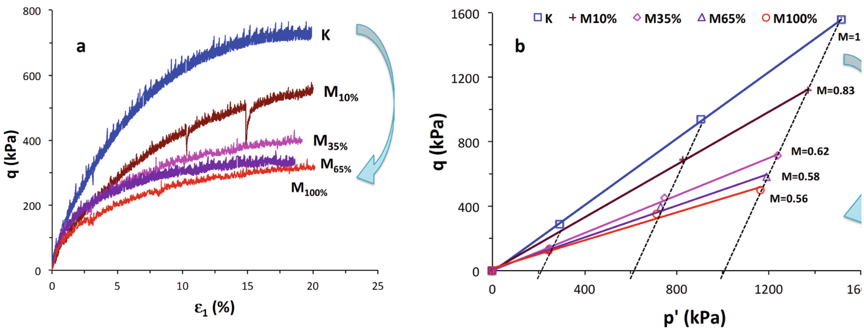

Fig. 2. Mix-Clay behaviour on triaxial path and ultimate critical state variation. (a) Axial strain versus the deviator - (b) Effective mean stress versus the deviator.

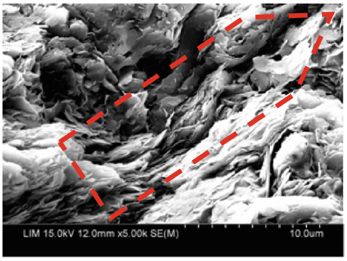

Fig. 3. Microstructural state in the last stages of loading (M35% case).

however exhibited in the mixtures: these privileged orientation planes are quasi-systematically constituted by groups of montmorillonite particles, constituting a weakness zones for micro-cracks development (Hattab 2011).

Mix-Clay Behaviour on Isotropic Path

Figure 4a shows that the straight line, identified in the case of kaolin isotropic path in the (log p′, e) plane, progressively disappears with the increase of montmorillonite fraction. Thus, the curves exhibit two compression indices depending on the stress domain. This behaviour appears as strongly related to Atterberg limits change, and show therefore how the physical-chemical properties affect the isotropic path. On the other side, the analyses of particles orientation show an isotropic microstructure of the clay during the isotropic loading (Fig. 4b).

Viewed at a micro-structural scale, it appears quite justified to consider clay as an assembly of aggregates, the aggregated clay structures can visually be observed from the SEM images as packings of assembled particles (Fig. 5). Other works, on different

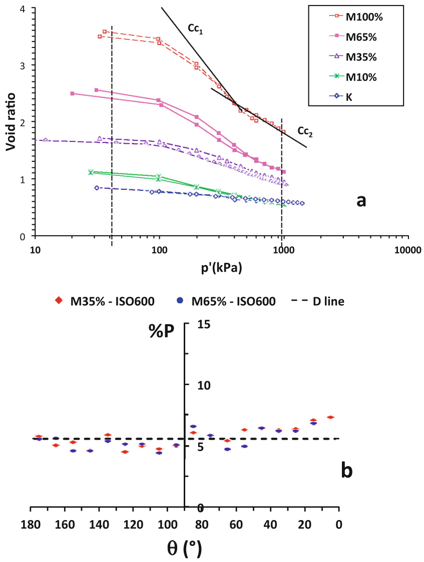

Fig. 4. The mix-clay behaviour on isotropic loading path and microstructural properties (a) Void ratio versus isotropic stress - (b) Percentage of particles versus their orientation.

clayey sediments, showed that the variation of porosity under the common levels of stresses is directly related to the pores inter-aggregates closure, while at the same time the intra-aggregates average pore diameter remains constant (Hattab et al. 2013, on Marine sediments; Delage 2010, on sensitive clays). This permits to conclude that the mechanisms of volumetric strain mainly take place between aggregates. Under the common stress levels, the pores within individual aggregate remain unaffected by loading. This observation will be fundamental to build the micromechanical approach that we proposed.

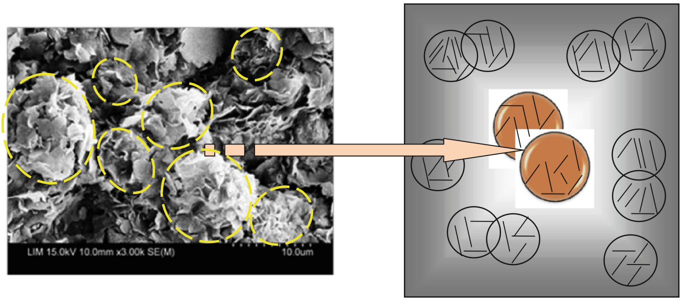

Fig. 5. Clay Microstructure ($M_{65\%}$ example) as a cluster assembly.

Micromechanical Approach and Physical-Chemical Effects – Case of Isotropic Loading

Microstructural Properties and Local Equations

The micromechanical model considers two neighbouring clusters (Fig. 6) of R radius and the length connecting the two centres is denoted as l_c. Under an isotropic loading, the deformation of the assembly is assumed to be caused by the change of l_c due to the change of inter-cluster pores. As consequence of the previous "microscopic structure" discussion, the change of intra-cluster pores is assumed as negligible. The interaction of two neighbouring clusters is governed by two types of potential: (1) repulsive type w_R, and (2) attractive type w_A.

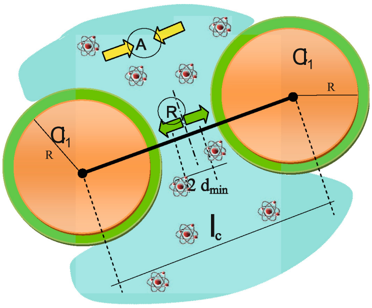

Fig. 6. Elementary system definition: cluster/water/cluster.

Simplified expressions are proposed for w_R and w_A as follows. $\mathrm{d}_{\mathrm{min}}$ is the mini distance between the clusters, $\widetilde{B}$ and $\widetilde{A}$ are the parameters related to the surface potential of clusters, these three parameters depend on the mineralogical nature of the clay and the properties of water between the clusters. Thus, the properties of surface potential symbolize, as a first approach, the physical-chemical properties of the clayey material.

$$w = w_R + w_A$$
$$\begin{cases} w_R = \widetilde{B}\,\mathrm{R}\,e^{-d_{\min}^{-1}(l_c-2R)} \\ w_A = -\widetilde{A_w}\left[\dfrac{2R^2}{l_c^2-4R^2} + \dfrac{2R^2}{l_c^2} + \ln\left(\dfrac{l_c^2-4R^2}{l_c^2}\right)\right] \end{cases}$$

From the derivation of the two potentials, we obtain in the inter-cluster force, which represents the sum of the repulsive and attractive forces.

$$f = -\widetilde{B}\mathrm{R}\ \mathrm{d}_{\mathrm{min}}^{-1}\, e^{-d_{\min}^{-1}(l_c-2R)} + \widetilde{A}R^2\left[\frac{l_c}{\left(l_c^2-4R^2\right)^2} + \frac{1}{l_c^3} - \frac{2}{l_c\left(l_c^2-4R^2\right)}\right]$$

Transition from Macro to Micro on the Isotropic Loading

The stress-strain relation at the continuous medium scale can be determined by the integration of local relations obtained at the "elementary level" (Fig. 6), the micro and macro variables can thus be related.

Following the kinematic approach represented in Fig. 7, the mean stress can be directly linked to the volumetric strain in an isotropic loading case using the following equation and Fig. 7.

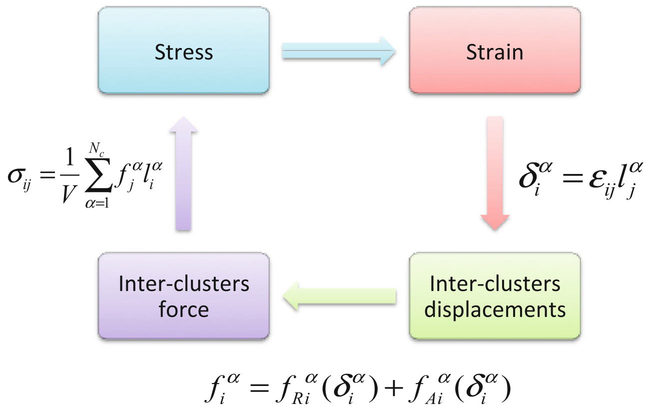

Fig. 7. Micro to Macro-transition kinematic method.

$$\sigma_m = \frac{f\, l_c N_c}{V}$$
$$w = w_0 + \frac{3\delta}{l_0}\left(\frac{100}{\gamma_s/\gamma_w} + w_0\right)$$

w here expresses the water content, σ_m the mean stress, δ the local displacement, N_c the total number of branches of the assembly and l_0 the distance between the center of two neighbouring clusters at the limit liquid state of the material. The calculations were performed using the model parameters given in Table 1. Those were calculated from the macro experimental data, assuming that the liquid limit and plastic limit correspond to the isotropic stresses of 6.7 kPa and 1000 kPa respectively according Biarez and Hicher (1994) correlations. Figure 8 shows a quite good agreement, in isotropic loading, between simulations and experimental results, achieved from the calculation of micro-macro transition.

Table 1. Model parameters for the Mix-clay.

Material	R_0 (μm)	l_0 (μm)	d_{min} (μm)	$\widetilde{B}(N)$	$\tilde{A}(N.\mu m)$	γ_s/γ_w
K	4	9.21	0.17	6.17 10^{-6}	3.84 10^{-7}	2.65
$M_{35\,\%}$	4.5	11.99	0.51	3.12.10^{-5}	3.54 10^{-5}	2.67
$M_{65\,\%}$	5	14.58	0.87	6.14.10^{-5}	2.61 10^{-4}	2.70
$M_{100\,\%}$	5	16.11	0.84	2.35.10^{-4}	3.36 10^{-4}	2.73

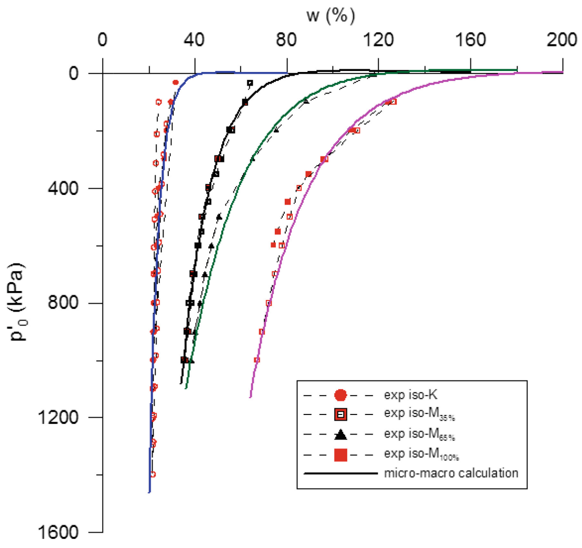

Fig. 8. Local behaviour and Micro-Macro Calculations for the Mix clay material.

Conclusion

The study contributes to show, at the macroscopic scale as well as at the microscopic scale, a behaviour on isotropic and triaxial paths which is particularly sensitive to the amount of montmorillonite in the mixture. Thus, the physical-chemical properties of the Montmorillonite wholly govern the behaviour of the mix-clays. Triaxial test results support this observations showing that the internal friction angle is also governed by the montmorillonite fraction, and, at the microscopic scale, privileged planes forming microcracks develop in different points of the montmorillonite fraction. These planes appear in the form of groups of oriented particles where slip planes can develop. Based on Chang and Hicher micromechanical approach, a new model for clay behaviour is developed which considers energy potentials in the local mechanisms between clay aggregates. This approach allows to introduce physical-chemical effects between clusters through repulsive and attractive forces. The parameters chosen for the local law, deduced from macroscopic curves, permit to estimate these forces between clusters. The results achieved from the calculation of micro-macro transition on isotropic paths appear in quite good agreement with experimental results.

References

Biarez J, Hicher PY (1994) Elementary mechanics of soils behaviour. Saturated remoulded Soils. A.A.Balkema/Rotterdam/Brookfield

Chang CS, Hicher PY (2005) An elastoplastic model for granular materials with microstructural consideration. Int J Solids Struct 42(14):4258–4277

Chang CS, Hicher PY, Yin ZY, Kong LR (2009) Elastoplastic model for clay with microstructural consideration. ASCE J Eng Mech 135:917–931

Chapman DL (1913) A contribution to the theory of electrocapillarity. Philos Mag 25:475–481

Delage P (2010) A microstructure approach to the sensitivity and compressibility of some Eastern Canada sensitive clays. Géotechnique 60(5):353–368

Gouy G (1910) Sur la constitution de la charge électrique à la surface d'un électrolyte. J Phys 9:457–468

Hattab M (2011) Critical state notion and microstructural considerations in clays. C R Méc. 339 (11):719–726

Hattab M, Chang CS (2015) Interaggregate forces and energy potential effect on clay deformation. J Eng Mech. 141(7):04015014

Hattab M, Hammad T, Fleureau JM (2015) Internal friction angle variation in a Kaolin/Montmorillonite clay mix and microstructural identification. Géotechnique 65(1):1–11

Hattab M, Fleureau JM (2010) Experimental study of kaolin particle orientation mechanism. Géotechnique 60(5):323–331

Hattab M, Hammad T, Fleureau JM, Hicher PY (2013) Behaviour of a sensitive marine sediment: microstructural investigation. Geotechnique 63(1):71–84

Van der Waals JD (1873) Ph.D. Thesis, State University of Leyden, Leyden

Van Olphen H (1977) An Introduction of Clay Colloid Chemistry, 2nd edn. Wiley, New York

Coupled Membrane and Diffusion Testing of Active Clays for Barrier Applications

Charles D. Shackelford(✉)

Department of Civil and Environmental Engineering, Colorado State University, Fort Collins, CO 80523-1372, USA
shackel@engr.colostate.edu

Abstract. Highly active clays, such as sodium bentonites, are known to behave as solute restricting, semipermeable membranes under specific physical and chemical conditions. This behavior has important implications for practical applications, including a reduction in solute mass flux due to diffusion. After description of a method for simultaneously measuring membrane behavior and solute diffusion of active clays, the results of experimental studies using the method to test bentonite-based barriers are presented. The effects of effective stress and/or void ratio (dry density) of the specimen, and deviations from anticipated coupled membrane and diffusion behavior resulting from extending the evaluation to the limit where membrane behavior becomes nil are illustrated. The presentation should be of interest to those evaluating the use of bentonite-based barriers for waste containment applications, such as dense bentonite-buffers for high level radioactive waste disposal.

Introduction

The results of extensive research conducted over the past approximate two decades indicate that active clays, such as sodium bentonites, commonly used as engineered barriers or components of engineered barriers for waste containment (e.g., geosynthetic clay liners (GCLs), bentonite buffers for high-level radioactive waste (HLRW) disposal, soil-bentonite backfills for vertical cutoff walls, compacted sand-bentonite liners) can behave as semipermeable membranes that restrict the migration of solutes (e.g., Shackelford 2013, Shackelford and Scalia 2016). Such membrane behavior can be beneficial to the containment function of these barriers, since solute restriction leads to chemico-osmosis and reduced solute (contaminant) mass flux. Also, under the common scenario whereby the hydraulic conductivity, k, of bentonite-based barriers is low (e.g., $\leq 1.0 \times 10^{-10}$ m/s), diffusion is expected to be a significant, if not dominant, component of solute mass flux (Shackelford 2014). Therefore, an understanding of coupled membrane and diffusion behavior of bentonite-based barriers can be important for design and evaluation of such waste containment barriers.

A. Ferrari and L. Laloui (eds.), *Advances in Laboratory Testing and Modelling of Soils and Shales (ATMSS)*, Springer Series in Geomechanics and Geoengineering,
DOI 10.1007/978-3-319-52773-4_11

Background

Membrane Behavior and Diffusion

Semipermeable membrane behavior results when solutes are restricted from movement through porous media. Restricted movement of charged solutes (i.e., ions) through clays occurs when the pore sizes of the clays are sufficiently small such that the electrical potentials of adjacent clay particles interact to the extent that the ions are prevented from entering the pores (Fritz 1986). The resulting restriction in solute migration gives rise to chemico-osmosis, or the migration of liquids (water) from regions of low solute concentration (high water activity) to regions of high solute concentration (low water activity) (Malusis et al. 2001, Malusis and Shackelford 2002a, b). Because solute restriction is largely associated with interacting electrical potentials of individual clay particles, semipermeable membrane behavior is likely to be significant only in high activity clays, such as bentonites and some shales, although membrane behavior also can be evident in low activity clays (e.g., kaolin) that are highly densified (e.g., Olsen 1969).

Clay membrane behavior is quantified in terms of a chemico-osmotic or membrane efficiency coefficient, ω, also commonly known as a reflection coefficient, σ (e.g., see Mitchell and Soga 2005). The magnitude of ω ranges from zero ($\omega = 0$) representing no solute restriction to unity ($\omega = 1$) representing "perfect" or "ideal" membrane behavior, whereby all solutes are restricted. In general, the membrane efficiency for clays that exhibit membrane behavior ranges between zero and unity (i.e., $0 < \omega < 1$) because of the variation in pore sizes comprising most clays, such that only a fraction of the solutes are restricted.

Because clays generally behave as imperfect (non-ideal) membranes, some solute migration via diffusion typically occurs through clay membranes. Such diffusion occurs in the direction opposite to that of chemico-osmosis, i.e., from a region of high solute concentration to a region of low solute concentration, and generally is described in accordance with Fick's first law for diffusive solute mass flux through porous media. The various forms of Fick's first law that have been used for this purpose are summarized in Table 1. Note that all tortuosity factors (τ_a, τ_m, τ_r) range from zero to unity, depending on the interconnectivity of the pores and the extent of solute restriction. For example, the matrix tortuosity factor, τ_m, represents the interconnectivity of the geometric pore structure and ranges from zero for no pore interconnectivity (e.g., unfractured rock) to unity for no soil (pure water). The restrictive tortuosity factor, τ_r, represents the degree of solute restriction due to membrane behavior, and ranges from unity ($\tau_r = 1$) for a porous medium that exhibits no solute restriction (sand) to zero ($\tau_r = 0$) for an ideal membrane. Diffusive solute restriction also has been described via an effective porosity that is less than the total porosity ($n_e < n$) instead of via τ_r. In this regard, $\tau_r = n_e/n$ (e.g., Manassero and Dominijanni 2003). Finally, values of τ_a, τ_m, and τ_r or n_e are determined indirectly via measurement of D^* or D_e.

For a given solute concentration gradient (i_c), solute diffusion is governed primarily by the diffusion coefficient of the specific solute with respect to the specific porous medium. Although all three forms for Fick's first law summarized in Table 1 have been reported in the literature, the form involving D^* is preferred on the basis that the total

Table 1. Definitions of diffusion coefficients in porous media (after Shackelford and Moore 2013).

Form of Fick's first law[a]	Form of diffusion coefficient[b]
$J_d = nD^* i_c$	$D^* = D_o\tau_a = D_o\tau_m\tau_r$
$J_d = D_e i_c$	$D_e = nD_o\tau_a = nD_o\tau_m\tau_r$
$J_d = n_e D_p i_c$	$D_p = D_o\tau_m$

[a] J_d = diffusive solute mass flux [ML^2T^{-1}; M = mass units; L = length units; T = time units]; i_c = solute concentration gradient [ML^{-4}]; n = total porosity [L^3L^{-3}]; n_e = effective porosity [L^3L^{-3}]; D^*, D_e = effective diffusion coefficient [L^2T^{-1}]; D_p = pore diffusion coefficient [L^2T^{-1}]
[b] D_o = aqueous-phase diffusion coefficient [L^2T^{-1}]; τ_a = apparent tortuosity factor [-]; τ_m = matrix tortuosity factor [-]; τ_r = restrictive tortuosity factor [-]

porosity (n) generally is known *a priori* such that including n within the definition of D_e is unnecessary, whereas n_e generally is not known *a priori*, such that the form involving n_e is problematic.

Method of Measurement

A method for simultaneously measuring membrane behavior and solute diffusion of clays was described by Malusis et al. (2001). In this method (see Fig. 1), an electrolyte (salt) solution and de-ionized water (DIW) are circulated continuously across the top and bottom of a clay specimen, respectively, to establish a salt concentration difference, ΔC (= $C_{ob} - C_{ot} = -C_{ot} < 0$, i.e., since $C_{ob} = 0$ for DIW), across the specimen of thickness L. If the specimen behaves as a semipermeable membrane, a tendency for chemico-osmotic liquid (water) flow, q_π, from the bottom to the top of the specimen will develop in response to ΔC. However, the top and bottom circulation systems are saturated with liquid and closed such that volume change is prevented ($\Delta V = 0$). In addition, the specimen is saturated and contained within a rigid-wall cell, such that no volume change of the specimen can occur. As a result, there is no space for liquid to flow (i.e., $q_\pi = 0$), resulting in the development of a chemico-osmotic pressure difference, ΔP, across the specimen to counteract the tendency for chemico-osmosis. The magnitude of ΔP is measured via a differential transducer, and used to calculate ω from the relationship, $\omega = \Delta P/\Delta\pi$, where $\Delta\pi$ = maximum chemico-osmotic pressure difference, which is a function of the boundary solute concentrations (Malusis et al. 2001).

Based on the assumption that the clay specimen exhibits non-ideal membrane behavior (i.e., $0 < \omega < 1$), the chemical species (solutes) derived from the salt solution introduced at the top of the specimen will diffuse through the specimen resulting in a solute mass flux, J_d, emanating from the bottom of the specimen in response to the applied ΔC. As a result, the concentrations of the solutes in the circulation outflow from the bottom of the specimen, C_b, will eventually increase such that $C_b > C_{ob}$ (Fig. 1). The measured C_b is converted to solute mass (m) via multiplication with the

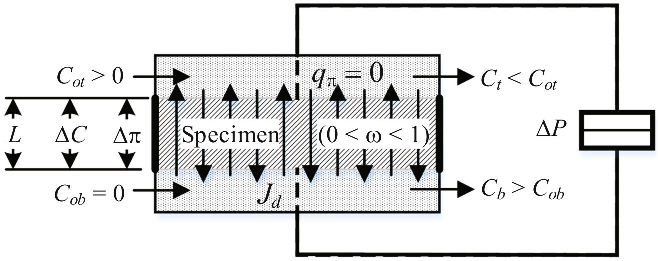

Fig. 1. Schematic illustration of method for the simultaneous measurement of membrane behavior and solute diffusion of clays (after Malusis et al. 2001).

volume of the circulation outflow, V_b (i.e., $m = V_bC_b$), such that the cumulative solute mass emanating from the specimen is determined by monitoring C_b and collecting all of the circulation outflow (i.e., $\Sigma m = \Sigma V_bC_b$). This cumulative solute mass is normalized with respect to the cross-sectional area, A, of the specimen, and designated as Q_t (= ΣV_bC_b/A). The resulting values of Q_t are plotted as a function of elapsed time, t (i.e., Q_t vs. t). Provided the boundary salt concentrations are maintained constant, solute diffusion eventually reaches steady state resulting in a constant slope of Q_t vs. t that is equivalent to the steady-state value of J_d. Based on the steady-state J_d, and known values for n and i_c (= $-\Delta C/L$), the steady-state D^* is determined for the solutes via Fick's first law (Table 1). This method of diffusion testing has been referred to as the time-lag, steady-state, or through-diffusion test method (Shackelford 1991, Malusis et al. 2001).

The original method for simultaneously measuring both membrane behavior and solute diffusion of clays described by Malusis et al. (2001) was based on the use of a rigid-wall (RW) cell. Kang and Shackelford (2009) developed a flexible-wall (FW) cell for use with the aforementioned procedure which offers the advantages of allowing for back-pressure saturation and complete control of the state of stress of the specimen prior to testing. Also, Sample-Lord and Shackelford (2014) describe a hybrid RW-FW cell developed to measure coupled membrane and diffusion behavior of unsaturated clays.

Results

General Trends in Coupled Membrane and Diffusion Behavior

The first experimental results using the aforementioned procedures were reported by Malusis and Shackelford (2002a,b). Their results pertained to a GCL that was permeated with DIW prior to testing to (1) saturate the specimen, (2) enhance the likelihood of significant membrane behavior, and (3) determine the initial k. Solutions of KCl with concentrations (C_{ot}) ranging from 3.9 to 47 mM were circulated across the top of the specimen while DIW ($C_{ob} = 0$) was circulated across the bottom. The measured ω decreased semi-log linearly from 0.63 to 0.14 as C_{ot} increased from 3.9 to 47 mM, respectively (Fig. 2a). In contrast, D^* of chloride (Cl^-), which served as a

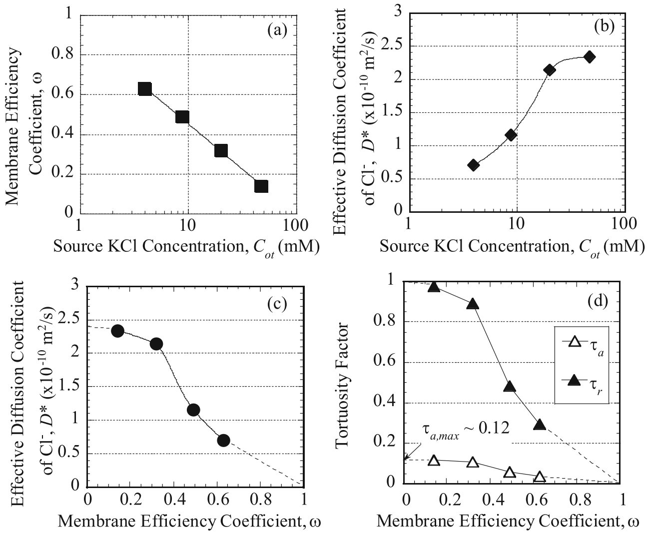

Fig. 2. General trends in coupled membrane and diffusion behavior for a GCL: (a) ω vs. C_{ot}; (b) D^* vs. C_{ot}; (c) D^* vs. ω; (d) τ_a and τ_r vs. ω (data from Malusis and Shackelford 2002a, b).

tracer, increased with increasing C_{ot} (Fig. 2b). These trends were explained on the basis of classical diffuse double layer (DDL) theory, whereby the electrostatic DDLs associated with the individual clay particles collapsed to a greater extent with increasing concentration of KCl in the pores, resulting in larger pore sizes, less solute restriction, and greater solute diffusion through the GCL. The overall effect (Fig. 2c) is that D^* decreased with increasing ω, and trended towards zero as ω approached unity ($D^* \rightarrow 0$ as $\omega \rightarrow 1$) as required by the definition of ideal membrane behavior. This trend was attributed to an increase in tortuosity (decrease in tortuosity factor) with increasing ω (Fig. 2d).

Effect of Effective Stress and Void Ratio

In general, an increase of effective stress, $\sigma'(= \sigma - u$, where σ = total stress and u = pore-water pressure), results in a decrease in void ratio, e, of the clay and smaller pores (Kang and Shackelford 2010). Thus, an increase in σ' correlates with an increase in ω and a decrease in D^* (Kang and Shackelford 2009, 2011, Malusis et al. 2015). Note that this definition of σ' does not include the effects of the chemical composition of the pore water, which may be significant in active clays via the difference in the repulsive and active forces between adjacent clay particles (Chatterji and Morgenstern 1990, Kang and Shackelford 2009).

For example, consider the results shown in Fig. 3a, which pertain to coupled membrane and diffusion testing of a GCL subjected to source solutions of KCl with C_{ot} ranging from 3.9 to 47 mM. The results in Fig. 3a were obtained using FW cells on specimens of a GCL that were permeated with DIW for periods ranging from 105 to 209 d

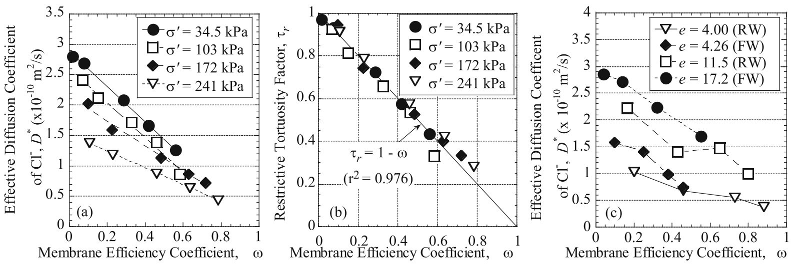

Fig. 3. Effect of effective stress (σ′) and void ratio (*e*) on coupled membrane and diffusion behavior of bentonite-based barriers: (a) D^* vs. ω for GCL; (b) τ_r vs. ω for GCL; (c) D^* vs. ω for polymerized bentonite (data for (a) and (b) from Malusis et al. 2015; data for (c) from Bohnhoff and Shackelford 2015).

to flush soluble salts from the pores of the bentonite, and the D^* values are for Cl^-. As shown in Fig. 3b, the reduction in D^* of Cl^- as reflected by τ_r appears to be well correlated with the relationship $\tau_r = 1 - \omega$ proposed by Manassero and Dominijanni (2003) on the basis of theoretical considerations, and this correlation appears to be independent of σ′.

The effect of *e* on coupled membrane and diffusion testing of a polymerized bentonite (PB) based on tests using both RW and FW cells and source KCl solutions with C_{ot} ranging from 4.7 to 54 mM is illustrated in Fig. 3c (Bohnhoff and Shackelford 2013, 2015, Bohnhoff et al. 2016). As expected, the results in Fig. 3c indicate that solute restriction becomes increasingly enhanced with decreasing *e*.

Limiting Behavior

The results of a study evaluating coupled membrane and diffusion behavior of a GCL in the limit as ω approaches zero ($\omega \rightarrow 0$) are shown in Fig. 4 (Meier et al. 2014, Shackelford et al. 2016). The test was similar to those previously conducted using RW cells and KCl solution except for two aspects. First, C_{ot} was increased until the limiting membrane behavior corresponding to $\omega = 0$ was achieved. Second, the GCL specimen was not flushed of soluble salts via permeation with DIW prior to coupled membrane and diffusion testing.

The results indicated that the membrane behavior of the GCL was effectively destroyed at a C_{ot} for KCl of 400 mM (Fig. 4a), and unlike the linear behavior in ω vs. log C_{ot} previously shown for lower C_{ot} (Fig. 2a), the membrane behavior was clearly nonlinear. As a result, the limiting C_{ot} of 400 mM was significantly greater than would have been anticipated based on an extrapolation of an assumed linear behavior (Meier et al. 2014). Also, the coupled membrane and diffusion behavior was nonlinear (Fig. 4b), and τ_r back-calculated on the basis of the measured D^* were lower than those predicted on the basis of the theoretical relation $\tau_r = 1 - \omega$ (Fig. 4c). Shackelford et al. (2016) attributed this latter observation to the possibility of physico-chemical interactions that resulted in an increase in τ_m, which generally is assumed to be constant,

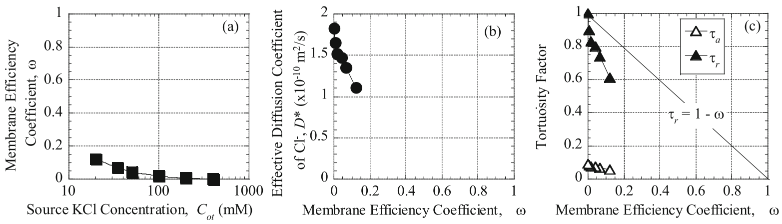

Fig. 4. Limiting membrane and diffusion behavior of a GCL in a RW cell subjected to KCl solutions: (a) ω vs. C_{ot}; (b) D^* vs. ω; (c) τ_a and τ_r vs. ω (data from Meier et al. 2014, Shackelford et al. 2016).

although the lack of flushing of soluble salts prior to membrane and diffusion testing also may have been a factor.

Summary

A testing method for measuring coupled membrane and diffusion behavior of active clays was described. Results illustrate the expected trend of decreasing D^* with increasing ω, such that D^* approaches zero as ω approaches unity corresponding to perfect (ideal) membrane behavior. The expected trend of increasing ω and decreasing D^* with increasing σ′ and/or decreasing e also was illustrated. The method should be applicable for bentonite-based containment barriers, such as dense bentonite buffers used for HLRW containment in geological depositories.

References

Bohnhoff G, Sample-Lord K, Shackelford C (2016) Advances in membrane behavior of bentonite-based barriers, geo-Chicago 2016. ASCE, Reston

Bohnhoff G, Shackelford C (2013) Improving membrane performance via bentonite polymer nanocomposite. Appl Clay Sci 86:83–98

Bohnhoff G, Shackelford C (2015) Salt diffusion through a bentonite-polymer composite. Clay Clay Miner 63:172–189

Chatterji P, Morgenstern N (1990) A modified shear strength formulation for swelling clay soils. In: Hoddinott K, Lamb R (eds) EdsPhysico-chemical aspects of soil and related materials. ASTM, Philadelphia, p 118–135

Fritz S (1986) Ideality of clay membranes in osmotic processes: a review. Clay Clay Miner 34:214–223

Kang J, Shackelford C (2009) Clay membrane testing using a flexible-wall cell under closed-system boundary conditions. Appl Clay Sci 44:43–58

Kang J, Shackelford C (2010) Consolidation of a geosynthetic clay liner under isotropic states of stress. J Geotech Geoenviron 136:253–259

Kang J, Shackelford C (2011) Consolidation enhanced membrane behavior of a geosynthetic clay liner. Geotext Geomembr 29:544–556

Malusis M, Kang J, Shackelford C (2015) Restricted salt diffusion in a geosynthetic clay liner. Environ Geotech 2:68–77

Malusis M, Shackelford C (2002a) Chemico-osmotic efficiency of a geosynthetic clay liner. J Geotech Geoenviron 128:97–106

Malusis M, Shackelford C (2002b) Coupling effects during steady-state solute diffusion through a semipermeable clay membrane. Environ Sci Tech 36:1312–1319

Malusis M, Shackelford C, Olsen H (2001) A laboratory apparatus to measure chemico-osmotic efficiency coefficients for clay soils. Geotech Test J 24:229–242

Manassero M, Dominijanni A (2003) Modelling the osmosis effect on solute migration through porous media. Géotechnique 53:481–492

Meier A, Sample-Lord K, Castelbaum D, Kallase S, Moran B, Ray T, Shackelford C (2014) Persistence of semipermeable membrane behavior for a geosynthetic clay liner. Proceedings of 7th international conference environment Geotech, Melbourne, Australia (ISBN 978-1-922107-23-7), p 496–503

Mitchell J, Soga K (2005) Fundamentals of soil behavior, 3rd edn. John Wiley, New York

Olsen H (1969) Simultaneous fluxes of liquid and charge in saturated kaolinite. Soil Sci Soc Am Pro 33:338–344

Sample-Lord K, Shackelford C (2014) Membrane behavior of unsaturated bentonite barriers. Geo-congress 2014: geo-characterization and modeling for sustainability, GSP 234, ASCE, Reston, p 1900–1909

Shackelford C (1991) Laboratory diffusion testing for waste disposal – a review. J Contam Hydrol 7:177–217

Shackelford C (2013) Membrane behavior in engineered bentonite-based containment barriers: state of the art. In: Proceedings of coupled phenomena environment geotechnics (CPEG), Torino, Italy, CRC Press/Balkema, Taylor & Francis Group, London, 1–3 July, pp 45–60

Shackelford C (2014) The ISSMGE Kerry Rowe lecture: the role of diffusion in environmental geotechnics. Can Geotech J 51:1219–1242

Shackelford C, Meier A, Sample-Lord K (2016) Limiting membrane and diffusion behavior of a geosynthetic clay liner. Geotext Geomembr 44:707–718

Shackelford C, Moore S (2013) Fickian diffusion of radionuclides for engineered containment barriers: diffusion coefficients, porosities, and complicating issues. Eng Geol 152:133–147

Shackelford C, Scalia J (2016) Semipermeable membrane behavior in bentonite-based barriers: past, present, and future. In: Proceedings of GeoVancouver 2016, Vancouver, BC, Canada, 2–5 Oct 2016

Evidences of the Effects of Free Gas on the Hydro-mechanical Behaviour of Peat

C. Jommi[1(✉)], S. Muraro[1], E. Trivellato[1,2p], and C. Zwanenburg[3]

[1] Delft University of Technology, Delft, The Netherlands
C.Jommi@tudelft.nl
[2] Laboratoire Navier, École Nationale des Ponts et Chaussées, Paris, France
[3] Deltares, Delft, The Netherlands

Abstract. Peats are soils containing a significant component of organic matter. Biochemical degradation of this fraction generates gases such as CO_2, H_2S and CH_4, which tend to saturate the pore water eventually resulting in exsolution and expansion. The effects of these gases on the hydro-mechanical behaviour of peats are under investigation at Delft University of Technology. The results of a series of triaxial tests are discussed, in which gas was exsolved under controlled conditions by flushing natural samples with carbonated water, and undrained isotropic unloading and shear were performed. A significant reduction in the effective stress acting on the soil skeleton was observed during undrained unloading due to gas exsolution. However, different stages were observed in time, which appear to be ruled by the very high compressibility of peat. The mechanical response upon shearing is dominated as well by the ratio between the compressibility of the fluid and the soil skeleton. Although the ultimate strength does not differ much between the samples tested, the mobilised shear strength for a given axial strain does, which has to be accounted for cautiously in the choice for an *operative* shear strength.

Introduction

Decomposition of the organic matter in peat layers tends to saturate the pore fluid with several species of gas, such as CO_2, H_2S and CH_4. The possibility of gas being trapped in peat layers was firstly advanced based on systematic different pore pressure measurements coming from vented and non-vented pressure transducers (Kellner et al. 2005; Acharya et al. 2015). Several attempts to quantify this amount of gas reached a consensus on a volumetric gas fraction ranging between 0.05–0.12 (Baird and Waldron 2003). However, atmospheric pressure changes, total stress reduction, lowering the water table and temperature oscillations are all potential causes of exsolution and expansion of these gases. Gas bubbles release due to total stress reduction were observed during field tests on dykes founded on peat layers (Zwanenburg 2013), which raised a concern about the value of shear strength to be used in their assessment. A comprehensive study was planned at Delft University of Technology in cooperation with Deltares, aimed at quantifying the influence of gas on the hydromechanical behaviour of peat. The study stemmed from previous knowledge on the hydrological response of peat layers (e.g. Kellner et al. 2005), and on the mechanical response of different gas bearing

A. Ferrari and L. Laloui (eds.), *Advances in Laboratory Testing and Modelling of Soils and Shales (ATMSS)*, Springer Series in Geomechanics and Geoengineering,
DOI 10.1007/978-3-319-52773-4_12

sediments, namely sands and marine clays (e.g. Sobkowicz and Morgenstern 1984; Sultan et al. 2012). Results from a series of triaxial tests are discussed here to evaluate the relevance of gas on the undrained unloading and shearing responses.

Laboratory Tests and Experimental Data

Material Properties and Experimental Set up

A series of isotropic undrained triaxial tests has been carried out on natural peat samples. Undisturbed peat samples were collected at Katwoude along the Markermeer dykes in the Netherlands, between 1.0 m and 2.5 m depth. The material was then stored in a climate controlled room at 10 °C and 90% relative humidity. Table 1 reports the index properties of the tested samples. Loss of ignition tests (Skempton and Petley 1970) gave an average organic content, *OC*, of 85.7%.

Table 1. Index properties of the undisturbed peat samples.

	γ [kN/m^3]	Gs [-]	γ_{dry} [kN/m^3]	n_0 [-]	e_0 [-]
Test 01	9.87	1.475	1.23	0.91	9.59
Test 02	10.97	1.371	1.12	0.92	12.04
Test 03	10.36	1.401	1.34	0.91	9.89
Test 04	10.20	1.454	1.37	0.91	10.03
Test 05	10.37	1.432	1.29	0.92	10.78

In order to generate a uniform gas distribution in the peat samples, dissolved gas was injected by flushing carbonated water, and exsolution was forced by means of isotropic undrained unloading. The experimental set up consisting in a GDS Triaxial load frame type, with standard back pressure and cell pressure volume controllers, was modified with a third external controller to flush the carbonated water solution. The solution was prepared before every test in a Perspex cell where CO_2 at 380 kPa was left in contact with de-aired water for few days at 22 °C. The same procedure had been successfully adopted by Lunne et al. (2001), Amaratunga and Grozic (2009) and Sultan et al. (2012). Two latex membranes with grease in between were used for gassy specimens in order to reduce gas leaking. All the tests were performed under controlled air temperature 13 °C, and relative humidity 68%.

Experimental Programme

Four tests (Tests 02, 03, 04, 05) have been conducted on carbonated gassy samples, while Test 01 has been performed on a fully saturated sample. For the latter, demineralized de-aired water instead of carbonated water was flushed into the sample, for full repeatability of the testing protocol. All the samples, 100 mm high with diameter 50 mm, experienced a similar imposed stress history in terms of cell pressure, σ_c, and back pressure, u_b: (a) isotropic undrained loading up to $\sigma_c = 406 \div 409$ kPa;

(b) flushing under a pressure difference of $u_f - u_b = 2 \div 3$ kPa; (c) isotropic consolidation $\sigma'_c = 20 \div 22$ kPa; and (d) isotropic undrained unloading to a final confining stress $\sigma_c = 51 \div 65$ kPa. During undrained unloading the pore fluid pressure u_f was measured at the bottom of the sample, and the final value was in the range $u_f = 38 \div 64$ kPa. Eventually, undrained shearing was performed at a controlled axial displacement rate of 0.02 mm/min.

Isotropic Undrained Unloading

In gassy soils the large amount of dissolved gas with high solubility in the pore fluid dominates the pore pressure response upon unloading. When the pore pressure decreases below the liquid-gas saturation pressure $u_{l/g}$, gas exsolution begins and despite the undrained external drainage conditions, the soil experiences volumetric strain (Sobkowicz and Morgenstern 1984). The volumetric strains during the isotropic undrained unloading are reported for all the tests in Fig. 1a. Compressive stresses and strains are assumed positive.

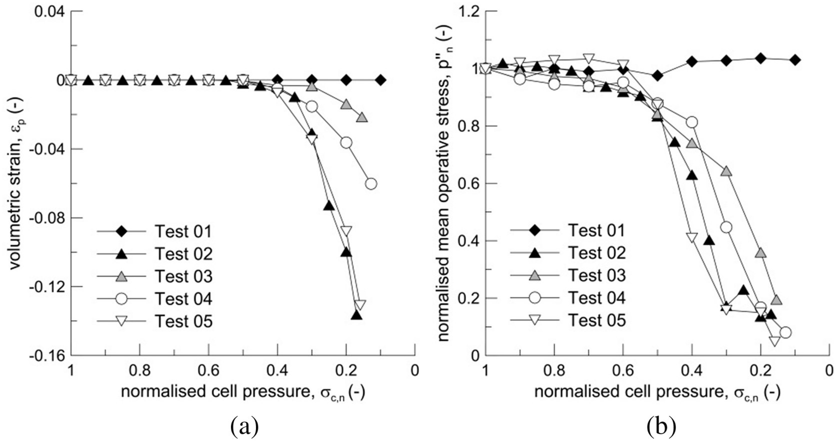

Fig. 1. (a) Volumetric strain, (b) Normalised mean operative stress, during the isotropic undrained unloading.

The unloading rate differed in the four tests on gassy samples. For Test 01 and Test 05 the unloading duration was 2 h, for Test 03 and Test 04 it lasted 4 h and in Test 02 a step by step procedure was adopted. According to the volumetric strain recorded for the gassy samples the generated gas content attains a volumetric fraction between 0.03 and 0.14, which mostly depended on the unloading stress rate. In the fully saturated Test 01 no volumetric strain was recorded.

The presence of gas bubbles increases the pore fluid compressibility, resulting in a significant decrease in the effective stress acting on the soil skeleton upon total stress reduction (Amaratunga and Grozic 2009). In Fig. 1b the evolution of the normalised mean operative stress $p''_n = (\sigma_c - u_f)/(\sigma_{c0} - u_{f0})$ (Sills et al. 1991) is reported as a function of the imposed normalised total stress reduction, where σ_{c0} and u_{f0} are the initial cell and pore fluid pressures at the start of unloading. The experimental data show that gas exsolution brings the mean operative stress nearly to zero, while virtually no change was observed during unloading of the sample saturated with de-aired water (Test 01). Similar results had been found on other gassy soils (Sobkowicz 1982; Sultan et al. 2012). However, the rate of exsolution differed in this case, as it will be discussed in the next section.

Undrained Shear

Results of the undrained shear stage for the fully saturated and the normally consolidated gassy samples are reported in Fig. 2. The gassy samples showed an initial partly drained response as in Nageswaran (1983) and Sills et al. (1991). The high compressibility of the pore fluid due to the exsolved gas causes a lower excess of pore fluid pressure and non-null volumetric strain despite external undrained conditions. As soon as the free gas is compressed and dissolved again, the observed response becomes closer to the fully saturated case. The compressibility of gas affects the stress-strain stiffness, but the ultimate stress ratio of the different samples is similar and hardly affected by the initial gas fraction, with all the samples approaching the tension cut-off line. A diffused failure mode eventually occurred for all the samples, at axial strains around 30%. The high ultimate strain and the contribution of big fibres on the asymptotic strength, typically suggest the definition of operative criteria for serviceability and ultimate limit states based on mobilised shear strength at given axial strain thresholds. The dramatic effect of gas on the operative shear strength parameters is demonstrated in Fig. 2b, where the mobilised friction angle is reported for axial strains of 2% and 5%.

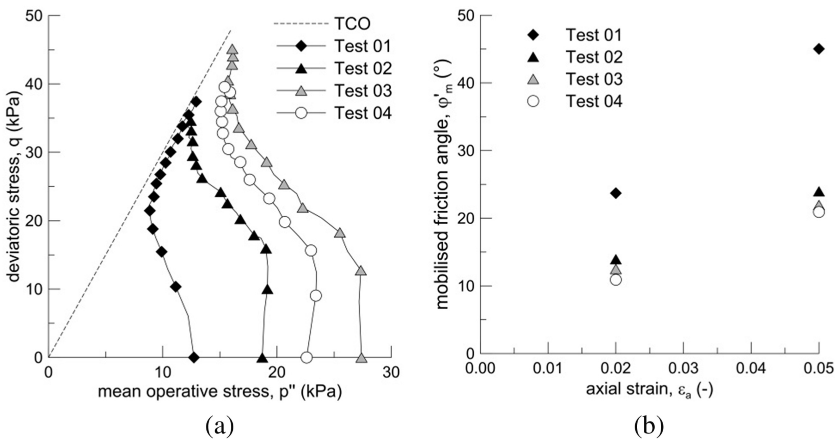

Fig. 2. (a) Stress paths in the mean operative - deviatoric stress plane (symbols are plotted every 2% axial strain increment), (b) Mobilised friction angles at given axial strains.

Interpretation and Discussion

The volumetric strains reported in Fig. 1a and the mean operative stress in Fig. 1b suggest that gas exsolution began at a normalised cell pressure $\sigma_{c,n}$ around 0.55–0.60, with $\sigma_c = 200 \div 248$ kPa. The corresponding measured pore fluid pressure ranged between $u_f = 185 \div 225$ kPa. Differently from Sobkowicz (1982) and Amaratunga and Grozic (2009) the measured pore fluid pressure at the initiation of gas exsolution was well below the pressure at which the water had been saturated with CO_2 ($u_{l/g}$ = 380 kPa). According to Henry's law, the concentration c_g of a gas in the aqueous phase is proportional to the absolute gas pressure u_g through Henry's coefficient H^{cp}:

$$H^{cp} = \frac{c_g}{u_g}$$

Henry's coefficient depends on the gas species, gas pressure and temperature (Sander 2015). It is worth remarking that the carbonated water was prepared in a room at 22° and it was then brought to the triaxial test room at 13 °C. Considering the dependence of the Henry's coefficient on the temperature, the gas concentration c_g reached at 22 °C and relative u_g = 380 kPa corresponds to a relative liquid-gas saturation pressure $u_{l/g}$ = 271 kPa at a temperature of 13 °C, at which the triaxial tests were performed. For $u_f > u_{l/g}$ the solution is therefore under saturated and only for $u_f < u_{l/g}$ gas exsolution can take place. The change in the liquid-gas saturation pressure with temperature may account for most of the difference between the pressure at which the gas was dissolved into the water and the pressure at which it started exsolving during undrained unloading of the peat samples, which was around 200 kPa. However, similar delay in gas exsolution was observed on a soft marine clay (Sultan et al. 2012), although no difference in temperature was reported. Also, gas loss by diffusion through the membrane might have contributed in delaying the exsolution of gas, despite the double membrane with grease used to prevent such diffusion.

It is worth remarking that the relative stiffness between the pore fluid and the soil skeleton plays the most important role in the fluid pressure evolution. While in sands the soil skeleton is very stiff with respect to water with gas, this is not always the case for very compressible peat, and possibly for soft clay soils. To provide further insight into the coupled process, the time evolution of the measured pore fluid pressure during undrained unloading is reported in Fig. 3a for Test 05. Three stages can be clearly identified: stage 1, where $\dot{u}_f \cong \dot{\sigma}_c$, stage 2 with $\dot{u}_f < \dot{\sigma}_c$ and stage 3 where again $\dot{u}_f \cong \dot{\sigma}_c$.

In stage 1, the pore fluid pressure decreases commensurately with the total stress, indicating that no gas exsolution is taking place. Both under saturated solution at the beginning of the stage and a relatively high stiffness of the water with respect to the soil skeleton (initial bulk modulus lower than 1.0 MPa) contribute in delaying gas exsolution. Gas starts exsolving when the fluid pressure reaches 200 kPa (stage 2) leading to a significant reduction in the mean operative stress (Fig. 1b). As a result of the free gas bubbles in the pore spaces, the pore fluid compressibility increases. With continuing gas exsolution, the operative stress decreases and the soil skeleton compressibility increases, eventually becoming smaller than that of the pore fluid. During the last stage

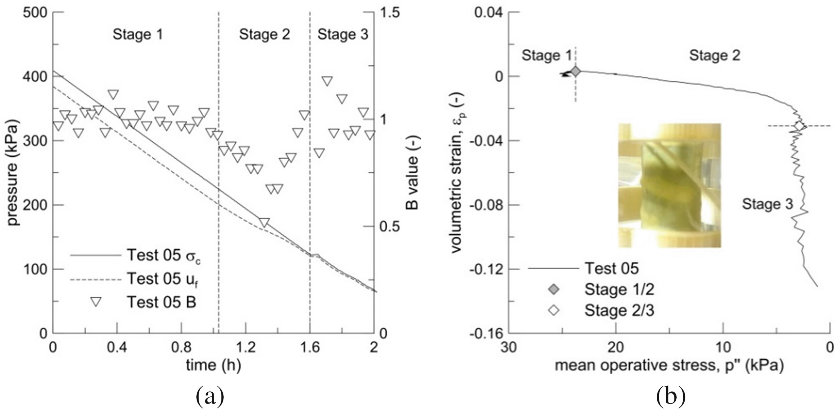

Fig. 3. (a) Evolution of cell pressure and measured pore fluid pressure during the isotropic undrained unloading for Test 05 together with the B value; (b) Volumetric strain versus mean operative stress.

of undrained unloading (stage 3), the pore fluid and the cell pressure decrease by the same amount. The pore pressure parameter B (Skempton 1954) derived from the experimental data, shown in Fig. 3a, is smaller than 1 during the second stage of unloading, while it becomes close to unity again at the end of the unloading stage.

The observed macroscopic behaviour is indeed the result of a complex process at the soil fabric-pore scale. As pointed out by Wheeler (1988) the gas bubbles behaviour and the surrounding matrix one are totally coupled, in the sense that the matrix deformation affects the gas pressure and vice-versa. To highlight this aspect, the volumetric strain recorded for Test 05 during the isotropic undrained unloading is plotted versus the mean operative stress in Fig. 3b. The three stages of Fig. 2 are superimposed on the data.

A clear dependence of the volumetric strain and thus of the exsolved gas fraction on the mean operative stress is evident. Once the gas starts to exsolve (stage 2), the volumetric strains are almost linearly dependent on the operative confining stress. During this stage, the volumetric strain increment is only about 0.04 for a relatively high change in the operative stress of ≈21 kPa. The vast majority of free gas is generated only during stage 3 under a low nearly constant operative stress, when previous gas exsolution and expansion have softened the soil fabric, as pointed out by Sobkowicz and Morgenstern (1984). Possible local softening of the soil fabric was suggested by the formation of gas pockets on the lateral side of the sample (Fig. 3b). These gas pockets were observed only during the last part of unloading as if the gas clusters inside the sample had locally damaged the soil matrix with preferential horizontal gas flow paths.

Concluding Remarks

Isotropic undrained unloading and shear tests on peat were performed, after flushing the samples with carbonated water in order to generate a uniform distribution of gas. The tests aimed at evaluating the role played by gas on the stiffness and the strength response of peat in anaerobic environment. As soon as the pore fluid pressure drops below the liquid-gas saturation pressure, which depends on temperature, gas exsolution starts. Free gas bubbles increase the pore fluid pressure and its compressibility, eventually reducing the operative stress on the soil skeleton and potentially softening the peat fabric, with a mutual gas-matrix interaction, depending on their current relative stiffness. The following stress-strain response is affected by gas, but the ultimate shear strength does not differ much between saturated and gassy samples. However, the mobilised shear strength for a given axial strain changes dramatically, which has to be accounted for cautiously in the choice for an operative shear strength based on strain thresholds.

References

Acharya MP, Hendry MT, Edwards T (2015) A case study of the long-term deformation of peat beneath an embankment structure. In: Manzanal D, Sfriso AO (eds) Proceedings of the 15th Pan-American conference on soil mechanics and geotechnical engineering, pp 438–445. doi:10.3233/978-1-61499-603-3-438

Amaratunga A, Grozic JLH (2009) On the undrained unloading behaviour of gassy sands. Can Geotech J 46(11):1267–1276. doi:10.1139/T09-056

Baird AJ, Waldron S (2003) Shallow horizontal groundwater flow in peatlands is reduced by bacteriogenic gas production. Geophys Res Lett 30(20). doi:10.1029/2003GL018233

Kellner E, Waddington JM, Price JS (2005) Dynamics of biogenic gas bubbles in peat: potential effects on water storage and peat deformation. Water Resour Res 41(8). doi:10.1029/2004WR003732

Lunne T, Berre T, Strandvik S, Andersen KH, Tjelta TI (2001) Deepwater sample disturbance due to stress relief. International conference on Geotechnical, geological and geophysical properties of deepwater sediments. Houston, TX, pp 64–85

Nageswaran S (1983). Effects of gas bubbles on the sea-bed behaviour. Ph.D. thesis, Oxford University

Sander R (2015) Compilation of Henry's law constants (version 4.0) for water as solvent. Atmos Chem Phys 15:4399–4981. doi:10.5194/acp-15-4399-2015

Sills GC, Wheeler SJ, Thomas SD, Gardner TN (1991) Behaviour of offshore soils containing gas bubbles. Géotechnique 41(2):227–241. doi:10.1680/geot.1991.41.2.227

Skempton AW (1954) The pore pressure coefficients A and B. Géotechnique 4(4):143–147. doi:10.1680/geot.1954.4.4.143

Skempton AW, Petley J (1970) Ignition loss and other properties of peats and clays from Avonmouth, King's Lynn and Cranberry Moss. Géotechnique 20(4):343–356. doi:10.1680/geot.1970.20.4.343

Sobkowicz JC (1982) The mechanics of gassy sediments. Ph.D. thesis, Civil Engineering Department, University of Alberta, Edmonton, Alta

Sobkowicz JC, Morgenstern NR (1984) The undrained equilibrium behaviour of gassy sediments. Can Geotech J 21(3):439–448. doi:10.1139/t84-048

Sultan N, De Gennaro V, Puech A (2012) Mechanical behaviour of gas-charged marine plastic sediments. Géotechnique 62(9):751–766. doi:10.1680/geot.12.OG.002

Wheeler SJ (1988) A conceptual model for soils containing large gas bubbles. Géotechnique 38(3):389–397. doi:10.1680/geot.1988.38.3.389

Zwanenburg C (2013) Dikes on Peat: analysis of field trials. Internal report, Deltares

Unsaturated Behavior of Soils and Shales

Use of Psychrometers, Capacitive Sensors and Vapour Transfer Technique to Determine the Water Retention Curve of Compacted Bentonite

María Victoria Villar(✉), Rubén Javier Iglesias, Carlos Gutiérrez-Álvarez, and Gemma Campos

Centro de Investigaciones Energéticas, Medioambientales y Tecnológicas (CIEMAT), Madrid, Spain
mv.villar@ciemat.es

Abstract. The FEBEX large-scale test simulating an underground repository of nuclear waste excavated in granite was dismantled after 18 years of operation. The engineered barrier between the heaters and the host rock consisted of compacted blocks of FEBEX bentonite which were retrieved during dismantling. The water content, dry density and suction of some of these blocks were measured at the laboratory and retention curves (WRC) were inferred from these values. The WRC of samples trimmed from the blocks was also determined using the vapour transfer technique. The results obtained with both methodologies were compared with the WRC obtained previously for the reference untreated FEBEX bentonite. The results are comparable, which indicates, on the one hand, that both methodologies give consistent results and, on the other, that the water retention capacity was not altered by 18 years operation under barrier conditions.

Introduction

The aim of FEBEX (Full-scale Engineered Barrier Experiment) was to study the behaviour of components in the near-field of a nuclear waste repository in crystalline rock. As part of this project, an in situ test under natural conditions and at full scale was performed at the Grimsel Test Site (GTS, Switzerland) underground laboratory (ENRESA 2006). The thermal effect of the wastes was simulated by means of two heaters which were placed horizontally in a drift excavated in granite and surrounded by a clay barrier constructed from highly-compacted bentonite blocks. The external surface temperature of the heaters was 100°C and the bentonite barrier was slowly hydrated by the granitic groundwater. After 5 years operation half of the installation was dismantled. The FEBEX Dismantling Project (FEBEX-DP) undertook the dismantling of the remaining half after 18 years operation (Fig. 1). The onsite analyses showed a variety of water content and dry density values across the barrier, caused by the combined effect of heating and hydration and the expansive potential of the material (Villar et al. 2016). Thus, the samples closest to the heater had overall the highest dry densities and lowest water contents (Fig. 2). Also, the bentonite barrier at the back of

A. Ferrari and L. Laloui (eds.), *Advances in Laboratory Testing and Modelling of Soils and Shales (ATMSS)*, Springer Series in Geomechanics and Geoengineering,
DOI 10.1007/978-3-319-52773-4_13

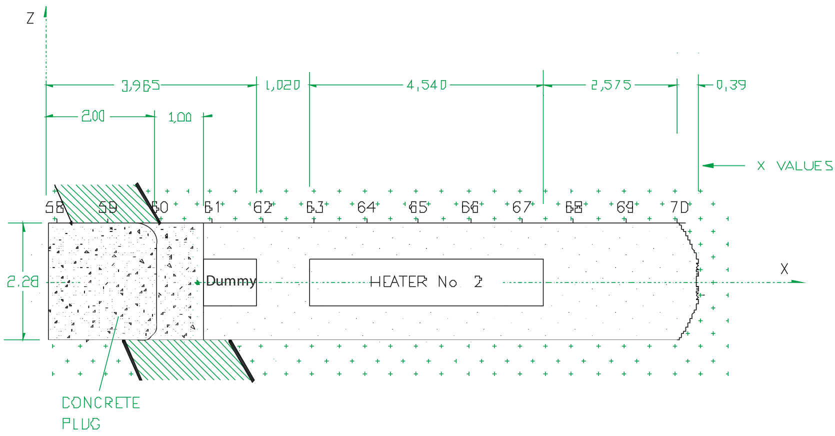

Fig. 1. General layout of the in situ test from 2002 to 2015 and location of bentonite sampling sections for onsite determinations (AITEMIN 2016).

the gallery was not affected by the heater and the temperatures in it were below 22°C during operation.

Numerous bentonite blocks were taken during dismantling and analysed at CIEMAT laboratories. The water retention curve (WRC) of the bentonite has been determined with the aim of checking the effect of prolonged drying on the water retention capacity of the bentonite by comparison with samples taken from non-heated parts of the barrier and with the reference bentonite.

Material: FEBEX Bentonite

The FEBEX bentonite was extracted in 1995 from the Cortijo de Archidona deposit (Almería, Spain) and the processing at the factory consisted on disaggregation and gently grinding, drying at 60°C and sieving by 5 mm, what gave place to a water content of 14%. The blocks used in the FEBEX in situ test were manufactured by uniaxial compaction of this material in the shape of 12-cm thick circular crown sectors using pressures of between 40 and 45 MPa.

The same material (hereafter called reference or untreated material) was thoroughly characterized in the laboratory over the years (ENRESA 2006). It contains 92 ± 3 wt% of montmorillonite, variable quantities of quartz (2 ± 1 wt%), plagioclase (3 ± 1 wt %), K-felspar (traces), calcite (1 ± 0.5 wt%) and cristobalite-trydimite (2 ± 1 wt%). The cation exchange capacity of the smectite is 102 ± 4 meq/100 g, with calcium, magnesium and sodium as main exchangeable cations. The density of solid particles is 2.70 ± 0.04 g/cm^3.

The retention curve of the reference bentonite was determined in samples compacted to different dry densities at different temperatures (Villar 2002; Lloret et al. 2004; Villar and Lloret 2004; Villar 2007; Villar and Gómez-Espina 2009). The volume of the samples remained constant during these determinations. From these data an

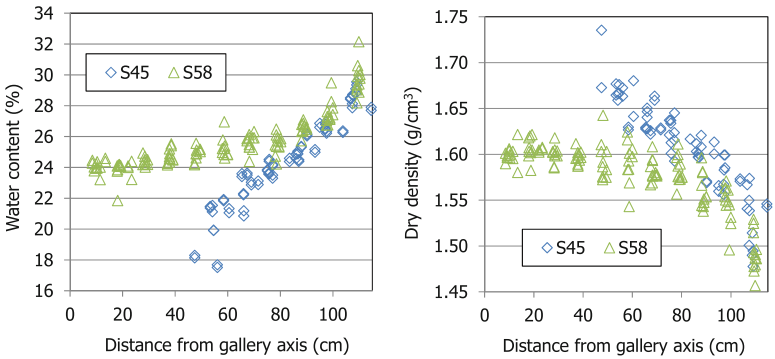

Fig. 2. Water content and dry density determined onsite of samples taken around the heater (S45) and at the back of the gallery (S58). See Fig. 1 for location of sections.

empirical expression relating water content to suction taking into account porosity and temperature was obtained and presented in Villar et al. (2012).

Methodology

The blocks retrieved at GTS were wrapped onsite with plastic film immediately after their extraction and put into two aluminized-PET bags which were vacuum sealed to avoid any humidity losses. More than 40 blocks were sent to CIEMAT for the study of their physical state and changes in thermal, hydraulic and geochemical properties. From their arrival the samples were kept in a RH-controlled storage room.

The relative humidity and temperature of the blocks was measured either with psychrometers or with capacitive sensors. The relative humidity of the blocks with higher water content was measured with 8 psychrometers Wescor Elitech PST-55-30-SF with stainless steel filters connected to a Wescor Elitech PSYPRO datalogger. These sensors, 6 mm in diameter and 30 mm in length, operate in a suction range from 50 to 6200 kPa, with a precision of ±1% FS. The capacitive transmitters used for the samples with lower water content were Sensirion SHT75, which have a precision of 2% RH in the range from 20 to 80%.

The blocks were taken from the storage room to the laboratory at least 1 h before the measurements to ensure thermal equilibrium. The aluminium foil bags were removed and, with the block wrapped in plastic foil, holes were drilled in the block to install the sensors inside (Fig. 3, left). The stabilisation of the measurement took about 1 h. To convert the values of relative humidity (RH, %) to suction values (s, MPa) the Kelvin's law was used:

$$s = -10^{-6} \frac{R \times T}{V_w} \ln\left(\frac{\mathrm{RH}}{100}\right) \tag{1}$$

where R is the universal constant of gases (8.3143 J/mol · K), T the absolute temperature and V_w, the molar volume of water ($1.80 \cdot 10^{-5}$ m^3/mol).

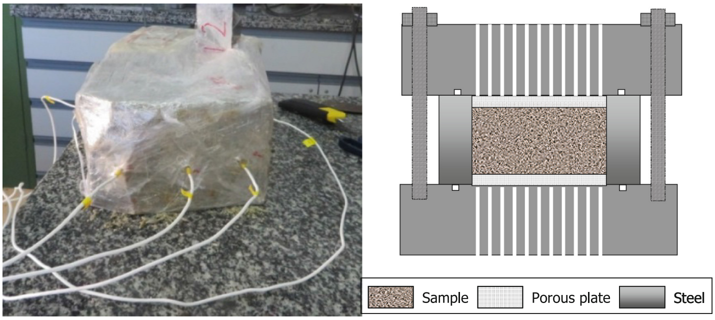

Fig. 3. Psychrometers inserted on a block prior to unpacking and schematic representation of the constant volume cell for WRC determination (Villar 2002).

The samples for the water content and dry density determinations were obtained by drilling the blocks with a crown drill bit. Two or three positions were drilled in each block, and from every core 1 or 2 subsamples were obtained.

The gravimetric water content (*w*) is defined as the ratio between the mass of water and the mass of dry solid expressed as a percentage. The mass of dry soil was determined by oven drying at 110°C for 48 h. Dry density (d) is defined as the ratio between the mass of the dry sample and the volume occupied by it prior to drying. The volume of the specimens was determined by immersing them in a vessel containing mercury and by weighing the mercury displaced. The same samples whose volumes had been determined were used for the water content determination.

The water retention curves (WRC) are being determined with the aim of checking the effect of prolonged drying on the water retention capacity of the bentonite. For this reason, samples from the blocks closest to the heater are being tested. For comparison, blocks of similar water content taken from cool parts of the barrier are also being tested. The samples were drilled from the blocks with a crown drill bit. The cores obtained were trimmed with cylindrical cutters to adjust their diameter to 3.8 cm and pushed into stainless steel rings which are the body of a cell (Fig. 3, right). The height of the resulting bentonite cylinders was between 1.1 and 1.2 cm. The cells were placed in desiccators with sulphuric acid solutions, so that to apply a given suction to the samples by means of the control of the relative humidity. The relative humidity inside the desiccators is related to total suction through Kelvin's equation (Eq. 1).

The samples have been initially submitted to suctions of 19–23 MPa, which were the suctions measured in the blocks with sensors as described above. Afterwards, the samples were submitted to suctions progressively lower to check their water retention capacity under confined conditions. The evolution of water content in the samples is checked by periodical weighing, and the suction step is not changed until stabilisation is reached. The determinations are being performed at 20°C. These tests are still ongoing.

Results

The suction values computed with Eq. (1) from the measurements taken with psychrometers or capacitive sensors are plotted in Fig. 4 as a function of the water contents and degrees of saturation determined in the same blocks and in the same positions. Capacitive sensors had to be used to measure the suction in blocks placed during operation at less than 44 cm from the heater, because their RH was below the range suitable for psychrometers. The values have been grouped according to the dry density of the samples. For suctions above 10 MPa, the water content and the degree of saturation decreased lineally as suction increased. The relationship between suction and water content or degree of saturation for lower suctions (those below 7 MPa that were measured with psychrometers) is basically dependent on dry density: the higher the dry density the lower the water content for a given suction. In terms of degree of saturation, the effect of density on the WRC is not noticeable.

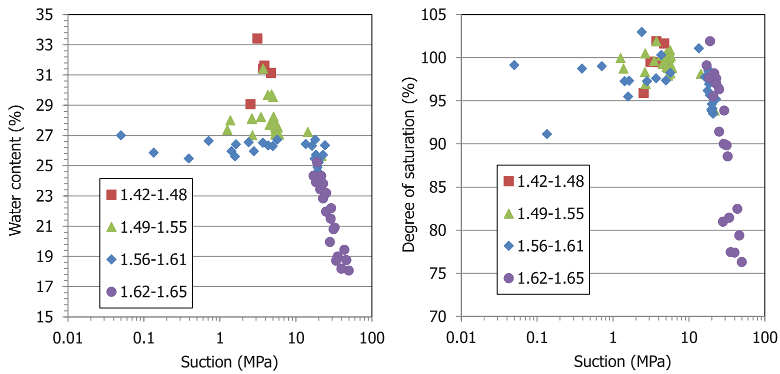

Fig. 4. Relationship between suction measured and water content and degree of saturation in the blocks sampled at CIEMAT's laboratory.

The samples that were subjected during operation to temperatures lower than 40°C (those closer to the granite or at the back of the gallery) followed a wetting path from the beginning of the in situ test, whereas those subjected to higher temperatures (those at less than 44 cm from the heater) followed a wetting-after-drying path. Hence, some hysteresis effect on the suction values measured could be expected. However, it has not been possible to ascertain this in the measurements performed in the laboratory, probably because the samples were subjected during operation to different temperatures and the densities among them were different (the heated samples had higher dry densities). Indeed, density has a relevant influence on the retention capacity.

The water retention curve of the retrieved bentonite is being determined with the vapour transfer technique following a wetting path in samples taken close to the heater, i.e. those subjected to higher temperature and wetting-after-drying during operation. The same determination is being performed in samples of similar water content but taken in a cool area. This will allow following the eventual saturation of the bentonite

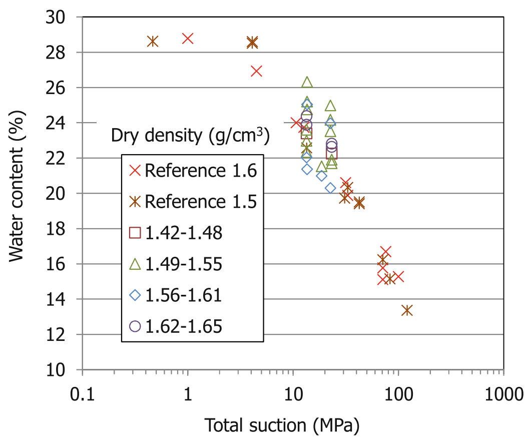

Fig. 5. Preliminary water retention curves obtained in cells with the vapour transfer technique.

in the hottest and cold areas, and evaluate the impact of the previous thermal treatment on the water uptake capacity. The preliminary results are shown in Fig. 5, where the values have been grouped according to the same dry density ranges as in Fig. 4. The figure shows also the results obtained with the same methodology for the reference untreated FEBEX bentonite compacted to dry density 1.6 and 1.5 g/cm^3 (Villar 2007). The results obtained in samples from Grimsel follow the same trend as that of the reference material, although there is a large dispersion in the results that could be partly due to the uncertainties in the density values, which have to be confirmed at the end of the tests.

Summary and Conclusions

The water retention curve of bentonite samples submitted to the conditions of the engineered barrier of a nuclear waste repository for 18 years has been determined in the laboratory following two approaches: measurement and imposition of suction. The suction was measured using either psychrometers (for suctions below 7 MPa) or capacitive sensors (for higher suctions) and these values were correlated to the water content and dry density determined in adjacent samples. This allowed obtaining water retention curves for different densities, given the large range of water content and dry density of the samples retrieved. Additionally, samples trimmed from the blocks retrieved were submitted to different suctions under isochoric conditions until their water content stabilised to determine their WRC through the vapour transfer technique. Both methods entail total suction, which could justify the coherence between the results obtained. Figure 6 shows all the results, along with the water retention curve for the FEBEX reference bentonite obtained previously using both methods for the same density as the average dry density of the barrier (1.6 g/cm^3).

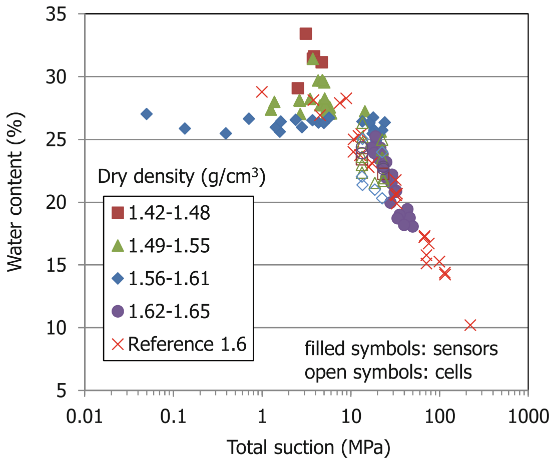

Fig. 6. Water retention curve of samples from the FEBEX-DP experiment determined with sensors (filled symbols) and with the vapour transfer technique (open symbols) and of the reference FEBEX bentonite determined with the vapour transfer technique and capacitive sensors (crosses).

The effect of dry density on the water retention capacity is evident, particularly for suctions below 10 MPa. Samples of lower density have higher water retention capacity, since their porosity is higher. For larger suctions the effect of density cannot be evaluated solely based on the results obtained with sensors, because the range of densities is not large enough, but the comparison with the preliminary results obtained in cells, seems to point to an inverse relation, i.e. higher density samples would have higher retention capacity.

The samples analysed had been submitted during in situ operation to wetting or wetting-after-drying paths, but the measurements performed with the sensors did not show any clear hysteresis effects.

During operation the bentonite blocks were submitted to high temperatures, and consequently the suctions during operation could have been lower than those measured in the laboratory. On the other hand, the samples retrieved suffered decompression during dismantling and this possibly increased their suction, because of the changes in porosity. Nevertheless the comparison of the WRC of the blocks retrieved with that of the reference material points to the preservation of the water retention capacity during operation.

Acknowledgements. This work has been financed by the FEBEX-DP consortium and through the Annex XLII of the ENRESA-CIEMAT framework agreement. Part of the laboratory work was performed by J. Aroz and F.J. Romero.

References

AITEMIN (2016) FEBEX-DP dismantling of the heater 2 at the FEBEX “in situ” test. Nagra Arbeitsbericht NAB16-011

ENRESA (2006) FEBEX full-scale engineered barriers experiment, updated final report 1994–2004. Publicación Técnica ENRESA 05-0/2006, Madrid, 590 pp

Lloret A, Romero E, Villar MV (2004) FEBEX II project final report on thermo-hydro-mechanical laboratory tests. Publicación Técnica ENRESA 10/04, Madrid, 180 pp

Villar MV (2002) Thermo-hydro-mechanical characterisation of a bentonite from Cabo de Gata. A study applied to the use of bentonite as sealing material in high level radioactive waste repositories. Publicación Técnica ENRESA 01/2002, Madrid 258 pp

Villar MV (2007) Water retention of two natural compacted bentonites. Clays Clay Miner 55 (3):311–322

Villar MV, Lloret A (2004) Influence of temperature on the hydro-mechanical behaviour of a compacted bentonite. App Clay Sci 26(1–4):337–350

Villar MV, Gómez-Espina R (2009) Report on thermo-hydro-mechanical laboratory tests performed by CIEMAT on FEBEX bentonite 2004–2008. Informes Técnicos CIEMAT 1178, Madrid, 67 pp

Villar MV, Martín PL, Bárcena I, García-Siñeriz JL, Gómez-Espina R, Lloret A (2012) Long-term experimental evidences of saturation of compacted bentonite under repository conditions. Eng Geol 149–150:57–69

Villar MV, Iglesias RJ, Abós H, Martínez V, de la Rosa C, Manchón MA (2016) FEBEX-DP onsite analyses report. Nagra Arbeitsbericht NAB 16-012, 106 pp

Water Content Effect on the Fault Rupture Propagation Through Wet Soil-Using Direct Shear Tests

M. Ahmadi(✉), M. Moosavi, and M.K. Jafari

International Institute of Earthquake Engineering and Seismology (IIEES), Tehran, Iran
mo.ahmadi@iiees.ac.ir

Abstract. Some fault rupture propagation tests were conducted in which wet soil were used to model a cohesion soil in real condition. Results of these tests show that by increase of water content, the shear band of fault rupture propagate in a narrower zone so the distorted area above the ground was decreased. Ductile soil has the ability to deform more before a developed shear band reaches to the surface. This behavior can be interpreted by strength parameters of the wet soil. For this purpose, some series of direct shear tests were conducted, studying the effect of water content on some strength parameter of granular soil. All of these tests were carried out in both low and high vertical stress. The results indicated that increase of water content to a certain value lead to increase in internal friction angle and beyond this limit it decreases. The response of cohesion was vice versa. Also the internal friction angle was increased as the vertical stress decreased. The results were discussed in both high and low vertical stress.

Introduction

Many efforts were devoted for understand the surface fault rupture phenomenon after 1999 due to the occurrence of three tremendous earthquakes in Turkey and Taiwan (Anastasopoulos et al. 2007; Lin et al. 2006; Loukidis et al. 2009; Moosavi et al. 2010; Rojhani et al. 2012; Ng et al. 2012; Fadaee et al. 2013). Real field evidences of surface fault rupture show a distinct scarp at surface that is created by fault movement. This kind of discontinuity can be made because of soil cohesion and its moisture. There were conducted many studies to investigate the effect of surface fault rupture by using physical modelling. Previous researches show that many efforts were devoted for investigation of non-cohesive granular soil. There are few researches that were studied fault rupture propagation through wet soils. As it is clearly known, in real condition, soil is not completely dry. This moisture can cause a soil to behave like a cohesive soil. So this can change the behavior of fault rupture propagation through wet soil.

Based on a research at soil laboratory of International Institute of Earthquake Engineering and Seismology (IIEES), a cohesive wet soil in real condition were be modeled in 1-g field by adding water to the pure sand. As the confinement stress decreases by the factor N (N is length scale achieved be dividing the length of prototype to corresponding length in model), the frictional portion of shear strength also

A. Ferrari and L. Laloui (eds.), *Advances in Laboratory Testing and Modelling of Soils and Shales (ATMSS)*, Springer Series in Geomechanics and Geoengineering,
DOI 10.1007/978-3-319-52773-4_14

decreases by factor N. This is despite the fact that cohesion portion of shear strength remains constant. So cohesion has a higher influence on the behavior of soil in model than prototype. To overcome this shortcoming in physical modeling, by reducing the dimensions of prototype, its cohesion also should be reduced. The conducted study used wet soil to model a cohesion soil in real condition. Figure 1 shows one of the tests that fault rupture propagated from bedrock to the surface. For modeling, a split box in 1 g field was employed as the faulting simulator apparatus. Also PIV method was used to visualize the formation of shear bands through soil and their propagation path. The main parameters that changed in these test is the water content of soil. Results show that by increase of water content, the shear band of fault rupture propagate in a narrower zone so the distorted area above the ground was decreased. It was believed that this behavior can be interpreted by strength parameters of the wet soil.

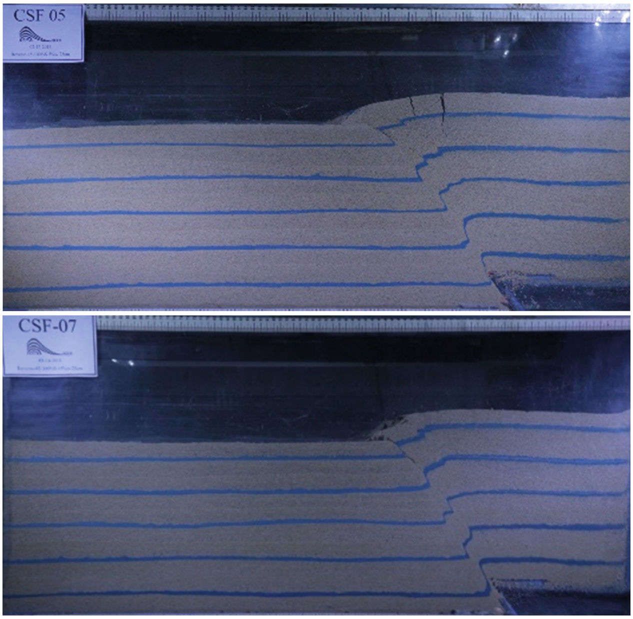

Fig. 1. Fault rupture propagation through wet soil by using 1-g physical modelling: (top) W.C. = 5%, (bottom) W.C. = 15%.

By variation of water content, soil can behave differently that resulted into changing of soil strength parameter. Here soil internal friction angle and cohesion were called as strength parameters. Water suction force between soil grains is the main cause of this change. The amount of water can affect these parameters, so for a correct result interpretation, an individual research was conducted to investigate the effect of water content on the strength parameter of wet soil. As shearing occurred during the tests, direct shear test seems to be the appropriate laboratory test for determining wet soil behavior.

Fault Rupture Tests Results

One of the important results that can be achieved in a fault rupture test is the knowledge that when the fault rupture trace reach to the surface and how much relative displacement (D) needed at bedrock for this. This parameter usually normalizes by the height (h) of the soil and expresses by percentage. D/h parameter is usually used to interpret the ability of soil to absorb the fault rupture. As soil behave more brittle, this parameter decreases. Ductile soil has the ability to deform more before a developed shear band reaches to the surface. Figure 2 shows the result of four tests in which the amount of (D/h) parameter was plotted against water content of soil.

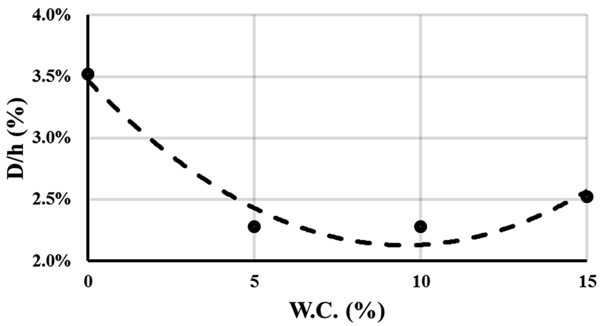

Fig. 2. D/h parameter results against water content of the soil.

Figure 2 shows that as the water content increase up to a certain value (between 5 to 10%) the D/h parameter decrease that shows the soil behaves more brittle. As the water increase more, soil act like a ductile material, so it can absorb more fault displacement. It is essential to verify the result of these tests by discovering the behavior of wet sand against water content. So a series of direct shear test were conducted that is described in the next section.

Soil Response to the Change of Water Content

Direct Shear Test Apparatus

Direct shear test apparatus is chosen to be the appropriate one for the purpose of this study. The diameter and height of the specimen are 60 and 20 mm, respectively. The applied velocity is 1 mm/min. This velocity is enough slow to assure the dissipation of probable pore water pressure due to the shearing. Shearing was continued at least 10% in shear strain. The relative density of samples are equal to 50%, corresponding to the soil density in physical modeling.

Tests Programs

In this study, five type of soil were examined by changing in their water content. Their water content percent are zero (dry condition), 5%, 10%, 15% and saturation condition (approximately 24%). As the soil response directly affected by its confining stress, all samples were examined under high and low vertical stress. As in physical modeling the dimensions of model is reduced, so its confining stress also decreased. This shows the importance of determining soil response at low stress. Low stress condition contains 0.015, 0.03 and 0.045 kgf/cm^2 normal stress. These are equal to the pressure of soil in 1/3, 2/3 and total height of the soil in fault rupture model. The vertical stress of 0.1, 0.25, 0.4, 0.6, 0.85 and 1.25 kgf/cm^2 is defined as high stress condition. It is discussed further why 0.1 kgf/cm^2 can be a limit between high and low stress condition.

Direct Shear Test Results

Shear Stress-Strain Curves

The shear stress-strain curves that were obtained from the tests up to 10% of shear strain for the dry and saturated soil were depicted in Fig. 3. The others couldn't be

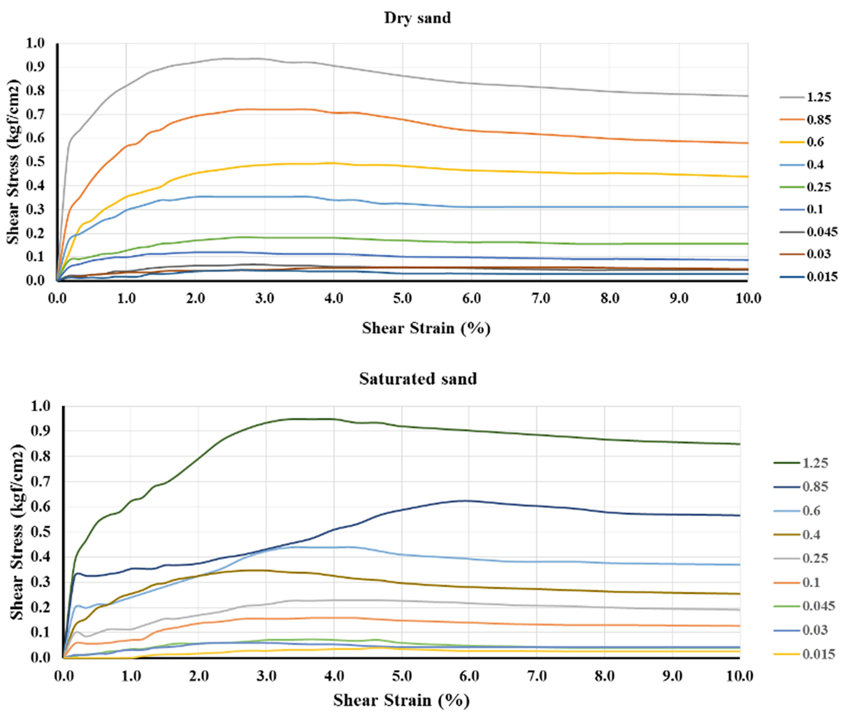

Fig. 3. Engineering behaviour of: (top) Dry sand, (bottom) Saturated sand for various normal stress (right values).

shown here due to the paper limitations. Dry and saturated sand show softening behavior when they sheared. Wet sands behave differently: increase of shear stress until failure and then reach to a steady state condition. The differences can show the importance of studying wet (unsaturated) soils.

Peak Strength Parameters

The main important results that were obtained in this study is determining soil strength parameters (here it was mentioned as internal friction angle (φ) and cohesion (C)) by changing its water content. The peak strength parameters are discussed in this paper. Residual behavior also can be discussed but due to paper limitation can't be paid. To determine a specific boundary between low and high vertical stress, Fig. 4 shows the shear stress at peak versus its corresponding vertical stress (that is related to confining stress) for the sand with 5% water content as an example. As it can be concluded from this figure, slope of the curve significantly change around normal stress equal to 0.1 kgf/cm^2. So this stress can be act as a divider between high and low vertical stress fields. The slope of the curve remain constant at high vertical stress. But it increase significantly at low stress that mean increase in internal frictional angle. So by dividing the gathered data into two fields, we can obtain two φ and C for both low and high normal stress. Similar trend also can be found in other studies (Fukushima and Tatsuoka 1984). Table 1 shows φ and C values for three conditions: (1) low stress, (2) high stress, (3) mean stress (determining φ and C by using all gathered data). It should be noted that low stress belongs to vertical stress less than 0.1 kgf/cm^2 and high stress equal and more than this value. The strength parameter for high and low condition were obtained base on the results of their data individually. In mean stress condition the results of all nine tests (low and high stress tests together) have been used to obtain strength parameter of the soil, so it is called mean stress condition.

The results of Table 1 were depicted in Figs. 5 and 6. As it can be seen in Fig. 5, in high normal stress tests, increase of water content up to 5–10% leads to decrease in φ and beyond this limit, φ was increased. Such a behavior was seen in the result of mean normal stress condition. Nevertheless, changing of φ observed to be completely reverse

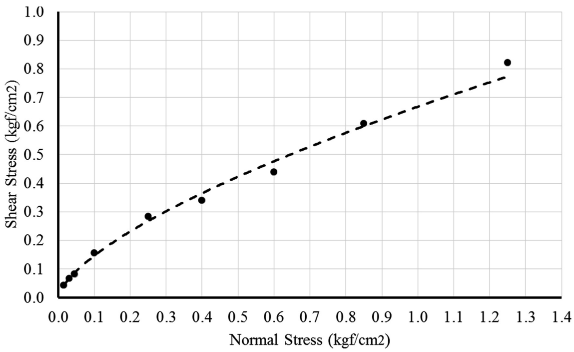

Fig. 4. Failure shear stress versus normal stress for the sand with 5% water content.

Table 1. Φ and C values of soil for different water content at high, low and mean normal stress

Soil W.C. (%)	High normal stress		Low normal stress		Mean normal stress	
	Φ (°)	C (kgf/cm^2)	Φ (°)	C (kgf/cm^2)	Φ (°)	C (kgf/cm^2)
Dry	37	0.04	37	0.03	37	0.04
5%	30	0.11	53	0.02	32	0.07
10%	30	0.09	50	0.01	32	0.06
15%	31	0.08	37	0.04	32	0.06
Saturate (24%)	34	0.06	49	0.02	35	0.05

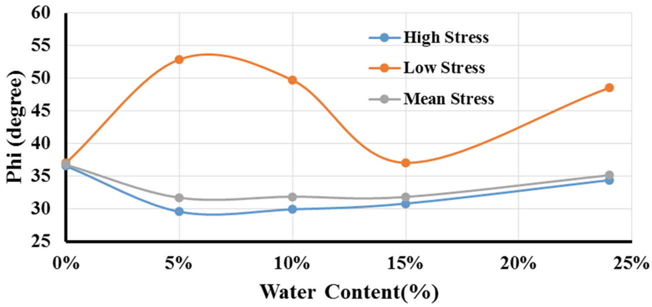

Fig. 5. Water content effect on φ in three normal stress conditions.

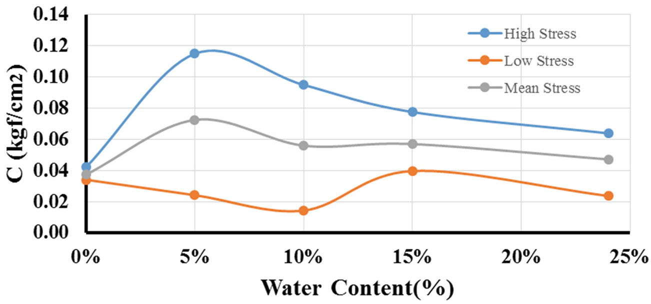

Fig. 6. Water content effect on cohesion in three normal stress conditions.

in low stress tests. In the last conditions, by increase of water content, φ at first increase then it decreased. The result of soil with 15% water content is a bit different in comparison with the other in low stress condition. This can be occurred due to laboratory errors or something like that. However, general trend can be observed by achieved data.

Also results show that internal friction angle of dry soil behaves independently from confining pressure. The result show a 37° of frictional angle for the dry soil both in high and low normal stress.

Figure 6 depicts the effect of water content on the observed cohesion of wet soil. At high stress, wet soil shows an increase in its cohesion till 5–10% and then decrease after this limit. Wet soil in low normal stress behave reversely.

It can be concluded that soil behavior can be affected by the water content percentage. This change in their behavior can reflected in their strength parameter. By focus on low stress condition, changing in cohesion of soil can be negligible. By this supposition, the shear strength of soil is produced by its frictional behavior. According to Fig. 5, by increase of water content, soils frictional angle also increase and then decrease. This leads to reaching its maximum shear strength at the water content between 5–10%. So by increase of soil strength, it behave more brittle. This can interpret the changing of D/h parameter as shown in Fig. 2. By increase of soils water content up to 5–10%, its shear strength increase and then decrease. This means that fault rupture can propagate faster through soil, then by increase of water content in faulting model samples, D/h parameter at first decrease and then increase.

Conclusion

- Existence of pore water in granular soils causes soil to behave more differently from dry or saturation condition.
- Dry or saturated sands show a softening behaviour that couldn't be seen obviously in wet sample.
- In samples with high confining pressure, as the water content increases up to 5–10%, friction angle decreases and beyond this limit increases. A completely reverse behaviour was seen for the samples with low confining pressure.
- In samples with high confining pressure, as the water content increases up to 5–10%, cohesion of the soil increases and beyond this limit decreases. A completely reverse behaviour was seen for the samples with low confining pressure.
- Internal friction angle of soil is significantly higher in low stress condition that in high stress tests.
- In high stress test, wet soil shows higher cohesion in comparison with low stress tests.
- In low stress condition that is corresponds to physical modelling situation, by neglecting the cohesion of soil (due to their small values), soils shear strength increases up to 5–10% water content and then decreases. This can explains the observed behavior in physical modeling tests (Fig. 2).

References

Anastasopoulos I, Gazetas G, Bransby MF, Davies MC, Nahas A (2007) Fault rupture propagation through sand: finite-element analysis and validation through centrifuge experiments. J Geotech Geoenviron Eng 113(8):943–958. doi:10.1061/(ASCE)1090-0241(2007)133:8(943)

Fadaee M, Anastasopoulos I, Gazetas G, Jafari M, Kamalian M (2013) Soil bentonite wall protects foundation from thrust faulting: analyses and experiment. Earthq Eng Eng Vib 12 (3):473–486. doi:10.1007/s11803-013-0187-8

Fukushima S, Tatsuoka F (1984) Strength and deformation characteristics of saturated sand at extremely low pressures. Soils Found 24(4):30–48

Lin M, Chung C, Jeng F (2006) Deformation of overburden soil induced by thrust fault slip. Eng Geol 88(1–2):70–89

Loukidis D, Bouckovalas G, Papadimitriou A (2009) Analysis of fault rupture propagation through uniform soil cover. Soil Dyn Earthq Eng 29:1389–1404

Moosavi SM, Jafari MK, Kamalian M, Shafiee A (2010) Experimental investigation of reverse fault rupture – rigid shallow foundation interaction. Int J Civil Eng 8(2):85–98

Ng CW, Cai QP, Hu P (2012) Centrifuge and numerical modeling of normal fault-rupture propagation in clay with and without a preexisting fracture. J Geotech Geoenviron Eng 138 (12):1492–1502. doi:10.1061/(ASCE)GT.1943-5606.0000719

Rojhani M, Moradi M, Galandarzadeh A, Takada S (2012) Centrifuge modeling of buried continuous pipelines subjected to reverse faulting. Can Geotech J 49:659–670. doi:10.1139/T2012-022

Specimen Preparation Techniques for Testing Fully and Partially Saturated Sands in Dynamic Simple Shear (DSS) Test Device with Confining Pressure

Derya Burcu Gulen and E. Ece Eseller-Bayat(✉)

Department of Civil Engineering, Istanbul Technical University, Istanbul, Turkey
ebayat@itu.edu.tr

Abstract. In this study, specimen preparation techniques for testing fully and partially saturated specimens were investigated. Various techniques were evaluated for obtaining loose to dense fully saturated sand specimens in a flexible membrane of DSS-C device, with minimal distortion to the specimen. Moist undercompaction technique in stages and then saturation with back pressure seem to be the best technique for obtaining loose to dense fully saturated uniform sand specimens. Gas/air entrapped partially saturated sand specimens were prepared by using a chemical powder: sodium percarbonate. The powder was mixed with water and predetermined amount of dry sand was rained into this solution. The chemical powder gets into reaction with water and generates oxygen gases which get entrapped in the sand voids. The techniques developed for obtaining uniform, repetitive sand specimens practically were discussed herein. The specimens prepared were tested under undrained conditions in Dynamic Simple Shear with Confining Pressure (DSS-C) testing device.

Introduction

The aim of this study is to get loose, uniform and undeformed fully saturated and partially saturated sand samples to be tested in DSS-C device for liquefaction tests. There are widely used techniques to get fully saturated sand samples which are dry pluviation, wet pluviation and moist undercompaction. In this study, all the three techniques were performed and advantages/disadvantages of these techniques are discussed herein.

The Induced Partially Saturation (IPS) technique by generating gas bubbles was improved by Yegian et al. (2007) as a new mitigation method against liquefaction problem. Also, the seismic response and mitigation of liquefaction failure of partially saturated sands were studied in details by Eseller-Bayat (2009). In the future research, partially saturated sand samples are planned to be tested in DSS-C device in liquefaction setup for undrained, cyclic loading conditions under high effective stresses. For preparation of partially saturated sand samples, degree of saturation is decreased by creating entrapped air inside the voids. The specimen preparation technique of partially saturated sands is also discussed in this paper.

A. Ferrari and L. Laloui (eds.), *Advances in Laboratory Testing and Modelling of Soils and Shales (ATMSS)*, Springer Series in Geomechanics and Geoengineering,
DOI 10.1007/978-3-319-52773-4_15

Dynamic Simple Shear w/Confining Pressure (DSS-C) Testing Device

Dynamic simple shear testing system with confining pressure by VJ Tech Soil Dynamics Laboratory in Istanbul Technical University, is shown in Fig. 1. It includes de-aired water tank, vacuum machine, air compressor, DSS-C apparatus, controller unit (DSC), air-water cylinder, pneumatic APC and hydraulic APC machines. Testing setups such as saturation, consolidation, static loading, cyclic loading and liquefaction can be performed by using Clisp Studio program.

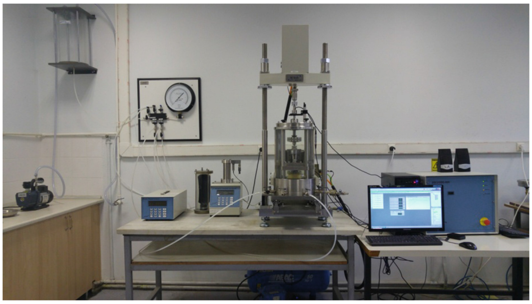

Fig. 1. VJ Tech Dynamic Simple Shear Testing System with Confining Pressure.

Fully Saturated Sand Specimen Preparation Techniques

For preparation of fully saturated sand specimens to be tested in simple shear devices, various techniques were developed in the literature. However, most of these techniques were developed for specimens prepared in a constrained ring or wire reinforced membrane. In DSS w/C the specimen is prepared inside the membrane where there is no constrain laterally. In this study, dry pluviation, wet pluviation and moist under-compaction techniques were performed.

In dry pluviation technique, the specimen is prepared by pouring sand though a funnel. During the pluviation process, the elevation of funnel is raised slowly. The relative density of the specimen depends on the drop height of the sample from the funnel to the top of the specimen. According to Ishihara (1996), this height must be constant and also the dry pluviation method creates denser specimens compared to wet pluviation and moist undercompaction techniques. In this research, for liquefaction tests, the aim is to achieve fully saturated loose specimens. Therefore, dry pluviation technique was challenging in getting loose as well as 100% saturated specimens.

The other technique that was also performed in this study was wet pluviation. In wet pluviation technique, sand is rained from a specific height into a predetermined amount of de-aired water which is needed to obtain fully saturated sand specimens. The soil can be pluviated though a funnel (Ishihara 1996) or from a sealed flask (Finn et al. 1971). In this study, at the beginning, wet pluviation technique was tried to get loose and fully saturated specimens. However, it is hard to get least deformed fully saturated sand samples inside the membrane. In wet pluviation, samples can easily bulge after the top cap is placed.

The third method is moist undercompaction that was improved by Ladd (1978). In this method, the initially prepared soil sample's degree of saturation is around 50%. The moist soil is placed into the mold in layers. Each layer is compacted to achieve uniform density all around the specimen. The samples were prepared around 35% relative density with this technique. The moist undercompaction was chosen in this study and fully saturation was gained by applying cell and back pressures to the sample.

Specimen Preparation for DSS Device w/Confining Pressure

In the sample preparation process, firstly the saturated porous stones and papers are placed into the bottom specimen plate and into the top cap. The membrane stretched around the base plate with two O rings. The split mold is placed on the base plate with O rings and the membrane is stretched over the split mold.

The specimen is prepared inside the DSS-C device and the security pin is placed to prevent the sample distortion during preparation process. Before the sample preparation starts, the pore pressure and the back pressure pipes are saturated.

In the moist undercompaction method, approximately 50% saturated sample is prepared and tamped gently to get a loose sample. After the sample is prepared, the height of the sample is measured. Later on, the top cap is placed over the sample and finally, the split mold is removed around the specimen. The height is measured again. At this step, it was observed that the height of the specimen decreased and the sample bulged from the top. Additionally, the top cap was not standing as vertically elevated and it wasn't touching over the sample at some points. It was discovered that the deformation was resulted from the shape of the split mold. As a result of this, a new mold was designed for this research. According to ASTM D6528-07 Standard for specimen size requirements, the new split mold was designed for preparing the samples 70 mm in diameter and around 28 mm in height. A 2.5 mm gap was created over the sample height to place the top cap over it in order to prevent the deformation of the sample before removing the mold. The new mold design is shown in Fig. 2. Specimen preparation procedure with the new mold is shown in Fig. 3.

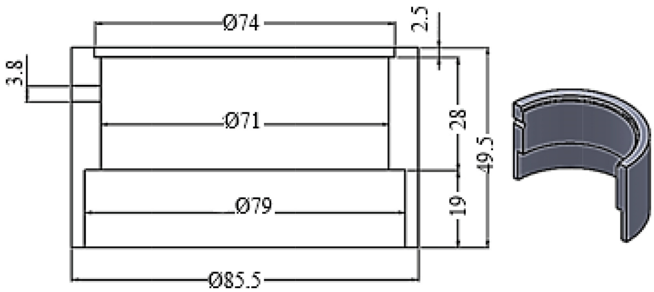

Fig. 2. Designed new split mold (dimensions in mm).

Fig. 3. Sample preparation (a) Membrane and O rings in the base plate, (b) Split mold over the membrane and O rings over the mold, (c) Specimen inside the mold, (d) Specimen in place in DSS-C device under cell pressure.

Saturation Setup

An example of the sample prepared with moist undercompaction method at 33% relative density and 51% degree of saturation was tested in DSS-C device. Saturation test process is presented in Fig. 4.

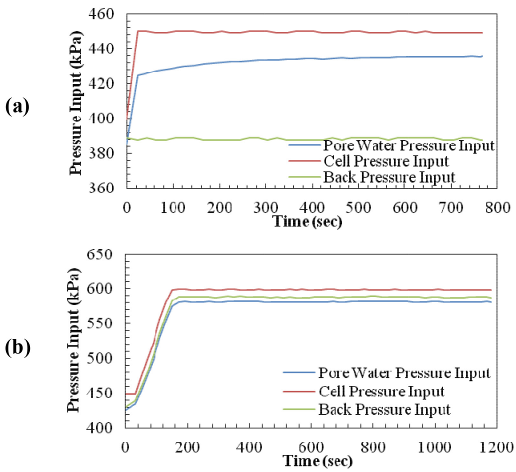

Fig. 4. Saturation test results for pressure inputs and time relations, (a) B check at 450 kPa cell pressure, (b) Cell pressure ramp up to 600 kPa.

B value is the ratio of excess pore water pressure Δu_c to the applied confining stress $\Delta\sigma_3$. After saturation test, the increment in pore pressure was measured as very close to the increment in confining stress which corresponds to fully saturation.

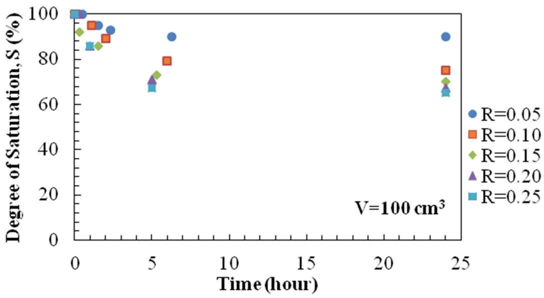

Fig. 5. The achieved degree of saturation with time for partially saturated samples during 24 h for 100 cm^3 volume.

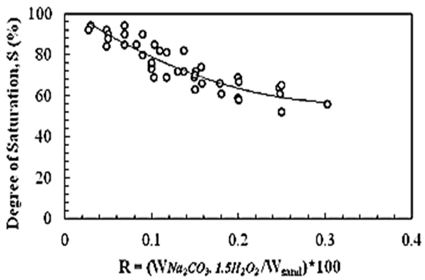

Fig. 6. Correlation between achieved degree of saturation and R values.

Partially Saturated Specimen Preparation Techniques

Gas/air entrapped partially saturated sand specimens were prepared by using a chemical powder: sodium percarbonate. This chemical is environmentally friendly and it is widely used for cleaning detergent. As reported by Nababan (2015), Gokyer (2015) and Kazemiroodsari (2016) the chemical powder gets into reaction with water, generates oxygen gases which get entrapped in the sand voids and decrease the degree of saturation. The chemical reaction is shown as follows:

$$Na_2CO_3.1.5H_2O_2 \rightarrow 2Na^{+1} + CO_3^{-2} + 1.5H_2O_2$$

$$1.5H_2O_2 \rightarrow 1.5H_2\text{O} + 0.75O_2$$

The sample preparation process with sodium percarbonate, the determination of the rate of gas generation and degree of saturation in partially saturated samples were investigated widely by Gokyer (2015) and by Kazemiroodsari (2016). As stated in their studies, the sample preparation has two phases: preparing the sodium percarbonate-water mixture and the wet pluviation of dry sand into this solution. The sodium percarbonate-water solution was prepared for different concentrations (expressed in w/w) in the range of 0.10% to 1.0%. The amount of sand and chemical were determined for varying ratios of R as follows:

$$R = \frac{\text{Weight of sodium percarbonate (g)}}{\text{Weight of dry sand (g)}} * 100$$

The sample volume was known and the amount of sand was calculated for target relative density. Also, the initial amount of water was calculated for aimed water content in fully saturation conditions. The samples were prepared in the range of 0.03 to 0.30 R values. Thus, the weight of chemical can be determined for the solution.

In the case of partial saturation, firstly water and chemical powder were mixed and uniformly distributed solution was obtained. Then, the predetermined amount of dry sand was rained into this solution with wet pluviation method.

Gas generation was determined by using volume calculations as in phase relation calculations. According to the chemical reaction, water is collected on the top of sand samples. Generated gases get entrapped into the sand voids and increase the water elevation. This change in water volume was assumed as same with generated air volume which decreases the degree of saturation.

Resulted Values of Degree of Saturation for Different R Values

Entrapped gas molecules decrease the degree of saturation of specimens. Decreasing degree of saturation and time relations were observed at different R values for 100 cm^3 sample volume as presented in Fig. 5. Kazemiroodsari (2016) mentioned that the specimen volume and relative density have an ignorable affect on the degree of saturation. The correlation between the resulted degree of saturation and R values are presented in Fig. 6.

Problems Faced During Sample Preparation

Some problems faced in the partially saturated sample preparation with sodium percarbonate. The samples were prepared according to the weight of chemical and the weight of sand ratios, at the same time; it was directly related with the concentration of the chemical-water solution. The samples were prepared in two different ways: (1) mixing the chemical with sand then raining this mixture into the predetermined amount of water and (2) firstly mixing chemical with water and then raining the sand into this solution. In both cases the samples were left for 24 h to allow sufficient time for the generation of gases inside the voids. The evaporation of water was prevented by closing the top of the containers. In the first case, it was observed that non-uniformly distributed air gaps occurred inside the sample. In the second case, it was observed that mixing the chemical with water first presents a uniformly distributed air gaps inside the sample. As a result of this, the second preparation technique was chosen.

Another problem faced was the change in the structure of the specimen when the samples were prepared at R values greater than 0.10. In that case, the generated air bubbles pushed away the soil grains and the voids volume got larger, by changing the structure of the specimen. These specimens could be still tested by incorporating the new relative density due to the enlarged volume of the voids.

Conclusion

In this study, the most suitable techniques for the preparation of uniform loose fully saturated and partially saturated sand samples to be tested in DSS w/C device for liquefaction tests were investigated. The moist undercompaction method was determined to be the best technique for preparation of uniform and fully saturated sand specimens. The loosest specimen was obtained at approximately 35% relative density and fully saturation was achieved for B value $\geq$ 0.95 by saturation test in DSS-C device. For achieving uniform loose partially saturated sand specimens a special chemical sodium percarbonate was used and specimens were prepared using wet pluviation technique. The partially saturated samples were produced by mixing water with sodium percarbonate and pluviating dry sand into this mixture. After chemical reaction completed, degree of saturation decreased down to the range of 80% to 60%. In the research plan, the partially saturated samples are going to be tested in DSS-C device for liquefaction studies.

Acknowledgement. This research is funded by TUBITAK (The Scientific and Technological Research Council of Turkey) under the grant No: 213M367. The support of TUBITAK is greatly appreciated. The support of VJ Tech Limited and DOTEK during and after the installation of DSS-C device is greatly appreciated. The authors present their gratitude to VJ Tech Technical Support Employee Prash Jeevagan and George Nikitas for their instant support. The support of Mr. Binaya Bhattarai is also greatly appreciated for the problems faced during the specimen preparation process. The authors also would like to thank our colleagues at ITU especially Dr. Mustafa Hatipoglu, Dr. Atila Sezen and Prof. Recep Iyisan for their guidance and support during our tests. Finally, the support of Istanbul Technical University in bringing the DSS-C device into our laboratory is greatly appreciated.

References

Eseller-Bayat E (2009) Seismic Response and Prevention of Liquefaction Failure of Sands Partially Saturated through Introduction of Gas Bubbles. *Ph.D. dissertation*, Northeastern University, Boston, MA

Finn WDL, Pickering DJ, Bransby PL (1971) Sand liquefaction in triaxial and simple shear tests. J Soil Mech Found Div, ASCE 97(SM4):639–659

Gokyer S (2015) Numerical Simulation of Partial Saturation in Sands Induced by Flow and Chemical Reactivity. Ph.D. dissertation, Northeastern University, Boston

Ishihara K (1996) Soil behaviour in earthquake geotechnics, 1st edn. Clarendon Press, Oxford 350 p.

Kazemiroodsari H (2016) Electric Conductivity for Laboratory and Field Monitoring of Induced Partial Saturation (IPS) in Sands. Ph.D. dissertation, Northeastern University, Boston

Ladd RS (1978) Preparing test specimens using undercompaction. Geotech Test J, GTJODJ 1 (1):16–23

Nababan FRP (2015) Development and Evaluation of Induced Partial Saturation (IPS), Delivery Method and its Implementation in Large Laboratory Specimens and in the Field. Ph.D. dissertation, Northeastern University, Boston

Yegian MK, Eseller-Bayat E, Alshawabkeh A, Ali S (2007) Induced partial saturation (IPS) for liquefaction mitigation: experimental investigation. J Geotech Geoenviron Eng, ASCE, 133 (4):372–380

Measurement of Vertical Strain of Compacted Bentonite Subjected to Hydration Effort on Creep Test

Tomoyoshi Nishimura(✉) and Keita Iwasaki

Department of Civil Engineering, Ashikaga Institute of Technology, Ashikaga, Japan
tomo@ashitech.ac.jp

Abstract. Compacted bentonite which is one component of structure framework of barrier system. The hydro-thermal-mechanical properties of compacted bentonite have been investigated in the past decades in the area such as geoenvironmental engineering (Olivella et al. Olivella et al. 1996). This study conducted creep test for bentonite using a modified relative humidity circulation system. Various vertical stresses were applied on basis of unconfined compressive strength that only relative humidity of 98% as hydration effort influenced to creep behaviour in deformation. Thus, either expansion or shrinkage in vertical direction was measured, and all specimens approached to be completely destruction due to apply the combined effort of mechanical effect and hydration effect.

Introduction

The radioactive waste disposals have been produced from atomic plant that geo-environment engineers should establish the extremely safety disposal management issue (Nagra 2015). Compacted bentonite is one component of structure framework of barrier system. It is likely that the compacted bentonite as well as host rock change various properties such transformation in quality due to hydration effect, thermal heating and chemical actions (Sanchcz et al. 2012). Geoenvironmental engineers would like to focus attention that unsaturated compacted bentonites are influenced by the combined effort such as hydration, thermal and chemical. There is a wide number of researches on the unsaturated behavior of bentonite. Therefore, experimental works should process more carefully into this aspect. This study investigated the creep behaviour of compacted bentonite from unsaturated soil mechanics point of view. Bjerum (1967) worked, and demonstrated as pioneer. After that, some experimental results and establish mathematical modellings have been published on the soil mechanics or geotechnical engineering field. Their researches close looked at limited saturated soil materials.

The effects of hydration on large deformation or destroy process for compacted bentonite are important for a various geotechnical construction conditions. Recently, two papers mentioned the creep mechanics for unsaturated soil that were Lai et al. (2014) and Nazer and Tarantino (2016). This study focused on the vertical strain of

A. Ferrari and L. Laloui (eds.), *Advances in Laboratory Testing and Modelling of Soils and Shales (ATMSS)*, Springer Series in Geomechanics and Geoengineering,
DOI 10.1007/978-3-319-52773-4_16

unsaturated, compacted bentonite under external vertical loading. Hydration due to increase relative humidity (i.e. increment of soil moisture) really developed micro-macro structure in bentonite, so that volume deformation obviously is indicated in expansion. The functions including shrinkage by vertical stress and expansion by hydration induced the critical deformation, and finally approached to destruction while test. This testing program used a modified relative humidity circulation system based on conventional triaxial apparatus, and the relative humidity of 98% was maintained in the triaxial chamber. The flow of air with RH 98% flow steady, circulated in the system. Also, the unconfined compressive strength was useful as certain parameter for creep test. What is appeared in this study is that suggest important issue to prediction of safety of barrier system in extremely long period.

Soil Materials and Testing Procedure

This testing programs consisted of creep test and unconfined compressive test that were conducted for describing the creep behaviour of compacted bentonite. The modified creep test apparatus was used for this study. The many cracks and destruction of bentonite were observed carefully. The time at begining of destroy was measured, and a trend was suggested as one of results.

Soil Material

Sodium bentonite (Kunigeru V1) was used for this test program which SiO_2 occupied 62% to all chemical components. The grain size distribution of bentonite were determined by Test method for particle size distribution of soils (JIS A 1204: 2009), and was shown in Fig. 1. Also, the soil-water characteristic curve of the bentonite used in this testing was indicated in Fig. 2. The determined SWCC had a wide range from 2.8 MPa to 296 MPa which was measured using the vapor pressure technique. Using a vapor pressure technique for high suction measurement is no longer a special suction application. The SWCC data sets were plotted against six different suctions in temperature of 20°. Most data sets were described a straight line on logarithmic scale. The evaluated inclination was 2.36. The specimens had a diameter of 50 mm, and a height of 100 mm. Statically compaction with only one layer was performed in the stiffness steel mould.

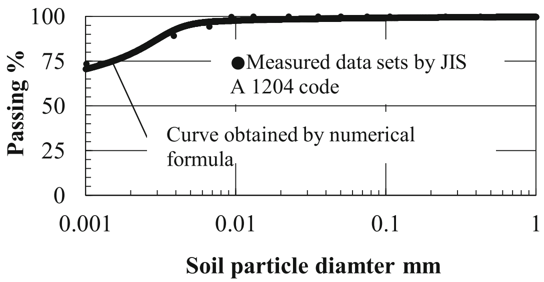

Fig. 1. Grain size distribution for bentonite.

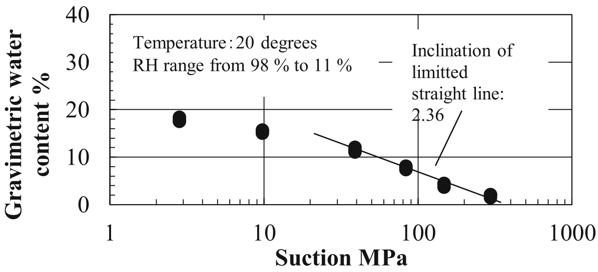

Fig. 2. Soil-water characteristic curve for bentonite.

Modified Creep Test Apparatus

The modified creep test apparatus was shown in Fig. 3. The modified creep test apparatus was employed along with a conventional cyclic relative humidity control system (Nishimura and Koseki 2013). The system having vapor pressure techniche was useful to measure the mechanical properties of unsaturated materials. This apparatus consist of triaxial chamber, air cyclic flow pump, the chamber including salt solution and basically functions in conventional triaxial apparatus. A dynamic activity of the conventional pump maintained a steady air flow. The suction corresponding to its relative humidity were imposed completely to the specimen in the triaxial chamber. The implication of hydration effort is that increasing of relative humidity induces the increment of soil moisture, namely, decrement of suction. As far as the air flow is circulated, the relative humidity is maintained in the triaxial chamber.

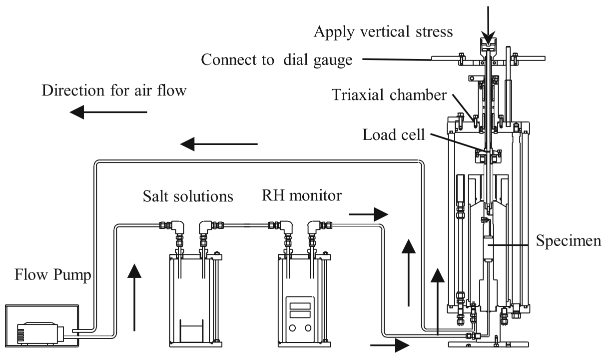

Fig. 3. Modified creep test apparatus.

Creep Test

The sample was statically compacted with water content of 8.0% that had a dry density of 1.600 g/cm^3 and degree of saturation of 30.9%. The reason why the specimen was compacted with one layer that there was the influence of boundary between layers in specimen on the mechanical properties. The axial compression force (i.e. creep stress) was applied to bentonite sample. Before the creep test, the unconfined compression test

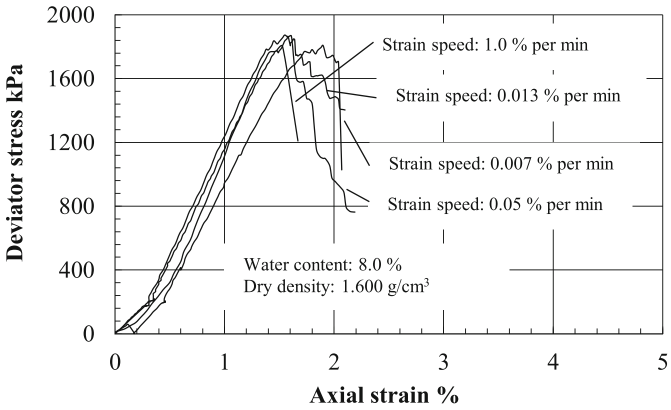

Fig. 4. Stress-strain curve for compacted bentonite with various strain speed.

was conducted out that was performed based on a Method for unconfined compression test of soils (JIS A 1216). The unconfined compressive strengths of intact specimen serve, refer as one of conventional strength parameters, and is very useful to consider the implication of applying the some vertical stresses. The stress-strain curves at different axial strain rates were described in Fig. 4. Almost of all stress-strain curves were approximately similar that the unconfined compressive strengths had a little difference among all specimens. Relationship between axial strain rate and the unconfined compressive strength was indicated in Fig. 5. According to increase the axial strain rate, the unconfined compressive strength slightly decease: its tendency was similar to the direct shear test results of unsaturated compacted bentonite with various suction by Nishimura (2015). The unconfined compressive strength of 1801.1 kPa at axial strain rate of 1.0% per min was used to determine the creep compression stress. The required stresses were summarized in Table 1 which had a range from 0.50 to 0.10 for ratio to the unconfined compressive strength of 1801.1 kPa. The relative humidity produced the hydration application which was 98%, and it corresponded the suction of 2.8 MPa.

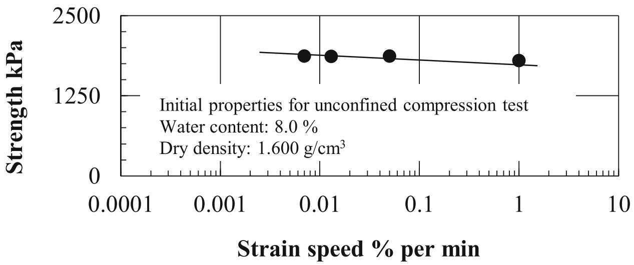

Fig. 5. Influence of strain speed on strength for bentonite.

Table 1. Confirmed vertical compression stress and ratio to unconfined compressive strength for creep test

	Case 1	Case 2	Case 3	Case 4	Case 5
Compression stress kPa	898.9	799.0	549.3	364.5	182.8
Ratio to unconfined compressive strength	0.50	0.40	0.30	0.20	0.10

Test Results

The creep tests with various axial compression stresses were carried out, and the vertical deformations were only measured with time. Such creep behaviour was mentioned as following.

The vertical deformations with elapsed time

The vertical compression stresses summarized in Table 1 were applied to all specimens, and the vertical deformations with elapsed time were described in Figs. 6(a) (b) (c) (d) and (e). The positive value for axial strain corresponds to shrinkage in volume. About all specimens, the vertical deformation was measured. Case 1 and 2 maintained the shrinkage condition, and the shrinkage deformation slowly increased till the creep destruction. The samples reached failure at a low axial deformations value. Other three cases indicated the shrinkage deformation when the vertical compression stress was just applied. However, all of three cases described were in contrast to Case 1 and 2. Particulary, for two samples (i.e. Case 4 and 5) expansion deformation occurred. Therefore, the expansion seem to be growing according to decrease the vertical compression stresses. It was accurately for hydration application to produce the definitely expansion. Case 3 occurred the creep destruction in shrinkage. In other words, the vertical compression stress was of important with hydration effort, that was rather utilized as feature parameter to interpret the creep behaviour.

Figure 7 shows the relationship between vertical compression stress and axial strains, which meant the shrinkage strain. It is strain at once when sample was applied stress in creep test. The strain increased clearly with vertical strain that was adjusted as straight line. Thus, the vertical compression stress had the influence on creep behaviour. As the following issue, the critical time was considered that the creep destruction of sample began. Each begining point (i.e., begining of destruction) was indicated in Fig. 6 which was mentioned. A numerical formula appeared the relevant curve, which was useful to understanding strong dependence of vertical compression stress. Equation (1) is indicated,

$$DT = 700e^{-0.025VCS} \tag{1}$$

where: DT is time (h) that the sample occurred just the destruction.

VCS is vertical compression stress (kPa)

The numerical formula equation above mentioned was not in conservation which was proposed at limited stress conditions. Many different testing conditions and performances are require to accurately evaluate, predict the creep behaviour and numerical formula simulation (Fig. 8).

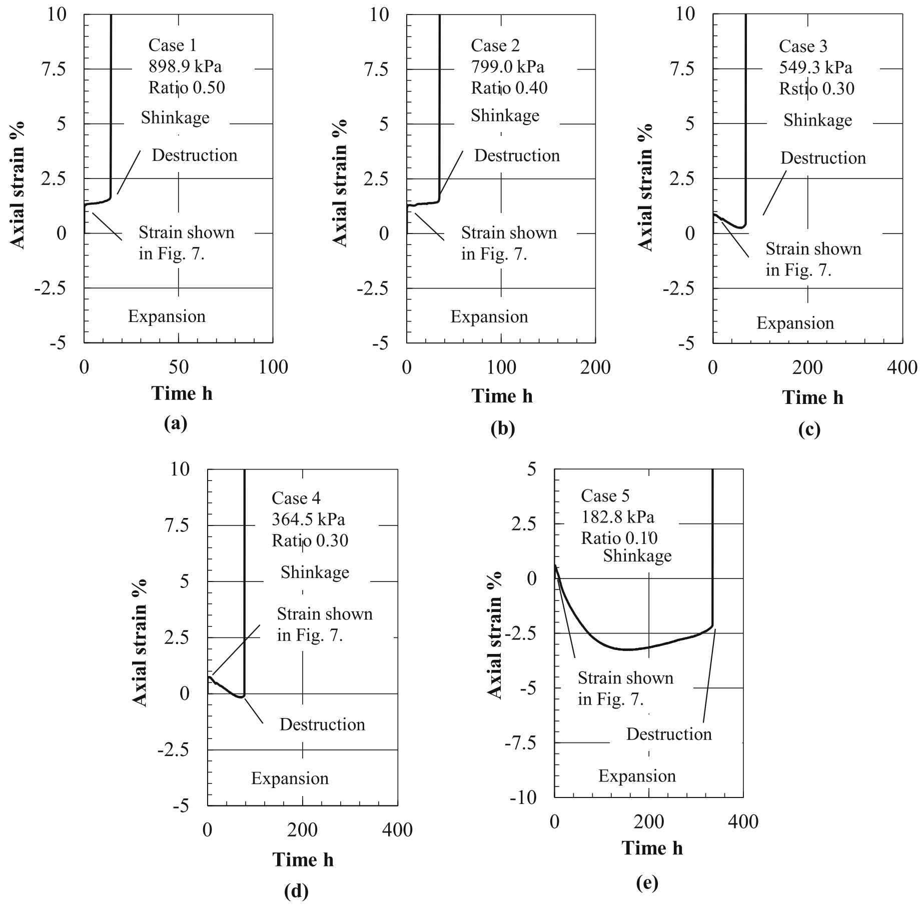

Fig. 6. Axial deformation with various vertical compression stress.

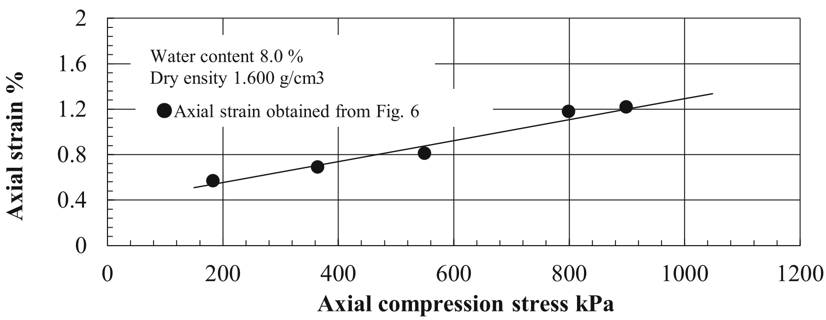

Fig. 7. Comparison of creep strain to axial strain during unconfined compression test.

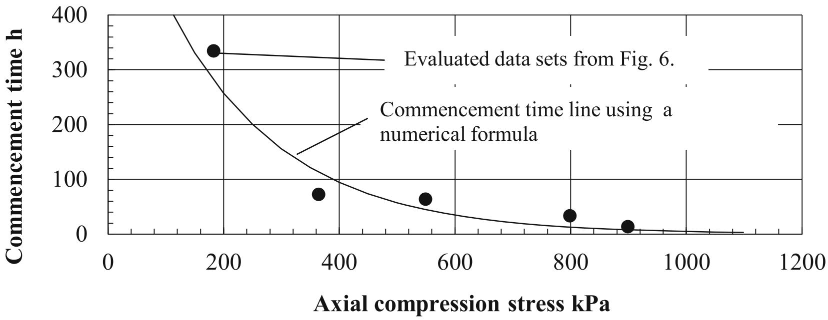

Fig. 8. Decreasing of commencement time with stress.

Conclusions

This study investigated the creep behaviour of compacted bentonite subjected to hydration process. In fact, bentonite was placed under constant relative humidity of 98%, and mechanical loading was applied. Thus, two difference efforts described the following important issue on creep behaviour of bentonite.

The stress ratio was accepted as one of strength parameters which was defined as ratio of vertical stress on unconfined compressive strength. It was useful to interpret that time at begining of destruction of bentonite clearly decreases according to an increase of the ratio. The expansion of the bentonite occurred due to the hydration process applied with the imposition of a relatively humidity to 98%. In spite of observation of expansion, all specimens approched to the destruction at end of test. Measured time at begining destruction and vertical stress was suggested as simple numerical formula. At least more experimental works are needed to make a tendency on basis of theoretical mechanism.

Acknowledgement. Ashikaga Institute of Technology accepted this study for research recipient on 2016. Authors express great appreciation to a subsidy program.

References

Bjerrum L (1967) Engineering geology of Norwegian normally-consolidated marine clays as related to the settlements of buildings. Géotechnique 17(2):83–119

Lai XL, Wang SM, Ye WM, Cui YY (2014) Experimental investigation on the creep behavior of an unsaturated clay. Can Geotech J 51(6):621–628

Nazer NSM, Tarantino A (2016) Creep response in shear of clayey geo-materials under saturated and unsaturated conditions. In: Proceedings of the 3rd European conference on unsaturated soils (E-UNSAT 2016). doi:10.1051/e3sconf/20160914023

Nagra. Annual report 2015, National Cooperative for the Disposal of Radioactive Waste (2015)

Nishimura T, Koseki J (2013) Influence of shear speed on direct shear strength for compacted bentonite with different soil suctions. In: Third international conference on geotechnique, construction materials and environment (Geo-Mate 2013), pp 598–603, Nagoya

Nishimura T (2015) Influence of shear speed on hydro-mechanical behavior for compacted bentonite. In: The 15th asian regional conference on soil mechanics and geotechnical engineering, 15ARC JPN-051

Olivella S, Gens A, Carrera J, Alonso EE (1996) Numerical formulation for a simulator (CODE-BRIGHT) for the coupled analysis of saline media. Eng Comput 13(7):87–112

Sanchez M, Gen A, Guimaraes L (2012) Thermal-hydraulic-mechanical (THM) behaviour of large-scale in situ heating experiment during cooling and dismantling. Can Geotech J 49 (10):1169–1195

Response of Clay Rock to Moisture Change

Chun-Liang Zhang(✉)

Gesellschaft für Anlagen- und Reaktorsicherheit (GRS),
38122 Braunschweig, Germany
chun-liang.zhang@grs.de

Abstract. Various kinds of laboratory experiments were carried out on the Callovo-Oxfordian and Opalinus claystones to investigate response of clay rock to moisture change, including swelling and shrinking with variations of the environmental humidity, stress-bearing capability of bound porewater or buildup of swelling pressure, influence of water content on the mechanical stiffness and strength, and moisture-enhanced sealing of fractures. Significant responses of the claystones were observed.

Introduction

In the context of geological deep disposal of radioactive waste in clay formations, very comprehensive investigations have been recently performed by GRS on the indurated Callovo-Oxfordian and Opalinus claystones to improve the understanding of moisture effects on clay rocks (Zhang and Rothfuchs 2007; Zhang et al. 2010; Zhang 2013, 2015, 2016). Significant responses of the claystones to moisture change were observed: swelling and shrinking with variations of the environmental humidity, stress-bearing capability of bound porewater up to the overburden pressure, influence of water content on the stiffness and strength, and moisture-enhanced sealing of fractures. Major findings are briefly summarized in this paper.

Characteristics of Studied Claystones

The Callovo-Oxfordian claystone (COX) at the Meuse/Haute-Marne-URL in France and the Opalinus claystone (OPA) at the Mont-Terri-URL in Switzerland were taken for the experimental studies. These claystones are composed of fine-grained minerals. The pore sizes mainly range from nano-scale (<2 nm) in between the parallel platelets of the clay particles to micro- and meso-scale (2–50 nm) between solid particles. The fraction of macro-pores (>50 nm) amounts to less than 10% (Andra 2005; Bock et al. 2010). The COX claystone contains 25–55% clay minerals, 20–38% carbonates and 20–30% quartz (Andra 2005), while the OPA claystone in the shaly facies has higher clay contents of 58–76%, less carbonates of 6–24% and quartz of 5–28% (Bock et al. 2010). However, the quantities of expansive clay minerals such as smectite are limited to 13–23% in COX (Tournassat et al. 2007) and 5–20% in OPA (Pearson and Arcos 2003). The clayey matrix consists of particles with strongly adsorbed interlayer water and strongly to weakly adsorbed water at external surfaces. Water in macro-pores is freely movable. The clayey matrix is embedding other mineral particles.

A. Ferrari and L. Laloui (eds.), *Advances in Laboratory Testing and Modelling of Soils and Shales (ATMSS)*, Springer Series in Geomechanics and Geoengineering,
DOI 10.1007/978-3-319-52773-4_17

Stress Concept

Up to now clay rocks are commonly treated as a conventional porous medium, in which porewater is assumed to be freely migrating and physico-chemical interactions of water with clay minerals are not explicitly taken into account. However, a considerable fraction of the porewater in the claystones is adsorbed on the internal and external surfaces of clay particles due to physico-chemical interactions, as mentioned above. Stress between clay particles must be transferred through the bound porewater rather than directly via solid-to-solid grain contacts.

Based on the knowledge of the microstructure and the porewater state in the claystones, a stress concept was proposed by Zhang (2016) for clay rock, which suggests that the effective stress in a compact clay-water system is transferred through both, the bound porewater in narrow pores and the solid-solid contact between non-clay mineral grains. This is schematically illustrated in Fig. 1 for any wavy surface that passes through contact areas between particles in a saturated claystone. The stress equilibrium can be expressed by

$$\sigma_t = \sigma_s + \sigma_l + p_w \quad \text{or} \quad \sigma_{eff} = \sigma_t - p_w = \sigma_s + \sigma_l \tag{1}$$

where σ_t is the total stress acting on the medium, σ_s is the contact stress between solid particles, σ_l is the disjoining (or swelling) pressure acting in the bound porewater between clay particles, p_w is the pressure acting in free water in macro-pores, and σ_{eff} is the conventional effective stress. In clay-rich and less cemented materials, the effect of solid-solid contacts between particles disappears, $\sigma_s \to 0$, so that the effective stress is mostly carried by the bound porewater and is equivalent to the swelling pressure, $\sigma_{eff} \Leftrightarrow \sigma_l$. Conversely, if a claystone contains large amounts of non-clay particles and/or strongly cemented, the effect of bound water is negligible, $\sigma_l \to 0$, and thus the externally applied load will be transferred through the solid-solid grain contacts, $\sigma_{eff} \Leftrightarrow \sigma_s$. This puts the meaning of the conventional Terzaghi's effective stress into perspective. This stress concept provides a reasonable view to the nature of the effective stress in argillaceous rock and forms the fundamental basis for studies of the hydro-mechanical properties and processes in clay formations.

The swelling pressure σ_l is dependent on saturation degree of bound porewater. Figure 2 illustrates schematically the saturation degrees of the different types of porewater (interlayer water, interpaticle bound water, free water). Taking the fractions of the contact areas (solid-to-solid, bound porewater and free porewater) into account, a linear relationship of the effective stress to the saturation degree of bound porewater is preliminarily proposed

$$\sigma_{eff} = \sigma_s + \sigma_l = \sigma_s + \pi_D S_e = \sigma_s + \pi_D \left(\frac{S_l - S_r}{1 - S_r} \right) \tag{2}$$

where π_D is the local net disjoining pressure in the interparticle bound porewater ($\pi_D S_e = \sigma_l$), S_e is the effective saturation degree of bound porewater, S_l is the saturation degree of total porewater, and S_r is the residual saturation degree of the remaining water

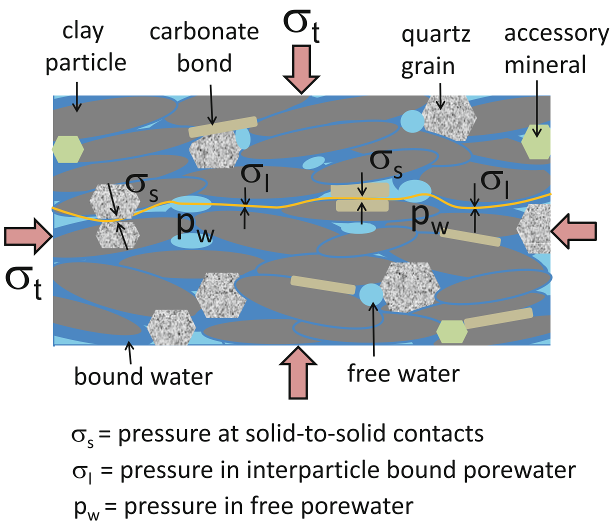

Fig. 1. Stress state in a representative element of a saturated claystone.

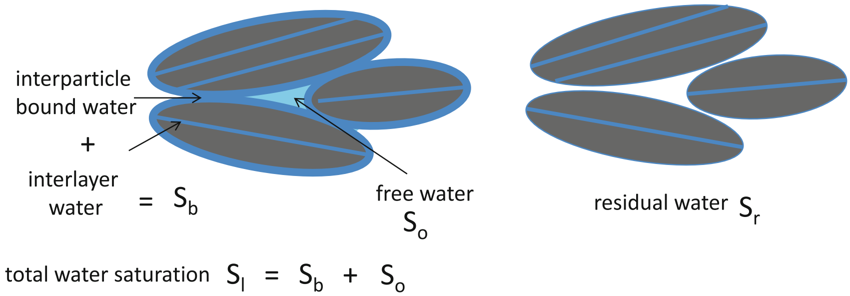

Fig. 2. Schematic of saturation of interlayer, interparticle bound and free porewater in clay.

in the interlayer and adsorbed on the external surfaces as the clay particles are disconnected.

Laboratory Observations

Stress Response to Humidity Change

The so-called uniaxial swelling test method was developed for investigating stress response to humidity change (Zhang and Rothfuchs 2007; Zhang et al. 2010). A sample was axially pre-loaded and then fixed at unconfined lateral condition (see Fig. 3a). The sample was then dried and wetted by circulating air with varying humidity around the surface, where response of the axial stress was monitored. The resulting variation of water content or saturation was measured on an accompanying sample of the same size in the same air circulating system outside the cell.

Figure 3b shows that the axial stress decreases with drying from the pre-load of 15 MPa down to nearly zero and then increases again with wetting to a high level of 10.5 MPa where failure occurred due to wetting-induced alteration of the inner structure (cf. Fig. 8). Actually, drying causes release of the adsorbed porewater and conversely wetting lets water molecules enter the pores, being adsorbed on internal and external surfaces of clay particles, forming double-layers being compressed in narrow pores and resulting in repulsive forces (swelling pressure) against the rigid confinement. This and many other tests (Zhang 2016) provided clear evidence for the proposed stress concept (Eq. 1). Since no radial stress was applied, $\sigma_r = 0$, the build-up of the uniaxial swelling pressure with wetting suggests that the adsorbed porewater is capable of carrying deviatoric stress.

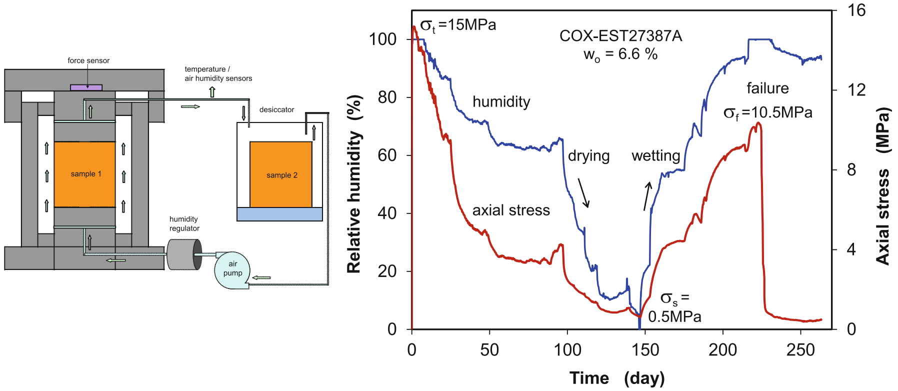

Fig. 3. Principle of uniaxial swelling test under axially-fixed and laterally-unconfined conditions (a) and stress response to humidity change surrounding a claystone.

Furthermore, the test data can be used for the determination of the effective stress in relation to the water saturation (Eq. 2). Figure 4 plots the axial stress as a function of water saturation degree. One can find out that:

(a) The pre-applied axial stress of σ_o = 15 MPa decreases with desaturation to a minimum value of σ_s = 0.5 MPa at a residual saturation degree of S_r = 15%, below which no stress changes occur;

(b) The resaturation increases the stress to σ_{ls} = 9.5 MPa at full saturation (S_l = 100%), which is the sum of the pressure acting in the bound water-films and on the contacts between solid particles, $\sigma_{ls} = \sigma_l + \sigma_s$, where σ_s = 0.5 MPa and $\sigma_l = \pi_D$ = 9 MPa;

(c) The linear relationship (Eq. 2) is confirmed by the stress–water saturation curve along drying path for a range of $S_r \leq S_l < 80\%$ and along wetting path for $S_r \leq S_l < 90\%$;

(d) Near and after the full saturation, the stress increase is more rapid to a maximum value of σ_p = 10.5 MPa, which might be mainly attributed to osmotic effects by π_O = 1 MPa.

The total maximum swelling pressure is the sum of $\pi_D + \pi_O$ = 10 MPa. So the osmotic swelling pressure shall be involved in the model as a function of water uptake Δw:

$$\sigma_{eff} = \sigma_s + \pi_D S_e + \pi_O(\Delta w) = \sigma_s + \pi_D \left(\frac{S_l - S_r}{1 - S_r} \right) + \pi_O(\Delta w) \tag{3}$$

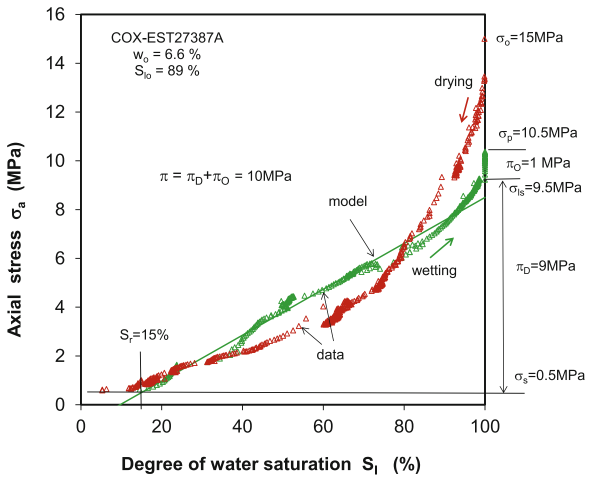

Fig. 4. Effective stress and swelling pressure as a function of degree of water saturation.

Strain Response to Humidity Change

Strain response of the claystones was examined under different load conditions. As an example, Fig. 5a shows the strain response of an unconfined sample to a drying-wetting cycle. The sample was firstly resaturated in water vapour (humidity RH = 100%). The wetting caused an expansion in all directions. The subsequent drying to RH ≈ 0 removed the porewater out of the pores, resulting in collapse of the pore structure and thus a macroscopic shrinkage. The following wetting up to RH = 100% increased the water content (not given here) and hence the thickness of the bound water-films between solid particles, yielding a recovery of the strains. However, the strain–water saturation curves depicted in Fig. 5b are different between the drying process and the wetting process.

The hysteric performance in strain as a result of drying-wetting cycle may be interpreted with help of a schematic illustration of a clay aggregate shown in Fig. 6. Drying causes release of adsorbed porewater successively from the large pores, from the narrow space between clay particles, and from the interlayer within the sheet

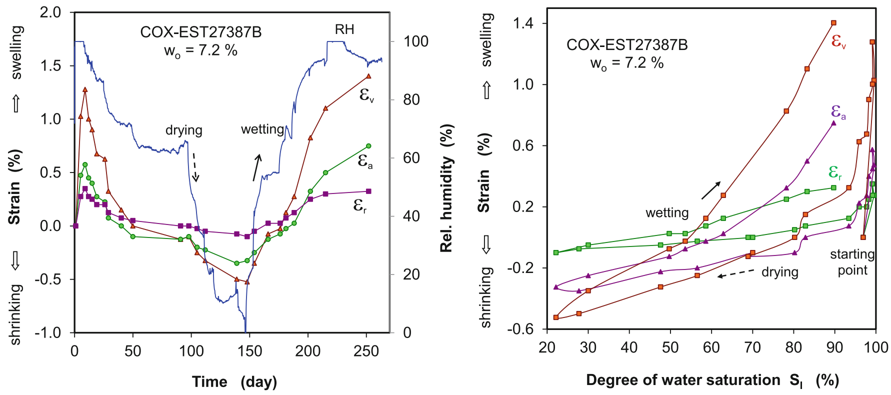

Fig. 5. Free shrinking and swelling of a claystone during a drying-wetting cycle.

structure. The release of the bound porewater as bearing element results in collapse of the pore structure and thus a macroscopic shrinkage. Contrary, wetting drives water molecules into the pores. Under the effect of physic-chemical potentials, water molecules are adsorbed on the surface of clay particles. The narrow pores will be firstly filled and expand by taking up more water. The air in some large pores may be enclosed there and even forever when the surrounding narrow pores are fully sealed. Thus, at a same volume, the degree of water saturation by wetting is lower than that by drying, and the strain–water saturation curve from wetting is above that from drying (Fig. 5b).

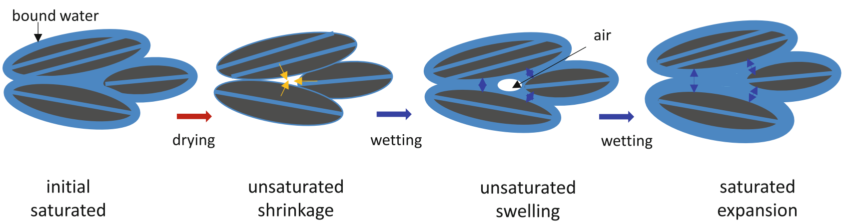

Fig. 6. Hysteric performance in strain as a result of drying-wetting cycle for claystone.

Because of the high water adsorption potentials, the unconfined claystones can take up great amounts of water up to 10–13% in water vapour, much more than that of 7–8% in the naturally confined state. The increase in water content can contribute to the volumetric expansion up to 7–12%, as shown in Fig. 7 comparing the swelling capacities of the COX and OPA claystones by wetting with water vapour and with synthetic porewater. The OPA claystone with higher clay content exhibits a larger swelling compared with the COX. As the claystone contacts with the synthetic water, the swelling takes place very quickly and then tends to constant, as shown by the COX

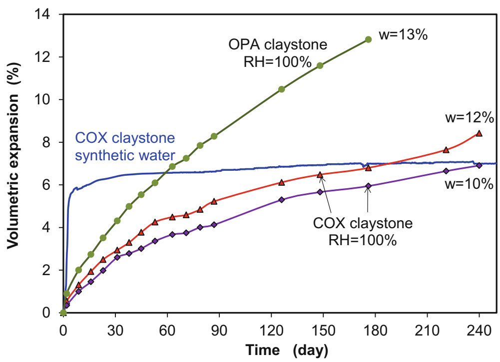

Fig. 7. Swelling of COX and OPA claystones by wetting with vapour and synthetic water.

sample. However, the final magnitudes of swelling by contacting with liquid water and water vapour are nearly the same.

Influence of Water Content on Strength

The influence of water content on the stress-strain and strength behaviour was investigated on COX claystone in uniaxial compression tests. The samples with different water contents from w = 1.5% to 7.7% were axially loaded at a rate of 0.2 MPa/min. Figure 8 summarizes the measured stress-strain curves, elastic stiffness and strength. The claystone behaves elasto-plastically. The linear elastic behaviour is dominating in the low stress region, where the volume is compacted. As micro-cracking starts at a stress σ_D, the compaction turns over to dilatancy. With the development of the micro-cracks to interconnection, macro-fractures are forming to failure at the peak stress σ_F. Because of the compaction of the air-occupied pores in the elastic region, the elastic stiffness increases with loading. But the inner structure of the claystone is largely altered by water. Increasing water content results in widening of the distances or thickness of bound water-films between clay particles and in turn degradation of the inherent cohesion and friction resistance. So the stiffness and strength are largely degraded with increasing water content. For instance, the minimum peak strength of 10 MPa obtained at a high water content of w = 7.7% is four times lower than the maximum of 50 MPa at a low w-value of 1.4%.

Moisture-Enhanced Sealing of Fractures

The high swelling capabilities of the claystones can enhance the self-sealing of fractures. This important issue for the safety of the repositories was examined by flowing humid gas and synthetic water through cracked claystones.

Figure 9 shows effects of humid gas flow on fracture sealing. A fractured sample was flowed through with wetted gas by increasing humidity from RH = 75% to 85% and 100% under confining stress of 1 MPa. During wetting the fractures, a gradual

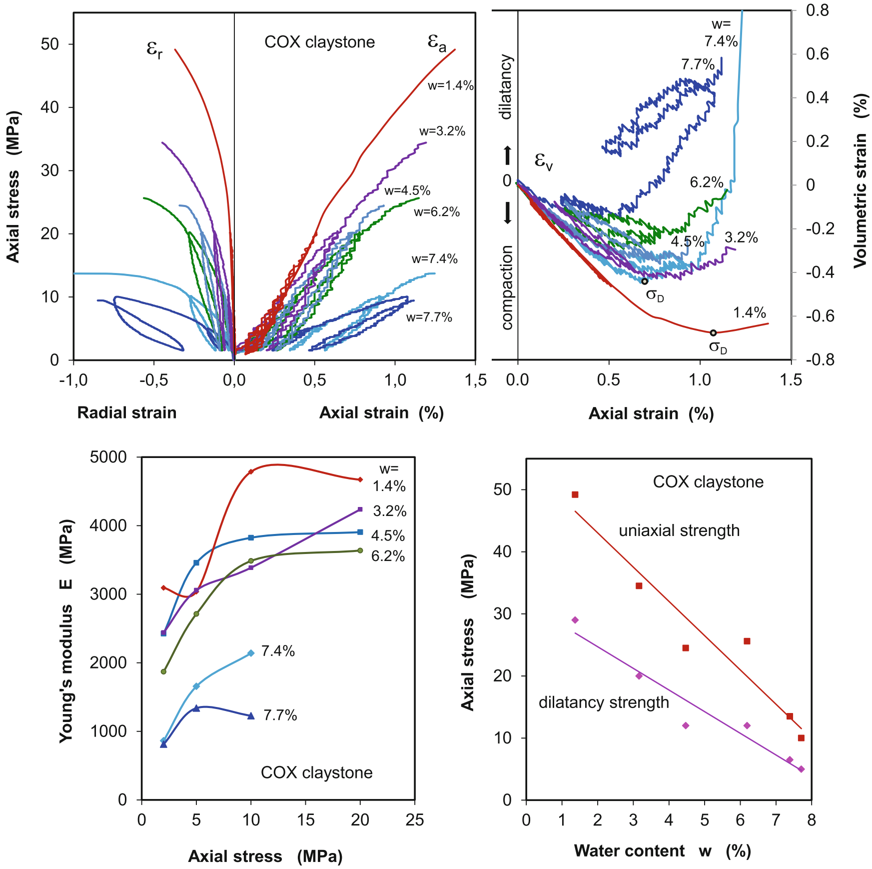

Fig. 8. Influence of water content on the uniaxial stress-strain behaviour, elastic stiffness, dilatancy and failure strength of COX claystone.

expansion was observed in the normal direction to the fracture planes, which was resulted from high local swelling pressures in contacting areas between fracture walls. Actually, the clay fracture walls must expand preferably into the unstressed fracture voids than elsewhere. This makes the flow pathway narrow and the permeability decreases, as observed from $3{\cdot}10^{-14}$ to $6{\cdot}10^{-16}$ m^2 in this test.

Another example is the water-enhanced sealing of fractures in claystone, as shown in Fig. 10. The fractured sample was loaded under an isostatic stress of 2 MPa. The initial permeability is quite high at 10^{-12} m^2 measured by dry gas. As the synthetic water was introduced into the fractures, the clay matrix expanded rapidly into the fracture voids, indicated by the swelling strain curve. Correspondingly, the hydraulic conductivity dropped down by several orders of magnitude to very low levels of $<10^{-18}$ m^2. This and many other tests (Zhang 2013) demonstrated the strong effects of water flow on the sealing of fractures in the claystones.

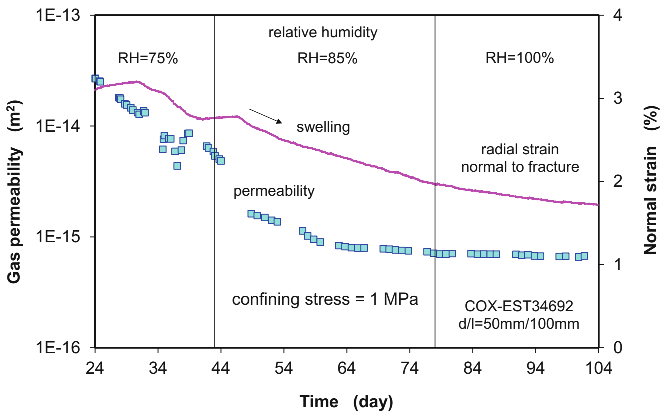

Fig. 9. Sealing of fractures in correspondence with swelling during humid gas flow.

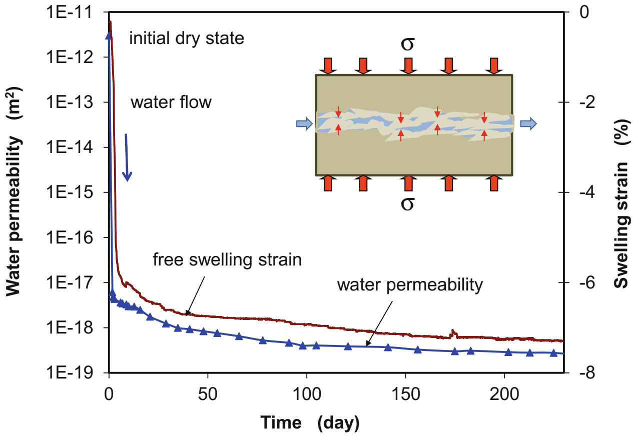

Fig. 10. Sealing of fractures in correspondence with swelling during water flow.

Conclusions

Significant responses of the COX and OPA claystones were observed in the laboratory experiments. The following conclusions can be drawn:

- The effective stress in the claystones is transferred through both, the adsorbed porewater in narrow pores and the solid-solid contact between non-clay mineral grains. This stress concept driven by Zhang (2016) is confirmed by the experiments showing that the applied effective stresses are mostly carried by the bound pore-water up to failure strength.
- The claystones exhibit high adsorption potentials, under which a great amount of water can be taken up from the humid environment, depending on the confinement.

The water uptake enlarges the distances between solid particles and causes macroscopic swelling. Conversely, drying causes release of porewater and collapse of the pore structure to a macroscopic shrinkage.

- The widening of the interparticle distances by water uptake leads to degradation of the inherent cohesion and friction resistance between solid particles, so that the stiffness and strength of the claystones decrease with increasing water content.
- The moisture-induced swelling, weakening and slaking of clay minerals can seal the fractures in the claystones.

References

Andra D (2005) Synthesis – evaluation of the feasibility of a geological repository in an argillaceous formation

Bock H, Dehandschutter B, Martin CD, Mazurek M, Haller AD, Skoczylas F, Davy C (2010) Self-sealing of fractures in argillaceous formations in the context of geological disposal of radioactive waste – review and synthesis. Clay club report, OECD 2010, NEA no 6184

Pearson FJ, Arcos D, Bath A et al (2003) Mont Terri project – geochemistry of water in the opalinus clay formation at the Mont Terri rock laboratory, no 5, Bern

Tournassat C, Gaucher EC, Fattahi M, Grambow B (2007) On the mobility and potential retention of iodine in the Callovian-Oxfordian formation. Phys Chem Earth 32(8–14): 539–551

Zhang CL, Rothfuchs T (2007) Moisture effects on argillaceous rocks. In: Schanz T (ed) Proceedings of the 2nd international conference of mechanics of unsaturated soils. Springer Proceedings in Physics, vol 112, pp 319–326. Springer, Heidelberg

Zhang CL, Wieczorek K, Xie ML (2010) Swelling experiments on mudstones. J Rock Mech Geotech Eng 2(1):41–47

Zhang CL (2013) Sealing of fractures in claystone. J Rock Mech Geotech Eng 5(2013):214–220

Zhang CL (2015) Deformation of clay rock under THM conditions. Geomech Tunn 8(5): 426–435

Zhang CL (2017) Examination of effective stress in clay rock. J Rock Mech Geotech Eng. doi:10.1016/j.jrmge.2016.07.008

Volumetric Behaviour of Lime Treated High Plasticity Clay Subjected to Suction Controlled Drying and Wetting Cycles

Marco Rosone, Camillo Airò Farulla(✉), Clara Celauro, and Alessio Ferrari

Department of Civil, Aerospace, Environmental and Materials Engineering (DICAM), University of Palermo, Palermo, Italy
camillo.airofarulla@unipa.it

Abstract. The paper presents some experimental results collected on samples recovered from an experimental embankment obtained by compacting a lime-treated clay. Samples were collected soon after the in situ compaction and they were cured in controlled environmental conditions for at least 18 months. Mercury intrusion porosimetry tests (MIP) were carried out on freeze-dried specimens to characterize the microstructure of the material. In order to assess the durability of the improved material, laboratory tests focused on the effects of cyclic variations of the degree of saturation on the water retention properties and the volumetric behaviour of the stabilized clay. Collected results show that the lime-treated clay undergoes an almost irreversible volumetric behaviour; this irreversible contraction is associated to severe drying processes.

Introduction

Lime stabilization of fine soils is an advanced technology among those that promote sustainable use of natural resources. The technique is aimed at improving the workability, the physical, chemical and mechanical properties of the clays that otherwise would not be suitable for these purposes. Then, it allows the re-use of clayey soils in the construction of transport infrastructures, minimizing the need for suitable materials from borrow-pits and the need to transport waste soils.

Basic reactions in the lime treatment process are quite well understood (Locat et al. 1990; Abdi and Wild 1993; Boardman et al. 2001) and so is the consequent mechanical improvement, mainly in terms of bearing capacity, shear strength and compressibility of the treated clays (Bell 1996; Croce and Russo 2003; Zhang et al. 2015). Furthermore, despite the quite wide use of the lime treatment technique, so far not many studies deal with the long term behaviour of the treated clay or the effect of repeated loading or variation in the boundary hydraulic conditions (Stoltz et al. 2012). In particular, a very interesting aspect to be clarified is the one related to the durability in time of the mechanical properties gained by the treatment, in relation to the repeated variations in the degree of saturation of the material.

The results presented in the paper refer to a wide experimental programme carried out during the construction of a main extra-rural state road in Sicily. A high plasticity

A. Ferrari and L. Laloui (eds.), *Advances in Laboratory Testing and Modelling of Soils and Shales (ATMSS)*, Springer Series in Geomechanics and Geoengineering,
DOI 10.1007/978-3-319-52773-4_18

clay, available in large quantities after the excavation work, was studied in order to define the technical and economic feasibility of the treatment. With the aim to characterize the microstructure of lime-treated high plasticity clay, mercury intrusion porosimetry (*MIP*) tests were carried out on a specimen sampled soon after the in situ compaction and cured in controlled environmental conditions. Finally, in order to assess the stability in time of the geotechnical characteristics, the paper presents test results of repeated wetting and drying cycles carried out in a suction-controlled oedometric device and by means of the vapour equilibrium technique.

Material Properties and Experimental Programme

The material was recovered from an experimental embankment built in the Favarella district, in the province of Caltanissetta (Sicily). Some geometric and constructive details of the experimental embankment are reported in Airò Farulla et al. 2014. Before the treatment and the compaction stage (corresponding to the Standard Proctor energy level), the clay was partly disaggregated by means of a motor grader, to obtain a material with apparent grain size distribution through d = 31.5 mm and d = 4.76 mm sieves, respectively, equal to $p_{31.5}$ = 100% and $p_{4.76}$ = 63%. Spreading controls carried out with measurement of the mass of lime spread on the surface, have shown that the quantity of lime considered as actually used in the layers is equal to 2.3% (Airò Farulla et al. 2014). The initial consumption of lime, obtained from laboratory tests was slightly less than 2% (Hilt and Davidson 1960; Eades and Grim 1966). The tested samples, recovered at the time of the construction of the embankment, were wrapped in multiple layers of plastic film, and treated for a period of 18 months in an air-conditioned cabinet with a temperature T = 20 °C and relative humidity $U_r \geq$ 90%.

The following properties were determined for the tested samples: grain size distribution consisting of gravel fraction $f_{gravel} = 1 \div 6\%$, sandy fraction $f_{sand} = 9 \div 17\%$, silty fraction $f_{silt} = 39 \div 59\%$, clayey fraction $f_{clay} = 24 \div 52\%$; liquid limit $w_l = 51 \div 53\%$, plasticity index $PI = 24 \div 28\%$ and activity index $I_a = 0.54 \div 1.0$; soil specific weight $\gamma_s = 26.3 \div 26.4$ kN/m^3; water content $w = 17.6 \div 21.8\%$; dry unit weight $\gamma_d = 15.9 \div 17.4$ kN/m^3; void ratio $e_0 = 0.52 \div 0.65$.

MIP tests were performed using a porosimeter attaining a maximum intrusion pressure of 200 MPa, which corresponds to an entrance pore diameter of approximately 7 nm. The advancing non-wetting contact angle between mercury and the clay minerals was assumed to be 140° (Romero and Simms 2008). *MIP* tests were carried out on an untreated sample, compacted at optimum standard Proctor condition (γ_d = 16.1 kN/m^3 and w = 20.3%), and on a lime treated clay sample coming from the embankment. Samples for the *MIP* tests were dehydrated by means of a freeze-drying technique consisting in quick freezing the samples by dipping them in liquid nitrogen (boiling temperature −198 °C) and sublimation with vacuum pump at −60 °C for 24 h.

In order to assess the water retention properties of the treated material in a wide range of suction, both in drying and in wetting paths, various techniques for suction control were used. The axis translation technique (air overpressure method) applied in an oedometric apparatus was used to control matric suction in the range of 0.01÷0.80 MPa, whereas the vapour equilibrium technique was used to impose total suction in the range of 2 $\div$ 110 MPa. When using the vapour equilibrium technique, the stationary condition was considered to have been achieved when the difference in weight of the specimen between two successive measurements, carried out at a distance of one week, was lower than 0.1%. A fluid displacement technique was used to measure the volume of each tested specimen after equalization at the imposed total suction.

Results Analysis

The most relevant results of the MIP are reported in terms of the cumulative intrusion void ratio e_i (Fig. 1a) and pore size density function ($-\Delta e_i/\Delta(logd)$) (Fig. 1b) which expresses the frequency of the pores, as a function of equivalent diameter d. Figure 1b shows how the untreated compacted clay presents a typical double porosity pore size distribution, characterized by a very well marked peak in the field of micropores (d = 0.5 μm) and a uniform distribution in the macropore field, that is the range of diameter between 3 and 100 μm. In particular, assuming as a boundary limit the diameter d = 1 μm, from the cumulated volume curve it can be calculated that macropores characterize a little less than 20% of the total intruded porosity. These results are typical for natural clay compacted in optimum conditions (Delage et al. 1996).

The intruded void ratio in the treated sample increases due to the lower state of compaction (γ_d = 16.5 kN/m^3). The treated clay has a bimodal pore size distribution, with a peak slightly more marked for $d \geq$ 10 μm, as could be expected for an aggregated structure. The modal value of the diameter in the field of the macropores is equal to about 60 μm, while the intrusion void ratio in the field of macropores is more greatly increased ($e_{i,M}$ = 0.20) than the untreated clay ($e_{i,M}$ = 0.08). Minor variations in terms of intruded volume are found in the field of micropores even though the pore distribution is somewhat different. In the field of micropores, untreated clay shows the modal value 0.41 μm while the treated clay has a much lower modal value (d = 0.06 μm). Furthermore, treatment with lime reduces intruded void ratio in the field of micropores (from 0.42 to 0.39 mm^3/g).

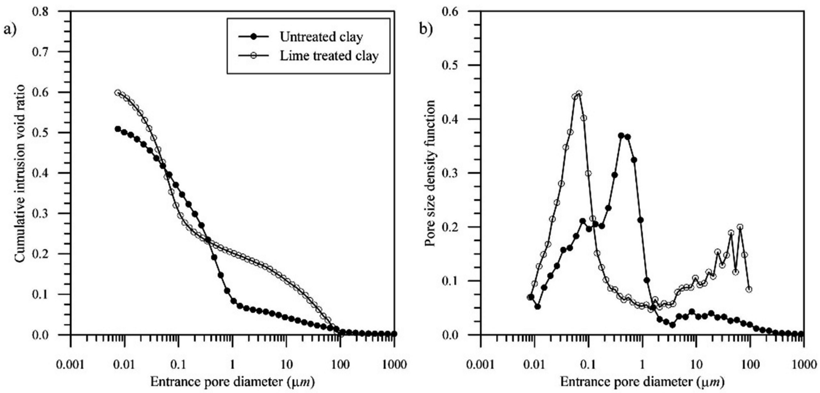

Fig. 1. Cumulive intrusion void ratio (a) and pore size density function (b) as a function of equivalent pore diameter for untreated clay and lime treated clay.

Although the improvement of the geotechnical properties of the treated clay is a well-known result (Cuisinier et al. 2011; Al-Mukhtar et al. 2012; Di Sante et al. 2014), the stability of such properties in time, especially with seasonal variation in weather, at the moment appears to be unclear and, at the same time, a key topic to evaluate the durability of the work.

Figure 2 shows the results, expressed in terms of void ratio and degree of saturation S_r, as a function of applied matric suction s, of the cycling matric suction tests performed at constant net vertical pressure ($\sigma_{v,net}$ = 50 kPa). The range of variation of suction during the test, $s = 0.01 \div 0.8$ MPa, was selected because minimum variation of water content ($\Delta w = -0.08\%$) at constant void ratio was measured during first equalization at 0.80 MPa. During the first cycle, the variation of suction was performed by steps while in subsequent cycles, the maximum variation of suction was applied instantaneously.

The evolution of the void ratio as applied matric suction varied (Fig. 2a) shows that during the wetting and drying cycles the sample undergoes a very low void ratio variation (Δe = 0.002), reversible in nature. During the first wetting, as well as during the subsequent, the specimen reaches almost complete saturation while in the following drying it starts significantly to desaturate for suction higher than 0.05 MPa. Variations in the degree of saturation take a different course varying the considered cycle. During the first cycle, the degree of saturation differences, at constant matric suction, are linked to the effect of the hydraulic hysteresis (Airò Farulla et al. 2011). In subsequent cycles, the cyclical variations of degree of saturation is reduced a lot, although it should be noted a slight tendency to reduce the degree of saturation in the third and fourth round of drying ($\Delta S_r = -0.003$). Then, it can be concluded that the degree of saturation S_r, as it is shown in Fig. 2b, cyclically varies in the range between 0.92 and 1.00 without significant variation in successive cycles of suction. On the basis of the collected results, it is possible to claim that the processes inducing a reduction of suction do not intervene significantly on the hydro-mechanical behaviour of such material.

Different behaviour can be observed in the case of wide cyclic variation covering a suction range greater than the level of suction operating on the specimen as a result of

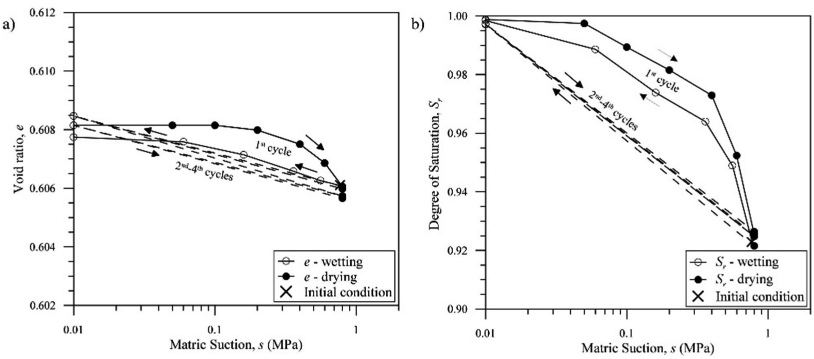

Fig. 2. Void ratio, e, (a) and degree of saturation, S_r, (b) during matric suction cycle between 0.01 and 0.80 MPa.

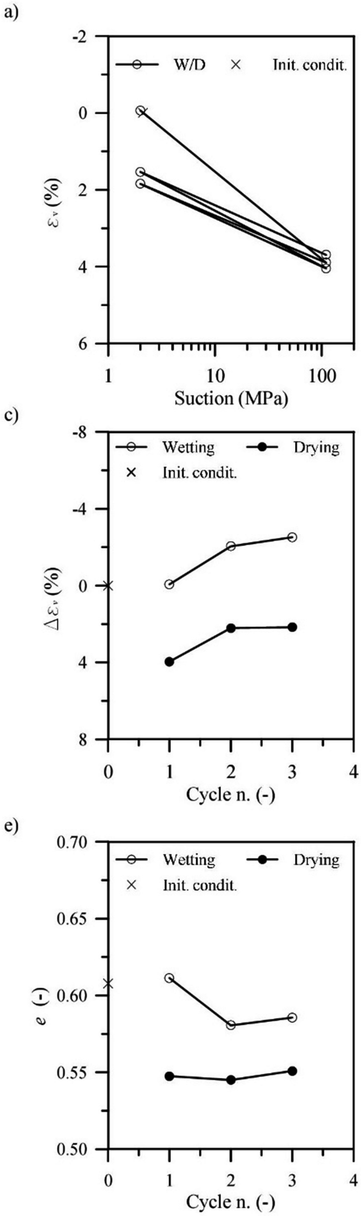

Fig. 3. Evolution of volumetric deformation ε_v, (a), water content w (b), volumetric deformation changes $\Delta\varepsilon_v$ (c), water content variations Δw (d), void ratio e (e) and degree of saturation S_r (f) during total suction cycles between 2 and 110 MPa.

the compaction process and following treatment. In order to highlight this peculiar behaviour, the results of several cycles of wetting and drying applied by varying total suction between 2 and 110 MPa (Fig. 3) are reported. The evolution of the volumetric strain ε_v (Fig. 3a) due to cyclic suction variations is characterized by the accumulation of significant deformations of shrinkage. Always in the same diagrams, it can be observed that these deformations occur, mainly, in the first cycle of wetting and drying. Such behaviour tends to become reversible in nature.

The evolution of the water content w of the specimens is shown in Fig. 3b. During the first equalization stage at 2 MPa, the specimen slightly decreases the water content ($\Delta w = -0.1\%$) at constant volume and only after the first equalization stage at total suction equal to 110 MPa, it significantly reduce the water content ($\Delta w = -15.6\%$). These results highlight that the initial total suction can be assumed to be equal to 2 MPa. However, the resulting reduction of water content is generally very significant during the equalization stage of the first cycle while it is more modest, but still significant in the second and the third cycles. The irreversible variations of water content occurring almost exclusively in the first cycle of suction, are primarily due to the hydraulic hysteresis phenomenon.

Volumetric deformation variation measured in the phases of wetting and drying the individual cycles are represented in Fig. 3c. In the first equalization step the specimen does not undergo a significant volumetric shrinkage ($\Delta\varepsilon_v = 0.02\%$).

In the following drying at 110 MPa a further deformation (volumetric shrinkage) occurs that obviously deeply influences behaviour in the subsequent cycles. Drying at 110 MPa produces volumetric shrinkage of about 5%, which is not totally recovered in later wetting stages.

In fact, after the second cycle, volumetric deformation changes are greatly reduced and they show opposite signs, i.e. swelling deformation in wetting and shrinkage deformation in drying. In addition, absolute values of deformation are very close and are further reduced in the third cycle.

Figure 3c represent the evolution of water content variation Δw as a function of the number of cycles assuming the following convention: the volumes of water expelled from the sample (i.e. water content reductions) are considered negative and those absorbed (water content increasing) positive. Water content variations Δw are negligible for the specimens equalized to the suction of 2 MPa (Fig. 3d). In the first cycle, the reduction in w during the drying step is higher (in absolute value) than that of the following phase of wetting, with a progressive reduction of w, as effect of the hydraulic hysteresis (Airò Farulla et al. 2011).

At the same time, despite the strong volumetric shrinkage, a reduction in the degree of saturation with the continuation of the cycles occurs (Fig. 3f). In the subsequent cycles, the volumes of water exchanged tend to decrease, although a tendency to reversible behaviour, particularly in terms of the degree of saturation, is not less clear.

The evolution of the void ratio with the cycles of suction (Fig. 3e) reflects, of course, the evolution of the volumetric strain already examined with the diagrams in Fig. 3c. After the second cycle series, the volume variations are quite moderate.

Conclusions

The analysis of obtained results from tests performed in the suction controlled oedometer suggests that the clay treated with lime does not suffer significantly from cyclic processes of wetting and subsequent drying which develop in a range of matric suction, between 0.8 to 0.01 MPa, lower than the initial matric suction of the specimen.

Conversely, the treated clay undergoes in a particular way the processes of drying develop in a range of total suction higher than the initial total suction of the specimen. In fact, cyclic variations of total suction, which determine a significant drying, give rise to significant irreversible deformations of shrinkage because during the wetting stages, the material is unable to recover most of the deformations developed in the previous drying stages. The volumetric behaviour undergoes an almost reversible pattern.

The observed behavior may be interpreted with reference to the various mechanisms that control the volume response of the material to the double porosity, then considering the interactions between the microstructure and the macrostructure (Alonso et al. 1999). The triggering mechanism is due to the mutual sliding of the aggregates for the reduction of the shear resistance along the areolae of contact. This reduction can be determined by the breaking of the bonds of cementation between the aggregates of clay particles, triggered by the great loss of water, which is fundamental for the formation and permanence of cementing pozzolanic products and, only after, by the disappearance of the menisci and of their stabilizing effect.

References

Al-Mukhtar M, Khattab S, Alcover JF (2012) Microstructure and geotechnical properties of lime-treated expansive clayey soil. Eng Geol 139–140:17–27

Abdi MR, Wild S (1993) Sulphate expansion of lime-stabilized kaolinite: I. physical characteristics. Clay Miner 28(4):555–567

Airò Farulla C, Battiato A, Ferrari A (2011) The void ratio dependency of the retention behaviour for a compacted clay. In: Unsaturated soils – proceedings of the 5th international conference on unsaturated soils, vol 1, pp 417–422

Airò Farulla C, Celauro B, Celauro C, Rosone M (2014) Field test of lime treatment of clayey soils for railways and road works. Ingegneria Ferroviaria 69(9):729–752

Alonso EE, Vaunat J, Gens A (1999) Modelling the mechanical behaviour of expansive clays. Eng Geol 54(1–2):173–183

Bell FG (1996) Lime stabilization of clay minerals and soils. Eng Geol 42(4):223–237

Boardman DI, Glendinning S, Rogers CDF (2001) Development of stabilisation and solidification in lime-clay mixes. Géotechnique 51(6):533–543

Croce P, Russo G (2003) Experimental investigation on lime stabilised soils. In: Proceedings of the XIII European conference of soil mechanics and geotechnical engineering (ECSMGE), Prague

Cuisinier O, Auriol JC, Le Borgne T, Deneele D (2011) Microstructure and hydraulic conductivity of a compacted lime-treated soil. Eng Geol 123(3):187–193

Delage P, Audigier M, Cui Y, Howat MD (1996) Microstructure of a compacted silt. Can Geotech J 33(1):150–158

Di Sante M, Fratalocchi E, Mazzieri F, Pasqualini E (2014) Time of reactions in a lime treated clayey soil and influence of curing conditions on its microstructure and behaviour. Appl Clay Sci 99:100–109

Eades J, Grim R (1966) A quick test to determine lime requirements of lime stabilization. Highw Res Rec 139:61–72

Hilt GH, Davidson DT (1960) Lime fixation in clayey soils. Highw Res Board Bull 262:20–32

Locat J, Berube MA, Choquette M (1990) Laboratory investigations on the lime stabilization of sensitive clays: shear strength development. Can Geotech J 27(3):294–304

Romero E, Simms P (2008) Microstructure investigation in unsaturated soils: a review with special attention to contribution of mercury intrusion porosimetry and environmental scanning electron microscopy. Geotech Geol Eng 26:705–727

Stoltz G, Cuisinier O, Masrouri F (2012) Multi-scale analysis of the swelling and shrinkage of a lime-treated expansive clayey soil. Appl Clay Sci 61:44–51

Zhang X, Mavroulidou M, Gunn MJ (2015) Mechanical properties and behaviour of a partially saturated lime-treated, high plasticity clay. Eng Geol 193:320–336

Crack Initiation and Propagation of Clays Under Indirect Tensile Strength Test by Bending Related to the Initial Suction

Lamine Ighil Ameur(✉) and Mahdia Hattab

Laboratoire d'Etude des Microstructures et de Mécanique des Matériaux, Metz, France
lamine.ighil-ameur@univ-lorraine.fr

Abstract. The aim of this research is to analyze, by experimental approach, the impact of suction in the tensile strength and cracking phenomenon of unsaturated clayey soils samples. Through a bending tests, and a clay submitted to different level of suction (361 MPa, 110 MPa and 38 MPa), the approach consisted first in estimating the tensile strength which controls the initiation of tensile cracks. Then, using digital image correlation method, the propagation of cracks was precisely followed through the local strains development around the crack and close the crack tip.

Introduction

Mechanical and hydraulic properties of clayey media can be significantly affected by the presence of cracking in the material. Drying phenomenon, which provokes suction development in the material, appears to be one of the causes of the cracking of clays. During drying, Wei et al. (2016) show that different mechanisms can provoke the initiation and the development of cracking; they demonstrated that cracking by tensile (by opening mode or by Mode I) was one of them.

Many researchers in the past have focused on the importance of the knowledge of the tensile strength, among of them: Bishop and Garga (1969), Ajaz and Parry (1975), Tang and Graham (2000); or more recently Lakshmikantha et al. (2012). The tensile cracking seems to occur when induced tensile stress exceeds the tensile strength.

Ajaz and Parry (1975) used the results of two different tests: the beam flexion test and the direct tensile test were used on two different clays (Gault clay and Balderhead clay). The results show that the failure tensile strain increases as water content increases. Depending on the percentage of water content, the authors show that failure tensile strain at the maximum tensile stress varies from 2% to 15% for beam flexion tests, and from 1% to 5% for direct tensile tests. Similar observations on the water content effect were obtained on a claystone subjected to different levels of suction in Wei et al. (2016b).

This study is mainly focused on the characterization and the understanding of the tensile strength properties of clayey soils, and their relationships with tensile cracks' initiation and propagation. Tensile tests were performed using an indirect tensile test apparatus by bending, which was developed in the laboratory.

A. Ferrari and L. Laloui (eds.), *Advances in Laboratory Testing and Modelling of Soils and Shales (ATMSS)*, Springer Series in Geomechanics and Geoengineering,
DOI 10.1007/978-3-319-52773-4_19

A series of small-beam flexion tests were then carried out on preconsolidated specimens. Test samples were initially subjected to suction. This experimental approach allows estimating indirectly the global tensile strength at different suction of the clay samples, as well as the local strains using digital image correlation method.

Material and Method

Material Properties and Specimen Preparation

The clayey soil used in this study was Kaolinite K13, which is an industrial clay marketed by *Sibelco* (Paris, France). This synthetic clay appears to be similar to the more known Kaolinite P300. Liquid and plastic limits are about 40% and 20%, respectively. The density of the solid grains is equal to $\gamma_s/\gamma_w = 2.65$. The elementary kaolinite particle consists of a set of stacked sheets (Hattab et al. 2014).

To prepare the soil specimens, the clay powder (being initially on dry state) was progressively hydrated up to water content about twice the liquid limit. Then, the slurry was introduced in a dual drainage consolidometer and gradually consolidated by one-dimensional compression under a vertical stress of 120 kPa (Fig. 1a).

A preconsolidated specimen was afterward extracted from the consolidometer, and cut into small beam samples of 35 mm length, 10 mm height and 10 mm width (Fig. 1b). The samples of small-beams were then submitted to three different levels of suction (361 MPa, 110 MPa and 38 MPa) into a vacuum desiccator using salt solutions (Fleureau et al. 1993).

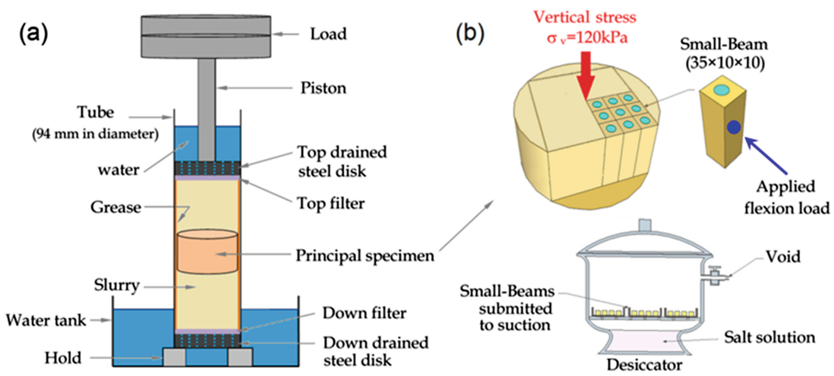

Fig. 1. Schematic representation of specimen preparation: (a) consolidometer apparatus; (b) cut and conditioned small-beams.

During the drying stage until the stabilization, for each imposed suction, the water content of the beams was measured on other similar small samples by the double weighing technique. This was done every day by extracting the small samples from the same desiccator for the weighing. The mean values are plotted on Fig. 2 as a function of time.

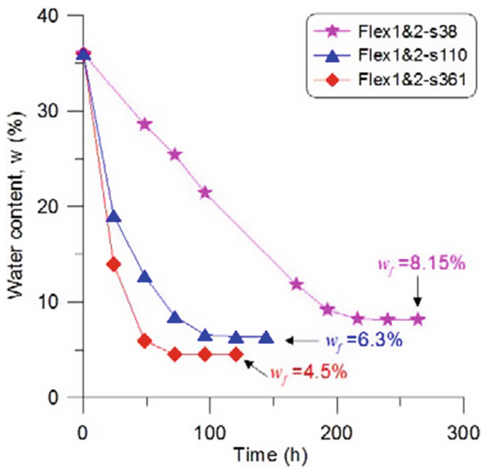

Fig. 2. Water content as a function of time during imposed suction stage.

Shrinkage velocity is defined by the ratio of the differential of water content divided by that of time (dw/dt), and computed between the beginning of shrinkage until the starting of the equalization phase. The results show that shrinkage velocity on the samples depends on the suction level. It was very fast at high suction level (361 MPa) and less important for the low suction (38 MPa). All the curves were afterwards stabilized at an equilibrium state, at given water content named w_f.

The properties of small-beam are presented in Table 1. For each level of suction, the tensile tests were performed with two different specimens.

Table 1. Beam flexion tests properties.

Imposed suction level		Low (38 MPa)	Mean (110 MPa)	High (361 MPa)
Names	Test 1	Flex1-s38	Flex1-s110	Flex1-s361
	Test 2	Flex2-s38	Flex2-s110	Flex2-s361
Relative humidity (%)		75.6	44.7	6.9
Shrinkage velocity dw/dt (%/h)		0.14	0.4	0.61
Water content after equilibrium (%)		8.15	6.3	4.5

Test Equipment

Before testing, the small beams removed from the desiccator at the end of the suction's imposition were immediately covered with the paraffin to avoid any relative humidity changes.

The apparatus was especially developed for small-beam flexion tests by Katti (2012). Then, the device was evolved to be adapted to the digital image correlation (DIC) tests. The system consists on a flexure beam device, a camera, a comparator and a control table equipped with a force sensor (Fig. 3).

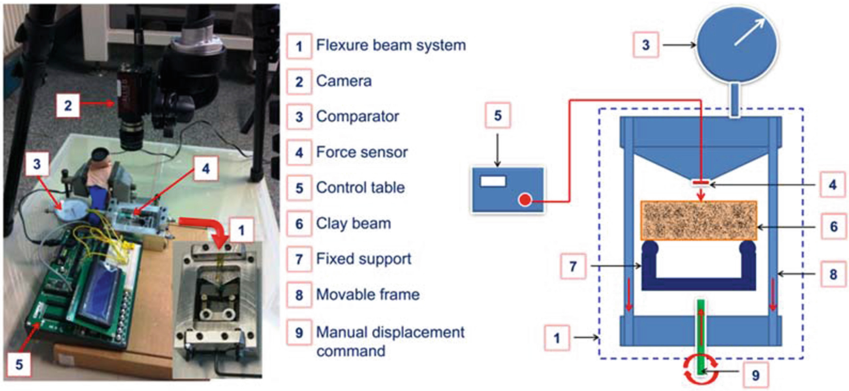

Fig. 3. Experimental flexure small-beam test apparatus.

The test starts by the displacement induces thanks to the one-dimensional free translation of the movable frame. The latter is equipped with force sensor in contact with the small-beam, which permits to capture the applied force on the sample. The imposed displacement to the movable frame was also measured. The displacement command was monitored with a rate of 10^{-3} mm/min. For each force value, images were simultaneously captured by the camera for the DIC analyses.

Results and Discussion

Analysis of the Global Behavior

As first approach, the tensile stress σ_t was estimated starting from the loading force applied to the sample, which was measured by sensor fixed on the sample. The used Eq. (1) was proposed by Ajaz and Parry (1975b) in the framework of the elastic bending theory. The method is based on the following assumptions: the plane sections remain plane after bending; the Young's modulus has the same value for the material of the beam in tension as in compression; the stress is linearly proportional to the strain; no creep occurs during bending.

$$\sigma_t = \frac{6M_f}{b.h^2} \tag{1}$$

M_f being the bending moment; b and h are the width and height of the small-beam respectively.

Figure 4 shows the results of tensile stress σ_t versus displacement of all performed tests. At a given suction level, the curves show consistent results. Tensile strength named σ_{tmax} corresponds to the maximum tensile stress. The results show the influence of the suction on the peak σ_{tmax} which clearly increase with the increase of suction. After the peak, more marked drop of the tensile stress is observed for higher suction.

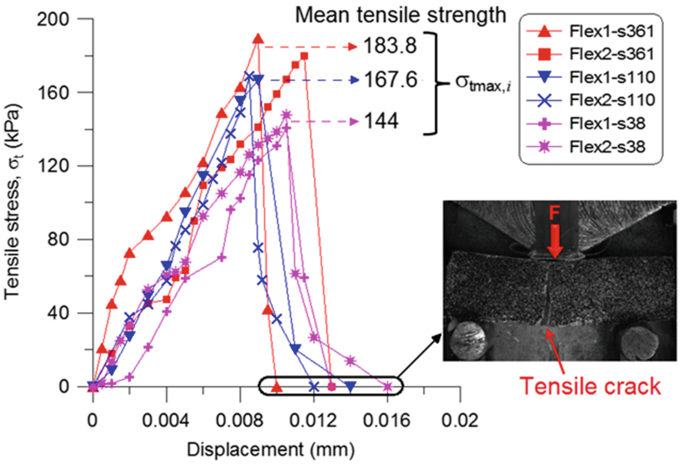

Fig. 4. Tensile stress as a function of the displacement during beam flexion loading.

Identification of the Local Behavior Using DIC Calculations

The initiation and the evolution of tensile strain can be shown through the longitudinal strain maps presented in Fig. 5. We choose here to present the results given by DIC on local strains for only the test Flex1-s38.

At tensile strength (σ_{tmax} = 140.6 kPa), referenced image i (Fig. 5a), the maximum and the minimum ε_{xx} are equal to +0.2% and −0.096%, respectively. The tension zone of the beam is shown in red, where the average ε_{xx} is equal to +0.2%. This stage defined crack initiation as it can be seen in the image.

Then, when the tensile stress decreases, the corresponding DIC (image i + 1 in the Fig. 5b) shows the propagation of the crack by tensile crack, the extension increasing up to +6.3%. At the end of the test, referenced image f (Fig. 5c), it can be clearly observed the directions of the displacement vectors (white vectors) indicating the opening mechanism of the crack.

Discussion

Relationship Between Tensile Strength and Water Content

Figure 6 shows the relation between the water content and tensile strength for all tests performed in this study. In this figure, the results obtained by Wei (2014) using a direct tensile method on the same material, are added. The objective here is to define a trend

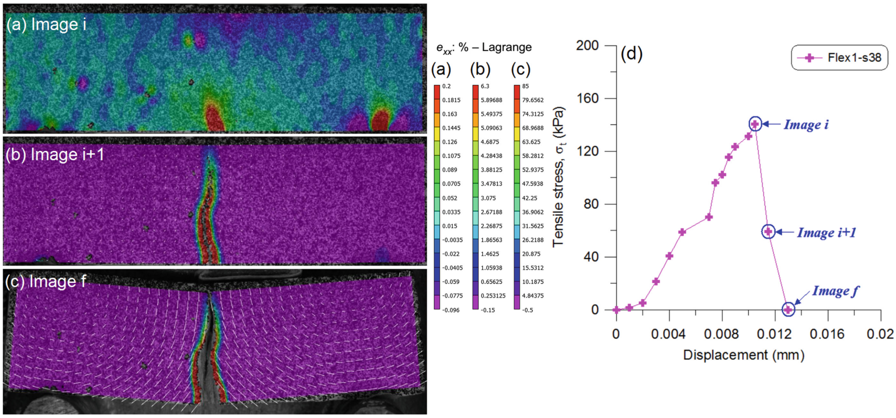

Fig. 5. Longitudinal local strain ε_{xx} at (a) image i; (b) image i + 1; (c) image f and (d) their positions on tensile stress curve (test Flex1-s38).

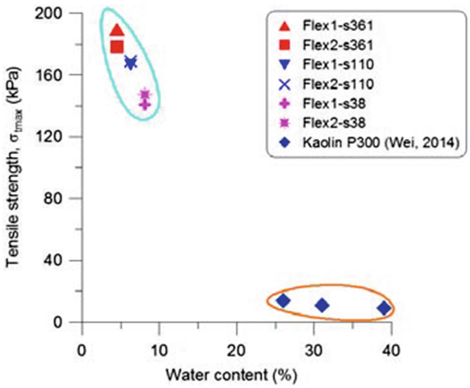

Fig. 6. Tensile strength as a function of water content.

in the evolution of the tensile strength, and not to precisely compare the results obtained by the two methods of the measurement.

As it can be seen from these results, which appear quite consistent with Ajaz and Parry (1975) observations, the decrease of water content seems to induce an exponential increase of the tensile strength σ_{tmax}.

Relationship Between Tensile Strength and Suction

The relationship between tensile strength and initial suction is plotted in Fig. 7 both as a function of the logarithm of suction (Fig. 7a) and suction (Fig. 7b). The results show how tensile strength increases with the initial suction. This relationship in Fig. 7b is nonlinear. Same trend was also shown by Tang and Graham (2000) on sand-bentonite

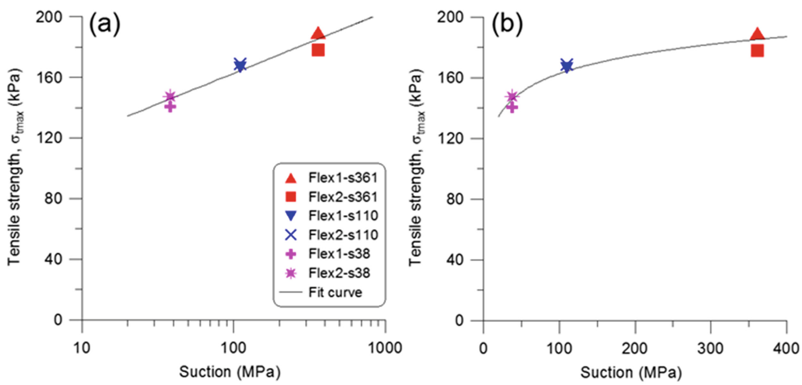

Fig. 7. Tensile stress as a function of suction.

mixture, and by Wei et al. (2016b) on claystone. The observed non-linearity at the global behavior is explained by some authors, for instance Taibi et al. (2008), as the result of local mechanisms which mainly concern the non-linear function of the local capillary stress versus suction.

Conclusion

In this study, an experimental indirect tension device by bending was designed in the laboratory, allowing to approach the tensile strength of a clayey material. This research is focused both on the relationships between tensile strength and suction on one hand, and the effect of tensile strength on tensile cracks' initiation and propagation on the other hand.

In the analysis of the global behavior, tensile strength values were calculated for all the tests in each level of the imposed initial suction. Moreover, using the digital correlation images allowed to identify the opening mode mechanism of the tensile crack. It can be seen that initiation of the crack starts at the tensile strength, then, propagates with the decrease of tensile stress until the complete breaking of the small-beams.

The results show that the tensile strength generally increases with decreasing water content, which is related to the initial suction. A relationship where tensile strength increases nonlinearly with increasing suction is also highlighted.

References

Ajaz A, Parry RHG (1975a) Stress-strain behaviour of two compacted clays in tension and compression. Geotechnique 25(3):495–512

Ajaz A, Parry RHG (1975b) Analysis of bending stresses in soil beams. Geotechnique 25(3):586–591

Bishop AW, Garga VK (1969) Drained tension tests on London Clay. Géotechnique 19:303–313

Fleureau JM, Kheirbek-Saoud S, Soemitro R, Taibi S (1993) Behaviour of clayey soils on drying-wetting paths. Can Geotech J 30(2):287–296

Hattab M, Hammad T, Fleureau JM (2014) Internal friction angle variation in a kaolin/montmorillonite clay mix and microstructural identification. Géotechnique 65(1):1–11

Katti A (2012) Etude expérimentale des fissurations dans les argilites de Bure et les argiles de synthèses soumises à des chargements statiques en flexion. Rapport de stage Master 2 MMSP, Université de Lorraine, Metz, France

Lakshmikantha MR, Prat PC, Ledesma A (2012) Experimental evidences of size-effect in soil cracking. Can Geotech J 49(3):264–284

Taïbi S, Fleureau JM, Hadiwardoyo S, Kheirbek-Saoud S (2008) Small and large strain behaviour of an unsaturated compacted silt. Eur. J. Environ. Civ. Eng. 12(3):203–228

Tang GX, Graham J (2000) A method for testing tensile strength in unsaturated soils. Geotech Testing J 23(3):377–381

Wei X (2014) Etude micro-macro de la fissuration des argiles soumises à la dessiccation. Doctoral dissertation, Ecole Centrale Paris, Châtenay-Malabry, France

Wei X, Hattab M, Bompard P, Fleureau JM (2016a) Highlighting some mechanisms of crack formation and propagation in clays on drying path. Geotechnique 66(4):287–300

Wei X, Duc M, Hattab M, Reuschlé T, Taibi S, Fleureau JM (2016b) Effect of decompression and suction on macroscopic and microscopic behavior of a clay rock. Acta Geotech 1–19, doi:10.1007/s11440-016-0454-8

Evaluation of the Instantaneous Profile Method for the Determination of the Relative Permeability Function

Anne-Catherine Dieudonné(✉) and Robert Charlier

University of Liege, Liège, Belgium
anne-catherine.dieudonne@epfl.ch

Abstract. Experimental determination of water permeability in unsaturated conditions is a critical issue. Among the existing experimental techniques, the instantaneous profile method is frequently used. When applied to bentonite-based materials, the method often shows that the water permeability–suction function significantly differs depending on the distance from the wetting face. Such behaviour has been interpreted as a consequence of structural changes in the sample which directly affect the water flow properties. In order to better understand the involved processes, a hydromechanical simulation of an infiltration test is performed. While structural changes are shown to affect the hydraulic properties, the computed water permeability–suction evolution is strongly affected by the interpretation of the raw experimental data.

Introduction

Unsaturated fluid flow is important in many engineering applications. For instance, a proper estimation of the time required to ultimately saturate bentonite buffers under *in situ* conditions is an important stake for the safe design of geological repositories for radioactive waste. In this context, good characterization and modelling of both water retention behaviour and unsaturated water flow are of paramount importance.

Yet, experimental determination of unsaturated water permeability is a critical issue. Among the different experimental techniques, the instantaneous profile method (Daniel 1982) has been frequently used to determine the permeability of unsaturated materials (Cui *et al.* 2008; Ye *et al.* 2009; Wang *et al.* 2013a; Schanz 2016). According to the method, a cylindrical sample is wetted from one extremity and the evolution of relative humidity is monitored over time at different heights of the sample. The results are plotted in terms of isochrones of suction and water content at different times. In order to determine the permeability, the hydraulic gradient and liquid flux are also computed.

When applied to bentonite-based materials, the instantaneous profile method often shows that the water permeability–suction function significantly differs depending on the considered distance from the wetting face. Such behaviour has been interpreted as a consequence of structural changes in the sample which directly affect the water flow properties. In order to better understand the involved processes, a coupled hydromechanical simulation of the infiltration test is performed in this paper. The determination

A. Ferrari and L. Laloui (eds.), *Advances in Laboratory Testing and Modelling of Soils and Shales (ATMSS)*, Springer Series in Geomechanics and Geoengineering,
DOI 10.1007/978-3-319-52773-4_20

of the relative permeability function by means of the instantaneous profile method is then discussed.

Hydromechanical Formulation for Bentonite-Based Materials

The theoretical framework is composed of two balance equations, namely the balance of momentum and water mass balance equations. The stress equilibrium equation is expressed as:

$$\nabla \cdot \boldsymbol{\sigma_t} + \boldsymbol{b} = 0$$

where $\boldsymbol{\sigma_t}$ is the total (Cauchy) stress tensor and $\boldsymbol{b}$ is the body force vector. The mass balance equation for water is given by:

$$\frac{\partial}{\partial t}(\rho_w \phi S_r) + \nabla \cdot (\rho_w \boldsymbol{q_w}) = Q_w$$

where ρ_w is the bulk density of liquid water, ϕ is the porosity, S_r is the degree of saturation, Q_w represents any external supply of water, and $\boldsymbol{q_w}$ is the Darcy flow. It is related to the water pressure u_w through:

$$\boldsymbol{q_w} = -\frac{k_{rw}(S_r) \cdot K_w}{\mu_w}(\nabla u_w + \rho_w \boldsymbol{g})$$

where μ_w is water dynamic viscosity, K_w is the water permeability in fully saturated conditions ($S_r = 1$) and k_{rw} is the so-called relative permeability function and is a function of the degree of saturation S_r according to:

$$k_{rw} = S_r^{n_k}$$

with n_k a model parameter. Kozeny-Carman law is extended to account for the double-structure of compacted bentonite-based materials, so that the saturated water permeability K_w is a function of the macrostructural void ratio $e_M = e - e_m$ (with e the total void ratio and e_m the microstructural void ratio) according to:

$$K_w = K_{W0} \frac{(1 - e_{M0})^M}{e_{M0}^N} \frac{e_M^N}{(1 - e_M)^M}$$

with K_{W0} a reference permeability measured on a material with a reference macrostructural void ratio e_{M0}, and N and M two model parameters. The microstructural void ratio is not fixed but evolves with the water ratio $e_w = S_r \cdot e$ according to Dieudonne *et al.* (2014) and Della Vecchia *et al.* (2015):

$$e_m = \beta_0 e_w^2 + \beta_1 e_w + e_{m0}$$

where e_{m0} is the microstructural void ratio for the dry material, and β_0 and β_1 are parameters quantifying the swelling potential of the microstructure. The water retention model developed by Dieudonne *et al.* (2016) is adopted. The model considers adsorbed water in the microstructure and capillary water in the aggregate-porosity. Accordingly, the degree of saturation is given by:

$$S_r = \frac{e_m}{e}\exp\left[-(C_{ads}s)^{n_{ads}}\right] + \frac{e-e_m}{e}\left\{1+\left[(e-e_m)\frac{s}{A}\right]^n\right\}^{-m}$$

where C_{ads} and n_{ads} are material parameters governing the microstructural water retention mechanism, A, m and n are material parameters governing the macrostructural water retention mechanism, and s is suction.

Finally, the Barcelona Basic Model (Alonso *et al.* 1990) is used to reproduce the mechanical behaviour of the material.

Numerical Modelling of an Infiltration Test

Description of the Test

Wang *et al*. (2013a) carried out an infiltration test on a compacted mixture of MX-80 bentonite and sand, with respective proportions of 70/30 in dry mass. The specimen (250-mm high and 50 mm in diameter) was compacted to a dry density of 1.67 Mg/m^3 and an initial water content of 11%. It was then introduced in a constant-volume cylindrical cell of the same diameter for the infiltration test. Four relative humidity sensors were installed every 50 mm along the sample as shown in Fig. 1. Water supply was done at atmospheric pressure from the bottom base. The top cover allows air expulsion but limited water evaporation.

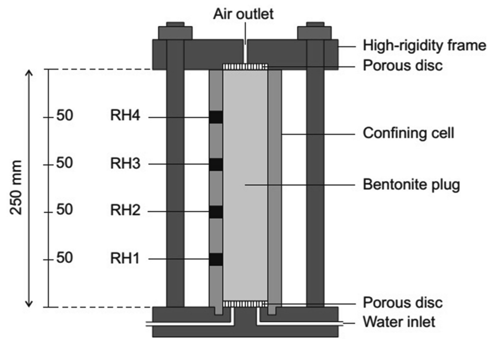

Fig. 1. Experimental set-up used for the infiltration test (after Wang *et al*. 2013a). RH1 to RH4 denote the relative humidity sensors.

Features of the Analysis

A hydromechanical model of the infiltration test is realized. The analysis assumes one-dimensional axisymmetric conditions around the longitudinal axis of the sample. An initial isotropic stress state of 0.1 MPa is considered in the whole sample, the effects of gravity being neglected. On the other hand, the initial suction in the sample is equal to 65 MPa.

The parameters of the hydromechanical model were calibrated against experimental data from Gatabin *et al.* (2008); Wang *et al.* (2013b) and Gatabin *et al.* (2016). They are given in Table 1. Finally, the exponent n_k of the relative permeability law is calibrated by best-fitting the responses of two relative humidity sensors, namely RH2 and RH3, located at distances of 100 and 150 mm from the injection front. Consequently, the model is validated by comparing the experimental and numerical results for the two other sensors, namely RH1 and RH4. A value of $n_k = 3.4$ is used in the reference analysis.

Table 1. Hydromechanical parameters of the MX-80 bentonite/sand mixture.

Microstructure evolution model			
e_{m0}	0.29		
β_1	0.18		
β_0	0.1		
Water retention model			
A (MPa)	0.2	C_{ads} (MPa^{-1})	0.0053
n	3	n_{ads}	0.79
m	0.15		
Water flow model			
K_{w0} (m²)	2.5 x 10^{-20}	N	2
e_{M0}	0.31	M	0.2
Barcelona Basic Model			
κ	0.025	$\lambda(0)$	0.12
κ_s	0.073	p_0^* (MPa)	1.40
ν	0.35	p_c (MPa)	0.01
$c(0)$ (MPa)	0.1	r	0.8
k	0.046	ω (MPa^{-1})	0.09
ϕ (°)	25		

Numerical Results

Figure 2 presents the evolution through of the relative humidity measured at different heights of the sample. The numerical results are compared to the experimental results.

As soon as hydration starts, an increase in relative humidity is detected by the sensor RH1, located at a distance of 50 mm from the wetting face. As water injection proceeds, the sensors RH2, RH3 and RH4 located at increasing distances from the

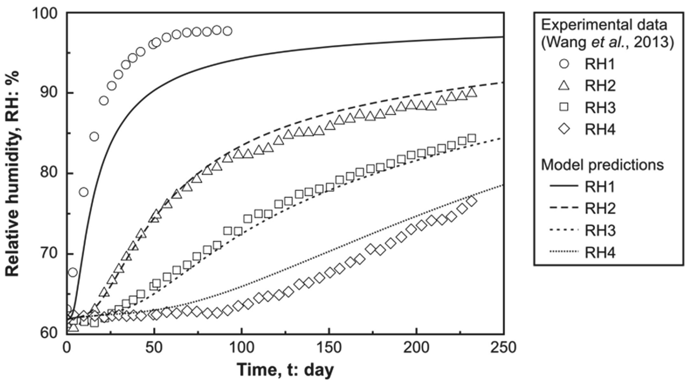

Fig. 2. Evolution of relative humidity during water infiltration. Comparison between experimental data (Wang *et al.* 2013a) and model predictions.

bottom progressively exhibit an increase in relative humidity. As observed in Fig. 2, the hydration rate is all the more important that the considered point is situated close to the injection water face. The progressive increase of relative humidity measured by the different sensors is well captured by the numerical model. A somewhat weaker agreement is obtained for RH1 which is located the closest from the injection front. Indeed, the very fast reaction of this sensor is not well reproduced numerically. This discrepancy of the model could be explained either by the assumed equilibrium between the microstructural and macrostructural levels, or by the fact that the infiltration cell is different from the compaction cell. In any case, the difference between the observed and modelled results should be balanced by the accuracy of the relative humidity sensors which is generally of the order of 1 to 3%.

Evaluation of the Instantaneous Profile Method for the Determination of the Relative Permeability Function

The instantaneous profile method has often been used to interpret infiltration tests and determine the water permeability of unsaturated porous materials. By monitoring of the injected water volume and the evolution of the relative humidity at different distances from the wetting front, the water permeability may be expressed as a function of suction. Figure 3 presents the evolution of the water permeability with suction predicted by the numerical model. These permeability values are obtained at four different points of the mesh and not computed using the instantaneous profile method. For the sake of comparison, the permeabilities computed by Wang *et al.* (2013a) using the instantaneous profile method are also represented.

Despite the good performance of the numerical model in reproducing the evolution of relative humidity in the sample, a very bad agreement is apparently obtained in terms of unsaturated water permeability. Indeed, Wang *et al.* (2013a) showed that the permeability evolution strongly depends on the considered height. At the bottom of the sample, an important decrease in permeability is observed between 65 MPa and

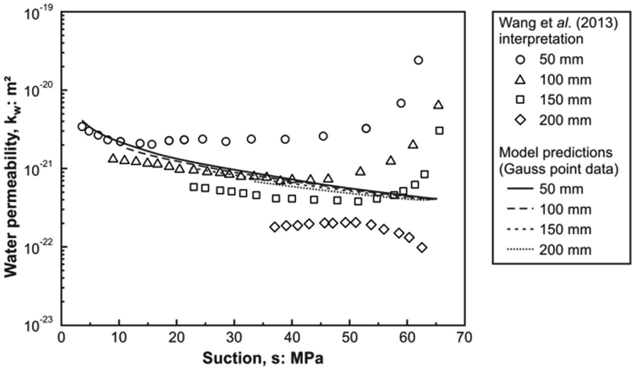

Fig. 3. Water permeability versus at different distances from the wetting end y. Comparison between Wang *et al.* (2013a) interpretation and the values obtained from the numerical model. Water permeabilities are obtained directly at different points.

50 MPa of suction Water permeability versus. The permeability is then relatively stable with decreasing suctions, although a slight increase is observed below 15 MPa. On the contrary, an increase in permeability is detected in the high suction range for the sensor located the furthest from the injection side. This trend is not reproduced by the numerical model which predicts a continuous increase of the water permeability with suction, regardless the distance from the wetting face. In addition, the evolution of the water permeability is less significant than the one predicted by Wang *et al.* (2013a) using the instantaneous profile method.

In order to determine the permeability of the partially saturated porous media, the hydraulic gradient i and the water flux q_w must be computed. In particular, the hydraulic gradient i is calculated as the slope of the isochrones (the tangent of the suction profile s at a height y and time t). It reads

$$i(t) = \left.\frac{\Delta s}{\Delta y}\right|_t$$

s and y being expressed in the same length units. On the other hand, using the water retention curve, the relative humidity profile can be converted into a water content profile. Considering the volumetric water content profiles at different times, the water flux can be determined according to

$$q_w(y_i) = A\frac{\int_{y_i}^{H}\theta(t+\Delta t)dy - \int_{y_i}^{H}\theta(t)dy}{\Delta t}$$

where A is the surface area of the sample face, H is the sample height and θ is the volumetric water content. Note that, in the previous relationship, the integrals are evaluated by trapezoidal rule. Then, knowing both hydraulic gradient and water flux, the permeability is obtained as (Daniel 1982)

$$k_w = -\frac{1}{A}\frac{q_w(y_i)}{\frac{1}{2}(i_t + i_{t+\Delta t})}$$

It can be computed as a function of suction at different heights of the sample corresponding to the positions of the relative humidity sensors. Here, the evolutions of relative humidity at 50 mm, 100 mm, 150 mm and 250 mm from the wetting end are used as input data for the instantaneous profile method (Fig. 4). The evolutions of water permeability computed in this way are in good agreement with those determined by Wang *et al.* (2013a), both qualitatively and quantitatively.

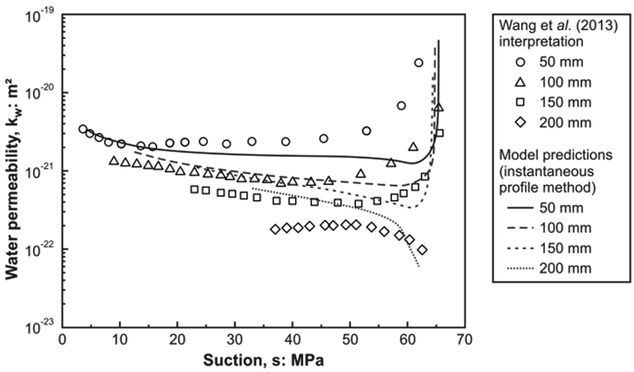

Fig. 4. Water permeability versus suction at different distances from the wetting end *y*. Comparison between Wang *et al*. (2013a) interpretation and the reinterpretation of the numerical results.

Conclusions

The instantaneous profile method is frequently used to determine the permeability of unsaturated soils. When applied to bentonite-based materials, it shows that the water permeability–suction function significantly differs depending on the distance from the wetting face. In this paper, a hydromechanical simulation of an infiltration test is performed. We show that the evolution of water permeability with suction as computed by the instantaneous profile method differs from the permeability values obtained at the Gauss points. In particular, the instantaneous profile method tends to overestimate the changes of unsaturated permeability during hydration. While infiltration column tests provide valuable and necessary data to assess the hydration kinetics of bentonite-based materials, their interpretation using the instantaneous profile method should be taken with caution.

References

Alonso EE, Gens A, Josa A (1990) A constitutive model for partially saturated soils. Géotechnique 40(3):405–430

Cui YJ, Tang AM, Loiseau C, Delage P (2008) Determining the unsaturated hydraulic conductivity of a compacted sand–bentonite mixture under constant-volume and free-swell conditions. Phys Chem Earth 33:S462–S471

Daniel DE (1982) Measurement of hydraulic conductivity of unsaturated soils with thermocouple psychrometers. Soil Sci Soc Am J 46(6):1125–1129

Della Vecchia G, Dieudonne AC, Jommi C, Charlier R (2015) Accounting for evolving pore size distribution in water retention models for compacted clays. Int J Numer Anal Meth Geomech 39(7):702–723

Dieudonne AC, Charlier R, Levasseur S, Della Vecchia G, Jommi C (2014) Evolution of clay fabric and water retention properties along hydromechanical stress paths. In: Proceedings of the 8th European conference on numerical methods in geotechnical engineering, NUMGE 2014, pp 971–975

Dieudonne AC, Gatabin C, Talandier J, Collin F, Charlier R (2016) Water retention behaviour of compacted bentonites: experimental observations and constitutive model. In: 3rd European conference on unsaturated soils – E-UNSAT 2016. E3S Web of Conferences, vol 9, 11012. doi:10.1051/e3sconf/20160911012

Gatabin C, Talandier J, Collin F, Charlier R, Dieudonne AC (2016) Competing effects of volume change and water uptake on the water retention behaviour of a compacted MX-80 bentonite/sand mixture. Appl Clay Sci 121–122:57–62

Gatabin C, Touze G, Imbert C, Guillot W, Billaud P (2008) ESDRED project, module 1-selection and THM characterization of the buffer material. In: Proceedings of the international conference underground disposal unit design & emplacement processes for a deep geological repository, Prague

Schanz T (2016) Transient boundary conditions in the frame of THM-processes at nuclear waste repositories. In: 3rd European conference on unsaturated soils – E-UNSAT 2016. E3S Web of Conferences, vol 9, 03001. doi:10.1051/e3sconf/20160903001

Wang Q, Cui YJ, Tang AM, Barnichon JD, Saba S, Ye WM (2013a) Hydraulic conductivity and microstructure changes of compacted bentonite/sand mixture during hydration. Eng Geol 164:67–76

Wang Q, Tang AM, Cui YJ, Delage P, Barnichon JD, Ye WM (2013b) The effects of technological voids on the hydro-mechanical behaviour of compacted bentonite–sand mixture. Soils Found 53(2):232–245

Ye WM, Cui YJ, Qian LX, Chen B (2009) An experimental study of the water transfer through confined compacted GMZ bentonite. Eng Geol 108(3–4):169–176

Advanced Laboratory Testing

A Double Cell Triaxial Apparatus for Testing Unsaturated Soil Under Heating and Cooling

Qing Cheng(✉), Raejee Kaewsong, Chao Zhou, and Charles Wang Wai Ng

Department of Civil and Environmental Engineering, Hong Kong University of Science and Technology, Kowloon, Hong Kong
qcheng@ust.hk

Abstract. To study thermo-hydro-mechanical behaviour of unsaturated soil, some apparatuses are developed and reported in the literature. Most of the existing apparatuses, however, cannot apply cooling and control temperature lower than room temperature. Moreover, an accurate measurement of thermal volume changes is still challenging, particularly for unsaturated soil. In this study, a triaxial apparatus with double cell total volume change measuring system is modified to fulfil temperature control in a wide temperature range (both higher and lower than room temperature). Temperature is regulated by circulating water with a controlled temperature in a spiral copper tube installed between the inner and outer cells. Detailed calibrations are carried out to determine the response of heating/cooling system and double cell to heating and cooling, such as the thermal equilibrium time and the volume change of inner cell. By using the new apparatus, a series of test is carried out to investigate the volume changes of normally consolidated intact and recompacted loess at different suctions over a wide thermal cycle ranging from 5 °C to 53 °C. It is found that contractive volumetric strain increases as temperature increases. During the cooling process, soil volume keeps contracting until the temperature decreases to 5 °C. An irreversible contraction at a much higher rate is observed from 13 °C to 5 °C. The observed plastic strain during cooling cannot be captured by existing thermo-mechanical models.

Introduction

Thermal effects on soil behaviour have a significant influence on many geotechnical problems, such as landfill engineering, pavement engineering and pipeline engineering (Gens 2010), thus the non-thermal condition must be considered. One of the first temperature controlled triaxial apparatus was described by Campanella and Mitchell (1968). From then on, some efforts have been made to develop apparatus for investigating the thermo-hydro-mechanical behaviour on saturated soils (Delage et al. 2000; Abuel-Naga et al. 2007; Di Donna and Laloui 2015) and unsaturated soils (Romero et al. 2003; Uchaipichat and Khalili 2009; Coccia and McCartney 2016). So far, most of the existing apparatuses in the literature can just control the temperature higher than room temperature, but cannot apply cooling and control temperatures lower than the

A. Ferrari and L. Laloui (eds.), *Advances in Laboratory Testing and Modelling of Soils and Shales (ATMSS)*, Springer Series in Geomechanics and Geoengineering,
DOI 10.1007/978-3-319-52773-4_21

room temperature. Furthermore, for unsaturated soils, an accurate measurement of thermal volume changes of unsaturated soil is still challenging (Ng et al. 2002).

In this study, a new thermal double cell triaxial apparatus is developed. Particular attention has been paid to the calibrations of the response of double cell subjected to heating and cooling. By using the new apparatus, four tests were carried out to study volume changes of intact and recompacted loess specimens during a heating and cooling cycle at different suctions. The temperature range is 5 °C to 53 °C.

A Temperature-Controlled Double Cell Triaxial Apparatus

A thermal double cell triaxial apparatus is developed in this study. Figure 1 shows a photograph of the newly developed apparatus. It consists of four main parts: the loading and suction control system, volume measuring system, flushing system and newly added temperature control system.

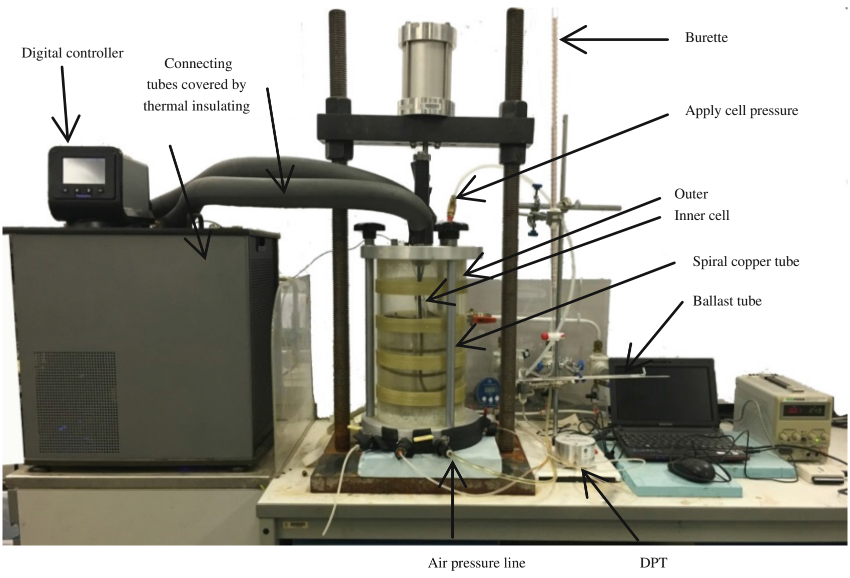

Fig. 1. Photograph of the temperature-controlled double cell triaxial apparatus.

The temperature control system includes a heating/cooling bath connected with a spiral copper tube installed between the inner cell and outer cell. The heating/cooling bath mainly consists of a digital controller which is able to adjust the output of the heating/cooling unit according to current and target temperatures, a thermostat, a heating/cooling unit, a water bath, an inbuilt pump and a thermocouple. During a test, the water is heated/cooled in the water bath and then circulated in the tube. Soil specimen is heated and cooled by heat exchanges between the specimen and water in the tube. In order to maintain the target temperature, a thermocouple is installed within the water of the inner cell to give feedback to the thermostat and the advanced digital controller. This will then automatically adjust the output of the heating/cooling unit according to the target temperature. Furthermore, a thermal insulating material is used to wrap the whole triaxial apparatus to minimize any heat loss and exchange with the surroundings.

The axis translation technique is used to control the matrix suction ($u_a - u_w$) in the soil specimen, where u_a and u_w are pore-air pressure and pore-water pressure, respectively. The total volume change of the specimen is measured by monitoring the change in the differential pressure between the water level inside the inner cell and that in the reference tube with a differential pressure transducer (DPT). The accuracy of DPT is within 0.1 mm. For the specimen size used in this research, 76 mm in diameter and 20 mm in height, this accuracy corresponds to a volumetric strain of about 0.03% (the diameter of the bottle neck is 20 mm).

The thermally induced volumetric strain of soil specimen is calculated using the following equation:

$$\varepsilon_v(T) = (\Delta V_m(T) - \Delta V_a(T) - \mu t)/V \tag{1}$$

where $\varepsilon_v(T)$ is the thermally induced volumetric strain (positive for contraction); $\Delta V_m(T)$ is the gross volumetric contraction measured by the DPT; $\Delta V_a(T)$ is the thermal contraction of volume change measurement system, including the inner cell, ceramic disk, top cap, membrane, water in the inner cell and drainage tubes; μ is the rate of water diffusion through the membrane and drainage tubes at a given pressure and temperature condition; t is the test duration; V is the volume of specimen. More details of the system were reported by Ng et al. (2012).

Calibrations of the Heating/Cooling System and Double Cell

Careful calibrations are carried out to determine the time to reach thermal equilibrium. During the calibration, the temperature in the water bath was increased from room temperature (23 °C) to 53 °C and then decreased to 5 °C step by step. Each step is around 10 °C. Apart from an inbuilt thermocouple in the heating/cooling bath, two thermocouples were installed in the water of the inner cell and in the middle of the soil specimen, respectively. Figure 2 shows the temperature monitored by the three thermocouples. It can be seen that within 1 h, the temperature in the heating/cooling bath reaches the target one. The temperatures of the water in the inner cell delays for about half an hour, while soil temperature reaches the target temperature within around 5 h. The time to reach thermal equilibrium is longer than some other apparatus in the literature (for example, 2 h in the study of Cai et al. (2014)), mainly because the inner cell in the current study decrease the rate of heat transfer. On the other hand, the slower heat transfer can enhance the stability of soil temperature. After reaching equilibrium, the temperature fluctuation is less than 0.2 °C.

The relationship between total volume change and output voltage of the DPT is determined in an approach similar to that reported by Ng et al. (2002). Furthermore, careful calibrations are carried out to determine the second and third terms on the right hand side of Eq. (1) at various pressure and temperature conditions.

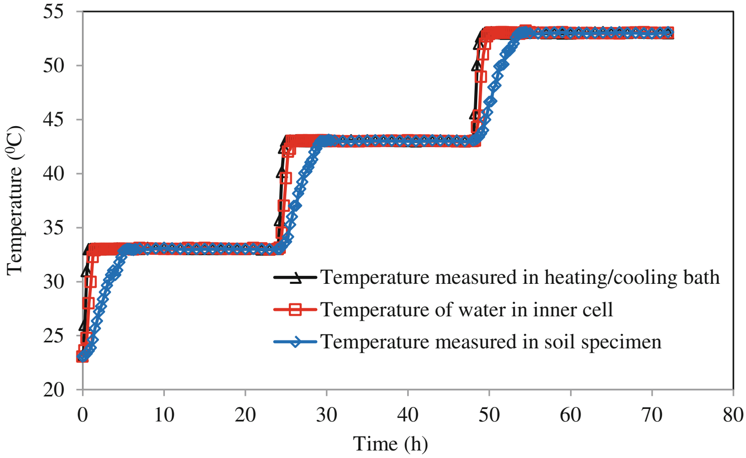

Fig. 2. The change of temperature with time during heating.

Test Material, Program and Procedures

This experimental study was performed on loess from Shaanxi Province, China. The index properties are summarized in Table 1. According to the Unified Soil Classification System (ASTM 2006), the test soil is classified as a clay of low plasticity (CL).

Table 1. Index properties of loess.

Specific gravity, Gs	2.69	Liquid limit (%)	36
Sand content (%)	0.1	Plastic limit (%)	19
Silt content (%)	71.9	Plastic index (%)	17
Clay content (%)	28.0		

Intact block loess samples were manually extracted using wooden cubic boxes with a length of 300 mm at a depth of 3.5 m. And the cutter ring with 76 mm diameter and 20 mm height was used to obtain the intact specimens. The initial void ratio is 1.17 while the initial suction is 200 ± 20 kPa. For recompacted specimens, static compaction is adopted. The compaction water content is about 10.9% and the initial void ratio is 1.17.

Four suction–controlled heating and cooling tests were carried out. Two of them (R0 and R100) were carried out on recompacted specimens, but at different suctions (0 and 100 kPa). The other two (I0 and I100) were carried out on intact specimens at suctions of 0 and 100 kPa.

Figure 3 shows the stress path. Each test consists of three stages: isotropic compression, wetting and thermal cycle. After set-up in the triaxial apparatus, the initial state of each specimen was fixed at Point A (or A’). For intact and recompacted specimens, the initial suction is about 200 and 180 kPa, respectively. Each specimen was firstly isotropically compressed to a net confining stress of 50 kPa (A → B). The next stage was to apply the target suction. The equilibrium state can be considered to be attained when the water flow rate is less than 0.1 ml/day, which is equivalent to a rate of 0.09%/day in gravimetric water content. In tests R100 and I100, soil specimens were wetted to 100 kPa (B → C1). Similarly, soil specimens in tests R0 and I0 were wetted to 0 kPa (B → C2). 7–10 days were required to reach the equilibrium condition. Then, the third stage was to change the temperature step by step. The heating process was from the typical room temperature (23 °C) to 53 °C (C1 → D1, C2 → D2), followed by cooling to 5 °C (D1 → E1, D2 → E2) and re-heating to the room temperature (E1 → F1, E2 → F2). The change of soil temperature is about 10 °C in each step. Each step lasted for 24 h in order to achieve thermal equilibrium.

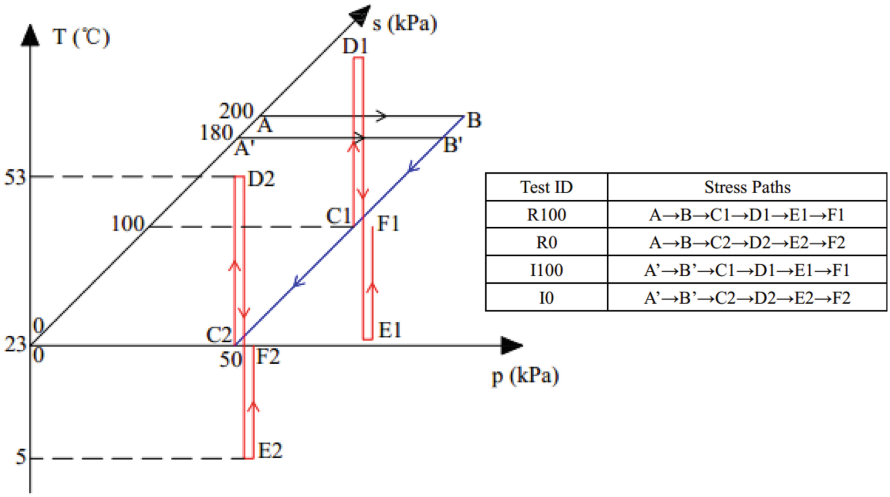

Test ID	Stress Paths
R100	A→B→C1→D1→E1→F1
R0	A→B→C2→D2→E2→F2
I100	A'→B'→C1→D1→E1→F1
I0	A'→B'→C2→D2→E2→F2

Fig. 3. Stress path during the test.

Volume Changes of Intact and Recompacted Loess During Heating and Cooling

Figure 4 shows the volume changes of intact and recompacted loess during heating and cooling at two different suctions (0 and 100 kPa). For recompacted soil, during the heating process, contractive volumetric strain increases with increasing temperature. During the cooling process, soil volume keeps contracting until temperature decreases to 13 °C at a slower rate of around 2×10^{-3}%/°C. However, when temperature decreases from 13 °C to 5 °C, there is a plastic contraction at a much higher rate of about 2.5×10^{-2}%/°C. This plastic volume changes during cooling are probably because cooling-induced contraction of soil particles leads to particle rearrangements in loess. Moreover, the cooling-induced plastic volume change, which only occurs when the cooling temperature is less than a critical value, cannot be captured by existing thermo-mechanical models (for example, Zhou and Ng (2015)), which predict elastic contraction during cooling.

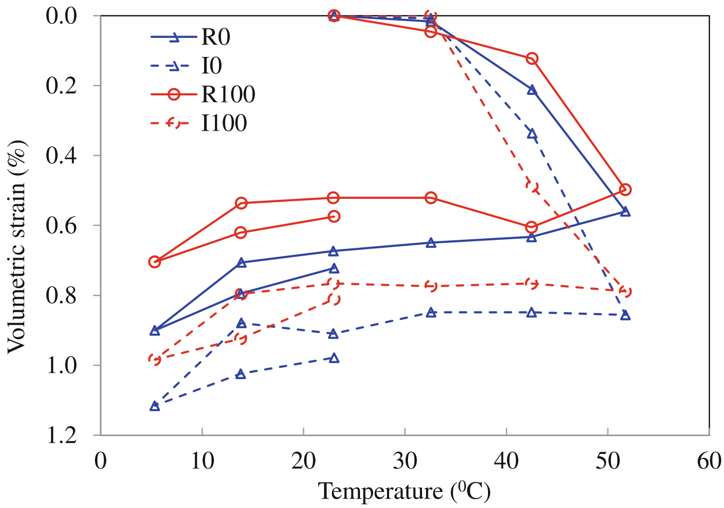

Fig. 4. Volume changes of intact and recompacted loess during heating and cooling at a confining stress of 50 kPa.

For suction effects, it is revealed in the figure that the cumulative thermal volume change at zero suction is larger than that at suction of 100 kPa. The difference, which varies with temperature in the range of 0 to 20%, is about 5% on average. For unsaturated loess in the current study, substantial volumetric contraction (about 17%, 25%, 13% and 19% for R100, R0, I100 and I0, respectively) was recorded during wetting. With a larger suction, the void ratio after wetting is larger. Effects of suction-induced hardening are compensated by effects of strain hardening induced by wetting collapse.

At a given suction, the cumulative volumetric strain of intact specimen is about 25% larger than that of recompacted one. The differences between intact and recompacted specimens may be attributed to their different soil structures. For intact specimen, there are a number of large pores with diameter over 200 µm while the pores of recompacted specimen are more uniform (Ng et al., 2016). In addition, the wetting induced volumetric strain of intact specimen (13% and 19% for I100 and I0) is much smaller than that of recompacted specimen (17% and 25% for R100 and R0), inducing a larger void ratio for intact specimen prior to heating and cooling. With more large pores and larger void ratio, the intact specimen shows larger volume change under heating and cooling cycle.

Summary and Conclusions

A temperature-controlled unsaturated soil triaxial apparatus with double cell total volume change measuring system is developed. Different from existing temperature-controlled triaxial apparatus in the literature, this apparatus can fulfil temperature control in a wider temperature range (both higher and lower than room temperature).

Furthermore, the new apparatus has a high accuracy (0.03%) in measuring the volumetric strain of unsaturated soil.

During the heating process, contractive volumetric strain of recompacted soil increase. During the cooling process, soil volume keeps contracting until the temperature decreases to 5 °C. An irreversible volume, when temperature decreases from 13 to 5 °C, is observed. The observed plastic behaviour during cooling cannot be described by existing thermo-mechanical models, which generally predict elastic contraction during cooling.

The thermal volume change behaviour of intact specimen is qualitatively similar to that of recompacted specimen. At a quantitative level, however, intact specimen shows a 25% larger strain than recompacted specimen due to the presence of some extra-large pores (>200 μm) in intact loess specimen.

Acknowledgements. The authors would like to acknowledge the financial support provided by the National Natural Science Foundation of China through the research grant 51509041. In addition, the authors would like to thank the Research Grants Council of the Hong Kong Special Administrative Region (HKSAR) for their financial support from Projects 616812 and 16209415.

References

Abuel-Naga H, Bergado DT, Bouazza A, Ramana GV (2007) Volume change behaviour of saturated clays under drained heating conditions: experimental results and constitutive modelling. Can Geotech J 44(8):942–956. doi:10.1139/t07-031

ASTM (2006) Standard practice for classification of soils for engineering purposes (unified soil classification system). American Society of Testing and Materials, West Conshohocken

Cai GQ, Zhao CG, Li J, Liu Y (2014) A new triaxial apparatus for testing soil water retention curves of unsaturated soils under different temperatures. J Zhejiang Univ Sci A 15(5):364–373

Campanella RG, Mitchell JK (1968) Influence of temperature variations on soil behaviour. J Soil Mech Found Div 94(3):709–734. ASCE

Coccia CJR, McCartney JS (2016) High-pressure thermal isotropic cell for evaluation of thermal volume change of soils. Geotech Test J 3(2):217–234. doi:10.1520/GTJ20150114. ASTM

Delage P, Sultan N, Cui YJ (2000) On the thermal consolidation of boom clay. Can Geotech J 37 (2):343–354. doi:10.1139/t99-105

Di Donna A, Laloui L (2015) Response of soil subjected to thermal cyclic loading: experimental and constitutive study. Eng Geol 190:65–76. doi:10.1016/j.enggeo.2015.03.003

Gens A (2010) Soil-environment interactions in geotechnical engineering. Géotechnique 60 (1):3–74. doi:10.1680/geot.9.P.109

Ng CWW, Cheng Q, Zhou C, Alonso EE (2016) Volume changes of an unsaturated clay during heating and cooling. Géotechnique Lett 6(3):1–7. doi:10.1680/jgele.16.00059

Ng CWW, Lai CH, Chiu CF (2012) A modified triaxial apparatus for measuring the stress path-dependent water retention curve. Geotech Test J 35(3):490–495. doi:10.1520/GTJ104203

Ng CWW, Zhan LT, Cui YJ (2002) A new simple system for measuring volume changes in unsaturated soils. Can Geotech J 39(3):757–764. doi:10.1139/t02-015

Romero E, Gens A, Lloret A (2003) Suction effects on a compacted clay under non-isothermal conditions. Géotechnique 53(1):65–81. doi:10.1680/geot.2003.53.1.65

Uchaipichat A, Khalili N (2009) Experimental investigation of thermo-hydro-mechanical behaviour of an unsaturated silt. Géotechnique 59(4):339–353. doi:10.1680/geot.2009.59.4.339

Zhou C, Ng CWW (2015) A thermo-mechanical model for saturated soil at small and large strains. Can Geotech J 52(8):1101–1110. doi:10.1139/cgj-2014-0229

A Suction- and Temperature-Controlled Oedometric Device

Hugo Troupel(✉), Jean-Michel Pereira, and Matthieu Vandamme

Université Paris-Est, Laboratoire Navier (UMR 8205), CNRS, ENPC, IFSTTAR, 77455 Marne-la-Vallée, France
hugo.troupel@enpc.fr

Abstract. To characterize the influence of temperature and relative humidity on the mechanical behavior of geomaterials, an experimental device was designed based on a conventional oedometer testing device. The aim of this work is to provide fundamental information about Thermo-Hydro-Mechanical coupling of unsaturated porous geomaterials such as sand or clay. Several methods were tested and compared to impose relative humidity and temperature. Two systems of control of relative humidity were developed: one using salt solutions to impose constant relative humidity with accuracy in the range of ±4% and the other one using the variation of the saturated vapor pressure of water with temperature to impose relative humidities and potentially make them vary over time. A special attention was paid to thermal insulation of the entire system to reduce temperature variations. A Proportional–Integral–Derivative controller (PID controller) permits to control temperature of samples between 20 and 60 °C for a week with accuracy in the range of ±0.5 °C. This system makes it possible to test 3 samples in parallel, at the same temperature but at potentially different relative humidities. For each sample the vertical displacement, the temperature close to the sample, the relative humidity of the air injected into the sample and the lateral pressure (since zero lateral strain boundary conditions are imposed) are measured. Finally the experimental device was tested on Hostun sand at two temperatures and three relative humidities.

Introduction

Thermo-Hydro-Mechanical (THM) coupling can strongly affect the behavior of clays in the context of disposing nuclear waste in deep geological formations, or granular soils in the context of thermo-active structure (Bidarmaghz et al. 2016). Experimental setup requires extreme caution to ensure relevant data. A suction- and temperature-controlled oedometric device was designed to study THM coupling of soils, in which zero lateral strain boundary conditions are imposed with lateral pressure measurement. Other experimental devices were created to characterize THM behavior under oedometric conditions (Recordon 1993; Romero et al. 2003, 2005; François et al. 2010, 2007 and Ye et al. 2012).

This paper presents the experimental device imagined to study THM behavior of geomaterials. Methods of control of suction and temperature are detailed. Then the influence of relative humidity on compression of sand at constant temperature is presented.

A. Ferrari and L. Laloui (eds.), *Advances in Laboratory Testing and Modelling of Soils and Shales (ATMSS)*, Springer Series in Geomechanics and Geoengineering,
DOI 10.1007/978-3-319-52773-4_22

Description of Oedometric Device

The oedometric device imagined is based on a standard oedometric device composed of a bench and three oedometer cells (Fig. 1). The three oedometer cells were modified to control temperature and relative humidity of the sample.

Fig. 1. Conventional oedometric device used before modifications (Controlab©).

Temperature Control

To ensure good stability of temperature, a special care was paid to thermal insulation of the whole oedometric bench. An 80 mm thickness isolating material (extruded polystyrene) was used to create an insulating box surrounding the whole oedometric device. Inside this box a heating cable, controlled by a PID (Proportional–Integral–Derivative) controller, permits to impose a constant temperature inside the box between 20 to 60 °**C** (Fig. 2). To increase thermal inertia of the box, the heating cable was disposed inside a container with about 20 kg of dry sand. This system is equipped with several

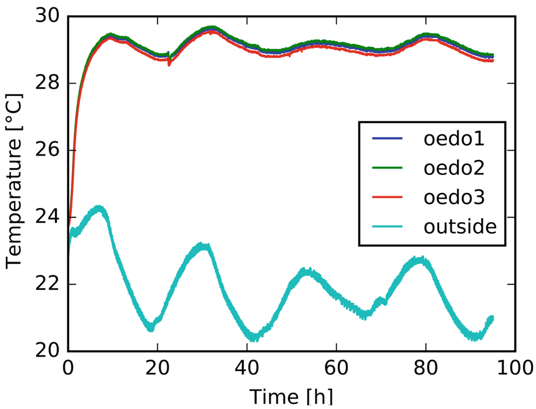

Fig. 2. Evolution of temperature outside and inside the insulating box with oedo1, oedo2 and oedo3 being the temperature close to the first, the second and the third oedometric cell, respectively.

temperature sensors, one next to each oedometer cell, one inside the thermal inertia box and one outside the insulating box. Figure 2 represents a comparison between the evolution of the temperature inside and outside the box for several days including the initial heating phase. The daily temperature variation in the room (± 2 °**C**) is well attenuated inside the box (±0.5 °**C**). The box is divided into two inner chambers, which makes it possible to load each oedometer without disturbing temperature control around the cells.

Relative Humidity Control

In the present article, two methods were chosen to impose relative humidity on samples, one, using vapors equilibriums with salts solutions, and another one based on the dependence of the saturated vapor pressure of water on temperature.

The first method uses salt solutions: knowing the relative humidity imposed by a salt solution to the air, the value of the suction imposed can be calculated using the celebrated Kelvin's law. However, the value of the relative humidity imposed by a salt solution evolves with temperature (Tang et al. 2005). Controlling relative humidity with salts proves to be a convenient method to impose constant relative humidity at constant temperature.

The other method is based on the variation of the vapor pressure with temperature (Désarnaud et al. 2013). The relative humidity is defined as: $H_r = p_v/p_v^{sat}$ with H_r the relative humidity, p_v the vapor pressure of water and p_v^{sat} the saturated vapor pressure of water. When air is heated, the vapor pressure of water does not change with temperature while saturated vapor pressure of water increases as a consequence the relative humidity decreases. Respectively, when air is cooled, the relative humidity increases. The Rankine equation gives an approximation of the saturated vapor pressure of water with temperature between 5 to 140 °**C**,

$$\ln\left(\frac{p_v^{sat}}{p_0}\right) = 13.7 - \frac{T_0}{T}$$

with $p_0 = 1$ atm, T the thermodynamic temperature and $T_0 = 5120$ K. To impose a relative humidity at a given temperature, air must be saturated at a precise temperature. For instance, to obtain a relative humidity of 80% at 30 °C, air must be saturated at 26 °C. Figure 3 shows the thermodynamic path of air: in blue a wetting path and in red a drying path from the same starting point (when considering that ambient air is at current temperature).

For this second method, the experimental device consists in a polystat with a bubbler flask which permits to saturate the air at a precise temperature with good accuracy (± 0.05 °C) (Fig. 4). To saturate the air, an air pump injects air bubbles at the bottom of the temperature-controlled flasks filled with water. Those bubbles will spontaneously migrate toward the water surface. Air from the top of bubbler flasks is then injected in the cells. The rest of this section evaluates if the time required for the bubbles to migrate through the flasks is sufficient for them to be saturated (at the temperature of the flask).

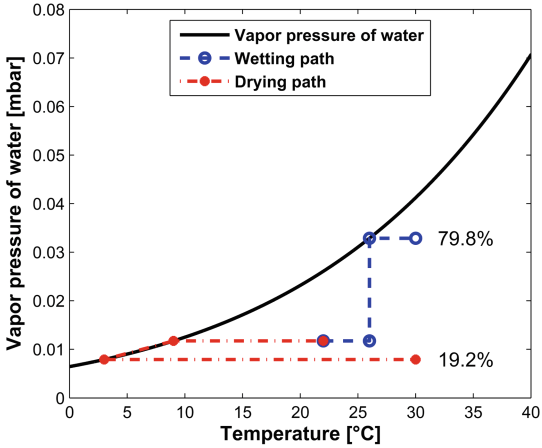

Fig. 3. Drying and wetting paths of air in the bubbler flask.

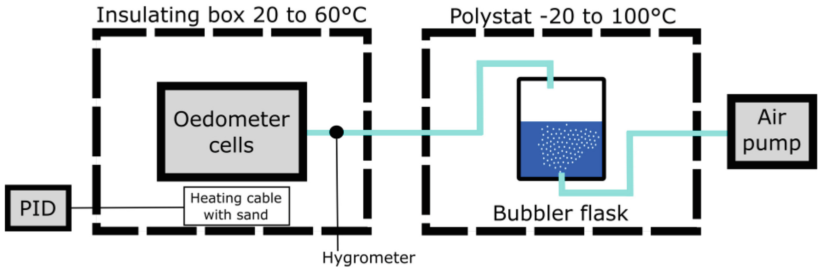

Fig. 4. Schematic representation of how temperature and relative humidity are controlled in our oedometric device, when using the dependence of saturated vapor pressure on temperature to control this latter.

Considering a bubble in the flask, if the bubble is subjected to Stokes' law, neglecting the density of air, according to Newton's second law, the maximum speed of the bubble is given by

$$v_{lim} = \frac{2}{9}\frac{\rho g R^2}{\mu}$$

with $\rho = 1000$ kg/m^3 the density of water, $g = 9.81$ m/s^2 the gravitational acceleration, R the radius of the bubble, and $\mu = 10^{-3}$ Pa·s the dynamic viscosity of water. So with a typical water level in the flask of $h = 15$ cm, the typical time of migration of each bubble through the water in the flask is: $t_w = \frac{9}{2} * \frac{\mu h}{\rho g R^2}$.

This time must be compared to the time of diffusion of water into the bubble. Considering Fick's law, the characteristic time of diffusion in one dimension could be written: $t_d = \frac{R^2}{D}$ with $D = 2.42 * 10^{-5}$ m^2/s at 25 °C being the coefficient of diffusion of water into air. The critical radius of a bubble well saturated at the end of the bubbler flask is obtained when typical time of diffusion and typical time of migration for a bubble inside the bubbler flask are equivalent. This radius is about 0.8 mm. This result is only slightly affected by temperature and water level. So bubbler flasks equipped with a porous stone of 1 µm was chosen to ensure that the radius of air bubbles in the flask is micrometric, and hence that air bubbles are saturated when they reach water level after having migrated through the flask.

The Oedometric Cell

The 50 mm-diameter cell used is equipped with lateral force sensor (capacity 5 MPa) to monitor the evolution of lateral stress (Fig. 5). This lateral force sensor is located at the base of the soil specimen. Axial displacements are monitored with a LVDT (Optimum Solartron©) of 3 mm stroke with accuracy in the range of ± 0.1 µm. The air at controlled relative humidity is force through the sample.

Comparison with Existing Devices

Table 1 compares the experimental device presented with other existing devices. Recordon (1993) imagined the first thermo-hydro-mechanical oedometric device where suction was measured using a tensiometer.

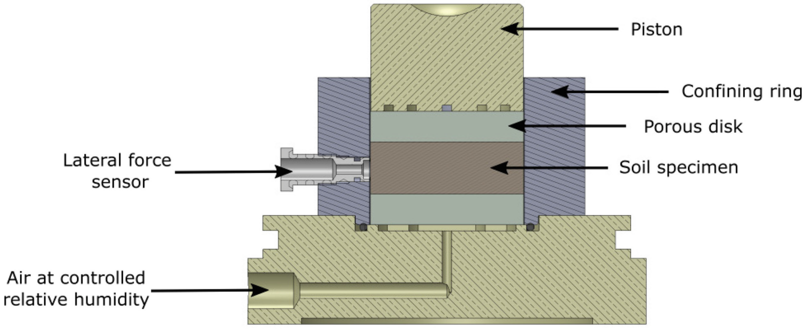

Fig. 5. Schematic representation of the modified oedometer cell used.

Table 1. Comparison of our experimental device with other devices.

Author	Maximum stress	Maximum suction	Maximum temperature
Romero et al. (2003)	1.2 MPa	450 kPa	80 °C
Romero et al. (2005)	4.5 MPa	14 MPa	65 °C
Francois et al. (2010)	1 MPa	500 kPa	80 °C
Ye et al. (2012)	80 MPa	110 MPa	80 °C
This study	5 MPa	150 MPa	60 °C

Different methods are used to impose suction such as axis-translation technique (Romero et al. 2003 and Francois et al. 2010). To extent the suction domain, Ye et al. (2012) imposed suction using salt solutions. But, in contrast to this study, they imposed suction by diffusion, by blowing air at controlled relative humidity through both the top and bottom porous stones: they did not force the air directly through the sample.

Results on an Unsaturated Sand

The device was tested on loose sand with high permeability to speed up the kinetics of hydraulic equilibration. Hostun sand was tested at two constant temperatures and three different relative humidities imposed with salt solutions. Six experiments were performed: all testing conditions are detailed in Table 2.

Table 2. Experimental conditions imposed to samples.

Sample	Initial void ratio e_0	Relative humidity imposed	Temperature (°C)
S25_50	0.98	50% ± 0.5%	25.6 ± 0.1
S25_73	0.98	73% ± 0.9%	25.6 ± 0.1
S25_91	0.98	91% ± 0.5%	25.5 ± 0.1
S41_41	0.98	41% ± 1%	41 ± 0.5
S41_68	0.99	68% ± 3%	41 ± 0.5
S41_76	0.95	76% ± 4%	41 ± 0.5

Figure 6 presents the influence of the relative humidity on the consolidation of the sand. At 25.6 °C, volumetric strain increases with relative humidity; but such trend is not so obvious at 41 °C.

The compression index C_c, the swell index C_s and the earth coefficient at rest $K_0 = \sigma_h^{'}/\sigma_v^{'}$ are presented in Table 3, in function of temperature and relative humidity. The swell index C_s increases with relative humidity and temperature and the Compression index C_c is quite independent of temperature and relative humidity.

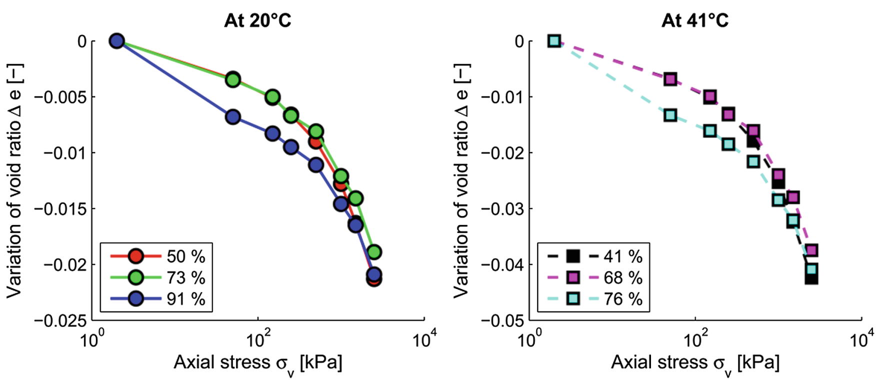

Fig. 6. Influence of relative humidity on consolidation of a sand at 25 °C and 41 °C.

Table 3. Influence of temperature and relative humidity on mechanical behavior of sand.

Temperature	25.6 °C	25.6 °C	25.5 °C	41 °C	41 °C	41 °C
Relative humidity	50%	73%	91%	41%	68%	76%
Swell index C_s	0.00013	0.0020	0.0025	0.0026	0.0027	0.0052
Compression index C_c	0.027	0.024	0.022	0.022	0.021	0.020
Earth coefficient at rest K_0	0.44	0.41	0.44	0.47	0.42	0.38

For all tests, the relation between the axial stress and the horizontal stress (Fig. 7) is almost linear. The earth coefficient at rest K_0 is estimated by linear regression for each test. Correlation coefficients are higher than 0.99. The obtained values are consistent with the range for K_0 from 0.4 to 0.45 for compact sand given by Schlosser (1990). At 25.6 °C, the relation between the axial stress and the horizontal stress (and hence K_0) does not depend on the relative humidity. In contrast, at 41 °C, K_0 decreases with relative humidity.

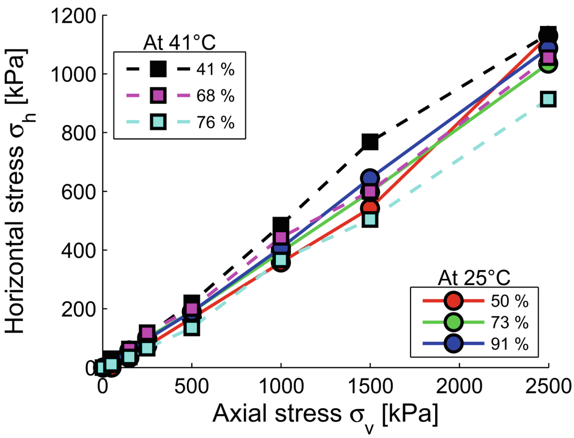

Fig. 7. Influence of relative humidity and temperature on axial and horizontal stress.

Conclusions and Perspectives

1. An oedometric device was designed to permits to control temperature (± 0.5 °C) and suction (± 4%) with good accuracy and to measure the lateral stress (up to 5 MPa).
2. For Hostun sand, C_s increases with relative humidity and temperature and C_c is quite independent of temperature and relative humidity. At 25.6 °C, the relation between the axial stress and the horizontal stress (and hence K_0) does not depend on the relative humidity. In contrast, at 41 °C, K_0 decreases with relative humidity.
3. The device could be modified to study stiff clays formations using the technique of control of suction based on (Ye et al. 2012).

References

Bidarmaghz A, Makasis N, Narsilio GA, Francisca FM, Carro Pérez ME (2015) Geothermal energy in loess. Environ Geotechnics 3(4):225–236

Désarnaud J, Bertrand F, Shahidzadeh-Bonn N (2013) Impact of the kinetics of salt crystallization on stone damage during rewetting/drying and humidity cycling. J Appl Mech 80(2):020911

François B, Laloui L (2010) An oedometer for studying combined effects of temperature and suction on soils. Geotechnical Test J 33(2):1–11

François B, Salager S, El Youssoufi M, Ubals Picanyol D, Laloui L, Saix C (2007) Compression tests on a sandy silt at different suction and temperature levels. In: Computer applications in geotechnical engineering, pp 1–10

Recordon E (1993) Déformabilité des sols non saturés à diverses températures. Rev Fr Géotech 65:37–56

Romero E, Gens A, Lloret A (2003) Suction effects on a compacted clay under non-isothermal conditions. Géotechnique 53(1):65–81

Romero E, Villar MV, Lloret A (2005) Thermo-hydro-mechanical behaviour of two heavily overconsolidated clays. Eng Geol 81(3):255–268

Schlosser F (1990) Ouvrages de soutènement: Poussée et butée. Techniques de l'ingénieur. Construction 1(C242):C242–1

Tang AM, Cui YJ (2005) Controlling suction by the vapour equilibrium technique at different temperatures and its application in determining the water retention properties of MX80 clay. Can Geotechnical J 42(1):287–296

Ye WM, Zhang YW, Chen B, Zheng ZJ, Chen YG, Cui YJ (2012) Investigation on compression behaviour of highly compacted GMZ01 bentonite with suction and temperature control. Nuclear Eng Des 252:11–18

Acoustic Emission Technology to Investigate Internal Micro-Structure Behaviour of Shear Banding in Sands

Wenli Lin[1(✉)], Wuwei Mao[2], and Junichi Koseki[1]

[1] The University of Tokyo, Tokyo, Japan
LWLCSU@geot.t.u-tokyo.ac.jp
[2] Chuo Kaihatsu Corporation, Tokyo, Japan

Abstract. Current experimental techniques used to understand the shear banding process in sands provide little insight into the internal micro-structure evolution. To this end, Acoustic Emission (AE), as a non-destructive testing technique, was proposed in this paper with great interest in characterizing the internal micro-structure response leading to the evolution of shear bands formed in laboratory triaxial compression. Silica sand was used to conduct consolidated-drained triaxial compression tests at a constant axial strain rate under an effective confining pressure of 100 kPa. AE events were collected and analyzed. Insights regarding relations of the deviatoric stress, source rates and dissipated energy rates of AE events with the increasing global axial strain are offered. The result indicated that with the increase of relative densities, the evolution envelope of AE source rates transits from a steep shape to a flat shape, and total amount of AE source events decreases gradually. According to the evolution of AE energy rate, shear banding process can be divided into four stages in terms of O-A, A-B, B-C and C-D, corresponding to the strain hardening regime, incipient strain softening regime, highest rate of strain softening regime and residual stress regime. From which point A could be considered as an omen of the initiation of strain localization, point B as the initiation of visible shear band and point C as the completion of shear banding. AE technologies can be provided as an alternative means to clarify and indicate the initiation and evolution of shear banding in sand.

Introduction

The strain localization and shear banding phenomenon have been attracting great attention because they are dominant in governing the strength and progressive failure of dense/cemented granular materials. Numerous pioneering works have been done experimentlly and theoretically (Vardoulakis 1979; Desrues and Chambon 1989; Tatsuoka et al. 1990; Chambon et al. 1994; Chambon et al. 2000; Alshibli et al. 2008; Rechenmacher et al. 2010) to advance understanding of the initiation and evolution of shear banding. Meanwhile, new advanced technologies were widely used in relevent researches, in which digital image techniques (Rechenmacher and Finno 2003; Rechenmacher 2006), grid point printed on the latex membrane (Alshibli and Sture 2000; Bhandari et al. 2012), etc. are engaged in grain-scale observation of shear

A. Ferrari and L. Laloui (eds.), *Advances in Laboratory Testing and Modelling of Soils and Shales (ATMSS)*, Springer Series in Geomechanics and Geoengineering,
DOI 10.1007/978-3-319-52773-4_23

banding, and computed tomography (Alshibli et al. 2003; Otani et al. 2000), resin-hardening specimens (Oda et al. 1998), etc. are employed regarding to the internal mechanism investigation. Shear bands, under plane strain condition, are prone to initiate around the peak strength and fully developed during the strain softening regime (Saada et al. 1999; Alshibli et al. 2003; Rechenmacher and Finno 2003), while Rechenmacher (2006) observed the incipient conjugate and multiple shear bands are burgeoned prior to the peak strength, i.e., in the strain hardening regime and fully developed until the critical residual stress. On the other hand, the initiation of complicated and multiple shear bands, under triaxial compression condition, were detected either as a strain hardening (Rechenmacher 2006; Bhandari et al. 2012) or softening phenomenon (Wang and Lade 2001, Alshibli et al. 2003). Though extensive important contributions have been achieved, it is evident that the initiation and evolution mechanism still remain dubious. Besides, the above-mentioned technologies are still limited in that either the surface deformation or discontinuous internal mechanism were observed to deduce the whole evolution of shear banding. Therefore, it is crucial to search another alternative means to clarify and indicate the initiation and entire evolution of shear banding.

Acoustic Emission (AE) method, as a non-destructive testing technique, has been widely used in many materials including metal, organic matrix composites and rock, etc. for detecting structure deformation and fracture. It has a superior advantage over other techniques in that it enables a direct analysis of the micro-structure response inside the detected material. A few literatures, recently, have even reported its successful applications in monitoring the sliding and crushing behavior in the sandy subsoil (Mao et al. 2015, Mao and Towhata 2015). Starting with these premises, in this paper, AE technique was proposed with great interest in understanding the internal micro-structure response leading to the initiation and evolution of shear banding in saturated silica sands subjected to triaxial compression. Relations of the deviatoric stress, the source rate and dissipated energy rate of AE events with increasing global axial strains were analyzed, and insights regarding them are offered.

Experimental Setup

Testing Materials and Apparatuses

The silica sand, having a mean particle size (d_{50}) of 0.471 mm, maximum void ratio (e_{max}) of 1.137, minimum void ratio (e_{min}) of 0.712 and a specific gravity (G_s) of 2.654, was used herein to prepare the specimen. Its particle size distribution curve is shown in Fig. 1.

Cylindrical specimens (100 mm in diameter and 200 mm in height) were prepared using air pluviation method in a split mould along with a thickness of 0.3 mm latex membrane. In this paper, four dense specimens with different relative densities (Dr = 80−96%) were tested under triaxial compression. Their relevant conditions tested herein are summarized in Table 1.

After the specimen preparation, the specimens were saturated using double vacuuming method with an effective confining pressure of 30 kPa. Besides, in order to fully

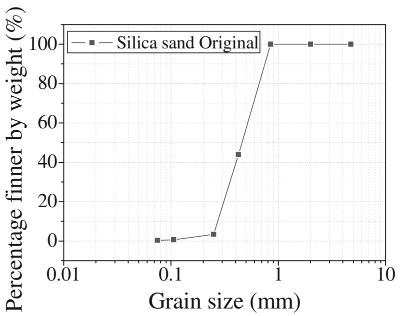

Fig. 1. Particle size distribution of Silica sand.

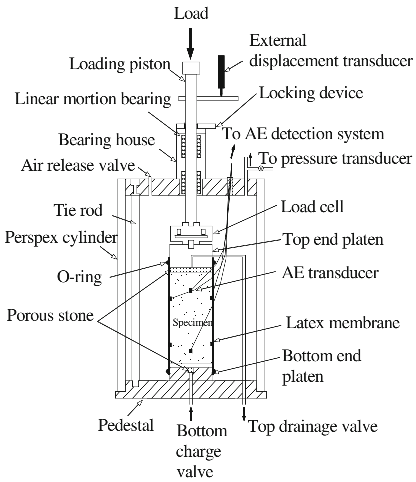

Fig. 2. Apparatus for triaxial compression test.

saturate the specimen, two porous stones and filter papers were embedded at both ends of the specimen. After the saturation of specimens, consolidated-drained triaxial compression tests were conducted at a constant axial strain rate under an effective confining pressure of 100 kPa, using the apparatus shown in Fig. 2.

Acoustic Emission (AE)

Acoustic Emission, sometimes known as stress wave emission, refers to the transient elastic waves generated by the rapid release of energy in the local stress concentration region inside a stressed material (ASTM E1316 2014). Generally speaking, as the stress

Table 1. Conditions for drained triaxial compression test.

No. of Test	Material	Effective confining pressure (kPa)	Strain-control rate (mm/min)	Relative density (%)
1	Silica sand	100	0.2	80.1
2	Silica sand	100	0.2	89.3
3	Silica sand	100	0.2	91.4
4	Silica sand	100	0.3	95.9

applied in the material increases, the generated elastic waves radiate out through the structure and excite the AE transducer to collect up the signal, which could be amplified by a preamplifier to avoid the influence of noises. Then the amplified signal could be further converted to an electrical signal and recorded by a data logger, and is

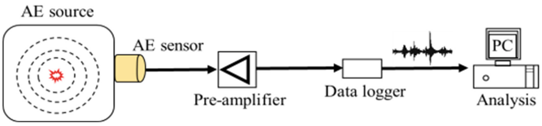

Fig. 3. Schematic of AE detection system.

finally transmitted to a computer for data display and feedback, as shown in Fig. 3.

In this paper, eight vibration transducers (with working frequency of 10 Hz–15 kHz, sensitivity of 20 dB and dimension size of 11.5 by 8.5 by 2.9 mm) produced by NEC/TOKIN Corporation, Model VS-BV210 were used and glued onto the latex membrane wrapping the specimen. The schematic arrangement of AE transducers is displayed in Fig. 4. AE data were collected using the NI PXIe-6366 data logger, which enables continuous data recording at a maximum analog input sampling rate of 2 MS/s (500 kS/s in this study) with a resolution of 16 bit for each channel.

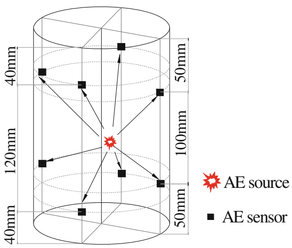

Fig. 4. Schematic arrangement of AE transducers.

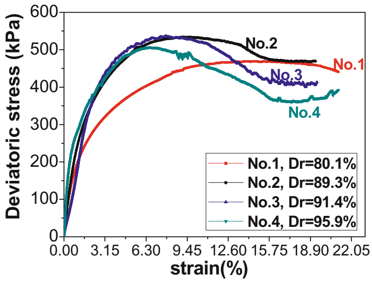

Fig. 5. Stress-strain relations of tests at different relative densities under drained triaxial compression.

Test Result

Global Deformation Monitoring and Analysis

Figure 5 demonstrates the corresponding stress strain relationships, in terms of deviatoric stress $q = \sigma_1'\text{-}\sigma_3'$ vs axial strain ε_1, for tests No.1 to No.4 with relative densities of D_r = 80.1%, 89.3%, 91.4%, 95.9% respectively.

For test No.1 on the relatively loose specimen, it is observed that the deviatoric stress increases initially with the axial strain and becomes essentially constant over a relatively large amount of strains to reach the peak strength. Significant strain softening is not observed during shear banding and the residual state is not reached even after terminating the test at an axial strain of 21.0%.

As the relative density increases from 80.1% to 95.9%, the peak strength becomes larger and considerable strain softening is observed. In addition, with the increase of relative densities, the amounts of strain at the peak strength decrease, while those at the critical residual state increase.

AE Event Monitoring and Analysis

Relation of deviatoric stress-strain and AE source rate. The AE source rate, as one of the important parameters indicating the amount of particles engaged in sliding and/or crushing, is analysed regarding to the evolution of deviatoric stress-strain, as shown in Fig. 6. Here, the source rate is designated as the source quantity in equal interval axial strains (set to 0.525% in this study). It indicates that, in general, the AE sources rate increases to a peak value (P_r) around the peak stress state (P_s) followed by a decrease in the post-peak regime, which is consistent with the evolution of the stress-strain response.

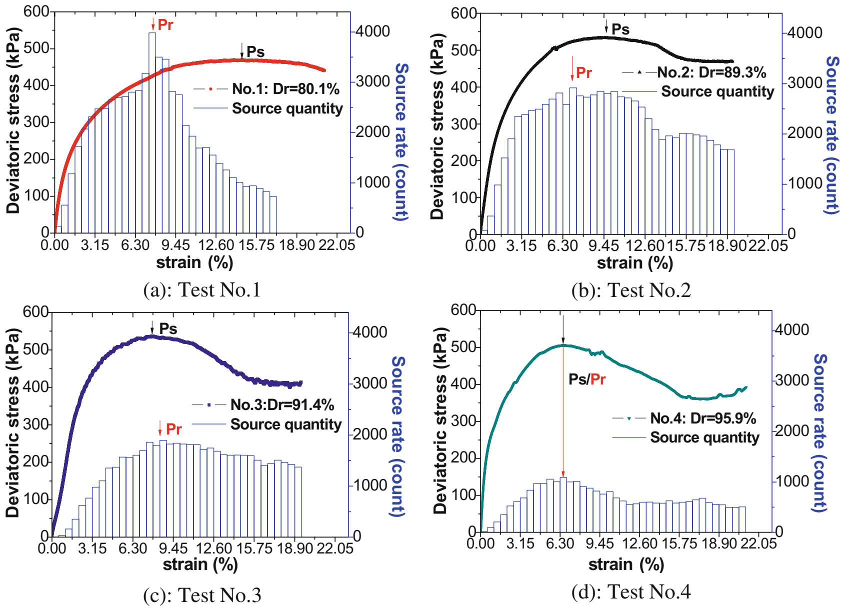

(a): Test No.1 (b): Test No.2

(c): Test No.3 (d): Test No.4

Fig. 6. AE source rate and stress path during shearing.

It is worth noting that with the increase of relative densities, the envelope of the source rate transits from a steep shape in looser sand to a flat shape in denser sand, i.e. the denser the sand specimens, the slower the source rate evolved during shear banding. In addition to different evolution shapes, the total amount of AE source events also decreases gradually as the increase of relative densities, in which the peak source rate in looser sand (around 4000 counts per 0.525% axial strain) is almost four times the rate in the densest sand (around 1000 counts per 0525% axial strain). It suggests that more intensive and extreme particles dislocation and/or crushing behaviour occur in looser sand, especially in the strain hardening regime.

Relation of deviatoric stress-strain and AE energy rate. The AE energy, referred to a measured area under the rectified signal envelope, is superior in interpreting the magnitude of AE source event as it is sensitive to both the signal amplitude and the duration (ASTM E1316 2014). Here, the energy rate was designated as the accumulation of energy in 10 s in this work. Results of its evolution law during shear banding in four dense sands under drained triaxial compression are displayed in Fig. 7. Based on the result of evolution of AE energy rate in the case of denser sand, it seems plausible to divide the process of shear banding into four stages, in terms of O-A, A-B, B-C and C-D as shown in the energy rate curve in Fig. 7(d). In which, the energy rate increases monotonically to a peak value (O-A) in the strain hardening regime followed by a steady or minor decreasing rate (A-B) around the peak strength, then increases sharply and rapidly (B-C) in the strain softening regime, and finally goes after with a

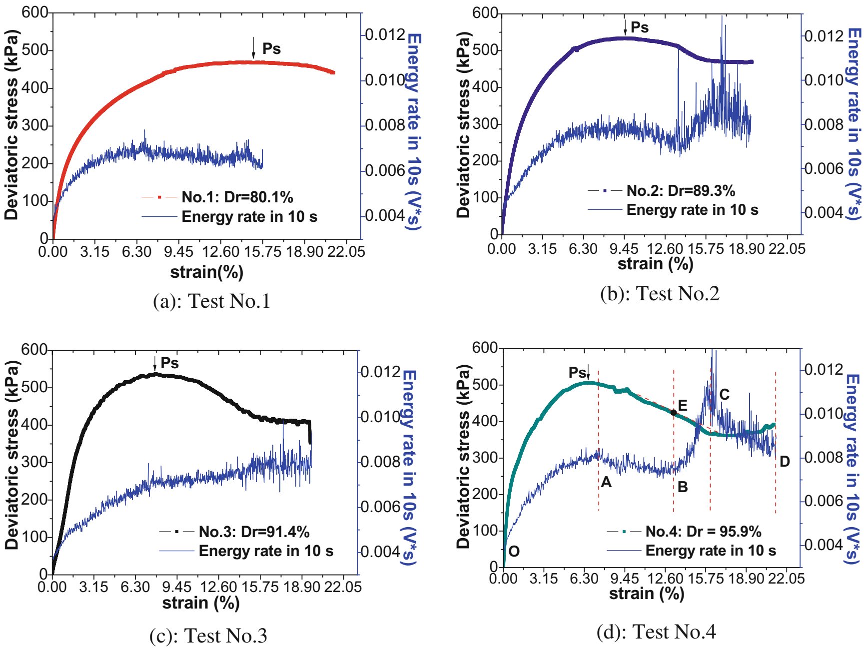

(a): Test No.1

(b): Test No.2

(c): Test No.3

(d): Test No.4

Fig. 7. AE energy rate and stress path during shearing.

significant decrease (C-D) in the residual stress regime. On the other hand, as to looser sand, only two stages are indicated as shown in Fig. 7(a), in which the energy rate increases rapidly to a peak value (O-A) followed by a stable or minor decreasing energy rate (A-B).

In O-A stage, as the increase of applied force, the specimen suffers from contraction, relative particle deformation, load columns collapse and buckling with regard to particle sliding, rotating and/or crushing under normal and tangential stresses, resulting in the rapid increase of energy rate. In A-B stage, strain localization starts to occur and becomes predominant. Visible strain localisation can be observed on the specimen, while evidence for shear band is not yet discovered. In B-C stage, generally, shear bands were fully developed in this stage. As a result, intensive energy released in a more rapid rate. While in C-D stage, since the shear band is completely developed, extreme deformation tends to slow down significantly and stress becomes constant, which results in the asymptotical decrease in the energy rate.

These high consistencies among AE source rate, AE energy rate and stress-strain behavior further suggest that AE technologies can be provided as an effective alternative means to clarify and indicate the initiation and evolution of shear banding in sand.

Conclusion

In this paper, Acoustic Emission (AE) technology was proposed to understand the micro-structure response leading to the initiation and evolution of shear banding. Relevant conclusions can be drawn as follows.

The evolution envelope of AE source rates transits from a steep shape in looser sand to a flat shape in denser sand and the total amount of AE source events decrease gradually as the increase of relative densities, suggesting that more intensive and extreme particles dislocation and/or crushing behaviour occur in looser sand.

According to the evolution of AE energy rate in denser sand, the process of shear banding can be divided into four stages in terms of O-A, A-B, B-C and C-D, corresponding to the strain hardening regime, incipient strain softening regime, highest rate of strain softening regime and residual stress regime, while the process of shear banding in looser sand only presents two stages, O-A and A-B. From which point A could be considered as an omen of the onset of strain localization, point B as the initiation of visible shear band and point C as the completion of shear banding.

References

Alshibli KA, Sture S (2000) Shear band formation in plane strain experiments of sand. J Geotech Geoenvironmental Eng 126(6):495–503

Alshibli KA, Batiste SN, Sture S (2003) Strain localization in sand: plane strain versus triaxial compression. J Geotech Geoenvironmental Eng 129(6):483–494

ASTM E1316–14e1 (2014) Standard Terminology for Nondestructive Examinations. ASTM International, West Conshohocken

Bhandari AR, Powrie W, Harkness RM (2012) A digital image-based deformation measurement system for triaxial tests. ASTM Geotech Test J 35(2):209–226

Chambon R, Desrues J, Hammad W et al (1994) CLOE, a new rate-type constitutive model for geomaterials theoretical basis and implementation. Int J Numer Anal Meth Geomech 18 (4):253–278

Chambon R, Crochepeyre S, Desrues J (2000) Localization criteria for non-linear constitutive equations of geomaterials. Mech Cohesive-frictional Mater 5(1):61–82

Desrues J, Chambon R (1989) Shear band analysis for granular materials: the question of incremental non-linearity. Ing Arch 59(3):187–196

Mao W et al (2015) Acoustic emission characteristics of subsoil subjected to vertical pile loading in sand. J Appl Geophys 119:119–127

Mao W, Towhata I (2015) Monitoring of single-particle fragmentation process under static loading using acoustic emission. Appl Acoust 94:39–45

Oda M, Kazama H, Konishi J (1998) Effects of induced anisotropy on the development of shear bands in granular materials. Mech Mater 28(1):103–111

Otani J et al (2000) Application of X-ray CT method for characterization of failure in soils. Soil Found 40(2):111–118

Rechenmacher AL, Finno RJ (2003) Digital image correlation to evaluate shear banding in dilative sands

Rechenmacher AL (2006) Grain-scale processes governing shear band initiation and evolution in sands. J Mech Phys Solids 54(1):22–45

Rechenmacher A, Abedi S, Chupin O (2010) Evolution of force chains in shear bands in sands. Geotechnique 60(5):343–351

Saada AS, Liang L, Figueroa JL et al (1999) Bifurcation and shear band propagation in sands. Geotechnique 49(3):367–385

Tatsuoka F et al (1990) Strength anisotropy and shear band direction in plane strain tests of sand. Soil Found 30(1):35–54

Vardoulakis II (1979) Bifurcation analysis of the triaxial test on sand samples. Acta Mech 32(1–3):35–54

Wang Q, Lade PV (2001) Shear banding in true triaxial tests and its effect on failure in sand. J Eng Mech 127(8):754–761

Direct and Indirect Local Deformations of Sand in Undrained Cyclic Triaxial Tests by Image Analysis Technique

Chuang Zhao[1(✉)], Junichi Koseki[1], and Yukika Miyashita[2]

[1] Department of Civil Engineering, University of Tokyo, Tokyo, Japan
zhaochuang@geot.t.u-tokyo.ac.jp
[2] Institute of Industrial Science, University of Tokyo, Tokyo, Japan

Abstract. A series of undrained cyclic triaxial liquefaction tests were conducted to observe directly and indirectly the local deformations of sand specimen through a transparent membrane. Black-colored silica sand, mixed in white-colored silica sand, was used for the direct evaluation. Black-colored dots, used for observing the local deformations indirectly, were pasted on membrane with a constant interval of 5 mm. Digital photographs were taken in front of the triaxial cell to evaluate the deformations of sand particles patterns and dots by Particle image Velocimetry method. The results indicated that image analysis is an efficient method for direct and indirect measurements of local deformation. Comparison of direct and indirect evaluations revealed that relative movement between sand particles pattern and an adjacent dot on the membrane had a leap when excess pore water pressure ratio reached unity.

Introduction

Conventional triaxial compression test is widely used by researchers and civil engineers to evaluate soil behavior in practice. Axial strain is deemed as a representative parameter of soil deformation by the assumption that the response of specimen is homogeneous under complex stress conditions. Recently, interests in strain localization especially on shear band evolution by continuously updated technologies have rapidly increased. Yoshida et al. (1994) took analog photos from the outside of a transparent cell to investigate deformation properties of shear band in sand subjected to plain strain compression test, by means of a photogrammetric system. Harris et al. (1995) also used plane strain compression tests to analyze the development of shear band in sand by stereophotogrammetry method. Desrues et al. (1996) conducted triaxial tests on sand for void ratio evaluation inside shear band by computed tomography. In addition, image analysis and digital correlation techniques have been applied in element tests on sand by researchers diffusely (e.g., Rechenmacher 2003; White et al. 2003; Mokni and Desrues 1998; Sadrekarimi and Olson 2010). In the above tests, local deformation properties have been detected and described both qualitatively and quantitatively.

However, researchers usually assume that uniform specimen would follow homogeneous strains during undrained tests, thereby little attention had been paid on

A. Ferrari and L. Laloui (eds.), *Advances in Laboratory Testing and Modelling of Soils and Shales (ATMSS)*, Springer Series in Geomechanics and Geoengineering,
DOI 10.1007/978-3-319-52773-4_24

strain localization in liquefaction tests. Undrained plane strain biaxial tests were carried out by Mokni and Desrues (1998) for strain localization by stereophotogrammetry method. It was found that shear banding also took place and the onset of localization was delayed, compared with drained tests. Kiyota et al. (2008) and Chiaro et al. (2013) claimed that specimen deformation became non-uniform after exceeding a certain level of overall shear strain, which was named as strain localization in torsional shear liquefaction tests. Fauzi and Koseki (2014) developed water sediment sample preparation method for segregated specimens in torsional shear tests, which was used for modeling reclaimed soil deposits by dredging and pumping in practice. During cyclic undrained torsional shearing, the specimen deformation got localized easily around fine layers. Direct and indirect evaluation methods, based on image analysis, were proposed by Hoshino et al. (2015) with a transparent membrane in triaxial liquefaction tests. The local deformation properties of a dense Toyoura sand specimen evaluated by indirect observation were consistent with those evaluated by direct observations up to a double amplitude axial strain of 5%.

In view of the above, the aim of this study is to investigate local deformation characteristics of colored silica sand in triaxial liquefaction tests, particularly focusing on direct and indirect deformation evaluations under large axial strian, based on Particle image Velocimetry method.

Test Materials, Apparatus and Procedure

The experimental materials employed in the current research were two types of colored silica sand with white and black colors, respectively. These two colored sand had the same physical properties, with a mean particle size of 0.52 mm, a uniformity coefficient of 2.0, a gradation coefficient of 0.92 and a specific gravity of 2.65. The maximum and minimum void ratios were measured at 1.085 and 0.659, respectively. The grain size distribution curve was obtained under Japanese Geotechnical Society standards as shown in Fig. 1.

A triaxial apparatus presented in Fig. 2 was used in this research. The axial deformation was measured by external displacement transducer (EDT). Through measuring the water height difference in two burettes by low-capacity differential pressure transducer (LCDPT), the volume change of saturated specimen could be obtained. The effective stress was measured by a high-capacity differential pressure transducer (HCDPT) which was connected to the specimen and the triaxial cell. The deviator stress was obtained from a load cell fixed between top cap and loading rod. In front of the cell, two lights were arranged to increase the brightness of specimen surface. A digital camera was used to record the side view of specimen with a resolution of 4912*7360 pixels.

After mixing white-colored and black-colored sands at a mass ratio of 10 to 1, cylindrical specimens with 150 mm in height and 75 mm in diameter were prepared by moist tamping method. In order to achieve target relative density, specimen was prepared in five layers, and the weight of each layer was controlled equally to maintain the

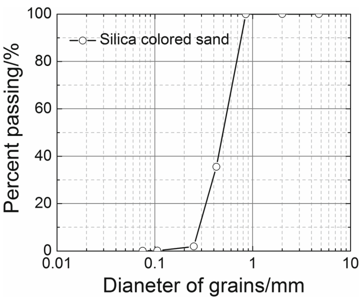

Fig. 1. Grain size distribution of colored-silica sand.

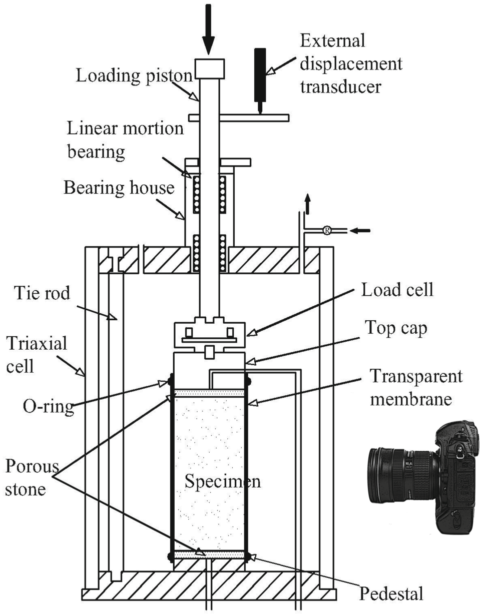

Fig. 2. Schematic diagram of triaxial apparatus with camera.

specimen homogeneity. In these tests, relative densities of specimens were kept in the range of 50% to 75%. After preparation, specimen was put in a fridge for 24 h freezing. After thawing, it was saturated by double vacuuming method to achieve a high B value which was more than 0.96. Then specimen was consolidated isotropically at an effective stress of 100 kPa. Undrained cyclic axial loading with a constant single amplitude deviator stress was applied. The single amplitude of deviator stresses were set as 60, 80 and 90 kPa to get the cyclic stress ratios of 0.3, 0.4 and 0.45 respectively. In all the tests, the axial strain rate was controlled to be 0.1% per minute.

Test Procedure of Image Analysis

In the current study, a transparent membrane made of silicone rubber was used for capturing the local deformations of membrane and sand particles, respectively. Black-colored latex dots were pasted on the membrane surface with an interval of 5 mm in both vertical and horizontal directions. Based on the resolution of digital image, one pixel described 0.025 mm. It meant that pixel and distance could be transformed to one another. In the analysis process, x axis was set horizontally at the bottom of specimen and y axis was vertical along the specimen. The coordinates of these black dots on membrane could be obtained to calculate the corresponding displacements on horizontal and vertical directions, which represented indirect evaluations of specimen deformations during loading. Similarly, the coordinates of distinct sand particles patterns also could be obtained by mixing white-colored and black-colored silica sands. The displacements of sand particles patterns were calculated to represent direct evaluations of specimen deformations. All the features of dots, sand patterns and the mixture effect of two colored sands were displayed in Fig. 3, which is an amplified zone of specimen.

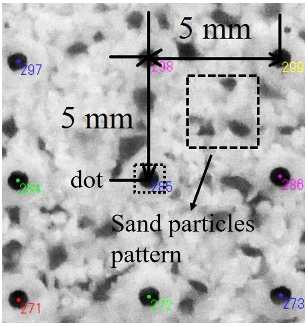

Fig. 3. An amplified zone of specimen surface with the details of sand particles patterns and dots.

Digital images were taken by a prescribed interval time of 10 s during undrained cyclic loading. The local strains from indirect evaluations on horizontal and vertical directions of each element, consisting of four dots in one grid, were calculated and analyzed to obtain indirect local strain distributions. Analogously, based on the four sand particles patterns in one grid, the local strains from direct evaluations could be obtained for the direct local strain distributions.

In order to compare the direct and indirect evaluations in a simplified manner, no geometric correction in terms of image distortion caused by cylindrical shape of specimen as well as the lens effect were applied in this study.

Based on the above descriptions of direct and indirect evaluations, the main steps of image analysis technique were summarized in Fig. 4. (1) During pre-processing stage, digital images were pretreated by graying and increasing proper contrast. Before selecting the origin of coordinate in the reference image, the scaling factor was decided by the ratio between real distance and pixel of reference points. In addition, the measurement points of dots and sand particles patterns were established in the reference image, respectively. (2) In the processing stage, the example of dot analysis, which was the same as sand particles pattern analysis, was introduced. The coordinates of each dot in every digital image were obtained. By using these coordinates, local displacements and strains in target digital image were computed by contrast to reference image. (3) During post-processing stage, local strain distributions, as well as the relative movement between sand particles pattern and adjacent dot, could be obtained.

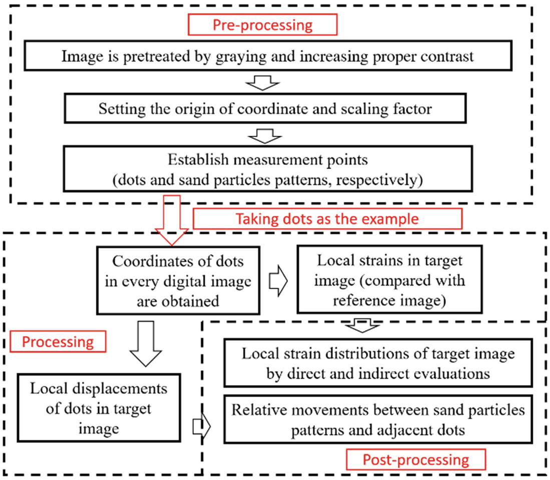

Fig. 4. Flow chart and structure of the image analysis technique.

Experimental Results and Discussion

One of the typical time histories of axial strain and excess pore water pressure ratio were shown in Fig. 5. One point, marked by red square in axial strain curve, was selected for the local strain analysis. Figure 6(a through d) gave local vertical and horizontal strain distributions by indirect and direct evaluations when global axial strain reached −4.3%. In Fig. 6a and b, red color scale meant local position was extended by the value of corresponding local strain. Similarly, yellow color scale meant local position was compressed by the corresponding local strain.

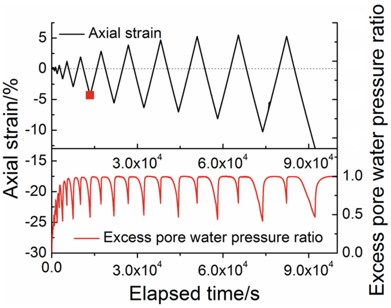

Fig. 5. Typical results of global axial strain and excess pore water pressure.

Compared with the original photo in Fig. 6e, strain localizations were shown visually and clearly by direct and indirect evaluations. The local strains of sand particles patterns from direct evaluations were consistent with those from indirect evaluations at a certain extent. However, some local parts such as specimen bottom and top exhibited different local strains. In order to compare these differences in detail, one position was chosen to reveal the time histories of vertical local strains and global axial strain as shown in Fig. 7. These curves indicated that local strains could follow the trend of global axial strain well, and the local strain from sand particles patterns had relatively larger values than the one from indirect evaluation by dots, especially at large axial strain condition.

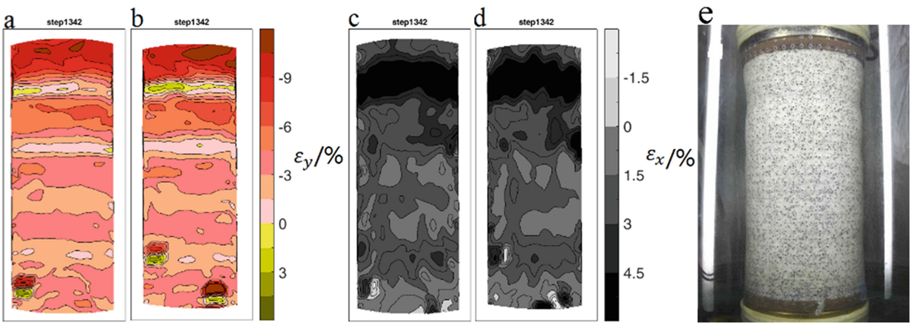

a) indirect vertical b)direct vertical c)indirect horizontal d)direct horizontal e)original photo

Fig. 6. Comparison of local strain distributions by moist tamping method and original photo at axial strain of −4.3%.

The local strain calculation method discussed above was based on the relative movements of four nodes of sand particles patterns or dots in a grid. The relative movements between sand particles patterns and dots at the same positions could not be recognized by local strains. In order to investigate these relative movements between sand particles patterns and adjacent dots, another new parameter was introduced and named as slippage, which could be calculated by the following equations.

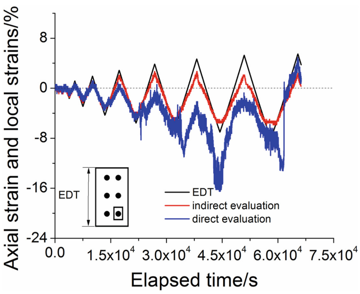

Fig. 7. Comparison of global axial strain and local strains at selected positions.

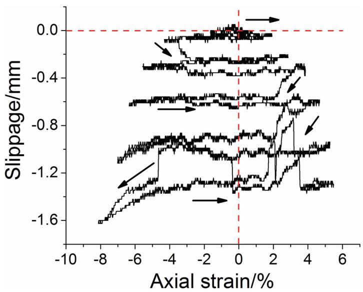

Fig. 8. Typical result of slippage with axial strain.

$$D_{dot,ydisp,i} = Y_{dot,original} - Y_{dot,i}$$

$$D_{sand,ydisp,i} = Y_{sand,original} - Y_{sand,i}$$

$$S_i = D_{dot,ydisp,i} - D_{sand,ydisp,i}$$

where i is the photo number during test. $D_{dot,ydisp,i}$ and $D_{sand,ydisp,i}$ are the displacements of dot and sand particles pattern on y direction at photo i; $Y_{dot,original}$ and $Y_{sand,original}$ are the original y coordinates of dot and sand particles pattern before loading; $Y_{dot,i}$ and $Y_{sand,i}$ are the y coordinates of dot and sand particles pattern at photo i. S_i is the slippage at photo i.

As for the local deformation, different from local strain showing the percentage of deformation, it could describe the actual displacement of each measurement point. Several local positions were selected randomly to describe the slippage between sand particles patterns and dots. Since the pedestal under the specimen was fixed and the top cap could slide upward and downward for unloading and loading, the vertical displacement of measured point near top part was larger than the one beneath it during loading. Therefore, at each local part, selected sand particles pattern was adjacent to the dot to avoid the effects from different positions. One typical result of slippage was shown in Fig. 8. The variation of slippage demonstrated that slippage was stable at small axial strain, and then some leaps of slippage occurred. However, slippage was accumulated in general.

In order to find the condition when slippage would occur during undrained cyclic loading, nine measurement points were selected at the top, middle and bottom parts of specimen. Relations between slippage and excess pore water pressure ratio during the whole cycles as indicated in Fig. 5 were shown in Fig. 9, based on this figure, the curves indicated that there was almost no slippage before excess pore water pressure

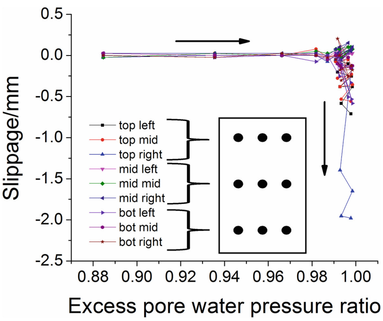

Fig. 9. Variation curves of slippage versus excess pore water pressure ratio at nine selected points.

ratio reached unity. Slippage would accumulate once excess pore water pressure ratio attained unity each time during cyclic loading, especially under large axial strain condition.

Conclusions

A series of undrained cyclic triaxial tests on two types of colored silica sand with white and black colors were conducted through a transparent membrane, to investigate the direct and indirect local deformations. In these tests, sand particle patterns and dots were analyzed by Particle image Velocimetry method without considering geometric corrections. The results could be summarized as follows:

(a) Image analysis could be used for measuring local deformations directly and indirectly with a high resolution of 0.025 mm/pixel. Additionally, local strains could be displayed visually and clearly by local strain distribution figures. Before liquefaction, the displacements of sand particles patterns and dots on membrane were almost same except some positions which were near the top cap and pedestal of specimen.

(b) Comparison of direct and indirect evaluations revealed that the space between dot and sand particles pattern, which were adjacent to each other, could not remain constant along cyclic loadings. Slippage had a significant leap when excess pore water pressure ratio reached unity especially under large axial strain condition.

References

Yoshida T, Tatsuoka F, Siddiquee MSA, Kamegai Y (1994) Shear banding in sands observed in plane strain compression. In: Localisation and bifurcation theory for soils and rocks, p 165–179

Harris WW, Viggiani G, Mooney MA, Finno RJ (1995) Use of stereophotogrammetry to analyze the development of shear bands in sand. Geotech Test J 18(4):405–420. doi:10.1520/GTJ11016J

Desrues J, Chambon R, Mokni M, Mazerolle F (1996) Void ratio evolution inside shear bands in triaxial sand specimens studied by computed tomography. Geotechnique 46(3):529–546. doi:10.1680/geot.1996.46.3.529

Rechenmacher AL (2003) Image based experimental soil mechanics. In: Proceeding of the 1st Japan-US workshop on testing, modelling and simulation, No. 156, pp 653–663

White DJ, Take WA, Bolton MD (2003) Soil deformation measurement using particle image velocimetry (PIV) and photogrammetry. Geotechnique 53(7):619–631. doi:10.1680/geot.53.7.619.37383

Mokni M, Desrues J (1998) Strain localization measurements in undrained plane strain biaxial tests on Hostun RF sand. Mech Cohesive Frictional Mater 4:419–441. doi:10.1002/(SICI)1099-1484(199907)4:4<419:AID-CFM70>3.0.CO;2-1

Sadrekarimi A, Olson SM (2010) Shear band formation observed in ring shear tests on sandy soils. J Geotech Geoenvironmental Eng 136(2):366–375. doi:10.1061/(ASCE)GT.1943-5606.0000220

Kiyota T, Sato T, Koseki J, Abadimarand M (2008) Behavior of liquefied sands under extremely large strain levels in cyclic torsional shear tests. Soils Found 48(5):727–739 http://doi.org/10.3208/sandf.48.727

Chiaro G, Kiyota T, Koseki J (2013) Strain localization characteristics of loose saturated Toyoura sand in undrained cyclic torsional shear tests with initial static shear. Soils Found 53(1):23–34. doi:10.1016/j.sandf.2012.07.016

Fauzi UJ, Koseki J (2014) Local deformation properties of segregated sand specimen in hollow cylindrical torsional shear tests. Bulletin of ERS, No. 47:27–36

Hoshino R, Miyashita Y, Sato T, Koseki J (2015) Local deformation properties of sand specimen in triaxial liquefaction tests evaluated by direct and indirect observations. Bulletin of ERS, No. 48:63–71

A New Laboratory Setup for Phase Equilibria Studies of Methane Hydrate in Porous Media

Brice Y. Kim(✉) and I. Yucel Akkutlu

Harold Vance Department of Petroleum Engineering,
Texas A&M University, College Station, USA
bricekim@tamu.edu

Abstract. Naturally-occurring hydrates are promising energy resource with abundant reserves that easily surpass the other resources all combined. Much work has been done in predicting the properties of gas hydrates. This is especially true for laboratory formed pure gas hydrates. But many physical properties of hydrates in reservoir are not completely understood yet. In effort to research the hydrate behavior in the subsurface conditions, a new laboratory technique is developed to effectively measure the formation and dissociation of the hydrates in pore space. This newly-developed method has other advantages, when compared with the conventional setup. Details of the experimental design and measurement procedure will be discussed. This chapter will also present the findings of the conducted experimental studies and test results on methane hydrate to illustrate the new technique's usefulness. It was found that the solution in the pore space retains a memory-effect when metane hydrate is melt at moderate temperatures. This can be eliminated only when the system is heated to sufficiently high temperature.

Introduction

Naturally-occurring hydrates are one of the most promising natural resources for the coming age. The potential value of gas accumulation in naturally-occurring gas hydrates can exceed 16 equivalent trillion tons of oil. Near 97% of these reserves are located offshore, mainly in continental shelf-oceanic slope transition zones, only 3% on land. (Makogon 2010).

The first documented laboratory-formed gas hydrate takes back as early as 1778 by Joseph Priestley. The more active research of gas hydrates started in 1934, when Hammerschmidt inspected and published a report concerning solid plugs that formed in pipelines during the winter time. This urgency led to rapid growth in research interests on gas hydrates. The scientific discovery of naturally-occurring gas hydrates was recorded in 1969 by Makogon for the Markhinskaya well in the north-western part of Yakutia. (Priestley 1778), (Hammerschmidt 1934), and (Makogon 1965).

Four conditions must be present in order for gas hydrate to form. (1) There must be hydrate forming gas, free or dissolved, (2) there also must be water (3) water and gas must be under hydrate stable pressure (4) and the environment must provide sufficient heat transfer. Under these conditions, a solid clathrate compound is formed and entrap significant amounts of gas. (Makogon 2010).

A. Ferrari and L. Laloui (eds.), *Advances in Laboratory Testing and Modelling of Soils and Shales (ATMSS)*, Springer Series in Geomechanics and Geoengineering,
DOI 10.1007/978-3-319-52773-4_25

There are many accurate findings on properties of gas hydrates. This is especially true for laboratory-formed gas hydrates, but many of definite physical properties, such as strength of the hydrogen bonds and the physical phenomena that lead to entrapment of the guest molecules, are not completely understood. More importantly, in terms of natural gas production point of view, the conditions of formation as well as stable existence of naturally occurring gas hydrate deposits are still unknown.

This research mainly focused on understanding phase equilibria of methane hydrate in both free water-gas contact and in pore-space. Many researchers have previously studied the formation and dissociation characteristics of hydrates. (Kobayashi and Katz 1949), (Makogon 1974, 1997), (Sloan et al. 1976), and Sloan and Koh (2008). However there has been limited research dedicated to the so-called memory effect phenomenon of gas hydrate re-formation. The general consensus among the hydrate researchers suggests that hydrates retain a form of structural memory when they dissociate at moderate temperatures. This phenomenon allows the previously hydrate-formed liquid to form hydrate again but with much less energy than that of the prior formation when the environment is brought to hydrate stable condition. There are still conflicting arguments regarding this curious effect. Some argue that it is due to residual structure, whereas some others argue that it is due to dissolved gas remaining in the solution, (Makogon 1974), (Chen 1980), (Rodger 2000) and (Sloan and Koh 2008). Further investigation is needed to understand this effect in the pore space and under typical subsurface conditions. The experimental overview and the results of hydrates in pore-space shall be discussed in this paper.

Phase Equilibria in Pore-Space

The phase equilibria studies in pore-space was conducted using the custom fabricated high-pressure stainless steel cylinder as shown in Fig. 1. To accommodate thermocouples and a pressure transducer, a copper plug was also designed and machined as shown in Fig. 2. The idea was to create an experimental chamber that can closely match the reservoir environment. Some research groups incorporated conventional Hassler type of core holders (Kneafsey et al. 2007). However, Hassler core holders are intended for permeability measurements, with limited porous medium bulk volumes. Our experimental approach, on the other hand, is devised to accommodate sufficient volumes of tightly packed sands for the hydrate formation.

Preparation

As shown in the dissected diagram along with the dimensions and the sizes of the parts in Fig. 3, the cylinder was divided into two main sections. Section A, pore-space, and Section B, empty-space filled with liquid. The apparatus consisted of three thermocouples in Section A. Measurement points and locations are circled in Fig. 3. One transducer was placed to measure the pore pressure P_1 in Section A and another transducer to measure pressure P_2 in Section B. Methane was supplied to pore-space.

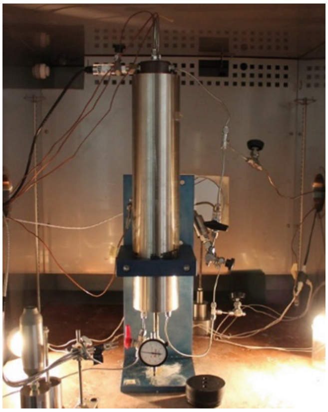

Fig. 1. Apparatus for methane hydrate stability study in pore-space.

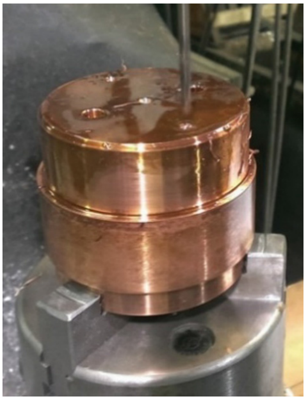

Fig. 2. Machined Copper cylinder plug to accommodate three thermocouples, one transducer, and two ports for gas injection and removal during the methane hydrate stability study in pore-space.

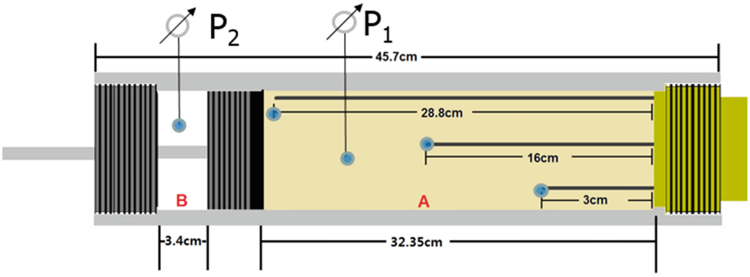

Fig. 3. Dissected diagram of the stainless steel cylinder.

A simple schematics for the experiment is shown in Fig. 4. Quartz sands were used for the experiment. The sieve analysis of the sand used is shown in Fig. 5.

Experimental sands were packed into the cylinder in Section A. For the experiment, 1,200 cm^3 of sands with 36.2% porosity, determined by the water saturation method, was saturated 50% with filtered water. Methane gas was then injected and flushed twice around 100 bar (about 18,500 scm^3 of methane injected in 217.2 cm^3 pore-space) to remove air inside of the cylinder. After flushing the pore-volume, the cylinder was pressurized with methane to 103 bar in the Section A. The final methane injection resulted 50% water saturation and 50% gas saturation in the pore-volume in section A. Then the sands in cylinder was confined by pumping the water into Section B up to 300 bar using the water pump until the piston separating the two sections stopped being displaced.

The experiments were conducted by first pressurizing the cylinder with water saturated sands to 103 bar at a room temperature, then the temperature-controlled

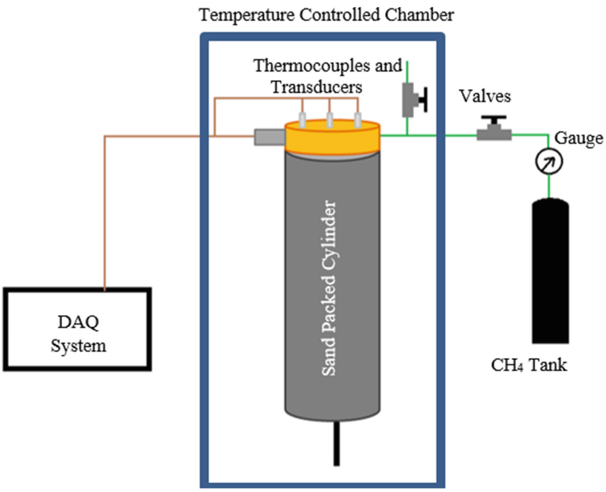

Fig. 4. Simple schematic for the methane hydrate formation in pore-space experiment.

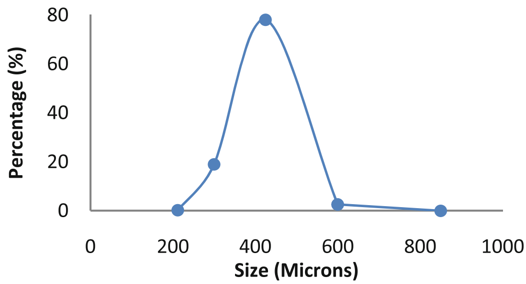

Fig. 5. Sieve analysis of beads sands (quartz) that was used for the experiment.

chamber was cooled to 1 °C, a hydrate forming temperature without triggering the ice formation. Then the system was kept in 1 °C for at least 12 h to observe the onset of hydrate formation, characterized by the exothermic reaction leading to localized temperature increase on the thermocouple. Once the hydrate formation stopped, the system was heated to a non-hydrate forming temperature to melt the hydrates in the system. Subsequent experiments and the results have been conducted by only changing the temperature; no depressurization was done.

Results

Figure 6 shows the course of the experiment by plotting the recorded pressure against the recorded temperature from the initial condition to the final condition of the experiment. The stainless steel cylinder was initially pressurized at a room temperature of 25.3 °C at 103.54 bar (Point A in Fig. 6). Then the system was cooled to 1 °C (Point B in Fig. 6) to trigger hydrate formation and kept for at least 12 h (Point C in Fig. 6). Then the system was heated to hydrate dissociation condition of 17 °C, 25 °C, 35 °C and 40 °C for another minimum of 12 h (Point D in Fig. 6). Then the procedures were repeated to determine initial hydrate forming temperature.

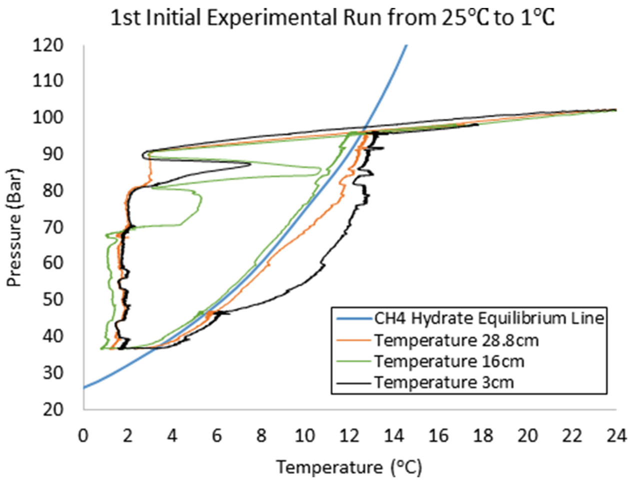

Fig. 6. Initial experimental result of the hydrate formation study in pore-space with three different lines representing the data collected from three different locations.

The theoretical methane hydrate stability line (Makogon 1997) is shown in blue to observe how the experimental results compare with the theoretical stability line. From the initial experiment, the first hydrate formation occurred at point B at 2.84 °C, more than a 9.16 °C sub-cooling. As shown in the Fig. 6, there is an evident temperature jump in the system due to the exothermic process of hydrate formation releasing the heat at point B.

The system at point C is then heated to 17 °C, point D, and kept for at least 12 h to ensure that all hydrates have been melted. In Fig. 7, it is shown that during the dissociation process, the thermocouple located in 16 cm, or about halfway from the one end of the cylinder, closely follows the theoretical methane hydrate curve when compared with thermocouples located in 28.8 cm and 3 cm. This is an indication that the most hydrates are concentrated in the center of the cylinder.

After keeping the system at 17 °C for sufficient time at point D, the experimental system was cooled to 1 °C, Point F, again to initiate hydrate formation. In Fig. 7, it is shown that the very first onset of hydrate formation for this experiment occurred at 8.71 °C, point E. This 3.29 °C sub-cooling is much less than the 9.16 °C sub-cooling of initial hydrate formation observed in Fig. 6. This 5.87 °C difference could be the evidence that the structural memory of water is present in the system. After keeping the system to 1 °C for more than 12 h, the system pressure and temperature reaches point G to completely form hydrates.

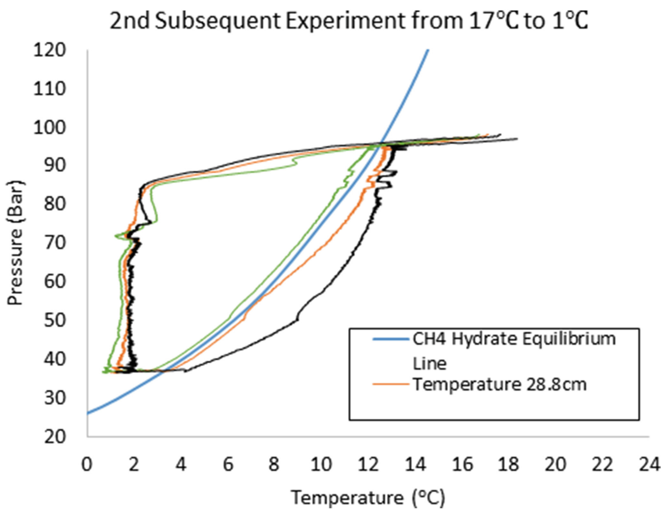

Fig. 7. Result of the 2nd subsequent experiment by melting system to 17 °C.

The setup was then heated to near room temperature of 25 °C and then cooled again which led to lower sub-cooling and hydrate formation temperature of 8.32 °C this is comparable to hydrate formation temperature when the system was cooled from 17 °C. Repeating the process and heating the system to 35 °C did not significantly alter the subsequent hydrate formation temperature, which led to hydrate formation at 8.49 °C. Thus indicating that the hydrate seeds are still present in the system even when the system was heated to 35 °C. It was only after heating the system to 40 °C, Point H in Fig. 8, that the apparent structural memory of water was completely disappeared, Point I.

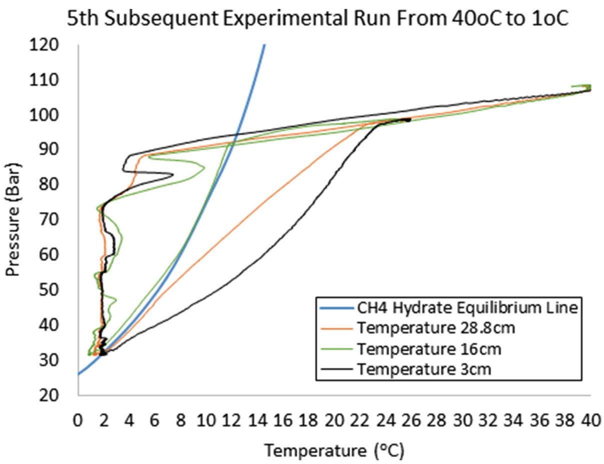

Fig. 8. Result of the 5th subsequent experiment by melting system to 40 °C.

The experimental data suggest that the system was reverted back to the initial condition when the system was heated to 40 °C as shown in Fig. 8. The onset of hydrate formation occurred at the temperature of 3.4 °C, Point I. This value is very similar to initial hydrate forming temperature of 2.84 °C, Point B in Fig. 6. Thus this experiment suggests that heating the hydrate system to 40 °C destroyed hydrate seeds in the system, hence, the system no longer exhibits a memory-effect within the liquid. The experimental results are summarized in Table 1.

Table 1. Summarized Experimental Results.

	Experiment initial temperature	Hydrate formation temperature	Sub-cooling temperature
Initial formation	25 °C	2.84 °C	9.16 °C
2nd subsequent	17 °C	8.71 °C	3.29 °C
3rd subsequent	25 °C	8.32 °C	3.68 °C
4th subsequent	35 °C	8.49 °C	3.51 °C
5th subsequent	40 °C	3.40 °C	8.60 °C

Discussions

In the previous works, not presented in this paper, the authors have conducted several preliminary experiments with just water and source gas in visual window cell to visually observe the formation and dissociation of hydrates in presence of memory effects. This paper was presented with intention of presenting the findings of the memory effect in pore-space with newly devised experimental setup. Through this setup it was determined that

1. When methane hydrates are melt at moderate temperature, the solution retains a structural memory-effect even in pore-space.
2. The system with previous hydrate history will lose its memory if the system is heated sufficiently to 40 °C. This shall be useful for flow assurance problems associated with hydrate plugs.
3. The hydrogen bond strength is dependent on the temperature, thus higher temperature effectively destroys more hydrate cages in the system.

Acknowledgment

The laboratory work presented in this chapter has been performed at Texas A&M University, Petroleum Engineering Department, Yuri F. Makogon Hydrate Laboratory. The authors thank Dr. Makogon for his support in designing the apparatus and for fruitful discussions on the structural memory.

References

Chen TS (1980) A Molecular Dynamics Study of the Stability of Small Pre-nucleation Water Clusters, Dissertation, U. Missouri-Rolla, University Microfilms No. 8108116, Ann Arbor, MI

Hammerschmidt EG (1934) Formation of gas hydrates in natural gas transmission lines. Ind Eng Chem 26:851–855

Kneafsey TJ, Tomutsa L, Moridis GJ, Seol Y, Freifeld BM, Taylor CE, Gupta A (2007) Methane hydrate formation and dissociation in a partially saturated core-scale sand sample. J Petrol Sci Eng 56:108–126

Kobayashi R, Katz DL (1949) J Petrol Technol 1: 66

Makogon YF (1965) A gas hydrate formation in the gas saturated layers under low temperature. Gas Indus. 5:14–15

Makogan YF (1974) Hydrates of Natural Gas, Moscow, Nedra, Izadatelstro. PennWell Books, Tulsa, 237 p. in Russian (1981) (in English)

Makogon YF (1997) Hydrates of Hydrocarbons. Penn Well, Tulsa, pp 10–16

Makogon YF (2010) Natural gas hydrates-A promising source of energy. J Natural Gas Sci Eng 2:49–59

Priestley J (1778–1780) Versuche und Beobachtungen Uber Verrshiedene Gattungen der Luft, Th. 1–3, 3:359–362. Wien-Leipzig

Rodger M (2000) Proc. gas hydrates: challenges for the future (Holder, G.D., Bishnoi, P.R., eds). Ann NY Acad Sci, vol 912, p 474

Sloan ED, Khoury FM, Kobayashi R (1976) Ind Eng Chem Fund 15:318

Sloan ED, Koh CA (2008) Clathrate hydrates of natural gases, 3rd edn., 721 pp. CRC Press, Boca Raton

An Experimental Platform for Measuring Soil Water Characteristic Curve Under Transient Flow Conditions

Guanxi Yan[1(✉)], Zi Li[1], Thierry Bore[1], Sergio Galindo-Torres[1], Stefan Schlaeger[2], Alexander Scheuermann[1], and Ling Li[1]

[1] School of Civil Engineering, Geotechnical Engineering Centre, University of Queensland, Brisbane, Australia
g.yan@uq.edu.au
[2] Science – Engineering – Measurement, Sceme.de, Horn-Bad Meinber, Germany

Abstract. Soil Water Characteristic Curve (SWCC) is the core of unsaturated soil mechanics. The accuracy of modeling unsaturated soil seepage and consolidation behavior are highly governed by SWCC. The conventional testing methods only measured two state variables under the equilibrium condition. Those investigations were usually conducted on a Representative Elementary Volume (REV) scale less than the full length of suction/moisture profile of sandy soil. To further investigate both point-wise and the global SWCC measurement under transient flow condition, a dynamic SWCC testing platform is set up in The University of Queensland. This experimental platform integrates Spatial Time Domain Reflectometry (Spatial TDR) technique, tensiometers and outflow logging by electrical bench scales, so that the consistent logging of moisture profile, suction profile and in/outflow can be achieved. In this study, the experimental platform is briefly presented with some preliminary outcomes and the potential problems of setup are discussed.

Introduction

Soil Water Retention Curve (SWRC) is the core constitutive relationship bridging the hydro-mechanical behavior of unsaturated soil. For currently standardized test of unsaturated soil mechanics, the unsaturated soil hydraulic properties are usually characterized on a one-dimensional REV-sized specimen using Axis Translation Technique (ATT) (Fredlund et al. 1993, Lu et al. 2004). However, this technique only provides the SWRC under equilibrium or quasi-steady state condition (Topp et al. 1967, Hassanizadeh et al. 2002), which could be far off the natural transient flow conditions, such as intensive rainfall infiltration and the fast rising groundwater table (Scheuermann et al. 2007). Under such conditions, the conventional testing method might not be sufficient in accuracy.

With an aim to quantify dynamic response, a dynamic SWRC testing platform is recently set up in The University of Queensland. To characterize the moisture and suction profile under transient conditions, the Spatial Time Domain Reflectometry

A. Ferrari and L. Laloui (eds.), *Advances in Laboratory Testing and Modelling of Soils and Shales (ATMSS)*, Springer Series in Geomechanics and Geoengineering,
DOI 10.1007/978-3-319-52773-4_26

(STDR) technique (Schlaeger 2002, Scheuermann et al. 2009) and tensiometers (Klute et al. 1962) are separately applied on logging moisture and suction profile by time step. The experiment will be executed in various transient pressure boundary conditions such as one-step or multi-step in/outflow. The experimental data will contribute to the investigation of dynamic effect in SWRC for a transient multiphase flow in porous media. As the first stage, the data of gravitational drainage of sand is presented with a discussion of limitations.

Experimental Methodology

The experimental platform for measuring SWCC under both transient and equilibrium conditions mainly consists of three automatically logging systems, which are applied on a soil column up to 2.4 m. The experimental setup refers to the literature (Yan 2015, Yan et al. 2016) in details with the validation of data logging systems. Two types of soil (sand and loam) are being tested on drying and wetting paths using this experimental setup as shown in Fig. 1. A concise summary of essential techniques applied on this experiment and corresponding configuration are given in this section.

Fig. 1. Experimental setup of dynamic SWRC (Drainage for Saturated Loam, Imbibition in Dry Sand, Imbibition in Dry Loam and Drainage in Saturated Sand from left to right).

Soil Column Configuration

There are four soil columns set up in Geotechnical Engineering Centre, The University of Queensland. Currently, two type of soil is being tested. One is medium sand collected from Bribe Island, Queensland, Australia, while the other is loam sourced from a construction site nearby Brisbane. Specification of two soil and corresponding packing condition are summarised int Table 1.

Table 1. Specification of two soil and packing condition in columns.

Soil type	Sand	Loam
D_{50} (mm)	0.34	0.27
Specific gravity	2.655	2.655
ρ_{dry} (g/cm3)	1.61	1.43
Mean Porosity	39% ± 2%	45% ± 4%

Moisture Profile Measurement

The moisture profile is measured using Spatial Time Domain Reflectometry (Spatial TDR) technique (Huebner et al. 2005, Scheuermann et al. 2009). The details of sensor development and validation can be sourced from Scheuermann et al. (2009). In principle, this technique is made up of four stages: (1) the electrical sensor design on the capacitance model of three-wire TDR transmission line (Huebner et al. 2005); (2) the assumptions on constant inductance (L) and resistance (R) in TDR's frequency domain, which cannot be applied to high-salinity or clay-rich geomaterial (Scheuermann et al. 2009); (3) the calibration of electrical and dielectric parameters (Scheuermann et al. 2009), and (4) the final core step-mathematical reconstruction of capacitance (C) and conductance (G) profile using inversion analysis of TDR waveform (Schlaeger 2002). In brief introduction, the TDR device sends the pulse into the electromagnetic waveguide (the sensor) and later receive the TDR waveform; the inverse analysis script developed by Schlaeger (2002) forward modelling telegraph equation to generate a TDR waveform; the optimisation is conducted between measurement and simulation result until the best fitting achieved; finally the input of conductance and capacitance for forward modelling can be extracted from the best fitting performance and later applied into the dielectric model in order to determine the permittivity profile along soil column. The moisture profile, therefore, can be given by a soil specific moisture-permittivity calibration (Rota et al. 1990) or robust empirical model (Topp et al. 1980).

The sensor and logging system are shown in Fig. 2(a) and (b). The Spatial TDR waveform is logged using the Campbell Scientific CR1000 data logger© chained with TDR100© and SDM X50 multiplexer©. Two-way Spatial TDR sensor was manufactured around 2 m long. The logging time interval is one minute.

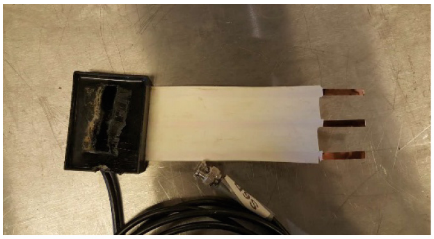

(a)

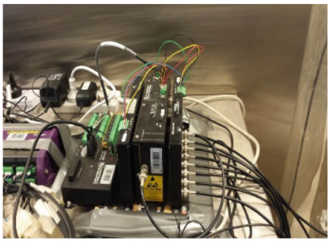

(b)

Fig. 2. (a) Spatial TDR flat ribbon sensor (b) TDR waveform logging system.

Suction Profile Measurement

In this experiment, the commercial tensiometer (T5 UMS©) is selected to measure the suction of sand and loam column at six different elevations of −16, 20, 40, 80, 120, 160 cm as shown in Fig. 3(a). Tensiometers are connected to a commercial datalogger (DT85G, Pacific Data© shown in Fig. 3(b)) to collect dynamic response of water pressure. The minimum time step can be 10 s. The calibration between water pressure and voltage sent to the logger are predetermined before test along positive pressure range as a linear equation (shown in Fig. 3(c)). The measuring range is from 100 kPa to −85 kPa with a precision of ±0.5 kPa.

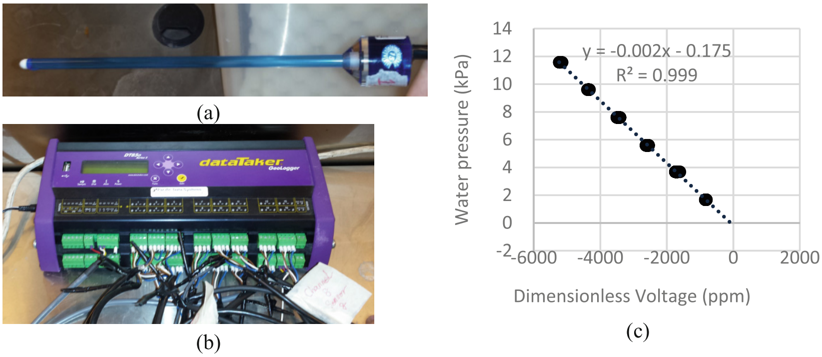

Fig. 3. (a) T5 tensiometer (b) DT85 Datalogger (c) The calibration between pressure and voltage.

Accumulative In/Outflow Measurement

The accumulative in/outflow measurement is shown in the lower part of Fig. 1(a). A constant head tank is attached to the bottom of each column to supply a 36 ± 1 cm total water head as pressure boundary condition. In front of each constant head tank, there is another set of tanks supplying the water into the constant head tank using the water pumps. Those tanks are individually located on each scale so that the increasing/decreasing mass of water can be directly logged by each scales within a time step of 30 s. The circulation of water between two tanks causes gravitational variation on scales less than 1 g. Another water tank with the same condition is set up nearby to calibrate the water loss by evaporation.

Result and Discussion

Validation of Experimental Platform

The validation of TDR logging system and measuring value given by sensor are shown in Figs. 4 and 5. The Fig. 4(a) and (b) illustrates the dynamics of TDR traces separately sent from bottom and top of the column, which prove the success of TDR logging system. The reduction of travel time between two inflection points successfully demonstrates the mean moisture decreasing in the soil column. Figure 4(c) shows the soil specific empirical relationship between permittivity and volumetric water content in comparison with the Topp's model which overestimate the mean moisture content.

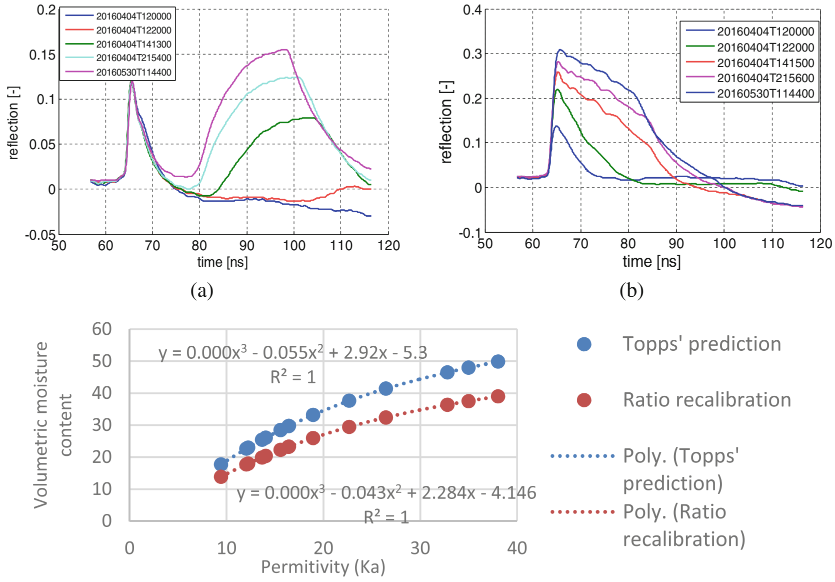

(a) (b) (c)

Fig. 4. (a) Spatial TDR traces sent from column bottom (b) Spatial TDR traces sent from column top (c) soil specific recalibration between moisture and apparent permittivity.

Figure 5(a) shows the comparison between soil suction measurement and theoretical suction. The suction measured by T5 tensiometer can exactly match hydrostatic pressure. The Fig. 5(b) shows the outflow logging. Based on this data, the mean volumetric water content dynamics are calculated in comparison to the moisture content measured by TDR sensor in Fig. 5(b). The agreement of moisture by two methods further proves the accuracy of the recalibration.

Preliminary result and reflection of setup problems

As the transient responses shown in both Fig. 6(a) and (b), the most significant reduction of both moisture and suction happened in the first few hours. However, in the following month, there was still a gradually decreasing of moisture and suction. This phenomenon indicates that under such a fast drainage process, some smaller capillary conduits might still hold more moisture which later results in this slow drainage in vadose zone. The final stage of SWCC is given in Fig. 6(c). The Air Entry Value is not precisely determined due to the moisture resolution of Spatial TDR technique (±3%).

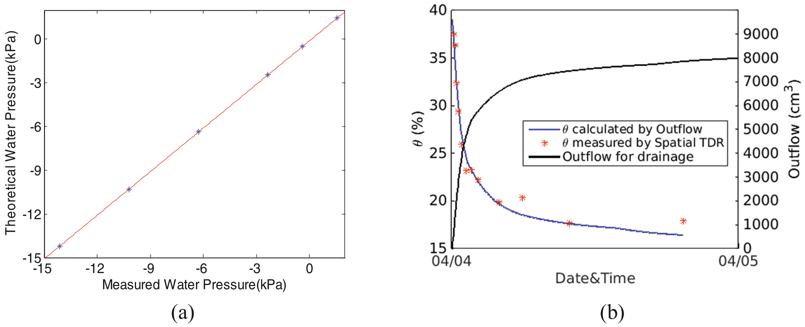

Fig. 5. (a) Theoretical water pressure vs water pressure measured by tensiometer (b) Outflow with a comparison between moisture measured by TDR and moisture calculated from outflow data.

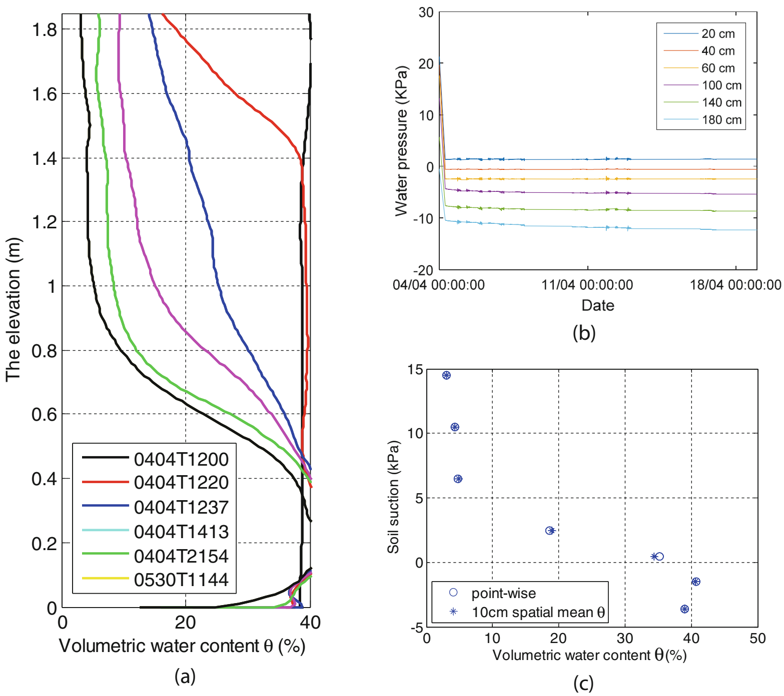

Fig. 6. (a) The moisture profile changed with time (b) water pressure response varying with time (c) the SWCC in final equilibrium (two months later).

Therefore, the accuracy of this platform is constrained by the resolution of moisture profile measurement.

This experimental platform so far has few limitations. First, the inverse analysis needs further improvement to enhance the precision of moisture profile. Second, for the imbibition test, tensiometers can easily lose hydraulic conductivity between dry soil and electrical sensor body. Once the air penetrating through the ceramic tip, the replacement is needed. Third, the tensiometer only works on lower suction range from −85 kPa to 0. Also, the Spatial TDR technique cannot work in the soil having high electrical conductivity. Therefore, this platform might be only suitable to investigate the dynamic effects in sand or silty sand.

Concluding Mark

The prediction of unsaturated soil mechanics and hydraulics is highly determined by Soil Water Characteristic Curve (SWCC). The conventional method only conducts the measurement on a REV-scale specimen under static condition. Applying a static measurement to modelling transient seepage is still debatable. This experimental platform provides a chance to investigate the moisture/suction profile dynamics. Some preliminary outcomes have validated the logging system. By improving the inversion analysis of TDR technique, this experiment will contribute to a better understanding of transient flow in unsaturated soil.

Acknowledgements. This work was funded by the Linkage Project (LP120100662), Multi-scale two-phase flow in complex coal seam systems, funded by the Australian Research Council and supported by a Queensland Science Fellowship awarded to A. Scheuermann.

References

Fredlund DG, Rahardjo H (1993) Soil mechanics for unsaturated soils, Wiley, New York

Hassanizadeh SM, Celia MA, Dahle HK (2002) Dynamic effect in the capillary pressure–saturation relationship and its impacts on unsaturated flow. Vadose Zone J 1(1):38–57

Huebner C, Schlaeger S, Becker R, Scheuermann A, Brandelik A, Schaedel W, Schuhmann R (2005) Advanced measurement methods in time domain reflectometry for soil moisture determination. In: Kupfer K (ed) Electromagnetic Aquametry. Springer, Heidelberg, pp 317–347

Klute A, Gardner W (1962) Tensiometer response time. Soil Sci 93(3):204–207

Lu N, Likos WJ (2004) Unsaturated soil mechanics. Wiley, New York

Rota K, Schulin R, Fluhler H, Attinger W (1990) Using a Composite Dielectric Approach. Water Resour Res 26(10):2267–2273

Scheuermann A, Bieberstein A (2007) Determination of the soil water retention curve and the unsaturated hydraulic conductivity from the particle size distribution. In: Schanz T (ed) Experimental unsaturated soil mechanics, vol 112, Springer Proceedings in Physics. Springer, Heidelberg, pp 421–423

Scheuermann A, Huebner C, Schlaeger S, Wagner N, Becker R, Bieberstein A (2009) Spatial time domain reflectometry and its application for the measurement of water content distributions along flat ribbon cables in a full-scale levee model. Water Resour Res 45(4)

Schlaeger S (2002) Inversion von TDR-Messungen zur Rekonstruktion räumlich verteilter bodenphysikalischer Parameter, Inst. für Bodenmechanik und Felsmechanik

Topp G, Davis J, Annan AP (1980) Electromagnetic determination of soil water content: measurements in coaxial transmission lines. Water Resour Res 16(3):574–582

Topp G, Klute A, Peters D (1967) Comparison of water content-pressure head data obtained by equilibrium, steady-state, and unsteady-state methods. Soil Sci Soc America J 31(3):312–314

Yan G (2015) Dynamic multiphase flow in granular porous media. The University of Queensland, Faculty of Engineering, Architecture and Information and Technology (EAIT)

Yan G, Scheuermann A, Schlaeger S, Bore T, Zi L, Ling L (2016) Application of spatial time domain reflectometry for investigating moisture content dynamics in unsaturated loam for gravitational drainage (prepared). J Measur Sci Technol, The University of Queensland

Determining Fluid Compressibility and Soil Permeability of Quasi Saturated Sand with the Alternating Flow Apparatus

Jeanne Ewers(✉) and Fabian Karl

Federal Waterways Engineering and Research Institute (BAW), Karlsruhe, Germany
jeanne.ewers@baw.de

Abstract. Predicting pore water pressures due to wave induced pressure fluctuations on quasi saturated porous beds is important e.g. for the design of bank protections in channels. Therefore, the influence of fluid compressibility and the coefficient of permeability both depending on the degree of saturation were analyzed by means of laboratory testing with the alternating flow apparatus of the Federal Waterways Engineering and Research Institute. A methodology for the determination of the saturation dependent parameters based on high precision pressure and discharge measurements is presented. As shown in the present paper, test results and finite element simulations based on the determined parameters coincide very well.

Introduction

Banks and bottoms of waterways are exposed to ship-induced waves that can cause failure mechanisms if excess pore pressures occur due to the presence of gas in the soil. Beside the hydraulic boundary conditions, the process is depending in particular on the compressibility of the fluid, meaning the water-gas-mixture, and the soil permeability. A test series was carried out on fine sand samples with the alternating flow apparatus, allowing for the application of variable pressure and flow boundary conditions. By means of high precision pressure and flow measurements, a determination of the compressibility of the water-gas-mixture and the saturation dependent permeability of the sand sample is possible.

The facility and the main results, including the conceptual analysis of a test series are shown. Here, in particular the effect of absolute pressure changes on the degree of saturation and the permeability coefficient is analyzed. Coupled numerical finite element simulations are shown to be in good agreement with the test data.

Conceptual Model of Quasi-Saturated Sands

An unsaturated soil is constituted of the solid skeleton, the free gas, the pore water, as well as the dissolved gas, which is part of the water volume and has a significant influence on the water compressibility (Fredlund 1976). Following Pietruszczak and

A. Ferrari and L. Laloui (eds.), *Advances in Laboratory Testing and Modelling of Soils and Shales (ATMSS)*, Springer Series in Geomechanics and Geoengineering,
DOI 10.1007/978-3-319-52773-4_27

Pande (1996), it is assumed that the different phases are equally distributed in the control volume, that the water phase is continuous and the gas phase embedded in the liquid phase in the form of small gas bubbles. The degree of saturation S – defined as water volume per void volume – of quasi-saturated soil is ranging between about 85% and 100% (Tarantino 2013).

The constitutive behavior of quasi-saturated soil depends both on the constitutive relation of the soil matrix and on the deformation relation of the water-gas-mixture linked by the concept of effective stress. The coefficient *B* (Skempton 1954) describes the change of pore pressure and effective stress under a change in total stress for undrained conditions, thus quantifying the interactions.

After Fredlund (1976), the compressibility of the water-gas-mixture β_m is defined as the compressibility of the gas phase following Boyle's law, the compressibility of the water phase with $\beta_w = 4.81 \cdot 10^{-7} \mathrm{m/kN}$ and the increased compressibility of the water phase due to the solution of gas in water following Henry's law with Henry's constant h assumed 0.02 for air. The compressibility of the mixture can then be written as

$$\beta_m = S\beta_w + \frac{1 - S}{p} + \frac{S \cdot h}{p} \tag{1}$$

In this formulation, neither surface tension between gas bubbles and water is applied nor are suction effects accounted for.

After the Kozeny-Carman equation the permeability coefficient *k* can be written as a function of porosity n (cf. Chapuis and Aubertin 2003). Accounting for the reduced effective porosity caused by the embedded gas bubbles in quasi-saturated soils and defined as the volumetric water content $S \cdot n$, following proportionality states the saturation-dependent coefficient of permeability:

$$k \propto \frac{(S \cdot n)^3}{(1 - S \cdot n)^2} \tag{2}$$

The Alternating Flow Apparatus

The alternating flow apparatus (see Fig. 1) is operated and developed by the Federal Waterways Engineering and Research Institute (BAW). The apparatus allows for the application of controlled static and dynamic pressure and flow conditions on soil samples. Essentially, the apparatus consists of two expansion tanks, a piping system, which connects the pressure tanks with the test cell, and a pressure control facility, which allows inducing different pressures and pressure regimes inside the tanks. The pressures are built up by use of compressed air. To avoid air entrainment, each expansion tank is equipped with a diaphragm separating water and air.

In order to vent the system of water pipes, the apparatus is fitted with automatic air bleed valves. These valves are mounted at the highest points of the apparatus. Thus, free air bubbles rising up to the highest point escape mechanically into the surrounding environment by means of a floater.

Fig. 1. Alternating flow apparatus and test cell with sand sample.

The alternating flow apparatus covers a pressure range of 2 to 90 mH2O. Pressure fluctuations up to 5 mH2O/S can be reached. To protect the employed test cell, the pressure range has been reduced to 2 to 50 mH2O for the presented test series.

The complex control process is carried out on a computer. The control algorithm contains a detailed model of the whole facility, describing compressible gas flow, thermodynamic changes due to compression and expansion of the air, flow resistance of the pipes, mass inertia of the water, hysteresis behaviour of the mechanical pressure regulators and others. On the basis of this model, the behaviour of the apparatus is predicted on-line. Thus, a very accurate control is achieved and even dynamic needs are met with high accuracy.

Due to its decentralized modular structure, the applied measuring system provides almost interference-free signals owing to the digitization nearby the sensor. The Setup permits simultaneously sampled signals with a sampling rate of 10 kHz, averaged to 100 values per second. The digitalized signals have a resolution of 24 bit.

The specially developed control software offers the possibility to stimulate the sample with diverse standard pressure and flow curve shapes, e.g. sinusoids, trapezia, constants and variable time series.

The test cell has been developed by the Leichtweiß Institute for Hydraulic Engineering and Water Resources at the Technical University of Braunschweig in cooperation with and modified by BAW. The development took place in the context of the "KOFIMARS" research project of the German Research Foundation (DFG OU 1/1661), see further application of the apparatus in Schürenkamp et al. (2015). The test cell essentially consists of an acrylic glass cylinder, equipped with 12 absolute pressure transmitters. These are mounted on nine different levels at a distance of 10 cm each, measuring pressure conditions within and above the sample. The cylinder has an inner diameter of 32.8 cm and is 1 m high. A controllable surface load can be applied by pneumatic cylinders with a pressure plate.

In the normal configuration the upper and lower hydraulic boundaries of the sample are open, thus pressure or flow controlled. The option to create a closed boundary condition on the lower edge of the sample is given by a knife-gate valve.

A further description of the apparatus can be found in Kayser et al. (2016).

Model Tests

The presented results concern a fine sand, also known as Karlsruhe fine sand, described in Wichtmann and Triantafyllidis (2015). The sand samples were constituted by pluviation of dry sand in tab water, in analogy to Dave and Dasaka (2012). After pluviation, the sample was drained and then refilled from the bottom, thus obtaining medium dense sand probes with S < 90% for p = 1.4 bar. During the whole test series, a load plate with about 25 kN/m^2 was applied to the top of the probe. Five pressure levels ranging from 1.4 to 4 bar were driven successively. For each pressure level, quasi linear pressure fluctuations simulating ship-induced waves were applied on the top of the sample, whereas the bottom boundary of the sample was closed. In order to determine the saturation dependent permeability, steady state hydraulic gradients inducing upward seepage were applied at each pressure level. For each test, three increasing hydraulic gradients were applied, with constant absolute pressure in the middle of the sample.

Compressibility of the Water-Gas-Mixture

Assuming that the measured outflowing fluid during pressure fluctuation $\int_{t_1}^{t_2} Qdt$ must be equal to the change in fluid volume dV_m due to a change in pressure, the compressibility of the water-gas-mixture is

$$\beta_m = -\frac{1}{V_v}\frac{dV_m}{p(t_1) - p(t_2)} \tag{3}$$

with pressures p measured at the bottom of the soil sample and V_v the constant void volume. Figure 2a) shows the results of compressibility as a function of absolute pressure p. The compressibility of the mixture decreases with increasing absolute pressure.

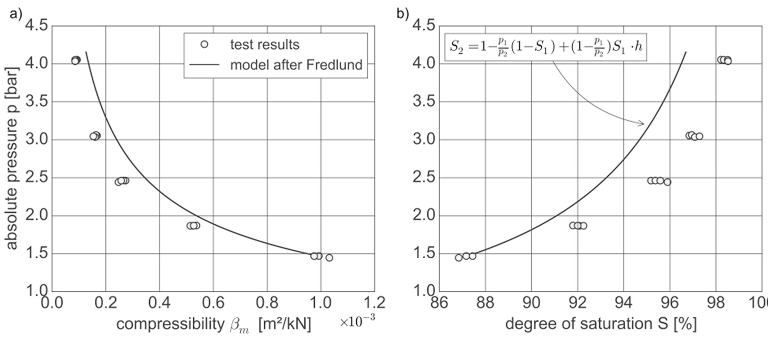

Fig. 2. (a) Mixture compressibility and (b) degree of saturation over absolute pressure.

Now, the degree of saturation can be calculated by transforming Eq. 1 which is shown in Fig. 2(b). The solid lines in the figures represent the model calculation based on Eq. 1 and the determination of the degree of saturation accounting for dissolved air (cf. the formula in the figure). By means of high precision measurements of discharge and pressure, a reliable determination of fluid compressibility is possible and can be approximated by Fredlund's model assuming h = 0.02.

Coefficient of Permeability

The coefficient of permeability k is a leading parameter for the development of excess pore pressures see e.g. the investigations of Kirca et al. (2014), thus a precise determination of the saturation-dependent k is important. Figure 3(a) shows a nearly linear dependency between seepage velocity and hydraulic gradient with increasing slopes for increasing average pressure levels. Steady state conditions during the permeability tests are assumed. Referring to Fig. 4, note that "pressure fluctuation 1" was performed before and "pressure fluctuation 2" after each permeability test stating negligible differences and indicating a nearly constant degree of saturation during seepage processes.

Figure 3(b) relates the permeability coefficient to the degree of saturation calculated in the previous section, showing an increase in permeability with increasing saturation. It is shown that the Kozeny-Carman proportionality between effective void space and permeability – see the solid line in Fig. 3(b) and Eq. 2 – is in good agreement with the measurements.

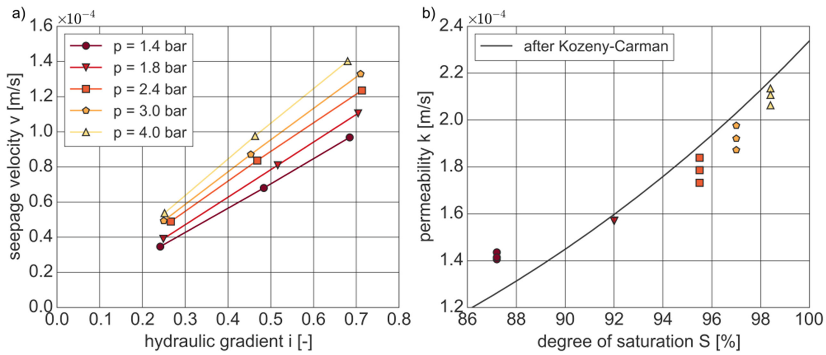

Fig. 3. Results of the permeability tests performed at different average absolute pressures. (a) seepage velocity over hydraulic gradient and (b) pressure-dependent permeability over degree of saturation extracted from Fig. 2(b).

Further quasi-saturated permeability models are presented in Faybishenko (1995) or Schaap and van Genuchten (2006). The simple Kozeny-Carman relation has the advantage that no further parameters are required for the calculation of changes in k.

Finite Element Simulations

The tests are simulated by means of Plaxis 2D using a fully coupled approach with mixed finite elements and linear elastic soil model, with the input data shown in Table 1. Figure 4 shows the development of excess pore pressures in the sample with respect to a linear water pressure change. The markers represent the test results at different pressure levels. The solid lines show the results of the numerical simulation with the input data according to Table 1 and the dashed lines represent the simulation with a constant permeability of $2.1 \cdot 10^{-4}$ m/s (cf. k(p = 4.0 bar) in Table 1) for all

Table 1. Soil and water simulation input data determined in the test series.

Pressure level	Young's modulus	Poisson's ratio	Void ratio	Mixture compressibility	Degree of saturation	Coefficient of permeability
p	E	υ	e	β_m	S	k
bar	MN/m^2	–	–	m^2/kN	%	m/s
1,4	14.0[a]	0.3[b]	0.85	$9.99 \cdot 10^{-4}$	87.2	$1.42 \cdot 10^{-4}$
1,8				$5.25 \cdot 10^{-4}$	92.0	$1.57 \cdot 10^{-4}$
2,4				$2.61 \cdot 10^{-4}$	95.5	$1.79 \cdot 10^{-4}$
3,0				$1.61 \cdot 10^{-4}$	97.0	$1.92 \cdot 10^{-4}$
4,0				$8.87 \cdot 10^{-4}$	98.4	$2.10 \cdot 10^{-4}$

[a] value from Wichtmann, Triantafyllidis (2015),
[b] empirical value

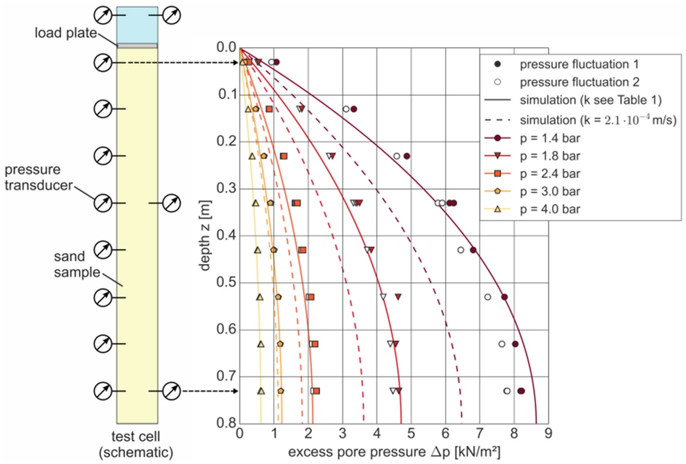

Fig. 4. Maximum excess pore pressures over depth during pressure decrease of 20 kN/m^2 in 20 s at different pressure levels.

pressure levels. Taking into account the change in compressibility and in permeability, the simulations are in excellent agreement with the test data.

Concluding Remarks

The alternating flow apparatus is perfectly equipped for the analysis of quasi-saturated sand samples. The saturation-dependent permeability as well as the mixture compressibility can be determined by means of precise pressure and flow measurements. The presented results coincide satisfactorily with Fredlund's compressibility equation. The permeability can be formulated as a function of volumetric water content based on the Kozeny-Carman equation. The coupled finite element simulations are in accordance with the test data. They show that resulting excess pore pressures increase with decreasing degree of saturation due to an increase in mixture compressibility and a reduction of the permeability coefficient.

As an outlook, the applicability of the conceptual model of quasi-saturated sands and its limits should be verified. Further numerical simulations can be applied to more complex boundary and model conditions.

References

Chapuis RP, Aubertin M (2003) On the use of the Kozeny Carman equation to predict the hydraulic conductivity of soils. Can Geotech J 40(3):616–628. doi:10.1139/T03-013

Dave TN, Dasaka SM (2012) Assessment of portable traveling pluviator to prepare reconstituted sand specimens. Geomech Eng 4(2):79–90. doi:10.12989/gae.2012.4.2.079

Faybishenko BA (1995) Hydraulic behavior of quasi-saturated soils in the presence of entrapped air laboratory experiments. Water Resour Res 31(10):2421–2435. doi:10.1029/95WR01654

Fredlund DG (1976) Density and compressibility characteristics of air–water mixtures. Can Geotech J 13(4):386–396. doi:10.1139/t76-040

Kayser J, Karl F, Schürenkamp D, Schwab N, Oumeraci H (2016) A test apparatus for alternating flow in geotechnical engineering. Geotech Test J 39(5):20150252. doi:10.1520/GTJ20150252

Kirca VSO, Sumer BM, Fredsøe J (2014) Influence of clay content on wave-induced liquefaction. J Waterway Port Coastal Ocean Eng 140(6):4014024. doi:10.1061/(ASCE)WW.1943-5460.0000249

Pietruszczak S, Pande GN (1996) Constitutive relations for partially saturated soils containing gas inclusions. J Geotech Eng 122(1):50–59. doi:10.1061/(ASCE)0733-9410(1996)122:1(50)

Schaap MG, van Genuchten MTh (2006) A modified Mualem–van Genuchten formulation for improved description of the hydraulic conductivity near saturation. Vadose Zone J 5(1):27. doi:10.2136/vzj2005.0005

Schürenkamp D, Oumeraci H, Kayser J, Karl F (2015) Numerical and laboratory experiments on stability of granular filters in marine environment. Int Conf Coastal Eng 1(34):17. doi:10.9753/icce.v34.structures.17

Skempton AW (1954) The pore-pressure coefficients A and B. Géotechnique 4(4):143–147. doi:10.1680/geot.1954.4.4.143

Tarantino A (2013) Basic concepts in the mechanics and hydraulics of unsaturated geomaterials, in mechanics of unsaturated geomaterials. Wiley, Hoboken doi:10.1002/9781118616871.ch1

Wichtmann T, Triantafyllidis T (2015): An experimental database for the development, calibration and verification of constitutive models for sand with focus to cyclic loading. Part I —tests with monotonic loading and stress cycles. In: Acta Geotech. doi:10.1007/s11440-015-0402-z

Effect of Specimen Confinement Method on Simple Shear Test of Clay

Bhagaban Acharya(✉) and David Airey

School of Civil Engineering, J05, The University of Sydney, Sydney, NSW 2006, Australia
bhagaban.acharya@sydney.edu.au

Abstract. The simple shear test has been employed regularly during the last few decades in soil characterisation studies for earthquakes, liquefaction, offshore construction and other applications. A variety of simple shear devices are available and the main difference between them is the method of applying the horizontal confining stress. According to the ASTM (D6528-07) standard for direct simple shear testing of cohesive soils, circular specimens are generally confined by a wire reinforced membrane or stacked rings. In this paper a comparison of results from monotonic undrained simple shear tests with wire reinforced and flexible membranes is reported. A simple shear apparatus is utilized in which lateral confinement of the specimens can be achieved, either by flexible membrane and confining pressure applied to the specimen through compressed air to maintain K_0 condition during compression, or by conventional wire reinforced membrane without confining pressure. It is shown that the membrane confinement method influences the measured undrained strength. For the normally consolidated specimens reported herein the shear strength using a flexible membrane is higher than for the wire reinforced membrane when the confining stress is adjusted to keep the vertical stress constant and is similar when the confining stress is kept constant throughout the shearing stage.

Introduction

The simple shear test has been employed regularly during the last few decades in the study of various engineering problems such as for earthquakes, liquefaction, offshore soil characterisation, design of pile shafts, embankment design and others. The simple shear state of strain is a plain strain mode of shearing in which all the strain components are zero except for the shear strain, γ_{yx}. During soil tests there can also be vertical normal strain, ε_{yy}, which is equal to the volumetric strain (Airey et al. 1985). In conventional undrained simple shear tests soil specimens are first consolidated under K_0 conditions followed by shearing under constant volume conditions. Constant volume conditions are generally achieved by preventing vertical strain assuming that the lateral confinement is sufficiently stiff to minimise lateral strains. In tests with the flexible membrane it is possible to prevent drainage so that, at least on average, the constant volume condition is satisfied. The simple shear test enables soil specimens to be tested with rotating major principal stress axes during shearing which replicates various loading conditions in the field. In contrast, rotation of the principal stress axes

A. Ferrari and L. Laloui (eds.), *Advances in Laboratory Testing and Modelling of Soils and Shales (ATMSS)*, Springer Series in Geomechanics and Geoengineering,
DOI 10.1007/978-3-319-52773-4_28

cannot be simulated with conventional triaxial tests which only allow an instantaneous rotation of the principal axes through 90°. However, the simple shear test is limited in its inability to apply complementary shear stresses on the vertical boundaries of the specimen resulting in complicated and non-uniform stress and strain distributions during shearing (Airey and Wood 1987, Budhu 1984) and this complicates test interpretation.

A wire reinforced rubber membrane or rubber membrane supported by a series of closely stacked rings are usually employed (ASTM standard D6528-07) in simple shear tests to enclose the specimen, provide confinement on the lateral boundaries and ensure the plane strain and no lateral strain conditions. An alternative confinement approach was suggested by (Franke et al. 1979). In this approach an unreinforced membrane is used and the apparatus is placed in a confining vessel so that confining pressure can be provided to maintain the zero lateral strain condition. Previous studies into the lateral confinement system have compared wire reinforced membranes and stacked rings and have shown that essentially identical results are obtained with cohesive soil sheared at constant volume (Baxter et al. 2010) and for clean dry sand sheared under constant vertical load conditions (Kwan and El Mohtar 2014). Apart from a limited study reported by Reyno et al. (2005) there appear to be no other studies investigating and comparing the effects of the flexible membrane confinement system with the more widely used reinforced membrane system. In addition the use of the flexible membrane introduces another question which is what should happen to the confining stress during shearing. In principle this should not be important if simple shear conditions are imposed as the specimen should follow the same effective stress response irrespective of the applied total stresses (Airey and Wood 1987). In this paper the effects of both adjusting the confining pressure to keep the total vertical stress constant and of holding the confining stress constant are investigated. These tests have been designed to evaluate the use of flexible boundary simple shear devices and provide recommendations for their test interpretation.

Materials, Apparatus and Procedure

Cylindrical soil specimens of kaolin clay with properties: liquid limit 43%, plasticity index 16%, specific gravity 2.6 and coefficient of consolidation 3 m^2/yr, were prepared for the tests as follows. Reconstituted specimens were prepared by mixing clay powder with de-aired water at a moisture content about 1.5 times the liquid limit. After mixing thoroughly the slurry was poured into a 90 mm diameter tube and consolidated in stages to a final vertical effective stress, σ'_{v0}, of 80 kPa. The specimens were then extruded from the consolidation tube and trimmed to 60 mm in diameter and 20 mm in height using a thin-walled sample cutter. The specimens were then extruded from the cutter onto the specimen base platen and confined between the platens by either flexible or wire reinforced membranes which were secured by O-rings to the top and bottom platens. The sample and end platens were then located and aligned in the simple shear apparatus.

The simple shear apparatus used in this study was designed at the University of Western Australia and is similar to the ‘Berkeley’ type simple shear apparatus

(Rau 1999). The apparatus can be configured to conduct the simple shear test with either flexible or reinforced membranes.

One of the advantages of the flexible membrane confinement system is that back pressures can be applied to ensure saturation of the specimen and pore water pressures can be measured in undrained tests. To allow back pressure application the apparatus is enclosed in a steel cylindrical confining cell and air pressure used to provide the confining stress. Internal load cells are used to measure vertical and horizontal loads and internal displacement transducers measure the vertical and horizontal movements of the top and bottom platens respectively. The specimens sit within a small 3 mm high rim around the platens to prevent slip along the horizontal soil-platen interface (Reyno et al. 2005). The test procedure consists of first saturating the specimens by slowly ramping up the cell pressure to 210 kPa and back pressure to 200 kPa, keeping an effective isotropic stress of about 10 kPa. This also requires control of the vertical drive to maintain a zero deviator stress. The B-value was checked at the end of saturation and an average of 0.98 was found with values of greater than 0.96obtained in every test. The specimens were then compressed to the desired normal stress by slowly increasing the deviatoric stress while also adjusting the confining cell pressure to ensure that the targeted stress ratio was maintained. A constant stress ratio K (σ'_h/σ'_v) = 0.55 was used throughout the compression stages and was found to result in essentially identical axial and volumetric strains, so that there is no lateral strain. This may be compared with the value of K_o (= 1 − sin ϕ') for normally consolidated soil which gives 0.56 based on the reported critical state friction angle from triaxial tests (Chow 2013). During undrained shearing the height of the specimen was kept constant by locking the vertical loading ram and the base of the specimen was driven horizontally at a rate of 25%/hr. Experiments conducted to evaluate the effect of rate of shearing for the same kaolin clay (Acharya 2017) showed that there was no significant effect on the stress–strain behaviour for tests conducted at a range of shear strain rates of between 2.5%/hr and 25%/hr. The confining pressure (σ_h) was either held constant or adjusted to maintain a constant total vertical stress (σ_v) on the specimen and pore water pressure was measured directly.

For the tests conducted using the reinforced membrane confinement the test procedure and control was much simpler. The specimens were enclosed in latex membranes which were reinforced by spiral windings of wire having diameter 0.6 mm and wound at 10 turns per cm. The confining cell is not required as the wire reinforcement provides the lateral restraint to the specimens. However, without the confining stress the application of back pressure to saturate the specimen is not possible. After setting up the specimen the vertical stress is slowly increased, at a similar rate as for the tests with the flexible membranes, to achieve the target value and the reinforced membrane is assumed to enforce one-dimensional conditions. During undrained shearing the vertical loading ram is locked and the base of the specimen driven horizontally just as for the tests with the flexible membrane. The vertical load acting on the specimen is recorded and is taken to be the effective vertical stress, and the pore pressure relevant to the field is then estimated by assuming a constant total vertical stress during shear (Dyvik et al. 1987).

Results

An extensive laboratory testing program has been conducted and results from nine representative tests are used to show the effects of membrane confinement. Table 1 shows the initial void ratios at the start of the tests (e_o), the final void ratios (e_f), the effective vertical stresses at start of shearing (σ'_{vc}), the peak shear stress or undrained strength (s_u), the normalised strengths (s_u/σ'_{vc}) and the friction angles ($\phi' = \tan^{-1}(\tau_{xy}/\sigma'_v)$) at the peak strength. In all tests the specimens were one-dimensionally compressed to the effective vertical stresses shown in Table 1. All the specimens were compressed to normally consolidated states with vertical stresses higher than the 80 kPa used during preparation. For the flexible membrane type A tests, the confining stress was varied during undrained shear to maintain a constant total vertical stress. For the type B tests the confining stress was maintained constant during shear.

Table 1. Monotonic undrained simple shear test program.

Confinement method	Test code	σ'_{vc} (kPa)	e_o	e_f	s_u (kPa)	s_u/σ'_{vc}	ϕ'
Reinforced membrane	R100	100	1.064	0.938	29.7	0.30	25.1°
	R200	200	1.057	0.907	59.5	0.30	26.1°
	R400	400	1.061	0.862	97.3	0.24	25.3°
Flexible membrane (type A: varying σ_h)	F100A	100	1.058	0.952	34.6	0.35	28.8°
	F200A	200	1.053	0.914	83.3	0.42	29.7°
	F400A	400	1.062	0.881	125.2	0.31	27.5°
Flexible membrane (type B: constant σ_h)	F100B	100	1.052	0.940	30.1	0.30	23.1°
	F200B	200	1.055	0.903	58.8	0.29	25.2°
	F400B	400	1.071	0.866	103.3	0.26	23.1°

Figure 1a shows the shear stress versus shear strain curves for flexible and reinforced membrane confinement systems at different effective vertical stresses. This figure clearly shows that the peak shear stresses (undrained strengths) obtained from the tests with the flexible membrane are higher than those obtained when using the standard reinforced membrane confinement for each normal stress taken into consideration. The effective stress paths shown in Fig. 1b indicate that the specimens behave similarly at the start of shearing but diverge as they approach failure. At failure, which is defined here as occurring at the peak shear stress, the average values of s_u / σ'_{vc} are 0.36 and 0.28 and the average values of ϕ', calculated as $\tan^{-1}(\tau_{xy} / \sigma'_v)$, are 28.7° and 25.5° for the flexible and reinforced membrane confinement systems, respectively. It is evident that the normalised undrained strengths and the estimated friction angles from the tests with the flexible membrane are significantly higher than when the reinforced membrane confinement system is used. As the same soil and same apparatus have been used the different responses must be associated with the different lateral boundary confinements. To maintain a constant vertical stress in the flexible membrane tests significant increases in the confining lateral stress must occur for these normally

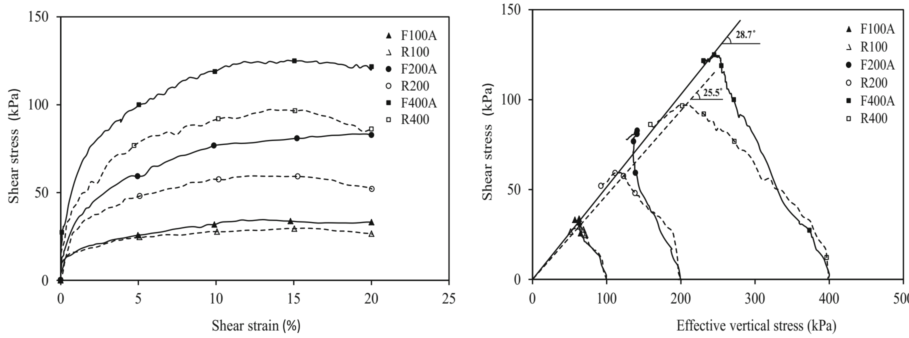

Fig. 1. Comparison of flexible membrane (σ_v constant) and reinforced membrane responses (a) Stress - strain responses, (b) Effective stress paths.

consolidated specimens and it is believed this contributes to the higher apparent strength, and to the different post-peak responses once a shear band has formed.

To further investigate the effect of the confining stress in the flexible membrane tests, a second group of tests was performed in which the confining stress was held constant during shearing. Results from these tests are compared with the standard reinforced membrane tests in Figs. 2a and b. Figure 2a presents the shear stress versus shear strain curves and Fig. 2b presents the effective stress paths for the two types of tests. In these tests the stress – strain responses as well as the effective stress paths for both flexible and reinforced confinement systems produced comparable results. The average peak value of s_u/σ'_{vc} found for each confinement system is 0.28 and average friction angles of ϕ' are 23.8° and 25.5° for the flexible and reinforced membrane confinement systems respectively. Only the tests with initial effective stress of 400 kPa show significant differences and further tests would be required to confirm the apparent difference in friction angles. In combination with the tests with the varying confining stress these tests confirm the important influence of the confining stress on the observed stress-strain-strength response.

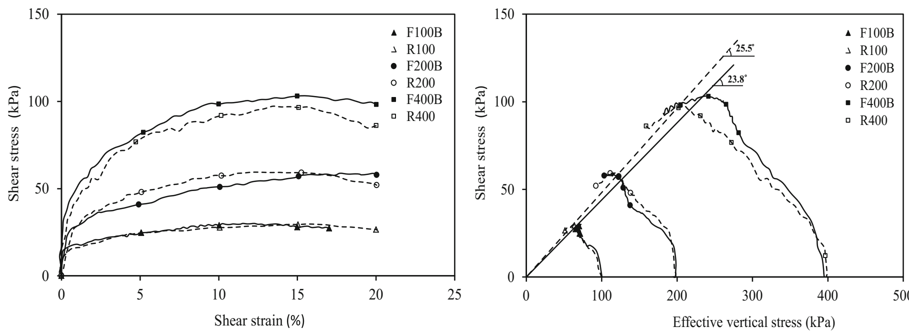

Fig. 2. Comparison of flexible membrane (σ_h constant) and reinforced membrane responses (a) Stress - strain responses, (b) Effective stress Paths.

To further investigate the differences in behaviour between the two types of tests using the flexible membrane the variations of total and effective stresses are presented in Fig. 3. It should be noted that the horizontal stress refers to the confining stress, which is not necessarily the same as the horizontal stress of a specimen undergoing simple shear, and in both of the test methods total effective vertical stress (σ'_v) and total effective horizontal stress (σ'_h) are obtained from the direct measurement of σ_v, σ_h and pore water pressure. Figure 3 shows the state of total and effective, vertical as well as horizontal, stresses acting on specimens during two typical tests conducted at 400 kPa.

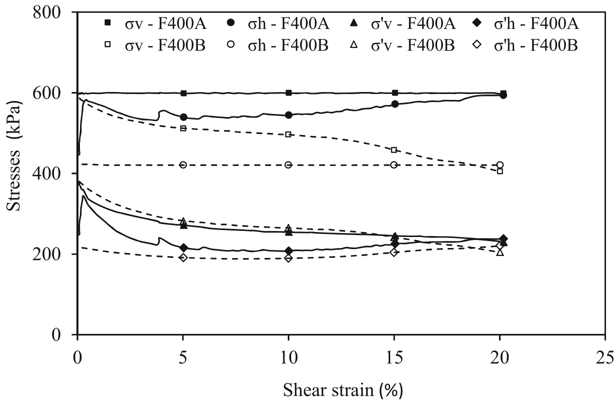

Fig. 3. State of stresses during shear stages in flexible membrane confinement system.

In test F400A the requirement to keep σ_v constant is achieved by adjusting σ_h throughout the shearing stage of the test. To maintain this prerequisite condition, σ_h increases quickly at the beginning of shearing, then reduces slowly up to about 5% shear strain followed by a slow increase until it almost reaches σ_v at the end of the test. In test F400B the requirement to keep σ_h constant results in a gradual decrease in σ_v throughout the shearing stage of the test, with both vertical and horizontal stresses reaching similar values at large strain. Comparison of the effective stress responses shows that the changes in σ'_v are similar in both tests. However, there are very significant differences in the horizontal effective stress, σ'_h which initially rises much higher in test F400A, a rise that is associated with the rapid increase of the confining stress at the start of shearing. Nevertheless, as the specimens approach failure the effective horizontal stresses in the test with the varying and greater confining pressure is only slightly higher than the test with the constant and lower confining stress. As these average boundary effective stresses are similar at failure it is surprising that there is such a significant difference in the apparent undrained strengths. It is believed that this is a consequence of the non-uniform boundary stresses that arise in simple shear tests and the effect of the confining stress on shear plane development.

In some simple shear studies the average horizontal stresses from tests with reinforced membranes have been estimated from the strain in the reinforcing wire.

For example Airey (1984) showed that the average horizontal total stress for normally consolidated specimens decreased by about 25% during shear. Thus it appears that applying a constant confining pressure may lead to pressures which are higher than in conventional simple shear tests and may result in overestimation of the undrained strength.

Summary and Conclusions

Results of monotonic undrained simple shear tests of reconstituted normally compressed kaolin have been presented. These tests have demonstrated the differences in undrained strength and interpreted friction angle that can occur when the standard reinforced membrane specimen confinement is replaced by a flexible membrane supported by confining pressure.

During compression of specimens confined by flexible membranes the confining pressure is adjusted to maintain one-dimensional loading and this controls the initial confining stress at the start of undrained shear. Tests in which the confining stress was raised during shear to maintain a constant total vertical stress, as assumed to replicate field loading, resulted in significantly higher apparent strengths and friction angles than tests performed in conventional wire reinforced membranes. However, when the confining pressure was held constant throughout shear the strengths and friction angles were similar to the reinforced membrane tests.

The tests have demonstrated the significant role that the confining stress can play when flexible membranes are used in place of standard reinforced membrane confinement.

The practice of employing flexible membrane confinement systems with adjustment of confining cell pressure to maintain constant vertical total stress over estimates the undrained shear strength and frictional angle of soft clay. It should be noted that the correct interpretation of test results is crucial to estimate the shear strength parameters of soft clay utilizing such simple shear devices.

References

Acharya B (2017) Simple shear tests of clays. Forthcoming PhD Thesis, University of Sydney

Airey DW (1984) Clays in circular simple shear tests. PhD Thesis, University of Cambridge

Airey DW, Budhu M, Wood DM (1985) Some aspects of the behaviour of soils in simple shear. Devel Soil Mech Found Eng 2:185–213

Airey DW, Wood DM (1987) An Evaluation of direct simple shear tests on clay. Geotechnique 37:25–35

Baxter CDP, Bradshaw AS, Ochoa-Lavergne M, Hankour R (2010) DSS test results using wire-reinforced membranes and stacked rings. Geotech Spec Publ 199:600–607

Budhu M (1984) Nonuniformities imposed by simple shear apparatus. Canad Geotech J 21:125–137

Chow SH (2013) Free falling penetrometer tests in clay. PhD Thesis, University of Sydney, Australia

D6528-07, A. Standard Test Method for Consolidated Undrained Direct Simple Shear Testing of Cohesive Soils, Astm Int'L

Dyvik R, Berre T, Lacasse S, Raadim B (1987) Comparison of truely undrained and constant volume direct simple shear test. Geotechnique 37:3–10

Franke E, Kiekbusch M, Schuppener B (1979) A new direct simple shear device. Geotech Test J 2:190–199

Kwan WS, El Mohtar C (2014) Comparison between shear strength of dry sand measured in CSS device using wire-reinforced membranes and stacked rings. Geotechn Spec Publ, 1111–1119

Rau GA (1999) Evaluation of strength degradation in seismic loading of Holocene Bay mud from Marin County, California. PhD Thesis, University of California, Berkeley

Reyno AJ, Airey DW, Taiebat HA (2005) Influence of height and boundary conditions in simple shear tests. In: Frontiers in offshore geotechnics, Proceedings of the 1st international symposium on frontiers in offshore geotechnics, pp. 1101–1107

Hydro - Mechanical Behaviour of Shales and Stiff Clays

Fractal Analysis of the Progressive Failure of Shales and Stiff Clays Under Shear

Luis E. Vallejo[1,2,3(✉)], Jairo M. Espitia[1,2,3], and Bernardo Caicedo[1,2,3]

[1] Department of Civil and Environmental Engineering, University of Pittsburgh, Pittsburgh, USA
vallejo@pitt.edu
[2] Departmento de Ingenieria de Minas, Universidad Pedagogica y Tecnologica de Colombia, Sogamoso, Colombia
[3] Departamento de Ingeneria Civil y Ambiental, Universidad de los Andes, Bogotá, Colombia

Abstract. Shales and stiff clays when deformed under direct shear stress conditions develop narrow shear zones within which different sets of discontinuities or cracks are present. These cracks form in the shear zone in a progressive manner. In the first stage of deformation, a small set of unconnected cracks called Riedel shears form. In the second stage of deformation, a series of cracks called Thrust shears form. They connect with the Riedel shears. In the third stage of deformation, The Riedel and Thrust discontinuities interact, forming an undulating and rough failure surface. In this study, the fractal dimension concept from fractal theory is used to evaluate the progressive degree of cracking in the shear zone that causes the failure of shales and stiff clays forming part of natural slopes and earth dams. It was established that the intensity of cracking in the samples was reflected in the fractal dimension values. High levels of cracking were associated with high values of the fractal dimension.

Introduction

Shales and stiff clays forming part of natural slopes, earth dams and the foundations for footings fail in the form of curved shear zones as shown in Figs. 1(A) and (B). Most of the displacements during failure occur within these shear zones that are relatively wide with thicknesses varying between 0.25 and 2.54 cm (Vallejo 1982). The direct shear test is the laboratory experiment that is used in practice to analyze the formation an evolution of the discontinuities that produce the shear failures in natural slopes, earth dams and the foundations for footings [Fig. 1(C)].

In the direct shear test, the shale or the stiff clay is placed in a split rectangular box and is subjected to a combination of normal and shear loads. The samples that can be tested in this apparatus usually measure 6 cm in length, 6 cm in width, and 4 cm in height. During testing, the normal load is kept constant while the shearing load is progressively increased until the samples fail in a shear zone between the two halves of the box.

A. Ferrari and L. Laloui (eds.), *Advances in Laboratory Testing and Modelling of Soils and Shales (ATMSS)*, Springer Series in Geomechanics and Geoengineering,
DOI 10.1007/978-3-319-52773-4_29

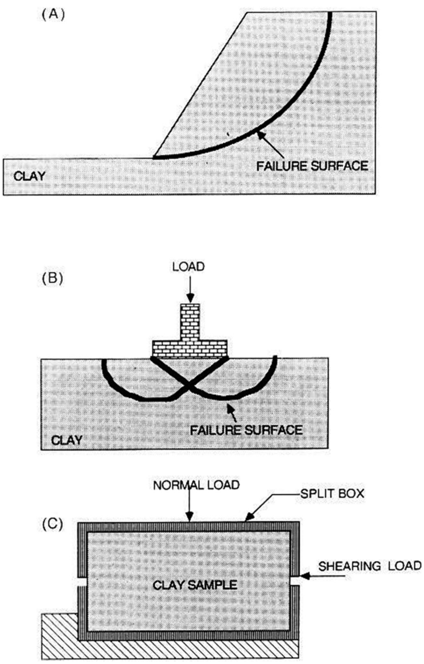

Fig. 1. (A) Failure surface in a shale or a stiff clay forming part of a slope. (B) Failure surface in a shale or stiff clay forming part of the foundation for a footing. (C) The direct shear test.

An example of the types of discontinuities produced during the shearing of a stiff clay sample in the direct shear apparatus is shown in Fig. 2 (Skempton 1966). An analysis of Fig. 2 indicates that the failure of the stiff clay as a result of shear takes place in a progressive manner. The sample develops different sets of cracks that progressively grow and interact until a final failure surface develops in the sample. In the first stage of deformation, a small set of unconnected cracks called Riedel shears form [stage (i) in Fig. 2]. In the second stage of deformation, a series of cracks called Thrust shears form. They connect with the Riedel shears [stage (ii) in Fig. 2]. In the third stage of deformation, the Riedel and Thrust discontinuities interact, forming an undulating and rough failure surface [stage (iii) in Fig. 2].

The purpose of this study is to analyze the progressive degree of cracking in the stiff clay subjected to direct shear that produces the failure of the sample (Fig. 2). The evaluation of the different levels of cracking shown in Fig. 2 will be made using the fractal dimension concept from fractal theory (Mandelbrot 1982).

Fractal Evaluation of the Degree of Cracking

Fractal theory is a relatively new mathematical concept first introduced by Mandelbrot in 1967 to measure the degree of roughness of the coast of Great Britain. Fractal theory has recently been applied in geotechnical engineering to measure the roughness and

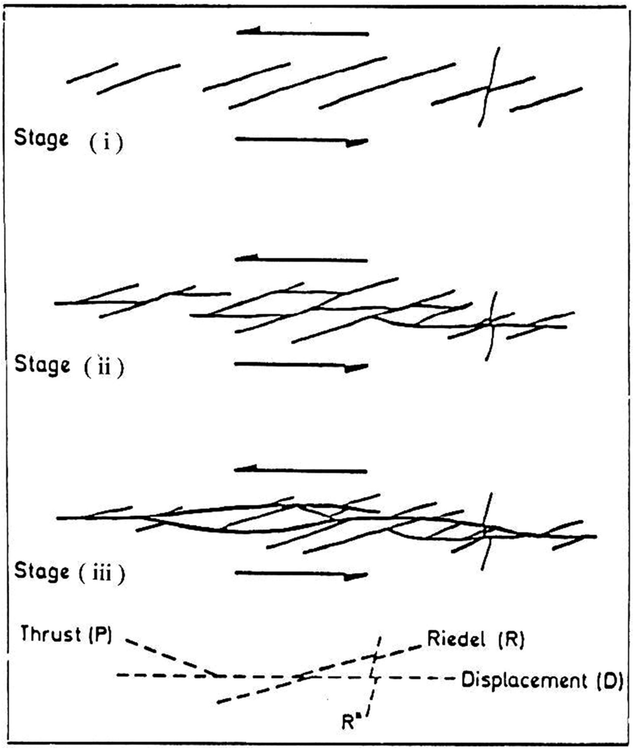

Fig. 2. Stages of crack formation and evolution in a stiff clay subjected to direct shear (after Skempton 1966).

size distribution of granular materials (Vallejo 1995; Hyslip and Vallejo 1997), the distribution of rock fragments resulting from blasting (Perfect 1997), the structure and distribution of pores in clays (Vallejo 1996), and the formation and propagation of cracks during the desiccation of clays (Vallejo 2009).

Fractal Dimension Concept to Measure the Degree of Cracking

For the purpose of this study, the fractal dimension concept from fractal theory will be used to evaluate the intensity of cracking in Fig. 2. The fractal dimension measures the spatial distribution and the tendency of crack traces to fill the area in which they are embedded (Hirata 1989**).** According to Hirata (1989), the fractal dimension, D, that measures the spatial distribution and the tendency of the crack traces to fill an area can be obtained using the box method (Figs. 3 and 4). The box method uses a sequence of square grids, each with a different square cell size r (Fig. 3). The sequence of grids is first drawn on transparent paper. Each grid is then placed over the area containing the traces of cracks. Next the number (N) of the cells intersected by the crack traces is counted (Fig. 3). The fractal dimension, D, can be obtained by plotting the number of

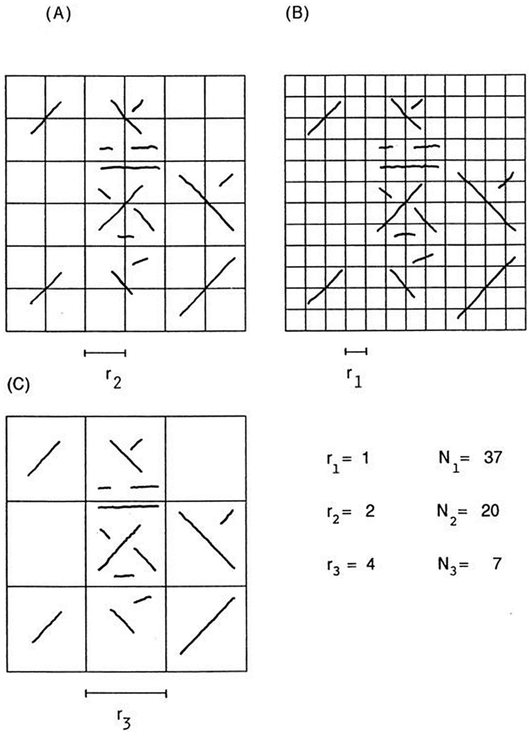

Fig. 3. Box method to calculate fractal dimension of crack pattern.

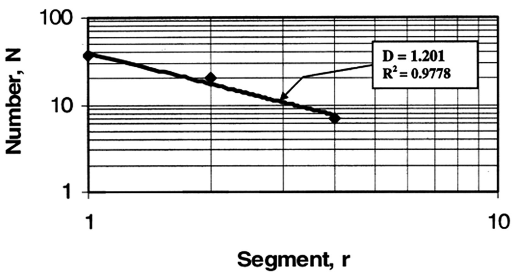

Fig. 4. Fractal dimension, D, for crack pattern shown in Fig. 3.

cells, N, versus the corresponding size of the cells used, r, on log-log paper. The points on the log-log paper are then connected with a best fitting straight line. The absolute value of the slope of this line represents the fractal dimension, D (Fig. 4). The higher the value of D, the higher is the degree of cracking of the clay surface being analyzed.

Fractal Analysis of the Degree of Cracking in a Stiff Clay Subjected to Shear

The box method from fractal theory was used to measure the fractal dimension for the crack patterns at different levels of shearing shown in Fig. 2. For the fractal analysis, two very important questions will be addressed. The first question deals with whether the fractal dimension can be used to measure the degree of cracking taking place in the shear zone of the sample subjected to shear. The second question deals with whether there is a fractal dimension associated with the crack interconnectivity that produced the failure surface in the clay under shear. Figures 5, 6, and 7 shows the calculation of the fractal dimension for stages (i), (ii) and (iii) shown in Fig. 2.

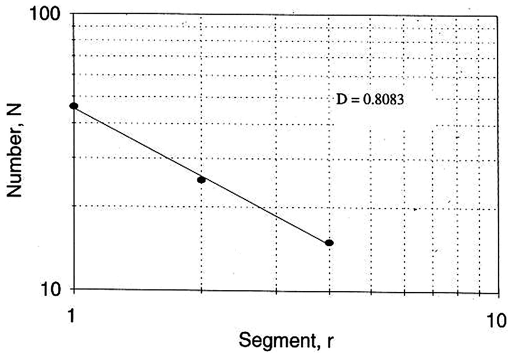

Fig. 5. Fractal dimension, D, for crack pattern in Fig. 2, Stage (i).

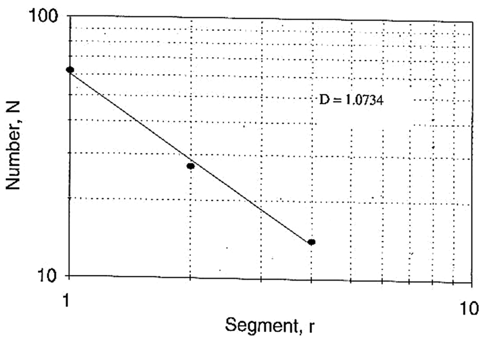

Fig. 6. Fractal dimension, D, for crack pattern in Fig. 2, Stage (ii).

Figures 5, 6, and 7 show linear plots of the number of cracks, N, versus the size of the grids, r, used to calculate the fractal dimension, D. A review of these figures indicate that the degree of cracking in the sample was reflected in the value of the fractal dimension, D. Low levels of cracking [stage (i) in Fig. 2] were associated with

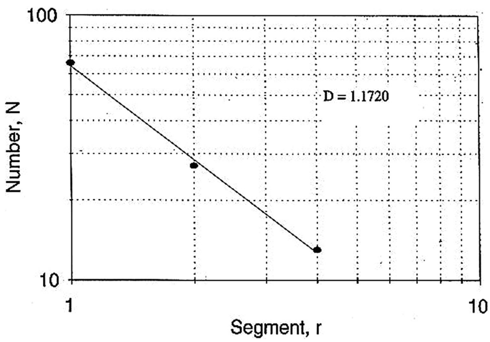

Fig. 7. Fractal dimension, D, for crack pattern in Fig. 2, Stage (iii).

low values of the fractal dimension (D = 0.8083). High levels of cracking [stage (ii) in Fig. 2] were associated with high values of the fractal dimension (D = 1.0734). The highest fractal dimension value (D = 1.1720) was associated with the final, rough failure surface [stage (iii) in Fig. 2].

Thus, the fractal dimension, D, can be appropriately be used to evaluate the degree of cracking in the stiff clay sample under shear. Also, it can be used to measure the interconnectivity of the cracks in the shear zone when this interconnectivity produces the final failure surface in the stiff clay under shear.

Conclusions

A theoretical analysis that makes use of the fractal dimension concept from fractal theory has been used to evaluate the evolution of cracking in a stiff clay sample under shear. From this analysis the following conclusions were reached:

(1) The degree of cracking in the sample was reflected in the fractal dimension values for the crack pattern. Low levels of cracking were associated with low values of the fractal dimension. High levels of cracking were associated with high values of the fractal dimension.
(2) The threshold for crack interconnectivity that produced the continuous failure surface in the clay sample was equal to 1.1720. This was the highest value measured in the sample under shear.
(3) The use of the fractal dimension concept from fractal theory proved to be an elegant and simple mathematical tool to measure not only the degree of cracking in the sample, but the level of crack interconnectivity that produced its failure.

References

Hirata T (1989) Fractal dimension of fault systems in Japan. Pure appl Geophys 131:157–170

Hyslip JP, Vallejo LE (1997) Fractal analysis of the roughness and size distribution of granular materials. Eng Geol 48:231–244

Mandelbrot BB (1967) How long is the coast of Great Britain? statistical self-similarity and the fractal dimension. Science 156:636–638

Mandelbrot BB (1982) The Fractal Geometry of Nature. Freeman, San Francisco

Perfect E (1997) Fractal models for the fragmentation of rocks and soils: a review. Eng Geol 48:185–198

Skempton AW (1966) Some observations on tectonic shear zones. In: Procedings of the 1st International Congress on Rock Mechanics, Lisbon, vol. 1, pp. 329–335

Vallejo LE (1982) Development of the shear zone structure in stiff clays. In: Procedings of the 4th international conference on numerical methods in geomechanics, Edmonton, Alberta, Canada, vol. 1, pp. 255–262

Vallejo LE (1995) Fractal analysis of granular materials. Geotechnique 45:159–163

Vallejo LE (1996) Fractal analysis of the fabric changes in a consolidating clay. Eng Geol 43:281–290

Vallejo LE (2009) Fractal analysis of temperature induced cracking in clays and rocks. Geotechnique 59:283–286. doi:10.1680/geot.2009.59.3.283

Recent Developments in Measurement and Use of Fully Softened Shear Strength in the USA

Bernardo A. Castellanos(✉) and Thomas L. Brandon

Virginia Tech, Blacksburg, USA
bernardo@vt.edu

Abstract. There has been a renewed emphasis in the U.S. on the use of fully softened shear strength for slope stability analysis of cuts in stiff clays and the stability of compacted clay embankments. A detailed investigation on the proper use and measurement of the fully softened shear strength has been recently undertaken, examining different test apparatuses and procedures. A summary of the recent development and guidelines on the use of this concept in slope stability analysis and the proper way to measure the fully softened shear strength in the laboratory is presented.

Introduction

The fully softened shear strength, defined as the drained shear strength of a clay in a remolded, normally consolidated state, is an semi-empirical concept presented by Skempton (1970) to explain the decrease in mobilized shear strength in first-time failures in cuts in stiff clays occurring several years after the cut was made. Skempton developed this concept based on back analyses of several failures in London (Skempton 1977). Kayyal and Wright (1991) and Wright (2005) extended this concept to first-time slope stability failures in compacted clay embankments of high-plasticity clay.

Virginia Tech Workshop

Problems concerning the performance of levees, earth dams, and natural slopes at several project sites in Texas in the early 2010s involved geotechnical engineers from many firms and organizations. This resulted in an increased interest the applicability and measurement of fully softened shear strength. A workshop focusing on fully softened shear strength was held at the Virginia Tech campus on August 16 and 17, 2011. This workshop brought together more than 50 engineering practitioners, academics, and researchers who shared their experiences and opinions related to the use and measurement of fully softened shear strength (Duncan et al. 2011; VandenBerge et al. 2013). Continuing the momentum, a panel discussion and a portion of the proceedings at the American Society of Civil Engineers (ASCE) Geo-Congress 2013 in San Diego, CA, was devoted to this topic. In 2013, a new subcommittee of the ASCE Embankments, Dams, and Slopes committee was formed to focus on fully softened shear strength parameters.

A. Ferrari and L. Laloui (eds.), *Advances in Laboratory Testing and Modelling of Soils and Shales (ATMSS)*, Springer Series in Geomechanics and Geoengineering,
DOI 10.1007/978-3-319-52773-4_30

The workshop at Virginia Tech consisted of a combination of presentations and break-out sessions on the softening process, measurement of fully softened strength, use of fully softened strength in stability analyses, and research needs. A summary of the workshop's conclusion was presented by VandenBerge et al. (2013). Some of the main conclusions, among others, were that:

(1) The fully softened shear strengths should be used, with appropriate long-term pore pressures, for analysis of the stability of excavated slopes in highly plastic fissured clays and for analysis of the stability of shallow potential slides in embankments where wet/dry climate cycles are likely to produce significant desiccation cracking.
(2) In general, the likelihood of reaching the fully softened condition probably increases with: (a) higher Plasticity Index, (b) existence of fissures or shrinkage cracks, (c) water contents much above the shrinkage limit, (d) higher clay size fractions, (e) lower silt and sand content, and (f) higher activity (ratio of PI divided by percent finer than two microns).
(3) Curved failure envelopes are more appropriate than linear envelopes for representing fully softened strength.
(4) The direct shear test is the most appropriate test for measuring fully softened shear strength.

Use of Fully Softened Shear Strength in Practice

Detailed guidelines on the use of fully softened are not readily available in any of State Department of Transportation or Federal agency manuals. The fully softened shear strength has historically been recommended to be used in cut-slopes in stiff clays and compacted clay embankments constructed of high plasticity clays without further specifications or details.

A comprehensive investigation based on a literature review of case histories where the fully softened shear strength was found to be the controlling shear strength was presented by Castellanos et al. (2015). Castellanos et al. collected more than 68 failures in stiff clays and 74 failures in compacted clay embankments related to fully softened shear strength. The liquid limits and plasticity indices of the soils involved in these slides are plotted in Fig. 1. Based on this plot, it can be seen that the fully softened shear strength applies to cut in stiff clays and compacted clay embankments for clays with liquid limits above 40 and plasticity index above 20.

Castellanos et al. (2015) used the same database of case histories to conclude that slides in stiff clays can occur over a wide range of depths. In compacted clay embankments, the failures tend to be shallower - usually less than 3.3 m deep. For first-time slides in cuts in stiff clays, they recommended that the fully softened strength be applied to the entire clay layer. This method should predict the correct factor of safety but may not give the correct location of the failure surface. A pore pressure ratio of 0.3 appears to be appropriate for preliminary design of cuts in stiff clays if better information is not available. For final designs, pore pressures corresponding to steady-state seepage conditions representing the expected worst case scenario should

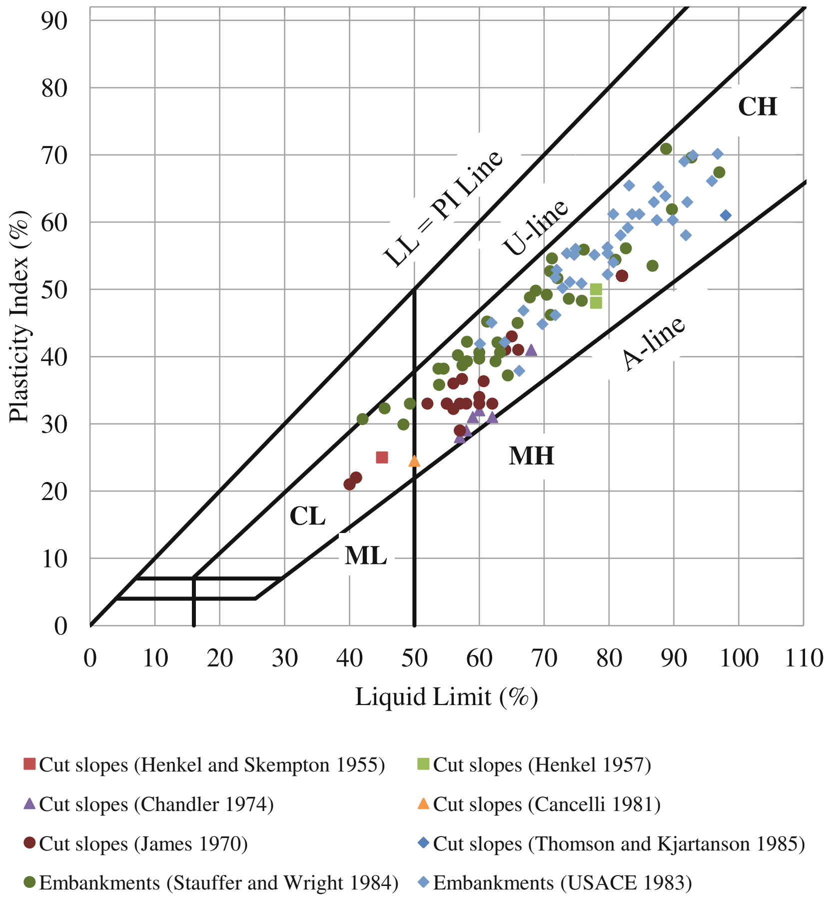

Fig. 1. Atterberg limits of soils involved in first-time failures where the fully softened shear strength produced a factor of safety ≈1 according to the original authors (Castellanos et al. 2015).

be used. Another method is available that requires more laboratory data and might produce a better estimate of the location of the failure surface was presented by Mesri and Shahien (2003) and Castellanos et al. (2015).

For long-term limit equilibrium analysis of compacted clay embankments, Castellanos et al. (2015) also recommended that the fully softened strength be applied to the entire embankment, while using pore pressures corresponding to a water table coincident with the slope surface, if better information is not available. For compacted embankments, assuming a 3.3 m depth of softening seem to be reasonable. The shear strength of the soil in the foundation of the embankment should be based on conventional shear strength tests performed using undisturbed samples. Softening of the foundation soil is not expected to occur after the embankment is constructed.

The curvature of the fully softened failure envelope has a significant influence on the factor of safety for slope stability and the location of the critical failure plane obtained (Duncan et al. 2011). A linear interpretation of fully softened shear strength envelope may result in deeper failure surfaces, and unconservative calculated factors of safety. Castellanos et al. (2015) recommended to use a factor of safety of 1.25 for shallow failures with low consequences of failure, 1.35 for deeper failures for situations with low to medium consequences of failure, and 1.5 for conditions with higher consequences of failure. These factors of safety were recommended for cases where the fully softened strength is judged to be appropriate and conservative pore pressures are used.

Laboratory Test Methods Comparison

The fully softened shear strength has been commonly measured using the direct shear and triaxial devices. Recently, the ring shear device has also been proposed to be used for this purpose, but a detailed investigation of the suitability of this device to properly measure the correct fully softened shear strength had not been conducted. Oddly enough, this is the only device with a standardized testing procedure for fully softened shear strength defined (ASTM D7608).

Castellanos et al. (2013) and Castellanos and Brandon (2014) presented a detailed investigation on the proper ways to measure the fully softened shear strength. They compared the fully softened shear strength measured with the direct shear, ring shear, and triaxial devices. A sample of the results are presented in Figs. 2, 3 and 4. From the results shown, it can be seen that the fully softened shear strength measured with the ring shear device is very low when compared to the direct shear and triaxial devices, with these two tests giving approximately the same results. The direct shear and triaxial devices have been historically proven to provide reliable results for peak shear strength measurements. The ring shear device, was designed and intended to be used to measure

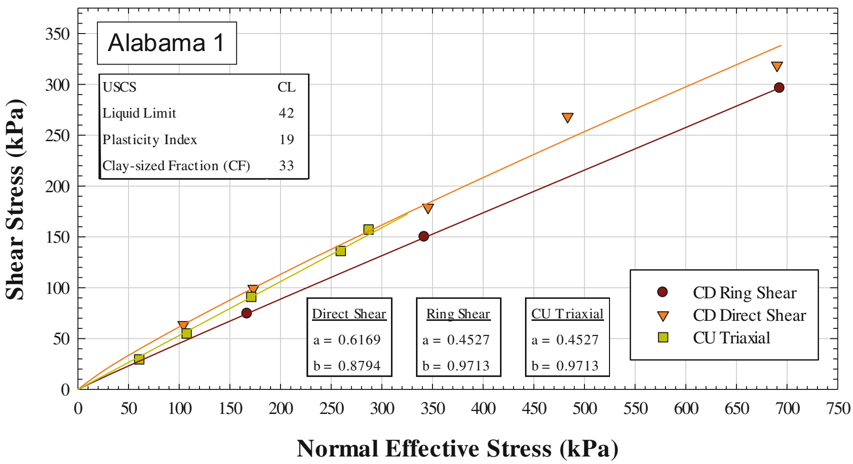

Fig. 2. Fully softened failure envelopes for Alabama 1.

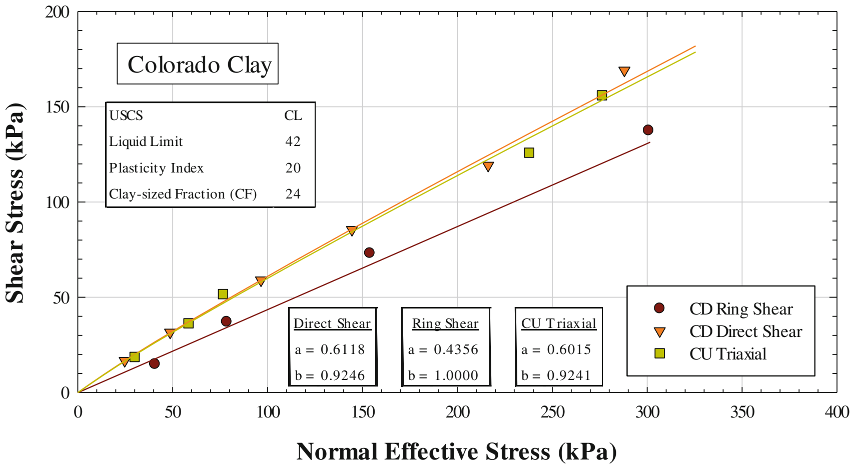

Fig. 3. Fully softened failure envelopes for Colorado Clay.

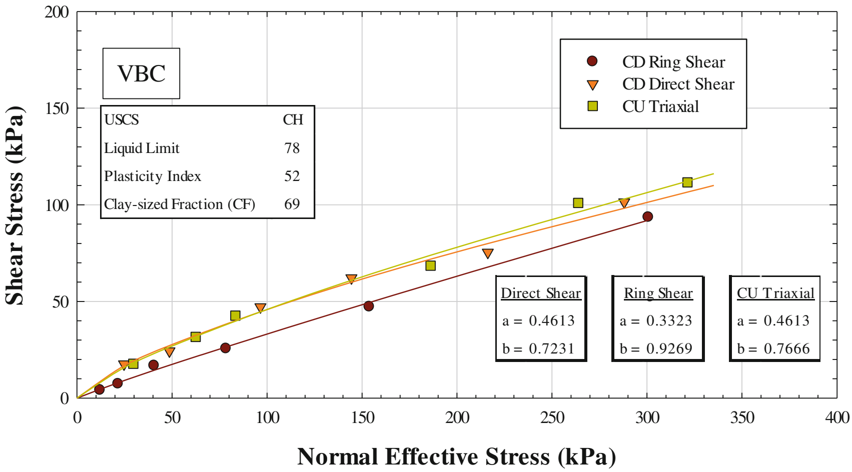

Fig. 4. Fully softened failure envelopes for VBC.

the residual shear strength of soil. Bromhead (1979), who designed a popular device that is commercially available, advised against the use of this device for peak shear strength measurements because of issues with progressive failure. Gamez and Stark (2014) also acknowledge that the results obtained with the ring shear device are too low when compared with the triaxial device. Although both the direct shear and triaxial devices provide reliable values for the fully softened shear strength, the former is recommended for this purpose because is easier and more convenient to use than the later.

Direct Shear Procedures

Measuring the fully softened shear strength using the direct shear device is simpler, faster, and more convenient than with the triaxial device. A test specimen is first sieved through a No. 40 sieve and then mixed to the desired water content. Usually a water content near the liquid limit is used, and a Casagrande liquid limit device can be used to infer the water content. The sample will be at the water content needed when about 24 to 26 blows are required to close the gap cut in the soil in the manner of a regular liquid limit test as specified in ASTM D4318. After the soil sample is at the desired water content, the test specimen is formed inside the direct shear box using a spatula or it can be "piped" in using a pastry bag. After the test specimen is formed, the direct shear tests is conducted as detailed in ASTM D3080. Because of the high water content usually used to form the test specimen, the consolidation stresses need to be applied in steps to prevent the test specimen from extruding out of the shear box. An initial consolidation stress of about 5 kPa is recommended. The final consolidation stress is then reached by using a load increment ratio of one (i.e. doubling the applied stress) until the desired stress is reached. More details about sample preparation procedures and test specimen preparation are presented by Castellanos and Brandon (2014).

Correlations for Fully Softened Strength Parameters

Different correlations have been proposed in the literature to obtain fully softened shear strength parameters (Wright 2005; Tiwari and Ajmera 2011; Gamez and Stark 2014). Castellanos et al. (2016), presented a detailed discussion of the issues concerning the existing correlations to estimate fully softened shear strength parameters. The correlation presented by Stark and Gamez (2014) is perhaps the most commonly used. As explained by Castellanos et al. (2016) this correlation is not recommended because: (1) it was developed using results obtained using the ring shear device, (2) an empirical and unconservative correction was applied, (3) inconsistency exists in the preparation methods used for measuring the index properties, (4) the correlation is not continuous throughout the whole spectrum of clay-sized fraction, among others.

The correlations presented by Castellanos et al. (2016) are shown in Figs. 5 and 6. These correlations were developed for the power function presented by Lade (2010) to characterize the curvature of the fully softened failure envelope shown in Eq. 1. The confidence limits presented in the correlations are provided to characterize the reliability. When the mean value is used, the probability of one of the parameter chosen being higher than the actual value is 50%. Using the mean minus one or two standard deviation decreases this probability to 16% and 2%, respectively. These reliability margins were calculated assuming that the error in the correlation follows a normal or log-normal distribution. Castellanos et al. (2016) also provided equations and details to use the correlations in a probabilistic framework.

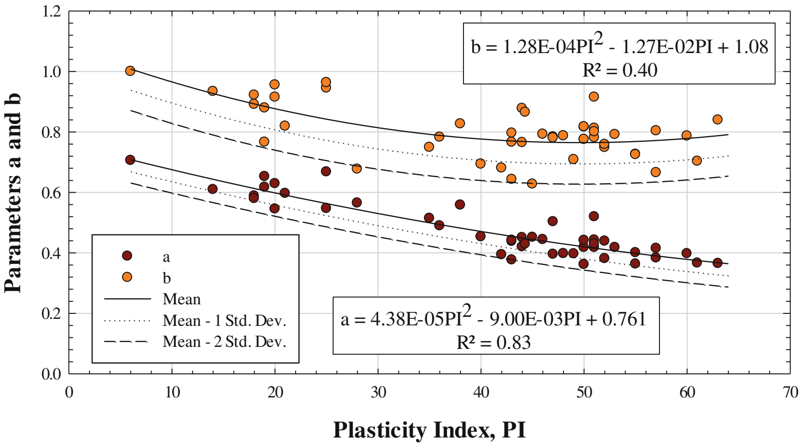

Fig. 5. Fully softened shear strength correlation as a function of PI (Castellanos et al. 2016).

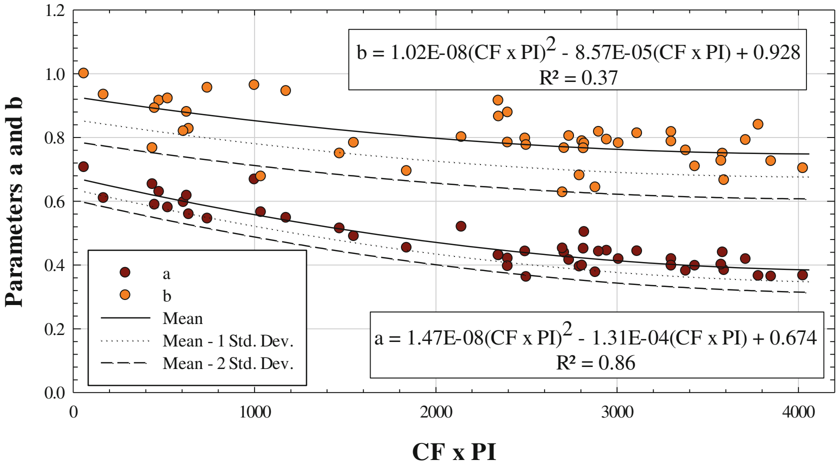

Fig. 6. Fully softened shear strength correlation as a function CF × PI (Castellanos et al. 2016).

$$s = aP_a\left(\frac{\sigma}{P_a}\right)^b \tag{1}$$

where s is the shear strength of the soil, a is equal to the tangent of the secant friction angle for an effective normal stress of one atmosphere, b is an empirical constant describing the curvature of the failure envelope, P_a is the atmospheric pressure, and σ' is the effective normal stress on the failure plane in the same units as atmospheric pressure.

Conclusions

Motivated by recent engineering projects in Texas dealing with high plasticity clays, a renewed interest in the concept of the fully softened shear strength exists in the US. Workshops and conference sessions have been held to identify important aspects of using the fully softened shear strength in practice. Methods of measuring the shear strength using different testing apparatuses have been investigated, and guidelines for using the direct shear test for measuring fully softened shear strengths are described. A new correlation providing shear strength parameters for non-linear failure envelopes for high plasticity clays is presented.

References

Bromhead EN (1979) A simple ring shear apparatus. Gr Eng 12:40–44

Castellanos BA, Brandon TL (2014) Use and measurement of fully softened shear strength, CGPR #79. Center for Geotechnical Practice and Research, Blacksburg

Castellanos BA, Brandon TL, Stephens I, Walshire L (2013) Measurement of fully softened shear strength. In: Proceedings of geo-congress 2013 stab perform slopes embankments, vol III, pp 234–244

Castellanos BA, Brandon TL, VandenBerge DR (2015) Use of fully softened shear strength in slope stability analysis. Landslides. doi:10.1007/s10346-015-0597-y

Castellanos BA, Brandon TL, VandenBerge DR (2016) Correlations for fully softened shear strength parameters. Geotech Test J 39:1–16

Duncan JM, Brandon TL, VandenBerge DR (2011) Report of the workshop on shear strength for stability of slopes in highly plastic clays, CGPR #67. Center for Geotechnical Practice and Research, Blacksburg

Gamez JA, Stark TD (2014) Fully softened shear strength at low stresses for levee and embankment design. J Geotech Geoenviron Eng 140:1–6. doi:10.1061/(ASCE)GT.1943-5606.0001151

Kayyal MK, Wright SG (1991) Investigation of long-term properties of paris and beaumont clays in earth embankments. Center for Transportation Research, University of Texas at Austin, Austin

Lade PV (2010) The mechanics of surficial failure in soil slopes. J Eng Geo 114:57–64. doi:10.1016/j.enggeo.2010.04.003

Mesri G, Shahien M (2003) Residual shear strength mobilized in first-time slope failures. J Geotech Geoenviron Eng 129:12–31

Skempton AW (1970) First-time slides in over-consolidated clays. Géotechnique 20:320–324. doi:10.1680/geot.1970.20.4.343

Skempton AW (1977) Slope stability of cuttings in brown london clay. In: Proceedings of the 9th international conference soil mech found eng, vol 3, pp 261–270

Tiwari B, Ajmera B (2011) A new correlation relating the shear strength of reconstituted soil to the proportions of clay minerals and plasticity characteristics. Appl Clay Sci 53:48–57. doi:10.1016/j.clay.2011.04.021

VandenBerge DR, Duncan JM, Brandon TL (2013) Fully softened strength of natural and compacted clays for slope stability. In: Proceedings of geo-congress 2013 stab perform slopes embankments, vol III, pp 221–233

Wright SG (2005) Evaluation of soil shear strengths for slope and retaining wall stability analyses with emphasis on high plasticity clays. Center for Transportation Research, University of Texas at Austin, Austin

Chemical Influence of Pore Pressure on Brine Flow in Clay-Rich Material

Etienne Cassini[1(✉)], Danila Mylnikov[1], and Roman Makhnenko[1,2]

[1] Laboratory of Soil Mechanics – Chair "Gaz Naturel" Petrosvibri, Swiss Federal Institute of Technology (EPFL), Lausanne, Switzerland
etienne.cassini@epfl.ch
[2] Department of Civil and Environmental Engineering, University of Illinois at Urbana-Champaign, Urbana, USA

Abstract. Hydromechanical properties of shales are complex due to the involved material structure, with the solid matrix being mainly formed by swelling clays and porosity dominated by nanometer scale tortuous voids with large aspect ratios. Intrinsic permeability of restructured Opalinus Clay (Swiss shale) brought to shallow geological storage conditions was measured with *in situ* brine. Under constant temperature, vertical stress, and downstream fluid pressure, steady-state flow experiments show a significant trend of permeability decrease with increasing differential (upstream minus downstream) fluid pressure, thus contradicting the conventional Darcy's description. To interpret these experimental measurements, brine permeability is derived using a one-step self-consistent homogenization scheme based on the knowledge of material's pore structure. While mechanical and thermal effects cannot explain the permeability decrease, the trend is reproduced with the correct order of magnitude by considering a chemical effect: a pore size reduction in the sample due to water adsorption at mineral surface.

Introduction

Shales are fissile rock formations composed of inert mineral inclusions embedded in a clay matrix (Weaver 1988). The amount of clay is usually very high, e.g. around 60% in Opalinus Clay - a Swiss shale (Bossart 2012), and as a consequence shales exhibit certain particular features, such as high level of anisotropy, self-healing capacity, and very low permeability. Because of the high specific surface area of the clay minerals and their *mille-feuille* structure, shale's behavior is also very sensitive to water saturation and its chemical composition. Shales now are broadly considered as seals for nuclear waste and CO_2 storage and in petroleum industry for unconventional gas exploitation. Therefore, fluid and gas permeability, including permeability to *in situ* water or brine, are the key parameters to study for the safety, the efficiency, and the scientific comprehensiveness of the material.

Permeability of a geomaterial is a macro-parameter, which is influenced by the structure of its pore system and eventual chemical phenomenon leading to pore size reduction or pore closure. Permeability measurements provide important information on the material's microstructure, especially in a case where direct investigations at

A. Ferrari and L. Laloui (eds.), *Advances in Laboratory Testing and Modelling of Soils and Shales (ATMSS)*, Springer Series in Geomechanics and Geoengineering,
DOI 10.1007/978-3-319-52773-4_31

the micro-scale are impossible. To conclude on material behavior at micro-level, permeability measurements should demonstrate high level of accuracy and confidence, which can be achieved by the steady-state flow technique. In this paper we discuss the results on permeability measurements for clay-rich material during steady-state flow of brine and interpret them considering water adsorption, with a one-step self-consistent homogenization scheme.

Experimental Methods

Remolded (i.e., reconstituted) shale – Opalinus Clay – saturated with natural brine (Pearson 2002) is studied in the current work. Remolded specimens are prepared by crushing the intact material in a grinder, sieving the particles with a size smaller than 0.5 mm, mixing with brine corresponding to approximately 1.5 times the liquid limit (or 60%), and consolidating at 350 kPa vertical stress for at least 72 h in one-dimensional conditions. Obtained cylindrical specimens have porosity of 0.33 and the degree of saturation is 0.85 – 0.90. Crushing of shale preserves the flake-like structure

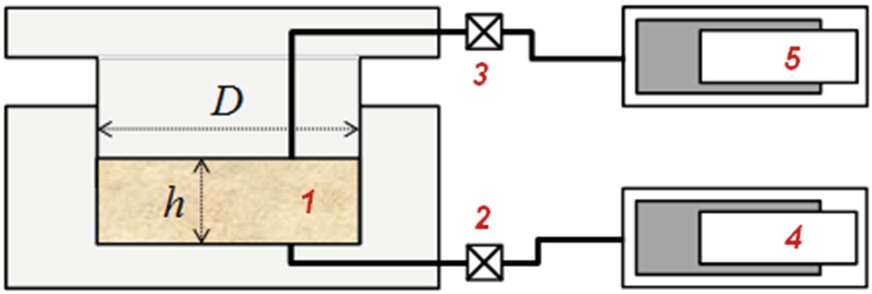

Fig. 1. Scheme of the experimental setup. 1 – rock specimen inside the oedometric cell; 2 and 3 – upstream and downstream pressure transducers respectively; 4 and 5 – upstream and downstream pressure/volume controllers respectively.

of an intact material and eliminates structural anisotropy.

Tested specimen (height h = 12.5 mm and diameter D = 35 mm) is then gradually brought to *in situ* conditions in the oedometric cell: 27 MPa axial total stress (σ_v) and 8 MPa pore pressure (p), which results in the porosity reduction to 0.15. Back pressure saturation method is implemented for 7 days with graduate increase of upstream and downstream pressures and promoting the flow through the specimen. It allows achieving full saturation (at p > 7 MPa) that is confirmed by measurements of constant Skempton's B coefficient values while the effective mean stress (P') is preserved to be the same (ASTM D4767 2011) and equal to 9 MPa. Recorded undrained pore pressure increments are corrected for the influence of "dead" volume (Makhnenko and Labuz 2016) and provide B = 0.85, while B is measured to be isotropic and equal to 0.99 in conventional triaxial cell at $P' = 0.2$ MPa. Effective mean stress and bulk modulus are calculated from applied vertical stress and vertical deformation by taking drained Poisson's ratio $v = 0.3$ (measured in conventional triaxial test at $P' = 0.2 - 0.7$ MPa). Biot coefficient α is calculated from measured unjacketed bulk modulus $K_s' = 8.9$ GPa and the bulk modulus of the brine at pressures above 3 MPa is found to be $K_{br} = 2.0$ GPa – slightly lower than the one of pure water. Summary of the material parameters of investigated remolded shale is given in Table 1.

Table 1. Material properties of remolded shale at $\sigma_v = 27$ MPa, $p = 8$ MPa.

Porosity n, [-]	Bulk modulus K, [GPa]	Skempton's coef. B, [-]	Biot coef. α, [-]	Poisson's ratio v, [-]
0.15	2.5	0.85	0.72	0.3

Results

Brine permeability of shale is reported as an intrinsic permeability k_{int} that is determined from Darcy's law after achieving steady-state flow conditions:

$$k_{int} = \frac{4\eta_{br} h \Delta V}{\pi D^2 \Delta p_{diff} \Delta t} \tag{1}$$

Here η_{br} is brine viscosity equal to 0.001 Pa·s, Δp_{diff} is the differential fluid pressure, and ΔV is the fluid volume that passed through the specimen during the time period Δt. The differential fluid pressure is determined as the difference in readings of the upstream and the downstream pressure transducers (Fig. 1). Upstream and downstream pressure/volume controllers provide measurements of brine volume that enters and exits the specimen respectively.

Considering all the contributing factors, permeability is reported with the accuracy of 2.5% when the duration of steady-state flow exceeds 12 h. Steady-state condition and the consistence of the measurements are ensured by obtaining constant permeability values with standard deviation of 2.5% for several consecutive flow cycles at a fixed differential fluid pressure.

Permeability of the material is measured at several differential pressure values after the steady-state flow of brine is established through the specimen. Downstream fluid

Table 2. Values of brine permeability for the remolded shale as a function of differential fluid pressure.

Differential pressure, MPa	1.5	3.0	6.0	8.0
Intrinsic permeability, m^2	1.3e-20	1.2e-20	9.0e-21	8.5e-21

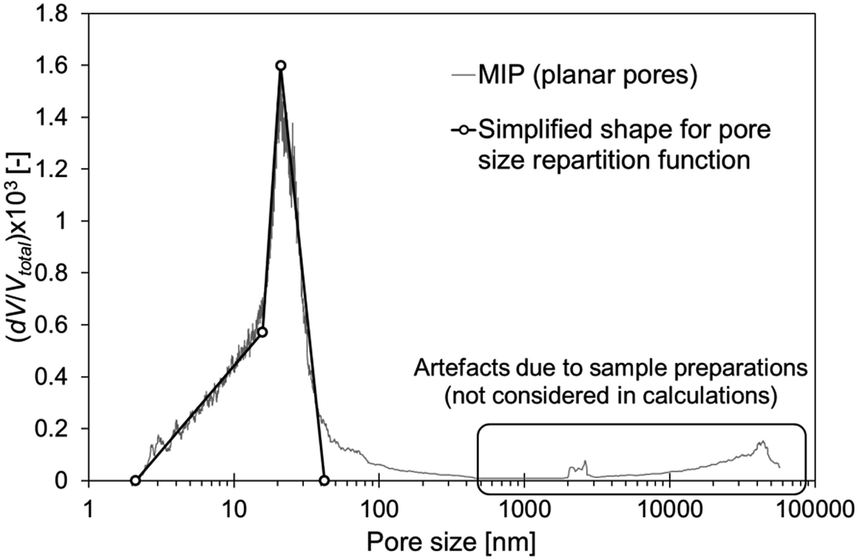

Fig. 2. MIP measurements of pore size distribution in tested remolded shale with hypotheses of planar pores (*V* - volume of intruded mercury).

pressure is kept at constant value of 8 MPa, while upstream pressure is increased several times. The results demonstrate consistent nonlinear decreasing trend of brine permeability with increasing differential fluid pressure (Table 2).

Measured values of remolded shale (Opalinus Clay) permeability are $\sim 10^{-20}$ m^2, while reported intrinsic permeability of the intact material ranges from 10^{-21} to 10^{-19} m^2 (Romero et al. 2013). Mercury intrusion porosimetry (MIP) measurements performed on the tested sample show a mono-modal pore size repartition with a peak at 21 nm inter-platelet distance (Fig. 2). Pores of this size are supposed to be flat (crack-like) and localized in the clay matrix.

Discussion

Observed decreasing trend of intrinsic brine permeability of remolded shale, with increasing fluid differential pressure at constant downstream pressure, cannot be explained using only the poromechanical considerations. An increase in brine pressure upstream with constant downstream pressure should lead to increase in both porosity and pores size upstream and preserve the microstructure downstream, leading to a global increase of the permeability. Moreover, this increase in porosity and permeability is evaluated using poroelastic relationships to be on the order of a few percent, whereas the decrease in permeability observed here is of 35%. Also, the observed trend cannot be explained by a thermal effect, e.g., for a conservative calculation that considers unidirectional flow between two adiabatic platelets. Using Stokes equations for non-isotherm viscous flow and brine thermal conduction at 24 °C of 0.6 $W \cdot m^{-1} \cdot K^{-1}$, the elevation of temperature along the flow can be shown to be much lower than 1 °C.

Suggested explanation of the experimental observations deals with chemistry and a reduction of the brine accessible porosity in the upstream section of the sample where brine pressure is higher. Due to the characteristic structure of shale, with very small pores and high specific surface area, brine adsorption at the clay surface, which increases with fluid pressure, should be considered. The thickness of a single layer of water is of 0.3 nm, so the adsorption of multiple water layers at the surface of clay minerals in the shale sample can lead to the closure of the smallest pores ($\sim$ nm) and cause a reduction of the effective pore size of the larger pores.

In this work, a numerical derivation of the sample permeability, assumed to be isotropic, is performed based on continuum fluid mechanics and homogenization theory (Dormieux et al. 2006). The goal of the modeling is to investigate if water adsorption is a good candidate for explaining the experimental data, both in terms of the trend and the order of magnitude. The simulation is based on a decomposition of the sample in 20 vertical layers where pressure is supposed to be constant. The permeability of each layer is calculated iteratively from upstream to downstream to determine the brine pressure in the next layer and then deduce its permeability. Flow is constant between the different layers and the convergence criterion is on the downstream pressure. Calculations are performed in MatLab©.

Based on continuum fluid mechanics considerations at the nanoscale and a slipping boundary condition between brine and mineral surface (Klinkenberg effect), the local tangential permeability k_t in a planar pore is

$$k_t = \frac{(h - 2\Delta h)^2}{4}\left(\frac{1}{3} + \frac{\beta}{h - 2\Delta h}\right) \tag{2}$$

Here h is the interplatelet distance, Δh is the thickness of the adsorbed layer of water, and β is a slipping parameter for the flow boundary condition. From molecular dynamics simulations (Botan et al. 2011), β value is fixed at 0.21 nm. The term (h - $2\Delta h$) represents the effective accessible pore size. Formally, this relationship holds for planar pores with an opening larger than the thickness of a few water layers (e.g., 10) and continuum mechanics is no longer valid in smaller pores, where the discreteness of water molecules should be considered. However, here we accept continuum mechanics considerations for pore openings larger than one water layer, i.e. 0.3 nm, and smaller pores are assumed to be impermeable.

Equation (2) is considered to be a fair approximation for oblate pores with high aspect ratios and the local permeability is used in a one-step self-consistent scheme similar to the one proposed by Cariou(2010). Although in the present work the mineral solid matrix is not spherical, but oblate with the aspect ratio $\gamma_s < 1$. In this case, a small variation of the aspect ratio can lead to an order of magnitude difference in the homogenized permeability (Fig. 3). The localization tensor in the case of oblate pores,

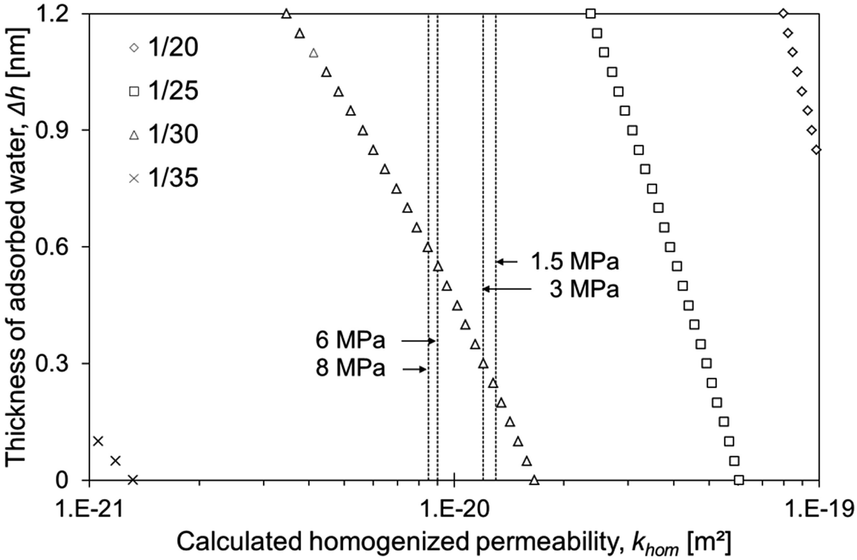

Fig. 3. Calculated homogenized permeability for different values of the thickness of the adsorbed water layer and different aspect ratio of the solid particles. The dashed vertical lines indicate the experimental results dependence on the differential fluid pressures.

or mineral inclusions, is calculated from equations provided by Giraud et al. (2015). This is a first order approach to derive shale properties, as a true homogenization scheme for shales should be two stepped: one step for the clay matrix and another one for the inert mineral inclusions.

The homogenization scheme is applied for different values of γ_s and Δh to investigate the influence of these parameters. Results are displayed in Fig. 3 and demonstrate the strong dependence on the solid aspect ratio, small variation of which can lead to an order of magnitude change in permeability. For a well-chosen solid aspect ratio, here 1/30, experimentally observed permeability decrease trend can be linked to the passage from one adsorbed water layer ($\Delta h \approx 0.3$ nm) to two layers ($\Delta h \approx 0.6$ nm). Adsorption of brine is then related to its pressure with a Toth (1971) adsorption isotherm:

$$\Delta h = \Delta h_m \frac{\left(p/p_{ref}\right)^t}{1 + \left(p/p_{ref}\right)^t} \tag{3}$$

where Δh_m is the maximum thickness of adsorbed water, chosen as a multiple of 0.3 nm, and p_{ref} and t are fitting parameters. Two examples of numerical simulations of sample permeability with this model are shown in Fig. 4, reproducing the decreasing permeability trend within the order of magnitude. Proper measurements of the adsorption parameters should be based on independent brine injection tests, while the intrinsic material permeability could be measured with an inert gas, providing further insight into the nature of complicated hydro-mechanical behavior of clays and shales.

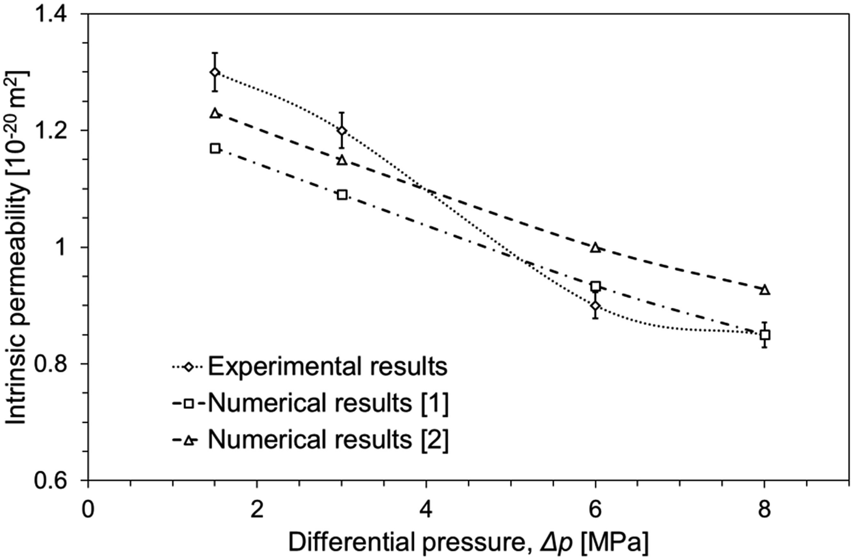

Fig. 4. Brine permeability evolution of remolded shale specimen with differential fluid pressure, experimental results (diamonds with error bars) and numerical simulations. Adsorption model parameters are Δh_m = 1.2 nm, p_{ref} = 13 MPa, and t = 3.5 in simulation [1] (squares), and Δh_m = 0.9 nm, p_{ref} = 12 MPa, and t = 4 in simulation [2] (triangles).

Conclusions

Flow measurements performed on a sample of remolded shale (Opalinus clay) show a significant decrease of brine permeability with increasing brine pressure. Influence of mechanical and thermal effects on this trend are negligible, while brine adsorption in the sample leading to a modification in the fluid accessible porosity has been considered as a possible option to explain the observed permeability decrease. Though numerical results are very sensitive to the hypothesis made for the pore structure (e.g., value of the solid particles aspect ratio) and the choice of parameters for the adsorption isotherm, they predict the decreasing permeability trend within the order of magnitude. For the better understanding of material behavior, permeability is suggested to be independently measured with an inert gas. Then, brine injection and flow tests could be used to determine the adsorption parameters and explain the complicated nature of hydro-mechanical behavior of clay-rich and shaley materials.

Acknowledgements. Opalinus clay cores were provided by Swisstopo in the framework of Mont Terri project, CS-C experiment. R. Makhnenko acknowledges the support from SCCER-SoE (Switzerland) grant KTI.2013.288 and Swiss Federal Office of Energy (SFOE) project CAPROCK #810008154.

References

ASTM D4767 (2011) Standard Test Method for Consolidated Undrained Triaxial Compression Test for Cohesive Soils

Bossart P (2012) Characteristics of the Opalinus Clay at Mont Terri. http://www.mont-terri.ch/internet/montterri/de/home/geology/key_characteristics.html

Botan A, Rotenberg B, Marry V, Turq P, Noetinger B (2011) Hydrodynamics in clay nanopores. J Phys Chem C 115(32):16109–16115

Cariou S (2010) Couplage hydro-mécanique et transfert dans l'argilite de Meuse/Haute-Marne: approches expérimentale et multi-échelle (Doctoral dissertation, Ecole des Ponts ParisTech)

Dormieux L, Kondo D, Ulm FJ (2006) Microporomechanics. Wiley, Chichester 327 p

Romero E, Senger R, Marschall P, Gomez R (2013) Air tests on low-permeability claystone formations. Experimental results and simulations. In: Laloui L, Ferrari A (eds) Multiphysical Testing of Soils and Shales., Springer Series in Geomechanics and Geoengineering, Springer, Heidelberg, pp 69–83

Giraud A, Sevostianov I, Chen F, Grgic D (2015) Effective thermal conductivity of oolitic rocks using the Maxwell homogenization method. Int J Rock Mech Mining Sci 80:379–387

Makhnenko RY, Labuz JF (2016) Elastic and inelastic deformation of fluid-saturated rock. Phil Trans R Soc A 374:20150422. doi:10.1098/rsta.2015.0422

Pearson FJ (2002) PC experiment: recipe for artificial pore water. Mont Terri Project, Technical Note 2002–17

Toth J (1971) State equations of the solid-gas interface layers. Acta Chim Acad Sci Hungar 69 (3):311–328

Weaver CE (1988) Clays, Muds, and Shales. Elsevier, Amsterdam, 819 p

Development of Classification Charts for Q Index of Shale from the Parameters

Nandyala Darga Kumar(✉), Ravikant R. Singh, Faijal Ali, and Efray'im

Fiji National University, Suva, Fiji Islands
darga.nandyala@fnu.ac.fj

Abstract. Construction of tunnels, slopes, deep basements, foundations and retaining walls are common in shale. Quality of shale can be assessed based on the Q index system. This paper presents the analysis of charts developed for Q index of shale from three different parameters such as block size (RQD/J_n), inter-block shear strength (J_r/J_a) and active stress (J_w/SRF). For the range of values chosen for RQD/J_n, J_r/J_a and J_w/SRF a Q index was estimated and charts were established between Q index and RQD/J_n for various values of J_r/J_a and J_w/SRF. The charts presented in the paper for Q index can be used to classify the shale. Shale should have minimum J_r/J_a, J_w/SRF and RQD/J_n as 0.5, 0.2 and 10 respectively to be classified as good to very good category.

Introduction

Shale is the most abundant sedimentary rock worldwide and is characterized by breaks along thin laminae, parallel layering, bedding less than one centimeter in thickness (Coveney 2003). Black shale contains organic material that sometimes breaks down to form natural gas or oil. Shale is commonly used to produce clay, cement and also used in construction of embankments and highways. The potential uses of shale in road construction include general fill, selected granular fill, capping and sub-base (Winter 2001). Shale is a rock composed mainly of clay-size mineral grains such as illite, kaolinite, and smectite. Shale has a very small particle size, so the void spaces are very small. Some soils which are derived from shale are troublesome for the construction of infrastructure because they undergo changes in volume upon wetting and drying (Derakhshandeh 1989). Landslides are common in most of the shale formations. Due to weathering, the shale becomes a clay-rich soil which normally has a very low shear strength, especially when wet. When these low-strength materials are wet and on a steep hillside, they can slowly or rapidly move down slope. Progressive undercutting and time dependent deformations can result in frequent rock falls and dangerously unstable conditions (Shakoor and Rodgers 1992; Bonini et al. 2009).

Shales of less than certain stiffness are not considered the best materials for hydraulic fracturing operations in construction (Britt and Schoeffler 2009). Swelling of shale can result in lot of maintenance cost (Einstein 2000). Predicting the ground response for tunnels in weak shales remains challenging (Derek Martin 2015). To understand the behavior of shale, it is required to develop empirical equations that relate unconfined

A. Ferrari and L. Laloui (eds.), *Advances in Laboratory Testing and Modelling of Soils and Shales (ATMSS)*, Springer Series in Geomechanics and Geoengineering,
DOI 10.1007/978-3-319-52773-4_32

compressive strength and internal friction angle of sedimentary rocks such as sandstone, shale, and limestone and dolomite to physical properties like velocity, modulus, and porosity. The empirical equations are more appropriate to estimate rock strength from parameters measurable with geophysical well logs (Chang et al. 2006).

Q Index

Design and support recommendations for underground excavations, retaining structures, foundations, tunnels are dependent on quality of the rock/shale mass which can be expressed in the form of Q index as presented in below equation (Barton et al. 1974; Barton 2002).

$$Q = \left(\frac{RQD}{J_n}\right)\left(\frac{J_r}{J_a}\right)\left(\frac{J_w}{SRF}\right)$$

where, *RQD* is the Rock Quality Designation, J_n is the joint set number, J_r is the joint roughness number, J_a is the joint alteration number, J_w is the joint water reduction factor, *SRF* is the stress reduction factor. The rock quality index Q can be considered to be a function of only three parameters which are block size (RQD/J_n), inter-block shear strength (J_r/J_a) and active stress (J_w/SRF). The Q-index is sufficiently flexible to identify the potential fall of ground hazard if it is properly used and also it can be used as a guideline to more cost-effective support designs (Hartman and Handley 2002). Bertuzzi and Pells (2002) presented different classes of shales (Table 1).

Table 1. Shale classification (Bertuzzi and Pells 2002)

Class/parameter	Class 1	Class 2	Class 3	Class 4	Class 5
RQD/J_n	22.5–50	17.5–22.5	6.7–15	4.2–10	–
J_r/J_a	1–3	0.25–2	0.17–1	0.04–0.25	0.17–0.33
J_w/SRF	1	0.5–1	0.2–1	0.066–0.4	0.066–0.2
$Q = \left(\frac{RQD}{J_n}\right)\left(\frac{J_r}{J_a}\right)\left(\frac{J_w}{SRF}\right)$	22.5 to 150	2.2 to 45	0.2 to 15	0.011 to 1	0.009 to 0.27
Classification of shale	Good to extremely good	Poor to very good	Very poor to good	Extremely poor to very poor	Exceptionally poor to very poor

Discussion on Q Index Variation and Classification Charts for Shale

The variation of Q index is discussed with the range of values chosen for three parameters such as RQD/J_n, J_r/J_a and J_w/SRF of shale. The values chosen for block size parameter, RQD/J_n, are 4, 8, 12, 16, 20, 24, 28, 32, 36, 40, 44, 48, 52 and for inter-block shear strength parameter, J_r/J_a, are 0.01, 0.05, 0.1, 0.5, 1, 2 and 3.

The values chosen for active stress parameter, J_w/SRF, are 0.05, 0.1, 0.2, 0.5 and 1. These range of values for the above three parameters are chosen as per the classification presented in Table 1.

The variations of Q index are presented in Figs. 1, 2, 3, 4, 5, 6 and 7. Figure 1 presents the Q index variation for J_r/J_a = 0.01. From this figure, it can be noticed that as the RQD/J_n varies from 4 to 54 the Q index is increasing for all the stress parameters, J_w/SRF. The increase in Q index is higher for the active stress parameters 0.5 and 1. Though the increase is noticed in Q index, this value is considerably below for all the active stress parameters considered. As per the classification of shale (Table 1), the Q index presented in Fig. 1 can be utilised to classify extremely poor to very poor shale for the given parameters such as block size, inter-block shear strength and active stress.

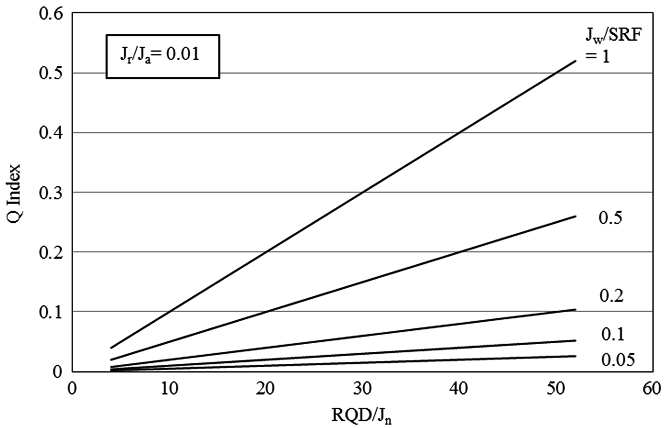

Fig. 1. Variation of Q index with RQD/J_n for J_r/J_a = 0.01

Figure 2 presents Q index variation corresponding to inter-block shear strength parameter, J_r/J_a = 0.05. For any value of RQD/J_n, as J_w/SRF increases from 0.05 to 1, the increase in Q index is noticed as 20 times. Similarly for J_w/SRF variations from 0.5 to 1, the increase in Q index is found to be 2 times for all values of RQD/J_n. The lowest and highest values of Q index shown in Fig. 2 are 0.01 and 2.6 and, as per the classification of shale presented in Table 1, this figure can be utilised to classify the shale of category very poor to poor and also moderately good. The variation of Q index for inter-block shear strength parameter J_r/J_a = 0.1 is presented in Fig. 3. The lowest and highest Q index values that can be noticed from the figure are 0.02 and 5.4. The Q index variations presented in figure for J_w/SRF = 0.05, 0.1 and 0.2 can be utilised for classifying the extremely poor to very poor category of shale. The lines drawn for J_w/SRF = 0.5 and 1 can be utilised to classify the shale of poor to good category.

From Fig. 4, it can be noticed that the lowest and highest values of Q index are 0.1 and 26 corresponding to an inter-block shear strength parameter, J_r/J_a = 0.5. This figure can be utilised to classify the very poor to good and poor to very good category of shale. For J_r/J_a = 1, the variation in Q index is presented in Fig. 5. From this figure,

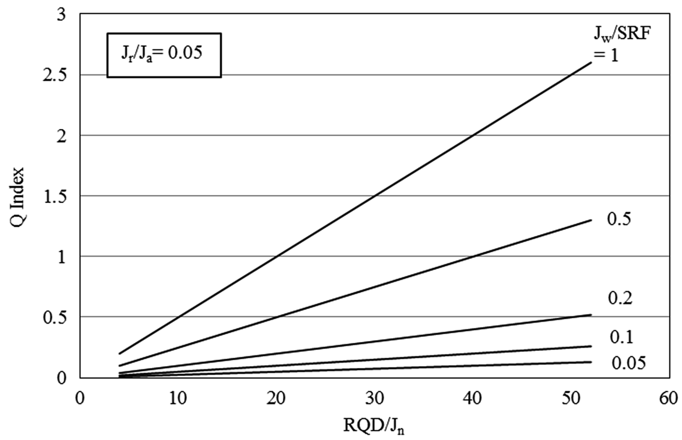

Fig. 2. Variation of Q index with RQD/J_n for J_r/J_a = 0.05

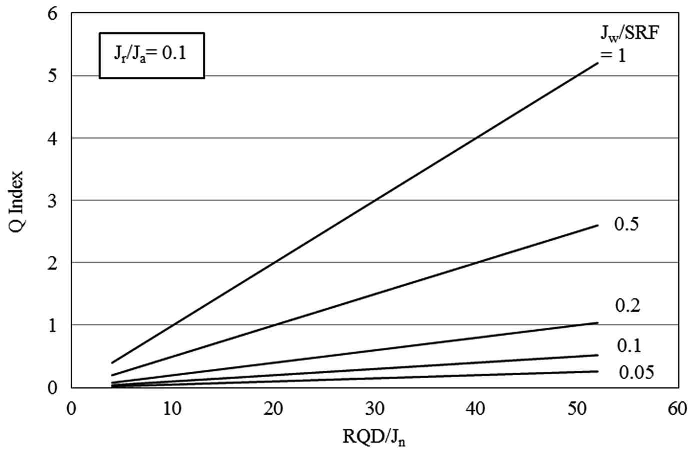

Fig. 3. Variation of Q index with RQD/J_n for J_r/J_a = 0.1

it can be seen that the lowest and highest values of Q index are 0.2 and 54. In this figure, the lines drawn for J_w/SRF = 0.05, 0.1 and 0.2 can be utilised to classify the shale of category extremely poor to good whereas the lines drawn for J_w/SRF = 0.5 and 1 can be utilised to classify the shale from very poor to very good.

For J_r/J_a = 2 and 3, the variation in Q index is presented in Figs. 6 and 7. These two figures present the Q index for higher values of inter-block shear strength parameters. A good increase in Q index can be seen even at low values of active stress parameter such as 0.05, 0.1 and 0.2 corresponding to higher values of RQD/J_n higher than 30. These two figures can be utilised to classify the shale of category poor to extremely good. The variations of Q index drawn for various RQD/J_n and J_w/SRF corresponding to inter-block shear strength parameter J_r/J_a = 0.01, 0.05 and 0.1 shown in Figs. 1, 2 and 3,

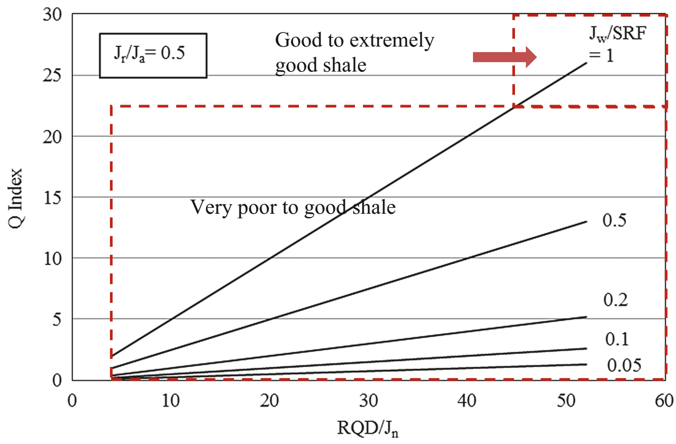

Fig. 4. Variation of Q index with RQD/J_n for J_r/J_a = 0.5

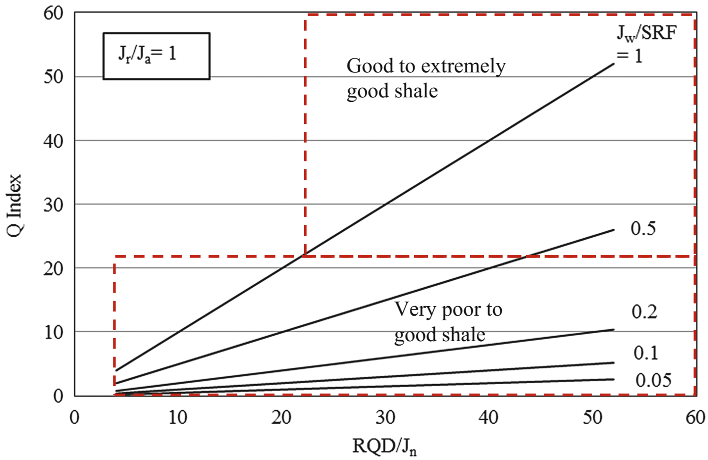

Fig. 5. Variation of Q index with RQD/J_n for J_r/J_a = 1

are none is representing the shale classification as good to extremely good. Whereas Figs. 4, 5, 6 and 7 are representing the good to extremely good classification of shale as the area shown in dotted lines.

From the Figs. 4, 5, 6 and 7, it can be noticed that the shale to be classified as good to extremely good, the three parameters which are contributing the Q index value such as J_r/J_a, J_w/SRF and RQD/J_n are supposed to be of minimum of 0.5, 0.2 and 10 respectively. The analysis presented in Figs. 1, 2, 3, 4, 5, 6 and 7 can be utilised for the classification of shale and for intermediate values, the Q index can be estimated from the linear interpolation.

From the above variations of Q index, it is noticed that J_r/J_a is the main parameter influencing the classification of shale. The parameter, J_r/J_a represents the roughness and

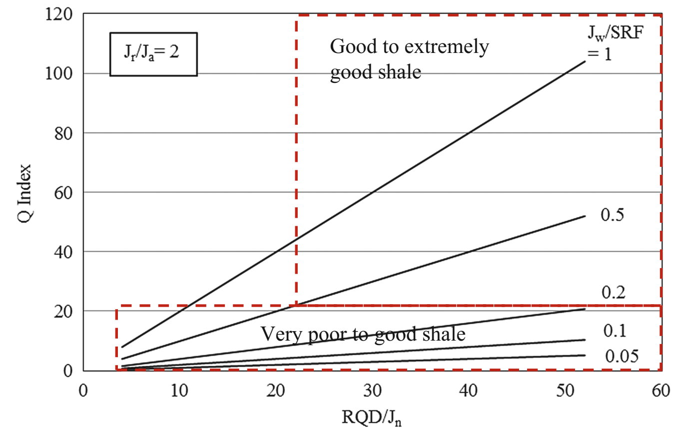

Fig. 6. Variation of Q index with RQD/J_n for J_r/J_a = 2

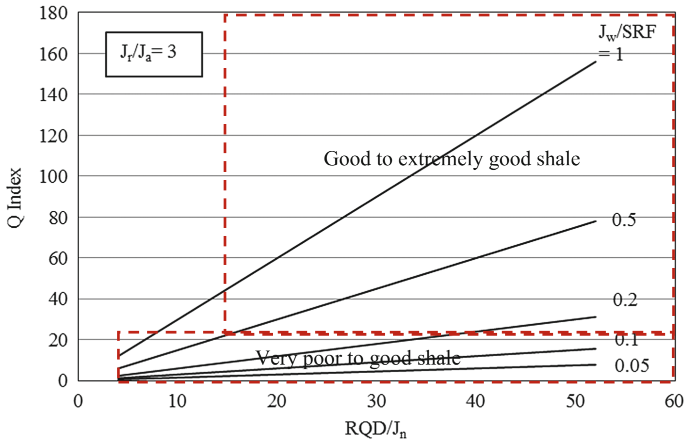

Fig. 7. Variation of Q index with RQD/J_n for J_r/J_a = 3

frictional characteristics of the joint walls or filling materials. This parameter is weighted in favor of rough, unaltered joints in direct contact. High values of this parameter represent better mechanical quality of the shale. The J_r of shale 0.5 and below and J_a 12 and above can result in J_r/J_a less than 0.1. This in fact leads to shale of classification extremely poor to poor quality.

As the inter-block strength parameter, J_r/J_a increases from 0.5 to 3, the RQD/J_n required qualifying the shale as good to extremely good is decreasing from 45 to 15. Similarly, as the J_r/J_a increases from 0.5 to 3, the J_w/SRF required qualifying the shale as good to extremely good is decreasing from 1 to almost 0.2.

Conclusion

The Q index value is low and it is less than 5.2 for inter-block shear strength parameter, $J_r/J_a = 0.01$, 0.05 and 0.1, irrespective of range of values chosen for block size, RQD/J_n, and active stress parameter, J_w/SRF. For the lower values of J_r/J_a the shale is falling in the very poor to poor category. For the range of values of $J_r/J_a = 0.5$ and above depending upon chosen values of RQD/J_n and J_w/SRF, the shale is falling under the category of very poor to good and good to extremely good. Overall, the inter-block shear strength parameter is the main deciding parameter for the classification of shale. In-situ shear strength measurement and estimation of index properties of shale is very important in classifying the shale towards quality assurance of any construction activity on shale.

References

Barton NR (2002) Some new Q-value correlations to assist in site characterization and tunnel design. Int J Rock Mech Min Sci 39(2):185–216. doi:10.1016/S1365-1609(02)00011-4

Barton NR, Lien R, Lunde J (1974) Engineering classification of rock masses for the design of tunnel support. Rock Mech Rock Eng 6(4):189–236. doi:10.1007/BF01239496 Springer

Bertuzzi R, Pells PJN (2002) Geotechnical parameters of Sydney stone and shale. Aust Geomech 37(5):41–54

Bonini M, Debernardi D, Barla M, Barla G (2009) The mechanical behaviour of clay shales and implications on the design of tunnels. Rock Mech Rock Eng 42:361. doi:10.1007/s00603-007-0147-6

Britt LK, Schoeffler J (2009) The geomechanics of a shale play: what makes a shale prospective. SPE Eastern Regional Meeting, Society of Petroleum Engineers, 9 pp

Chang C, Zoback MD, Khaksar A (2006) Empirical relations between rock strength and physical properties in sedimentary rocks. J Petrol Sci Eng 51:223–237. Elsevier

Coveney RM (2003) Metalliferous paleozoic black shales and associated strata. In: Lenz DR (ed) Geochemistry of sediments and sedimentary rocks Geotext, vol 4. Geological Association of Canada, pp 135–144

Derek Martin C (2015) Behaviour of shales in underground environments. In: 13th ISRM international congress of rock mechanics, 10–13 May, Montreal. International Society for Rock Mechanics. ISBN 978-1-926872-25-4

Einstein HH (2000) Tunnels in Opalinus clay shale-a review of case histories and new developments. Tunn Undergr Space Technol 15(1):13–29. Elsevier Science Ltd.

Hartman W, Handley MF (2002) The application of the Q-tunneling quality index to rock mass assessment at Impala Platinum mine. J S Afr Inst Min Metall 102(3):155–165

Derakhshandeh M (1989) Monitoring of nondurable shale fills in semi – arid climates, Report No. CDOH-DTD-R-89-8, Colorado Department of Highways, Colorado

Shakoor A, Rodgers JP (1992) Predicting the rate of shale undercutting along highway cuts. Environ Eng Geosci. doi:10.2113/gseegeosci.xxix.1.61

Winter MG (2001) Spent oil shale use in earthwork construction. Eng Geol 60(1–4):285–294. Special issue on geoenvironmental engineering

Exploring Fissure Opening and Their Connectivity in a Cenozoic Clay During Gas Injection

Laura Gonzalez-Blanco[1], Enrique Romero[1](✉), Cristina Jommi[2], Xavier Sillen[3], and Xiangling Li[4]

[1] Universitat Politècnica de Catalunya, Barcelona, Spain
Enrique.romero-morales@upc.es
[2] Delft University of Technology, Delft, The Netherlands
[3] ONDRAF/NIRAS, Brussels, Belgium
[4] EIG EURIDICE, Mol, Belgium

Abstract. Gas transport properties in argillaceous rocks are becoming an important issue within different contexts of energy-related geomechanics (disposal of radioactive waste, production of shale gas, CO_2 sequestration). The present investigation aims at describing the pathways generated on a deep Cenozoic clay during gas injection using different microstructural techniques. Mercury intrusion porosimetry results have allowed detecting fissures after gas injection tests that have not been observed on intact samples. The opening of these pressure-dependent fissures plays a major role on gas permeability. A complementary insight into the connectivity of these fissures has been quantified by micro-computed tomography.

Introduction

The migration of gases through argillaceous rocks is an important issue in energy-related geoengineering applications, such as CO_2 geological sequestration, extraction of gas shale and nuclear waste geological storage. Within this last context, gases can be produced in the post-closure phase of the disposal system and may have a significant impact on the long-term performance of the host rock formation (ONDRAF/NIRAS 2013; Shaw 2013). The pressure resulting from the gas generation in an almost impermeable host rock will increase, and micro-cracks and fissures (gas pathways) may develop as a consequence of the deformation induced by stress and gas pressure changes, as well as by taking advantage of the material heterogeneity, anisotropy or rock discontinuities. These pathways have an important impact on gas intrinsic permeability, as a consequence of the strongly coupled response of the gas flow and the mechanical behaviour.

Evidence of fissure opening induced by air injection has been detected with mercury intrusion porosimetry (MIP) (Gonzalez-Blanco *et al.* 2016). This technique presents data on entrance pore sizes and their distribution, but does not provide information on their shape (pore or fissure) – unless fractal analysis is used – or on their connectivity. The use of new tomographic techniques in the geotechnical field, such as

A. Ferrari and L. Laloui (eds.), *Advances in Laboratory Testing and Modelling of Soils and Shales (ATMSS)*, Springer Series in Geomechanics and Geoengineering,
DOI 10.1007/978-3-319-52773-4_33

X-ray micro-computed tomography (μCT), nuclear magnetic resonance (NMR) or focussed ion beam-scanning electron microscopy (FIB-SEM), appear to be encouraging to complement the microstructural characterisation (Muurinen *et al*. 2013; Fleury and Canet 2014; Desbois *et al*. 2014; Hemes *et al*. 2015).

This work particularly addresses the changes in the pore network of Boom Clay induced by air injection using MIP and μCT. Boom Clay is a potential Cenozoic sedimentary clay formation in Belgium for the geological disposal of long-living and heat-emitting radioactive waste. MIP tests will allow quantifying the pore volumes associated with the micro and macroporosity, as well as the pore size distribution changes before and after air injection, whereas μCT images will be mainly used to quantify the connectivity of the pore network.

Air Injection Tests on Boom Clay

Boom Clay (Northwest European Tertiary Basin) with dominant kaolinitic-illitic clay fraction was retrieved at a depth of 223 m in the Underground Research Laboratory facility of EURIDICE at Mol, Belgium. The void ratio of the retrieved clay was between 0.56 and 0.61 with an air-entry value around 4.8 MPa. Main geotechnical properties are described in Gonzalez-Blanco *et al*. (2016).

An instrumented high-pressure and high-stiffness oedometer cell (20-mm thick samples and 50 mm in diameter) was used to perform the air tests and to determine the soil volume changes during air injection and dissipation stages. The air injection (bottom cap) was performed at a constant volume-rate of 100 mL/min on a sample with bedding planes parallel to air flow and at a constant total vertical stress of 6 MPa (A to

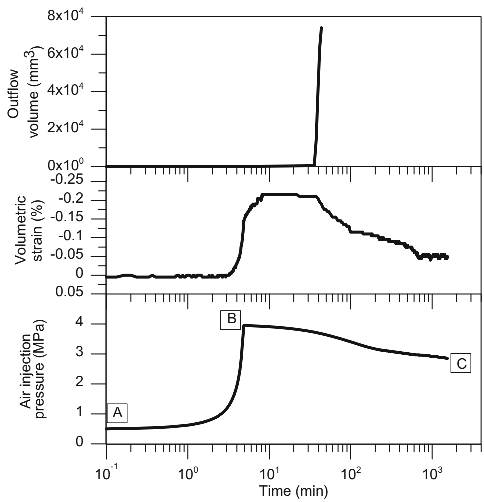

Fig. 1. Time evolution of outflow volume, volumetric strain and air injection pressure during the air injection/dissipation test (A to B: air injection stage; B: shut-off; B to C: dissipation stage).

B in Fig. 1). When air pressure reached a maximum of 4 MPa (below the air-entry value of the material), the air injection piston was stopped (shut-off at point B in Fig. 1), and then allowed decaying at constant air volume of the inlet line (B to C in Fig. 1). The sample at constant total vertical stress displayed some small expansion (negative volumetric strain) during the air injection stage. After shut-off, expansion continued as the air pressure front propagated into the sample, inducing the pore fluid pressure to increase and the constitutive stress to decrease. Some elapsed time later after shut-off, the air injection pressure started to decline along the dissipation stage towards point C with a sharp increase of the outflow volume through the top cap (upper graph in Fig. 1). Consequently, the constitutive stress increased inducing compression on the material. The expansion deformation induced during the air injection and early shut-off stages may cause some damage on the material (Gonzalez-Blanco *et al*. 2016).

Mercury Intrusion Porosimetry

MIP tests were performed on intact Boom Clay and after air injection tests (Autopore IV 9500, Micrometrics). Instantaneous freezing was carried out by plunging small samples (around 1000 mm^3) into liquid nitrogen and then applying vacuum to ensure microstructure preservation. Desbois *et al*. (2014) showed that no significant changes in the quantification of pore sizes and pore morphologies were produced due to this sublimation process.

Figure 2a presents the pore size density functions for the intact material and after the air tests in terms of the intruded volume of mercury referred to the volume of solids (non-wetting void ratio e_{nw}) for different entrance pore sizes x (Romero and Simms 2008). As indicated in the figure, a new family of large pores, which was not detected on intact samples and on loaded samples without air injection, was observed after the air tests. This new dominant pore size at entrance sizes larger than 2 µm appeared to be

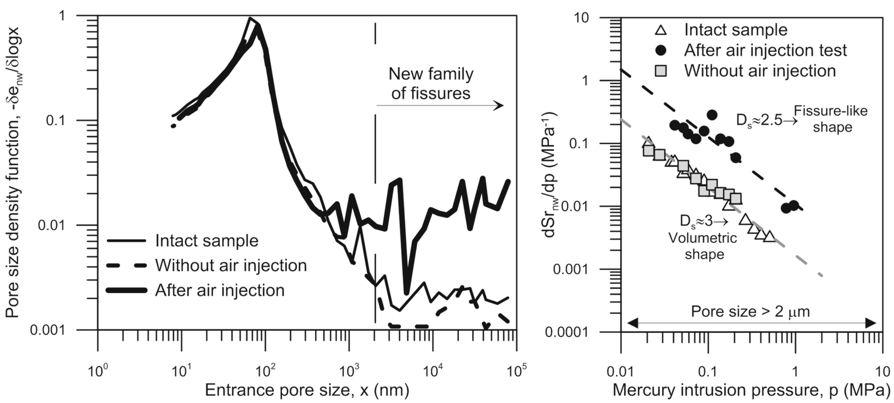

Fig. 2. (a) Pore size density function changes before and after air tests. (b) Fractal analyses of MIP results showing fissure-like shape after the air tests.

associated with the expansion undergone by the material during the air injection and early shut-off stages and the possible opening of fissures (Gonzalez-Blanco *et al.* 2016). MIP data were also interpreted in terms of the fractal character of the porous network admitting self-similarity of the hierarchical void structure. Figure 2b shows the fractal dimensions D_s of the porous medium on intact material and after the air tests, obtained from the change of the intruded degree of saturation Sr_{nw} with respect to the change in injection pressure p. As observed, the fractal analyses suggested a fissure-like structure after the air tests.

Micro-computed Tomography and Image Analyses

μCT scans were carried out on a Phoenix Nanotom equipment (GE Oil & Gas) to analyse the internal 3D microstructure of the intact material and after the air tests (Andò *et al.* 2011; Josh *et al.* 2012; Saba *et al.* 2014; Deng *et al.* 2016). Although the technique did not need any sample pre-treatment, the same freeze-drying process as in the MIP tests was followed for further comparison of results. The samples (15 mm height, 15 mm in diameter) were scanned using 720 projections on 360º with a voxel size of 20 μm. The final 3D images were 16-bit grayscale with a size of 825 × 825 × 875 voxels.

Figure 3 presents two slices that corresponded to intact material and after the air test. Differences between them could be readily observed: the intact sample presented a homogeneous aspect (except for calcium carbonate inclusions in white due to their higher density), whereas after the air injection test some fissures were visible throughout the cross-section that were oriented along bedding planes.

The main goal of the image analysis was to study fissures induced by the air passage, as well as to quantify their total volume and connectivity. The multiscale Hessian

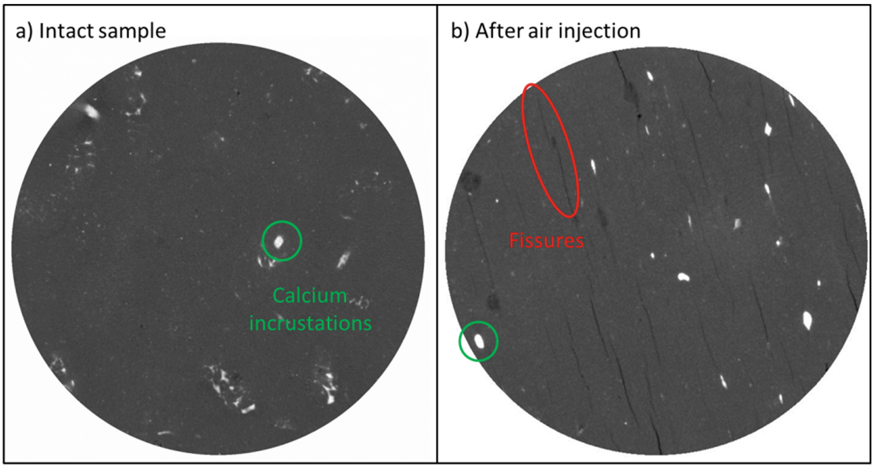

Fig. 3. μCT images of intact sample (left) and after the air tests (right).

fracture filtering (Voorn *et al*. 2013) was used to analyse μCT-scan images. It was implemented in a multiplatform of the public domain software ImageJ (Rasband 2012) that allowed the segmentation of narrow fractures in 3D image data. The connectivity filtering, which works through a MATLAB® script, allowed generating the connected fracture pattern.

After multiscale filtering, the fissures obtained using adequate parameters are depicted in Fig. 4, where two types of fissures can be distinguished: the connected ones in green and the non-connected in maroon. The figure also shows the total volume of the sample, in which the bedding plane orientation is indicated with a blue plane. The fissure pattern was consistent with the opening of fissures during the expansion undergone by the material along the air injection and early shut-off stages and revealed that the air pathways followed the bedding planes.

Quantitative Comparison of Both Techniques

This section compares the volume of fissures induced by the air tests obtained by both techniques. As previously indicated, MIP results considered fissures with entrance sizes larger than 2 μm, whereas μCT voxel resolution was limited to 20 μm. Therefore, only fissures larger than 20 μm were considered to obtain comparable results between both techniques.

A fissured void ratio $e_{fissured}$, defined as the area below the pore size density function after the air test (Fig. 2a), was used to quantify the volume of fissures (respect to the volume of solids) induced by air migration (refer to Table 1). This fissured void ratio was normalised with respect to the total void ratio e = 0.56 ($e_{fissured}/e$ in Table 1).

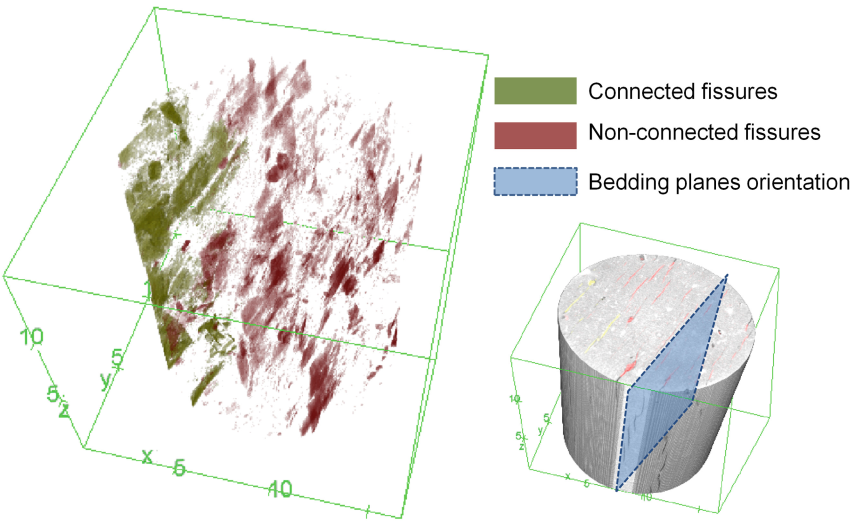

Fig. 4. 3D reconstruction of the fissure pattern in the sample after the multiscale Hessian and connectivity filtering (left) together with the total volume of the sample (right).

Table 1. Quantification of fissured void ratios using MIP and μCT results.

Technique	$e_{fissured}$	$e_{fissured}/e$
MIP (x > 2 μm)	0.038	0.068
MIP (x > 20 μm)	0.026	0.047
μCT (x > 20 μm, all fissures)	0.028	0.050
μCT (x > 20 μm, connected fissures)	0.007	0.013

This ratio was useful to provide information on the expected value of the final degree of saturation of the clay after the air tests, $Sr = 1 - e_{fissured}/e$, when all fissures were desaturated (and clay matrix pores were still saturated). Final Sr = 0.932 and 0.953 could be estimated when all fissures larger than 2 μm and 20 μm, respectively, were desaturated.

The quantitative analysis of the fissures (x > 20 μm) obtained after the filtering process of the μCT images resulted in a fissured volume of 34.5 mm^3, of which only 8.6 mm^3 were connected. The total volume of the analysed sample was 1900 mm^3 (volume of solids: 1218 mm^3). The fissured void ratio obtained by this technique is also reported in Table 1. As observed, only 25% of the fissures were connected, which indicated a final degree of saturation after the tests of Sr = 0.987 if only connected fissures larger than 20 μm were desaturated.

A good consistency is observed in the table for $e_{fissured}$ when comparing both techniques at the same range of fissure sizes (x > 20 μm).

Concluding Remarks

Air injection/dissipation stages on Boom Clay systematically displayed expansion deformation that induced damage on the material and the opening of preferential air pathways (fissures). These fissures played a major role on the dissipation stage, in which the air injection pressure started to decline with a sharp increase of the outflow air volume.

Two different microstructural techniques were used to analyse the changes in the pore network before (on intact material) and after the air test, namely mercury intrusion porosimetry (MIP) and micro-computed tomography (μCT).

MIP provided information on the entrance pore sizes and the distribution of the pore space (pore size density function), which resulted in the detection of a new family of pores at entrance sizes larger than 2 μm after the air passage. The technique also allowed the quantification of the volume of fissures larger than 2 μm. A fractal analysis of the mercury intrusion data confirmed this fissure-like structure after the air test.

μCT images also confirmed the existence of fissures after the air test that followed the orientation of the bedding planes. Image analysis through multiscale Hessian fracture filtering allowed the quantification of the volume of fissures after the air tests. To obtain comparable results between both techniques, only fissures larger than 20 μm (μCT voxel resolution) were considered. The volume of fissures respect to the volume of solids (fissured void ratio) was 0.026 and 0.028 for MIP and μCT, respectively. In addition, the image analysis allowed quantifying the connectivity of the fissure network, resulting in 25% of connected fissures. This information was useful to provide the expected value of the final degree of saturation of the clay after the air test, when all connected fissures larger than 20 μm were desaturated ($Sr = 0.987$).

Acknowledgements. The authors are grateful to the Belgian agency for radioactive waste management (ONDRAF/NIRAS) for their financial support ('Laboratory investigation of the gas transport processes in a repository located in Boom Clay', ref. XSI/AV/2012-1952, 2012-2016).

References

Andò E, Hall SA, Viggiani G (2011) Grain-scale experimental investigation of localised deformation in sand: a discrete particle tracking approach. Acta Geotech 7(1):1–13. doi:10.1007/s11440-011-0151-6

Desbois G, Urai JL, Hemes S, Brassinnes S, De Craen M, Sillen X (2014) Nanometer-scale pore fluid distribution and drying damage in preserved clay cores from Belgian clay formations inferred by BIB-cryo-SEM. Eng Geol 179(4):117–131. doi:10.1016/j.enggeo.2014.07.004

Deng H, Fitts JP, Peters CA (2016) Quantifying fracture geometry with X-ray tomography: Technique of Iterative Local Thresholding (TILT) for 3D image segmentation. Comput Geosci 20(1):231–244. doi:10.1007/s10596-016-9560-9

Fleury M, Canet D (2014) Water orientation in smectites using NMR nutation experiments. J Phys Chem C 118(9):4733–4740. doi:10.1021/jp4118503

Gonzalez-Blanco L, Romero E, Jommi C, Li X, Sillen X (2016) Gas migration in a Cenozoic clay: experimental results and numerical modelling. Geomech Energy Environ 6:81–100. doi:10.1016/j.gete.2016.04.002

Hemes S, Desbois G, Urai JL, Schöppel B, Schwarz J-O (2015) Multi-scale characterization of porosity in Boom Clay (HADES-level, Mol, Belgium) using a combination of X-ray μ-CT, 2D BIB-SEM and FIB-SEM tomography. Microporous Mesoporous Mater 208:1–20. doi:10.1016/j.micromeso.2015.01.022

Josh M, Esteban L, Delle Piane C, Sarout J, Dewhurst DN, Clennell MB (2012) Laboratory characterization of shale properties. J Petrol Sci Eng 88–89:107–124. doi:10.1016/j.petrol.2012.01.023

Muurinen A, Carlsson T, Root A (2013) Bentonite pore distribution based on SAXS, chloride exclusion and NMR studies. Clay Miner 48(2):251–266. doi:10.1180/claymin.2013.048.2.07

ONDRAF/NIRAS (2013) Research, Development and Demonstration (RD&D) plan for the geological disposal of high-level and/or long-lived radioactive waste including irradiated fuel of considered as waste, state-of-the-art report as of December 2012," ONDRAF/NIRAS, Rep NIROND-TR 2013-12 E

Rasband WS (2012) ImageJ. U.S. National Institutes of Health, Bethesda. http://imagej.nih.gov/ij/

Romero E, Simms PH (2008) Microstructure investigation in unsaturated soils: a review with special attention to contribution of mercury intrusion porosimetry and environmental scanning electron microscopy. Geotech Geol Eng 26(6):705–727. doi:10.1007/s10706-008-9204-5

Saba S, Delage P, Lenoir N, Cui YJ, Tang AM, Barnichon JD (2014) Further insight into the microstructure of compacted bentonite-sand mixture. Eng Geol 168:141–148. doi:10.1016/j.enggeo.2013.11.007

Shaw RP (ed) (2013) Gas generation and migration. In: International symposium and workshop 5th to 7th February 2013 Luxembourg, Proceedings FORGE Report, p 269

Voorn M, Exner U, Rath A (2013) Multiscale Hessian fracture filtering for the enhancement and segmentation of narrow fractures in 3D image data. Comput Geosci 57:44–53. doi:10.1016/j.cageo.2013.006

Profiling the *In Situ* Compressibility of Cretaceous Shale Using Grouted-in Piezometers and Laboratory Testing

Laura Smith[1], S. Lee Barbour[2(✉)], M. Jim Hendry[1], and D. Elwood[2]

[1] Department of Geological Sciences, University of Saskatchewan, Saskatoon, SK, Canada
[2] Department of Civil and Geological Engineering, University of Saskatchewan, Saskatoon, SK, Canada
lee.barbour@usask.ca

Abstract. Grouted-in vibrating wire pressure transducers (VWPs) can be used to measure the *in situ* constrained (1-D) compressibility (m_v) of deep claystone aquitards through measurement of barometric loading efficiency. Measurements of *in situ* m_v for a Cretaceous shale in southern Saskatchewan, Canada, were undertaken using data collected from 27 VWPs installed in multiple boreholes at two sites over depths of 10 to 325 m below ground. The measured m_v profiles at both sites produced similar trends of decreasing m_v with increasing depth. 1-D consolidation testing was used to measure pre-consolidation pressure (Pc'), compression index (C_c), and the swelling index (C_r) on nine core samples collected from Site 1. These tests yielded C_c values ranging from 0.1–0.5 ($\bar{x} = 0.29 \pm 0.12$), and C_r from 0.03–0.07 ($\bar{x} = 0.05 \pm 0.02$). Laboratory measurements of C_c and C_r were used to estimate variations in *in situ* m_v with depth. A theoretical relationship between *in situ* void ratio (e) and effective stress (σ') was determined using the laboratory determined Pc' values, compression indices (C_c, C_r), and measurements of *in situ* e. Varying the values of Pc', C_c, or e exerted minor influences on these profiles relative to C_r. The resulting theoretical patterns of *in situ* m_v with depth (or σ'), exhibited a similar pattern to the laboratory and field observations, however to replicate the *in situ* profiles the C_r values had to be an order of magnitude lower than the laboratory values. The good agreement between the theoretical and measured m_v profiles with depth highlight the potential to combine *in situ* measurements of m_v with laboratory consolidation test results to characterize the mechanical properties of deep claystone aquitards and potentially improve upon our understanding of how the stress history of these formation has resulted in their present day geomechanical properties.

Introduction

Argillaceous sediments (clay-rich aquitards, commonly referred to as shales) with low hydraulic conductivity ($K \leq 10^{-8}$ ms^{-1}) make up 2/3 of all sedimentary rocks on Earth. These shales typically control recharge and chemical transport to adjacent aquifers, and can also act as isolating units to protect shallow groundwater from

A. Ferrari and L. Laloui (eds.), *Advances in Laboratory Testing and Modelling of Soils and Shales (ATMSS)*, Springer Series in Geomechanics and Geoengineering,
DOI 10.1007/978-3-319-52773-4_34

contamination by fluid or gas migration from deeper formations. Therefore, managing and protecting groundwater resources is often dependent on accurate determinations of the geotechnical properties of a formation. However, characterizing the hydraulic and geomechanical properties of such deposits has been difficult due to the slow response times of field-based methods, and the difficulty of collecting representative and competent core samples for laboratory analysis. Even when intact samples are carefully collected, laboratory tests tend to overestimate stiffness properties such as m_v and underestimate hydraulic properties such as K (Smith et al. 2016). The majority of the constrained compressibility (m_v) estimates in the literature are obtained from laboratory testing. The objective of this study was to develop a better understanding of the stress behaviour of argillaceous aquitards by comparing the depth profiles of m_v obtained using *in situ*, laboratory, and theoretical methods. Additional details related to this study are provided in a technical note of the same title by Smith et al. (submitted).

Hydrogeologic Setting

The Williston Basin (WB) is a sedimentary basin within the larger Western Canada Sedimentary Basin (WCSB) that underlies approximately 250,000 km^2 of North Dakota, South Dakota, Montana, Manitoba, and Saskatchewan (Vigrass 2006). The mid-Jurassic to Tertiary age of the sedimentary rocks in the upper succession of rocks in the WB are predominantly low-K shale and sandstone. Economically, these shales are important because they contain one of the world's richest reserves of petroleum and natural gas, which has led to considerable attention both academically and in industry. The Cretaceous deposits (predominantly shales) were previously overlain by 1–3 km of tertiary sediment that was eroded during the mid to late Tertiary (Dawson et al. 2008), as well as the Laurentide ice sheets (up to 3 km thick) during the Quaternary. This loading history resulted in the overconsolidation of the Cretaceous shales (Sauer and Misfeldt 1993).

Methods

Two sites in the WB were investigated. Site 1 is located on the northeast portion of the WB where the surficial till is thin (<10 m) relative to other regions in the basin (Fig. 1a). Site 2 is located approximately 350 km southwest of Site 1, and closer to the center of the basin (Fig. 1a). A single borehole was continuously cored at Site 1 in 2009 (total depth: 325 m BG) and five boreholes were continuously cored at Site 2 between 2012 and 2014 (total depth: 100–200 m BG). The five boreholes at Site 2 were within a 180 km^2 area and although the formations were the same, the depth to the till/shale contact varied from 35–75 m BG. Nested Geokon vibrating wire pressure transducers (VWPs) ($n = 3 - 10$) were installed in the 5 boreholes at the two sites (Fig. 1b) to measure fluid pressure. The scale of the Geokon VWPs ranged from –0.1 to 0.35, 0.7, 1, 2, and 3 MPa (absolute accuracy of ±0.1% full scale (FS) and resolution of ±0.025% FS). At both sites, the transducers were attached to the outside of a steel tremie pipe and lowered into the borehole. A bentonite/cement grout mixture was pumped down the tremie pipe until grout returned to surface, indicating the entire borehole was filled with grout and the transducers were secured in place directly within the grout. The grout used at both sites was a mixture of 4% bentonite-96% cement. It was regularly tested during installation to ensure the specific gravity was approximately 1.7 (density of 1700 kg m^{-3}).

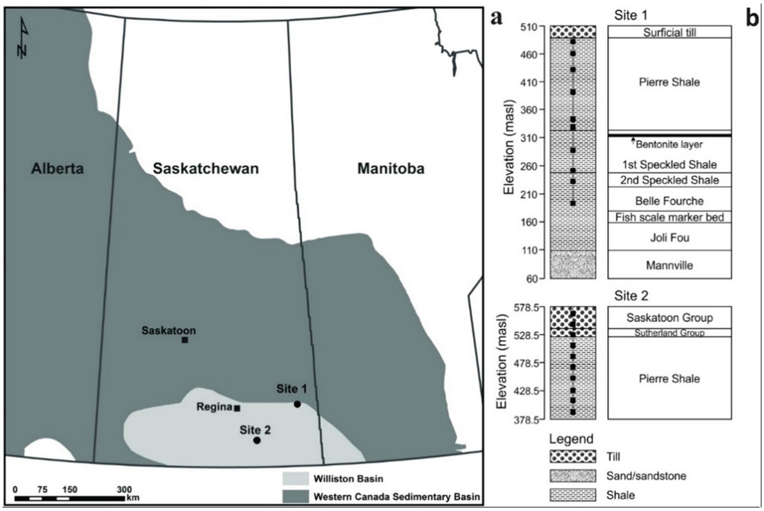

Fig. 1. Map of the eastern portion of the WCSB through Saskatchewan and Manitoba, as well as the Canadian portion of the WB (a). The locations of Site 1 and Site 2 are shown on the map along with the corresponding stratigraphic sections of each borehole (with the transducer depths identified by a black square (b). Only one of the five boreholes from Site 2 is presented here and although the till/shale contact varies from 35–70 m BG at Site 2, this profile is intended to illustrate the high frequency of VWP installations through both the till and the Pierre Shale.

The transducers were connected to a datalogger and programmed to record pressure and temperature at 30 min increments after installation. Stabilized hydraulic heads were corrected for barometric pressure following the method described in Smith et al. (2013), in which the loading efficiency (γ) for the formation at the location of each transducer was determined and pore pressure records corrected accordingly to define hydraulic head. Values of m_v were then calculated for each VWP location at Site 1 and Site 2 using (van der Kamp and Gale 1983):

$$m_v = \frac{\gamma n \beta}{1 - \gamma}$$

where n is porosity, and β is the bulk compressibility of water (4.6×10^{-7} kPa^{-1}).

Core samples were collected for 1-D consolidation testing (ASTM D2435-04) from the shale formations at Site 1 at depths of 47.4, 87.0, and 128.4 m (Pierre Shale), 174.1, 184.9, 212.0 and 249.0 m (1st Speckled Shale), 283.6 (2nd Speckled Shale) and 307.0 m (Belle Fourche Shale). Each sample was 63.3 to 63.5 mm in diameter and

12.5 to 13 mm in height. Incremental loading stages (n = 8 – 10), each lasting 10–12 h to ensure excess pore pressure dissipation, were applied to each specimen (increasing from approximately 0.06 and up to 58 MPa). The results were corrected for compressibility of the apparatus by loading a steel blank to full load range. Additional core samples were obtained from the shale at both sites to calculate total porosity (n_T) in accordance with ASTM D4531-86 (n = 45 from Site 1; n = 28 from Site 2).

Results and Discussion

The glacial till (often referred to as Quaternary drift) is composed of the Sutherland and the Saskatoon Group. These two groups are composed of overconsolidated silt and clay; and are only distinguishable using laboratory testing (e.g. carbonate content, Atterberg limits, preconsolidation pressure) and geophysical signatures (c.f. Christensen 1968a, b). The Pierre Shale is a grey-dark grey, non-calcareous, overconsolidated silt and clay with multiple horizons of shell fragments, fossils, pyrite mineralization and bentonite. The 1st and 2nd Speckled Shale are calcareous mudstone with abundant coccoliths and coccospheres, which produce a 'speckled' appearance. Generally, the 1st and 2nd Speckled Shale are only distinguished by the high total carbon content and hydrogen indices of the 2nd Speckled Shale. The underlying Belle Fourche and Joli Fou are composed of greyish black shale and are separated by the 'fish scales zone' at the base of the Belle Fourche Formation. The mean total porosity of the shale at Site 1 and 2 is 0.33 $\pm$ 0.04 (n = 45), and 0.33 $\pm$ 0.02 (n = 28), respectively.

At both sites, m_v decreases with increasing depth and spans about one order of magnitude, ranging from 3.0×10^{-6} to 2.0×10^{-7} kPa^{-1}. Similar lithology and geotechnical parameters at both sites suggest that the trend in m_v with depth can be attributed to increasing effective stress (σ'). The results also indicate that the Pierre Shale at Site 1 is less compressible than the Pierre Shale at Site 2. This could be due to differences in the evolution of the basin at each site (i.e. thicknesses of the overburden, glacial loading/unloading). The results of the 1-D consolidation tests conducted on core samples from Site 1 also indicate that the m_v of a sample decreases with increasing stress levels. It is expected that the deformation behaviour observed during the sequential incremental loading of a sample will depend on the *in situ* stress level for the sample relative to its stress history (e.g. preconsolidation pressure, Pc').

These consolidation tests provide two compression indices. The compression index (C_c) is the slope of the e-log (σ') curve during the first loading of the sample or the slope when the sample is re-loaded to stresses higher than it has previously experienced in its stress history. The recompression (or swell) index (C_r) is obtained from the slope of the e-log (σ') during unloading (or reloading at stress levels that are less than the preconsolidation stress. Pc' was determined from the laboratory samples and used to estimate a profile of pre-consolidation pressures with depth.

Theoretically, core samples of similar texture collected from the same borehole (or location) should follow a similar loading curve if they have experienced the same stress history. The results of a representative consolidation tests conducted on a core sample of the Pierre Shale (185 m BG) obtained from Site 1 is illustrated in Fig. 2. The C_c and C_r compression indices measured for the Pierre Shale (0.29 $\pm$ 0.12 and 0.05 $\pm$ 0.02, respectively) were consistent with those measured by Smith (1978) for undisturbed core samples of Pierre Shale in Colorado of 0.34 and 0.026, respectively, and by Peterson (1958) for similar shale samples from the Bearpaw Formation in southern Saskatchewan of approximately 0.68 and 0.06, respectively.

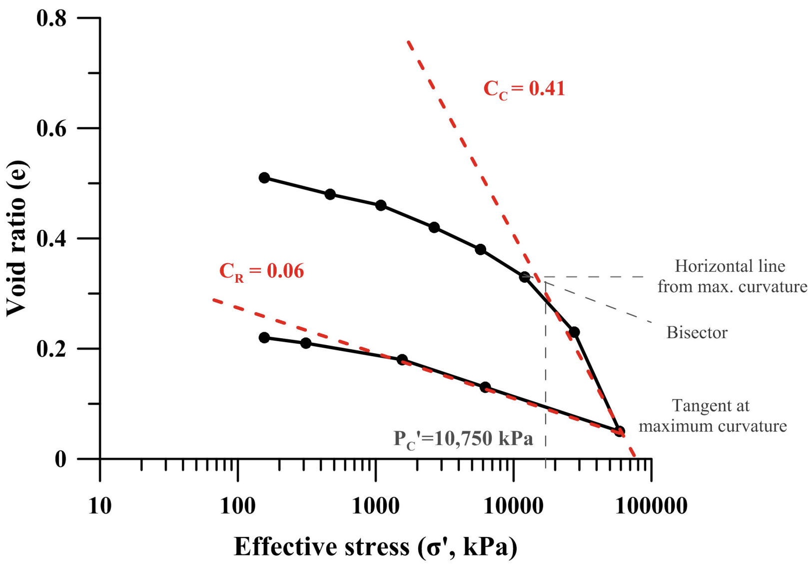

Fig. 2. 1-D consolidation test results of a core sample obtained from the Pierre Shale at Site 1 (185 m BG) (black solid line). The slope of the compression line (C_c) and recompression line (C_r) are identified by dashed red lines. A Casagrande construction to define the preconsolidation pressure (Pc') is illustrated in grey dashed lines (Casagrande 1936).

Installing multiple VWPs in the same profile provides a natural analogue to a laboratory consolidation test. Although there are differences between the m_v values and the compression indices of laboratory and *in situ* observations, the pattern of decreasing m_v with increasing depth observed in both cases was consistent. A comparison between the compressibility behaviour for *in situ* samples as observed in barometric loading vs the laboratory (1-D consolidation tests) could provide insight as to whether the pattern of m_v with depth is consistent with the known dependency of m_v on *in situ* stress levels and stress history.

A comparison between the two methods was undertaken by calculating a hypothetical m_v with depth using the following procedure. The initial e was based on measurements done on the core samples and the σ' values were calculated based on *in situ* depth and observed hydraulic head conditions. The void ratio (e) of the core samples at their Pc' value was estimated by extrapolating the relationship between e and σ' with depth and using the average value of C_c determined from 1-D consolidation tests (0.29). The e of each sample under its current σ' was calculated assuming a value of C_r (using final void ratios observed for both the field and laboratory data sets).

The m_v at the *in situ* (or final laboratory) stress levels were then estimated by calculating the coefficient of compressibility (A_v, kPa^{-1}) using the equations described in Jorgensen (1980):

$$A_v = 0.434 \frac{C_r}{\sigma'}, \quad \text{(and)}$$

$$m_v = \frac{A_v}{1 + e_o}$$

A sensitivity study was conducted to determine the influence of Pc', C_c, C_r, and e on the resulting m_v. The results indicate that varying the values of Pc', C_c, or e have a minor influence on these profiles relative to C_r. As such, by varying the C_r over a small range for each site and the laboratory data, a range of m_v values resulted in an envelope of calculated values. These values are plotted with the measured field and laboratory values in Fig. 3. The C_r values used to calculate a range of m_v with depth to compare with the laboratory results were similar to those observed in the laboratory consolidation tests (0.02–0.06). However, the ranges of C_r values for each of the sites were lower than the laboratory values; specifically, 0.005–0.01 for Site 1 and 0.001–0.003 for Site 2. It is not known why a low range of C_r was required to fit the *in situ* data; however, the differences between laboratory and *in situ* stress behaviour has been noted previously (Bjerrum 1967; Smith 1978). For example, swell behaviour can be affected

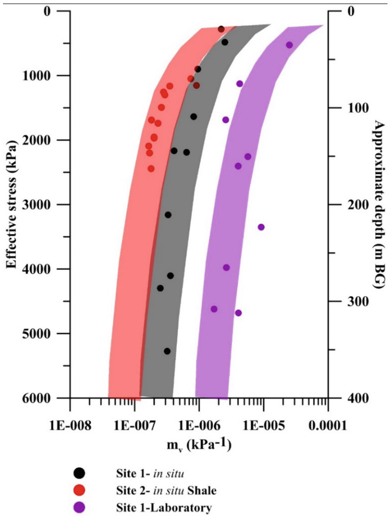

Fig. 3. Depth profile of σ′ and m_v of both Site 1 (red) and Site 2 (black), along with the laboratory estimates at *in situ* σ′ (purple). The coloured regions represent a range of calculated m_v from the laboratory determined C_c and C_r. The purple shaded region was produced using C_c and C_r consistent with the laboratory tests (0.29 and 0.02–0.06, respectively). The black and red shaded regions were produced using C_c consistent with laboratory testing (0.29) but C_r estimates of 0.005–0.01 and 0.001–0.003, respectively.

by both clay structure and diagenetic bonds (Bjerrum 1967; Smith 1978); therefore, it would follow that core samples that were disturbed would result in the breaking of diagenetic bonds or clay structure, resulting in a larger C_c and C_r values.

The advantage of having both field and laboratory m_v data is the ability to compare not only the results of the two methods, but to determine if the deformation behaviour is similar for comparable materials. All of the core samples used to determine C_r were obtained from the Cretaceous Shales at Site 1, and while similar to the shales at Site 2, they do differ slightly in lithology (i.e. Atterberg limits, mineralogy, etc.). Regardless, the primary goal was to determine if the stress behaviour observed from the laboratory tests would highlight a pattern (predicted m_v with depth) that could be applied to the *in situ* results at both sites. The reason why the C_r required to produce a range of m_v values consistent with the *in situ* observations varied between sites is unknown. However, it appears that the stress behaviour (and resulting trend) determined in the laboratory can be applied to both Site 1 and Site 2.

Conclusions

Laboratory consolidation tests overestimated the m_v of the shale compared to the *in situ* estimates using VWP data. In both cases, the compressibility decreased with increasing depth. Disturbances caused by sampling appears to underestimate the stiffness of a sample and overestimate C_r, presumably due to breaking of diagenetic bonds or rearranging clay structure. However, the general trend of the stress behaviour (e relationship to σ') observed during the 1-D consolidation tests was present in the *in situ* observations, although offset by about an order of magnitude. Further, the agreement between the theoretical and measured m_v depth profiles highlight the potential to combine *in situ* measurements of m_v with laboratory consolidation tests results to characterize the mechanical properties of aquitards. These results could potentially be used to improve upon the understanding of how the stress history of formations led to their current geomechanical properties.

Acknowledgements. Funding was provided by NSERC-IRC (184573) and by the Mosaic Company, Cenovus Energy, PotashCorp, and the Saskatchewan Potash Producers Association (MJH).

References

Bjerrum L (1967) Progressive failure in slopes of overconsolidated clay and clay shales. Proc J Soil Mech Found Div 93:1–49. American Society of Civil Engineers

Christensen EA (1968a) Pleistocene stratigraphy of the Saskatoon area, Saskatchewan, Canada. Can J Earth Sci 5:1167–1173

Christensen EA (1968b) A thin till in west-central Saskatchewan. Canada. Can J Earth Sci 5:329–336

Casagrande A (1936) The determination of the pre-consolidation load and its practical significance. In: Proceedings of the international conference on soil mechanics and foundation engineering. Harvard University Cambridge, pp 60–64

Dawson FM, Evans CG, Marsh R, Richardson R (2008) Uppermost Cretaceous and tertiary strata of the western Canada sedimentary basin. In: Geological atlas of the western Canada sedimentary basin. Canadian Society of Petroleum Geologists and Alberta Research Council, Special Report 4

Jorgensen D (1980) Relationships between basic soils-engineering equations and basic ground-water flow equations, Geological Survey Water-Supply Paper 2064, Washington, DC

Peterson R (1958) Rebound in Bearpaw Shale. West Can Bull Geol Soc Am 69:1113–1124

Sauer KE, Misfeldt GA (1993) Preconsolidation of Cretaceous clays of the western interior basin in southern Saskatchewan. In: Proceeding of the 46th annual Canadian geotechnical conference, Saskatoon, 27–29 September 1993

Smith LA, van der Kamp G, Hendry MJ (2013) A new technique for obtaining high-resolution pore pressure records in thick claystone aquitards and its use to determine in situ compressibility. Water Resour Res 49:732–743. doi:10.1002/wcwr.20084

Smith LA, Barbour SL, Hendry MJ, Novakowski K, van der Kamp G (2016) A multiscale approach to determine hydraulic conductivity in thick claystone aquitards using field, laboratory and numerical modeling methods. Water Resour Res. doi:10.1002/2015WR018448

Smith LA, Barbour SL, Hendry MJ Profiling the in situ compressibility of Cretaceous shale using grouted-in piezometers and laboratory testing. Can Geotech J. (submitted)

Smith TJ (1978) Consolidation and other geotechnical properties of shales with respect to age and composition. PhD thesis, University of Durham

van der Kamp G, Gale JE (1983) Theory of earth tide and barometric effects in porous formations with compressible grains. Water Resour Res 19(2):538–544

Vigrass L (2006) Williston basin. Encyclopedia of Saskatchewan. http://esask.uregina.ca/entry/williston_basin.html. Accessed 23 Nov 2015

Influence of Surface Roughness of the Fracture on Hydraulic Characteristics of Rock Mass

Wenquan Zhang(✉), Jiudang Yuan, Guibin Zhang, and Bo Li

College of Mining and Safety Engineering,
Shangdong University of Science and Technology, Qingdao 266590, China
54334416@qq.com

Abstract. To obtain the influence of surface roughness of the fracture on hydraulic characteristics of rock mass. Firstly, the roughness of three kinds of fracture surfaces were determined using TR600 roughness profiler. The vertical stress and horizontal stress and water head pressure of samples are simulated by normal load, shear load, and seepage water pressure respectively. The coupled shear-seepage tests were carried out using a JAW-600 shear–seepage coupled test system. The changes in hydraulic opening and permeability with shear displacement were obtained under different initial normal stress and normal stiffness conditions. This study shows that the hydraulic opening and permeability of fracture rock mass can be divided into three stages of reduction, accelerated rise and stability with the increase of the shear displacement. Larger initial normal stress correspond to greater the hydraulic opening and transmission rate of the rock mass. Greater roughness of the fracture surfaces correspond to greater hydraulic opening and transmission rate, and worse stability. The water infiltration is proportional to three times the degree of hydraulic opening. A small change in the degree of hydraulic opening can cause great changes in the transmission rate. Under the same stress condition, the degree of the fracture surface roughness will produce important influence on the volume of gushing water.

Introduction

Excavations may result in the expansion of cracks in the jointed surrounding rock mass. Large changes in the permeability of a rock mass occur when cracks undergo closure and shear expansion. Olsson and Barton (2001) have conducted theoretical and experimental studies on the mechanism of coupled shear and seepage in fractured rock. Sharp and Maini (1972) conducted a coupled seepage-shear experiment on the splitting surface of slate without a normal load and found the shear dilation of a jointed face is not restricted. Makurat et al. (1992) conducted a coupled shear-seepage experiment under the conditions of low shear displacement and gravity. They concluded that the shear displacement can lead the permeability coefficient of joints to increase dramatically. Caihua et al. (2002, 2003) simultaneously applied a normal load, shear load, and seepage pressure using a coupled shear-seepage test system. However, because of the way it affects water infiltration to the surrounding area, the seepage pressure differed from the actual pressure. In this study, firstly, the roughness of three kinds of fracture surfaces were determined using TR600 roughness profiler. Then, according to stress

A. Ferrari and L. Laloui (eds.), *Advances in Laboratory Testing and Modelling of Soils and Shales (ATMSS)*, Springer Series in Geomechanics and Geoengineering,
DOI 10.1007/978-3-319-52773-4_35

changes of the rock during mining, a coupled compression-shear seepage experiment was carried out using a JAW-600 shear-seepage coupled test system. The change in hydraulic opening and permeability with shear displacement and load in jointed rock were obtained under different initial normal stress and normal stiffness conditions. This paper provides the theoretical basis for the initiation and evolution of permeability in a fractured rock mass made up of permeable channels.

Coupled Shear-Seepage Test of the JAW-600

Composition and Function of the Test System

The basic composition of the JAW-600 shear-seepage coupled test system is as follows (Fig. 1).

The coupled shear-seepage test for fractures with different roughness was conducted by a maintaining constant normal load (CNL) and constant normal stiffness (CNS) in the normal direction for fractured samples.

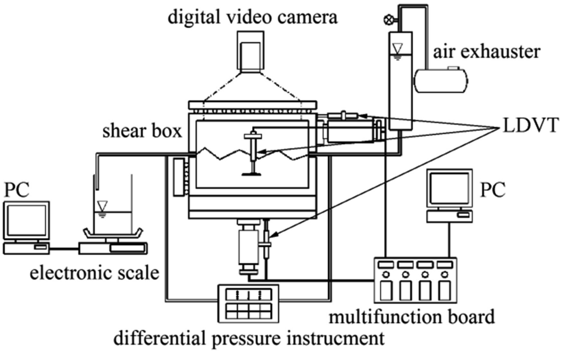

Fig. 1. Schematic diagram of JAW-600 coupled shear-seepage test system.

Preparation of the Fractured Samples with Different Roughness

In order to ensure sealing of the shear box, a slot was first cut along the surface of the sample. Then, the sample was split using rock mechanical test equipment. The samples are marked as 1, 2 and 3 respectively according to the fracture surface roughness of three samples. The samples are shown in Fig. 2. The roughness of the samples were measured using a TR600 roughness profiler. Sample 1 was smooth, and the convex surface was small with uniform distribution. There was a big bulge in the middle of the fracture surface of sample 2. There was a large protrusion in the boundary of the fracture surface of sample 3. There were many small projections in other regional entities of sample 3. The surface roughness of the sample is shown in Fig. 3. The Z_2 method was used to determine the range of joint roughness coefficient (JRC) values for the fractures by Hongfa et al. (2002).

(a) Sample 1 (2) sample 2 (3) sample 3

Fig. 2. Fine sandstone samples with different roughness.

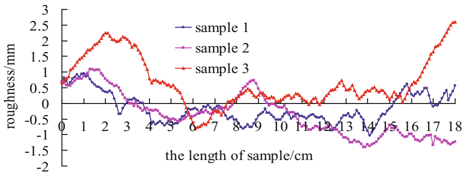

Fig. 3. The surface roughness of different samples.

Experimental Conditions

In all cases, the direction of water flow was parallel to the direction of shear, operated as fissure flow in low confining pressure, and obeyed cubic standards. The upper and lower part of the effective contact length decreased along with shear. If the hydraulic head stays constant, the hydraulic gradient will rise. This will affect the size of the

Table 1. Experimental cases under constant normal load (CNL) and constant normal stiffness (CNS) conditions.

Sample number	Cases		Range of joint roughness coefficient (JRC)	Boundary conditions	
				Initial normal stress/MPa	Normal stiffness/MPa · m^{-1}
1	CNL	J1_1	4–6	0.5	–
		J1_2		1.5	–
		J1_3		2.5	–
	CNS	J1_4		2.0	300
		J1_5		2.0	500
2	CNL	J2_1	10–12	0.5	–
		J2_2		1.5	–
		J2_3		2.5	–
	CNS	J2_4		2.0	300
		J2_5		2.0	500
3	CNL	J3_1	16–18	0.5	–
		J3_2		1.5	–
		J3_3		2.5	–
	CNS	J3_4		2.0	300
		J3_5		2.0	500

transmittance. The shear displacement corresponding to the hydraulic gradient can be reduced to eliminate this effect. The experiments were conducted with both CNL and CNS conditions, the specific working conditions are shown in Table 1.

Experimental Procedure

(1) The two pieces of each sample were assembled.
(2) To obtain the greatest possible closure between the two pieces of each sample, cyclic loading and unloading were carried out on the sample. A reasonable normal stress-displacement curve was obtained according to the results of the third cyclic loading and unloading test used to calculate the mechanical gradient of fractures.
(3) The seepage coupling shear experiments are carried out.

Analysis of the Influence of Surface Roughness on Hydraulic Opening

The hydraulic opening-shear displacement curves for samples with different roughness under different initial normal stresses are shown in Fig. 4. The following features can be observed.

The fracture surface roughness of rock mass has a significant effect on the degree of hydraulic opening. The jointed samples have negative expansion due to normal compaction. The degree of hydraulic opening becomes smaller with an increase in the shear displacement when the initial shear displacement is within the range of 2 mm. The hydraulic opening is almost zero. When the shear displacement is greater than 2 mm, the hydraulic opening increases rapidly to a certain value and then keeps stable. Under the same shear displacement condition, a larger initial normal stress, and a greater roughness of the fracture, corresponds to a greater degree of hydraulic opening. A larger shear displacement, corresponds to a higher maximum value of hydraulic opening. Under the same initial normal stress conditions, a smaller surface roughness of the sample, corresponds to a lower ultimate hydraulic opening value, and a faster time to the peak value of hydraulic opening. The maximum hydraulic opening is more stable at higher initial normal stress values. The roughness and flow area of sample 3 is the largest, the residual hydraulic opening value of the fracture shows the upward trend in the later period of the experiment.

The hydraulic opening-shear displacement curves for samples with different roughness under different normal stiffness are shown in Fig. 5. The following features can be observed.

The hydraulic opening gradually becomes larger and maintains stability with an increase in shear displacement. Larger values of normal stiffness, correspond to lower hydraulic opening values. These graphs show that the normal stiffness has a inhibiting effect on the degree of hydraulic opening. Under same normal stiffness condition, greater surface roughness of the sample, correspond to smaller hydraulic opening value is. The residual degree of hydraulic opening has a tendency to increase with an increase

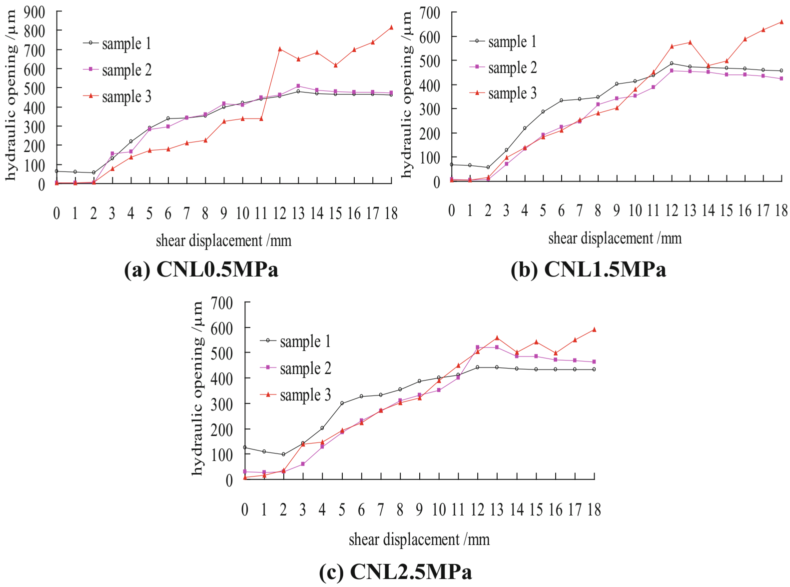

Fig. 4. Hydraulic opening-shear displacement curves for samples with different roughness under different initial normal stress.

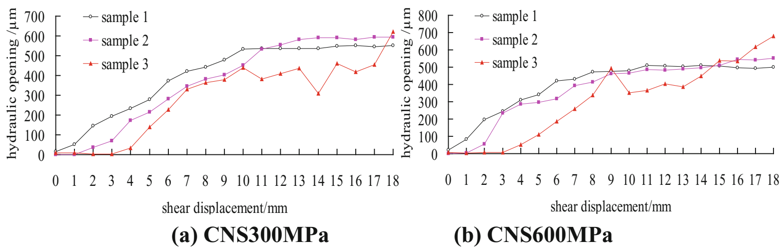

Fig. 5. Hydraulic opening-shear displacement curves for samples with different roughness under different normal stiffness.

in shear displacement toward the end of the experiment because the surface roughness of the sample 3 is the largest. The degree of hydraulic opening is slightly larger under the CNL condition compared to that under the CNS condition.

Analysis of the Influence of Joint Roughness on Transmission Rate

The transmission rate-shear displacement curves for the samples with different roughness under different initial normal stress and normal stiffness condition are shown in Figs. 6 and 7. The following features can be observed.

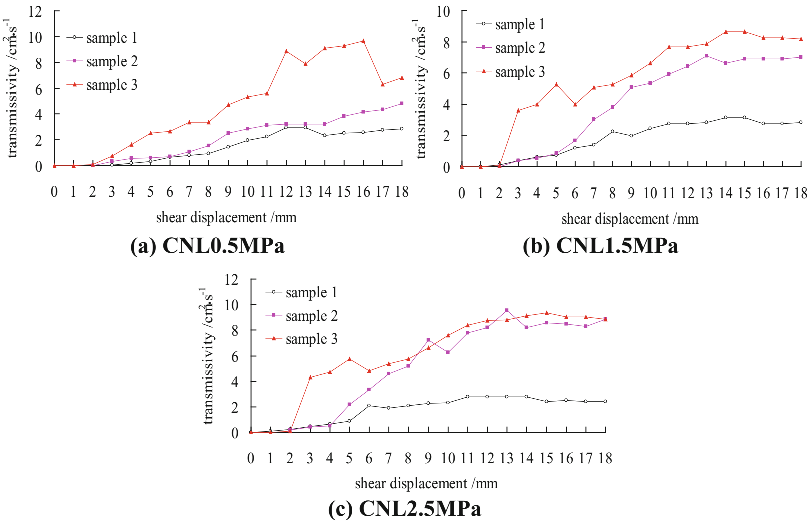

Fig. 6. Transmission rate-shear displacement curves for samples with different roughness under different initial normal stress.

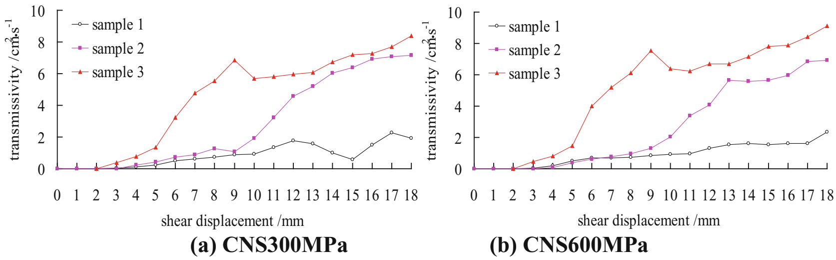

Fig. 7. Transmission rate-shear displacement curves for samples with different roughness under different normal stiffness.

(1) The transmission rate increases with an increase in the shear displacement. The transmission rate decreases with an increase in the initial normal load.
(2) The transmission rate increases with an increase in shear displacement. A larger normal load corresponds to a smaller transmission rate in the sample. The more rough the fracture surface is, the more the transmission rate is.
(3) The surface roughness of the sample has a great influence on the stability of the transmission rate during the test. The larger the surface roughness of the sample is, the worse the stability of the transmission rate is, the more obvious the fluctuation of transmission rate is.

Conclusions

Coupled shear-seepage coupling experiments on three groups of jointed slate samples with different roughness were carried out using a JAW-600 coupled shear-seepage test system. The change in hydraulic opening with shear displacement were obtained under different initial normal stress loading and normal stiffness conditions. The following results were obtained.

(1) The changes in the degree of hydraulic opening include the effects of shear stress, water head pressure, and horizontal crustal stress. The shear stress and water head pressure enhance the degree of hydraulic opening, and the horizontal crustal stress inhibits the degree of hydraulic opening. The change in the degree of hydraulic opening degree is divided into three stages associated with the change in shear displacement. (a) In the first stage, the hydraulic opening decreases at the beginning of shear deformation. (b) In the second stage, the hydraulic opening increases rapidly with an increase in shear displacement. (c) In the third stage, the hydraulic opening increases slowly and reaches a maximum value at a low rate. The variation in the degree of hydraulic opening is caused by shear dilation and consolidation. The final stable value of the hydraulic opening is influenced by the roughness of the fracture surface. Greater fracture surface roughness results in greater final stability in the degree of hydraulic opening. The water infiltration is proportional to three times the degree of hydraulic opening. A small change in the degree of hydraulic opening can cause great changes in the transmission rate. Under the same stress condition, the degree of the fracture surface roughness will produce important influence on the volume gushing water.

(2) The transmission rate increases with increasing shear displacement. Larger normal loads correspond to smaller transmission rates in the samples. The more rough the fracture surface is, the more the transmission rate is. The surface roughness of the sample has a great influence on the stability of the transmission rate during the test. The larger the surface roughness of the sample is, the worse the stability of the transmission rate is, the more obvious the fluctuation of transmission rate is. The trend of the transmission rate for the jointed sample is the same under the two boundary conditions of CNL and CNS, but the transmission rate is larger under the CNL condition than that under the CNS condition.

References

Olsson R, Barton N (2001) An improved model for hydromechanical coupling during shearing of rock joints. Int J Rock Mech Min Sci 38:317–329. doi:10.1016/s1365-1609(00)00079-4

Sharp JC, Maini YNT (1972) Fundamental considerations on the hydraulic characteristics of joints in rock. In: Proceedings of the international symposium on percolation through fissured rock, Stuttgart, [s. n.], pp 1–15

Makurat A, Barton N, Rad NS et al (1992) Joint conductivity variation due to normal and shear deformation. In: Barton N, Stephansson O (ed) Proceedings of the international symposium on rock joints. A.A. Balkema, Rotterdam, pp 535–540

Caihua LIU, Congxin CHEN, Shaolan FU (2003) Testing study on seepage characteristics of single fracture with sand under shear displacement. Chin J Rock Mech Eng 22:1457–1461. doi:10.3321/j.issn:1000-6915.2003.10.014

Caihua LIU, Congxin CHEN, Shaolan FU (2002) Testing study on seepage characteristic of a single rock fracture under two- dimensional stresses. Chin J Rock Mech Eng 21:1194–1198. doi:10.3321/j.issn:1000-6915.2002.08.018

Xu H, Li Y, Liu X et al (2002) Fractal simulation of joint profiles and relationship between JRC and fractal dimension. Chin J Rock Mech Eng 21:1663–1666. doi:10.3321/j.issn:1000-6915.2002.11.017

Opalinus Clay Shale

The Role of Anisotropy on the Volumetric Behaviour of Opalinus Clay upon Suction Change

Alberto Minardi(✉), Eleonora Crisci, Alessio Ferrari, and Lyesse Laloui

Laboratory of Soil Mechanics (LMS), Swiss Federal Institute of Technology in Lausanne (EPFL), Lausanne, Switzerland
alberto.minardi@epfl.ch

Abstract. An experimental investigation to analyse the anisotropic volumetric response of shaly and sandy facies of Opalinus Clay upon suction variations is presented. Obtained results demonstrate the different behaviour of the tested facies to a wetting-drying cycle. The shaly facies exhibits higher water retention capacity and stronger volumetric response than the sandy facies. Anisotropic response is experienced by both facies with the strain perpendicular to bedding higher than in the parallel direction. The sandy facies exhibits a more pronounced anisotropic behaviour in particular during the drying phase. A detailed analysis of the response in the two directions with respect to the bedding orientation proves that the different anisotropic behaviour between the two facies is mainly caused by a different response parallel to bedding rather than perpendicular.

Introduction

Opalinus Clay is a shale formation currently under consideration to serve as the host geomaterial for the underground storage of high-level nuclear wastes in Switzerland. Among the several aspects of Opalinus Clay that have been investigated, its anisotropic fabric and water retention properties have been identified to play a significant role over the lifespan of the repository, during which the shale formation is subjected to a sequence of hydro-mechanical loadings.

The anisotropic response to the mechanical loading of shales has been observed and analysed in several studies (e.g., McLamore and Gray 1967; Niandou et al. 1997; Delle Piane et al. 2011), particularly on Opalinus Clay shale (e.g., Popp and Salzer 2007; Salager et al. 2013); for example, this aspect must be considered to properly predict the development and extent of the excavation damage zone around the tunnel (Popp et al. 2008). However, due to the high water retention properties of the Opalinus Clay (Ferrari and Laloui 2013; Ferrari et al. 2014) and the volumetric response sensitive to suction variations (Minardi et al. 2016; Soe et al. 2009), an anisotropic behaviour might be observed also upon suction changes. A proper understanding of this coupling may have a relevant impact on the prediction of the behaviour of Opalinus Clay during the tunnel excavation and ventilation, where the material might experience shrinkage due

A. Ferrari and L. Laloui (eds.), *Advances in Laboratory Testing and Modelling of Soils and Shales (ATMSS)*, Springer Series in Geomechanics and Geoengineering,
DOI 10.1007/978-3-319-52773-4_36

to the drying processes, and during resaturation phase of the repository, where a swelling of the host rock is expected due to the wetting process.

The objective of this study is to provide a detailed analysis of the role of anisotropy on the volumetric response during wetting and drying processes for two facies of Opalinus Clay. An advanced experimental methodology is used for this purpose. The laboratory test results demonstrate the anisotropic response of the materials upon suction variation, and the different behaviour of the two tested facies.

Opalinus Clay: Shaly and Sandy Facies

Opalinus Clay (OPA) is a fine-grained sedimentary geomaterial with a mineralogical composition consisting mainly of silicates, carbonates and quartz (Mazurek 1999). The core samples used in this study are collected from the Mont Terri Underground Laboratory (URL), in northern Switzerland, located at a depth of about 300 m. Two different facies of the Opalinus Clay shale are tested: the shaly and sandy facies. The shaly core sample is cored in the FE gallery at the tunnel wall. The sandy core sample is cored in the niche TT. The main difference between the two facies is clearly highlighted by their grain size distribution. The shaly facies is dominated by the silt and clay fractions (10% of sand, 57% of silt and 33% of clay), whereas the sandy facies shows higher values for the coarser fractions (11% of gravel, 29% of sand, 42% of silt and 18% of clay). Different mineralogical composition is also highlighted (Table 1); the shaly facies is dominated by the clay minerals while a more homogeneous composition is exhibited by the sandy facies.

Table 2 reports the geotechnical properties of the tested specimens measured after preparation (particle density ρ_s, bulk density ρ, initial water content w, initial void ratio e, porosity n, degree of saturation Sr, initial total suction Ψ_0).

Table 1. Mineralogical composition of the tested facies of the Opalinus Clay.

OPA facies	Calcite	Quartz	Clay	Other
SANDY	19%	37%	36%	8%
SHALY	16%	12%	66%	6%

Table 2. Index and geotechnical properties of the tested specimens.

Properties		ρ_s (g/cm^3)	ρ (g/cm^3)	w (%)	e (-)	n (-)	S_r (%)	Ψ_0 at 25°C (MPa)
OPA	Sandy	2.76	2.44	2.4	0.16	0.14	42	74.8
OPA	Shaly	2.75	2.30	3.1	0.23	0.19	36	96.0

Experimental Methodology

To analyse the impact of anisotropy on the response of the tested facies upon suction changes, an advanced testing methodology is adopted that combines total suction control with a precise assessment of the deformations in two orthogonal directions.

The vapour equilibrium technique is used for the application of wetting/drying processes. The technique allows for the control of the relative humidity inside a closed desiccator with saturated saline solutions. Considering the psychrometric law (Fredlund and Rahardjo 1993), relative humidity can be converted to total suction (Ψ). Saturated saline solutions are used to impose different total suction values. The used salts are: Magnesium nitrate (Ψ = 86 MPa), Sodium chloride (Ψ = 39 MPa), potassium chloride (Ψ = 23 MPa), and potassium nitrate (Ψ = 10 MPa). Total suction values are measured by means of a dew-point chilled mirror psychrometer (WP4C, e.g., Leong et al. 2003; Cardoso et al. 2007). Tests are performed at a reference temperature of 25 °C; the unwanted temperature fluctuation during the entire test period is in the range of ±1 °C.

To assess the anisotropic volumetric response upon suction variations, the specimen deformations are measured in directions perpendicular ($\varepsilon^{\perp}$) and parallel ($\varepsilon^{//}$) to the bedding. All of the tested specimens are equipped with two biaxial temperature-compensated strain gauges, two perpendicular and two parallel to the bedding, that provide strain measurement with microstrain resolution.

Cylindrical specimens are used (diameter of 25 mm and height of 20 mm), with bedding orientation perpendicular to the axis of the cylinder. For each facies, two specimens are placed inside the desiccator (Fig. 1). One specimen is equipped with strain gauges; the second specimen is used to monitor the mass variation during each step of total suction in order to assess the water content changes.

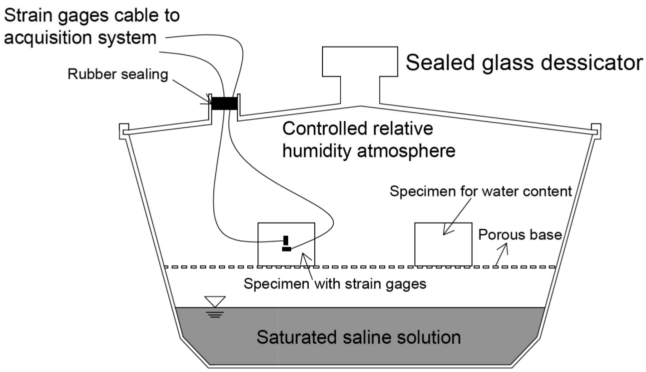

Fig. 1. Schematic representation of the testing set-up adopted for the investigation. Glass desiccator with saturated saline solution at the bottom and tested specimens.

To comprehensively analyse the role of anisotropy on the volumetric behaviour, a wetting/drying cycle is performed. The first value of total suction is defined near the initial condition of the specimens (assessed with the WP4C). At each suction step, the achievement of the equilibrium condition is assessed by checking the stabilization of both the strains and the mass of the specimen without the strain gauges. After the achievement of the equalization, the specimens are moved in few seconds into a new desiccator prepared with the saline solution corresponding to the next total suction value to be imposed. At the end of the cycle, the specimen for water content determination is dried in an oven at 105 °C until a constant mass is reached. This allowed for the back-calculation of the water content evolution throughout all of the steps.

Results

Figure 2 shows the obtained results for the shaly and sandy specimen respectively; each graph reports the evolution with total suction of volumetric deformations and water content. As the two specimens have different initial conditions, the equalization at suction of 86 MPa is considered as the initial point in order to make a comparison between the tested facies.

The water content evolution highlights the different water retention capacity of the two tested facies. Indeed, the shaly specimen has higher water content over all the total suction values investigated with respect to the sandy specimen; in addition, the shaly facies experience a higher water content variation for the same changes of total suction. This aspect is related to the different mineralogical composition of the two geomaterials where the higher clay content of the shaly facies is responsible for its higher water retention capacity.

As a consequence of the different water content variation experienced by the two facies upon suction variations, a significant different volumetric behaviour is observed. Both specimens show swelling and shrinkage response during the wetting and drying processes respectively. However, the shaly specimen exhibits a more pronounce response: at the end of the wetting, its volumetric swelling is 1.6 times higher than the expansion experienced by the sandy facies while, regarding the drying phase, the shrinkage is 1.5 times higher than the sandy specimen.

Finally, both water content and volumetric strain show a non-linear trend with more significant variations for low values of total suction. This aspect indicates the strong coupling between the water retention capacity and the volumetric behaviour.

Besides the mutual influence between the volumetric response and the water retention properties, the response of the tested facies of Opalinus Clay is highly anisotropic. Figure 3 presents the relationship between the anisotropic ratio (ratio between the strain perpendicular and parallel to bedding) and total suction for the two facies. As the ratio has always values greater than one, it means that the specimens' response perpendicular to bedding is always stronger than the response in the direction parallel to bedding. Comparing the response of the two facies, the sandy specimen exhibits an anisotropic behaviour upon suction variations more pronounced than the shaly specimen. All these aspects are observed both during wetting and drying processes performed. At the end of the wetting phase, the ratio is 2.7 and 4 for the shaly and sandy specimens respectively. Considering the end of the drying phase, the ratio is 2.4 and 5.5 for the shaly and sandy specimens respectively.

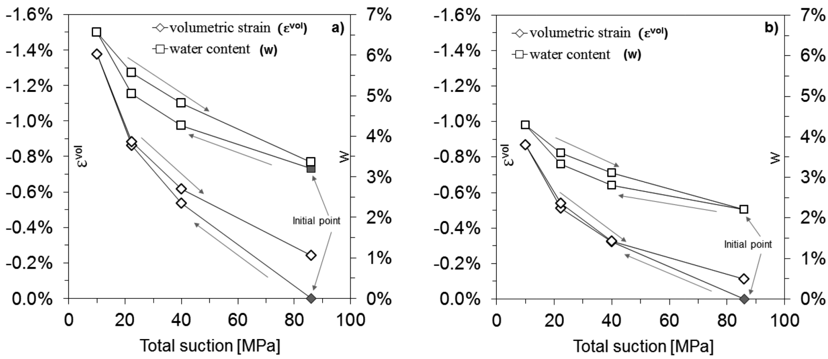

Fig. 2. Experimental results: volumetric strain (ε^{vol}) and water content (w) evolution with suction for the (a) shaly facies, (b) sandy facies. Negative strain means expansion.

Figure 3 highlights also a different evolution of the anisotropic ratio for the two tested facies of the Opalinus Clay. Generally, for suction values higher than 23 MPa, the anisotropic ratio is fairly constant during both wetting and drying processes. However, for lower suction values (below 23 MPa), the anisotropic ratio shows a deviation from this trend and some differences are observed. Considering the wetting phase, a similar trend is observed for both facies with a decrease of the ratio when suction is reduced to 10 MPa; this means that both facies experience a similar response in the directions perpendicular and parallel to bedding. In particular, at the end of the wetting process, the swelling of the shaly specimen is 1.4 and 2 times higher in the directions perpendicular and parallel to bedding respectively (Figs. 4a and b). Considering the drying phase, a stronger difference is observed between the two facies of the Opalinus Clay; during the first drying step, the ratio decreases for the shaly facies and increases for the sandy facies. This aspect is strictly related to the different specimens' response in the direction parallel to bedding. Indeed, as illustrated in Fig. 4c, both facies experienced a similar

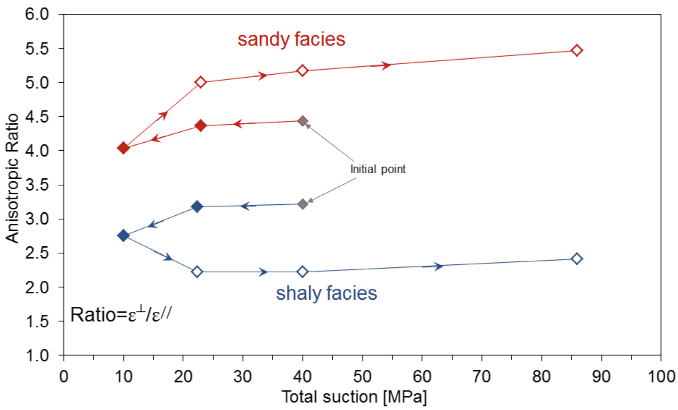

Fig. 3. Relationship between the anisotropic ratio ($\varepsilon^{\perp}/\varepsilon^{//}$) and total suction ($\Psi$) for the shaly and sandy OPA.

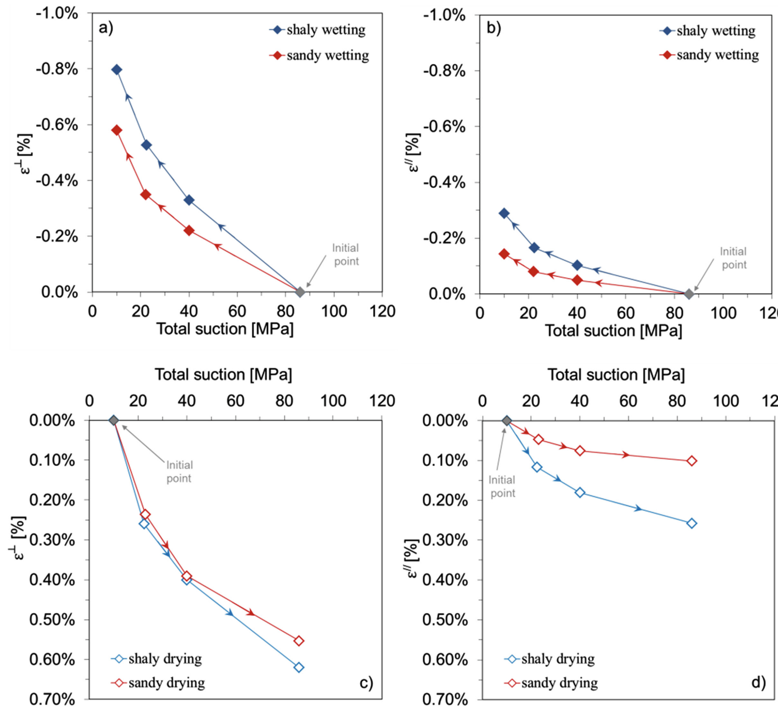

Fig. 4. Response of the tested specimens (shaly and sandy OPA) upon suction variation in the directions perpendicular ($\varepsilon^{\perp}$) and parallel ($\varepsilon^{//}$) to bedding during wetting and drying processes. (a) Perpendicular strain during wetting. (b) Parallel strain during wetting. (c) Perpendicular strain during drying. d) Parallel strain during drying.

shrinkage behaviour perpendicular to bedding (the contraction of the shaly specimen is 1.1 times higher than the sandy specimen); however, a more remarked different response is exhibited in the direction parallel to bedding, where the shrinkage of the shaly facies is 2.5 higher than the sandy facies (Fig. 4d).

Conclusions

The obtained results highlight significant features of the anisotropic behaviour of the tested facies of the Opalinus Clay upon total suction variations. The different volumetric behaviour is observed where the shaly OPA exhibits a stronger response (swelling and shrinkage during wetting and drying respectively) than the sandy OPA. The main feature of the observed behaviour during the wetting-drying cycle is the anisotropic response; both tested facies show a higher deformation in the direction perpendicular to bedding than parallel to bedding during both wetting and drying phases. In particular, the sandy facies exhibits a stronger anisotropic ratio than the shaly facies. This aspect is mainly due to a different response in the direction parallel to bedding. Indeed, a similar response is observed in the direction perpendicular to bedding during both wetting and drying phases; however, a greater discrepancy is observed in the direction parallel to bedding, in particular if the drying process is considered.

Finally, considering the behaviour of the facies observed during the wetting phase, the obtained results might have an impact on the swelling pressure expected during the resaturation process of the host rock occurring under in-situ condition; taking into account the different stiffness of the facies, different swelling pressure dependent on bedding orientation might be expected for the analysed facies.

Acknowledgement. The support of the Swiss National Cooperative for the Disposal of Radioactive waste (NAGRA) for this research is acknowledged.

References

Cardoso R, Romero E, Lima A, Ferrari A (2007) A comparative study of soil suction measurement using two different high-range psychrometers. Experimental unsaturated soil mechanics. Springer, Heidelberg, pp 79–93

Delle Piane C, Dewhurst D, Siggins A, Raven M (2011) Stress-induced anisotropy in brine saturated shale. Geophys J Int 184(2):897–906

Ferrari A, Favero V, Marschall P, Laloui L (2014) Experimental analysis of the water retention behaviour of shales. Int J Rock Mech Min Sci 72:61–70

Ferrari A, Laloui L (2013) Advances in the testing of the hydro-mechanical behaviour of shales. In: Laloui L, Ferrari A (eds) Multiphysical testing of soils and shales. Springer, Heidelberg, pp 57–68

Fredlund DG, Rahardjo H (1993) Soil Mechanics for Unsaturated Soils. Wiley, New York

Leong EC, Tripathy S, Rahardjo H (2003) Total suction measurement of unsaturated soils with a device using the chilled-mirror dew-point technique. Géotechnique 53(2):173–182

Mazurek M (1999) Mineralogy of the opalinus clay. In: Results of the hydrogeological, geochemical and geotechnical experiments, performed in 1996 and 1997. Swiss National Geological and Hydrogeological Survey. Geological report 23, pp 15–18

McLamore R, Gray KE (1967) The mechanical behavior of anisotropic sedimentary rocks. J. Eng. Ind. 89:62–73

Minardi A, Crisci E, Ferrari A, Laloui L (2016) Anisotropic volumetric behaviour of Opalinus Clay shale upon suction variation. Geotechnique Lett. 6:1–5

Niandou H, Shao JF, Henry JP, Fourmaintraux D (1997) Laboratory investigation of the mechanical behaviour of Tournemire shale. Int J Rock Mech Min Sci 34(1):3–16

Popp T, Salzer K (2007) Anisotropy of seismic and mechanical properties of Opalinus clay during triaxial deformation in a multi-anvil apparatus. Phys Chem Earth 32(8):879–888

Popp T, Salzer K, Minkley W (2008) Influence of bedding planes to EDZ-evolution and the coupled HM properties of Opalinus Clay. Phys Chem Earth 33:374–387

Salager S, François B, Nuth M, Laloui L (2013) Constitutive analysis of the mechanical anisotropy of Opalinus Clay. Acta Geotech 8(2):137–154

Soe AKK, Osada M, Takahashi M, Sasaki T (2009) Characterization of drying-induced deformation behaviour of Opalinus Clay and tuff in no-stress regime. Environ Geol 58(6):1215–1225

1D Compression Behaviour of Opalinus Clay

Valentina Favero(✉), Alessio Ferrari, and Lyesse Laloui

École Polytechnique Fédérale de Lausanne (EPFL), Lausanne, Switzerland
valentina.favero@epfl.ch

Abstract. One of the main concerns related to tunnel excavations, drilling operations and wellbore stability in shales is the generation of excess pore water pressure due to changes in mechanical stress; therefore the consolidation of shales is a fundamental process that must be considered. This paper presents a comprehensive methodology for analysing the compression and consolidation behaviour of shales. An apparatus to perform high-pressure oedometric tests is presented and an analytical method is introduced to analyse the shale consolidation behaviour, which allows information to be gathered on the coefficient of consolidation, stiffness, poroelastic properties, and permeability of the tested material as a function of the applied stress conditions. Results obtained on Opalinus Clay shale using the developed methodology are presented and discussed.

Introduction

Opalinus Clay is the shale formation currently considered for the construction of a nuclear waste repository in Switzerland. Different stress levels and the consequent changes in porosity affect the stiffness and permeability of the material, which are fundamental parameters in the assessment of the performance of the shale as host formation for waste disposal. Although the compaction and consolidation processes induced by the application of loads have been well understood for soils since the pioneering work of Terzaghi (1923), important issues remain unresolved in the analysis of the hydro-mechanical behaviour of shales. Additional factors related to the hydro-mechanical couplings in shales, such as the pore pressure coefficients and poroelastic properties (Biot 1941; Skempton 1954) as well as their dependency on the stress level (Detournay and Cheng 1993), must be included in the analysis of settlement evolution (Savage and Braddock 1991; Gutierrez et al. 2015) and in the assessment of porosity changes induced by loading. This paper presents a methodology for analysing the compression and consolidation behaviour of shales. The developed methodology allows oedometric tests to be performed on shales under a wide range of vertical effective stresses and allows the displacement evolution over time to be analysed through an analytical procedure. For this purpose, an apparatus was designed to perform high-pressure oedometric tests by applying a maximum vertical total stress of 100 MPa and simultaneously controlling the pore water pressure of the specimen. The proposed analytical method combines (i) a modified form of the classical Biot (1941) theory to account for the behaviour of shales under oedometric conditions and (ii) an extended one-dimensional consolidation theory to consider the poroelastic behaviour of shales and time-dependent loading conditions. The proposed analytical method allows

A. Ferrari and L. Laloui (eds.), *Advances in Laboratory Testing and Modelling of Soils and Shales (ATMSS)*, Springer Series in Geomechanics and Geoengineering,
DOI 10.1007/978-3-319-52773-4_37

information to be gathered on the coefficient of consolidation, stiffness, poroelastic properties and permeability of the tested material as a function of the applied stress.

Tested Shale

The Opalinus Clay cores studied in this work were retrieved from two different areas and depths in the north of Switzerland: the Mont Terri Underground Rock Laboratory (URL) in north-western Switzerland and the Schlattingen site in the Molasse basin. The Opalinus Clay from the Mont Terri URL (OPA-shallow) is located at a depth of approximately 300 m, while the Opalinus Clay formation at the Schlattingen site (OPA-deep) is found at a depth of approximately 830 m until a depth of approximately 950 m. The index properties of the tested cores at the as-extracted state are reported in Table 1. OPA-deep is characterized by considerably lower void ratio values with respect to OPA-shallow; this is likely due to both burial compaction and diagenetic phenomena (Favero et al. 2016).

Table 1. Geotechnical characterization of the tested cores.

Core	Depth (m)	ρ_s (Mg/m^3)	ρ (Mg/m^3)	w (%)	e (−)	S_r (%)	w_L (%)	w_P (%)	PI (%)
OPA-shallow	~300	2.75	2.46	7.5	0.21	98	38	23	15
OPA-deep	~890	2.71	2.49–2.55	3.3–4.9	0.10–0.15	93–96	29–36	19–25	9–13

Experimental Methodology

A high-pressure oedometric cell, which was developed to analyse the hydro-mechanical behaviour of shales at high confining stresses (Ferrari and Laloui 2013a), is used in this study. The cell is designed to hold cylindrical specimens (12.5 mm in height and 35 mm in diameter). The oedometer cell is put into a rigid stainless steel frame. The vertical load is applied by a hydraulic jack connected to a volume/pressure controller. The loading ram is positioned in the lower part of the system to prevent the specimen from being loaded before the test starts. The maximum vertical stress that can be imposed on the specimen is 100 MPa. The volumetric strains are measured by three LVDTs (with a resolution of 1 μm), which are fixed to the frame and are in contact with the loading ram. Two pumps are used to control the pore water pressure at the bottom and top basis (up to 2 MPa) and to measure the volume changes of the pore water.

The shale specimens were initially cut from the original cores and immediately placed inside the cell, in order to preserve as much as possible the initial conditions, since these materials are very sensitive to changes in relative humidity (Ferrari et al. 2014). The specimens were then saturated in isochoric conditions by applying a back pressure between 50–200 kPa, and the developed swelling pressure was measured. Afterward, loading-unloading cycles were performed in stages, allowing for the complete dissipation of the excess pore water pressure (drained conditions). The settlement versus time curves obtained from each loading step of the oedometric tests were analysed using an analytical model presented in Ferrari et al. (2016): the most relevant equations are briefly recalled here. The continuity equation in the zdirection which describes the one-dimensional consolidation process in shales is expressed as:

$$c_v \frac{\partial^2 u_e}{\partial z^2} = \frac{\partial u_e}{\partial t} - C \frac{\partial \sigma_z}{\partial t} \tag{1}$$

where u_e is the excess pore water pressure, σ_z is the vertical total stress, C is the coefficient defining the ratio of the increment in pore water pressure to the increment in vertical total stress under one-dimensional and undrained conditions, and t is time. The coefficient of consolidation c_v is defined as:

$$c_v = \frac{k_z E_{oed} C}{\alpha_{oed} \gamma_w} \tag{2}$$

where E_{oed} is the oedometric modulus, k_z is the coefficient of permeability in the vertical direction, γ_w is the specific weight of water, and αoed is the Biot's coefficient, here defined for the oedometric case as the ratio of the variation in the fluid content to the volumetric deformation when the development of radial strain is prevented. The solution of Eq. (1) allows to express the evolution of the primary consolidation settlement. The settlement versus time curves obtained in each loading step of the oedometric tests were analysed using the introduced model, which takes into account not only the primary consolidation settlement for a non-instantaneous loading, but also the deformation of the apparatus and the secondary compression. The curve fitting was performed based on the principle of the least-squares method, by minimizing the sum of the squared differences between the computed and measured settlements for the different time steps. The coefficient of permeability can be estimated based on the definition of the coefficient of consolidation, as expressed in Eq. (2):

$$k_z = \frac{c_v \alpha_{oed} \gamma_w}{C E_{oed}} \tag{3}$$

Equation (3) highlights that an assessment of the poroelastic parameters is required for the calculation of the coefficient of permeability. All the parameters that appear in the expression are obtained by fitting the experimental results in terms of time-settlement curves with the considered model. The optimization process is guided by certain restrictions on the values of the parameters and by preliminary estimations.

Results and Analysis

One-Dimensional Compression Behaviour

In this section the results of two high-pressure oedometric tests are presented: Test 1 is carried out on OPA-shallow, while Test 2 is carried out on OPA-deep. The section has

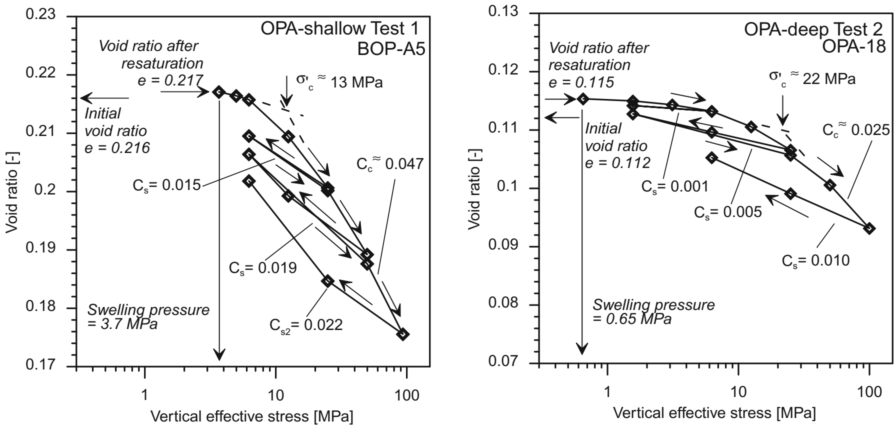

Fig. 1. End-of-primary oedometric curves for OPA-shallow and OPA-deep cores (after Ferrari et al. 2016).

the aim to describe the volume change behaviour of Opalinus Clay cores retrieved from different depths, during oedometric compression. The end-of-primary oedometric curves for the two considered Opalinus Clay specimens are depicted in Fig. 1.

The swelling pressures developed during the saturation phase were 3.7 MPa and 0.65 MPa for the first and second tests, respectively, for void ratio increments from 0.216 to 0.217 in Test 1 and from 0.112 to 0.115 in Test 2. Beginning with the saturation phase, the plots in Fig. 1 depict the volumetric response of the OPA-shallow specimens along the applied loading-unloading stress path. A pre-yield to post-yield transition is observable for both specimens, with vertical effective yield stresses obtained with the Casagrande's graphical method equal to approximately 13 MPa and 22 MPa for the first test and second test, respectively. The computed values of the compression index (C_c) and swelling index (C_s) are also reported in Fig. 1. An increase in the swelling index is observed with an increase in the maximum stress level reached during the loading history: greater swelling occurs upon mechanical stress release when greater vertical stresses are reached. The compression indexes suggested that the OPA-deep is less compressible than OPA-shallow since the C_c shows values equal to 0.047 for OPA-shallow and 0.025 for OPA-deep.

The values of the oedometric modulus are depicted in Fig. 2 as a function of the vertical effective stress at the beginning of the loading/unloading steps. An increase in the oedometric modulus with increasing vertical effective stress is evident, showing that the material becomes stiffer with increasing stress. The oedometric moduli measured during the unloading phases are also reported; in accordance with the trend reported for the swelling index, a reduction in the stiffness for the same vertical effective stress is observed in cases in which a higher vertical stress was previously reached.

Figure 3 presents the values of the coefficient of consolidation as a function of the vertical effective stress. For both tests, the variation in this coefficient with the vertical effective stress shows a trend similar to that typically observed for soils (Lambe and Whitman 1979): during the first loading phase, it is observed to decrease as the vertical

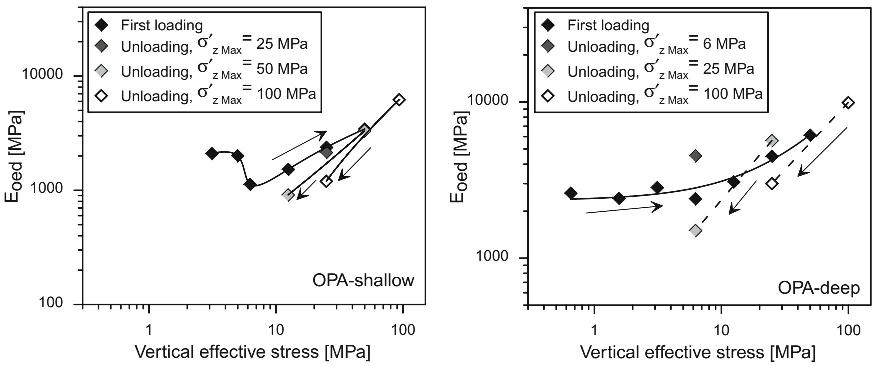

Fig. 2. Oedometric modulus as a function of the vertical effective stress.

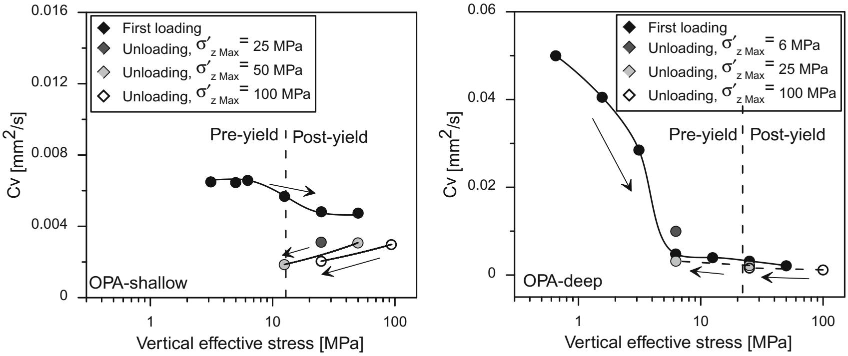

Fig. 3. Coefficient of consolidation as a function of the vertical effective stress.

effective stress approaches the yield stress, whereas afterwards, it remains approximately constant in the post-yield region; during unloading, the coefficient decreases as the vertical effective stress is released.

The values of the Biot coefficient α_{oed} obtained from the analysis of several oedometric tests on both OPA-shallow and OPA-deep are reported in Fig. 4 as a function of the vertical effective stress for the main loading path. The reduction in the α_{oed} with increasing vertical effective stress is observed for both OPA-shallow and OPA-deep, and this trend agrees well with the increase in the oedometric modulus.

Figure 5 reports the values of the pore pressure coefficient C as a function of the vertical effective stress. The obtained values are observed to decrease as the maximum vertical stress increases. This is a common trend that is often observed in stiff geomaterials in which the poroelastic properties play a significant role (Cook 1999): C values lower than one mean that under undrained compression, part of the load is carried by the solid constituents rather than by pore water alone.

A correct evaluation of the coefficient of permeability requires knowledge of the poroelastic properties of the material because they are relevant to the hydro-mechanical behaviour of stiff geomaterials. Consequently, a rigorous means of including the

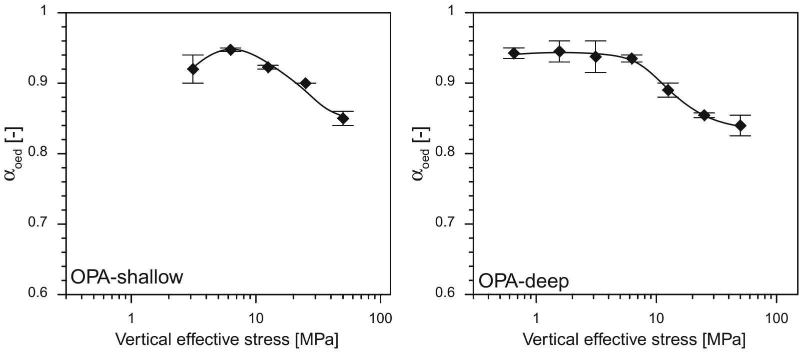

Fig. 4. Poroelastic parameter α_{oed} for Opalinus Clay samples from two different depths as a function of the vertical effective stress (after Ferrari et al. 2016).

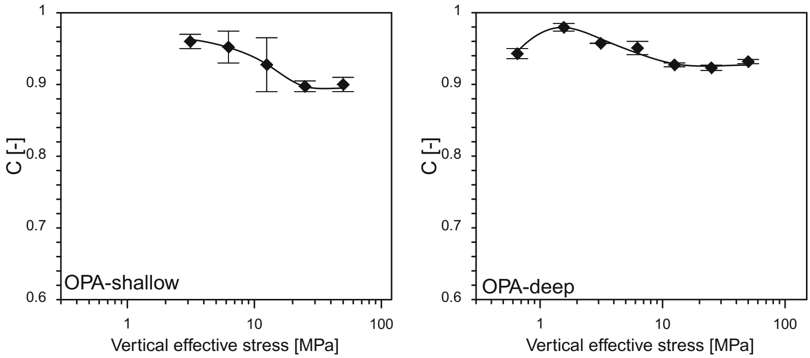

Fig. 5. Poroelastic parameter C for Opalinus Clay samples from two different depths as a function of the vertical effective stress (after Ferrari et al. 2016).

poroelastic features in the analysis is strongly needed. In this work, the expression used for the coefficient of permeability (Eq. 3) was derived from the consolidation equation for a poroelastic geomaterial, and all parameters that appear in the expression were obtained by fitting the experimental results. To validate the presented procedure, values of the coefficient of permeability for OPA-deep in the post-yield phase are presented as a function of the void ratio in Fig. 6. A comparison of the obtained results with direct measurements from constant-head permeability tests conducted on a core sample of the same material (Romero et al. 2013) reveals good agreement, especially when the possible heterogeneity of the different tested cores is considered.

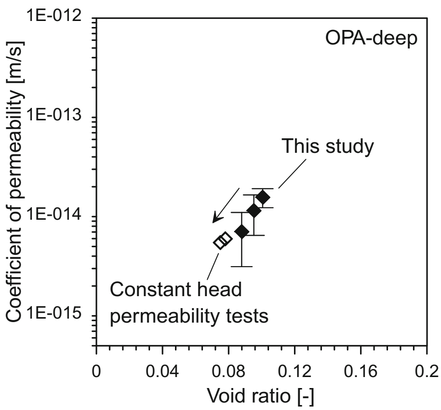

Fig. 6. Coefficient of permeability of OPA-deep as a function of the void ratio, as obtained from the analysis of the settlement versus time curves and compared to results from Romero et al. (2013) (after Ferrari et al. 2016).

Conclusions

This paper presented an advanced experimental tool and a comprehensive technique for investigating the oedometric volumetric behaviour and consolidation of shales. Testing materials with high yield stresses requires the design of a high-pressure oedometric cell, as presented here; the proposed approach enabled the successful testing of the mechanical behaviour of Opalinus Clay shale specimens and the observation of the transition from the pre- to the post-yield phases. An analytical solution was presented to enable the analysis of the time-dependent settlement curves of the tested shales; the developed method allows for the interpretation of the experimental results in light of the deformation of the testing device and secondary consolidation phenomena. The correct assessment of the hydro-mechanical behaviour of Opalinus Clay shale is particularly relevant because this material is a candidate host rock for the construction of deep geological repositories for high-level nuclear waste in Switzerland. The results of this work can provide guidance regarding consolidation and settlement during tunnel excavation, as well as regarding swelling phenomena.

References

Biot MA (1941) General theory of three-dimensional consolidation. J Appl Phys 12(2):155–164

Cook J (1999) The effects of pore pressure on the mechanical and physical properties of shales. Oil Gas Sci Technol 54(6):695–701

Detournay E, Cheng A (1993) Fundamentals of poroelasticity. In: Hudson J (ed) Comprehensive rock engineering: principles, practice & projects. Pergamon Press, Oxford vol. 2, p 113–171

Favero V, Ferrari A, Laloui L (2016) On the hydro-mechanical behaviour of remoulded and natural Opalinus clay shale. Eng Geol 208:128–135

Ferrari A, Favero V, Laloui L (2016) One-dimensional compression and consolidation of shales. Int J Rock Mech Mining Sci 88:286–300

Ferrari A, Favero V, Marschall P, Laloui L (2014) Experimental analysis of the water retention behaviour of shales. Int J Rock Mech Mining Sci 72:61–70

Ferrari A, Laloui L (2013a) Advances in the testing of the hydro-mechanical behaviour of shales., Multiphysical Testing of Soils and Shales. Springer, Heidelberg, pp 57–68

Gutierrez M, Katsuki D, Tutuncu A (2015) Determination of the continuous stress-dependent permeability, compressibility and poroelasticity of shale. Marine Petrol. Geol. 68:614–628

Lambe TW, Whitman RV (1979) Soil mechanics. Wiley, New York

Romero E, Senger R, Marschall P, Gómez R (2013) Air tests on low-permeability claystone formations. Experimental results and simulations., Multiphysical Testing of Soils and ShalesSpringer, Heidelberg, pp 69–83

Savage WZ, Braddock WA (1991) A model for hydrostatic consolidation of Pierre shale. Int J Rock Mech Mining Sci Geomech Abstracts

Skempton A (1954) The pore-pressure coefficients A and B. Geotechnique 4(4):143–147

Terzaghi K (1923) Die berechnung der durchlassigkeitsziffer des tones aus dem verlauf der hydrodynamischen spannungserscheinungen. Sitzungsber. Akad. Wissen., Wien Math. Naturwiss. Kl., Abt. IIa 132:105–124

Consolidated-Undrained Triaxial Test Results of Opalinus Clay and Comparison with Caprock Shales

Silvio Giger[1(✉)], Russell Ewy[2], and Rudy Stankovic[3]

[1] Nagra, Wettingen, Switzerland
Silvio.Giger@nagra.ch
[2] Chevron Energy Technology Co., Houston, USA
[3] RSTD Co., Southport, UK

Abstract. Specific equipment and procedures developed for geomechanical testing of hydrocarbon caprocks were adopted to conduct truly undrained triaxial tests with Opalinus Clay. The amount of pore pressure development during consolidation, and the resulting effective stress, is managed by equilibrating the samples in vacuum desiccators of different relative humidities (vapor equilibration technique) prior to assembling into the test apparatus. We present test results of five Opalinus Clay samples covering a laboratory mean effective consolidation stress range from 5 MPa to 50 MPa. A drained consolidation test was first conducted to determine the appropriate strain rate for consolidated-undrained (CU) triaxial testing. The Skempton 'B' parameter was quantified prior to the deformation tests and found to be stress dependent. A distinct stress dependency of elastic moduli is also observed, but normalized with the undrained shear strength there is only a relatively small variation. Within the explored stress range the different stress paths to peak indicate a transition from over consolidated to rather normally consolidated state. However, failure is in all cases dilatant, i.e. associated with a drop in pore pressure and strain-softening (more so at low effective stress). Caprock shales of similar porosity to the Opalinus share many similarities in overall behavior, but also exhibit some slight differences.

Introduction

Triaxial testing of low permeability argillites (shales, claystones) is challenging as elements of traditional soil mechanics testing must be adapted in the stress realm more typical of rock mechanics. Such procedures are required for geomechanical testing of Opalinus Clay, the designated host rock for high-level radioactive waste and one possible host rock for long-lived and intermediate to low level waste in Switzerland. It exhibits a very low hydraulic conductivity of the order of 1×10^{-14} to 1×10^{-12} m/s, but its mechanical behavior must be studied to elevated stresses given its relatively high strength (compared to clays) and given the planned repository depth range of approximately 400 to 900 m below ground.

The hydrocarbon industry faces similar challenges for geomechanical assessment of caprock shales and growingly also for tight shales from unconventional reservoirs. Special equipment and procedures were therefore developed for undrained triaxial

A. Ferrari and L. Laloui (eds.), *Advances in Laboratory Testing and Modelling of Soils and Shales (ATMSS)*, Springer Series in Geomechanics and Geoengineering,
DOI 10.1007/978-3-319-52773-4_38

testing (e.g. Steiger and Leung 1991, Ewy et al. 2003). Here we report on consolidated-undrained (CU) triaxial test results of Opalinus Clay using the same established procedures, which have been continuously used and improved as Chevron's and RSTD's shale testing standard for nearly 20 years.

Methodology

Sample Characterization

The core material used for this study stems from a borehole drilled in the village of Lausen (Switzerland) and was sourced from a shallow depth of approximately 33 m below ground. Preliminary analyses indicate a bulk density of approximately 2.47 g/cc and a mineralogy dominated by clay minerals ($\sim$50 wt%) and quartz (30 wt%). Water content (from oven drying) is between 5.3 to 6.0 wt% and calculated physical porosity approximately 12 to 15%. Hence, relating to the facies subdivision commonly used at the Mont Terri Underground Laboratory, the sample characteristics are considered more alike the "sandy" facies than the "shaly" facies (e.g. Bossart and Thury 2008).

Determination of Appropriate Strain Rate

To determine the allowable loading rate, a special test was performed to measure the consolidation coefficient, c_v (perpendicular to bedding). A sample 19 mm diameter by 13 mm length was subject to 10 MPa hydrostatic confining stress and 3 MPa pore pressure using 8.29 wt% NaCl brine. This test setup allows for applied fluid pressure at one end, while sample pore pressure is measured at a fully-undrained boundary at the other end. Once pore pressure was stable, it was increased to 6 MPa at the applied pressure end. After reaching a stable pressure at the no-flow end it was decreased back to 3 MPa at the applied pressure end. This is essentially a one-dimensional pressure diffusion test. The consolidation coefficient is approximated as the value of pressure diffusivity that explains the observed pressure change vs. time.

The results of this test are shown in Fig. 1. The pressure increase behavior and pressure decrease behavior are fit by slightly different values of c_v. The average value is 0.0034 mm^2/s. Using the equations in Head (1998), the allowable axial strain rate for undrained triaxial compression is 6E-08/s without side drains and is 1.3E-06/s with side drains, for strain at failure of 1%. Because our side drains consist of thin strips along two opposite sides and do not provide complete circumferential coverage, a compromise strain rate of 2E-07/s was used.

Sampling and Testing Procedure

Opalinus Clay was cored using a water-base drilling fluid with a polymer additive. Immediately after recovery core sections of approximately 100 cm in length and 10 cm in diameter were wrapped and sealed in aluminium foil and resin-impregnated into a plastic barrel to keep it preserved. Samples for triaxial testing were then sub-cored in

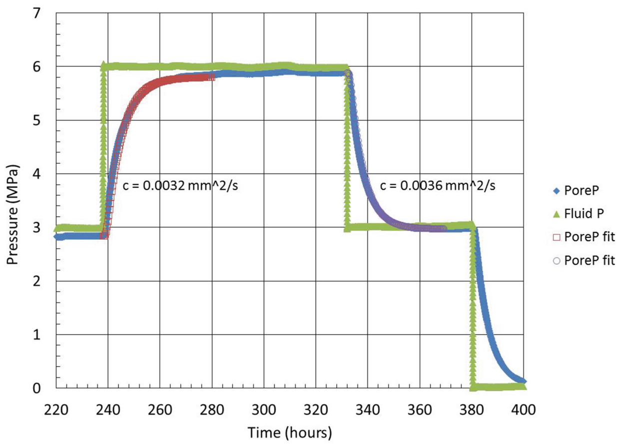

Fig. 1. Pressure diffusivity (consolidation coefficient) test, with fitted values.

the laboratory (19 mm diameter and 38 mm length), parallel to the core axis and perpendicular to bedding. Decane was used for sampling. The edges of the core were avoided, due to possible alteration by the coring fluid. Next the samples were equilibrated to a relative humidity of 92 to 98% (Table 1) in vacuum desiccators. The purpose of this step is twofold: (1) it assures a very high level of fluid saturation in the sample, and (2) the subtle differences in the relative humidities are used to control the amount of pore pressure (and hence effective stress) developing during consolidation. This is required as the set-up does not use a pore fluid line which would allow dynamic control of fluid pressure (see below).

The apparatus used for the CU test is described in detail in Ewy et al. (2003). It does not contain a pore fluid line to ensure the external pore fluid volume is a small fraction of the sample pore volume. The key innovation of the apparatus is that pore fluid pressure can still be measured continuously right near the sample face. In this way truly undrained tests can be conducted at the expense of the capability to actively adjust pore fluid pressure during the consolidation stage. This is managed by adjusting the samples to slightly different water contents as described above. The consolidation stage requires that confining stresses are raised at least until a positive pore fluid pressure is recorded. Before applying deviatoric loading, Skempton-B tests were conducted in three steps by increasing the confining stress by 1 MPa in each step (Fig. 2).

Deviatoric loading is then applied using a constant loading rate as determined from the consolidation test (see above). The combination of preconditioning the samples in a desiccator and using small samples with side drains enabled a relatively short test duration between 10 to 20 days (including several days for Skempton B steps), depending on the targeted stress range.

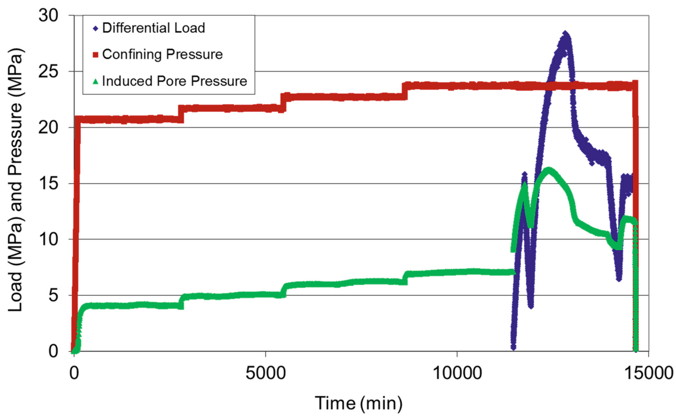

Fig. 2. Stress/pressure vs. time sequence for one of the samples.

Results

Undrained Elastic Parameters and Strength

Test conditions and test results for the various experiments are summarized in Table 1. It comprises of information of the isotropic effective mean consolidation stress (p'_c) prior to deviatoric loading, the interpreted undrained elastic parameters (Young's Modulus E_u, Poisson ratio v_u) as well as Skempton's pore pressure coupling parameter B and the effective mean and deviator stresses at failure (p'_f and q_f, respectively) defined as:

$$p'_f = \left(\sigma'_1 + 2 \cdot \sigma'_3\right)/3 \tag{1}$$

$$q_f = \sigma'_1 - \sigma'_3 \tag{2}$$

where σ'_1 and σ'_3 are the vertical and lateral effective stress magnitudes during triaxial compression tests with axial (vertical) loading.

Table 1. Overview of samples, test conditions and test results. Note: cylindrical samples were cored with the axis perpendicular to bedding.

Sample-ID	LSN1-1-9	LSN1-1-10	LSN1-1-7	LSN1-1-8	LSN1-1-5
RH [%]	98	98	96	96	92
p'_c[MPa]	5.1	14.6	18.1	43.6	51.7
B [-]	0.89	0.93	(0.70)	(0.50-0.70)	0.52
v_u [-]	0.46	0.49	0.38	0.36	0.41
E_u[MPa]	2690	4240	4960	5860	6870
q_f [MPa]	19.4	28.0	28.3	43.2	50.0
p'_f[MPa]	8.3	18.2	19.4	39.3	48.9
E_u:c_u [-]	277	303	351	271	275

The test results in Table 1 are arranged in columns with increasing consolidation stress to the right to better illustrate the general trends of the derived parameters with increasing effective mean consolidation stress. Skempton-B appears to decrease with stress, although it is noted than in two test results it was difficult to derive robust values (indicated in brackets). With increasing stress, the Poisson ratios broadly decrease and deviate from $v_u = 0.5$, the theoretical value for soil materials for which fluid and mineral grains can be considered as incompressible. Hence this trend can be considered an indication that the material becomes stiffer with greater stress and that the mineral grains and the fluid can no longer be regarded as incompressible compared to the skeleton. The undrained Young's modulus E_u was constrained from primary loading, and the derived values confirm a clear stress dependency, i.e. values for E_u increase non-linearly and by more than a factor two across the applied effective stress range.

Defining the undrained shear strength as $c_u = q_f/2$ to normalize the undrained E-Modulus it is found that the ratio Eu:cu is fairly constant around 300:1, varying less than 10% except for one test (Table 1).

The stress paths (Fig. 3) of tests starting from $p'_c \leq 15$ MPa are more typical of an over consolidated behavior, with a pronounced positive slope curvature before peak and indicative of pore pressure reduction and dilation. Stress paths for tests starting at $p'_c \leq 43$ MPa indicate a somewhat more normally-consolidated type behavior with positive pore pressure generation close to failure. However, failure is in all tests associated with dilation.

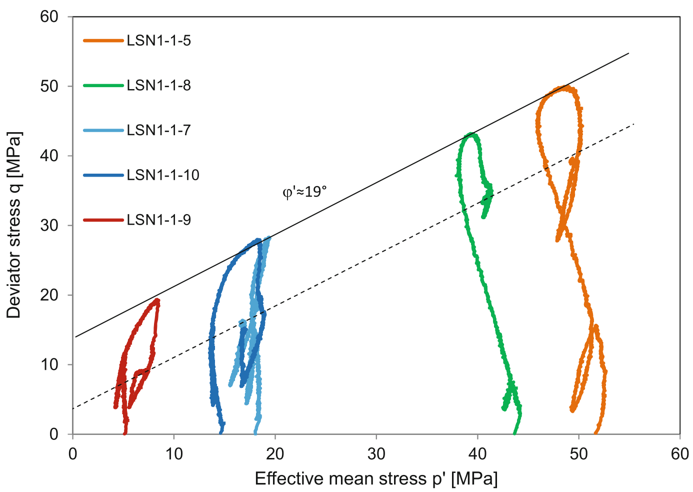

Fig. 3. Undrained stress paths for the five tested samples.

From the stress path a failure line with a slope of approximately 0.74 can be interpreted. This translates to a Mohr-Coulomb effective friction angle of approximately 19°. Unloading and reloading the sample to shear after failure suggests that the same slope is also suited to depict values of post-peak or residual strength. Essentially, the transition from peak to post-peak mainly affects the intercept value, but not the slope. This is qualitatively and quantitatively (friction angle) consistent with drained test results by Favero et al. (2016) with Opalinus Clay samples from the Mont Terri Underground Laboratory, and also with recent studies conducted with the Callovo-Oxfordian claystone from the Bure Underground Laboratory (Hu et al. 2014, Menaceur et al. 2015).

Stress-Strain Behaviour

The stress-strain behavior to peak is in all tests clearly non-linear (Fig. 4). All tests do exhibit strain-softening associated with failure. This finding is consistent with the dilative behavior associated with peak as observed in the stress paths. Strain-softening is much more pronounced for tests deformed at lower effective confining stresses. At the highest effective mean stress, deviator stress seems to peak in a more ductile manner (prolonged peak) before eventually dropping.

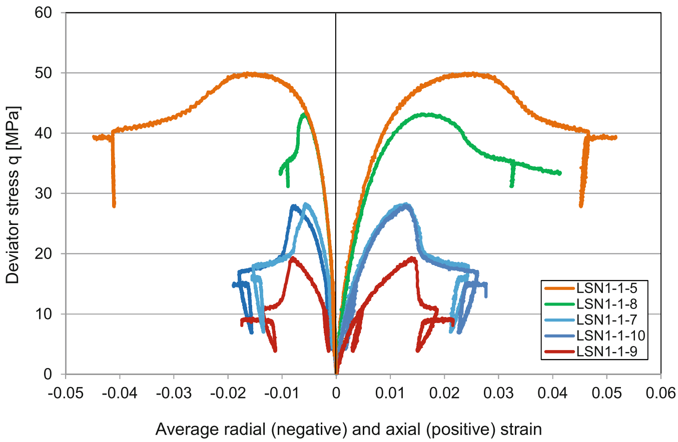

Fig. 4. Stress-strain (radial and axial) plot, undrained.

Comparison with Caprock Shales

From a dataset of over 80 caprock shales tested using these same protocols, covering a porosity range of ~10% to ~30%, two examples are selected here for comparison. Both shales are roughly similar to the tested Opalinus core; Shale X has bulk density 2.49 g/cc, porosity (oven-drying) 14% to 15%, is 64% clay (all illite/smectite) and has a bulk CEC of ~25 meq/100 g. Shale Y has bulk density 2.43 g/cc, porosity ~16%, is 77% clay (half kaolinite and half illite/smectite) and has a bulk CEC of ~18 meq/100 g. Additional test results on Shale Y, including strength anisotropy, are presented as 'Shale E' in Ewy et al. (2010).

Undrained stress paths for both shales are shown in Fig. 5. Several similarities with the Opalinus (Fig. 3) are apparent. Firstly, the interpreted cohesion and apparent UCS of these shales are roughly similar to the tested Opalinus Clay, being only slightly

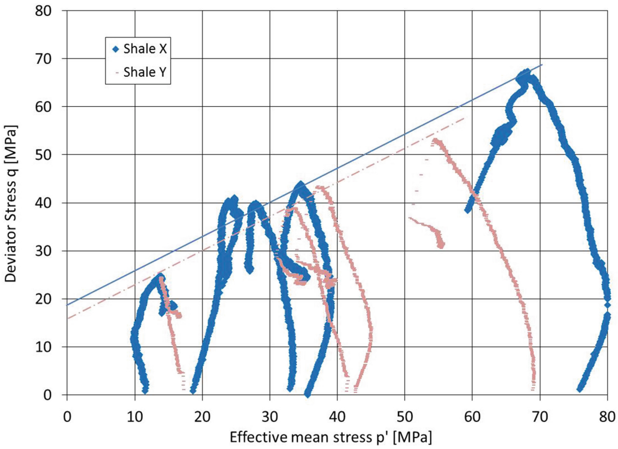

Fig. 5. Stress paths from two example caprock shales.

stronger. Secondly, the friction angle for these two shales is $\sim 18.6°$, also quite similar to the Opalinus (this may be mostly coincidence; measured friction angles for any clay-rich shale can usually be anywhere in the range 11° to 22°). Thirdly, at high stress the undrained stress paths tend to the left, exhibiting normally-consolidated behavior. Fourthly, a strength drop following peak stress occurs for all stress conditions, just as for the Opalinus.

In addition, Shale X shows an over consolidated stress path direction (to the right) at low stress, similar to Opalinus, although Shale Y does not. A small difference compared to Opalinus is that the high-stress stress paths for both of these shales continue to the left at peak and post-peak, whereas they turn to the right for the Opalinus. The slight differences in behavior among these two caprock shales, and compared to the Opalinus, could be due to differences in mineralogy or to fabric, including possible effects of anisotropic deformation behavior. But all three shales demonstrate both clay-like behavior and rock-like behavior. In general, the more a shale has been compacted in the earth to low porosity, the more its behavior deviates from that of high-porosity clay soils. Some examples, including stress-strain curves as well as stress paths, are given in Ewy et al. (2003).

References

Bossart P, Thury M (eds) (2008) Mont Terri Rock Laboratory – Project, Programme 1996 to 2007 and Results. Reports of the Swiss Geological Survey No. 3 – Swiss Geological Survey, Wabern

Ewy RT, Stankovich RJ, Bovberg CA (2003) Mechanical behavior of some clays and shales from 200 m to 3800 m depth. In: 39th U.S. Rock Mechanics Symposium/12th Panamerican Conference Soil Mech & Geotech Eng. MIT, Cambridge, USA, 22–26 June 2003

Ewy RT, Bovberg CA, Stankovic RJ (2010) Strength anisotropy of mudstones and shales. In: 44th U.S. Rock Mechanics Symposium/5th U.S.-Canada Rock Mechanics Symposium, Salt Lake City, USA, 27–30 June, 2010. paper ARMA 10-114

Favero V, Ferrari A, Laloui L (2016) Consolidated-drained triaxial testing of Opalinus Clay. Nagra Int. Ber

Head KH (1998) Manual of Soil Laboratory Testing, vol 3., Effective Stress TestsWiley, Chichester

Hu DW, Zhang F, Shao JF (2014) Experimental study of poromechanical behavior of saturated claystone under triaxial compression. Acta Geotech 9:207–214

Menaceur H, Delage P, Tang A-M, Conil N (2015) The thermo-mechanical behaviour of the Callovo-Oxfordian claystone. Int J Rock Mech Min Sci 78:290–303

Steiger RP, Leung PK (1991) Consolidated undrained triaxial test procedure for shales. In: Proceeding 32nd U.S. Rock Mechanics Symposium, Balkema, pp 637–646

One Dimensional Consolidation of Opalinus Clay from Shallow Depth

Eleonora Crisci[1(✉)], Alessio Ferrari[1], Silvio Giger[2], and Lyesse Laloui[1]

[1] Swiss Federal Institute of Technology, EPFL, Lausanne, Switzerland
eleonora.crisci@epfl.ch
[2] National Cooperative for the Disposal of Radioactive Waste, NAGRA, Wettingen, Switzerland

Abstract. First experimental results on Opalinus Clay from shallow depth (<30 m depth) are presented and compared to results on cores from Mont Terri Underground Rock Laboratory ($\sim$300 m depth). Samples were tested in one dimensional condition using an advanced experimental technique. The samples from the two sites show similar properties in terms of geotechnical characterization and one dimensional compressibility/swelling indexes, despite the different source depths.

Introduction

In the context of the deep underground disposal of nuclear waste, Switzerland has selected Opalinus Clay, a Jurassic shale, as a suitable host geo-material. Opalinus Clay is found throughout the north-eastern part of the country where the candidate repository sites are situated. The current depth distribution of Opalinus Clay in this area varies, notably due to the gentle dip of the Mesozoic sediments towards south-east. The dip developed by flexural loading during Alpine orogeny. Tectonic and erosional processes in Miocene to Quaternary times further contributed to the complexity of current depth distribution.

A relevant part of the research until now was conducted on cores from the Mont Terri Underground Rock Laboratory (URL), where Opalinus Clay, interpreted to have reached a maximum burial depth of approximately 1350 m (Mazurek et al. 2006), is found nowadays at about 300 m depth. Recently a borehole was drilled in a site in North-Western Switzerland where Opalinus Clay is encountered immediately at the base of Quaternary sediments at a depth of only 8 to approximately 70 m. Cores at different depths were retrieved, and an experimental campaign started in order to analyse the variability of the mechanical properties with depth.

Considering the long lasting life-time required to radioactive waste disposals of up to one million years, it is necessary to assess the potential effects of exhumation of the repository on barrier integrity. In this context, the cores from the shallow subsurface are investigated to study how the mechanical characteristics of the material may change with depth.

Complete geotechnical characterization and a high pressure one-dimensional consolidation test were performed, using an advanced experimental technique. The results

A. Ferrari and L. Laloui (eds.), *Advances in Laboratory Testing and Modelling of Soils and Shales (ATMSS)*, Springer Series in Geomechanics and Geoengineering,
DOI 10.1007/978-3-319-52773-4_39

are then compared to results from a core of Opalinus Clay from Mont Terri with very similar index properties and mineralogy.

Tested Material

Opalinus Clay shale is a fine grained sedimentary geomaterial mainly composed by silicates sheets minerals, carbonates and quartz (Mazurek 1999). In the presented work, results from a core of Opalinus Clay retrieved at 23 m depth near the village of Lausen, hereafter indicated as OPA-Lau, are presented. Geotechnical characterization and experimental results are compared to oedometric tests on Opalinus Clay (results from Ferrari et al. 2016) from the Mont Terri Underground Rock Laboratory (OPA-MT), in northern Switzerland. OPA-Lau presents index properties and mineralogy very similar to OPA-MT samples belonging to the shaly facies of the formation: a homogeneous, laminated, argillaceous and marly shale with low sand content (Bossart 2011), composed of 55–65% clay minerals, 10–20% of quartz, 10–20% of calcite.

The index properties of the two cores are reported in Table 1 (particle density ρ_s, liquid limit w_L, plastic limit w_P and plasticity index *PI)*, along with the void ratio *e* of the specimens, measured after the preparation for oedometric tests.

Table 1. Index properties of the Opalinus Clay cores used in this investigation and void ratio of the specimens used in the oedometric tests.

	Depth	ρ_s	w_L	w_P	PI	e
	m	Mg/m^3	%	%	%	–
OPA-Lau	~23	2.77	30	23	7	0.23
OPA-MT	~300	2.75–2.76	38	23	15	0.22

A specific procedure for the definition of the grain size distribution was developed to properly quantify the different grain size fractions. The technique includes manual crushing of the materials with a rubber hammer, particle dispersion in distilled water, wet sieving and sedimentation analysis. Figure 1a depicts the grain size distributions for the two tested cores. The cores show similar grain size distribution with the following percentage of grain size fractions: 8% sand, 64% silt and 28% clay for OPA-Lau; 10% sand, 58% silt and 32% clay for OPA-MT. Mercury Intrusion Porosimetry (MIP) tests were also performed on cubic specimens with side of 0.8 cm, showing a single dominant pore diameter of 20–30 nm for both cores (Fig. 1b).

Experimental Device and Techniques

Specimen Preparation

Specimens for oedometric tests were prepared using a workflow which was developed by Ferrari and Laloui (2013). The procedure consists in cutting a slice from the core with a thickness of approximately 20 mm without unpacking the core from the black

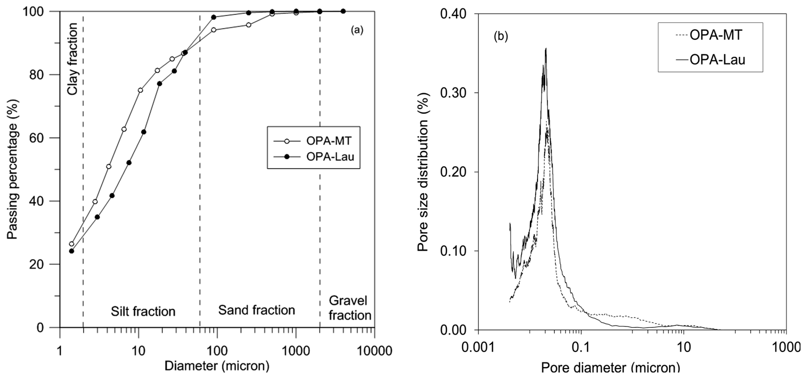

Fig. 1. (a) Grain size distribution and (b) Mercury Intrusion Porosimentry (MIP) results on cores from Mont Terri (OPA-MT) and from a shallow depth borehole (OPA-Lau).

PVC tubes in which the material is stored, in order to minimize the disturbance to the sample. Afterward the slice is sawn in a smaller piece suitable to be handled in a lathe machine. The diameter of the slice is progressively reduced in order to obtain a disk with a diameter slightly larger than the final confining ring. The height of the sample is reduced using the lathe machine, obtaining parallel and plane lower and upper faces. Re-coring with the oedometric ring is performed by using a hydraulic press. Finally, the lower and upper faces of the specimen are smoothed using sand paper. The specimen for the one-dimensional consolidation test was prepared with the bedding orientation perpendicular to the loading direction. The same preparation procedure and bedding orientation was used for tests performed on Opalinus Clay from Mont Terri (Ferrari et al. 2016). Thus, it is assumed that no differences in the behaviour can be addressed to the sample preparation technique adopted.

High-Pressure Oedometric Cell

The tests were performed in a multi-purpose oedometric set-up, designed to perform loading-unloading cycles at high stress levels (Ferrari and Laloui 2013). The cell was designed to hold cylindrical samples (12.5 mm in height and 35 mm in diameter). The oedometer ring is inserted into a rigid stainless steel frame. The loading ram is positioned in the lower part of the system and the vertical load is applied by a hydraulic jack connected to a volume/pressure controller. The maximum vertical total stress applied on the specimens was 100 MPa.

The volumetric strains are measured by two LVDTs (with a resolution of 1 μm), which are fixed to the frame and are in contact with the loading ram. The tests are performed in incremental loads, and a pore water pressure controller is used to control the pore water pressure at the bottom and top basis of the specimen.

The OPA-Lau specimen was saturated at 50 kPa of backpressure. The specimen was allowed to saturate and the swelling was constrained (within a range of ±12 μm, corresponding to 0.1% of the vertical strain) increasing the vertical load in steps. The vertical swelling pressure was achieved. After the saturation phase, loading/unloading cycles were performed in steps. After the application of each load/unload, 24 h were allowed to completely dissipate the excess pore water pressure. Displacements over time were recorded.

Tests were performed using synthetic water, in order to reproduce the chemical composition of the in situ pore water. The pore water used for Mont Terri specimen (Pearson 1998) has an osmotic suction of 1.4 MPa (Ferrari et al. 2014). The water prepared for the shallow specimen has a salt concentration (and consequently an osmotic suction) considerably lower.

Testing under high confining stresses is required to observe the transition from pre- to post-yield compaction behaviour of shales; however, the instantaneous application of high vertical stresses in the laboratory is hardly feasible. As mentioned in the previous section, a volume/pressure controller is adopted for the application of the vertical stress, therefore few minutes are required to reach the selected vertical load. To analyse the settlement over time curve for each loading increment, an analytical solution was adopted that considers the time-dependent load (Ferrari et al. 2016). The solution combines a modified form of the classical Biot theory (Biot 1941), to account for the behaviour of shales under oedometric conditions, and an extended one-dimensional consolidation theory, to consider the poroelastic behaviour of shales and time-dependent loading conditions. For each loading step the method allows for the identification of the primary consolidation settlement, related to the water overpressure dissipation.

Test Results

Lausen Core (Shallow Subsurface)

Test result on the specimen from the Lausen borehole (OPA-Lau) is presented in Fig. 2a in terms of vertical effective stress $\left(\sigma'_{\mathrm{v}}\right)$ versus void ratio (e).

The swelling was accurately restrained and the void ratio was not affected significantly by the saturation phase. The pressure generated in the saturation phase, called the swelling pressure, is equal to 0.95 MPa, and it is higher than the in situ vertical stress, estimated considering an overburden load at 23 m of depth ($\sim$0.5 MPa). After the first loading step at 2 MPa of total vertical stress, an unloading reloading cycle was performed to assess that the behaviour of the shale was in the elastic regime. The second unloading reloading cycle was performed at a maximum vertical effective stress of 5 MPa. The specimen recovered only partially the deformation, highlighting that the shale behaviour at that stress level was already in an elasto-plastic regime.

Moreover, upon unloading-reloading cycles, the material exhibits a strong degradation of the elastic properties, represented by the swelling index C_s, that increased of an order of magnitude (from the initial 0.002 to 0.025 at 100 MPa of maximum effective vertical stress). The vertical effective yield stress σ'_{y} was assessed at 6.3 MPa by Casagrande's construction. Figure 2a reports also the compressibility C_c, and swelling C_s indexes for the various unloading-reloading cycles.

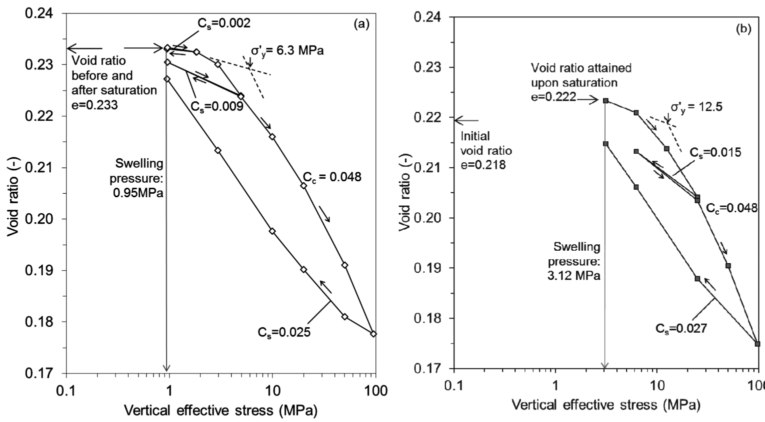

Fig. 2. Oedometric test results on (a) core from Lausen (~23 m depth) and (b) the core from Mont Terri (~300 m depth).

Comparison with Mont Terri Core

An oedometric test result on a Mont Terri core (data from Ferrari et al. 2016), is reported in Fig. 2b. The specimen from Mont Terri shows a slightly smaller void ratio. The compressibility C_c and the swelling C_s indexes are equal to 0.048 and 0.027, respectively. The swelling index was evaluated on the final unloading path. The C_s was also evaluated for the unloading-reloading cycle performed at 20 MPa of maximum vertical effective stress, and it is equal to 0.015. The swelling pressure, the initial void ratio, the void ratio after saturation and the vertical effective yield stress, assessed by Casagrande's construction, are reported in Fig. 2b.

Tests results are combined in Fig. 3. Interestingly, comparing the results on OPA-Lau and OPA-MT, the compressibility indexes appear to be equivalent and a unique trend of the compression lines is detectable. Elastic paths are also reported in Fig. 3: a common trend in the elastic properties degradation (increase of C_s as load increases) and in the final unloading path can be recognised.

This similarity is clear when the values of the swelling indexes are examined versus the maximum vertical effective stress experienced by the specimen before the unloading-reloading cycles (Fig. 4). In Fig. 4, three *Cs* values refer to OPA-Lau, two to OPA-MT. The index corresponding to the first loading step on OPA-MT is also depicted, assuming that in this first phase the specimen behaved elastically. The degradation of the swelling index with the applied stress follows the same trend for the two specimens: all the values are aligned in the semi-logarithmic plane of Fig. 4.

The similarities in terms of compressibility and swelling indexes can be attributed, as preliminary deduction, to the comparable composition, both in terms of grain size distribution and mineralogy, and to the fact that no significant differences were highlighted between the cores by the pore size distribution (determined by MIP).

However, concerning the yield stress, the specimen from Mont Terri site shows a higher vertical effective yield stress compared to the one of the shallower core.

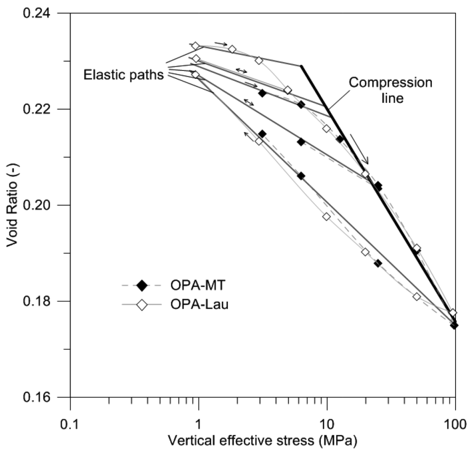

Fig. 3. Tests result from OPA-MT and OPA-Lau: identification of a unique compression line and common elastic paths, highlighting the degradation of the elastic properties with the applied vertical effective stress.

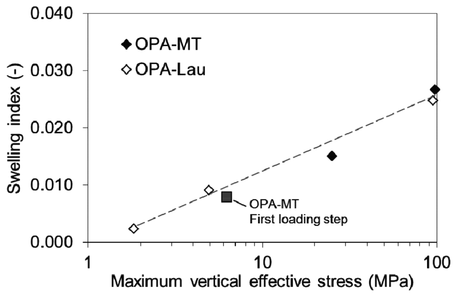

Fig. 4. Evolution of the swelling index with the maximum vertical effective stress for the specimen from Mont Terri and Lausen.

This difference could be related to the different geological history: at Lausen, Opalinus Clay was strongly decompacted by exhumation, assuming similar maximum burial depth as at Mont Terri; at Mont Terri the formation experienced the Jura folding (Bath and Gautschi 2003). Further investigation is needed to assess the validity of the hypothesis raised.

Concluding Remarks

Considering the long lasting life-time required to radioactive waste disposals, it is necessary to assess the potential effects of exhumation of the repository on barrier integrity. In this context, Opalinus Clay cores from the shallow subsurface are investigated to study how the mechanical characteristics of the material change with depth.

In this contribution, a core retrieved from a borehole near the village of Lausen, at a depth of ~23 m, was tested and results were compared to Mont Terri core.

Lausen core presents an initial void ratio slightly higher compared to the core retrieved at Mont Terri site. Moreover, it has similar grain size distribution and pore density function. Interestingly, the Lausen core shows compressibility and swelling indexes similar to the MT core. This could be related to the comparable composition and pore size distribution of the two cores. On the other hand, vertical effective yield stress is higher for MT core, compared to Lausen, and an impact of the geological stress history is envisaged. Further investigations would give a clear picture of the effect of the depth on the mechanical behaviour of the Opalinus Clay shale.

Acknowledgement. The support of the Swiss National Cooperative for the Disposal of Radioactive Waste (NAGRA) for this research is acknowledged.

References

Bath A, Gautschi A (2003) Geological setting and sample locations. In: Pearson FJ, Arcos D, Bath A, Boisson J-Y, Fernández AM, Gäbler H-E, Gaucher E, Gautschi A, Griffault L, Hernán P, Waber HN (eds.) Mont Terri Project – Geochemistry of Water in the Opalinus Clay Formation at the Mont Terri Rock Laboratory. Rapports de l'Office fédéral des eaux et de la géologie (OFEG), Berne

Bossart P (2011) Characteristics of the Opalinus Clay at Mont Terri. http://www.mont-terri.ch/internet/mont-terri/en/home/geology/key_characteristics.html

Biot MA (1941) General theory of three-dimensional consolidation. J Appl Phys 12(2):155–164

Ferrari A, Favero V, Laloui L (2016) One-dimensional compression and consolidation of shales. Int J Rock Mech Min Sci 88:286–300

Ferrari A, Favero V, Marschall P, Laloui L (2014) Experimental analysis of the water retention behaviour of shales. Int J Rock Mech Min Sci 72:61–70

Ferrari A, Laloui L (2013) Advances in the testing of the hydro-mechanical behaviour of shales. In: Laloui A, Ferrari L (eds) Multiphysical Testing of Soils and Shales. Springer, Heidelberg, pp 57–68

Mazurek M (1999) Mineralogy of the opalinus clay. In: Results of the Hydrogeological, Geochemical and Geotechnical Experiments, Performed in 1996 and 1997. Swiss National Geological and Hydrogeological Survey. Geological Report 23, pp 15–18

Mazurek M, Hurford AJ, Leu W (2006) Unravelling the multi-stage burial history of the Swiss Molasse Basin: integration of apatite fission track, vitrinite reflectance and biomarker isomerisation analysis. Basin Res 18:27–50

Pearson FJ (1998) Opalinus Clay experimental water: A1 Type, Version 980318. PSI Internal report TM-44-98-07, Paul Scherrer Institut, Villigen PSI, Switzerland

Lessons Learned from Electron Microscopy of Deformed Opalinus Clay

Ben Laurich[1(✉)], Janos L. Urai[1,2], Guillaume Desbois[2], Jop Klaver[2], Christian Vollmer[3], and Christophe Nussbaum[4]

[1] Federal Institute for Geosciences and Natural Resources (BGR), Stilleweg 2, 30655 Hannover, Germany
Ben.Laurich@bgr.de

[2] Structural Geology, Tectonics and Geomechanics, RWTH Aachen University, Lochnerstrasse 4-20, 52056 Aachen, Germany

[3] Institute for Mineralogy, University Münster, Correnstraße 24, 48149 Münster, Germany

[4] Swiss Geological Survey, Federal Office of Topography Swisstopo, Seftigenstrasse 264, 3084 Wabern, Switzerland

Abstract. Using a combined approach of ion-beam milling and electron microscopy, we observe, describe and quantify the microstructure of naturally and synthetically deformed Opalinus Clay (OPA) and deduce its microstructural evolution and underlying deformation mechanisms. The investigated samples derive from the so-called Main Fault, a 10 m offset fold-bend thrust fault crossing the Mont Terri Rock Laboratory in the Swiss Jura Mountains. The samples are slightly overconsolidated, experienced a burial depth of 1350 m and a maximum temperature of 55 °C. Most impact on strain is attributed to frictional sliding and rigid body rotation. However, trans-granular fracturing, dissolution-precipitation of calcite, clay particle neoformation and grain deformation by intracrystalline plasticity have a significant contribution to the fabric evolution. The long-term in-situ deformation behavior of OPA is inferred to be more viscous than measured at laboratory conditions.

Introduction

Several geoscience disciplines evaluate the suitability of the Opalinus Clay formation (OPA) to host a repository for nuclear waste. Most of them benefit from or even rely on insight of the OPAs' microstructure. In particular, hydro-mechanical studies profit from the understanding of microstructural processes. In this contribution, we present a summary of our results in observing, describing and quantifying the microstructure of naturally and synthetically deformed OPA (Laurich 2015; Laurich et al. 2016, Laurich et al. 2014). From this description, we further deduce the microstructural evolution from undeformed protolith to intensely deformed tectonite and aim to uncover underlying deformation mechanisms.

Rock fabric and rheological behavior depend on lithological and environmental controls (Rutter et al. 2001), both of which are fairly known for the well-researched OPA formation (e.g. Amann and Vogelhuber 2015; Clauer et al., accepted; Houben et al. 2013; Mazurek et al. 2006; Nussbaum et al. accepted). However, a comprehensive,

A. Ferrari and L. Laloui (eds.), *Advances in Laboratory Testing and Modelling of Soils and Shales (ATMSS)*, Springer Series in Geomechanics and Geoengineering,
DOI 10.1007/978-3-319-52773-4_40

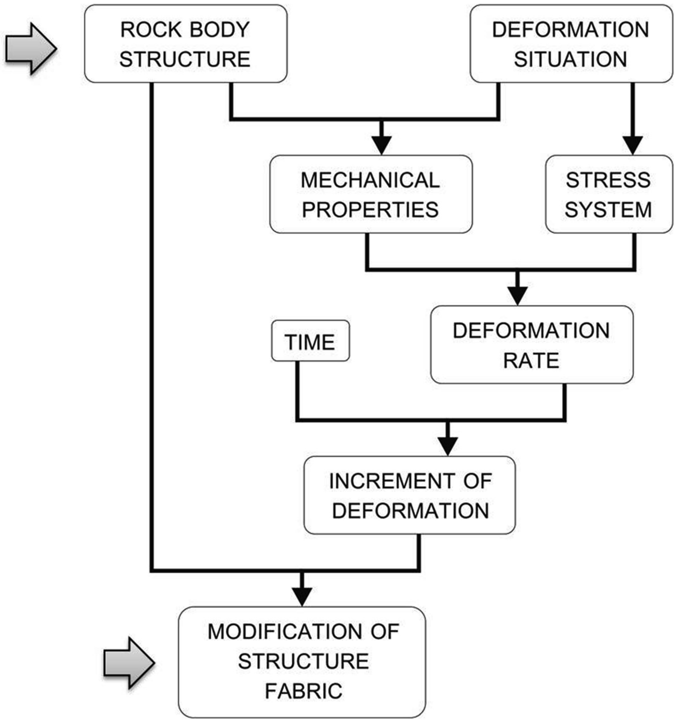

Fig. 1. General scheme of interacting factors that produce microstructural changes. Arrows point towards the factors that we optically examined, the remaining factors are intensely studied by other authors. Yet, a comprehensive, self-consistent model linking all elements is complex and missing. See text for details. Simplified after Hobbs et al. (1976).

self-consistent model on the deformation of OPA (Fig. 1) is missing, in particular for long-term in-situ deformation.

Using mostly electron microscopy techniques, we found five major deformation features in OPA from the Mont Terri Rock Laboratory: (1) slickensides, which are in cross-sectional view associated to (2) a μm-thin zone of slickenside-parallel oriented particles, (3) gouge, (4) calcite and celestite veins and (5) scaly clay.

Methods

All samples originate from the shaly facies of OPA from the Mont Terri Rock Laboratory (CH). They were retrieved either as outcrop or as drill core samples in vacuum sealed bags and got resin-stabilized in the laboratory. The samples were stored at dry conditions at room temperature. The wide majority of samples is from the so-called Main Fault, an up to 5 m wide fold-bend thrust fold with an offset in the rage of 10 m (Nussbaum et al. accepted).

Here presented results are obtained by: (1) Broad-Ion-Beam Scanning Electron Microscopy (BIB-SEM), JEOL SM09010 Ar-BIB, Zeiss Supra 55 SEM; (2) Focused-Ion-Beam Transmission Electron Microscopy (FIB-TEM), FEI Strata 205 FIB, Zeiss Libra 200FE.

The BIB (1) produces a smoothly polished (+/−5 nm surface roughness, Klaver et al. 2012) 2 mm^2 large surface free from mechanical polishing artifacts. Figure 2 illustrates the BIB-milling setup, where a combination of resin and cover glass minimizes any 'curtaining effects' by the BIB. The FIB (2) was conducted at samples with a thick W-coating (>50 nm) to preserve the structure directly underlying the sample surface. All procedures cut the samples parallel to shear direction and perpendicular to the faults' strike orientation (Fig. 2).

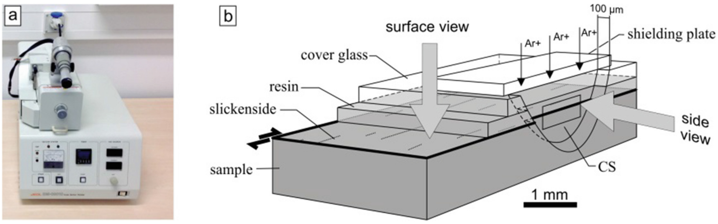

Fig. 2. (a) JEOL SM09010 Ar-BIB cross-section polisher, (b) Sketch of the BIB-milling setup from Laurich et al. (2014). CS = cross-section.

Results and Discussion

With a gentle force by hand, the samples from the Main Fault split perfectly along cohesionless slickensided surfaces, which show various types of kinematic indicators for frictional sliding (e.g. striae in Fig. 3a). An SEM-EDX map (Fig. 3b) illustrates Ca patches at slickenside risers, while Ca is scarce at restraining surfaces between. This Fig. 3 shows that despite cataclastic processes (e.g. frictional sliding), diffuse mass transport by pressure solution precipitation of calcite is an important deformation mechanism. This time-dependent mechanism cannot be easily reproduced at laboratory conditions (cf. Niemeijer et al. 2008).

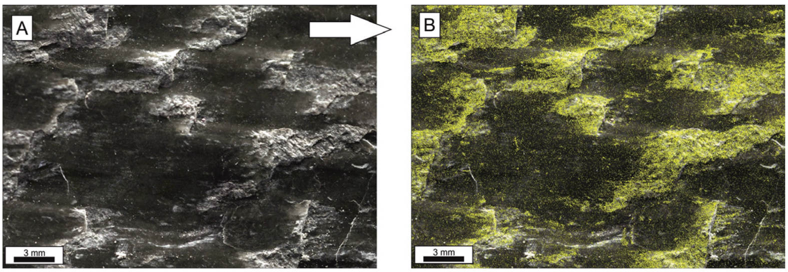

Fig. 3. Photograph (A) and SEM-EDX Ca distribution map of a slickensided surface from the Main Fault in the Mont Terri Rock Laboratory. Note that Ca patches correspond to brighter areas in the photograph, which are associated to risers (from Laurich 2015).

In side-view (Fig. 4), the slickensided surfaces are only a few microns wide, show a drastic loss in porosity, and nano-meter wide clay particles that enchase larger grains to build an absolutely flat surface. Figure 4a and b derive from the same FIB lamellae yet show indicators for different deformation mechanisms. (b) gives the impression of rigid body rotation, with larger grains wrapped by smeared clay particles and porosity in strain shadow regions. Contrary, (a) shows no porosity and strict face-to-face aligned larger minerals. This finding might be a product of clay neoformation as postulated

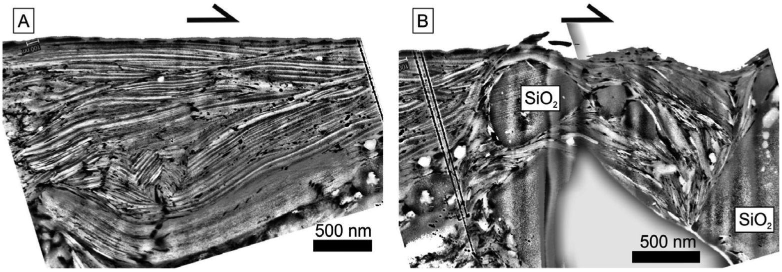

Fig. 4. TEM (HAADAF) images of an FIB lamella (from Laurich et al. 2014).

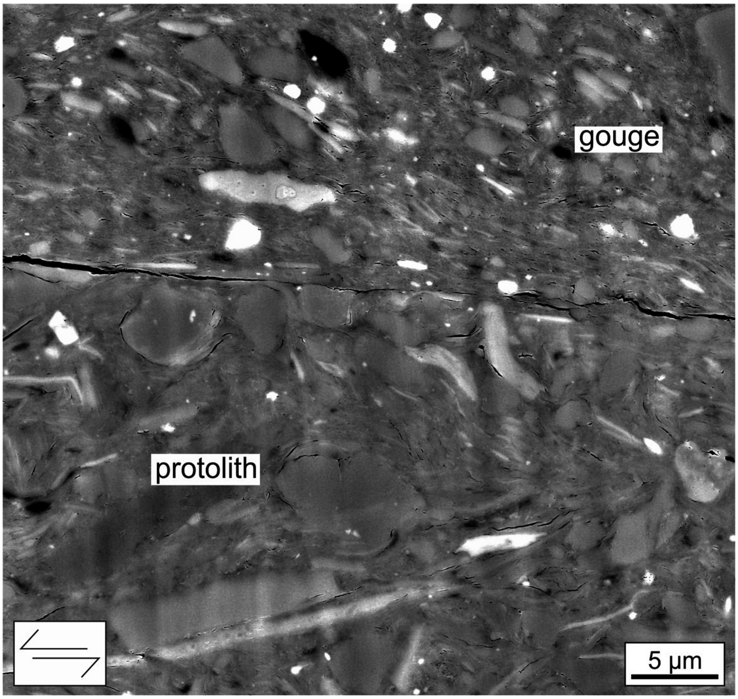

Fig. 5. BIB-SEM image of gouge next to protolith. Gouge and protolith are separated by a µm-thin shear zone that opened during sampling (black crack). Note the high fabric intensity in P-foliation and the grain size reduction for gouge.

elsewhere by geochemical analysis (Clauer et al. accepted; Warr et al. 2014) and/or a product of strong intracrystalline plasticity, both leaving no inter-grain porosity.

We interpret paleo fluid flow along but not perpendicular to the slickensides, which are µm-thin shear zones of sharp localized deformation: neighboring areas show the same microstructure as the undeformed protolith.

The µm-thin shear zone can be regarded as an elemental building block of other microtectonic features, such as gouge from the Main Fault. Figure 5 displays a µm-thin shear zone resembling a boundary of an gouge-internal shear band. Particles next to the shear zone are passively rotated into strict P-foliation, reduced in grain size, and frequently fractured. By EDX (not shown), gouge contains almost no calcite.

From our findings, we infer that gouge has a very low permeability, yet evolved from highly strained scaly clay by an abrasive dissolution process and deforms in a viscous manner with solid lubrication by nm-sized clay particles.

Conclusion and Relevance

We provide a microphysical basis to relate microstructures to macroscopic observations of strength and permeability. However, more work is necessary to link the factors in Fig. 1. We emphasize a strong collaboration of deformation testing and corresponding microstructural analysis in order to deduce the impact of each rheology controlling factor on the constitutive behavior of OPA.

Numerical modellers of long-term deformation behaviour of clays should not rely on laboratory derived parameters only, but implement more time-dependent processes to obtain realistic hydro-mechanical properties, resulting in a viscous long-term deformation. Our findings are also relevant to earthquake research, in particular to scaly clay fabrics in accretionary prisms.

References

Amann F, Vogelhuber M (2015) Expert Report - Assessment of Geomechanical Properties of Intact Opalinus Clay

Clauer N, Techer I, Nussbaum C, Laurich B (accepted) Geochemical signatures of paleofluids in calcite from microstructures and matrix of the main fault in the opalinus clay: a contribution to the regional evolutionary model. Swiss J Geosci

Hobbs B, Means W, Williams P (1976) An outline of structural geology. Wiley, New York

Houben ME, Desbois G, Urai JL (2013) Pore morphology and distribution in the shaly facies of opalinus clay (Mont Terri, Switzerland): insights from representative 2D BIB–SEM investigations on mm to nm scale. Appl Clay Sci 71:82–97. doi:10.1016/j.clay.2012.11.006

Klaver J, Desbois G, Urai JL, Littke R (2012) BIB-SEM study of the pore space morphology in early mature posidonia shale from the hills area. Germany Int J Coal Geol 103:12–25. doi: 10.1016/j.coal.2012.06.012

Laurich B (2015) Evolution of microstructure and porosity in faulted Opalinus Clay. RWTH-Aachen

Laurich B, Urai JL, Desbois G, Vollmer C, Nussbaum C (2014) Microstructural evolution of an incipient fault zone in opalinus clay: insights from an optical and electron microscopic study of ion-beam polished samples from the main fault in the mt-terri underground research laboratory. J Struct Geol 67:107–128. doi:10.1016/j.jsg.2014.07.014

Laurich B, Urai JL, Nussbaum C (2016) Microstructures and deformation mechanisms in opalinus clay: insights from scaly clay from the Main Fault in the Mont Terri Rock Laboratory (CH). Solid Earth Discuss, 1–30. doi:10.5194/se-2016-94

Mazurek M, Hurford AJ, Leu W (2006) Unravelling the multi-stage burial history of the Swiss Molasse Basin: integration of apatite fission track, vitrinite reflectance and biomarker isomerisation analysis. Basin Res 18:27–50. doi:10.1111/j.1365-2117.2006.00286.x

Niemeijer A, Marone C, Elsworth D (2008) Healing of simulated fault gouges aided by pressure solution: results from rock analogue experiments. J Geophys Res 113:B04204. doi:10.1029/2007JB005376

Nussbaum C, Kloppenburg A, Caer T, Bossart P (accepted) Tectonic evolution of the Mont Terri region, northwestern Swiss Jura: constraints from kinematic forward modelling. Swiss J Geosci

Rutter EH, Holdsworth RE, Knipe RJ (2001) The nature and tectonic significance of fault-zone weakening: an introduction. Geological Society, London, Special Publications, vol. 186, pp. 1–11. doi:10.1144/GSL.SP.2001.186.01.01

Warr LN, Wojatschke J, Carpenter BM, Marone C, Schleicher AM, van der Pluijm BA (2014) A “slice-and-view” (FIB–SEM) study of clay gouge from the SAFOD creeping section of the San Andreas fault at $\sim$2.7 km depth. J Struct Geol 69:234–244. doi:10.1016/j.jsg.2014.10.006

The Rock Mechanical Behavior of Opalinus Clay – 20 Years of Experience in the Mont Terri Rock Laboratory

David Jaeggi(✉), Paul Bossart, and Christophe Nussbaum

Swisstopo, Wabern, Switzerland
David.jaeggi@swisstopo.ch

Abstract. Monitoring the behavior of the rock mass combined with a sound knowledge of rock mechanical properties is of great importance. Already in the very beginning of the Mont Terri rock laboratory in 1996, rock samples were extracted for the assessment of elastic parameters. The transverse isotropic Opalinus Clay exhibits a strong dependence on its orientation with respect to the applied load. Furthermore, rock strength is dependent on water content/suction and microcracking due to desiccation and/or mechanical load. Swelling potential, very low hydraulic conductivity and non-linear temporal behavior are further important properties of Opalinus Clay, which require well-defined sampling procedures, sample conditioning and test setup in the lab. Monitoring deformation and pore water pressure of the temporal behavior of galleries and niches prior, during and after excavation is standard procedure in the Mont Terri rock laboratory. Besides classical survey of deformation as well seismic, and geoelectric methods are applied in order to assess sedimentary heterogeneity, tectonic discontinuities and the extent of the excavation damaged zone (EDZ). Swisstopo has furthermore developed a technique based on resin impregnation, which allows for characterizing geometry, properties and temporal behavior of the EDZ. These datasets allow for establishing and continuously improving conceptual models of the rock mechanical situation and behavior in the Opalinus Clay. Conceptual models and long-term datasets are important for the calibration and validation of HM coupled models. In the framework of the Mont Terri Project, several numerical models have been developed and tested for the specific use in consolidated shales, which are important instruments for future predictions.

Introduction

The understanding of the rock mechanical behavior in a future repository for nuclear waste is of major importance for safety and long-term stability of the galleries. The excavation of galleries in the Opalinus Clay with low stiffness and rock mechanical strength compared to other rock types, such as granites or limestones is a challenging task, especially at depths of 400 to 900 m, where this host rock is available at the potential sites for a high level waste (HLW) repository. The Opalinus Clay generally consists of a lower shaly sequence and an upper sandy sequence. Due to similar self-sealing and retention properties but much better elastic parameters compared to the shaly facies, the sandy facies is getting more important within research programs

A. Ferrari and L. Laloui (eds.), *Advances in Laboratory Testing and Modelling of Soils and Shales (ATMSS)*, Springer Series in Geomechanics and Geoengineering,
DOI 10.1007/978-3-319-52773-4_41

(Table 1). This short paper covers some aspects and problems encountered with sampling and conditioning of specimens for rock mechanical characterization. Furthermore examples of in-situ observations will be given, which yield important data for the validation of numerical codes.

Table 1. Comparison of selected parameters from the shaly and from the sandy facies of the Opalinus Clay at Mont Terri for S-samples (perpendicular to the bedding) and P-sample (parallel to the bedding). The different groups of parameters are illustrated with different colors: petrophysical = orange, rock mechanic = grey, hydraulic = blue, total cation exchange capacity (CEC) = green; where available, the number of measurements is given in brackets (data from Jaeggi et al. 2014).

Parameter	Shaly facies		Sandy facies	
	Range	Best estimate	Range	Best estimate
Water content [weight %]	5.0-8.9 (22)	6.6	2-6 (112)	4
Density (wet) [g/cm³]	2.40-2.53 (239)	2.45	2.42-2.63 (65)	2.52
Total (physical) porosity [Vol %]	14-25 (17)	18	5.3-17.7 (17)	11.1
Waterloss porosity [Vol %]	13-21	16	4.9-17.5 (19)	10.5
Uniaxial compressive strength, UCS (S) [MPa]	5-10 (19)	7	6-37 (51)	16
Uniaxial compressive strength, UCS (P) [MPa]	4-17 (22)	10.5	4-37 (60)	18.0
Elastic module, E-Module (S) [GPa]	2.1-3.5 (34)	2.8	0.4-19.0 (51)	6.0
Elastic module, E-Module (P) [GPa]	6.3-8.1 (39)	7.2	2.0-36.7 (60)	13.8
Poisson's ratio (S) [-]	0.28-0.38 (73)	0.33	0.06-0.42 (51)	0.22
Poisson's ratio (P) [-]	0.16-0.32 (73)	0.24	0.13-1.23 (59)	0.44
Hydraulic conductivity (S) [m/s]	2E-14-1E-12 (57)	2E-13	1E-13-5E-12 (10)	1E-12
Total cation exchange capacity CEC (Co-Hexamin, **Ni-en in bold**) [meq/100 g rock]	**9.4-13.4 (24)** -	**11.1** 16 (24)	7.3-21.9 (13)	14.4

Sampling and Conditioning of Opalinus Clay

Sampling for rock mechanical testing is a challenging task in Opalinus Clay. Thorough planning of the campaign starts with the choice of the drilling location and the appropriate drilling technique already. The transverse isotropic material makes a well-defined orientation of the borehole with respect to bedding anisotropy necessary. Generally samples are extracted from larger diameter cores by later subcoring for achieving subsamples parallel (P-samples) or perpendicular (S-samples) to bedding anisotropy. P-samples generally remain stable, whereas S-samples are often subjected to discing, where while drilling the sample shears off along bedding. Recent calibrations of numerical models have shown, that with these two orientations only, the rock mass behavior cannot be deduced entirely and that testing samples at angles other than 0° or 90° is needed; the so called Z-samples (Parisio 2016). In future campaigns, testing should be performed particularly at an angle of 60° in order to capture the observed behavior of galleries and boreholes. Besides orientation towards bedding anisotropy, as well heterogeneity plays an important role. In most studies on rock mechanical testing, the homogeneous shaly facies was sampled, where sample size is not so relevant for capturing a representative elementary volume (REV). In the sandy facies type however, depending on the location in the rock mass, sample properties may differ a lot (Fig. 1a, b). Heterogeneity of the sandy facies is considerable on the borehole scale, which is highlighted for instance on the wide ranges of UCS results for S-samples with ranges of 6–10 MPa and 5–37 MPa for shaly and sandy facies respectively (Table 1). Once the location and orientation of a sampling borehole is defined, appropriate drilling technique has to be chosen. At Mont Terri for rock mechanical purposes mostly double core or triple core drilling techniques, using air as flushing media are deployed. These techniques, if used with adapted low drilling advances, guarantee best core quality.

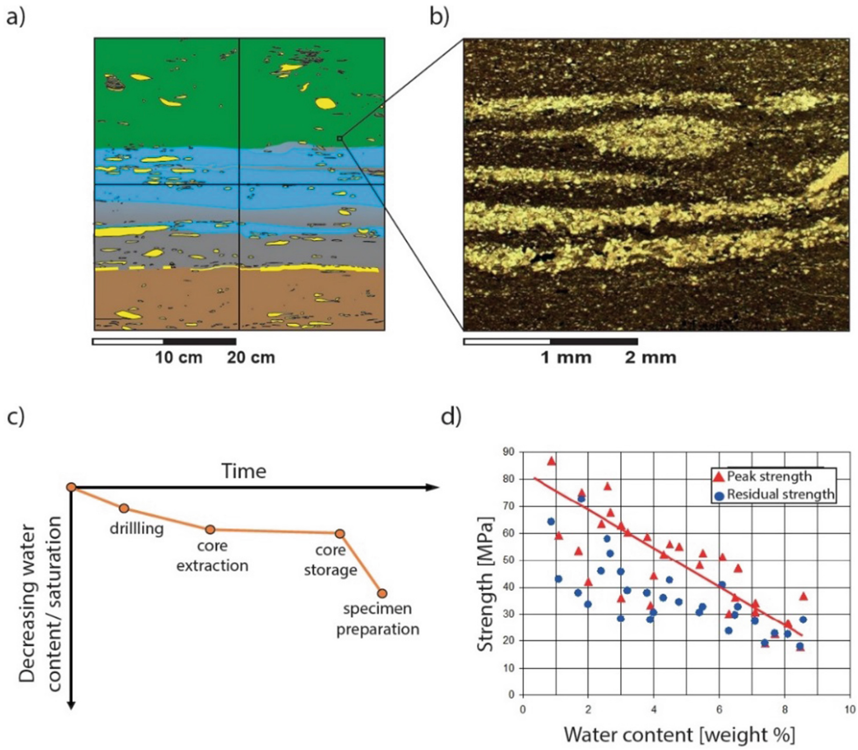

Fig. 1. (a) Heterogeneity of the sandy facies shown on a small scale map and example of a photomicrograph (b), (c) sketch, showing temporal desiccation path during a sampling campaign (adapted after Wild and Wymann (2015)), (d) graph of water content versus strength.

In order to minimize desiccation, the air flushing needs to be reduced to a minimum. Triple core drilling, minimal air flushing and low drilling speed help in mitigating desiccation, frictional temperature, impact of stress relief or deconfinement, excess pore water pressure and hence mechanical damage of the core specimen. Water content in any case decreases during drilling, core extraction and specimen preparation in the lab (Fig. 1c). Reducing the time of exposure and immediate appropriate conditioning by using resin impregnation techniques, sealing in vacuumed aluminum foil or storage in pressurized containers is important. Early discing and micro cracking of specimens is a known problem, e.g. detected by CT-scanning. Core handling by the drilling crew and shipping over longer distances, even in stiff liners, seem to be critical factors. Furthermore resin stabilized samples might be subjected to excess heat during the exothermal polymerization of the resin. Opalinus Clay exhibits a strong dependency of strength on water content or suction (Fig. 1d). The lower the water content of a specimen, the higher is its rock mechanical strength. Consequently, the knowledge of the initial water content of a sample right at the time of extraction is important in order to re-saturate the sample in the lab to the original in-situ value. However, it has to be noted, that under certain circumstances, re-saturation in the lab can lead to decomposition of samples.

In-Situ Observations and Conceptual Models

Coupled hydro-mechanical (HM) behavior of the rock mass is best investigated during so-called mine-by experiments, where the near field as well as the far field is extensively monitored with pore water pressure sensors and deformation sensors before, during and after an excavation. However, numerical data often lacks direct information on geometry of fractures and in most cases, conclusions have to be based on assumptions. This gap of knowledge can be filled-up for instance by in-situ observations in a rock laboratory. These observations are important data for the elaboration of conceptual models, which in turn are needed for the qualitative validation of results from numerical modeling. Many investigations on excavation damaged zone (EDZ) around galleries or boreholes (BDZ) have been carried out during the past 20 years. These investigations yielded valuable information on geometry and extension of this artificially induced zone (e.g. Bossart et al. 2002). The failure mechanisms and the temporal evolution in particular have been studied recently on a horizontal borehole, drilled parallel to bedding (Kupferschmied et al. 2015). By using a resin impregnation technique, they found, that within hours after a drilling, tangential shear fractures develop parallel to bedding (S_0). These tangential fractures form as so-called wing cracks (Fig. 2a, b). Wing cracks typically develop at shear fracture tips and are associated with a sudden decrease in slip velocity along the tangential fracture. Parallel to the tangential shear fractures in both opposite directions parallel to bedding further fractures develop, building a typical buckling chimney (Fig. 2c, d). For boreholes and galleries oriented parallel to bedding, this buckling chimney can extend up to 3 times the radius into the rock mass on both opposite sides, as interval velocity measurements along these directions have shown. This buckling chimney, consisting of bedding-parallel shear fractures (F1) and bordered by extensional fractures (F2), is

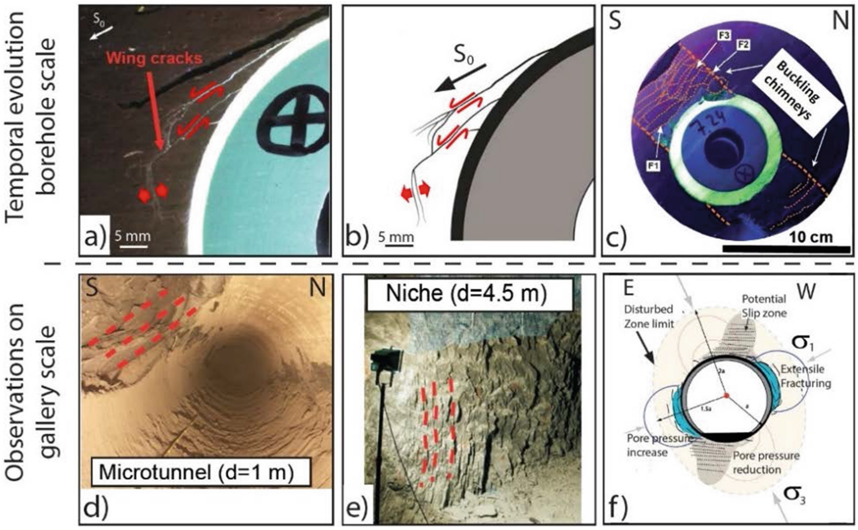

Fig. 2. (a) Detail of tangential shear fractures, so-called wing cracks with shear sense, (b) sketch of same detail (adapted after Kupferschmied et al., (2015), (c) photograph under UV light conditions showing the development of two buckling chimneys in opposing directions, F1: bedding parallel fractures, F2: border of central zone, F3: en-échelon fractures, (d) mechanically controlled breakouts at 11 and 5 o'clock in a microtunnel, (e) photo of extensile fracturing in niche sidewall, and (f) conceptual model of a gallery oriented N-S and in dip-direction (after Martin and Lanyon, 2004).

termed as anisotropy-induced breakouts. The evolution of those breakouts is closely linked to rock anisotropy.

Further observations on gallery scale are stress-induced breakouts in the sidewalls (Fig. 2e). These breakouts occur in the zone with pore water pressure increase, where the high deviatoric stresses lead to extensile fracturing (Martin and Lanyon 2004) (Fig. 2f).

Conclusions and Recommendations

During the past 20 years, a plethora of data has been acquired in the Mont Terri rock laboratory. There is still relatively few data available from the sandy facies. The main reason for this is its heterogeneity, which turns representative sampling quite challenging. Generally, big efforts are taken during sampling and conditioning in order to reduce external effects, which are acting on the specimen. However, recent investigations have shown, that despite these efforts, micro-cracking is quite common, which could affect the rock mechanical behavior of specimens from the Opalinus Clay. Consequently, procedures for sampling and conditioning need to be improved in the future.

In-situ observations and deduced from these, conceptual models, are both important for the validation of numerical models. With conceptual models, the relevance of numerical results and the validity of assumptions and simplifications of the model setup and the numerical implementation can be judged. By means of mine-by tests, data is acquired before, during and after excavations. These datasets of the temporal behavior of the rock mass during an excavation are further important data for the validation and calibration of numerical models. Based on this experience, numerical models have been improved continuously and led to recent developments, which enable reliable predictions for future experiments and the planned extension of the Mont Terri rock laboratory.

References

Bossart P, Meier P, Möri A, Trick T, Mayor JC (2002) Geological and hydraulic characterization of the excavation disturbed zone in the Opalinus Clay of the Mont Terri Rock Laboratory. Eng Geol 66:19–38

Jaeggi D, Bossart P, Wymann L (2014) Kompilation der lithologischen Variabilität und Eigenschaften des Opalinus-Ton im Felslabor Mont Terri. Expertenbericht der Landesgeologie 09 August 2014, 66 pp. swisstopo, Seftigenstrasse 264, 3084 Wabern, Switzerland

Kupferschmied N, Wild KM, Amann F, Nussbaum C, Jaeggi D, Badertscher N (2015) Time-dependent fracture formation around a borehole in a clay shale. Int J Rock Mech Min Sci 77:105–114

Martin CC, Lanyon GW (2004) Excavation Disturbed Zone (EDZ) in Clay Shale. Mont Terri, Mont Terri Technical report TR2001-01, 207 pp. swisstopo, Seftigenstrasse 264, 3084 Wabern, Switzerland

Parisio F (2016) Constitutive and numerical modeling of anisotropic quasi-brittle shales. PhD thesis EPFL Lausanne

Wild KM, Wymann LP (2015) Water retention characteristics and State-Dependent Mechanical and Petrophysical Properties of a Clay shale. Rock Mech Rock Eng 48:427–439

Advanced Laboratory Testing for Site Characterization and In – situ Application Studies

Cyclic Testing on Low-Density Chalk

Svend Pilgaard Larsen(✉), Nataša Katić, and Niels Trads

Geo, Kgs, Lyngby, Denmark
spl@geo.dk

Abstract. A short series of cyclic triaxial tests has been carried out on chalk samples from the English Channel. The specimens are installed with a minimum of handling. The state of specimens after the cyclic testing ranged between no apparent changes to the structure (no degradation) and total loss of structure (degradation); whereas pronounced failure planes were observed in some of the specimens. The current article summarizes details of geological description and handling of the tested specimens in respect to the failure mode of the chalk.

Introduction

Problematics of cyclic resistance of chalk has lately gained plenty of attention, especially from the offshore renewable energy industry. For this purpose, cyclic testing on chalk samples is being in an increasing demand. Samples of low-density chalk are generally sufficiently soft to be tested in a set-up suited for soils, and the testing is commonly carried out in agreement with the standards developed for cohesive soils.

In connection to an Offshore Wind Farm project, samples of chalk from the English Channel have been tested in the laboratory. The sampling has been successful and the chalk samples of very good quality were recovered.

The laboratory program included a short series of cyclic triaxial testing on the chalk. In total eight cyclic triaxial tests were carried out. The samples are installed with a minimum of handling.

The cyclic tests included the saturation with backpressure, followed by consolidation and static adjustment of stresses, and finally a cyclic undrained shear phase. Chalk specimens are consolidated to the estimated in-situ stress level before shearing.

The state of specimens after the cyclic testing ranged between no apparent changes to the structure (no degradation) and total loss of structure (degradation); whereas pronounced failure planes were observed in some of the specimens. Due to variations in chalk properties and very few specimens, it has not been possible to provide a statistical evaluation.

The current article summarizes details of geological description and handling of the tested samples in order to tackle the prediction of the failure mode of chalk. The results are compared to the findings of Coyne et al. (2015).

A. Ferrari and L. Laloui (eds.), *Advances in Laboratory Testing and Modelling of Soils and Shales (ATMSS)*, Springer Series in Geomechanics and Geoengineering,
DOI 10.1007/978-3-319-52773-4_42

Sampling and Samples Description

The sampling was conducted by Shelby tubes and coring.

Shelby tubes are mainly used for soil sampling, where the tube is forced into the target soil layer through the bottom of a borehole. Typically, the sample is preserved within the Shelby tube until it is extruded in the laboratory for description and testing.

The cores are samples drilled with the Geobor-S system. In soft materials, the drilling process can cause severe damage to the cores. The damage can be imposed by drill bits or by flushing necessary to eliminate the cuttings.

Within the current test series, the samples from the upper 20 m were obtained from the Shelby tubes, and the samples from below 20 m were obtained from the cores. The recovery of the cores varies between 73 and 100% and may be roughly associated to the frequency of fractures found in the cores.

The discontinuity spacing varies within the tested material. According to the discontinuity aperture based on CIRIA (Lord et al. 2002), the samples include chalk of grades A (structured, with closed fractures) and D (unstructured). The subdivisions of the grades according to the discontinuity spacing are listed in the geological descriptions of the test specimens in Table 1. The listed geological descriptions are based on the geological descriptions of the originating samples, rather than on particular specimens. Table 1 also presents the sample types and the respective sizes of the test specimens.

All the test specimens are described as Low-density chalk according to CIRIA. Some of the specimens slightly exceed the dry density limit of the low-density chalk (1.55 g/cm^3). However, this inconsistency is found not critical since other identification criteria have been satisfied, e.g. small lumps of chalk could be crushed between finger and thumb and remoulded to putty.

During the preparation of the specimens for the laboratory testing (“handling”), it was observed that the samples from the cores were of apparently better quality than the samples from the Shelby tubes. This is related to the rock grade (see Table 1) as a

Table 1. Description of the test specimens for cyclic triaxial testing.

Test no.	Boring no.	Lab. no.	Sample type	Height [mm]	Diameter [mm]	Rock grade (CIRIA)	Recovery [%]
1	A	1	Shelby tube	140	70	Dm	NA
2	A	2	Core	200	100	A4/A5	73
3	B	1	Core	196	101	A2/A3	100
4	C	1	Shelby tube	140	70	Dm or Dc	NA
5	C	2	Shelby tube	140	70	Dm or Dc	NA
6	C	3	Core	199	101	A3	85
7	C	4	Core	200	100	Dm	93
8	D	1	Core	200	100	A1–A3	87

criterion for selection of the sampling method. It is considered that taking the cores is possible only in a more competent chalk. Where more fragile and softer chalk was expected, the sampling with Shelby tubes was chosen.

Handling

In order to minimize further disturbance of the core specimens, the cyclic triaxial tests were carried out on specimens with the diameter of the core sample (100 mm). The Shelby tube specimens were also prepared for testing with the entire Shelby tube sample diameter (70 mm).

The Shelby tubes were transported and stored in upright condition to preserve the structure in the soft material. The chalk was extruded from the Shelby tubes directly into a steel ring with the length of the specimens. This allowed the ends of the specimens to be smoothened with a minimum of disturbance. Finally, the specimens were extruded from the ring and placed in the triaxial apparatus.

Although of a good quality, the core samples had uneven surfaces. Uneven surfaces generally present a risk of damaging the membrane during the installation and testing, and may cause stress concentrations in the most exposed parts of the specimens. The uneven surfaces originated from the drilling process and consisted of indentations following the direction of the drill bit. Indentations were typically up to 5 mm deep, except in one occurrence, where the indentation approached 10 mm.

In order to minimize the influence of the uneven surfaces, it was decided to plaster the sides of the specimens from the cores. The plaster used for covering the sides of the specimens had the bulk density in the range of 1.42–1.52 g/cm^3, Young's modulus in the range of 350–1010 MPa, and the unconfined compressive strength in the range of 0.7–1.1 MPa. As the preliminary testing of plaster showed that it typically fails due to pore-collapse, rather than in pronounced shear, it has been assumed that it would not cause localization of strain nor affect the failure of the specimen. Therefore, although of a similar strength as the tested chalk, the plaster is considered suitable for the purpose.

Test Specification

The cyclic tests are linked to monotonic reference tests through ratios of average and cyclic loads to the static strength obtained in monotonic tests.

Average shear stress and cyclic shear stress to be applied during the test, τ_{avg} and τ_{cy}, respectively, were planned as $0.3 \times s_u$, where s_u is the undrained shear strength obtained in the relevant reference monotonic test. The reference tests were carried out on the sample closest to the sample for cyclic testing, with the same geological description. The reference tests were carried out as unconfined compression tests (UCS) or undrained triaxial tests (CIUc), depending on the availability of the material. No reference test was available for the test no. 8. In cases where the reference is

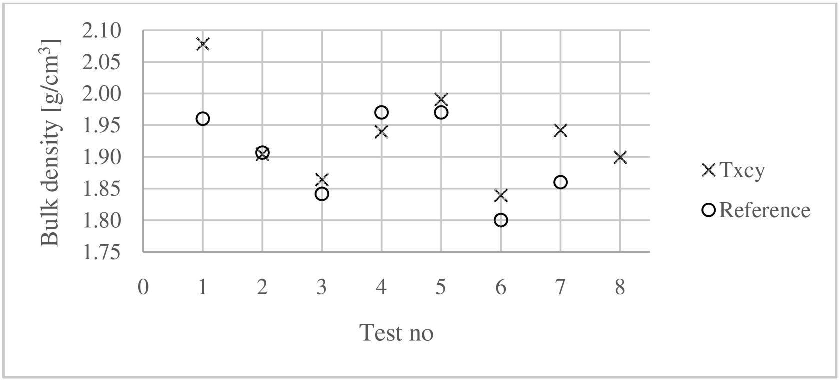

Fig. 1. Bulk density of the specimen for the cyclic testing (Txcy) and the corresponding reference test (Reference).

obtained from the UCS test, half the compression strength was used as the estimate of the undrained shear strength, s_u.

Figure 1 shows the comparison of the bulk density of the eight specimens for cyclic testing and the corresponding references. In general, the reference tests were made on the specimens of somewhat lower density, except for the tests 4. Therefore, it is considered that the reference strength may generally be slightly lower than the realistic strength of the specimen to be subject to cyclic testing.

The testing was carried out in accordance with ASTM D5311. Tests included the following steps:

(1) Installation at 25 kPa with dry filters.
(2) Flushing with de-aerated water.
(3) Back pressure application, followed by Skempton B-test.
(4) Drained isotropic loading to the estimated in situ stress.
(5) Undrained shear loading to average shear stress $\tau_{avg} = 0.3 * s_{u.}$
(6) Cyclic loading at 0.1 Hz with cyclic shear stress $\tau_{cy} = 0.3 * s_{u.}$

The stop criteria for the cyclic tests were based on the concept that the chalk should sustain a given number of load cycles (1500) below a deformation threshold critical for the construction (10% average axial strain or 10% cyclic axial strain).

Observations

In general, all of the specimens from the Shelby tubes failed. Out of the core specimens (more competent), only one failed and three passed the cyclic test.

The failed core sample test (test no. 7) is carried out with $\tau_{cy} = 0.4 * s_u$ instead of $\tau_{cy} = 0.3 * s_u$. Due to this, the specimen was expected to reach failure faster than the other specimens would. Table 2 lists that this specimen failed after 211 cycles when the

Table 2. Summary of the test specification and the test results. For all tests $\tau_{avg}/s_u = 0.3$.

Test no.	Boring no.	Lab. no.	Sample type	τ_{cy}/s_u [–]	ε_{avg} [%]	ε_{cy} [%]		N evaluation
1	A	1	Shelby tube	0.3	10.04	0.08	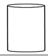	254 failed
2	A	2	Core	0.3	1.16	0.08	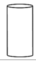	>1500 passed
3	B	1	Core	0.3	0.88	0.03	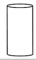	>1500 passed
4	C	1	Shelby tube	0.3	10.28	0.49	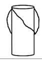	5 failed
5	C	2	Shelby tube	0.3	10.01	0.08		361 failed
6	C	3	Core	0.3	1.51	0.07	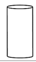	1500 passed
7	C	4	Core	0.4	10.38	0.39		211 failed
8	D	1	Core	0.3	1.92	0.07		>1500 passed

average axial strain exceeded 10%, thereby confirming the initial assumption. The test specification and a summary of the test results are presented in Table 2.

Figure 2 shows the specimen from test no. 7 before and after testing. The failure pattern forms a distinct coupled shear planes (cross), and a sketch of the failure figure is given in the Table 2.

The highest degradation from the cyclic loading was observed during test no. 4. It failed after five cycles, when the average axial strain exceed 10%. Figure 3 shows the specimen after testing. It can be seen that the degradation is so pronounced that it is

Fig. 2. Test no. 7. Before (left) and after failure by cyclic testing (right).

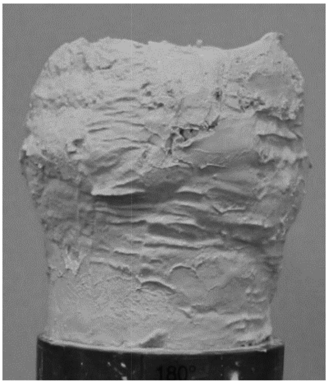

Fig. 3. Test no. 4 after failure by cyclic testing.

difficult to identify the failure figure. Figure 3, however, shows that the degradation is pronounced in the upper 2/3 of the specimen (approximately), while the deformation of the lower part of the specimen is significantly smaller.

Figure 4 shows the accumulation of axial deformation over the number of cycles for the tests no. 1, 5 and 7 which failed within 211–361 cycles.

In test no. 7, axial strain showed acceleration towards failure. Similar tendency, although much less pronounced, is observed in test no. 5. These two specimens both showed a distinct coupled shear failure. As opposite to this, in test no. 1, no failure planes were observed, and the strains did not accelerate towards failure. This indicates that the localization of strain might be observed on the plot of the curves of axial strain vs cycle no. as acceleration of strains after a certain threshold.

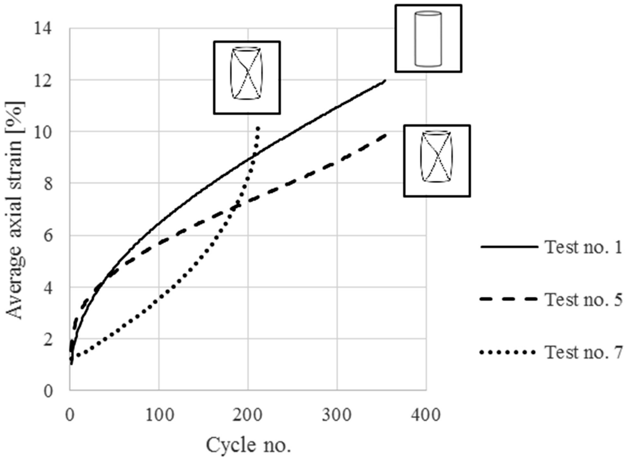

Fig. 4. Average axial strain vs cycle no. with outlined failure figures.

Discussion

Chalk is a very variable material whose strength and stiffness properties are often discussed in relation to various density measures (see e.g. CIRIA). The variation of the bulk density between the reference monotonic test specimens and the specimens to be subject to cyclic testing, shown on Fig. 1, indicates that the applied ratios τ_{avg}/s_u and τ_{cy}/s_u may differ from the assumed. Although the shear strength in monotonic tests for the low-density chalk can vary over two scales (see e.g. Katić and Christensen 2016), for the given set, the variation of strength is smaller and could cause a variation of assumed ratios of up to $\pm$ 0.05.

As noted by Coyne et al. (2015), it is anticipated that the cyclic degradation of chalk may be relatively quick once a threshold value has been exceeded. Although the current test series is made on the chalk of a lower density, and hence a lower static strength than in the cited reference, tests on specimens no. 4, 5 and 7 are in agreement with this observation. However, due to the high τ_{avg} used in the tests performed here, the average strain increased (as shown in Fig. 4), rather than the strain amplitude as observed by Coyne et al. (2015).

The threshold at about 250 cycles can be observed in test no. 5, after which the acceleration of the axial strains occurred (change of curvature of the axial strains vs. N curve). In test no. 7, the acceleration of strains occurs from the onset of cycling. Both tests, no. 5 and 7, show a strain localization in specific planes. A low number of cycles and a rather irregular failure figure of the specimen 4 may have been caused by the natural variability of the specimen material, but due to the natural sensitivity of chalk, a possibility of disturbance during sampling and handling should not be ruled out. Due to these uncertainties, the results of test no. 4 should be excluded from further considerations. Unlike in the tests no. 4, 5 and 7, in the test no. 1 no acceleration was observed and the specimen smoothly progressed towards a failure without any apparent failure planes.

It is worth noting that all the failed specimens are classified as unstructured chalk (grade D), out of which only test no. 7 is made on a cored sample. Due to the difference in the typical mode of failure of plaster to the observed mode of failure of the specimen, it is considered that the specimen has not been influenced by the plaster. Consequently, this test result is considered representative of the set of tests on unstructured chalk.

Neither of the tests performed on samples of structured chalk failed. Despite the possible minor departure from the designed stress ratios, it can be observed that the stability criterion cited by Coyne et al. (2015),

$$\tau_{cy}/s_u < 0.17 - \tau_{avg}/s_u$$

is very conservative with respect to the tested samples.

References

Coyne DL, Rattley M, Houlston P, Alobaidi I, Benson A, Russel C (2015) Cyclic laboratory testing of chalk to improve the reliability of piled foundation design. In: Meyer V (ed) Frontiers in Offshore Geotechnics III. Taylor and Francis Group, London, pp 1185–1190

Katić N, Christensen HF: Investigation of soft carbonate rocks in small and large scales: an overview of laboratory and field test methods. In: Proceedings of the 15th International Symposium on Engineering Geology and Geotechnics (2016, in print)

Lord JA, Clayton CRI, Mortimore RN: Engineering in Chalk. CIRIA Publication C574, CIRIA, London (2002)

Long Duration Oedometric Tests to Analyse the Creep Behaviour of Lacustrine Sediments

Luca Bonzanigo[1(✉)] and Fabrizio Jauch[2]

[1] geolog.ch SA, Bellinzona (CH), Switzerland
luca.bonzanigo@geolog.ch
[2] Consultest SA, Giubiasco (CH), Switzerland

Abstract. Some deep recognition boreholes were executed in relation to the construction of the Gotthard Base Tunnel, in the locality of Bodio. They reached about 200 m under the surface. From about 100 m, laminated lacustrine sediments were encountered, in the form of fine sands, argilleous silts and sandy clays. Two probes were submitted to an oedometric creep test lasting about eight months, under constant load. The purpose was to assess the parameters needed to for see tertiary settlement. The paper presents the results and discuss the method.

Introduction

A boring campaign was performed in the years 2010 and 2011 in order to explore the alluvial sediments to define the risk of settlements. Together with already performed bore-campaigns in 1995 and 2007, a dozen of boreholes were deepened, in 2010 two of them close to 200 m deep. The location is indicated in Fig. 1. It is situated in the southern Alps, canton Ticino, Leventina valley, at an altitude of about 320 m.s.l. The boreholes have been equipped with piezometers at various levels, and several geotechnical in situ measurements were performed as well as extensive sampling for laboratory testing. Two samples of lacustrine sediments were used for long lasting oedometric tests for creep analysis.

Geological Context

The valley of the Ticino river cuts perpendicularly the alpine structures of the southern Alps, through the crystalline Penninic nappes, as shown in Fig. 1. The characteristic U-shape is due to the deep erosion of the glaciers of the main Quaternary glaciation from about 2.6 myr to circa 20,000 years ago. Some decades ago it was assumed that successive glaciations are sole responsible for the deep erosion. Recent studies demonstrated that before the quaternary glaciations, during the so called Messinian Salinity Crisis (MSC, about 6 to 5.3 myr years BP), deep canyons could be dug by rivers following an uplift of the crust (Finkh 1978, Rogenmoser 1981) and or the drop

A. Ferrari and L. Laloui (eds.), *Advances in Laboratory Testing and Modelling of Soils and Shales (ATMSS)*, Springer Series in Geomechanics and Geoengineering,
DOI 10.1007/978-3-319-52773-4_43

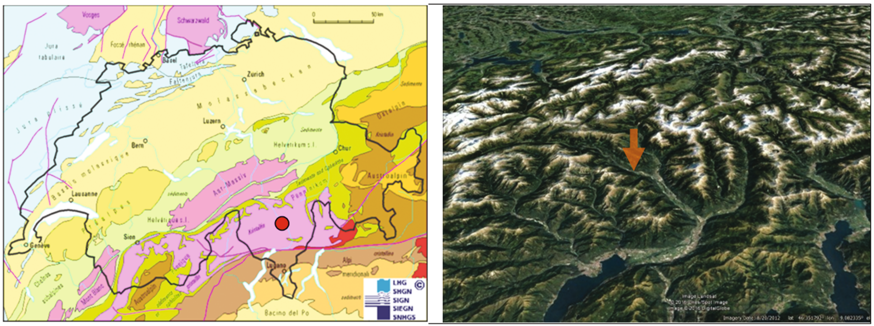

Fig. 1. Geographic and tectonic situation of the probe sampling. Location of the bore-campaign where lacustrine sediments were found.

of the Mediterranean Sea level. At the late Messinian the bottom of such canyons could have reached more than 500 m under sea level, followed by detritic sedimentation (Cita et al. 1990). With the reentering of Atlantic water through the reopened Gibraltar strait, the rivers transformed in fjords and lakes, similar to the today's lakes of the southern Alps, like Lago Maggiore, Como lake, Ceresio lake and smaller. Most of them are crypto-depressions (bottom of Lago Maggiore lies at −180 m.s.l., Como Lake at −230 m.a.s.l.). These fjord-similar lakes built hundreds of meters of lacustrine deposits. Temporary lakes could be formed also by the stepwise progressive erosion on terraces, without direct connection with sea level.

The fine-grained sediments encountered in the described boreholes could be explained according to these theories (Finckh 1978, Pirocchi 1992, Krijgsman et al. 1996, Yu and Eicher 2001, Gargani and Rigollet 2007, Antognini et al. 2012). The hypothetical lake where the encountered lacustrine sediments formed (Figs. 2, 3 and 4) could be related to the end of the last glaciation, as indicated by the C^{14} datation of about 15.300 years BP on a wooden remain above these sediments (−78 m, 242 m a.s.l). The observed lamination of these deposits (Fig. 4) are not interpretable as seasonal "varves" s.s., but rather as result of sudden changes in sedimentation regime following strong meteorological events, thunderstorm, floods etc. Recent studies show that such lakes could be filled rather quickly (Antognini et al. (2012) and Volpers 2002). It has been shown that 30 m of such sediments need only few centuries to deposit.

The retreat of the glaciers left the tills on the sides of the lacustrine valleys and successive erosion produced the alluvial and colluvial deposits filling their bottom which covered the fine-grained sediments. Lateral colluvial cones and rock-falls indented in these alluvia, but probably also earlier with the lacustrine sediments. The few meters of coarser, poorly rounded and highly permeable deposits found under the lacustrine sediments at the bottom of borehole SB8B are likely the sole encountered trace of this colluvial activity during the hypothetical lake existence (Figs. 2 and 3).

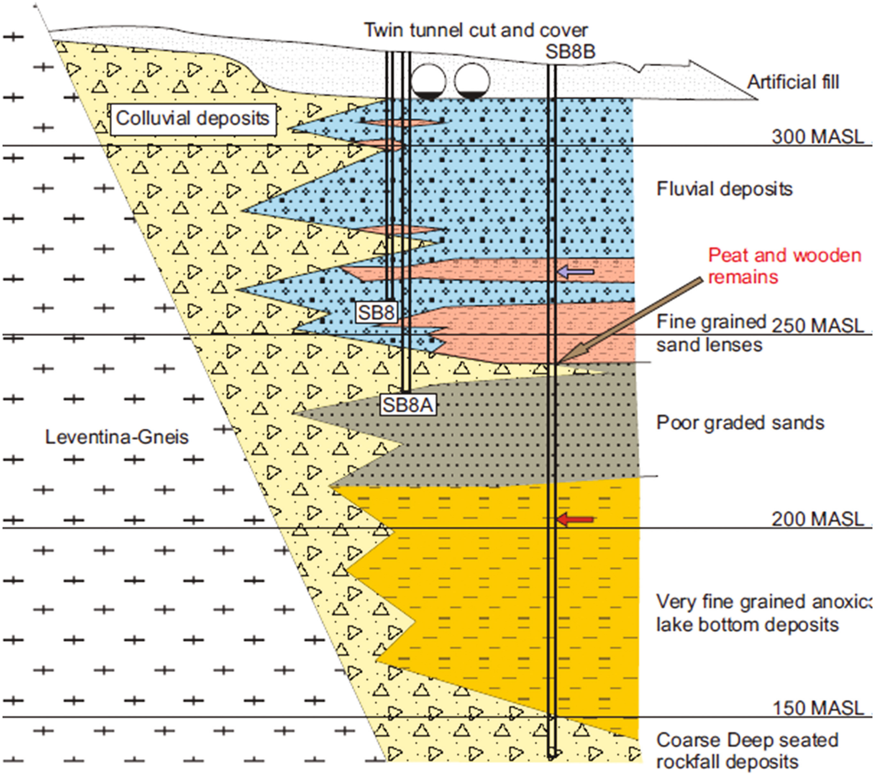

Fig. 2. Geological section with position of the two samples for creep test indicated by blue and red arrows.

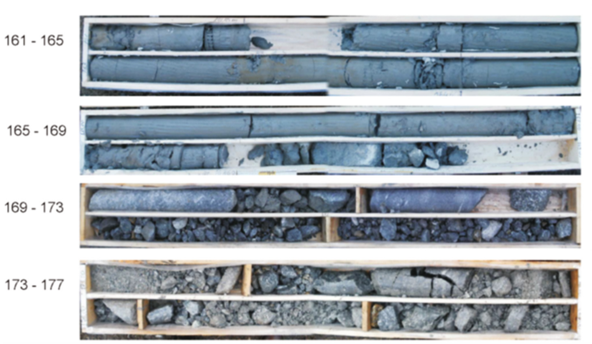

Fig. 3. Coarse colluvial deposits under the 65 m of lacustrine sediments.

Fig. 4. Laminated lacustrine sediments at ca 110 m of depth (ca 210 m.s.l).

Instrumentation and Methodology

The analysis were run on 2 front loading oedometer devices built by Wykeham Farrance in 2009 (Controls Group). On these instruments the soil specimen is laterally confined and subjected to a number of successive steps of load increments applied along the vertical direction. The oedometer cell consists of a rigid aluminium alloy frame to avoid any distortion under load, which is applied through calibrated weight sets that are hanged on a support located at the end of a lever arm performing a 10:1 ratio. The vertical consolidation of the specimen is recorded at various intervals of time until a constant settlement amount is reached. The vertical deformation is measured at a resolution of 1 μm with linear, high quality potentiometric transducers connected to a data acquisition unit allowing the recorded values to be immediately transmitted to a PC. During all the duration of the analysis the specimens have been constantly maintained fully immerged in water.

The two samples have been first consolidated with an usual oedometric procedure. For the specimen SB8B-3 the following loading steps were applied: 12.5 kPa, 25 kPa, 50 kPa, 200 kPa and 600 kPa. For the specimen SB8B-11 the sequence was: 12.5 kPa, 25 kPa, 50 kPa, 200 kPa, 600 kPa and 1200 kPa. Each loading step last 24 h before proceeding to the next on. After this phase the loads have been kept constant at the final amount reached, and the data recording rate has been modified in order to provide 1 value every 6 h. This phase of the analysis lasted 235 days for the sample SB8B-3 and 234 days for the sample SB8B-11, between April and December 2011. Table 1 describes the characteristics of the two samples that were tested for creep (Fig. 5).

Table 1. Parameters of the two tested samples.

ID	Depth (m)	USCS	Clay (w%)	Silt (w%)	Sand (w%)	w_L (%)	I_P	$\varepsilon_{\text{end-preconsol}}$	E_{oed} (kPa)
SB8B-3	52	SM	2	37	61	38.2	10.0	7.53	13800
SB8B-11	117	CM	33	66	1	45.7	23.0	8.55	27238

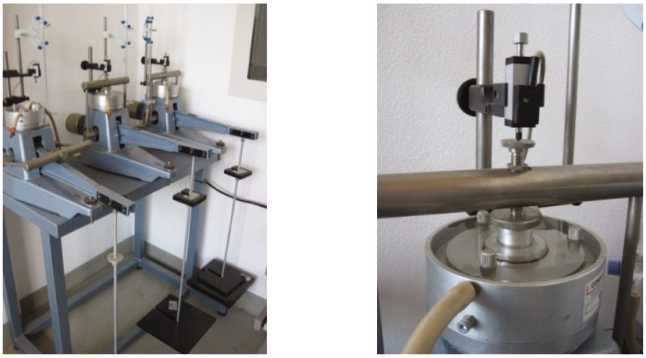

Fig. 5. Oedometers equipped with high quality electronic sensors, connected to an automatic data logger for the entire duration of the tests (about 8 months).

Results and Interpretations

The raw results of the long lasting oedemeter tests are shown in the diagrams of Figs. 6 and 7. The variability of the data is intense. With the sampling of 4 values per day strong oscillations are observed. The Fig. 6 shows the interpolations of the data in order to obtain the requested parameters, according to the usual theories and constitutive laws of creeping (secondary or "tertiary" settlement Janbu 1969 in Vermeer and Neher 2000, Vaid and Campanella 1977, Martins 1992). It illustrates the plot of the strain of the samples as percentage of the initial height of the sample after pre-consolidation as function of the log of time. According to Janbu, the slope of the linear portion of the curve gives the creep "C" parameter.

Various theories and constitutive laws can be applied to these results. An excellent compilation of proposed laws or prediction was made in 2013 (Alexandre et al. 2013) and Thesis were written on the theme (Havel 2004, Olsson 2010). They cite in particular Vaid and Campanella. Basing upon the obtained creep parameters in form of the slope of semi logarithmic plot of test-datas, which slightly differs by the basic expression of deformation, engineering strain, void ratio, etc. A 3D prediction could be performed using supplementary parameters (Vermeer and Neher 2000), but it was not the scope of the study.

In this paper, the methodology and his technical difficulties is emphasized, with regard to the influence of external actions that can influence the quality of the results. To explain the oscillating of the values, because the tests were conducted in a temperature and moisture controlled environment, the eventual effect of tides on the weights of the oedometers are herein suggested (Fig. 6). With eodometers activated hydraulically the hypothetic tidal effect should disappear.

The interpolations are performed according to the following function of time:

$$\frac{t}{A} + Bt + C\ sqrt(t)$$

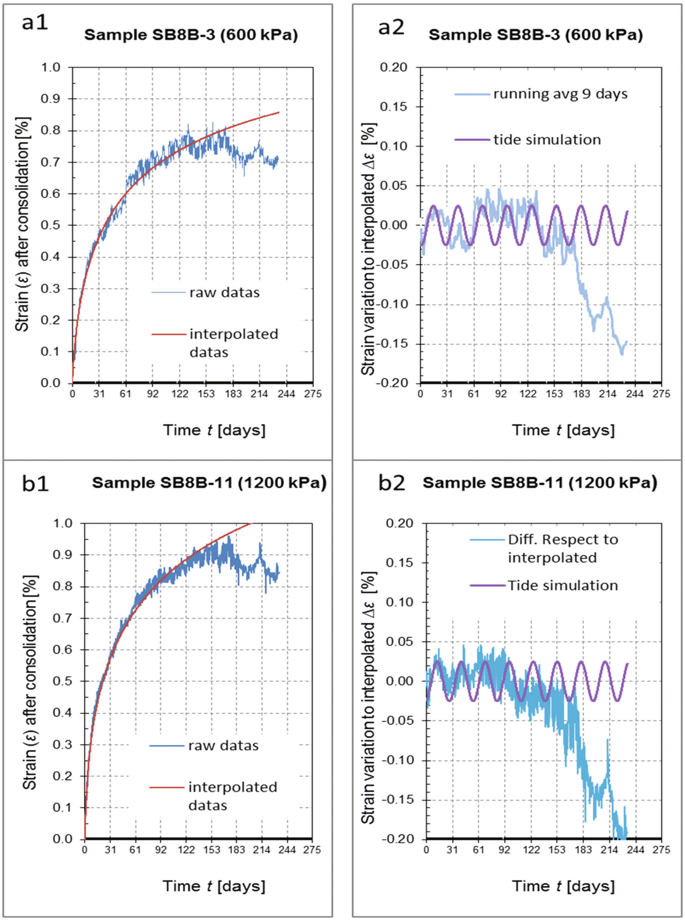

Fig. 6. Results of the 235 days creep test of the samples from 52 and 117 m of depth. The right-hand graphs shows the variability of all the values as function of the interpolated values. The eventual correlation of a 28 days tidal effect is shown.

were A, B and C are coefficients trimmed by regression. The daily tide effect can obviously not be correlated with a sampling rate of 4 values per day, and is maybe superposed to slight temperature, air-moisture day-night variations or atmospheric pressure, even if the laboratory was under controlled climatic conditions. The a2 and b2 graphics of Fig. 6 show a visual correlation between the variation of values respect to the interpolated ones, which well match with a 28 days sinusoidal function.

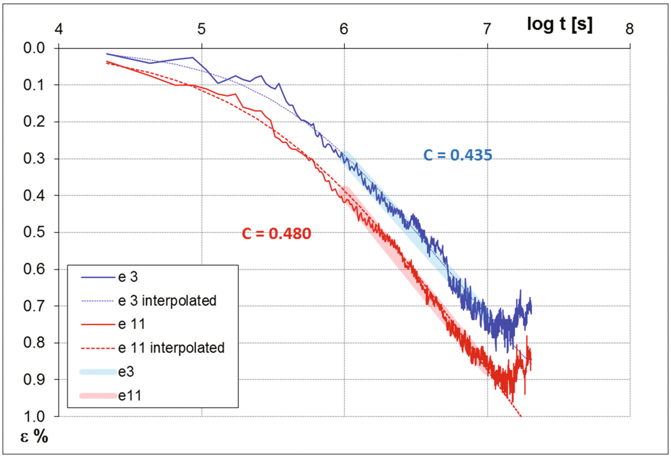

Fig. 7. Regression curves of creep values (only along thick red and blue lines) to gain the creep C parameter according to Janbu (1969), in Vermeer and Neher 2000).

Conclusions

Long lasting oedometer tests allow to assess the creep settlement parameters of fine sediments. The costs of such operation is affordable only using automatic recording devices that do not require any further assistance other than periodical surveillance of the measurements. Very sensitive, highest quality deformation sensors are compulsory, in this case with a resolution of 1 µm. The sensitivity has as consequence that every small variation of the records due to external or internal disturbance must be taken into account, like temperature, moisture or atmospheric pressure variations. The good correlation with a 28 days cycle suggest tidal effect on the eodemeter weights but every other influence on the sample and on the transducers are possible. The best way to analyze the data is to proceed to adjustments to correct external effects by different types of interpolation.

The creep could be recorded and clearly identified through cleaning of disturbances through interpolations. Furthermore, creep could still develop even if the applied load was smaller than the assumed natural lithostatic pressure. The observed reversed deformation, if not due to instrumental disturbing factors, could be explained with a strain-hardening due to changes in mineral structure and composition (begin of diagenesis, cementation). The question remains open if the same would occur in case of constant load higher than the effective lithostatic one.

A possible answer to that hypothesis could be obtained by repeating the test after unloading and reloading the samples under the same conditions and again over a long time, but such a procedure can be done only within the scope of a research project, unfortunately not in the context of a construction site with its terms. It is also interesting to observe that even if the grain size distribution of the two samples is quite different, the first being rich on fine sand, the resulting creep parameters are very close.

References

Alexandre GF, Martins ISM, Santa Maria PEL (2013) Creep prediction of an undisturbed sensitive clay. HAL. https://hal.archives-ouvertes.fr/hal-00880388

Antognini M, Volpers R (2002) A late pleistocene age for the chironico rockslide (Central Alps, Ticino Switzerland). Bull Appl Geol 7(2):113–125

Antognini M, Oppizzi P, Patocchi P, Scapozza C (2012) Stratigrafia, morfodinamica, paleoambienti della piana fluvio-deltizia del Ticino dall'Ultimo Massimo Glaciale a oggi: proposta di sintesi. Bollettino della Società ticinese di scienze naturali, vol 100, pp 89–106. ISSN 0379-1254

Cita MB, Bini A, Corselli C (1990) Superfici di erosione messiniana: una ipotesi sull'origine dei laghi sudalpini. In: Barabanti L, Giussani C, De Bernardi R (eds) Il Lago Maggiore dalla ricerca alla gestione. Documenta dell'Istituto Italiano di Idrobiologia, Pallanza, vol 22, pp 33–54

Finckh P (1978) Are southern Alpine lakes former Messinian canyons? Geophysical evidence for preglacial erosion in the southern lakes. Marine Geol 27:289–302

Gargani J, Rigollet C (2007) Mediterranean sea level variations during the messinian salinity crisis. Geophysical research letters. Willey

Havel F (2004) Creep in soft soils. Thesis submitted to the Faculty of Engineering, Science and Technology, Norwegian University of Science and Technology

Janbu N (1969) The resistance concept applied to deformation of soils. In: Proceedings of 7th ICSMFE, Mexico, vol 1, pp 191–196

Krijgsman W, Garcés M, Langereis CG, Daams R, van Dam J, van der Meulen AJ, Agustì J, Cabrera L (1996) A new chronology for the middle to late Miocene continental record in Spain. Earth and Planet Sci Lett 142(3–4):367–380. Elsevier

Martins ISM (1992) Fundamentals of a behavioral model for saturated clayey soils. D.Sc. thesis, COPPE/UFRJ, Rio de Janeiro, Brazil. (in Portuguese)

Olsson M (2010) Calculating long-term settlement in soft clays - with special focus on the Gothenburg region. Thesis for the Degree of Licenciated of Engineering, Chalmers University of Technology, Göteborg, Sweden

Pirocchi A (1992) Laghi di sbarramento per frana nelle Alpi: tipologia ed evoluzione. Tesi Università di Pavia, pp 1–154

Rogenmoser G (1981) Magnetische Untersuchungen im Pliozän von Balerna. Dipl. thesis ETH Zürich

Vaid Y, Campanella RG (1977) Time-dependent behaviour of undisturbed clay. ASCE J Geotech Eng Div 103(GT7):693–709

Vermeer PA, Neher HP (2000) A soft soil model that accounts for creep. In: Bexond 2000 in computational geotechnics - 10 years of PLAXI inernational, Balkema. ISBN 905809040X

Yu Z, Eicher U (2001) Three amphi-atlantic century-scale cold events during the Bølling – Allerød warm period. Géographie physique et Quaternaire

Deep Soil Mixing Method for the Bio-cement by Means of Bender Element Test

Keeratikan Piriyakul(✉) and Janjit Iamchaturapatr

Department of Civil and Environmental Engineering Technology,
Center of Excellence in Structural Dynamics and Urban Management,
College of Industrial Technology, King Mongkut's University
of Technology North Bangkok, Bangkok, Thailand
keeratikanp@kmutnb.ac.th

Abstract. This article presented the effect of mixing patterns for the bio-cement in two different soils (Kaolin clay and Bangkok sand). Bio-cementation process initiated the crystal forms of calcium carbonate ($CaCO_3$) to bind the soil particles. Soil samples were mixed with the solution containing 250 mM of $CO(NH_2)_2$, 250 mM of Ca^{2+} (by $CaCl_2$) and 20% (v/v) of urease. In simulated deep mixing of Kaolin clay, the research found that blades used in solution mixing affected the strength development of Kaolin clay after bio-cementation. The V_s of 210 m s^{-1} was found in comb blade mixer. In simulated deep mixing of Bangkok sand, the research found that solution injecting method affected the V_s of Bangkok sand. The period drop and the period injecting methods provided better V_s results than the one time pouring and the continuous injecting methods.

Introduction

An extensive amount of research investigated ground improvement techniques and studied the enhancing soil properties on demand by stimulating bio-chemo processes in-situ as described by De Jong et al. (2010), Van Paassen et al. (2010), Whiffin et al. (2005) and Ivanov and Chu (2008). One of these techniques was the bio-cementation which used the microbial-induced calcium carbonate ($CaCO_3$) precipitation. This bio-cementation technique was a environmentally friendly, low-energy input method and also the microorganisms were non-pathogen. Bacteria in the medium contained urea ($CO(NH_2)_2$) and calcium ion (Ca^{2+}) could induce precipitation of $CaCO_3$. Figure 1 illustrated bio-chemical reactions involving the induction of $CaCO_3$ precipitation. Ureolytic bacteria produced the enzyme urease which hydrolyzed $CO(NH_2)_2$ to ammonium (NH_4^+) and carbonate (CO_3^{2-}). The production of NH_4^+ resulted in the increase of pH and the formation of $CaCO_3$, which filling the pore space and increasing solid content in soils. Several studies have shown that this process could be used to improve the mechanical properties of porous materials as described by De Jong et al. (2010), Whiffin et al. (2005), Ivanov and Chu (2008), Piriyakul and Iamchaturapatr (2013) and Ketklin et al. (2013). Figure 1 showed the formation of $CaCO_3$ with amount of CO_3^{2-} derived from biological degradation of $CO(NH_2)_2$ by ureolytic bacteria. This research studied the possibility to use the deep mixing method of bio-cement solution in Bangkok area by means of the non destructive testing method (so called "bender element test").

A. Ferrari and L. Laloui (eds.), *Advances in Laboratory Testing and Modelling of Soils and Shales (ATMSS)*, Springer Series in Geomechanics and Geoengineering,
DOI 10.1007/978-3-319-52773-4_44

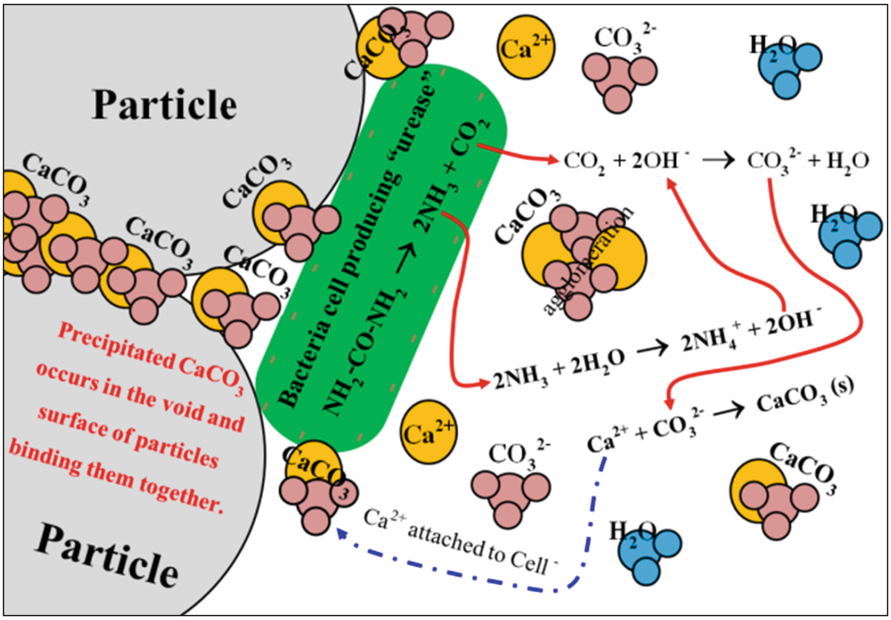

Fig. 1. Overview of biological and chemical processes via ureolysis inducing calcium carbonate precipitation: Bacteria produce enzyme urease that hydrolyzes urea ($CO(NH_2)_2$) or NH_2-CO-(NH_2) to ammonium (NH_4^+) and carbonate (CO_3^{2-}) ions.

Methodology

Testing Materials

This research used 2 types of soils. Firstly, the research used Kaolin clay to study the deep mixing technique for bio-cent in clay soils. Lastly, the research used Bangkok sand and studied the mixing patterns as described in details at the next sub-section.

Kaolin Clay

The Kaolin clay has the unit weight of 2,360 kg m^{-3}, the liquid limit of 46% and the plastic limit of 34%. The solution was contained 250 mM of $CO(NH_2)_2$ and 250 mM of Ca^{2+} (by $CaCl_2$) with the urease concentrations of 20% (v/v) as described by APHA, AWWA, WEF (2012). The samples are prepared at 2 times of the liquid limit and mixed by the motor at 100 RPM and penetrated at 0.1 mm s^{-1} with 3 types of mixing blades with diameter of 5 cm; (a) rectangle blade (b) spiral blade and (c) comb blade as shown in Fig. 2.

Bangkok Sand

The natural Bangkok sand was collected, dried in oven (105 °C for 24 h) and sieved passing through the ASTM sieve mesh no. 100 and retaining on the sieve mesh no. 200. Then, the dry Bangkok sand with the unit weight of 1470 kg m^{-3} was placed into

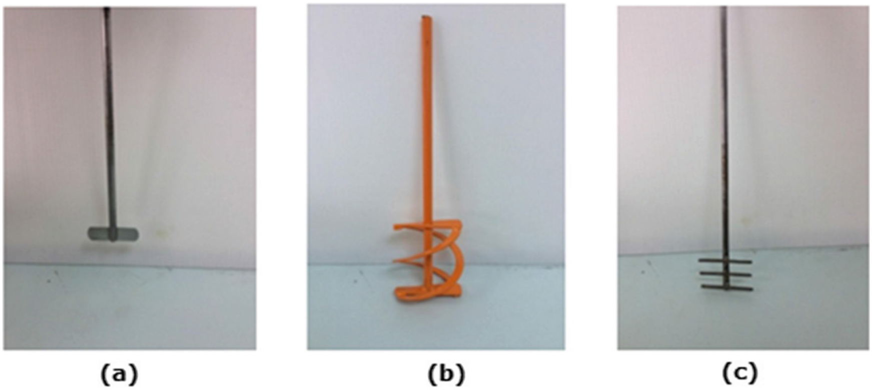

Fig. 2. (a) rectangle blade (b) spiral blade and (c) comb blade.

the plastic container (called biocemented sand reactor or BSR) with dimensions (width × length × depth): 15 × 15 × 25 cm. The bio-cement solution of 315 mL which contained 250 mM of $CO(NH_2)_2$ and 250 mM of Ca^{2+} (by $CaCl_2$) with the enzyme urease of 20% (v/v) was prepared and kept as stock solutions (APHA, AWWA, WEF 2012). There are 4 injection methods for filling the solution in to the BSR containers; (a) pour all the solution by one time with the pouring rate of 157.5 mL h^{-1} (b) drop the solution continuously with the dropping rate of about 3.3 mL h^{-1} (c) drop the solution periodically by each time of 78.75 mL with the dropping rate of about 13.5 mL h^{-1} for 4 days and (d) inject the solution periodically by each time of 78.75 mL with the injecting rate of about 39.5 mL h^{-1} for 4 days through the porous pipe as shown in Fig. 3.

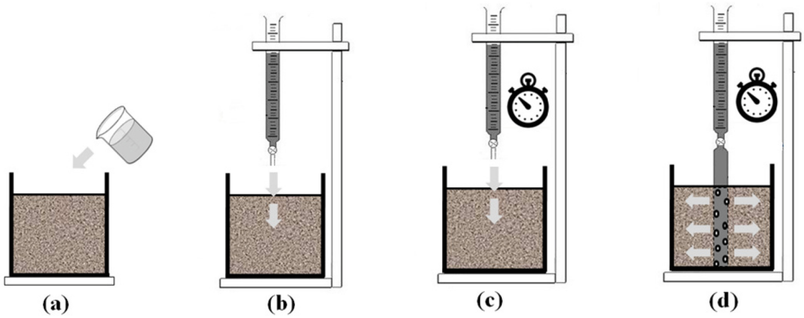

Fig. 3. (a) pour all the solution at one time with the rate of 157.5 mL h^{-1} (b) continue drop the solution with the dropping rate of 3.3 mL h^{-1} (c) periodically drop the solution of 79 mL per day with the dropping rate of 13.5 mL h^{-1} for 4 days and (d) periodically inject the solution 79 mL per day with the injecting rate of 39.5 mL h^{-1} for 4 days through the porous pipe.

Bender Element Test

The soil strength was measured for shear wave velocity *(V_s)*. The shear wave was sent and received by piezoelectric ceramic sensors placed at opposite ends of the soil sample. Figure 4 showed the schematic test set-up. A computer generated a signal through a sound card. This signal was amplified and sent to BSRs. An oscilloscope was used to measure the arrival time between a sending signal and a receiving signal. V_s was calculated from the Tip-to-tip distance between the two sensors and the time required by the shear wave to cover this distance and time as shown in Eq. 1.

$$V_s = \frac{L}{t} \tag{1}$$

where V_s is the shear wave velocity, L is the tip to tip distance between two sensors and t is the required time to cover this distance.

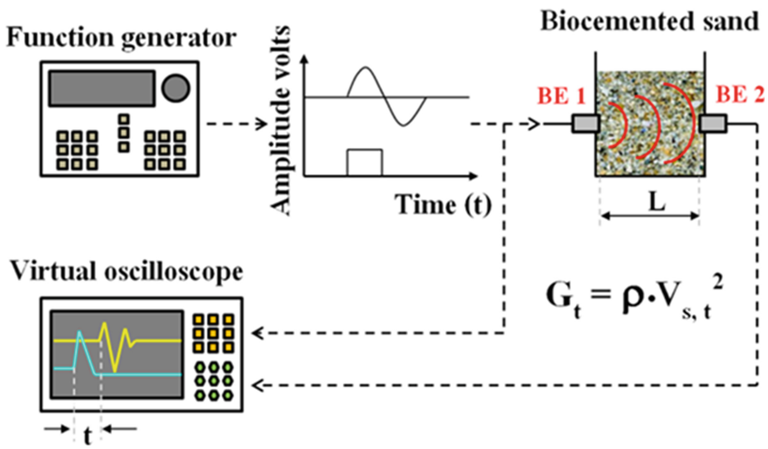

Fig. 4. Schematic of bender element test set-up.

Test Results

Figure 5a showed the Kaolin clay sample mixed by the rectangle blade. This Kaolin clay sample was cored and tested by the bender element test. The shear wave velocity of 167.3 m s^{-1} was measured and calculated by Eq. 1 as seen in Fig. 5b. In a similar way, Fig. 5c showed the coring Kaolin clay sample mixed by the spiral blade with the shear wave velocity of 150.6 m s^{-1} as seen in Fig. 5d. Figure 5e showed the coring Kaolin clay sample mixed by the comb blade and the shear wave velocity of 210.5 m s^{-1} is measured as seen in Fig. 5f. Table 1 summarized the bender element test results for Kaolin clay.

For Bangkok sand, Fig. 6a showed the bender element test result of the method (a) which has the maximum shear wave velocity of 184.5 m s^{-1} at the bottom depth of 15 cm and the minimum shear wave velocity at the top of 2 cm. This showed all the

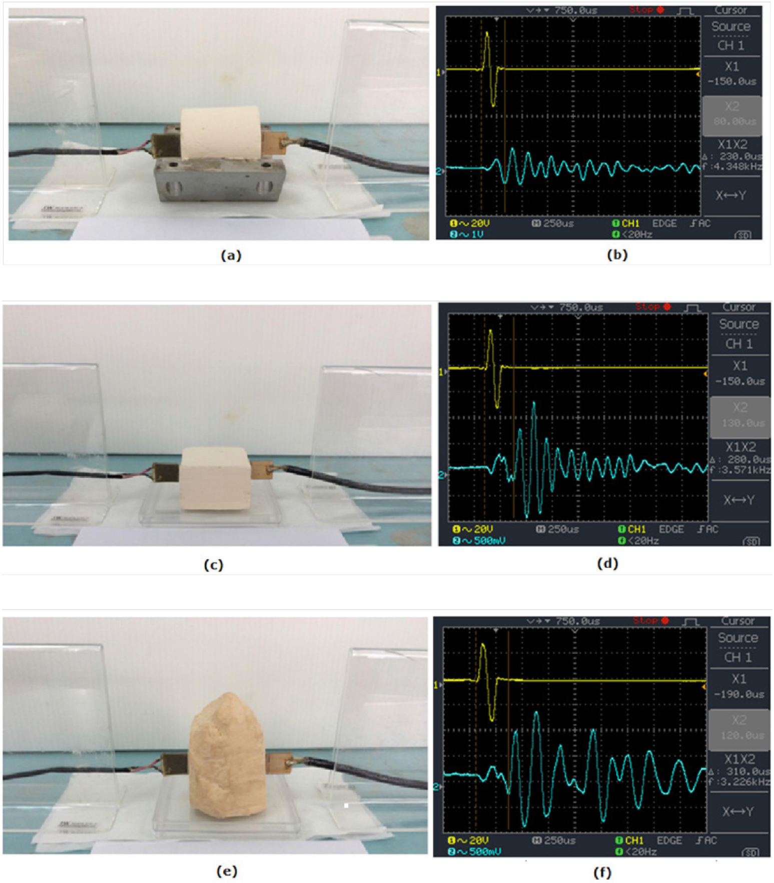

Fig. 5. (a) Sample mixed by rectangle blade (b) V_s of Sample mixed by rectangle blade (c) Sample mixed by spiral blade (d) V_s of Sample mixed by spiral blade (e) Sample mixed by comb blade (f) V_s of Sample mixed by comb blade.

Table 1. Bender element test results for Kaolin clay.

Blade type	Shear wave velocity [m s^{-1}]
Rectangle blade	167.3
Spiral blade	150.6
Comb blade	210.5

bio-cement reaction was done at the bottom area. On the other hand, Fig. 6b showed the bender element test results of the method (b) that the maximum shear wave velocity was 159.4 m s^{-1} at the depth of 5 cm and the minimum shear wave velocity was

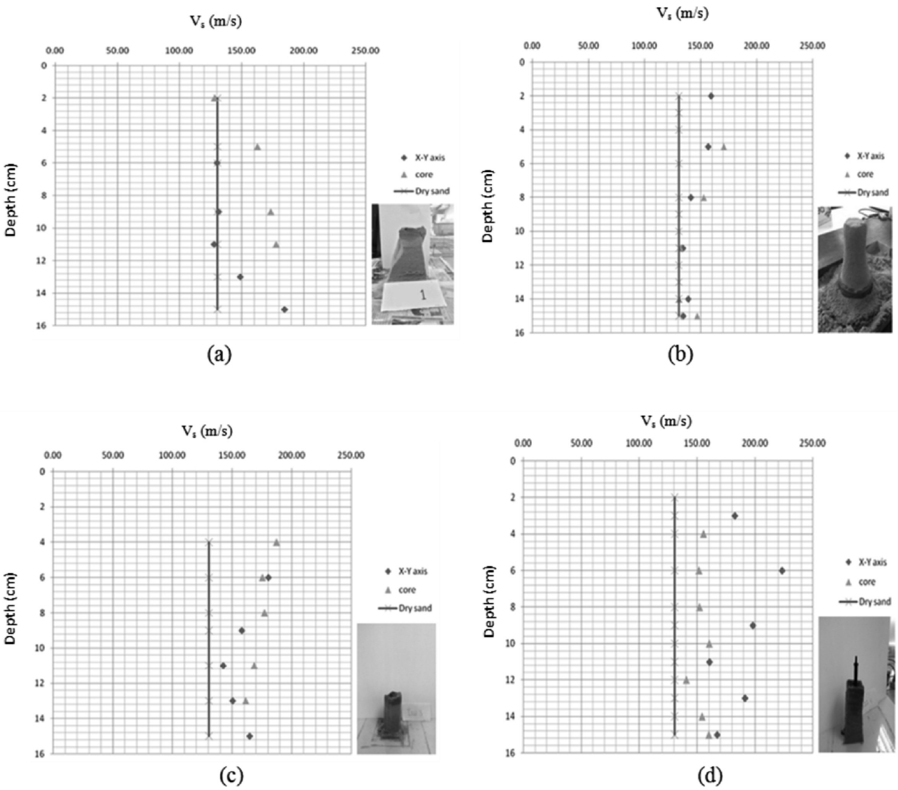

Fig. 6. Bender element test results: (a) pour all the solution at one time with the rate of 157.5 mL h^{-1} (b) continuous drop with the dropping rate of 3.3 mL h^{-1} (c) period drop of 79 mL with the dropping rate of 13.5 h^{-1} for 4 days and (d) period injection of the solution of 79 mL with the injecting rate of 39.5 mL h^{-1} for 4 days through the pipe.

Table 2. Bender element test results for Bangkok sand.

Injection method	V_s (Max.) [m s^{-1}]	V_s (Min.) [m s^{-1}]	V_s (Avg.) [m s^{-1}]
A	184.5	127.8	144.5
B	159.4	134.4	144.3
C	180.4	142.4	159.2
D	223.5	167.5	187.4

The controlled shear wave velocity of dry sand sample is 130.7 m s^{-1}

134.4 m s^{-1} at the depth of 11 cm. So, the bio-cement reaction was done at the top surface area. Figures 6c and d showed the homogenous bio-cement reaction which has the average shear wave velocity of 159.2 m s^{-1} for the method (c) and 187.4 m s^{-1} for the method (d). Table 2 summarized the bender element test results for Bangkok sand.

Conclusions

The bio-cement was an environmental friendly technique for deep mixing method ground which initiated the crystal forms of calcium carbonate ($CaCO_3$) to bind the soil particles resulting in soil mechanical improvement. For deep soil mixing in Kaolin clay, the research found that the comb blade type was the best mixing blade type. The rectangle blade type was the second efficient blade type and the spiral blade type was the last efficient mixing blade type. For deep soil mixing in Bangkok sand, the research found that the one time solution pouring method or the method (a) was a disadvantageous method since it improved the ground only at the bottom area. In a same way, the solution continuously drop method or the method (b) was also a disadvantageous method because it improved the ground only at the top area. The most recommended methods were the solution periodically drop method or the method (c) and the solution periodically inject method or the method (d) which improved the ground strength continuously along the depth.

Acknowledgement. The authors are grateful for the scientific research fund of the King Mongkut's University of Technology North Bangkok No. KMUTNB-Gov-59-09.

References

De Jong JT, Mortensen BM, Martinez BC, Nelson DC (2010) Bio-mediated soil improvement. Ecol Eng 36:197–210

Van Paassen LA, Daza CM, Staal M, Sorokin DY, Van der Zon W, Van Loosdrecht MCM (2010) Potential soil reinforcement by biological denitrification. Ecol Eng 36:168–175

Whiffin VS, Lambert JWM, Van Ree CCD (2005) Biogrout and biosealing-pore-space engineering with bacteria. Geo-Strata-Geo Inst ASCE 5:13–16

Ivanov V, Chu J (2008) Applications of micro-organisms to geotechnical engineering for bioclogging and biocementation of soil in situ. Rev Environ Sci Biotechnol 7:139–153

Piriyakul K, Iamchaturapatr J (2013) Biocementation through microbial calcium carbonate precipitation. J Ind Technol 9(3):1–21. (Thai Journal)

Ketklin T, Piriyakul K, Iamchaturapatr J (2013) Biocementation for ground improvement. In: The annual concrete conference (ACC9), Phitsanulok, Thailand

APHA, AWWA, WEF (2012) Standard methods for the examination of water and wastewater, 22nd edn. American Public Health Association, American Water Work Association and Water Environment Federation, Washington, DC

Studying of Shale Organic Matter Structure and Pore Space Transformations During Hydrocarbon Generation

Dina Giliazetdinova(✉) and Dmitry Korost

Lomonosov Moscow State University, Moscow, Russia
Gilyazetdinova_91@mail.ru

Abstract. In this study, we focus on organic matter structure and its interaction with the pore space of shales during hydrocarbon (HC) generation. Rock samples collected from Domanic horizon of South-Tatar arch were heated in the pyrolyzer to temperatures closely corresponding to different catagenesis stages. X-ray microtomography method was used to monitor changes in the morphology of the pore space and organic matter structure within studied shale rocks. By routine measurements we made sure that all samples had similar composition of organic and mineral phases. All samples in the collection were grouped according to initial structure and amount of organics. They were processed separately to: (1) study the influence of organic matter content on the changing morphology of the rock under thermal effects; (2) study the effect of initial structure on the primary migration processes for samples with similar organic matter content. After heating the morphology of altered rocks was characterized by formation of new pores and channels connecting primary voids. However, it was noted that the samples with a relatively low content of the organic matter had less changes in pore space morphology, in contrast to rocks with a high organic content. Second part of the study also revealed significant differences in resulting pore structures depending on initial structure of the unaltered rocks and connectivity of original organics.

Introduction

Currently studies of oil shale as unconventional sources of HC are highly relevant. In most cases this is motivated by depletion of conventional HC reserves, making it necessary to search for HC in other types of rock. The main feature of oil shales is that HC contained within the shale are a result of the generation of organic matter from the same formation. And as any process, process of HC generation can't pass without a trace. Newly-formed HC, pressure and temperature lead to pore space structure transformations in shales. It has been proved that the degree of rock pore space alterations depends on the degree of maturity and organic matter content in the rock (Tisot 1967; Tiwary et al. 2013). Generation of new HC can lead both to crack formation (Kobchenko et al. 2011), as well as formation of new pores, which are associated with kerogen interlayers (Tiwary et al. 2013). Thereby kerogen distribution in the rock also plays an important role (Tiwary et al. 2013). Still it remains unclear

A. Ferrari and L. Laloui (eds.), *Advances in Laboratory Testing and Modelling of Soils and Shales (ATMSS)*, Springer Series in Geomechanics and Geoengineering,
DOI 10.1007/978-3-319-52773-4_45

why the same processes in different rocks lead to different pore space alteration. We set the task to identify the main features that can control changes in the rock pore space. Taking into account that one of the main rock characteristics is texture, which is a feature that characterizes the location of the particles relative to each other in the rock, it will be considered as the main factor capable to influence changes in the pore space. In this study also organic matter content will be considered as the controlling factor.

Materials and Methods

Research Methods

The composition of the rocks was studied by XRD on Ultima-IV equipment of Rigaku (Japan) company. From each sample, thin sections were made to determine the internal structure of the rocks in the optical laboratory microscope Leica DM EP. Geochemical characteristics of organic matter were obtained on pyrolyzer Rock-Eval-6 according to the method developed by the French Institute of Petroleum (Espitalié et al. 1984; Tissot and Welte 1984 and others). It is worth noting that shales have pores size in order of magnitude less than traditional resources. In this regard, standard laboratory methods are not sufficient to study pore shale. Therefore, for detailed study of the rock pore space structure we used multi-scale imaging techniques. The study of samples by X-ray computed microtomography was produced using microtomograph SkyScan-1172. Samples of 3 mm in diameter were scanned with a resolution of 1.2 μ using Al + Cu filter at 100 keV voltages and current of 100 mA.

Experimental Procedure

Laboratory experiment aimed to model HC generation in the intact rock sample by heating in a nitrogen atmosphere at a predetermined temperature program and by observations of changes in the structure of the pore space. Simulation of HC generation was conducted on pyrolyzer RockEval 6.

To monitor the relevant changes in the structure of the rock we used X-ray microtomography. X-ray absorption depends on the density of mineral and non-mineral rock components. The X-ray absorption for organic matter will be minimal due to the low density component of kerogen. Given the fact that the microporosity of studied rocks is negligible, i.e. filled with organic matter, all materials with low absorption was considered to be organic matter. Using this approach it was possible to calculate the content of organic matter in volume in the unaltered samples, as well as organic matter and newly formed pores in the heated samples. Evaluation of organic matter (porosity) was based on a computer analysis: separation of X-ray contrast in brightness phase. According to the selected brightness corresponding to the pore space of the rock, volumetric calculation phase was produced. To assess transformation of sample pores we computed the volume of connected pores. This analysis also allows us to calculate the volume and connectivity parameters of each individual object (pore). Based on the analysis, we estimate the volume fraction of the largest cluster, which characterizes the highest connectivity in the rock. The connectivity allows us to estimate the degree of transformation, as in the process of pore alteration is related to merging of lenses and interlayers into a single system of pores.

Samples Collection

We studied a collection of rock samples from Domanik horizon from the South Tatar crest, Volga-Ural oil and gas basin, Russia. The composition of rocks is mainly dominated by siliceous-carbonate material; some are highly enriched with kerogen (>10%). Some samples are almost pure carbonate rocks, highly transformed, recrystallized with a low content of organic matter. The organic material in the rocks in most of the samples is immature under protocatagenesis Tmax = 420 °C. Special attention was devoted to the study of structures in the collection of the studied samples. Two types of structures have been identified: laminated and spotty. The laminated structure is most often characterized by alternating layers intensely saturated by organic matter and layers, folded with formed siliceous and carbonate components. Massive structure refers to a uniform distribution of organic matter in rock.

Results and Discussions

The first step of the experiment was devoted to the study of the rock structure. In our opinion, the structure may be an important factor that can affect the rate of sample pore space alteration in result of new HC generation. To confirm or refute this assumption we selected 3 samples with the same content of organic matter and different structures: a parallel-laminated and spotty (Table 1).

Table 1. Rock collection characteristics.

Sample	TOC, %	Tmax, C	Composition	Structure
1	10,46	430	Siliceous-carbonate	Laminated
2	3,44	423	Siliceous-carbonate	Spotty
3	3,92	427	Siliceous-carbonate	Laminated

Sample 3 is characterized by organic matter content 3.92%. After heating the volume of the rock void space has changed slightly, but its structure has undergone some changes. During heating, the individual cavities were transformed into the pore system, forming a crack with length 0.2 mm (Fig. 1).

Sample 2 with the organic matter content of 3.44% has spotty texture. After heating the sample to 500 °C a significant change in the pore space morphology was observed (Fig. 2). X-ray absorption of organic matter decreased, due to its transformation. Excessive pressure in the generation of new HC was compensated by the formation of channels connecting the pores.

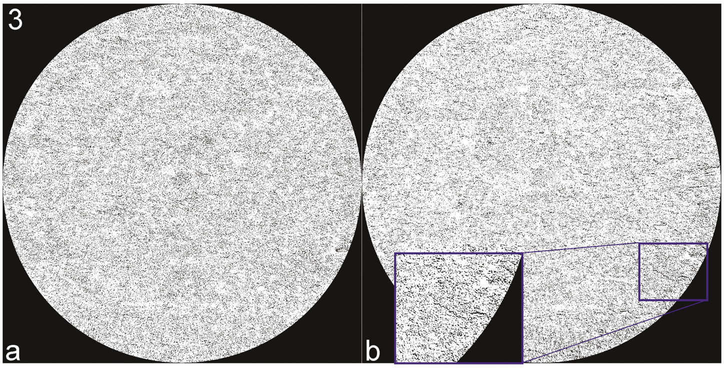

Fig. 1. a – binaries tomographic sample 3 slice before heating, b – binaries tomographic sample 3 slice after heating.

In contrast to the sample 2, in sample 3 cracks parallel to bedding were observed. The pores are connected with each other in both samples, but pore connectivity in spotty sample is smaller. Volumes of pore space changes in both samples are the same, which is consistent with the same content of organic matter in these rocks.

It follows that the transformation of pores due to primary migration processes in rocks with different structures can take place in different ways. In sample 2 with spotty structure organic matter is evenly distributed throughout the rock. Therefore, the result of the rock heating is a loose connectivity. In sample 3, organic matter is concentrated in certain isolated interlayers. Such rock structure upon heating results in the formation of cracks due to newly HC discharge under high pore pressure.

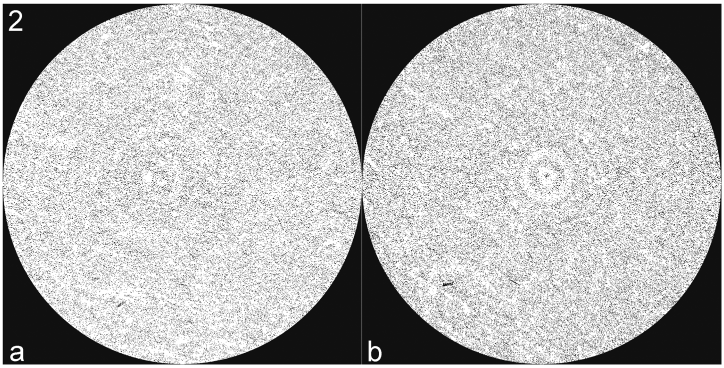

Fig. 2. a – binaries tomographic sample 2 slice before heating, b – binaries tomographic sample 2 slice after heating.

Significant changes in the morphology of the rock pore space also occurred in sample 1 (Fig. 3). Initial unaltered rock is characterized by numerous small (30 micron) pores which are weakly interconnected. After heating the sample, it was noted that the formation of new pores and cracks was oriented to the bedding of the rock. Pore space, in this case represented by organic matter and newly formed pores of altered rocks, exceeded the original twice (Table 2).

Thus, we can conclude that the organic content of the rock plays an important role in the transformation of the rock pore space in depths corresponding to the temperatures of HC generation. The results at this study stage are consistent with the work of predecessors (Korost et al. 2012; Lafargue et al. 1993; Tisot 1967; Tiwary et al. 2013; Kobchenko et al. 2011; Zhao et al. 2012).

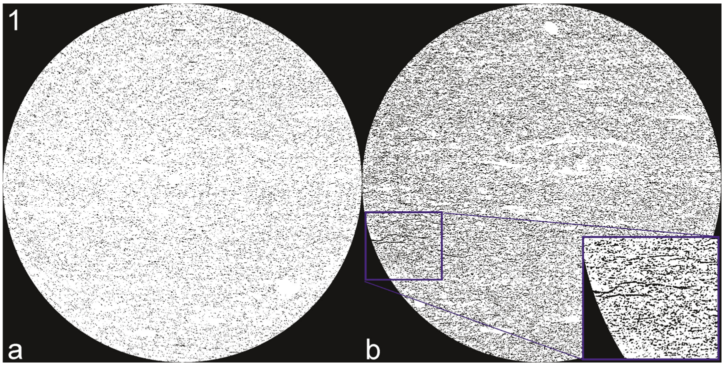

Fig. 3. a – binaries tomographic sample 1 slice before heating, b – binaries tomographic sample 1 slice after heating.

Table 2. The calculated values of porosity and connectivity before and after rock heating.

Sample	CT connectivity, before heating, %	CT connectivity, after heating, %	Porosity, before heating, %	Porosity, after heating, %
1	13,3	94	5,5	19,9
2	34	59,1	9,7	13,8
3	86	94,3	17,7	20,1

Conclusions

Structural features, just like the amount of organic matter in the rock have a significant role in the transformation of the pore space. Pore space of rocks with laminated structure, as noted earlier, is converted into the cracks during heating. This fact is probably due to the high concentration of organic matter in the interlayers. The new generation of HC leads to the formation of cracks. Formation of this type of alterations occurs under the action of pore pressure excess. Cracking requires isolation layers, saturated by organic matter. The situation is different with rocks with spotty structure. Due to the uniform distribution of organic matter in rock, cracks are not formed, since the newly formed portion of the HC fluids migrate into the open pore system.

Acknowledgements. This work was supported by RFFR grant № 16-35-00576 and RSF № 14-17-00658.

References

Espitalié J, Marquis F, Barsony I (1984) Geochemical logging. In: Voorhess KJ (ed) analytical pyrolysis. Butterworths, Boston, pp 53–79

Zhao J, Yang D, Kang Z, Feng Z (2012) A micro-ct-study of changes in the internal structure of Daqing and Yan'an oil shales at high temperatures. Oil Shale 29(4):357–367. doi:10.3176/oil.2012.4.06 ISSN 0208-189X

Kobchenko M, Panahi H, Renard F, Dysthe DK, Malthe-Sørenssen A, Mazzini A, Scheibert J, Jamtveit B, Meakin P (2011) 4D imaging of fracturing in organic-rich shales during heating. J Geophys Res 116:B12201. doi:10.1029/2011JB008565

Korost D, Nadezhkin D, Akhmanov G (2012) Pore space in source rock during the generation of hydrocarbons: laboratory experiment. Vestnik Moskovskogo Universiteta. Geologiya. – 2012. – No. 4. – c. 32–37

Lafargue E, Espitalie IJ, Broks TM, Nyland B (1993) Experimental simulation of primary migration. Adv Org Geochem 22:575–586

Tisot PR (1967) Alterations in structure and physical properties of Green River oil shale by thermal treatment. J Chem Eng Data 12:405–411

Tiwary P, Deo M, Lin CL, Miller JD (2013) Characterization of oil shale pore structure before and after pyrolysis by using X-ray micro CT. Fuel 107:547–554

Tissot BP, Welte DH (1984) Petroleum Formation and Occurrence, vol 699. Springer, Berlin

On the Application of Microbially Induced Calcite Precipitation for Soils: A Multiscale Study

Dimitrios Terzis(✉) and Lyesse Laloui

Laboratory for Soil Mechanics, Swiss Federal Institute of Technology, Lausanne, Switzerland
dimitrios.terzis@epfl.ch

Abstract. Two laboratory experiments are used to provide preliminary evidence towards upscaling the microbially induced calcite precipitation (MICP) for soils. Fine sand is packed and subsequently subjected to MICP treatment in 11-liter cylindrical tanks. Different conditions are tested regarding the bacteria injection source as well as their propagation in the porous medium. The goal is to associate the adopted application strategy with the final shape, size and total mass of precipitated calcite in the yielded bio-cemented soil volume. Observations carried out at the micro-scale reveal the presence of calcified biofilms as a distinct "habit" of $CaCO_3$ precipitate. Finally, a series of drained triaxial shear tests is carried out on fine and medium MICP-treated sands. Results reveal a more pronounced enhancement in terms of strength for the medium sand, despite the same $CaCO_3$ content.

Introduction

Microbially induced calcite precipitation (MICP) for soils has been seen by researchers and engineers as a technique to provide sustainable solutions for soil strengthening applications (Mitchell and Santamarina 2005, Dejong et al. 2013) due to the significantly improved mechanical properties, obtained post-treatment. Results show that the bio-cemented geo-material is endowed with improved strength, that reaches up to 8 MPa under unconfined compressive conditions (Van Passeen 2009) and improved cohesion reaching values in the order of hundreds of kPa (Terzis et al. 2016).

The MICP technique has at its core the metabolic activity of the soil bacterium *Sporosarcina Pasteurii* (Yoon et al. (2001)) which is responsible for hydrolyzing urea and generating favorable conditions for the precipitation of solid calcium carbonate crystals ($CaCO_3$). The urea hydrolysis completes 10^{14} faster (Hausinger 2013) under the presence of *S. Pasteurii* compared to the uncatalysed reaction. This allows considering the MICP technique for engineering works, with the foreseen completion time of the process ranging from a couple of hours to few days, based on the desired final content in $CaCO_3$.

The MICP technique has been so-far implemented mainly at the small laboratory scale for producing samples that can be subsequently subjected to conventional geotechnical testing (Van Paaseen 2009, DeJong et al. 2013, Carmona et al. 2016,

A. Ferrari and L. Laloui (eds.), *Advances in Laboratory Testing and Modelling of Soils and Shales (ATMSS)*, Springer Series in Geomechanics and Geoengineering,
DOI 10.1007/978-3-319-52773-4_46

Cheng et al. 2016, Terzis et al. 2016, Venuleo et al. 2016, Zamani et al. 2016). Fewer studies have investigated the reactive and transport mechanisms involved in the process (Fauriel and Laloui 2012, Akimana et al. 2015). Less evidence is available for the application and the response of the MICP technique at larger scales. Among the available results are those from Van Paseen (2009), who implemented the MICP in 100 m^3 experiments. Results showed significant spatial variation of the induced cementation. More recently, Gomez et al. (2015) implemented the MICP by surface percolation in order to investigate the technique's capacity to stabilize sands against erosion, for fugitive dust control. A cemented crust of 2 cm in depth is reported in this latter work.

The present paper condenses a series of findings, obtained at different scales, in order to contribute to an efficient passing towards a larger experimental scale. We identify the position of the bacteria cells as the most crucial parameter, which governs the final size and shape of the bio-cemented soil volume. We consider the shape, size and total mass of $CaCO_3$ of the bio-cemented soil volume as the main parameters to be controlled during application.

Experimental Details

Materials

Two types of sand are used for the application of the treatment technique: a fine sand with average particle diameter (D_{50}) equal to 190 μm (Itterbeck, Netherlands) and a medium sand with D_{50} = 390 μm (Bernasconi, Switzerland). For the shake of brevity in the current paper we refer to Terzis et al. (2016) for details regarding the bacteria and sample preparation, as well as the $CaCO_3$ measurement.

Study at the Microscale

Scanning Electron Microscopy (SEM) is used to carry out surface analyses of the sand grains and calcite crystal bonds. Subsequently, observations on planar sections are carried out using the Back-scattered Electron Detector of an XLF30-FEG microscope, available at EPFL. To this purpose, samples are firstly subjected to ion-beam bombardment in order to obtain smoothened planar sections. All samples are coated with a 15 nm gold or carbon layer using an Osmium plasma coater, prior to carrying out the observations.

Mechanical Testing on Bio-cemented Samples

Samples of 100 mm in height and 50 mm in diameter are cored from cemented columns, produced using the treatment pattern «TP4» described in Terzis et al. (2016). Bio-cemented and untreated samples of fine and medium sand are fully saturated, subjected to drained triaxial shear under three confining pressures of 30, 100 and 200 kPa respectively. The shearing rate is fixed at 0.040 mm/min.

Scaling-up the Application of the MICP with Two Different Strategies

Fine sand is compacted in layers under wet pluviation to an estimated initial dry density of 1650 g/cm^3 in plastic tanks, of a total maximum volume of 11 L. Two peristaltic pumps (Masterflex) are used for the injection and/or extraction of the bacteria and reactant elements. The following strategies are adopted:

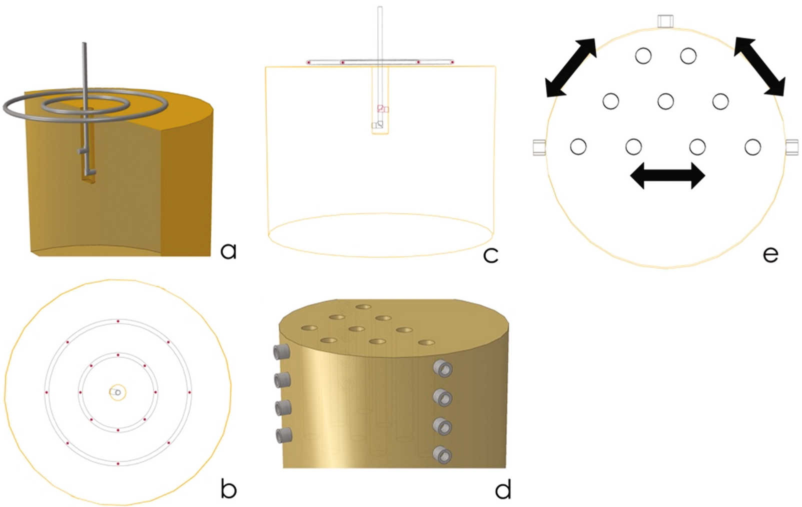

Fig. 1. Schematic representation of the two application strategies used; (a, b, c) surface percolation (d, e) grid of bores.

Strategy 1: Surface Percolation

This tests aims at evaluating the total depth of cemented soil, yielded when applying the MICP via injection points on the surface. To this purpose a total of 16 injection points are placed (red points in Fig. 1b) using two circular rings as shown in Fig. 1a, b, c. Injections take place for 8 h daily (1 h per injection point using two peristaltic pumps). Solutions of 0.5 M Urea-CaCl are introduced; at a speed of 20 ml/min. Free gravity flow is allowed via ten apertures, opened at the bottom of the tank. A bore is opened in the center of the tank where a vertical probe with a flow outlet is rotated manually, 180^o every one hour and 2 cm upwards every four hours (Fig. 1c). The probe is used to induce the cementation of the borehole wall.

Strategy 2: Mixing in a Grid of Bores

The adopted strategy, consists of mixing the bacteria in a triangular grid of boreholes of 1.8 cm in diameter and 13 cm in depth. Cementation solutions of 0.5 M urea-CaCl are provided along the paths shown in Fig. 1e (black arrows). A total of six injection/extraction points are used, placed vertically every 2 cm on the wall of the tank. Each source is activated for 1.5 h daily, for a total of 4 days.

Results

Study at the Microscale

The study at the microscale revealed the presence of calcified biofilms. Biofilms are found to grow around the contact points between soil grains, where bacteria cells are less exposed to advective fluxes. SEM observations reveal these bulb-shaped biofilms acting as precipitation sites for $CaCO_3$, with bacterial traces observed on the surface of the precipitated crystals (inlet in Fig. 2c) as well as in their core (Fig. 2b). This new finding holds a significant importance since it implies that bacterial communities grow inside soils, provided they are allowed the necessary time and nutrients, with the diameters of the calcified biofilms exceeding 100 μm.

Mechanical Response Under Drained Triaxial Shear

Figure 3 presents the mechanical response in the deviatoric stress-axial strain plane, for three different confining pressures (30 kPa–100 kPa–200 kPa) and the corresponding volumetric response on the normalized specific volume-axial strain plane. Both fine and medium sand yielded similar behaviour in the untreated state, reaching similar values of peak and residual strength. Though, in the treated state, the samples of medium sand reach significantly higher values of peak resistance for the three confining pressures applied. Both materials yield similar dilatancy angles with the medium sand being more contractive.

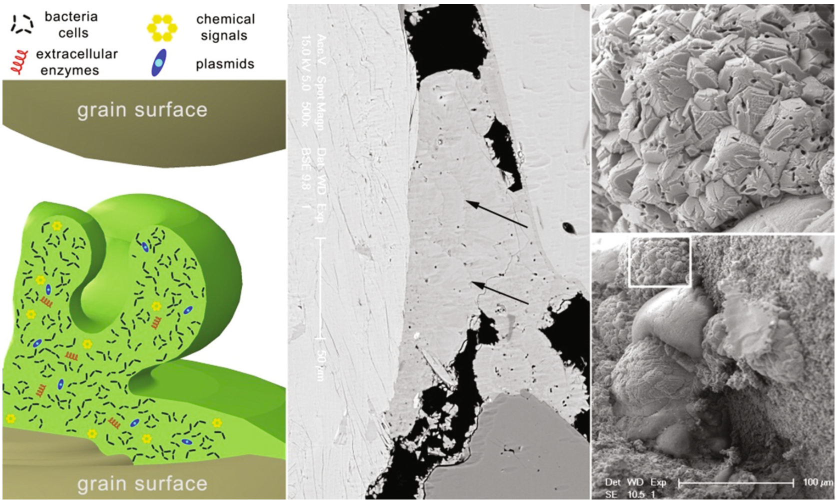

Fig. 2. (a) Schematic representation of a bulb shaped biofilm with its constituent elements (adapted from Ikuma et al. 2013); (b) image obtained through BSE showing the interior of a calcified biofilm and traces of the growth phases of the particle (arrows); (c) bacterial traces on the surface of the calcified bio-films.

Upscaling Strategies for the Application of MICP

Strategy 1: Surface Application

Figure 4 presents the spatial variation of the $CaCO_3$ content (w/w %) after introducing the bacteria and reactant elements through: (i) surface percolation, allowing free gravity flow and (ii) using a vertical probe for stabilising the borehole walls. Figure 1 presents the spatial distribution of $CaCO_3$ (w/w %). A cemented crust of approximately 4.5 cm in depth is obtained as seen in Fig. 4b and c, which is double the depth reported by Gomez et al. (2015). A rotating hydraulic jack is used to core a sample of 5 cm in diameter (arrows in Fig. 4b).

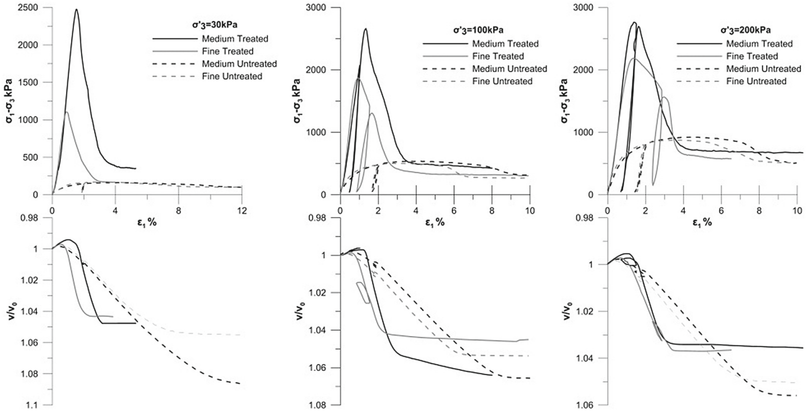

Fig. 3. Mechanical response for the untreated and MICP-treated fine and medium sand; (top) deviatoric stress versus axial strain; (bottom) normalized specific volume versus axial strain.

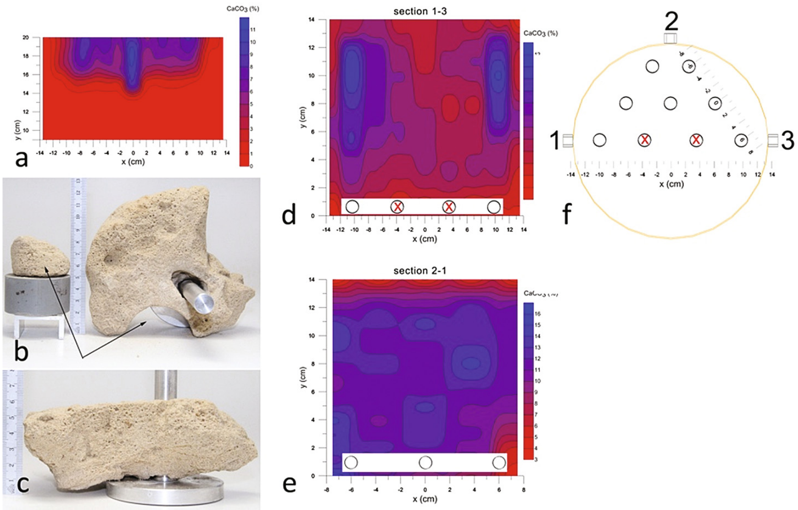

Fig. 4. MICP treated soil after applying strategies 1 (a, b, c) and 2 (d, e, f); spatial distribution of calcite along two representative planes (d, e). Bacteria are not mixed in the bores marked wit "x" in f.

Strategy 2: Grid of Injection Points

Figure 4d and e presents the spatial distribution of the calcite content along two representative planes. Soil was rinsed with water under pressure and the intact cemented volume reveals that cementation occurred around two bores (glass tubes) where bacteria were not introduced (Fig. 5).

Fig. 5. Obtained bio-cemented soil volume after applying treatment strategy 2.

Conclusions

The study provides three substantial observations regarding the application of the MICP. By allowing S. Pasteurii to grow and biofilms to form, we identify calcified biofilms as a distinct form of precipitate "habit". We observe that by applying the same treatment conditions to materials of different initial grain size, the yielded mechanical behaviour varies significantly despite the same final mass of $CaCO_3$ obtained. The improvement in terms of strength is found to be more pronounced for the coarser material. Finally inoculating bacteria by mixing is found to induce homogenous calcite distribution along the flow path. A series of experiments is under progress to further support these findings.

References

Akimana RM, Seo Y, Li L, Howard L, Dewoolkar M, Hu LB (2015) Exploring X-ray computed tomography characterization and reactive transport modelling of microbially-induced calcite precipitation in sandy soils in Geo-Chicago, pp 62–71

Dejong JT, Soga K, Kavazanjian E et al (2013) Biogeochemical processes and geotechnical applications: progress, opportunities and challenges. Géotechnique 63(4):287–301

Fauriel S, Laloui L (2012) A bio-chemo-hydro-mechanical model for microbially induced calcite precipitation in soils. Comput Geotech 46:104–120

Gomez MG, Martinez BC, DeJong JT, Hunt CE, deVlaming LA, Major DW, Dworatzek SM (2015) Field-scale bio-cementation tests to improve sands. Proc Inst Civil Eng Ground Improv 168(3):206–216

Hausinger RP (2013) Biochemistry of Nickel. Springer Science & Business Media, USA

Ikuma K, Decho AW, Lau BL (2013) The extracellular bastions of bacteria-a biofilm way of life. Nat Educ Knowl 4(2):2–19

Mitchell J, Santamarina J (2005) Biological considerations in geotechnical engineering. J Geotech Geoenviron Eng 131:1222–1233

Terzis D, Bernier-Latmani R, Laloui L (2016) Fabric characteristics and mechanical response to bio-improved sand to various treatment conditions. Géotech Lett 6(1):50–57

Van Paassen, LA (2009) Biogrout, ground improvement by microbially induced carbonate precipitation. Ph.D. thesis, Delft University of Technology, Netherlands

Venuleo S, Laloui L, Terzis D, Hueckel T, Hassan M (2016) Microbially induced calcite precipitation effect on soil thermal conductivity. Géotech Lett 6(1):39–44

Yoon JH, Lee KC, Weiss N, Kho YH, Kang KH, Park YH (2001) Sporosarcina aquimarina sp. nov., a bacterium isolated from seawater in Korea, and transfer of Bacillus globisporus (Larkin and Stokes 1967), Bacillus psychrophilus (Nakamura 1984) and Bacillus pasteurii (Chester 1898) to the genus Sporosarcina as Sporosarcina globispora comb. nov., Sporosarcina psychrophila comb. nov. and Sporosarcina pasteurii comb. nov., and emended description of the genus Sporosarcina. Int J Syst Evol Microbiol 51:1079–1086

Zamani A, Montoya BM (2016) Permeability reduction due to microbial induced calcite precipitation in sand in Geo-Chicago, pp 94–103

Carmona JP, Oliveira PJV, Lemos LJ (2016) Biostabilization of a sandy soil using enzymatic calcium carbonate precipitation. Procedia Eng. 143:1301–1308

Cheng L, Shahin, MA (2016) Urease active bio-slurry: a novel soil improvement approach based on microbially induced carbonate precipitation. Can. Geotech. J. 53(9):1376–1385

Determination of Intergranular Strain Parameters and Their Dependence on Properties of Grain Assemblies

Sparsha Nagula(✉) and Jürgen Grabe

Institute of Geotechnical Engineering and Construction Management, Hamburg University of Technology, Hamburg, Germany
sparsha.nagula@tuhh.de

Abstract. Intergranular strain parameters of the extended Hypoplastic model are determined from laboratory experiments. Simple static triaxial setup coupled with controlled stress path test method is employed to determine the parameters. Parameters are determined for 4 different naturally existing sands acquired from field. The dependence of the intergranular strain parameters, on density and stress state of the sand is studied and recommendations are made for the selection of mean values in the relevant range of stresses and densities. The variation in the magnitude of intergranular strain parameters is studied in accordance with the varying grain assembly properties. The strain range within which the incremental stiffness remains constant after strain reversal is studied in conjunction with the grain properties and the validity of the assumption that the governing parameter is a material independent constant is commented upon.

Introduction

The Hypoplastic model describes the mechanical behavior of granular materials. The Hypoplastic model is well suited to model the nonlinear and inelastic behavior of dry granular soils. Typical soil characteristics like dilatancy, contractancy, different stiffnesses for loading and unloading as well as the dependency of stiffness on pressure and void ratio can be modeled. The first version of the hypoplastic model was formulated by Kolymbas (1991). The most widely used version was developed by von Wolffersdorff (1996). Niemunis and Herle (1997) enhanced the model with the intergranular strain concept. The determination of Hypoplastic model parameters is well documented and is supported by substantial experimental date whereas the intergranular strain parameters are often assumed similar to the standard values as quoted by Niemunis and Herle (1997) and has been observed to provide satisfactory results in modeling various granular materials. However recent literature on resonant column tests on sands have revealed that these parameters are density and stress state sensitive. This paper hence focuses on the variation of the primary intergranular strain parameters with varying grain assemblies.

A. Ferrari and L. Laloui (eds.), *Advances in Laboratory Testing and Modelling of Soils and Shales (ATMSS)*, Springer Series in Geomechanics and Geoengineering,
DOI 10.1007/978-3-319-52773-4_47

Hypoplastic Model

In the Hypoplastic model (von Wolffersdorff 1996) the objective stress rate tensor $\dot{T}'$ is defined as a tensor valued function h of the effective Cauchy stress T', the deformation rate D and the void ratio e as follows.

$$\dot{T}' = h(T', D, e)$$

The Hypoplastic model without the intergranular strain parameter predominantly consists of 8 parameters. The first set of parameters consist of the limiting void ratios $e_{i0,}$ e_{c0} and e_{d0} corresponding to the upper bound void ratio, critical state void ratio and lower bound void ratio at zero pressure. These parameters are estimated from the minimum and maximum void ratio values of the granular material. The critical friction angle Φ_c which determines the resistance of the granular material in monotonic shearing in critical state is evaluated from drained triaxial tests or by the simplified approach from the determination of angle of repose. The parameter granulate hardness h_s and exponent n which describe the isotropic compression of loose sands are determined from oedometer tests in loose samples of granular materials. The exponent α governs the peak friction angle and also indirectly influences the dilatancy of the material and is calibrated with the results of drained triaxial tests on dense samples. The parameter exponent β which governs the stiffness of the granular materials is often calibrated from triaxial test data and in case of lack of experimental data a value of $\beta = 1$ has proven to yield good results. One of the primary advantages of the usage of the Hypoplastic model to mode granular materials is the ease with which the material parameters can be determined from standard laboratory tests such as shear and oedometer tests.

Intergranular Strain

The Hypoplastic model yields good results for deformations due to the rearrangement of granular skeleton but leads to large accumulation of deformations on being subjected to excessive stress cycles of small amplitude called as ratcheting. Hence the Hypoplastic model was extended and the intergranular parameters were introduced. These extended model took into account the behavior of the granular material under small strains due to change of direction of stress of strain path. The intergranular strain extension leads to the addition of the intergranular strain tensor (δ) which stores the most recent deformation history and also leads to an increase in the incremental stiffness ($E = dT/d\varepsilon$) of the material on change in direction of deformation (D).

The extension of the model states that if the state of stress and density of the material at point * is similar even after being subjected to different deformation histories as indicated in Fig. 1 for the material, a reversal in direction of deformation would lead to different increase in incremental stiffness depending on the nature of the reversal. A 180° reversal as indicated in first figure on top left, would lead to an increase in stiffness $E_R = m_R E_0$ and a 90° reversal (middle figure to left) would lead to an increase in stiffness $E_T = m_T E_0$ where m_R and m_T are intergranular strain parameters and E_0 is the stiffness after long monotonic shearing in same state. After being subjected to sufficient deformation ε_{SOM} the effect of change in direction of deformation is swept out of memory which is marked by the constancy of the incremental stiffness. The elastic range R describes the strain range over which the stiffness of the material is strain independent and is marked with higher magnitudes. The size of the elastic range R is assumed to be constant irrespective of the state of stress and void ratio as indicated in Fig. 1 (right) but whereas the magnitude of the elastic stiffness varies as per the stress state and void ratio. The intergranular strain model includes two other exponents β_χ and χ which govern the decay of $E_{R/T}$ after the change in deformation direction.

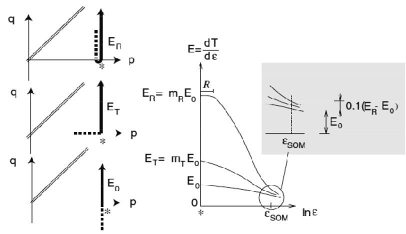

Fig. 1. Incremental stiffness according to change in direction of deformation.

Determination of Intergranular Strain Parameters

The intergranular strain parameters can be determined from dynamic tests or static tests with strain reversal (Niemunis and Herle 1997). The exponential parameters need be calibrated as per the experimental data. In this work static triaxial tests have been used to determine the intergranular strain parameters m_R, m_T and R. The experimental data was calibrated as per Niemunis and Herle (1997) to attain the exponential parameters. The parameters as determined by Niemunis and Herle (1997) for Hochstetten sand has been seen to work quite reasonably for finite element simulations and hence not much work has been done on the determination of these parameters. There has been some literature which states that the parameters are density and stress state sensitive (PLAXIS 2D Reference Manual 2014). In this work the primary intergranular strain parameters m_R, m_T and R have been evaluated from basic static triaxial tests on four different types of sands obtained from field. The variation of the parameters with the granular properties of the sand assemblies has then been compared.

Stress Path Experiments

Static triaxial tests were performed in order to determine the intergranular strain parameters m_R, m_T and R. Stress path method of testing was used in order to subject the material strain reversal after being subjected to different deformation histories. The tests were performed in the automated stress path type module of the GDS (GSD Instruments, Hampshire, United Kingdom) Triaxial Testing System (GDSTTS). As the strain ranges are low and need to be measured accurately, sensitive on sample GDS

Liner Variable Differential Transformer (LVDT) Local Strain Transducers were installed. These LVDTs can measure small strains and are well suited for accurate stiffness measurements.

Material Properties

The intergranular strain parameters tests were performed on four different kinds of sands obtained from field. The basic characterisation tests were performed on the sands and the results of the same have been tabulated in Table 1. It can be observed that all the four sands are of varying granulate properties and hence the resulting evaluated intergranular strain parameters would provide an insight on the inter relationship between grain assembly properties and intergranular strain parameters.

Table 1. Basic properties of four sands.

Sand	e_{max}	e_{min}	γ_{max} (g/cc)	γ_{min} (g/cc)	C_u
A1	0.799	0.385	1.914	1.473	2.32
A2	1.000	0.514	1.75	1.325	1.5
A3	0.774	0.400	1.893	1.494	1.7
A4	0.851	0.435	1.846	1.431	2.17

Sample Preparation

Triaxial samples of sand of 50 mm diameter and a height of 125 mm were prepared using vacuum suction method. Both dense and loose samples according to the maximum and minimum density of the sands as per Table 1 were prepared with sufficient quantity of water in order to ensure complete saturation of the sample during testing. Proper density and void ratio of the samples at start of the test were ensured.

Stress Path Controlled Triaxial Test

Simple static triaxial test setup was used in order to determine the intergranular strain parameters. GDS Triaxial Testing System equipped with automated stress path module is based on the classic Bishop & Wesley type stress path triaxial cell which controls stress directly on the sample. Sand samples at dense and loose states were tested. The sand probes were casted at the required density and were placed in the triaxial chamber with the on sample LVDTs as described in the preceding section. The probe were installed with extension load cap to ensure that they could be even subjected to extension during the test. The probe was first made to undergo saturation ramp at a radial pressure of 410 kPa and back pressure of 400 kPa. Samples were ensured to have a B-check value of at least 0.98 in order to ensure satisfactory saturation. The samples were then subjected to and isotropic consolidation of two different pressures of 100 kPa and 200 kPa. The two different consolidation pressures were chosen in order to study the variation of the intergranular strain parameters with varying stress state conditions. The stress path controlled testing enabled the sample to be driven to desired the p (mean stress) and q (deviator stress) stresses as depicted in Fig. 1. The module ensures independent linear control of p and q on the sample, hence the samples were subjected to similar stress paths as depicted in Fig. 1. Each form of sand sample was

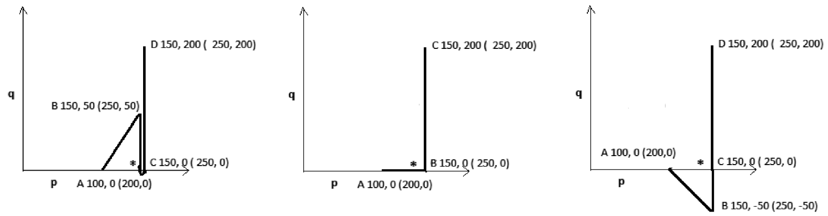

Fig. 2. Stress paths for (a) 180° (b) 90° and (c) 0° reversal.

subjected to three kinds of stress paths (1) 180° strain reversal (2) 90° strain reversal (3) no reversal.

180° Reversal

The sample is made to undergo the preliminary stages of saturation and consolidation as described in the preceding section. At the start of the stress path module the sample is subjected to 0 q stress and 100 kPa p stress (excluding back pressure) marked as point A in Fig. 3(a). The q and p stresses are then linearly increased to reach 50 and 150 kPa (Point B Fig. 3(a)), followed by next stage where q is reduced to 0 kPa and constant p of 150 kPa to reach point C (Fig. 2(a)). This stage marks extension of the sample as q is reduced. As soon as q reaches 0 kPa, the stress paths are programmed to make a 180° reversal. The q is increased to reach 200 kPa at constant p of 150 kPa to reach point d (Fig. 3(a)). This stage marks the compression of the sample as q is increased hence the material undergoes a 180° deformation reversal from extension to compression leading to the evaluation of the E_R which is ratio of incremental stress to strain after strain reversal.

90° reversal

The sample is subjected to the 90° reversal in similar manner as in the previous stage. After consolidation, the material is made to undergo further isotropic consolidation by increasing p to reach a value of 150 kPa as depicted in Fig. 3(b) (Point B). The sample is then subjected to monotonic shearing by an increase in q to reach a value of 200 kPa at constant p of 150 kPa to reach point C (Fig. 3(b)). This change from

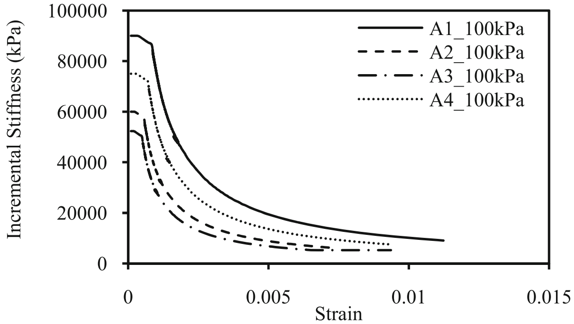

Fig. 3. Stiffness variation with strain for 180° reversal.

isotropic consolidation to compression marks a 90° reversal leading to the evaluation of E_T, similar to the evaluation of E_R.

0° reversal

The sample is made to undergo extension after consolidation by reducing q to reach −50 kPa and by increasing p to 150 kPa to reach point B (Fig. 3(c)). The sample is then subjected to monotonic shearing in the form of increase of q to reach 200 kPa at constant p of 150 kPa. The incremental stiffness E_0 is evaluated after the stress path crosses point C (Fig. 3(c)).

The points marked as * in Fig. 2 were checked to ensure that they all were marked by same density and void ratio. This was made possible by casting similar samples (dense or loose) and subjecting them to similar preliminary stages and ensuring that all samples reached the same stress state point by different stress paths. The above stages were described for an initial consolidation pressure of 100 kPa and similar tests were performed for 200 kPa pressure and correspondingly q and p were scaled in each stage as depicted in brackets in Fig. 3.

Results and Discussion

The incremental stiffness after 180° was evaluated for all the four sands (dense state) as depicted in Fig. 3. It can be seen that the sand with lesser void ratio and higher co-efficient of uniformity (C_u) showed higher stiffness values than the other sands. The difference in stiffness evolution for a 180° and 90° reversal can be clearly observed in Fig. 4 which shows that a 180 reversal increases the stiffness to an order of around 1.5–2 times to the stiffness for 90° reversal.

The incremental stiffness varied as per the density of the sand as can be observed in Fig. 5(a). Sand in denser state showed higher stiffness values than in loose state suggesting that the corresponding intergranular strain parameters would be density dependent.

The dependence of the incremental stiffness on the stress state can be observed in Fig. 5(b). It can be observed that the stiffness values increase as the material is subjected to higher consolidation pressure and eventually a higher p and q stresses. This observation shows that the intergranular strain parameters would be stress state sensitive and are not unique for a particular granular material.

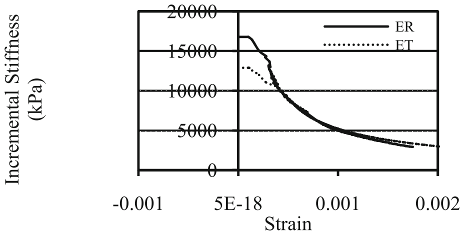

Fig. 4. Stiffness variation with strain for 180° and 90° reversal for A3 sand (Loose).

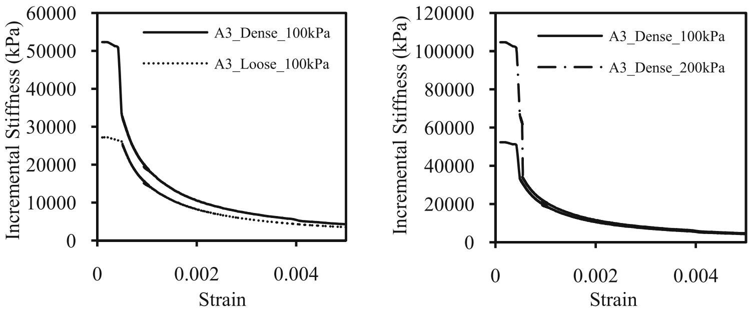

Fig. 5. Stiffness variation with (a) density and (b) stress state for A3 sand.

It can be observed (Figs. 3, 4 and 5) that the elastic strain range R in which the incremental stiffness is constant is 0.0001 irrespective of the form of granular material and its stress state and density.

Conclusions

The intergranular strain parameters are sensitive to the kind of granular material and vary as per the grain size distribution of the granular material. The parameters are stress state and density sensitive and hence should be evaluated for the expected on field conditions and not be assumed as material constants. R can be treated as a material independent constant for all practical purposes.

References

Kolymbas D (1991) An outline of hypoplasticity. Arch. Appl. Mech. 61:143–151

Niemunis A, Herle I (1997) Hypoplastic model for cohesionless soils with elastic strain range. Mech. Cohes. Fric. Mater. 4(2):279–299

PLAXIS 2D Reference Manual-Anniversary Edition: Calibration of hypoplastic parameters. Plaxis BV, Delft, Netherlands (2014). http://www.plaxis.nl/plaxis2d/manuals/

Wolffersdorff PV (1996) A hypoplastic relation for granular materials with a predefined limit state surface. Mech. Cohes. Fric. Mater. 1:251–271

Soil-Structure Interactions

Experimental and Numerical Study of the Thermo-Mechanical Behaviour of Energy Piles for Belgian Practice

M. Allani[1(✉)], G. Van Lysebetten[1], and N. Huybrechts[1,2]

[1] Belgian Building Research Institute (BBRI), Geotechnics Division, Limelette, Belgium
malek.allani@bbri.be
[2] Department of Civil Engineering, Catholic University of Leuven, Leuven, Belgium

Abstract. The use of energy piles remains a topic of discussion in Belgian practice. The main concern is the lack of knowledge and documented experience with regard to the energy performance. Another issue is the potential impact of temperature changes and temperature cycles on the pile response (bearing capacity, settlements), in particular for piles with a relative small diameter. To address this challenge, an extensive full-scale test campaign on several types of energy piles has been set up. The energy piles are instrumented over their entire length with Fibre Bragg Grating (FBG) optical sensors and thermocouples. The tests aim at thermally characterizing the piles, as well as determining the combined thermo-mechanical behaviour. This paper presents an overview of the first, preliminary results of the test campaign and assesses the potential of a fully coupled analysis with the Finite Element Method (FEM) in Plaxis 2D software, showing a good agreement with the measurements.

Introduction

The application of shallow geothermal energy systems (i.e. common depths of about 50 to 150 m in Belgian practice and low temperature levels of about 10 to 12°) has become a widely used technique during the last decade for the heating and cooling of all types of buildings. The continuously decreasing thermal energy demand of buildings offers opportunities to underground infrastructure. Even when the depth of the foundation is limited and the concerned zone is influenced by seasonal temperature fluctuations, thermal activated foundation piles have shown their potential internationally. Nevertheless, Belgian building owners and project developers remain sceptical about the thermal activation of foundation elements, while the additional investment cost is competitive with traditional UTES systems. Several international studies and test cases already investigated the thermo-mechanical behaviour of foundation piles (McCartney and Murphy (2012), Mimouni and Laloui (2015), Sutman et al. (2015)), which resulted in a framework of the thermo-mechanical behaviour with respect to the end-restraint boundary conditions and mobilized shaft shear friction. Moreover, numerical simulations on single piles and pile groups have been performed with different numerical methods (Di Donna et al. (2016), Caulk et al. (2016), Rotta Loria et al. (2015)).

A. Ferrari and L. Laloui (eds.), *Advances in Laboratory Testing and Modelling of Soils and Shales (ATMSS)*, Springer Series in Geomechanics and Geoengineering,
DOI 10.1007/978-3-319-52773-4_48

This paper presents the first results of an experimental thermo-mechanical test campaign on energy piles. Next, a Finite Element (FE) model of the test setup is elaborated in Plaxis 2D and compared to the in-field measurements.

Experimental Test Campaign

On a test site in Ostend (Belgium), 5 energy piles were installed. In this paper, the first results of a soil displacement screw pile with screw shaped shaft are discussed. The internal and external pile diameter equal 360 mm and 560 mm, respectively. The total pile length is about 11.5 m. A single U-loop heat exchanger (PE-Xa 32 $\times$ 2.9 mm) has been mounted on the reinforcement cage before installation, as well as 2 steel hollow reservation tubes for instrumentation purposes. Based on a CPT and samples taken from a drilling, the soil stratigraphy of the upper 14 m can be characterized as follows: 0 m–5 m: soft clay; 5 m–6 m: peat; 6 m–10 m: dense sand; 10 m–11 m: soft clay; 11 m–12 m: dense sand; 12 m–12.5 m: soft clay; 12.5 m–14 m: dense sand. The mechanical loading is applied by a reaction system consisting of 2 micropiles. The applied force is measured by a dynamometer. An LVDT measures the pile head displacements. Pile strains (FBG sensors) and temperatures (thermocouples) are measured every meter along the pile length. A thermal installation has been designed to allow performing Thermal Response Tests (TRT, i.e. constant temperature difference between in- and outlet at constant flow rate) as well as supplying a constant temperature between −5 °C and +40 °C at the inlet of the energy pile.

After pile installation, a static pile test was performed to charge the pile at approximately service load according to Belgian design standards. The pile was loaded stepwise up to 400 kN. The load settlement curve is shown in Fig. 1a. It should be remarked that this load settlement curve is a reload curve, as the pile had already been loaded up to 400 kN before. The pile head settlement is limited and less than 2.5 mm at the end of the reloading test. Consecutively, the applied load was kept constant during the thermo-mechanical test phase. This phase was started with a TRT to verify the possibility of determining the pile thermal resistance and soil thermal conductivity. This was followed by heating and cooling the pile at constant temperatures within a range of +40 °C and −4 °C. Each temperature step was applied during at least several days resulting in a concrete temperature change at the position of the FBG sensors of about +15, +10 and −12 °C for respectively the heating and cooling phases of 40, 30 and –4 °C at the inlet of the energy pile. Figure 1b shows the axial force distribution in the pile during the SLT and at the end of each heating and cooling phase. The axial force at 0 m is taken from the dynamometer measurements. As the FBG sensors do not auto-compensate for thermal dilation of their support and only measure physical deformation, the measured strains are temperature compensated using the coefficient of linear thermal expansion of reinforced concrete, α_c (equal to 12 microstrain/°C) and the measured temperature change at the sensor, ΔT. The axial force, F_{axial}, can then be calculated as $F_{axial} = E \cdot A \cdot (\varepsilon_{measured} - \alpha_c \cdot \Delta T)$ where A is the pile cross section and E the Young's modulus of the reinforced concrete. Note that for $\varepsilon_{measured} = 0$ (i.e. fully constrained by the end-restraint boundary conditions or the mobilised side shear friction (Stewart and McCartney, 2014)), the axial force is maximum and equal to

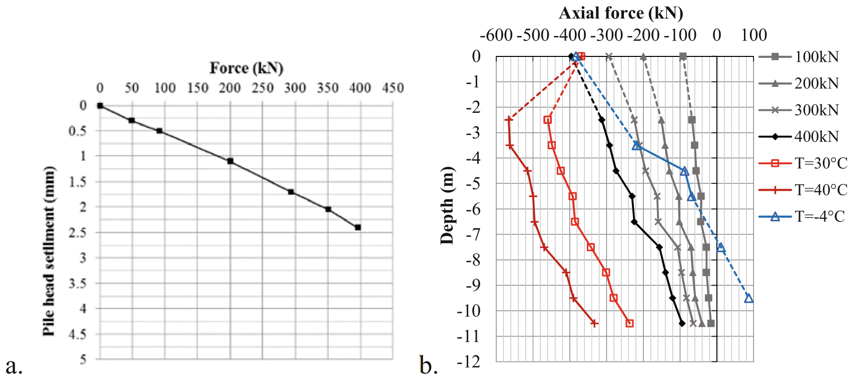

Fig. 1. (a) Load settlement curve of the Static Load Test (reloading) and (b) Axial force in the pile during the SLT and at the end of the heating phases at 30 and 40 °C and cooling phase at −4 °C (the sign of compression is negative).

$F_{axial} = E \cdot A \cdot (-\alpha_c \cdot \Delta T)$. If the pile would be free to move, then $\varepsilon_{measured} = \alpha_c \cdot \Delta T$ and $F_{axial} = 0$. In reality, boundary conditions are likely to be between unconstrained and constrained conditions.

The measurements show that shaft friction prevents the pile partially from dilating during the heating phases, leading to an increase of axial compressive strains in the pile. The increase is rather uniform over the entire pile length and accounts for about 40% of the thermally induced deformation (i.e. thermal deformation is about 60% of $\alpha_c \cdot \Delta T$). Only the upper 2 m allow a larger thermal deformation. No increased end-restraint is observed at the pile base. During cooling some of the FBG sensors failed. However, it can still be observed that the upper part of the pile (up to 3.5 m) undergoes a thermal deformation of more than 85%. At larger depths, pile contraction due to cooling is prevented increasingly (30 to 45% of the thermally induced deformation), resulting in decreasing axial forces in the pile and even tensile axial forces at the lower pile part. All these observations are in accordance with the framework for understanding energy pile behaviour proposed by Bourne-Webb et al. (2013).

Finite Element Model

The Finite Element software Plaxis 2D is used where a fully coupled thermo-hydro-mechanical formulation is implemented (mass balance, linear momentum balance and energy balance). Thermal plastic strains are not considered and the temperature dependence of the mechanical behaviour is limited to linear elastic thermal expansion. An axisymmetric configuration is considered. The modelled area measures 20 × 20 m^2 and the mesh comprises 15-node triangle elements with a refined mesh zone around the pile-soil interface. Note that the U-shaped heat exchangers imply a three-dimensional representation of the thermal loading. This was not possible with the current software and a concentric heat exchanger was thus assumed at the centre of the energy pile by means of a thermal flow boundary at the neutral line of the pile. This simplifies the problem and properly meets the adopted axisymmetric configuration. A conversion analysis from three-dimensional to an axisymmetric problem should be performed to justify this assumption. However, such heavy work is out of the scope of the current study. A mean pile diameter of 460 mm is assumed. No installation effects were considered for the pile, which means that the pile was 'wished into place'.

In this study, the Hardening Soil (HS) Model with Small-Strain-stiffness (HSsmall) is used. The required soil parameters are: E_{50}^{ref}, the secant stiffness in standard drained test; E_{oed}^{ref}, the tangent stiffness for primary oedometric loading and representing the plastic straining due to primary compression; E_{ur}^{ref}, the unloading/reloading stiffness; M, the power of stress level dependency of stiffness; c_{ref}, the cohesion according to the Mohr-Coulomb failure; $\varphi^{'}$, the angle of internal friction to the Mohr-Coulomb failure; ψ, the dilatancy angle; $\gamma_{0.7}$, the shear strain at which the shear modulus is equal to 0.72 G_0^{ref}; G_0^{ref}, the shear modulus at very small strain; γ_{unsat}, the soil unit weight above phreatic level; γ_{sat}, the soil unit weight below phreatic level. A rigid interface is considered between the pile and the soil. Initial soil stresses are generated automatically based on the HS model. All calculations are performed using drained analysis for the sand and silt layers and with undrained analysis for the clay layer. The pile is considered as non-porous with a linear-elastic material model. The required thermal soil and material parameters, are: c_s, the specific heat capacity; λ_s, the thermal conductivity; ρ_s, the density; α_x α_y and α_z, the x, y and z component of thermal expansion. As Plaxis 2D does not easily allow to apply a nonlinear temperature profile, the measured temperature gradient at about 7.5 m depth (0.012 °C/m) is imposed on the model. The soil temperature profile was considered constant during the pile installation and during the static loading test (SLT). For the following phases (TRT, heating up to 40 and 30 °C and cooling down to −4 °C), thermal-flow boundary conditions are imposed at the axisymmetric line of the pile. The same depth and time temperature evolution as measured inside the heat exchangers was introduced.

Comparison Between Experimental and Numerical Results

Before comparing the thermo-mechanical energy pile behaviour, it is important to calibrate the pure mechanical loading applied at the pile head. Soil strength parameters (φ' and c_{ref}) are first estimated from empirical CPT correlations available in the national Belgian Appendix of Eurocode 7 and in literature (Robertson et al. 1977). For the dilatancy angle, ψ, zero value was considered for $\varphi^{'}$-values less than 30°. Otherwise, an order of magnitude of $\psi = \varphi^{'} - 30$ was assumed. Considering the power of stress level dependency of stiffness, m, values of 0.5 and 1 were assumed for sandy and clayey soils, respectively (Plaxis manuals). Stiffness parameters are more difficult to define. As recommended by Schanz et al. (1999) and in Plaxis manuals, E_{oed}^{ref} is usually taken equal to E_{50}^{ref} while E_{ur}^{ref} is typically about 3 times E_{50}^{ref}. E_{50}^{ref} was initially estimated using Robertson et al. (1977) where correlations between CPTs and soil Young modulus are proposed. As a next step, E_{50}^{ref} is progressively adapted until a good match between the measured and simulated load-settlement curve was obtained. Small strain parameters ($\gamma_{0.7}[-]$,G_0^{ref}[kPa]) are considered according to the experimental data in Plaxis manuals and according to the empirical relationships of Alpan (1970) and Benz and Vermeer (2009). For the calculation of the threshold shear strain $\gamma_{0.7}[-]$ the relationship of Hardin and Drnevich (1972) was used. The calibrated soil parameters are listed in Table 1. For the pile parameters, a Young modulus E = 20 GPa and Poisson ratio ν = 0.15 were considered.

Table 1. Mechanical soil parameters.

Parameters	Clay	Peat	Sand
γ_{unsat} $[kN/m^3]$	15	12	17
γ_{sat} $[kN/m^3]$	16	14	20
E_{50}^{ref} $[kPa]$	8000	5000	20000
E_{oed}^{ref} $[kPa]$	8000	5000	20000
E_{ur}^{ref} $[kPa]$	24000	15000	60000
m	1	1	0.5
c_{ref}/c_u $[kPa]$	40	5	0
φ' $[^\circ]$	/	25	40
ψ $[^\circ]$	0	0	10
$\gamma_{0.7}$ $[/]$	0.0001	0.001	0.0001
G_0^{ref} $[kPa]$	50000	25000	120000

Figure 2a shows the comparison between the measurements and the numerical simulation of the load-settlement curve of the performed SLT. A satisfactory matching was obtained. This ensures a good correspondence for the global pile-soil behaviour. To make sure that mechanical properties for each layer are consistent, Fig. 2b shows the comparison between the measured and calculated strains along the pile depth. Very good agreement is obtained. On the other hand, it is important to investigate the thermal pile and soil response after the SLT. The vertical force is kept constant to allow the determination of pure thermal effects. Thermal soil properties were selected based on experimental tests on undisturbed and disturbed samples while classical thermal concrete properties (validated with laboratory tests) are retained. Pile and soil parameters used for the thermal calibration are listed in Table 2.

Figure 3a shows the comparison between the measured and simulated thermal soil response at 0.5 m distance from the pile centre at 7.5, 10.5 and 13.5 m depth. Note that a good agreement is observed between the measurements and the simulations at 7.5 m and 10.5 m depth. At 13.5 m depth, the calculated soil temperature is not affected by the pile heating and cooling, which is also observed in the measurements. The transition between heated soil and earth gradient temperature is well captured in the measurements. As an axisymmetric model has been applied, the U-loop heat exchangers are modelled as a line source. Because of this assumption, the measured temperatures in the pile concrete cannot be compared directly to the simulation results, as the geometry is not exactly the same. A good correspondence between temperature measured in the steel

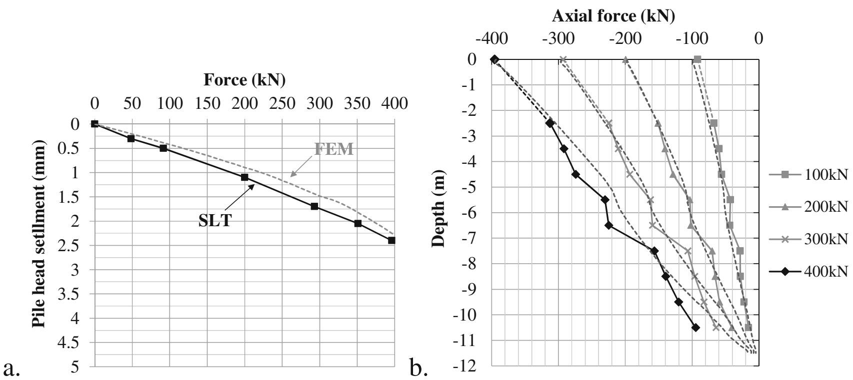

Fig. 2. (a) Load-settlement curve of the SLT: comparison between measurements and Plaxis simulation and (b) Strains in function of the pile depth at different steps of the SLT: comparison between measurements and Plaxis simulations (dashed lines).

Table 2. Thermal pile and soil parameters.

Parameters	Clay	Peat	Sand	Pile
$c_s[J/t/K]$	1	0.85	1	0.8
$\lambda_s[W/m/K]$	1.5	1.5	2	2.5
$\rho_s[t/m^3]$	2.5	2.2	2.5	2.5
$\alpha_{x,\,y\,and\,z}[10^{-6}/K]$	5	5	5	12

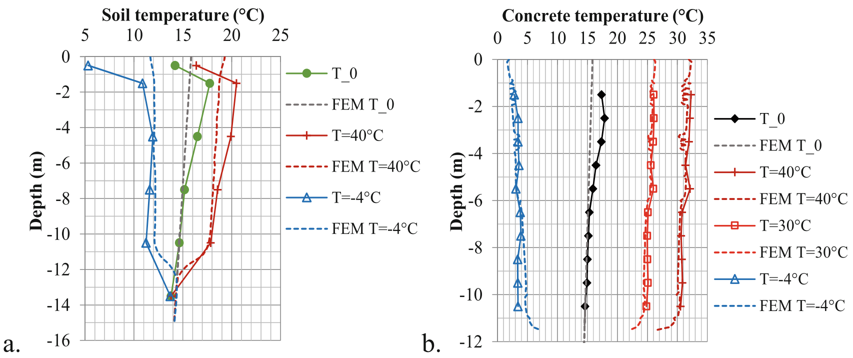

Fig. 3. Comparison (a) of the soil temperature at 0.5 m from the pile centre: measurements vs. Plaxis calculations and (b) of the concrete temperatures as measured in the reservation tubes and as calculated by Plaxis at 30 mm from the pile centre.

reservation tubes and calculated by Plaxis was found at a distance of about 30 mm from the thermal-flow boundary condition (Fig. 3b). In reality, the distance between the border of the heat exchanger and the centre of the steel reservation tube is about

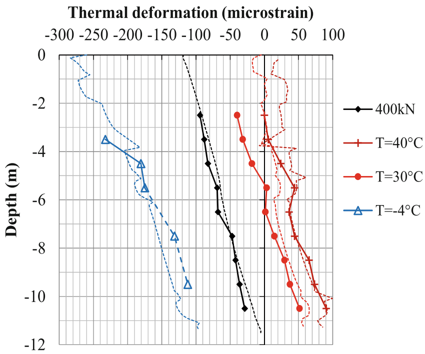

Fig. 4. Comparison of the thermal deformation of the pile as measured and as simulated by Plaxis (dashed line).

40 to 50 mm. As (deformations and) stresses depend on the temperature of the concrete, it is important to compare them at positions where temperature is rather similar.

Once mechanical and thermal calibrations are conducted, it is possible to investigate the thermo-mechanical coupling. For the consistency of comparison, pile strains at 30 mm distance from the pile centre are considered (the distance at which the concrete temperatures in Plaxis correspond to these measured in the pile). Figure 4 shows the comparison between the measured and simulated thermal strains along the pile length for the different temperature phases. Below 6 m depth, a good matching is observed.

Conclusions

This paper discussed the in-situ testing of an energy pile (displacement pile with diameter 460 mm), equipped with a U loop heat exchanger and instrumented with FBG strain sensors and thermocouples. Nearby soil temperature evolution during pile testing was monitored as well. With respect to the purely mechanical loading, the experiments show an increase of the axial stresses in a range of 50–150% and 80–250% when heating the pile 10 and 15 °C, respectively (i.e. a stress increase of 1.5–2.0 MPa and 0.8–1.1 MPa). When cooling the pile 12 °C, axial stresses decrease with 25–170% (i.e. a stress decrease of 0.4–1.3 MPa), resulting in tensile axial stresses at the lower pile part. Pile head displacement due to temperature changes (and at constant load) remained small during testing (less than 3 mm). In general, the results of the FE model were satisfactory. The thermal behaviour was well captured by the numerical model. With respect to the mechanical behaviour and thermo-mechanical coupling, further study is needed to improve the correspondence between measurements and numerical modelling. For example, the way the pile installation is modelled, the conversion of the 3D to a 2D thermal and the thermal climate effects of the subsoil temperature.

References

Alpan I (1970) The geotechnical properties of soils. Earth Sci Rev 6:5–49

Benz T, Vermeer PA (2009) A small strain overlay model. J Numer Anal Meth Geomech 33: 25–44

Bourne-Webb PJ, Amatya B, Soga K (2013) A framework for understanding energy pile behaviour. Proc Inst Civ Eng 166:170–177

Caulk R, Ghazanfari E, McCartney JS (2016) Parametrization of a calibrated geothermal energy pile model. Geomech Energy Environ 5:1–15

Di Donna A, Rotta Loria AF, Laloui L (2016) Numerical study on the response of a group of energy piles under different combinations of thermo-mechanical loads. Comput Geotech 72(1):126–142

Hardin BO, Drnevich VP (1972) Shear modulus and damping in soils. Measurement and parameter effects. J Soil Mech Found Div ASCE 6:603–624

McCartney JS, Murphy KD (2012) Strain distributions in full-scale energy foundations. DFI J 6(2):26–38

Mimouni T, Laloui L (2015) Behaviour of a group of energy piles. Can Geotech J 52(12):1913–1929

Robertson PK, Lunne T, Powell JJM (1977) Cone penetration testing in geotechnical practice. Blackie Academic/Routledge Publishing, New York

Rotta Loria AF, Gunawan A, Shi C, Laloui L, Ng CWW (2015) Numerical modelling of energy piles in saturated sans subjected to thermos-mechanical loads. Geomech Energy Environ 1(1):1–15

Schanz T, Vermeer PA, Bonnier PG (1999) The hardening soil model: formulation and verification. Balkema, Rotterdam, pp 281–290

Stewart MA, McCartney JS (2014) Centrifuge modelling of soil-structure interaction in energy foundations. J Geotech Geoenviron Eng 140(4):04013044

Sutman M, Olgum C, Brettmann T (2015) Full-scale field testing of energy piles. In: Proceedings of IFCEE 2015. ASCE, vol 1, pp 1638–1647

Drained and Undrained Analysis for Foundations Based on Triaxial Tests

André Arnold[1(✉)], Manuel Krähenbühl[1], and Andreas Schmid[2]

[1] Lucerne University of Applied Sciences and Arts, Horw, Switzerland
andre.arnold@hslu.ch
[2] Geotechnisches Institut, Brig, Switzerland

Abstract. The analysis of foundations in fine grained, mostly soft soils leads to the question if either an undrained or drained analysis is appropriate to describe the ultimate limit state of a certain structure. Triaxial tests show that the undrained shear strength s_u is no proper soil parameter but strongly dependent on the initial conditions (OCR-value) and on the developing stress path. The analytical modelling of raft foundations in drained and undrained conditions shows the difficulties of using s_u based on triaxial tests. More triaxial tests and the study of different geotechnical structures are needed to give advice whether the short term behaviour (undrained) or the long term behaviour (drained) is supposed to be most critical.

Introduction

The analytical derivation of the ultimate limit state of foundations is well known for both undrained and drained behaviour (Terzaghi 1943; Prandtl 1920). Atkinson (2007) recommends doing an effective stress analysis in case of fully drained conditions and well known pore pressures. A total stress analysis with the use of the undrained shear strength s_u should be done in case of undrained behaviour. In case of uncertainty he recommends conducting both drained and undrained analysis to consider the worst case.

The undrained behaviour is often neglected in practise as experienced in some consulting projects. Uncertainty about the mechanical behaviour in undrained conditions (Alonso et al. 2010) as well as an often unknown undrained shear stress s_u due to inappropriate geotechnical site investigation (mostly only the friction angle φ' is established in geotechnical reports) lead to this approach. This procedure might be sufficient in many cases since few of the clay deposits in Switzerland are overconsolidated due to glacial loading.

This contribution will compare fully drained and fully undrained conditions on the example of a foundation based on the results of triaxial tests. The triaxial tests were conducted under different initial conditions which will show some effects on the undrained shear strength. Finally, it will be shown how the initial conditions influence the ultimate limit state and will give some advice on how to deal with those facts in geotechnical reports and in the dimensioning of raft foundations.

A. Ferrari and L. Laloui (eds.), *Advances in Laboratory Testing and Modelling of Soils and Shales (ATMSS)*, Springer Series in Geomechanics and Geoengineering,
DOI 10.1007/978-3-319-52773-4_49

Expected Behaviour of Raft Foundations in Drained and Undrained Conditions

The undrained behaviour is expected to be the most critical in the dimensioning of raft foundations in normally consolidated clays. Figure 1 shows in the framework of the critical state soil mechanics and the Modified Cam Clay (MCC) soil model (Roscoe and Burland 1968) the stress path in undrained conditions which will reach the critical state line (CSL) at a lower deviatoric stress compared to the drained stress path. This behaviour is mostly influenced by the excess pore water pressure Δu (Fig. 1c).

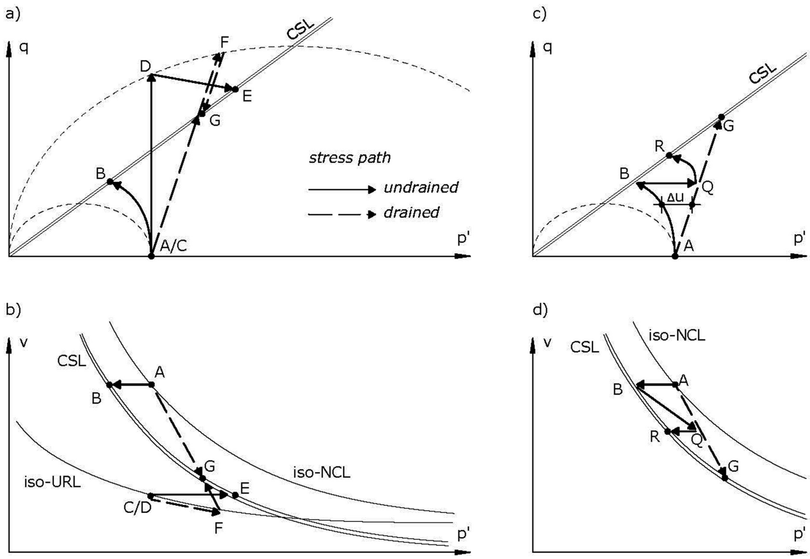

Fig. 1. Critical state theory of drained and undrained triaxial test for normally consolidated and heavily overconsolidated clay (after Muir Wood 1990).

If a foundation is loaded stepwise to allow for consolidation, more safety concerning the ultimate limit state can be reached because the excess pore water pressure is also lowered stepwise (Fig. 1c). A finally higher deviatoric stress and therefore a greater value of s_u will be reached due to lower water content (Fig. 1d).

During undrained conditions overconsolidated clay reacts theoretically elastic (no change of p’) as long as it remains inside the yield-surface (Fig. 1a, C-D). Reaching the current yield surface the softening process starts with a decreasing deviator reaching the critical state line. It is now not straightforward whether the drained or undrained stress path meets the critical state line first. The change of volume in relation to p’ is regarded in Fig. 1b: The undrained stress path meets the critical state line at a lower volume (C-D-E) and therefore at a greater deviator than the drained stress path (C-F-G).

Undrained Consolidated Triaxial Test on Clay

The clay material "Birmensdorfer Seebodenlehm" was sediment near Zurich, Switzerland. Its mechanical behaviour is well investigated by Trausch-Giudici (2004) and Weber (2007). The clay was reconstituted for the triaxial tests and for the standard classification.

The consistency of the soil and the classification after USCS is determined as follows (Table 1).

Table 1. Soil consistency using the Atterberg Limits.

USCS soil classification	CH - fat clay
Plastic Limit w_P	19%
Liquid limit w_L	56%
Plasticity index I_P	37%

The triaxial specimens were prepared by mixing clay powder with water under partial vacuum. The clay slurry has had a water content of 102% and has been filled up in a consolidometer. The slurry was consolidated one-dimensionally during two months with increasing load steps up to 200 kPa. The 1d-consolidated clay has been cut out with cylinders and prepared for the triaxial tests.

Test Procedure for Normally Consolidated Clay

The soil specimen is saturated stepwise by increasing the backpressure to a B-value greater than 0.95. The specimen has been subsequently consolidated isotropically to a mean effective pressure of 200 kPa. The undrained compression test has been conducted under constant volume (closed pore pressure valves) with a velocity of 0.03 mm/min which has been set after the recommendation of Lade (2016) to enable a uniform excess pore water distribution all over the soil specimen.

Results for Normally Consolidated Clay

The consolidation phase gives the model-parameters κ and λ of the MCC soil model. The parameters are shown in Table 2.

Table 2. Test results of undrained triaxial tests.

	OCR = 1	OCR = 4
Friction angle ϕ'_{crit}	26.3°	20.0°
Gradient of CSL M	1.04	0.77
Gradient of compression line λ	0.073	0.105
Gradient of swelling line κ	–	0.093

The gradient M and therefore the critical angle of friction φ'_{crit} of the critical state line which is given in Figs. 2 and 3 is derived directly from the conducted tests and also compared to values from Trausch-Giudici (2004) and Weber (2007).

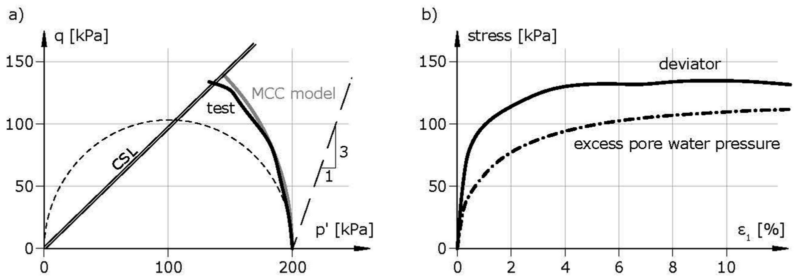

Fig. 2. Undrained triaxial test results for normal consolidated clay ("Birmensdorfer Seebodenlehm").

The value of κ is obviously too high compared to λ. Test results of Trausch-Giudici (2004) show a relationship of $\lambda/\kappa \approx 3$ and values for λ of about 0.12.

The focus of the test lies on the shape of the effective stress path and therefore on the amount of excess pore water pressure compared to the MCC model (Fig. 2). The clay reaches the critical state line as given in Fig. 2 with an almost constant deviatoric stress.

Test Procedure for Heavily Overconsolidated Clay

The soil specimen has been saturated and isotropically consolidated to an effective pressure of 800 kPa. After completion the consolidation phase at 800 kPa the effective pressure has been reduced to 200 kPa and consolidated at this stress stage. The heavily overconsolidated test has therefore an OCR-value of 4. The undrained compression test has been conducted under the same conditions as the normal-consolidated test.

Results for Heavily Overconsolidated Clay

The results of the triaxial tests are given in Fig. 3. The shape of the effective stress path shows that in a first stage, the MCC model fits quite well to the observed behaviour: elastic behaviour of the soil specimen inside the yield surface. In a second stage the effective stress path turns inside the yield surface to the right while the MCC model stress path remains elastically with no change in p'. A softening behaviour can be observed with a constant deviatoric stress at the end.

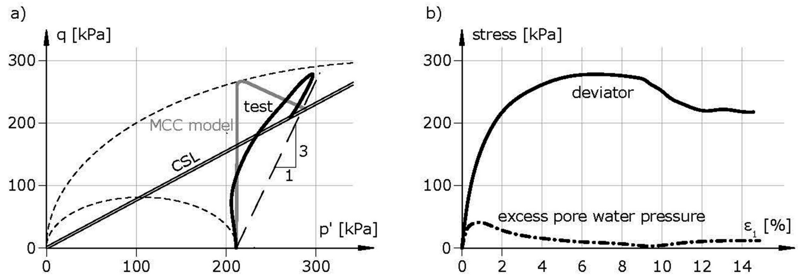

Fig. 3. Undrained triaxial test results for heavily overconsolidated clay ("Birmensdorfer Seebodenlehm").

Discussion of the Test Results

The test results show for normally consolidated clay soil good agreement to the expected behaviour given by the MCC soil model. For heavily overconsolidated clay the MCC soil model gives no good prediction of the effective stress path. The effective stress path turns to the right with decreasing excess pore water pressure while the MCC soil model stress path remains elastically with rising excess pore water pressure. Schädlich and Schweiger (2011) show different effective stress paths for heavily overconsolidated clay soils which also turn to the right and follow the critical state line instead of an elastic development up to the yield surface with subsequent softening. Schädlich and Schweiger (2011) model this behaviour on the basis of the Hvorslev surface (Price and Farmer 1981). The Hvorslev surface basically cuts the elastic range of heavily overconsolidated clays as the elastic development to the yield surface of MCC cannot be observed in triaxial compression tests (Fig. 3). Therefore it can be concluded that the MCC model works well for normally consolidated and slightly overconsolidated (OCR < 2) clays while some extensions as the Hvorslev surface should be added to the basic model of MCC to describe the behaviour of heavily overconsolidated soils.

Analytical Modelling of Raft Foundations in Undrained and Drained Conditions

The analytical modelling of raft foundations is basically restricted to the derivation of the bearing capacity in undrained conditions after Prandtl (1920):

$$q = (2 + \pi) \cdot s_u$$

In drained conditions after Terzaghi (1943):

$$q = \frac{1}{2} \cdot b \cdot \gamma \cdot N_\gamma$$

The undrained shear strength s_u of a certain soil does only depend on the water content of the soil (provided the soil is fully saturated) and is therefore strongly dependent on the initial conditions and on the depth below the soil-surface. The undrained shear strengths derived from the triaxial test cannot be used directly in the analytical modelling, as the shown triaxial tests are conducted at a higher mean effective normal stress p' than it will occur in the analytical modelling of the ultimate limit state of the foundation. To derive suitable undrained shear strength for normally consolidated and slightly over-consolidated conditions for the foundation, the MCC model is taken in account as follows (after Trausch-Giudici 2004 with $\lambda = 0.12$, $\kappa = 0.04$, $M = 1.02$, $r = 2$, $\sigma'_{v0} = 11.5$ kN/m^2):

$$s_u = \frac{1}{2} \cdot \sigma'_{v0} \cdot OCR^{0.8} \cdot M \cdot \left(\frac{1}{r}\right)^{((\lambda - \kappa)/\lambda)}$$

For heavily overconsolidated soil s_u is derived after the following empirical equation (Springman 1993) with the use of the parameters $a = 0.26$ and $b = 0.73$ after Trausch-Giudici (2004):

$$s_u = \sigma'_{v0} \cdot a \cdot OCR^b$$

The comparison of the drained and undrained ultimate bearing capacity of a foundation with width equal to 2 m is given in Table 3.

Table 3. Analytical ultimate bearing capacity for a drained and undrained foundation with b equal to 2 m for normal consolidated and heavily overconsolidated clay.

	b = 2 m	
	OCR = 1	OCR = 4
Drained	73 kPa	73 kPa
Undrained	19 kPa	42 kPa

Conclusions and Outlook

The stress paths from the triaxial tests fit quite well the general behaviour of raft foundations as mentioned in Atkinson (2007) and Muir Wood (1990). Foundations on normally consolidated clay will reach the critical state first in the undrained stage due to excess pore water pressures Δu. With consolidation Δu disappears and the soil hardens and becomes stronger. The used material model MCC estimates this behaviour well. Foundations on heavily overconsolidated clay are supposed to reach the critical state line for drained conditions at a lower deviatoric stress than in undrained conditions due to negative pore water pressures (Fig. 1). The negative pore water pressure sticks the soil grains together. With the dissipation of the negative excess pore water pressures the soil will expand and therefore soften. This means that for normally consolidated clays the short term behaviour of foundations is the most critical whereas for heavily over-consolidated soils the long term behaviour is supposed to be the most critical.

The effective stress path in the presented triaxial test turns to the right already inside the yield surface which was already mentioned by Muir Wood (1990) and other authors. So the theoretical development of the effective stress path in undrained conditions (Fig. 1) mentioned in the MCC-model could not strongly be verified. The presented undrained triaxial test on heavily overconsolidated soil did not show negative pore water pressures. More undrained triaxial tests would be needed to elaborate a clear statement on the development of the excess pore water pressures. The analytical model shows that even for OCR = 4 undrained conditions give a smaller bearing capacity than drained conditions. The uncertainty lies in the derivation of s_u in function of depth below soil surface (derivation of σ'_{v0}).

The triaxial tests show well, that with different initial conditions different undrained shear strengths will occur. The undrained shear strength is no state parameter of the soil (Atkinson 2007). Instead it is strongly dependent on the water content and therefore on the OCR-value. This behaviour is shown in Fig. 4 where one can see that with less specimen-volume which is equal to less water content the yield surface of the soil will expand and therefore give a higher undrained shear strength.

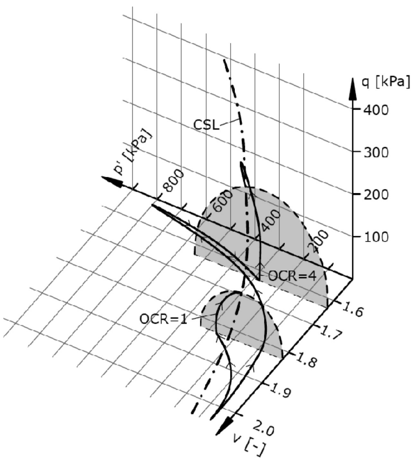

Fig. 4. 3-dimensional undrained stress path of consolidation and triaxial compression test for normally consolidated and heavily overconsolidated clay.

During the investigation of soil parameters in soft soil it is important to elaborate s_u-values with suitable water contents. It is also important to account for the behaviour of the soil due to the load of a foundation. The initial conditions such as OCR-value and the development of the effective stresses are of great importance to correctly describe the undrained shear strength for a certain geotechnical structure. Therefore undrained behaviour should clearly not be neglected in the dimensioning of a geotechnical structure in soft soil. It is indeed of great importance to well understand the loading behaviour and the development of the undrained shear strength s_u in undrained conditions, even for overconsolidated clays.

In a next step more undrained triaxial tests will be conducted to study the development of the excess pore water pressures. The studies of undrained conditions will be enlarged to other geotechnical structures such as excavations to get information about the short and long term behaviour in saturated soft soils.

Acknowledgements. We are most grateful to the help of Ralf Herzog from the Institute for Geotechnical Engineering at ETH Zurich. He supported us preparing the soil specimens for the triaxial tests.

References

Alonso EE, Pinyol NM, Puzrin AM (2010) Geomechanics of failures. In: Advanced topics. Springer Netherlands, Dordrecht

Atkinson J (2007) The mechanics of soils and foundations, 2nd edn. CRC Press, London; New York

Lade PV (2016) Triaxial testing of soils. Wiley, West Sussex

Muir Wood D (1990) Soil behaviour and critical state soil mechanics. Cambridge University Press

Prandtl L (1920) Nachrichten von der Gesellschaft der Wissenschaften zu Göttingen, Mathematisch-Physikalische Klasse 1920. Über Die Härte Plastischer Körper 1920:74–85

Price AM, Farmer IW (1981) The Hvorslev surface in rock deformation. Int J Rock Mech Min Sci Geomech Abstr 18:229–234

Roscoe KH, Burland JB (1968) On the generalised behaviour of ‘wet’ clay. In: Heyman J, Leckie, FA (eds) Engineering Plasticity. Cambridge University Press, pp 535–610

Schädlich B, Schweiger HF (2011) A multilaminate soil model for highly overconsolidated clays. In: Proceedings of the XV European Conference in Soil Mechanics and Geotechnical Engineering, Athens, pp 569–574

Springman SM (1993) Centrifuge modelling in clay: marine applications. In: Proceedings of the 4th Canadian Conference on Marine Geotechnical, Newfoundland (Vol. 3), pp 853–896

Terzaghi K (1943) Theoretical soil mechanics. Wiley, New York, London

Trausch-Giudici JL (2004) Stress-strain characterisation of Seebodenlehm. ETH, Zürich

Weber TM (2007) Modellierung der Baugrundverbesserung mit Schottersäulen. ETH, Zürich

Impact of Thermally Induced Soil Deformation on the Serviceability of Energy Pile Groups

Alessandro F. Rotta Loria(✉) and Lyesse Laloui

Laboratory of Soil Mechanics, LMS, Swiss Federal Institute of Technology in Lausanne, EPFL, Lausanne, Switzerland
alessandro.rottaloria@epfl.ch

Abstract. This paper expands on the impact of the thermally induced deformation of the soil on the serviceability mechanical performance (i.e., deformation-related) of energy pile groups. The work is based on the results of a full-scale *in-situ* test that was performed on a group of energy piles at the Swiss Tech Convention Centre, Lausanne, Switzerland, and on a series of 3-D thermo-mechanical finite element analyses that were carried out to predict the considered experiment. This study proves that the serviceability mechanical performance of energy pile groups crucially depends on the relative thermally induced deformation of the soil to that of the energy piles. The relative thermally induced deformation of the soil to that of the energy piles is governed by (i) the thermal field characterising the energy pile group and (ii) the relative thermal expansion coefficient of soil to pile. Considering these aspects in the analysis and design of energy pile groups is key because they profoundly characterise the deformation of such foundations.

Introduction

The serviceability mechanical performance of energy piles is markedly dependent on the deformation that is associated to any given temperature change applied to these elements as a consequence of their geothermal operation. The reason for this is that, for any considered energy pile-related problem of given specific geometry, material properties and boundary conditions, the contribution of developed (i.e., observed) thermally induced deformation causes displacement in the energy piles whereas the contribution of restrained deformation causes stress within the energy piles. These phenomena deserve to be considered in the analysis and design (e.g., geotechnical and structural) of energy piles (Di Donna et al. 2016).

Over the last two decades, the deformation of energy piles caused by the application of any given thermal load to such foundations has been generally interpreted with reference to the thermal expansion coefficient of these elements. Limited attention has been devoted to the thermal expansion coefficient of the soil surrounding the energy piles and the thermal field characterising the soil-pile system. Bourne-Webb et al. (2016), Rotta Loria and Laloui (2016) have recently remarked noteworthy drawbacks arising from such an analysis approach and have consequently highlighted novel insights for thoroughly addressing the serviceability mechanical performance of energy piles.

A. Ferrari and L. Laloui (eds.), *Advances in Laboratory Testing and Modelling of Soils and Shales (ATMSS)*, Springer Series in Geomechanics and Geoengineering,
DOI 10.1007/978-3-319-52773-4_50

This paper expands on the impact of the thermally induced deformation of the soil on the serviceability mechanical performance of energy pile groups based on the analysis of a series of results obtained by Rotta Loria and Laloui (2016) through a full-scale *in-situ* test and coupled finite element predictions.

In the following, the experimental and numerical methods are first summarised. The experimental and numerical results are then compared and discussed. Finally, concluding remarks that can be drawn from this work are presented.

Experimental Testing

The Foundation and Site

The pile foundation that was considered for the experimental test is located under the recently built Swiss Tech Convention Centre, Lausanne, Switzerland (cf., Fig. 1(a)). The foundation supports a $9 \times 25\ m^2$ water retention tank and comprises a group of four end-bearing energy piles (labelled EP1, EP2, EP3 and EP4 in Fig. 1(b)) and sixteen semi-floating conventional piles (labelled P1-16 in Fig. 1(b)) below a heavily reinforced 0.9 m-thick slab. The energy piles are 28 m long and 0.9 m in diameter, and the conventional piles are 16 m long and 0.6 m in diameter. All of the piles were bored, cast onsite and are made of reinforced concrete. Vertical loads of 0, 800, 2200 and 2100 kN are applied to energy piles EP1, 2, 3 and 4, respectively. Vertical loads of 300 kN are applied to each of the conventional piles. The energy piles were equipped with four 24-m-long high-density polyethylene U-loops that are connected in series. The inlets and outlets of the absorber pipes were thermally insulated to a depth of 4 m below the pile heads to limit the influence of the climatic conditions on the heat exchange process. All of the energy piles were instrumented with strain gauges, optical fibres and thermocouples along their lengths as well as with pressure cells at their toes. Piezometers and thermistors were installed in two boreholes in the soil (labelled P + T1 and P + T2 in Fig. 1(b)). More detailed information on these instruments is reported by Mimouni and Laloui (2015), and by Rotta Loria and Laloui (2016). The soil stratigraphy of the site is reported in Fig. 1(c).

Features of the Experimental Test

The experimental test involved the application of a heating-passive cooling cycle to energy pile EP1 (for approximately 5 and 10 months, respectively), which was the only energy pile of the group that operated as a geothermal heat exchanger. This paper focuses on the heating phase of the test, during which the mechanisms and phenomena occurring in the operating energy pile EP1, in the three surrounding non-operating energy piles EP2, 3 and 4, and in the soil were recorded.

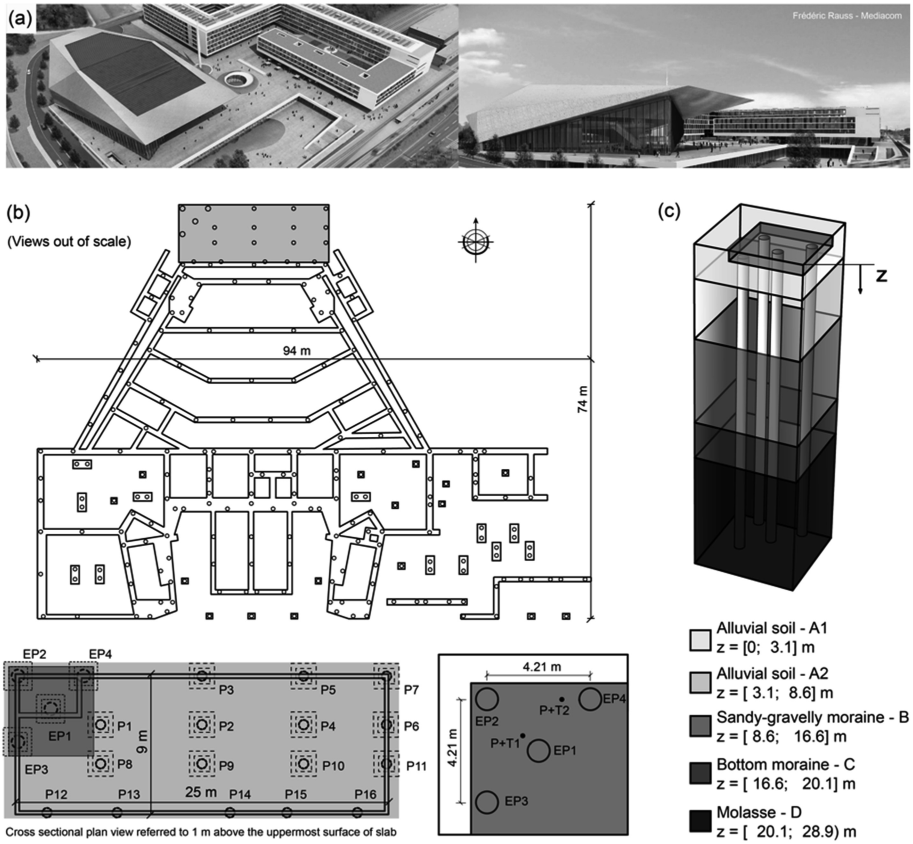

Fig. 1. (a) The EPFL Swiss Tech Convention Centre (modified from the original image, courtesy of Richter Dahl Rocha & Associés architectes SA); (b) plan view of the foundation including the four energy piles; (c) schematic of the soil stratigraphy

Numerical Modelling

Finite Element Model

A 3-D finite element model of the site was developed using the software COMSOL Multiphysics (COMSOL, 2014) (cf., Fig. 2). The model reproduces the foundation supporting the water retention tank. It also accounts for the presence of the pipes in the energy piles through linear entities in which a heat carrier fluid is assumed to flow, which allows the problem of the heat exchange that occurs in the pipes-pile-soil system to be considered.

Modelling Choices, Boundary and Initial Conditions

The numerical analyses are based on the following assumptions: (i) the displacements and deformations of all of the materials can be representatively described through a linear kinematic approach under quasi-static conditions; (ii) the materials that constitute the pile foundation are considered to be isotropic with pores that are fully filled by air and are assumed to be purely conductive domains with equivalent thermo-physical properties that are given by the fluid and the solid phases; (iii) the materials that make up the soil layers are assumed to be isotropic, fully saturated by water and purely conductive domains with equivalent thermo-physical properties that are given by the fluid and the solid phases; (iv) the loads that are associated with this problem have a negligible impact on the variation of the hydraulic field in the soil; and (v) the materials that compose the foundation and surrounding soil are considered to be representatively described by linear thermo-elastic behaviours.

Under these conditions, a thermo-mechanical mathematical formulation is employed. More detailed information about the mathematical formulation used for the numerical analyses performed for this study is reported by Batini et al. (2015).

In the finite element analyses, restrictions are applied to both the vertical and horizontal displacements on the base of the model (i.e., pinned boundary) and to the horizontal displacements on the sides (i.e., roller boundaries). The initial stress state due to gravity in the foundation and the soil is considered to be geostatic and assumes a coefficient of Earth pressure at rest of $K_0 = 1$. No residual stresses from the installation of the piles are considered in these elements and in the adjacent region of soil. This hypothesis may not be completely representative of reality but can be applied successfully in almost all methods of pile groups deformation analysis by choosing appropriate values of the soil moduli (Poulos and Davis, 1980). The temperature is fixed on each of the external boundaries of the model (T = 13.3 °C). The initial temperature in the pipes, energy and conventional piles, slab and soil is set to T_0 = 13.3 °C, which is the average temperature that was recorded at the beginning of the experimental test between depths of z = 4.9 and 28.9 m from the surface of the site (this temperature corresponds to the portions of the energy piles that are not thermally insulated). The fluid that circulates inside the pipes is water. The inner diameter of the pipes is ϕ = 26.2 mm (the outer diameter is 32 mm and the wall thickness is 2.9 mm). A thermal conductivity of $\lambda_p = 0$ W/(m °C) is imposed in the shallowest 4 m of the inlet and outlet of the pipes to simulate the thermal insulation near the ground surface. The trends of the inlet temperature and velocity of the fluid in the pipes that were experimentally recorded throughout the test are considered as input parameters for the numerical simulations (Rotta Loria and Laloui 2016).

Classification of the Numerical Simulation and Material Properties

Two kinds of numerical simulations were performed in this study: Class B1 and Class C1 predictions (Lambe 1973).

A Class B1 prediction was carried out while the modelled *in-situ* tests was performed and with the associated results available. This prediction employed the material properties proposed by Di Donna et al. (2016) for the characterisation of the site.

Different Class C1 predictions were carried out after the modelled *in-situ* test was performed and with the associated results available. The final Class C1 prediction employed the material properties proposed by Di Donna et al. (2016) with two main changes. These changes included the linear thermal expansion coefficient of the soil layers B, C and D as well as the thermal conductivity of the solid particles of all of the soil layers. Detailed justification of the considered changes is presented by Rotta Loria and Laloui (2016). Table 1 summarises the material properties used for the numerical simulations (in brackets are proposed the values of the material properties that were initially used for the Class B1 prediction).

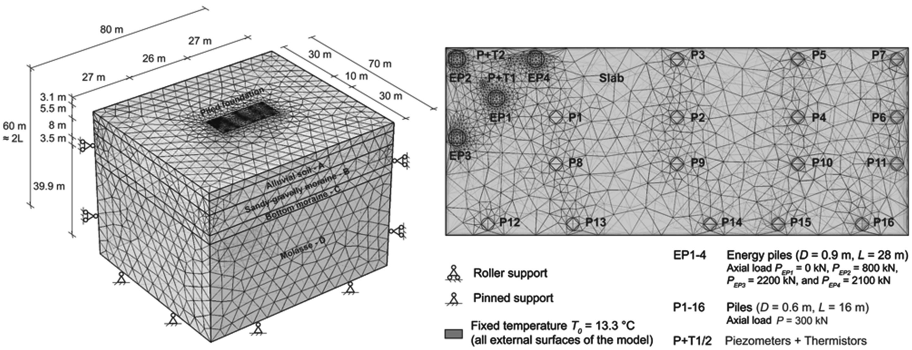

Fig. 2. Geometry and boundary conditions of the finite element model

Comparison Between Experimental and Numerical Results

Figure 3 shows the comparison between the variations in vertical strain that were determined through the Class B1 and final Class C1 numerical predictions along the lengths of energy piles EP1 and 2 when the former pile was characterised by average temperature changes along its unisulated portion of ΔT = 5, 10, 15 and 20 °C. The experimental results are plotted for reference. Expansive strains are considered to be negative.

At the early stages of the heating phase of energy pile EP1, a small difference between the variations in vertical strain that were determined through the numerical analyses was observed and the results agreed well with the experimental observations. At these stages, a limited volume of soil was subjected to a temperature change. Thus, despite the different values of thermal expansion coefficient used in the Class B1 and C1 predictions, the thermally induced deformation of the soil was limited and a small impact of the deformation of this material on that of both the operating and non-operating energy piles was observed.

At the successive stages of the heating phase of energy pile EP1, an increasing difference between the variations in vertical strain that were estimated through the

Table 1. Material properties used for the Class C1 and B1 numerical predictions.

	Young's modulus, E [MPa]	Poisson's ratio, ν [-]	Porosity, n [-]	Density of solid particles, ρ_s [kg/m^3]	Specific heat of solid particles, $c_{p,s}$ [J/(kg °C)]	Thermal cond. of solid particles, λ_s[W/(m °C)]	Linear thermal exp. coeff., α [1/°C]
Soil layers							
A	190	0.22	0.1	2769	880	1.49 (3.38)	$3.3 \cdot 10^{-6}$
B	84	0.4	0.35	2735	890	3.68 (4.45)	$3.3 \cdot 10^{-6}$ ($3.3 \cdot 10^{-5}$)
C	90	0.4	0.3	2740	890	3.46 (4.17)	$3.3 \cdot 10^{-6}$ ($3.3 \cdot 10^{-5}$)
D	3000	0.3	0.1	2167	923	3.82 (3.38)	$2.3 \cdot 10^{-5}$ ($3.3 \cdot 10^{-7}$)
Reinforced concrete piles and slab							
Piles	28000	0.25	0.1	2722	837	1.628	$1 \cdot 10^{-5}$
Slab	35000	0.25	0.1	2722	837	1.628	$1 \cdot 10^{-5}$
	Young's modulus, E [MPa]	Poisson's ratio, ν [-]	Porosity, n [-]	Density of solid particles, ρ_s [kg/m^3]	Specific heat of solid particles, $c_{p,s}$ [J/(kg °C)]	Thermal cond. of pipes, λ_p [W/(m °C)]	Linear thermal exp. coeff., α [1/°C]
High-density polyethylene pipes							
Pipes	–	–	–	–	–	0.42	-

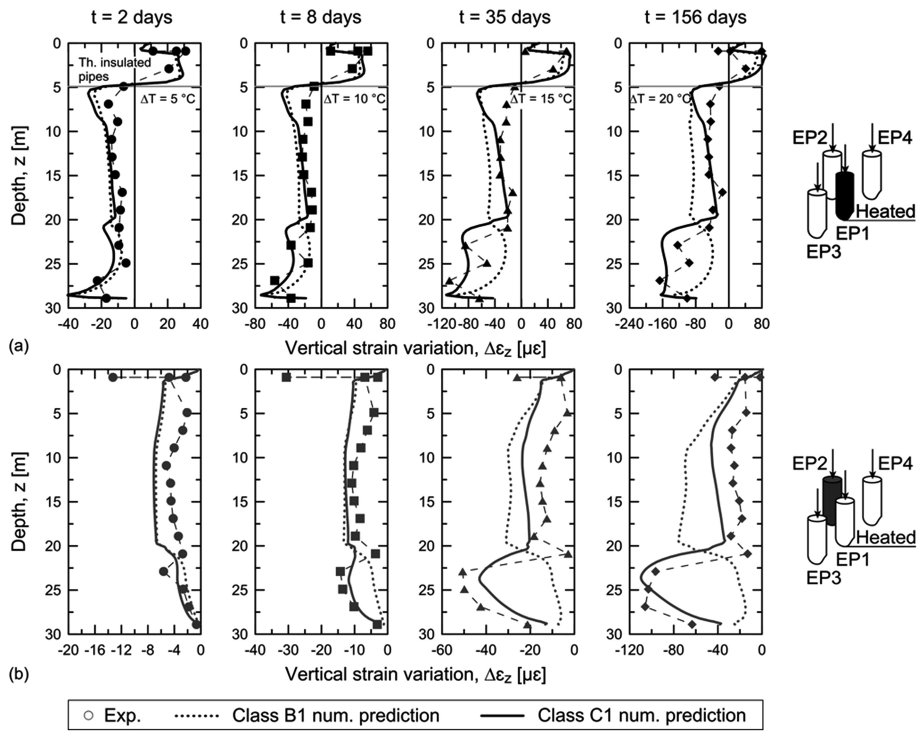

Fig. 3. Comparison between the experimental and numerical results

numerical analyses was noted. The results of the Class B1 prediction indicated an opposite evolution in vertical strain along the lengths of the energy piles compared to the experimental observations and, at a later stage, of the Class C1 prediction results. In general, greater variations in vertical strain were observed in the layers characterised by the greater thermal expansion coefficients. Greater strain variations were determined in the shallower portions of the energy piles by the Class B1 prediction compared to the smaller variations determined experimentally and by the Class C1 prediction. Smaller strain variations were determined in the deeper portions of the energy piles by the Class B1 prediction compared to the greater variations determined experimentally and by the Class C1 prediction. Marked differences between the variations in vertical stress along the lengths of all of the energy piles resulted as a consequence of this occurrence. The reason for the observed difference between the Class B1 prediction results and the experimental and Class C1 prediction results is because at the successive stages of the heating phase of energy pile EP1, a noteworthy volume of soil was subjected to a temperature change. This phenomenon involved a thermally induced deformation of the soil with a marked impact on the variation of the deformation of both the operating and non-operating energy piles.

Conclusions

The results presented in this paper highlight that the serviceability mechanical performance (i.e., deformation-related) of energy pile groups crucially depends on the relative thermally induced deformation of the soil to that of the energy piles. This fact is governed by (i) the thermal field characterising the energy pile group and (ii) the relative thermal expansion coefficient of soil to pile. Aspect (i) involves that the greater the volume of soil subjected to a temperature change is, the more pronounced the impact of the deformation of the soil on that of the pile is. Aspect (ii) can be assessed through the soil-pile thermal expansion coefficient ratio, i.e., the ratio between the linear thermal expansion coefficient of the soil and the linear thermal expansion coefficient of the pile, $X = \alpha_{soil}/\alpha_{EP}$.

At the early stages of geothermal operations of the energy piles, the deformation of energy pile groups is governed by the thermally induced deformation of the piles, almost irrespectively of whether $X \leq 1$ or $X > 1$.

At the successive stages of geothermal operations of the energy piles, values of $X \leq 1$ correspond to a deformation of energy pile groups that is governed by the thermally induced deformation of the piles; values of $X > 1$ correspond to a deformation of energy pile groups that is governed by the thermally induced deformation of the soil surrounding the piles.

Considering these aspects in the analysis and design of energy pile groups is key because they profoundly characterise the deformation of such foundations.

Acknowledgments. The financial support of N. 160117 (Division I-III) from the Swiss National Science Foundation is acknowledged.

References

Batini N, Rotta Loria AF, Conti P, Testi D, Grassi W, Laloui L (2015) Energy and geotechnical behaviour of energy piles for different design solutions. Comp Geotech 86:199–213

Bourne-Webb P, Bodas Freitas T, Freitas Assunção R (2016) Soil–pile thermal interactions in energy foundations. Géotech 66:167–171

Di Donna A, Rotta Loria AF, Laloui L (2016) Numerical study on the response of a group of energy piles under different combinations of thermo-mechanical loads. Comp Geotech 72:126–142

Lambe T (1973) Predictions in soil engineering. Géotech 23:151–202

Mimouni T, Laloui L (2015) Behaviour of a group of energy piles. Can Geotech J 52:1913–1929

Poulos HG, Davis EH (1980) Pile foundation analysis and design. Wiley, New York

Rotta Loria AF, Laloui L (2016) Thermally induced group effects among energy piles. Géotech 6:1–20. http://dx.doi.org/10.1680/jgeot.16.P.039

Numerical Analysis of Seismic Soil-Pile-Structure Interaction in Soft Soil with Strong Nonlinearity and Its Validation by 1g Shaking Table Test

Kheradi Hamayoon[1(✉)], Ye Bin[2], Morikawa Yukihiro[3], and Zhang Feng[1]

[1] Graduate School of Engineering, Nagoya Institute of Technology, Showa Ward, Nagoya 466-8555, Japan
hamayoon.k@gmail.com
[2] Department of Geotechnical Engineering, Tongji University, Shanghai 200092, China
[3] Nagoya Institute of Technology, Nagoya 466-8555, Japan

Abstract. The failure of pile foundations in recent strong earthquakes showed that the current analysis and design method of pile foundation need improvement. In strong earthquakes, the mechanical behavior of the pile foundations, the surrounding soil and the structure are completely nonlinear. Considerations of their nonlinearities are important in improving the analysis method. In recent years, the nonlinearity of the soil and the piles have become inevitable in the analysis of pile foundations. However, the nonlinearity of the structure is simplified. In this paper, a section of an elevated bridge supported by a 3×3 group-pile foundation in model scale is considered. 1g shaking table test and three-dimensional nonlinear dynamic finite element method (FEM) are conducted to investigate the seismic behavior of the mentioned model. In the numerical analysis, a FEM program called DBLEAVES is used. In the numerical modeling, the soil, the piles and the structure are modeled by nonlinear constitutive equations. The purpose of this study is to confirm the accuracy of the mentioned nonlinear analysis method by the 1g shaking table test. The recorded data of the shaking table test are reproduced qualitatively and quantitatively by the numerical test. This implies that the discussed numerical method is a comprehensive tool. Applicability of the method is to study the seismic behavior of piles with a high accuracy. Study of reinforcing of existing piles with the ground improvement is its other applicability.

Introduction

The failure of pile foundations in recent strong earthquakes such as 1995 Hyogoken-Nanbu Japan earthquake has shown the necessity of an accurate and comprehensive analysis method. A proper analysis method will help the designers to predict the seismic behavior of the pile foundations and design a safe structure. The seismic behavior of pile foundations in soft soil is a complex soil-pile-structure interaction (SPSI) problem. The long span bridges such as cable-stayed bridges will deflect relatively large in a strong

A. Ferrari and L. Laloui (eds.), *Advances in Laboratory Testing and Modelling of Soils and Shales (ATMSS)*, Springer Series in Geomechanics and Geoengineering,
DOI 10.1007/978-3-319-52773-4_51

earthquake. In the analysis of such structures, the consideration of geometric and material nonlinearity is important. Combining the nonlinearities of the soil, the piles, and structure together will increases the complexity of SPSI.

The SPSI has been studied by many researchers, for instance, Kimura and Zhang (2000), Zhang et al. (2000), Carbonari et al. (2011), Morikawa (2012) and Kheradi et al. (2015) conducted researches in this field. The use of proper constitutive equations in the numerical analysis provides a better understanding of seismic SPSI. In the realistic analysis of SPSI problems, the soil, the piles and the structure are involved in the calculation; on the other hand, they exhibit nonlinear behavior during strong earthquakes; hence, to develop a numerical method the considerations of their non-linearities are the most important.

In the recent researches by the geotechnical engineers, the nonlinearity of the soil and the pile foundations are inevitable considerations. Among these researchers, Zhang et al. (2007, 2011) introduced a nonlinear rotating-hardening type elastoplastic constitutive model for the behavior of the soil, with the name of Cyclic Mobility model (CM model). Furthermore, Zhang and Kimura (2002), introduced an axial-force dependent model (AFD model) for the nonlinear behavior of pile foundations. In the present study the CM model and AFD model are adopted for the behavior of the soil and the pile foundations respectively.

The nonlinearity of the structure usually is not considered by the geotechnical engineers. In the structural engineering field, Goto et al. (1995) and Li (1997) developed nonlinear beam elements that take geometric and material nonlinearities of the structures into consideration. Bao et al. (2012) embedded the Goto et al. (1995) and Li (1997)'s nonlinear beam elements into a geotechnical engineering finite element method (FEM) program called DBLEAVES (Ye 2007, 2011). In the present numerical calculation, the structure is modeled by the discussed nonlinear beam elements.

The DBLEAVES is a three-dimensional (3D) static and dynamic soil-water coupling FEM program.

In this paper, a section of an elevated bridge supported by a 3 × 3 group-pile foundation in model scale is considered. 1g shaking table test and three-dimensional (3D) nonlinear dynamic FEM are conducted to investigate the seismic behavior of the mentioned model. In the numerical analysis, a FEM program named DBLEAVES is used. The purpose of this study is to confirm the accuracy of the mentioned fully nonlinear analysis method, especially the accuracy of nonlinear beam elements for the behavior of structure by the 1g shaking table test. As it was mentioned before, fully nonlinear analysis method is a comprehensive numerical tool for future study of seismic SPSI problems.

1g Shaking Table Test Method

The shaking table device used in the present study is shown in Fig. 1(a). It has the maximum payload, acceleration and displacement of 16 kN, 9.8 m/s^2 and 0.05 m respectively. The dimension of the shaking table, shear box is 1.2 × 1.0 × 0.8 m (length, width and height). The shaking table unit has a laminate shear box that can avoid the influence of the fixed boundary condition during shaking. In order to prepare

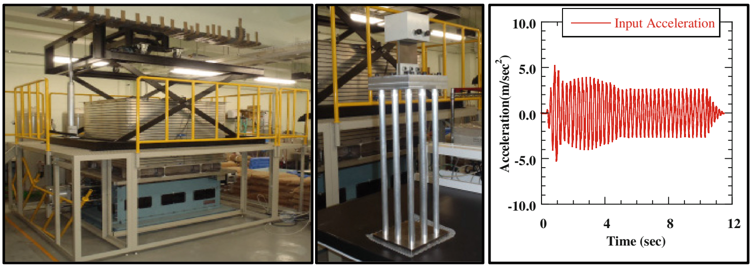

Fig. 1. (a) Shaking table test device, (b) Model group-piles (c) Input acceleration.

a uniform model ground with a prescribed density, the shaking table has a sand-dropping device. The model ground in the tests is made from Toyoura sand with a relative density of 80% in the dry state. The depth of model ground is 0.5 m. Table 1 shows the material parameters of the model ground.

In the shaking table tests, a section of an elevated bridge supported by a 3 × 3 group-pile foundation in model scale is investigated. The model group-piles, the pier as the structure of the model and the mass of the girder located on the top of the pier have a similarity ratio of 1/50. The model group-piles are made of aluminum pipes with a modulus of elasticity of 70 GPa. The pier is made of the 0.01 m thick aluminum bar with a modulus of elasticity of 70 GPa. A steel cube with a modulus of elasticity of 210 GPa is considered as the weight of girder. The model group-piles with its pier and weight of girder are shown in Fig. 1(b).

Table 1. Material parameters of Toyoura sand in CM model.

Parameter of ground material	Symbol	Toyoura sands	Note
Compression index	λ	0.050	Same parameters as Cam Clay model
Swelling index	κ	0.0064	
Stress ratio at critical state	M	1.300	
Reference void ratio (p′ = 98 kPa on N.C.L)	N	0.870	
Poisson's ratio	υ	0.300	
Degradation parameter in overconsolidation	m	0.010	New parameter
Degradation parameter of structure	a	0.500	
Evolution parameter of anisotropy	br	1.500	
Initial structure	R_0*	0.990	Initial values of state variables
Initial void ratio	e_0	0.650	
Initial degree of overconsolidation	OCR ($1/R_0$)	7.500	
Initial anisotropic	ζ_0	0.000	

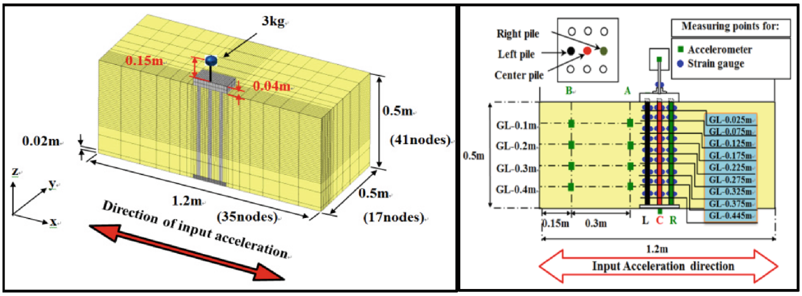

Fig. 2. (a) 3D FEM mesh (b) Measuring point.

The input acceleration of the shaking table test, as shown in Fig. 1(c), is in the horizontal direction and lasts for 11.5 s with a maximum amplitude of 5.0 m/s^2. The same input acceleration is used for the numerical test as well.

In order to measure the bending strain and the responding acceleration of the model test, strain gauges and accelerometers are installed at different depths. The strain gauges are installed on the three piles located on the center line of the model ground. These three piles are labelled as L, C and R, representing left, center and right pile, respectively. The measuring points are shown in Fig. 2(b). In the same measuring points the numerical test results are also plotted to compare them.

FEM Modelling and Numerical Test

In the numerical test, 3D nonlinear dynamic FEM with the program named DBLEAVES is used. The DBLEAVES program is based on the finite element-finite difference (FE-FD) scheme. The accuracy and applicability of DBLEAVES have been reported by many researchers, for instance, its accuracy can be seen in the work of Ye et al. (2007). The calculation is conducted on the model scale; additionally, the ground, the group-piles, the pier and the mass of the girder located on the top of the pier are considered in the same way as described in the previous section. Due to the symmetric geometric and loading conditions, only half of the domain is considered in the calculation; therefore, the mass of the girder is half of the shaking table test.

As discussed before, in the numerical test and shaking table test the ground is made of Toyoura sand and its nonlinear mechanical behavior is described by CM model. The CM model is a rotating-hardening type elastoplastic constitutive model that takes into account the overconsolidation, the soil structure and the stress-induced anisotropy simultaneously. The main feature of the model is its ability to describe the static and dynamic behavior of soils subjected to different loading under the different hydraulic condition in a unified way. The CM model has eight parameters, among them five parameters, M, N, λ, κ and υ are the same as those in the Cam Clay model. The other three parameters are a: the parameter controlling the collapse rate of the structure, m: the parameter controlling the losing rate of the overconsolidation ratio or the change in density of the soil, and b_r: the parameter controlling the developing rate of the stress-induced anisotropy are different. These three parameters have clear physical meanings and can be easily determined by undrained triaxial cyclic loading tests and drained triaxial compression tests. A detailed description of this model can be found in the work of Zhang et al. (2007, 2011). The properties of Toyoura sand are listed in Table 1.

In the numerical test, the nonlinear behavior of the pile foundations is modeled with the AFD model. The AFD model can take into consideration proper the axial-force dependency in the nonlinear moment-curvature relations. The detailed description of this model can be found in the work of Zhang and Kimura (2002).

The pier that is considered as the structure for the group-piles is modeled by the nonlinear beam elements. The nonlinear beam element is able to take both the geometric and material nonlinearities into consideration. The detailed description of this model can be found in the work of Bao et al. (2002).

The input acceleration in the numerical test is applied at the bottom of the ground along x-direction (Fig. 2). In the analysis, initial-stiffness-proportional Rayleigh damping with h1 = 0.05 is used for the ground and the structure. The dynamic analysis is conducted by the Newmark-β method (β = 0.60). The time interval is 0.010 s and the calculation for the vibration is performed for 11.5 s.

The boundary conditions of the ground are assumed to be fixed at the bottom, and the equal-displacement boundary condition is introduced in all directions at the right- and left-side boundaries. The boundary condition at piles toes is that the displacements along x, y, and z directions are fixed but the rotations are free. The FEM mesh with 23,585 nodes and 20,996 elements is shown in Fig. 2(a).

Shaking Table Test Vs. Numerical Test

In this section the dynamic calculation of numerical test is compared with the shaking table test and the comparisons are plotted in Figs. 3 and 4. The measuring points of computed and recorded data are shown in Fig. 2(b).

Due to the similar time history of response acceleration in the ground at the Point A and Point B are shown in Fig. 2(b), in both the recorded and calculated data the time history of response acceleration of point B is presented. Figure 3(a)–(d) show the time history of response acceleration at the ground level of −0.10 m, −0.20 m, −0.30 m and −0.40 m. Moreover, the recorded and computed time history of response acceleration at the top of the footing and pier are shown in Fig. 3(e) and (f) respectively. The time history of response accelerations on the ground in the numerical prediction is in very good agreement with the recorded data. On the ground level of −0.10 m, however, there is a minor difference. The minor difference is mainly ascribed to the difference between the assumed soil damping, stiffness and confining pressure and their actual values during the test.

From Fig. 3(e) and (f) it is known that the recorded data are reproduced almost the same by the numerical test. There is a minor difference between the recorded and computed data. In general the representation of the actual behavior seems to be reasonable enough.

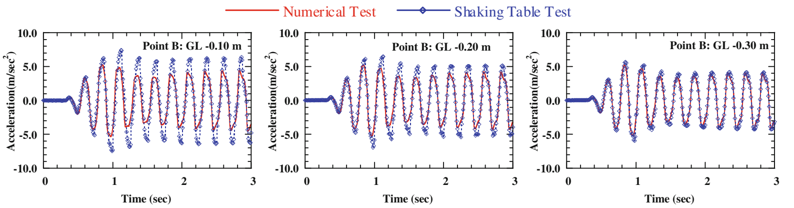

(a) Response Acceleration in GL -0.10 m *(b) Response Acceleration in GL -0.20 m* *(c) Response Acceleration in GL -0.20 m*

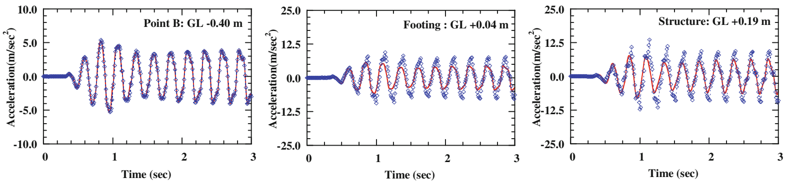

(d) Response Acceleration in GL -0.40 m *(e) Response Acceleration in Footing GL +0.04 m* *(f) Response Acceleration in Structure GL +0.19 m*

Fig. 3. Recorded and computed time history of response acceleration.

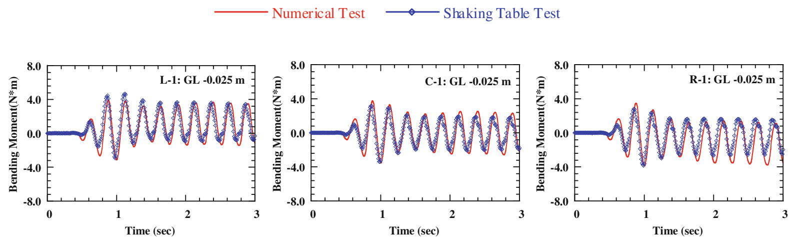

(a) Bending moment in GL -0.025 m at L-1, C-1 and R-1

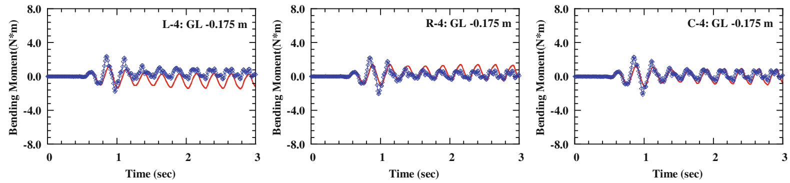

(b) Bending moment in GL -0.175 m at L-4, C-4 and R-4

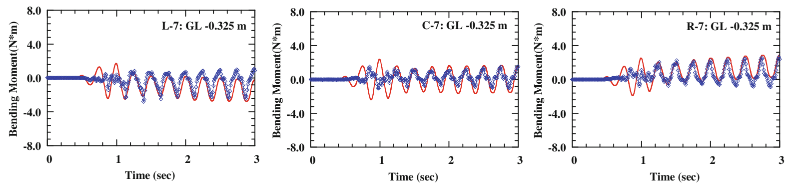

(c) Bending moment in GL -0.325 m at L-7, C-7 and R-7

Fig. 4. Recorded and computed time history of bending moments of the piles.

The time history of recorded and computed bending moment in the three piles and three different measuring depths marked in Fig. 2(b) are compared and plotted in Fig. 4. The Fig. 4 shows that the recorded time history of bending moment is reproduced with a good accuracy by the numerical test.

Based on the conformity of recorded and computed data was shown in Fig. 3 and 4 this is reasonable to assess that the present nonlinear analysis method has a high accuracy. In addition, the numerical method in the present study will be an accurate and comprehensive tool for future study of SPSI problem, especially for the structures in a seismically active region that behave relatively large deflection during the earthquake. The study of bending, buckling and settlement failure of piles during an earthquake are the serious problems that can be investigated using the current analysis method. Study of strengthening of existing piles in seismically active region with the ground improvement is an other applicability of the method.

Conclusions

In the present paper, 1g shaking table test and 3D dynamic FEM of SPSI both in the model scale were conducted. In shaking table test and numerical test a section of an elevated bridge supported by a 3 × 3 group-piles in the model scale were investigated. In the numerical modeling, the soil, the piles and the structure are modeled by nonlinear constitutive equations, namely, cyclic mobility model, axial-force dependent model and nonlinear beam element model respectively. The following conclusions can be given for the present investigation.

(a) The assessment of response acceleration on the ground, footing and structure show that the time histories of response accelerations in the numerical prediction are in very good agreement with the recorded data of the shaking table test.
(b) The assessment of bending moments in the pile foundations show that the recorded data by shaking table test were reproduced qualitatively and quantitatively by numerical tests.
(c) Based on results (a) and (b), it is reasonable to assess that the nonlinear consultative equations for the soil, the pile foundations and the structure were used in the present study have higher accuracy in the analysis of soil-pile-structure interaction. In addition, the numerical method in the present study will be an accurate and comprehensive tool for future study seismic SPSI.

References

Bao Y, Ye G, Ye B, Zhang F (2012) Seismic evaluation of soil-foundation-superstructure system considering geometry and material nonlinearities of both soils and structures. Soils Found 52 (2):257–278

Carbonari S, Dezi F, Leoni G (2011) Linear soil-structure interaction of coupled wall-frame structures on pile foundations. Soil Dyn Earthquake Eng 31:1296–1309

Goto Y, Li XS, Kasugai T, Obata M (1995) Analysis of greenhill problem by a co-rotational method. J Struct Eng 41A:411–420

Kheradi H, Oka R, Zhang F (2015) Numerical analyses and shaking table tests on seismic performance of existing group-pile foundation enhanced with partial-ground-improvement method. In: Proceedings of 15th Asian regional conference on soil mechanics and geotechnical engineering, vol 2, no 38, pp 1383–1388. JGS Special Publication

Kimura M, Zhang F (2000) Seismic evaluation of pile foundations with three different methods based on 3D elasto-plastic FEA. Soils Found 40(5):113–132

Li XS (1997) A rigorous numerical method for analysis of geometric and material nonlinear dynamic behavior of space frames. Doctoral dissertation, NITech

Morikawa Y (2012) Clarification of the mechanism of reliquefaction and its application to evaluate seismic enhancement effect of various kind of ground improvement. Doctoral dissertation, NITech

Ye B (2007) Experiment and numerical simulation of repeated liquefaction-consolidation of sand. Doctoral dissertation, Gifu University

Ye B, Ye GL, Zhang F, Yashima A (2007) Experiment and numerical simulation of repeated liquefaction-consolidation of sand. Soils Found 47(3):547–558

Ye GL (2011) DBLEAVES user's manual Ver 1.6, Shanghai Jiaotong University

Zhang F, Kimura M (2002) Numerical prediction of the dynamic behaviors of an RC group-pile foundation. Soils Found 42(3):77–92

Zhang F, Kimura M, Nakai T, Hoshikawa T (2000) Mechanical behavior of pile foundation subjected to cyclic lateral loading up to the ultimate state. Soils Found 40(5):1–17

Zhang F, Ye B, Ye GL (2011) Unified description of sand behavior. Int J Front Struct Civil Eng 5(2):121–150. Springer

Zhang F, Ye B, Noda T, Nakano M, Nakai K (2007) Explanation of cyclic mobility of soils: Approach by stress-induced anisotropy. Soils Found 47(4):635–648

On the Interface Shearing Behavior Between Granular Soil and Artificial Rough Surfaces

Xue-Ying Jing[1], Wan-Huan Zhou[1,2(✉)], Hua-Xiang Zhu[1], Zhen-Yu Yin[3], and Yangmin Li[4]

[1] Department of Civil and Environmental Engineering, Faculty of Science and Technology, University of Macau, Zhuhai, Macau, China
hannahzhou@umac.mo
[2] UMacau Research Institute, Zhuhai, Guangdong, China
[3] LUNAM University, Ecole Centrale de Nantes, GeM UMR CNRS 6183, Nantes, France
[4] Department of Electromechanical Engineering, Faculty of Science and Technology, University of Macau, Zhuhai, Macau, China

Abstract. The soil-structural interface is involved in many geotechnical engineering problems. Previous investigations have mainly relied on the macro-scale observations from laboratory experiment. However, soil is a type of granular material, and recent research works reveal that the macroscopic responses of granular materials originate from the evolution of the microstructures. Therefore, to understand well the shearing behavior of soil adjacent to an artificial interface, it is necessary to explore this problem on the particle scale. In this study, an interface shear test is modeled using the three-dimensional discrete element method. Five shear boxes of distinct size are modeled to verify the scale effect. According to the comparison between the interface shear tests in terms of computation time, shear strength measured on the interface and volumetric strain of the specimen, an interface shear box containing 14,000 particles is sufficient for this study. Then, a series of three-dimensional interface shear tests with distinct normalized roughness "R_n" is modeled. The results show that (1) two failure modes exist in an interface shear test, elastic-perfectly plastic for a smooth surface and stress softening observed for a rough surface, and (2) the shear strength of the soil-structural interface increases with the increasing of the roughness of the interface. The displacement field is obtained by interpolating the movement of each particle. The field of u_x (displacement in the direction of shearing) indicates that a narrow zone of intense shearing deformation, called the shear band, emerges from the contact interface and expands during the shearing process. A discontinuous feature is characterized after the shear band appears.

Keywords: Soil-rough interface · Discrete element method · Scale effect · Formation of shear band

Introduction

The soil-artificial rough interface is frequently encountered in geotechnical engineering, such as in the pile foundation, the retaining wall and the geotextile reinforcing engineering. Many efforts have been devoted to exploring the mechanical behavior of

A. Ferrari and L. Laloui (eds.), *Advances in Laboratory Testing and Modelling of Soils and Shales (ATMSS)*, Springer Series in Geomechanics and Geoengineering,
DOI 10.1007/978-3-319-52773-4_52

the soil-structure interface. The soil properties (DeJong and Westgate 2009; Tang et al. 2010; Khoury et al. 2011), the geometry, the roughness and the stiffness of the contact surface are found to affect the shearing behavior of interface (Uesugi and Kuroda 1986; Uesugi et al. 1988; Paikowsky et al. 1995; Hu and Pu 2005; Wang et al. 2007). These investigations provide a basic understanding about the mechanical properties of interface but cannot properly explain the micro-mechanism beneath these macroscopic responses. Accordingly, an in-depth investigation using the micro-approach is attracting growing attention from the research community.

A narrow zone with intense shearing deformation, called the "shear band", is observed in the soil-rough interface shearing test (IST) with the assistance of the micro-observation approach and numerical modeling (Hu and Pu 2005; DeJong et al. 2006; Zhang et al. 2006; Wang et al. 2007). After the shear band appears, two deformation patterns evolve in the granular material, including the non-linear stress-strain behavior in the shear band and the quasi-elastic deformation outside the shear band. In another sense, the discontinuity of the granular material is characterized. This feature is in conflict with the hypothesis of continuum mechanics. To better describe the constitutive behavior of a soil-rough interface, it is necessary to distinguish the shear band from the remaining homogeneous region. Although some investigations to demonstrate the existence of the shear band have been carried out, the literature lacks research exploring the formation of the shear band using the three-dimensional discrete element method (DEM).

This study aims to investigate the shearing behavior of the soil-rough artificial surface. A series of interface shear tests with varying roughness were modeled using 3D DEM. The scale effect is a critical issue for both the physical experiments and the numerical simulations. The dimensions of the shear box may affect the mechanical properties of the soil in the aspects of shear strength, volumetric change and peak friction angle (Barton and Bandis 1980; Lutenegger and Cerato 2006; Wang and Gutierrez 2010). For this reason, a representative volume of the specimen is confirmed in Sect. "Scale Effect". The shearing behaviors of IST with varying roughness in terms of shear stress and volumetric change are discussed in Sect. "Macroscopic Response of the Soil-Structural Interface". Formation of the shear band in the specimen shearing on a rough artificial surface is analyzed in the last section.

Model Set-up in PFC 3D

The interface shear test is modeled by PFC 3D (Fig. 1a). The shear box is composed of six rigid boundaries, including four fixed vertical boundaries and two moveable boundaries, one at the top and one at the bottom. Although the surface asperity is random in nature, in this study, a standard saw-tooth is chosen to represent the rough surface. The geometry of the rough surface is shown in Fig. 1b. The surface roughness is quantified by reference to the research of Uesugi and Kuroda (1986) by introducing a normalized roughness index "R_n", which is equal to h/d_{50} (h is the vertical distance between the peak and the bottom of a valley).

A linear rolling resistance model was adopted in the simulation. The force-displacement relationship between particles contains two parts: (1) the contact

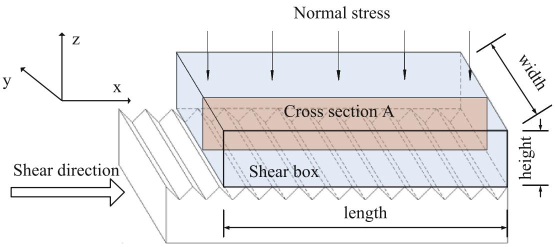

(a)

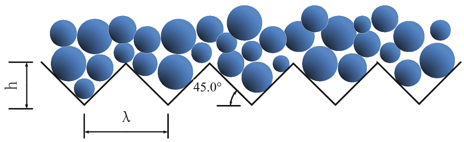

(b)

Fig. 1. (a) Schematic diagram of the interface shear test; (b) front view of the rough surface.

forces arise linearly from constant normal stiffness (k_n), tangential stiffness (k_s) and a damping coefficient until sliding occurs when the Coulomb criterion is met. (2) The internal moment is incremented linearly with the accumulated relative rotation between particles. This accumulation occurs up to a maximum limiting value M_r which is defined as $M_r = \mu_r \bar{r} F_n^l$, where $\bar{r}$ is the effective radius of the contact, F_n^l is the current normal contact force and μ_r is the rolling resistance coefficient. The particles start rolling as soon as the inertial moment reaches the threshold value M_r.

The input parameters are summarized in Table 1. The spherical particles were generated inside the shear box with radii following a uniform size distribution. To obtain a dense specimen, the radius of each particle was expanded gradually in a fixed space and the inter-particle friction angle remained at zero in this phase (Cui and O'Sullivan 2006). Then, a constant vertical force was applied on the top plate of the shear box by a servo system. The bottom plate started to move horizontally in the x-direction at a steady rate of 0.015 mm/s. The macroscopic behaviors of the specimen were obtained from the boundaries of the shear box, including (1) the shear stress "τ"

Table 1. Summary of input parameters for the DEM simulation.

Parameters	Value	Parameters	Value
k_n (N/m)	9.0×10^9	Range of particle's diameter (mm)	2.46–4.03
k_n/k_s	2.0	Internal particle friction coefficient	0.35
Particle density (kg/m^3)	2880	Particle-wall friction coefficient	0.2
C_u (d_{60}/d_{10})	1.2	Rolling resistance coefficient μ_r	0.17
d_{50} (mm)	3.48	Damping coefficient	0.7

on the bottom plate; (2) the normal stress "σ_n" on top plate; and (3) the volumetric strain "ε_v", which is taken to be the ratio of the vertical displacement of the top plate to the initial height of the specimen.

Scale Effect

As mentioned in the introduction, the dimensions of the shear box, including the length (L), width (W), height (H) and ratio of the length to height (L\H) may affect the soil's shearing behavior. To choose an appropriate dimension of shear box for the simulation, a total number of 20 simulations with 5 different shear boxes are carried out (Table 2). Figure 2 shows that the initial porosities n_0 of the specimen for all the ISTs are close to each other under the same normal stress. The peak shear stress τ_p measured in the IST with a larger L/H ratio is a little higher than the others (Fig. 3a). The difference in the volumetric change is not significant (Fig. 3b). The results demonstrate that the scale effect for the five ISTs is small enough to be ignored. Moreover, it is time-consuming if the number of particles exceeds 20000. Thus the dimension of IST1 (100 mm 100 mm × 25 mm) is chosen for the following study.

Table 2. Summary of interface shear tests with different shear boxes.

No. of shear box	Length/d_{50}	Width/d_{50}	Height/d_{50}	L/H	Particle number	R_n
IST1	28.7	28.7	7.2	4.0	13359	0.5
IST2	34.5	28.7	8.6	4.0	19267	0.5
IST3	40.2	28.7	10.1	4.0	26212	0.5
IST4	28.7	28.7	8.6	3.3	16039	0.5
IST5	28.7	28.7	10.1	2.8	18719	0.5

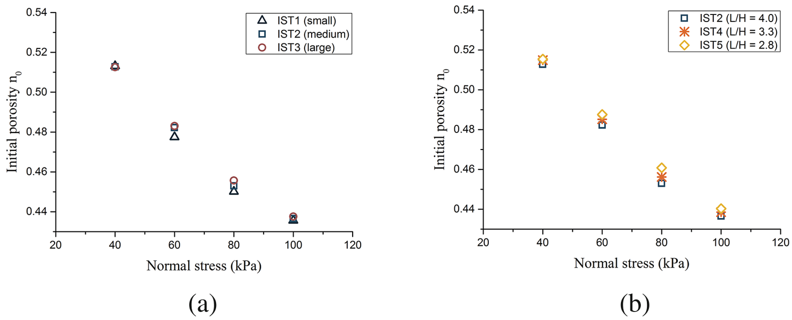

Fig. 2. Initial porosity n_0 as a function of the normal stress and: (a) the shear box size (L, H); (b) the ratio of L/H.

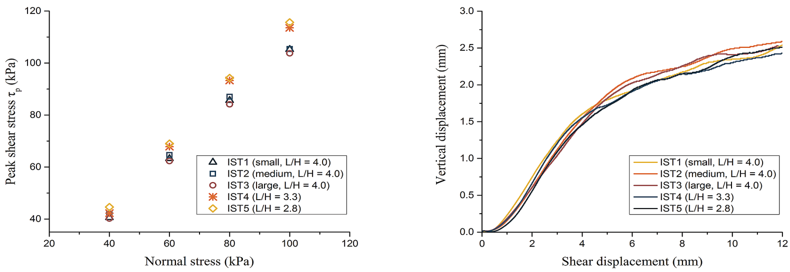

Fig. 3. (a) Peak shear stress τ_p vs. normal stress with different shear box sizes (L, H); (b) vertical displacement of the top plate vs. normal stress with different shear box sizes (L, H).

Macroscopic Response of the Soil-Structural Interface

The shearing behaviors of the soil-rough interface under σ_n of 80 kPa are analyzed in this section. The curves of τ and ε_v versus shear displacement for different normalized roughness R_n are plotted in Fig. 4. Apparently the R_n has a significant impact on the peak shear stress τ_p and bulk dilatancy, which is consistent with the laboratory experiments (Uesugi and Kuroda 1986; Paikowsky et al. 1995; Hu and Pu 2005). The shear strength of the soil-structural interface increases with an increase in R_n. Two failure modes exist for the IST with distinct R_n: (1) elastic-perfectly plastic if shearing on a relative smooth surface ($R_n \leq 0.1$) and (2) the stress softening and the bulk dilatancy are observed if the specimen is shearing on a rough surface ($R_n \geq 0.3$).

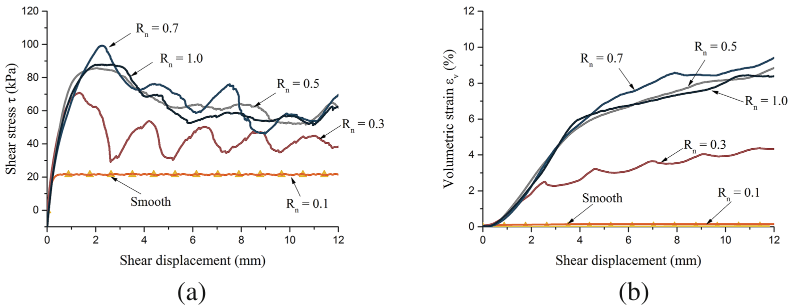

Fig. 4. Macroscopic responses of the soil-structural interface: (a) shear stress τ versus shear displacement; (b) volumetric strain ε_v versus shear displacement.

Formation of the Shear Band

The kinematics of the granular system are traced and recorded during the shearing process. At a given strain state, the displacement of nodes on a three-dimensional grid was interpolated according to the movement of each particle using a linear interpolation method.

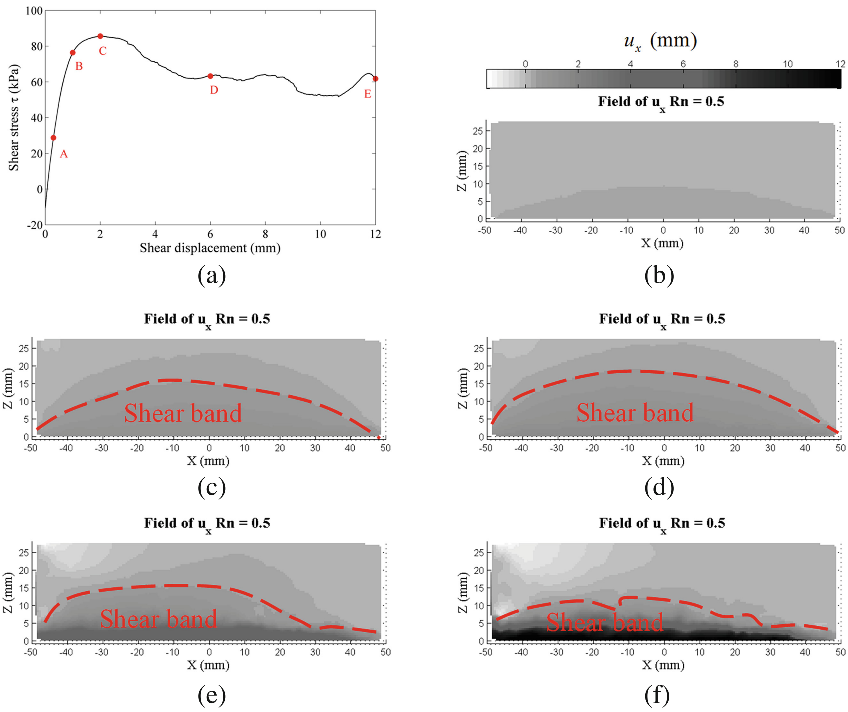

Fig. 5. (a) Shear stress-displacement relationship of the interface shear test ($R_n = 0.5$) under normal stress of 80 kPa; (b) displacement field in the x-direction at point A, 0.3 mm displacement; (c) displacement field in the x-direction at point B, 1 mm displacement; (d) displacement field in the x-direction at point C, 2 mm displacement; (e) displacement field in the x-direction at point D, 6 mm displacement; (f) displacement field in the x-direction at point E, 12 mm displacement.

The cross section A (Fig. 1a) of the specimen is chosen to analyze the formation of the shear band. Fields of displacement in the x-direction (u_x) of cross section A in the IST ($R_n = 0.5$) colored according to the value of u_x at different shearing states are illustrated in Fig. 5. It shows that the granular material deforms homogeneously at the early shearing phase (Fig. 5b). The particles close to the contact surface tend to have a large deformation on the progress of shearing. The area beneath the red dashed line is the shear band area ($u_x \geq 0.4$ mm). The contour of the shear band is irregular and unstable. It expands with increasing τ until it approaches the peak shear stress and shrinks in the stress softening phase. The shape of the shear band tends to be steady at the residual stress state (point D and point E). These results show that there is a correlation between the formation of the shear band and the shear stress.

Conclusions

The scale effect of IST is discussed in terms of the initial porosity and macro-response of IST with five different shear boxes (IST1 ~ IST5). The results show that the effect on the shearing strength and volumetric strain is not significant. Taking into account both of the affordable computation time and the macro-response of IST, a representative dimension of the shear box is confirmed.

The macroscopic responses of specimens subjected to interface shearing with various R_n are compared in terms of shearing stress and volumetric change. The elastic-perfectly plastic stress-strain curve is obtained for the soil shearing on a relative smooth surface. By contrast, the stress softening after τ_p and the bulk dilatancy are observed when the specimen shears on a rough surface.

The evolution of the strain localization in the IST (R_n = 0.5, σ_n = 80 kPa) at several monitoring stress states is analyzed. The results illustrate that a shear strain is localized in a narrow zone adjacent to the contact surface, called the shear band. The formation of the shear band correlates with the shear stress. It emerges at a certain stress state and expands gradually until the peak shearing stress is approached. Then, this domain narrows, accompanied with stress softening. As a result, the shear band is steadily shaped at the steady stress state.

Acknowledgements. The authors gratefully acknowledge the financial support from the Macau Science and Technology Development Fund (Grant nos. FDCT/125/2014/A3 and FDCT/011/2013/A1), the National Natural Science Foundation of China (Grant no. 51508585), the University of Macau Research Funds (Grant nos. MYRG2015-00112-FST and MYRG2014-00175-FST) and the Region Pays de la Loire of France (project RI-ADAPTCLIM).

References

Barton N, Bandis S (1980) Some effects of scale on the shear strength of joints. Int J Rock Mech Min Sci Geomech Abs. 17(1):69–73

Cui L, O'Sullivan C (2006) Exploring the macro- and micro-scale response of an idealised granular material in the direct shear apparatus. Géotechnique 56(7):455–468

DeJong JT, Westgate ZJ (2009) Role of initial state, material properties, and confinement condition on local and global soil-structure interface behavior. J Geotech Geoenvironmental Eng 135(11):1646–1660

DeJong JT, White DJ, Randolph MF (2006) Microscale observation and modeling of soil-structure interface behavior using particle image. Soils Found 46(1):15–28

Hu LM, Pu JL (2005) Testing and modeling of soil-structure interface. J Geotech Geoenvironmental Eng 130(8):851–860

Khoury CN, Miller GA, Hatami K (2011) Unsaturated soil-geotextile interface behavior. Geotext Geomembr 29(1):17–28

Lutenegger AJ, Cerato AB (2006) Specimen size and scale effects of direct shear box tests of sands. Geotech Test J 29(6):1–10

Paikowsky SG, Player CM, Connors PJ (1995) A dual interface apparatus for testing unrestricted friction of soil along solid surfaces. ASTM Geotech Test J 18(2):168–193

Tang CS, Shi B, Zhao LZ (2010) Interfacial shear strength of fiber reinforced soil. Geotext Geomembr 28(1):54–62

Uesugi M, Kishida H, Tsubakihara Y (1988) Behavior of sand particles in sand-steel friction. Soils Found 28(1):107–118

Uesugi M, Kuroda H (1986) Frictional resistance at yield between dry sand and mild steel. Soils Found 26(4):139–149

Wang J, Gutierrez MS (2010) Discrete element simulations of direct shear specimen scale effects. Géotechnique 60(5):395–409

Wang JF, Marte SG, Joseph ED (2007) Numerical studies of shear banding in interface shear tests using a new strain calculation method. Int J Numer Anal Meth Geomech 31:1349–1366

Zhang G, Liang DF, Zhang JM (2006) Image analysis measurement of soil particle movement during a soil-structure interface test. Comput Geotech 33(4–5):248–259

Constitutive and Numerical Modelling of Soils and Shales

Constitutive Framework for Unsaturated Soils with Differentiation of Capillarity and Adsorption

Yafei Qiao[1,2(✉)], Wenqi Ding[1], and Lyesse Laloui[2]

[1] Department of Geotechnical Engineering, College of Civil Engineering, Tongji University, Shanghai 200092, China
yafei.qiao@epfl.ch
[2] Soil Mechanics Laboratory, École Polytechnique Fédérale de Lausanne, EPFL, Station 18, 1015 Lausanne, Switzerland

Abstract. This paper presents a hydromechanical coupled framework for unsaturated soils, which differentiates the capillarity and adsorption. The proposed framework is a thermodynamic-based modelling framework and it was derived from energy-conjugate variables. Independent hydromechanical models are considered for each mechanism, including independent measures of effective stresses and water retention curves. Hydromechanical coupling at each mechanism is efficiently achieved by liking the effective stress formulation with the water retention model. Finally, the models are linked through a structure parameter to obtain the global response. The framework will pave the way for developing constitutive models for unsaturated soils, in particular the expansive soils.

Introduction

The pore water in unsaturated soils is stored by two mechanisms: capillarity and adsorption (Tuller et al. 1999; Romero et al. 2011; Lebeau and Konrad 2010). The capillary water exists in big pores between aggregated particles/grains and its properties are similiar to those of free water. The capillary force affects the contact stress between particles, resulting in a contribution to the effective stress (Konrad and Lebeau 2015; Zhou et al. 2016). The adsorbed water is attached to the surface of particles/grains (water film) or exists in the smaller pores. Its motion is limited and it has a higher viscosity and density than free water because of the physicochemical interactions between adsorbed water and particles/grains. In principle, the pressure of adsorption water acts on the surface of particles/grains uniformly, leading to a null resultant force. As a consequence, the adsorptive force almost has no effect on the contact stress (Zhou et al. 2016). Therefore, these two types of water should be distinguished when analysing the hydromechanical behaviour of unsaturated soils.

Conventional water retention models are limited by the representation of pore space as a bundle of cylindrical capillaries, which ignores the adsorptive forces and liquid films at high suctions. As a consequence, these models would underestimate hydraulic conductivity under dry conditions and overestimate hydraulic process of activated clays

A. Ferrari and L. Laloui (eds.), *Advances in Laboratory Testing and Modelling of Soils and Shales (ATMSS)*, Springer Series in Geomechanics and Geoengineering,
DOI 10.1007/978-3-319-52773-4_53

(Navarro et al. 2015). Moreover, the dominated transport processes of capillary and adsorbed water are different, as well as the definition of relative and intrinsic permeabilities. To overcome these shortcomings, Or and Tuller (1999) proposed a new water retention model that differentiates the capillarity and adsorption. This concept was later used by Lebeau and Konrad (2010) to describe the hydraulic flow of capillary water and thin film. Recently, Navarro et al. (2015) validated these concepts using the experimental data of MX80 bentonite.

When using the general effective stress concept (Nuth and Laloui 2008), the conventional water retention models could overestimate the shear strength of unsaturated soils and predict unrealistic effective stress path (Qiao 2016). The reason is that the contributions to effective stress of capillary and adsorbed water are different. The effective water saturation concept was proposed to eliminate the error induced by adsorbed water (Vanapalli et al. 1996), which results in a better description of shear strength of soils. Therefore, the different mechanical contributions of capillary and adsorbed water should also be considered.

In summary, capillarity and adsorption should be differentiated to analyse the hydromechanical behaviour of unsaturated soils. This paper presents a thermodynamic analysis of unsaturated soils and derives the corresponding input work with the consideration of capillarity and adsorption. Then the energy-conjugate pairs are analysed and a constitutive framework is defined and discussed.

Thermodynamic Derivation and Justifications

General Assumptions

Using mixture theory and the first law of thermodynamics, many authors derived the input work to unsaturated soils and discussed the formulation of effective stress (e.g., Houlsby 1997). However, these works ignored the effect of adsorbed water or did not distinguish the capillary water and adsorbed water. Therefore we extended the framework proposed by Houlsby (1997) to include the influence of adsorbed water. In the presentation, the sign convention that compression is positive is used. The main assumptions are listed below.

(1) Adsorbed water exists around the surface of grains/particles and inside the aggregated particles that are micropores. It moves along with the solid part.
(2) Capillary water exists in pores between aggregated particles/grains, which are indentified as macropores.
(3) The solid, liquid and gas phases have the same, constant temperature. The solid and liquid is incompressible, while the gas phase stays in ideal condition.
(4) No mass, entropy or internal energy is transferred among the three phases.
(5) When analysing the macroscopic balance, the soil consists of aggregates/grains, capillary water and pore air. The aggregates/grains consist of solid phase, adsorbed water and pore air, and their average density changes.
(6) The pressure of capillary water affects the contact stress between particles/grains. The adsorptive pressure is an internal force acting on particles/grains that has no effect on the contact stress.

(7) Capillary water and adsorptive water have the same water potential.

In the following presentation, super(sub)scripts M and m mean the macropores and micropores respectively. Subscripts ag, g and l mean aggregates, gas phase and liquid phase respectively. The gas and liquid phases are named as fluid phase, represented as α. The porosity n and water saturation S_r are defined as,

$$n_M = \frac{V_l^M + V_g^M}{V_{ag} + V_l^M + V_g^M}, \quad n_m = \frac{V_l^m + V_g^m}{V_{ag} + V_l^M + V_g^M}, \quad n = n_M + n_m \tag{1}$$

$$S_r^M = \frac{V_l^M}{V_l^M + V_g^M}, \quad S_r^m = \frac{V_l^m}{V_l^m + V_g^m}, \quad V_{ag} = V_s + V_l^m + V_g^m \tag{2}$$

where V_c^d means the volume of c phase in d scale. The macroscopic stress is the summation of stresses acting on each phase. Thus,

$$\sigma_{ij} = (1 - n_M)s_{ij} + nS_r^M u_l \delta_{ij} + n\left(1 - S_r^M\right)u_g \delta_{ij} \tag{3}$$

where s_{ij} is the stress acting on the aggregates, u_l and u_g are water and gas pressures in macroscopic pores. δ_{ij} is Kronecker tensor. The soils' density ρ is,

$$\rho = (1 - n_M)\rho_{ag} + nS_r^M \rho_l + n\left(1 - S_r^M\right)\rho_g \tag{4}$$

The excess pore pressure gradients in water and air phases are defined by:

$$\tilde{u}_{l,i} = u_{l,i} - \rho_l g_i, \; \tilde{u}_{g,i} = u_{g,i} - \rho_g g_i \tag{5}$$

where g_i is the gravitational acceleration vector and a comma notation is used to indicate differentiation with respect to spatial coordinate. The strain rate is,

$$\dot{\varepsilon}_{ij} = -v_{(j,i)} \tag{6}$$

where v_i is the velocity vector of aggregates, the superposed dot indicates the time differential.

The total stress equilibrium equation is,

$$-\sigma_{ij,j} + \rho g_i = 0 \tag{7}$$

If the average velocities of the water and air phases are f_i^l and f_i^g, the artificial seepage velocities of the water $\left(w_i^l\right)$ and air $\left(w_i^g\right)$ phases are,

$$w_i^l = n_M S_r^M \left(f_i^l - v_i\right), \quad w_i^g = n_M\left(1 - S_r^M\right)\left(f_i^g - v_i\right) \tag{8}$$

The input work to a volume V with a bounding area A is the sum of the input work at the boundary and the work done by gravitational forces (Houlsby 1997),

$$W = -\left[u_l w_i^l + u_g w_i^g + \sigma_{ij} v_i\right]_{,j} + \left[\rho_l w_i^l + \rho_g w_i^g + \rho v_i\right] g_i \tag{9}$$

Submitting Eqs. (5) and (7) into Eq. (9) gives,

$$W = -\tilde{u}_{l,i} w_i^l - \tilde{u}_{g,i} w_i^g - u_l w_{i,i}^l - u_g w_{i,i}^g - \sigma_{ij} v_{i,j} \tag{10}$$

Macroscopic Mass Balance

At the macroscopic scale, the mass balance equations of aggregates, water and gas phases are,

$$\int_A \rho_{ag}(1-n_M) v_i n_i dA - \int_V c_{ag} dV = -\int_V \frac{d\left[\rho_{ag}(1-n_M)\right]}{dt} dV \tag{11a}$$

$$\int_A \rho_l n_M S_r^M f_i^l n_i dA - \int_V c_l dV = -\int_V \frac{d\left(\rho_l n_M S_r^M\right)}{dt} dV \tag{11b}$$

$$\int_A \rho_g n_M \left(1 - S_r^M\right) f_i^g n_i dA - \int_V c_g dV = -\int_V \frac{d\left[\rho_g n_M \left(1 - S_r^M\right)\right]}{dt} dV \tag{11c}$$

where c_{ag}, c_l and c_g are the exchange mass of aggregates, water and air between the macrosocpic scale and microscopic scale, respectively. Since the volume V is arbitrary and the liquid is incompressible, Eqs. (11a), (11b) and (11c) can be simplified as,

$$v_{i,i} = \frac{\dot{n}_M}{(1-n_M)} - \frac{\dot{\rho}_{ag}}{\rho_{ag}} + \frac{c_{ag}}{\rho_{ag}(1-n_M)} \tag{12a}$$

$$f_{i,i}^l = -\frac{\dot{n}_M}{n_M} - \frac{\dot{S}_r^M}{S_r^M} + \frac{c_l}{\rho_l n_M S_r^M} \tag{12b}$$

$$f_{i,i}^g = -\frac{\dot{n}_M}{n_M} + \frac{\dot{S}_r^M}{\left(1 - S_r^M\right)} + \frac{c_g}{\rho_g n_M \left(1 - S_r^M\right)} - \frac{\dot{\rho}_g}{\rho_g} \tag{12c}$$

Submitting Eqs. (12a), (12b) and (12c) into Eq. (8) gives,

$$w_{i,i}^l = S_r^M \dot{\varepsilon}_v - n_M \dot{S}_r^M - (1-n_M) S_r^M \frac{\dot{\rho}_{ag}}{\rho_{ag}} + \frac{c_l}{\rho_l} + S_r^M \frac{c_{ag}}{\rho_{ag}} \tag{13a}$$

$$w_{i,i}^g = \left(1 - S_r^M\right)\dot{\varepsilon}_v + n_M \dot{S}_r^M - (1 - n_M)\left(1 - S_r^M\right)\frac{\dot{\rho}_{ag}}{\rho_{ag}} + \frac{c_g}{\rho_g} + \left(1 - S_r^M\right)\frac{c_{ag}}{\rho_{ag}} - n_M\left(1 - S_r^M\right)\frac{\dot{\rho}_g}{\rho_g} \tag{13b}$$

where $\dot{\varepsilon}_v = -v_{i,i}$.

Microscopic Mass Balance

The mass exchange term c_{ag} is achieved through the exchange of water and air between aggregates and macropores, so the density of aggregates is related to c_{ag},

$$\dot{\rho}_{ag} = \rho_{ag}\frac{\dot{n}_M}{(1 - n_M)} + \frac{c_{ag}}{(1 - n_M)} - \rho_{ag} v_{i,i} \tag{14}$$

Considering,

$$\dot{n}_M = \frac{\dot{e}^M}{1+e} - \frac{e^M}{(1+e)^2}\dot{e} = -\dot{\varepsilon}_v^M + n_M\dot{\varepsilon}_v, \quad \dot{\varepsilon}_v = -\frac{\dot{e}}{1+e} = -\frac{\dot{e}^M + \dot{e}^m}{1+e} = \dot{\varepsilon}_v^M + \dot{\varepsilon}_v^m \tag{15}$$

where $\dot{\varepsilon}_v$ is the total volumetric strain rate, $\dot{\varepsilon}_v^M$ and $\dot{\varepsilon}_v^m$ are macroscopic and microscopic volumetric strian rate respectively. Submitting Eq. (15) into Eq. (14),

$$\dot{\rho}_{ag} = \frac{\dot{\varepsilon}_v^m}{(1 - n_M)}\rho_{ag} + \frac{c_{ag}}{(1 - n_M)} \tag{16}$$

The mass balance equations of water and air phases in aggegrates are,

$$\int_A \rho_l n_m S_r^m f_i^{lm} n_i dA - \int_V c_{lm} dV = -\int_V \frac{d\left(\rho_l n_m S_r^m\right)}{dt} dV \tag{17a}$$

$$\int_A \rho_g n_m\left(1 - S_r^m\right) f_i^{gm} n_i dA - \int_V c_{gm} dV = -\int_V \frac{d\left[\rho_g n_m\left(1 - S_r^m\right)\right]}{dt} dV \tag{17b}$$

where f_i^{lm} and f_i^{gm} are the velocities of water and air in aggregates repectively. Considering that V is arbitrary and applying the divergence theorem of Gauss,

$$-\rho_l \dot{n}_m S_r^m - \rho_l n_m \dot{S}_r^m + c_{lm} = \rho_l n_m S_r^m f_{i,i}^{lm} \tag{18a}$$

$$-\dot{\rho}_g n_m\left(1 - S_r^m\right) - \rho_g \dot{n}_m\left(1 - S_r^m\right) + \rho_g n_m \dot{S}_r^m + c_{gm} = \rho_g n_m\left(1 - S_r^m\right) f_{i,i}^{gm} \tag{18b}$$

Since,

$$f_i^{lm} = f_i^{gm} = v_i, \quad c_{lm} + c_l = 0, \quad c_{gm} + c_g = 0 \tag{19}$$

$$\dot{n}_m = \frac{\dot{e}^m}{1+e} - \frac{e^m}{(1+e)^2}\dot{e} = -\dot{\varepsilon}_v^m + n_m\dot{\varepsilon}_v \tag{20}$$

Equations (18a) and (18b) can be simplified as,

$$S_r^m\dot{\varepsilon}_v^m - n_m\dot{S}_r^m + \frac{c_{lm}}{\rho_l} = 0 \tag{21a}$$

$$\left(1 - S_r^m\right)\dot{\varepsilon}_v^m + n_m\dot{S}_r^m + \frac{c_{gm}}{\rho_g} = 0 \tag{21b}$$

Submitting Eqs. (16), (19), (20), (21a), (21b) into (13a), (13b) gives,

$$w_{i,i}^l = S_r^M\dot{\varepsilon}_v - n_M\dot{S}_r^M - n_m\dot{S}_r^m - \dot{S}_r^M\dot{\varepsilon}_v^m + \dot{S}_r^m\dot{\varepsilon}_v^m \tag{22a}$$

$$w_{i,i}^g = \left(1 - S_r^M\right)\dot{\varepsilon}_v + n_M\dot{S}_r^M + n_m\dot{S}_r^m - \left(S_r^m - S_r^M\right)\dot{\varepsilon}_v^m - n_M\left(1 - S_r^M\right)\frac{\dot{\rho}_g}{\rho_g} \tag{22b}$$

Total Input Work to Unsaturated Soils

The total strain ε_{ij} can be decomposed into macroscopic strian ε_{ij}^M and microscopic volumetric strian ε_v^m. Therefore,

$$\varepsilon_{ij} = \varepsilon_{ij}^M + \frac{1}{3}\varepsilon_v^m\delta_{ij} \tag{23}$$

Submitting Eqs. (22a), (22b) and (23) into Eq. (10) gives:

$$\begin{aligned} W = {} & \left[\sigma_{ij} - u_g\delta_{ij} + \left(u_g - u_l\right)S_r^M\delta_{ij}\right]\dot{\varepsilon}_{ij}^M + \left[p - u_g + \left(u_g - u_l\right)S_r^m\right]\dot{\varepsilon}_v^m \\ & - n_M\left(u_g - u_l\right)\dot{S}_r^M - n_m\left(u_g - u_l\right)\dot{S}_r^m - \tilde{u}_{l,i}w_i^l - \tilde{u}_{g,i}w_i^g + u_g n_M\left(1 - S_r^M\right)\frac{\dot{\rho}_g}{\rho_g} \end{aligned} \tag{24}$$

Equation (24) is the input work to unsaturated soils. The first and second terms demonstrate the work done by effective stresses and strains in the macroscopic and microscopic scales respectively. The third and fourth terms are the work done by water retention processes in macropores and micropores respectively. The fifth and sixth terms are the power dissipated by the flow of water and air through the soil. The last term means the work used to compress the gas phase.

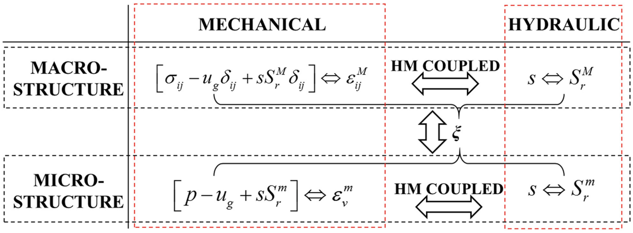

Fig. 1. Hydromechanical coupled framework for unsaturated soils.

Conclusions

As indicated in Eq. (24), four Energy-Conjugate Pairs (ECP) are necessary to describe the hydromechanical behaviour of unsaturated soils with the differentiation of adsorption and capillarity, which are summarized in Fig. 1. There are two mechanical ECPs and two water retention ECPs.

Therefore, the constitutive framework for unsaturated soils consists of four parts, including (1) the macroscopic mechanical law; (2) the capillary water retention model; (3) the microscopic mechanical law and (4) the adsorbed water retention model. The terms (1) and (2) are coupled through the macroscopic effective stress and used to describe the hydromechanical behaviour in the macro-structure. The terms (3) and (4) are linked by microscopic effective stress and used to capture the hydromechanical behaviour in the micro-structure. These two levels of models are then liked through a structure parameter ξ to obtain the global response of unsaturated soils. ξ indicates the contribution proportion of adsorptive mechanism and changes with hydraulic state, thermal loadings and mechanical loadings (Qiao 2016). Recently, some authors have reported constitutive models that belong to the framework illustrated in Fig. 1, such as Della Vecchia et al. (2013), Mašín (2013). If we neglect the microscopic parts, the framework becomes the conventional hydromechanical framework for unsaturated soils.

References

Houlsby GT (1997) The work input to an unsaturated granular material. Géotechnique 47 (1):193–196

Konrad JM, Lebeau M (2015) Capillary-based effective stress formulation for predicting shear strength of unsaturated soils. Can Geotech J 52(12):2067–2076

Lebeau M, Konrad JM (2010) A new capillary and thin film flow model for predicting the hydraulic conductivity of unsaturated porous media. Water Resour Res 46:W12554

Mašín D (2013) Double structure hydromechanical coupling formalism and a model for unsaturated expansive clays. Eng Geol 165:73–88

Navarro V, Asensio L, Morena DLG, Pintado X, Yustres A (2015) Differentiated intra- and inter-aggregate water content models of MX-80 bentonite. Appl Clay Sci 118:325–336

Nuth M, Laloui L (2008) Effective stress concept in unsaturated soils: clarification and validation of a unified framework. Int J Numer Anal Met 32(7):771–801

Or D, Tuller M (1999) Liquid retention and interfacial area in variably saturated porous media: upscaling from single-pore to sample-scale model. Water Resour Res 35(12):3591–3605

Qiao Y (2016) Thermoviscoplastic constitutive model and double-structure swelling model: application to nuclear waste geological disposal. PhD thesis, Tongji University

Romero E, Della Vecchia G, Jommi C (2011) An insight into the water retention properties of compacted clayey soils. Géotechnique 61(4):313–328

Tuller M, Or D, Dudley LM (1999) Adsorption and capillary condensation in porous media: liquid retention and interfacial configurations in angular pores. Water Resour Res 35(7):1949–1964

Vanapalli SK, Fredlund DG, Pufahl DE, Clifton AW (1996) Model for the prediction of shear strength with respect to soil suction. Can Geotech J 33(3):379–392

Della Vecchia G, Jommi C, Romero E (2013) A fully coupled elastic–plastic hydromechanical model for compacted soils accounting for clay activity. Int J Numer Anal Met 37(5):503–535

Zhou A, Huang RQ, Sheng D (2016) Capillary water retention curve and shear strength of unsaturated soils. Can Geotech J 53:1–14

Coupled Analysis of CO_2 Injection Induced Stress Variation in the Caprock

Chao Li(✉) and Lyesse Laloui

Laboratory of Soil Mechanics - Chair "Gaz Naturel" Petrosvibri,
Swiss Federal Institute of Technology, EPFL, Lausanne, Switzerland
chao.li@epfl.ch

Abstract. Caprock stability is crucial to be assessed in the carbon dioxide underground storage. The CO_2 injection not only generates pressurization but also induces thermal stresses because of the difference in injected CO_2 and *in situ* temperature. Exhibiting the combination of both effects, the caprock stability needs to be investigated. Numerical simulations are carried out to investigate the effects of thermo-mechanical coupled properties on the caprock stability. The results indicate that for a given geometrical configuration and a given temperature difference between injected CO_2 and reservoir, the deviatoric stress may increase or decrease, depending on the combination of thermal-hydro-mechanical properties: thermal expansion coefficient, stiffness and Poisson's ratio. Therefore the effects of material properties on the caprock stability should be addressed in a combined way for CO_2 injection problems.

Introduction

A large volume of CO_2 injections generates high overpressure in the reservoir which perturbs rapidly the stress field upon injection within the aquifer and extends to the caprock, as results of the main HM coupled processes (Li et al. 2015). In addition, the injection temperature is usually lower than that of the aquifer (Bissell et al. 2011), adding the thermal factor to the HM coupling. Both effects may be counterbalanced or superposed depending on the specific configuration of the problem, which deems a fully coupled thermal-hydro-mechanical THM investigation (Li and Laloui 2016). The low temperature injection may cause a reduction of compressive stress or even induce tensile stress in the caprock (Preisig and Prévost 2011) whereas an increase in stresses within the caprock has been concluded by (Vilarrasa et al. 2014). These studies are contradictory but they are actually complementary as demonstrated in this study. The main goal of this study is to investigate such problems with aid of numerical simulations and to elaborate a more rigorous conclusion for assessing the stress variation under low temperature CO_2 injection.

Thermal-Hydro-Mechanical Formulation

The compositional approach is employed for this study, as implemented for water and perfect gas by (Collin, 2003) in the finite element code *Lagamine*. This approach brings the advantage of writing the mass balance equation for two phase fluids in a

A. Ferrari and L. Laloui (eds.), *Advances in Laboratory Testing and Modelling of Soils and Shales (ATMSS)*, Springer Series in Geomechanics and Geoengineering,
DOI 10.1007/978-3-319-52773-4_54

straightforward manner. Based on this, we improve the current code with supercritical fluid properties, including terms for storage of both water and CO_2 in supercritical liquid, liquid and gashouse form, advective flow of both fluid, and non-advective flow of dissolved CO_2 in the water. Detailed formulation can be found in (Li and Laloui, 2016). Hereafter the THM governing equations are recalled. Water phase pressure p_w, CO_2 phase pressure p_c, temperature T and solid displacement field $\boldsymbol{u}$ are chosen as primary state variables to describe the state of the material. The mass balance equations (Eqs. 1 & 2), the energy balance Eq. 3 and the momentum balance Eq. 4 are expressed

$$\frac{\partial(nS_w\rho_w)}{\partial t} + \mathbf{div}(\rho_w\mathbf{q}_w) = 0 \quad \text{(mass balance of water)} \tag{1}$$

$$\begin{aligned}&\frac{\partial(n(1-S_w)\rho_c)}{\partial t} + \mathbf{div}(\rho_c\mathbf{q}_c)\\ &+ \frac{\partial(nS_w\rho_{dc})}{\partial t} + \mathbf{div}(\rho_{dc}\mathbf{q}_w) + \mathbf{div}(\mathbf{i}_{dc}) = 0 \quad \text{(mass balance of } CO_2\text{)}\end{aligned} \tag{2}$$

$$\frac{\partial H}{\partial t} + \mathbf{div}(\boldsymbol{\Gamma}) + \mathbf{div}(\mathbf{f_T}) = 0 \quad \text{(energy balance)} \tag{3}$$

$$\begin{aligned}&\mathbf{div}(\boldsymbol{\sigma}) +\\ &[(1-n)\rho_s + nS_w\rho_w + n(1-S_w)\rho_c]\mathbf{g} = 0 \quad \text{(momentum balance)}\end{aligned} \tag{4}$$

where $\boldsymbol{\sigma}$ is the Cauchy stress tensor, $\mathbf{g}$ the gravity acceleration vector, and n the porosity of the medium. ρ_w and ρ_c the densities of water, CO_2 and dissolved CO_2, respectively and S_w is the water saturation. ρ_{dc} represents the mass fraction of CO_2 dissolved in water and it is obtained through extended Henry law with CO_2 fugacity (Li and Laloui 2016). The liquid water is considered as a compressible and dilatant fluid, of which the linearized relationship for the density ρ_w definition is:

$$\rho_w = \rho_{w0}[1 + \kappa_T(p_w - p_{wr}) - \beta_w(T - T_r)] \tag{5}$$

where ρ_{w0} is the reference density for a given salinity at reference pressure p_{wr} and reference temperature T_r. κ_T is the isothermal water compressibility, β_w the volumetric thermal expansion coefficient of water. CO_2 cannot be considered as a perfect gas for its high pressure high temperature condition. Its properties (density and enthalpy) are calculated through Peng and Robinson's equations of state (EOS) (Peng and Robinson, 1976).

Among these terms, the liquid water flow $\mathbf{q}_w$ and supercritical/liquid CO_2 flow $\mathbf{q}_c$ are governed by the generalized Darcy's law:

$$\mathbf{q}_{w,c} = -\frac{\mathbf{k}k_{rw,rc}}{\mu_{w,c}}\left[\mathbf{grad}\left(p_{w,c}\right) + \rho_{w,c}\mathbf{g}\right] \tag{6}$$

where $\mathbf{k}$ is the intrinsic permeability and k_{rw}., k_{rc} are water and CO_2 relative permeability, which are geomaterial dependent parameters. μ_w is the dynamic viscosity of water and μ_c is the dynamic viscosity of $CO_{2.}$ which is valid for the range of temperatures and pressures considered here.

A van Genuchten function is used to describe the retention behaviour of rocks, and a power law for relative permeability:

$$S_w = \left(1 + ((p_c - p_w)/P_r)^{1/(1-m)}\right)^{-m} \tag{7}$$

$$\begin{aligned} k_{rw} &= S_w^{CKW} \\ k_{rc} &= (1 - S_w)^{CKC} \end{aligned} \tag{8}$$

where m and P_r are a material parameter and a reference pressure, CKW and CKC are material parameters.

The CO_2 diffusion in waters governed by Fick's law:

$$\mathbf{i}_{dc} = -nS_w\tau D_c\rho_w \mathbf{grad}\left(\frac{\rho_{dc}}{\rho_w}\right) \tag{9}$$

in which D_c is the diffusion coefficient of the dissolved CO_2 in the water phase and τ is the tortuosity of the porous media.

The heat transfer is composed of the heat conduction $\mathbf{\Gamma}$ and the convection $\mathbf{f_T}$. The mixture enthalpy H is defined as the sum of the heat of each constituent with neglect of the contribution of dissolved CO_2 in the water:

$$H = (1-n)\rho_s c_{p,s}(T - T_0) + nS_r\rho_w c_{p,w}(T - T_0) + n(1 - S_r)\rho_c h_c \tag{10}$$

where $c_{p,\alpha}$ is the heat capacity of the component α. The term h_c corresponds to the specific enthalpy of CO_2 which is temperature and pressure dependent. It is determined through the fundamental thermodynamics relationship by integrating the Peng and Robinson EOS (Li et al. 2016).

The heat transfer is governed by the heat conduction and convection:

$$\begin{aligned} \mathbf{\Gamma} + \mathbf{f_T} = &-(nS_w\lambda_w + n(1-S_w)\lambda_C + (1-n)\lambda_S)\mathbf{grad}T \\ &+ c_{p,w}(T - T_0)\rho_w\mathbf{q}_w + h_c\rho_c\mathbf{q}_c \end{aligned} \tag{11}$$

The total stress is decomposed into the generalized effective stress tensor $\boldsymbol{\sigma}'$ and fluid pressures:

$$\boldsymbol{\sigma} = \boldsymbol{\sigma}' + b(S_w p_w + (1 - S_w)p_c)\mathbf{I} \tag{12}$$

where $\mathbf{I}$ is the identity matrix. An important ingredient that contributes to the thermo-mechanical coupling is accounted for the definition of strain, due to the phenomenon of thermal expansion. The following description of thermo-elastic strains is used:

$$d\boldsymbol{\varepsilon} = \mathbf{E}^{-1} d\boldsymbol{\sigma}' - \alpha_s \mathbf{I} dT \tag{13}$$

where $d\boldsymbol{\varepsilon}$ is the total strain tensor increment, $\mathbf{E}$ the linear elastic tensor, α_s the thermal expansion coefficient. Using Young's modulus E and Poisson's ratio v to characterize the elastic geomaterial, we can write this expression in a more explicit form with indexed notation:

$$d\sigma'_{ij} = \frac{E}{1+v}\left\{d\varepsilon_{ij} + \frac{v}{1-2v} d\varepsilon_{kk}\delta_{ij}\right\} + \frac{E\alpha_s dT}{1-2v}\delta_{ij} \tag{14}$$

One can noticed from the above equation that the stress will reduce on the increment of the product of elastic properties, the temperature variation and the thermal expansion coefficient, when the material is evolving under the decrease of temperature in the absence of fluid pressure variation. A large temperature increment and high magnitude of the elastic modulus will certainly reduce more stress as illustrated by (Preisig and Prévost 2011).

Conceptual Model Characteristics

Figure 1 presents the geometry and the boundary conditions of the model under investigation. The model consists of three essential geology stratum involved in the CO_2 storage problem, sealing caprock, storage aquifer and underburden rock, which are porous media.

To understand the coupling of the overpressure, the temperature effect and thermal diffusion to the deformable porous media mechanics, it is necessary to define the

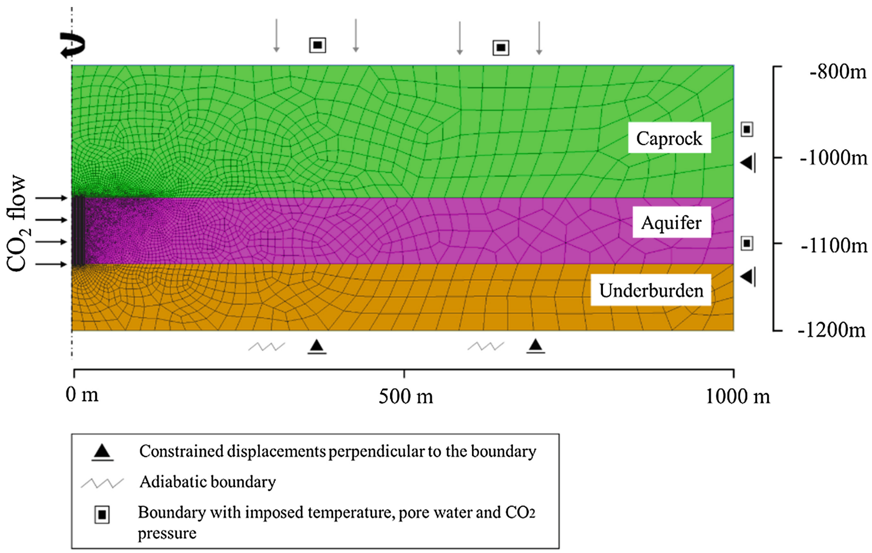

Fig. 1. Geometry, mesh and boundary condition of the model.

appropriate conditions that are encountered in a CO_2 storage project. The injection of CO_2 is modelled as a prescribed CO_2 mass flow at one million tonne per year through a vertical well along the thickness of the aquifer in a normal faulting system. The initial temperature of the reservoir is set as 330 K. The injection temperature is imposed at 300 K. The aquifer is considered to be water saturated prior to the injection, and acts as a host medium for CO_2. The caprock is nearly impermeable to prevent CO_2 from leakage. A constantly distributed stress of 13.5 MPa is applied along the top of the caprock, being equivalent to the overburden's dead load. The displacement on the right-hand side and bottom of the model is constrained in the perpendicular direction.

The sealing caprock usually involves very low permeability and porosity while the aquifer is much more porous, whereupon we consider clayey shale as caprock, and sandstone as storage rock as in most on-going CO_2 storage project (Metz et al. 2005). The fluid thermodynamic properties and geomaterial parameters are taken as typical averaged values from (Rutqvist and Tsang 2002). The model consists of 8723 quadrilateral elements and is run as an axisymmetric model. The initial stress equilibrium is obtained between the application of the body force and the lithostatic stress along the top of the caprock. The lateral earth pressure ratio is taken as *K0* = 0.6 as for a normal stress faulting system (Table 1).

Table 1. Material parameters for the reference model.

Thermal parameters	Symbol	Unit	Seal	Aquifer	Underburden
Saturated thermal conductivity	λ_s	W/(m.K)	1.50	2.50	1.50
Water thermal conductivity	λ_w	W/(m.K)	0.67	0.67	0.67
CO_2 thermal conductivity	λ_a	W/(m.K)	0.08	0.08	0.08
Solid specific heat capacity	$c_{p,s}$	J/(kg.K)	950	850	950
Water specific heat capacity	$c_{p,w}$	J/(kg.K)	4183	4183	4183
Solid thermal expansion coef.	α_s	K^{-1}	1×10^{-5}	1×10^{-5}	1.5×10^{-5}
Water thermal expansion coef.	β_w	K^{-1}	4.5×10^{-5}	4.5×10^{-5}	4.5×10^{-5}
Flow parameters					
Intrinsic permeability	k_{int}	m^2	1×10^{-18}	1×10^{-13}	1×10^{-18}
CO_2 relative permeability	k_{rc}	–	S_c^6	S_c^3	S_c^6
Water relative permeability	k_{rw}	–	S_w^6	S_w^3	S_w^6
Van Genuchten parameter	m	–	0.80	0.50	0.80
Van Genuchten parameter	P_r	MPa	0.60	0.02	0.60
Initial porosity	n_0	–	0.01	0.10	0.01
Tortuosity	τ	–	0.50	0.50	0.50
Other parameters					
Solid specific mass	ρ_s	kg/m^3	2700	2400	2700
Water specific mass	ρ_w	kg/m^3	1000	1000	1000
Mechanical parameters					
Young modulus	E	GPa	5.0	2.5	5.0
Poisson ratio	ν	–	0.30	0.30	0.30
Initial stress factor	$K0$	–	0.60	0.60	0.60

Influence of the Thermal-Mechanical Properties on the Caprock Stability

The thermal expansion coefficient governs the shrinkage level of the rocks upon cooling. Cooling induced stress reduction is sensitive to the thermal expansion coefficient and elastic properties as shown in Eq. 14. The quantitative influence of these parameters is interesting to be investigated.

For all the cases considered in Fig. 2, the reduction of the vertical effective stress is slightly higher than the values in Fig. 2e because the thermally induced stress variation in the vertical direction is very few as the material can contract freely. Figure 2a–c show graphs of the horizontal stress reduction at 100 day for three thermal expansion coefficients of the caprock $\alpha_c = \alpha_a$, $1.5\alpha_a$ and $2\alpha_a$ with α_a = *1.0E-5* in three cases. For the sake of clarity, the displacement is shown at 4 times of the first year only for $\alpha_c = 2\alpha_a$ in Fig. 2 as the other cases show very similar results. Nevertheless, the horizontal displacement is very constrained at the interface. Under such deformation constrained condition, the increase in the thermal expansion coefficient triggers a severe reduction of the horizontal stress consequently. The deviatoric stress is therefore increased for the cases 2a-2c. Note that for the case of $\alpha_c = \alpha_a$ (Fig. 2a), the horizontal stress drops more in the caprock than in the aquifer because the Young modulus of caprock is twice higher than that of the aquifer. This observation is confirmed with the Eq. 14, the cooling induced stress reduction is indeed controlled by the combination of

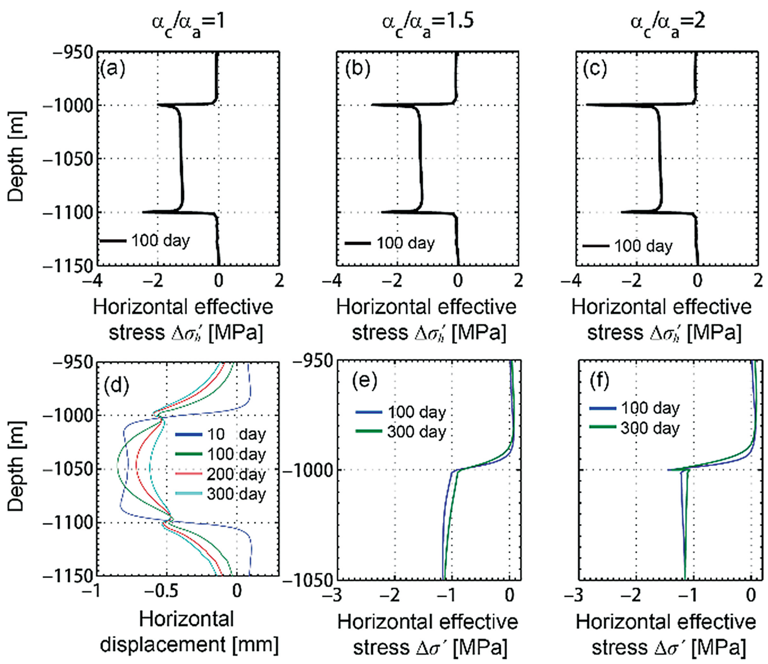

Fig. 2. Effect of the THM coupled parameters of the caprock on the horizontal stress variations and the horizontal displacement at 5 m away from the injection well.

three THM parameters as $\frac{E\alpha}{1-2\upsilon}$ for a same temperature diminution. At the interface aquifer-caprock, the ratio $R = \frac{E_c \alpha_c}{1-2\upsilon} / \frac{E_a \alpha_a}{1-2\upsilon}$ could indicate the stress reduction difference between the point in the caprock and that in the aquifer, if both are subjected to the same temperature drop.

Caprock's stiffness is thus investigated to discriminate the effect of $\frac{E\alpha}{1-2\upsilon}$ of caprock and aquifer. As shown in the Figs. 2e and f, two stiffness of the caprock $E_c = 1$ and 2 GPa are considered for a setup of thermal expansion coefficient $\alpha_c = 1.5\alpha_a$, $E_a = 2.5$ GPa for the aquifer and $\upsilon = 0.3$ for both caprock and aquifer. The results are shown for 100 days and 300 days after the beginning of injection. For the lowest value of $E_c = 1$ GPa, the ratio $R = \frac{E_c \alpha_c}{1-2\upsilon} / \frac{E_a \alpha_a}{1-2\upsilon}$ between the caprock and aquifer is small as $R = 0.6$. The decreased horizontal effective stress upon cooling is therefore lower in the caprock than that in the aquifer. The decrease in the vertical effective stress is higher than the horizontal one with this combination inside the caprock. The deviatoric stress is thus decreased. In the case that the stiffness of the caprock is equal to $E_c = 2$ GPa, shown in Fig. 2f, that is though smaller than that of the aquifer, $\frac{E\alpha}{1-2\upsilon}$ of the caprock becomes slightly higher due to a higher thermal expansion coefficient, leading to $R = 1.2$. The decrease in horizontal effective stress is thereby lightly more in the caprock than that in the aquifer. Slightly increase of the deviatoric stress is then occurring. As long as the ratio is high as $R = 4$ as illustrated in Fig. 2c, the horizontal stress has a major reduction and a sharp difference in the stress reduction is observed.

Conclusion

The interaction between the low temperature injection of CO_2 and the sealing caprock of a deep aquifer has been investigated by means of parametric studies. The study has revealed a high importance of the low temperature injection in relation to the stress variation caprock stability which are influencing by the coupled nature of the thermal, hydraulic, and mechanical phenomena that occur. It has been shown that the deviatoric stress (thus the caprock stability) may increase or decrease depending on the contrast of thermal-mechanical properties between the caprock and the aquifer.

References

Bissell RC, Vasco DW, Atbi M, Hamdani M, Okwelegbe M, Goldwater MH (2011) A full field simulation of the in Salah gas production and CO_2 storage project using a coupled geo-mechanical and thermal fluid flow simulator. Energy Procedia 4:3290–3297. doi:10.1016/j.egypro.2011.02.249

Collin F (2003) Couplages thermo-hydro-mécaniques dans les sols et les roches tendres partiellement saturés. University of Liège, Belgium

Li C, Barès P, Laloui L (2015). A hydromechanical approach to assess CO_2 injection-induced surface uplift and caprock deflection. Geomech Energy Environ. doi:10.1016/j.gete.2015.06.002

Li C, Laloui L (2016) Coupled multiphase thermo-hydro-mechanical analysis of supercritical CO_2 injection: Benchmark for the In Salah surface uplift problem. Int J Greenh Gas Control 51:394–408. doi:10.1016/j.ijggc.2016.05.025

Metz B, Davidson O, de Coninck H, Loos M, Meyer L (2005) IPCC Special Report on Carbon Dioxide Capture and Storage, IPCC. doi:10.1002/anie.201000431

Peng D-Y, Robinson DB (1976) A new two-constant equation of state. Ind Eng Chem Fundam 15:59–64. doi:10.1021/i160057a011

Preisig M, Prévost JH (2011) Coupled multi-phase thermo-poromechanical effects. Case study: CO_2 injection at In Salah. Algeria Int J Greenh Gas Control 5:1055–1064. doi:10.1016/j.ijggc.2010.12.006

Rutqvist J, Tsang C-F (2002) A study of caprock hydromechanical changes associated with CO_2 injection into a brine formation. Environ Geol 42:296–305. doi:10.1007/s00254-001-0499-2

Vilarrasa V, Olivella S, Carrera J, Rutqvist J (2014) Long term impacts of cold CO_2 injection on the caprock integrity. Int J Greenh Gas Control 24:1–13. doi:10.1016/j.ijggc.2014.02.016

Efficient Parameter Identification for THM Behaviour of Claystone Using Optimization Methods

Roger Schlegel(✉) and Johannes Will

Dynardo GmbH Weimar, Steubenstraße 25, 99423 Weimar, Germany
Roger.Schlegel@dynardo.de

Abstract. In the framework of the research for the thermo-hydro-mechanical effects of the clay host rock of a deep repository a numerical model to analyse the rock behaviour in response to heating was developed. The paper shows the developement of a 3D Thermal-Hydraulic-Mechanical (THM) simulator by coupling parametric modeling and implicit FE simulation environment in ANSYS. To calibrate the numerical model to the in-situ experimental results, powerfull methods of sensitivity analysis using optimized stochastic sampling strategies and optimization algorithms where used.

Project Aim

As a part of the nuclear waste management research powerful numerical solutions to study the thermo-hydro-mechanical effects of the rock behaviour in response to heating are necessary (Gens et al. 2006). The aim of the computational analysis was the parameter identification of calovo oxfordian claystone by Thermal-Hydraulic-Mechanical (THM) coupled recalculation of a heating experiment using a 3-dimensional simulation model. Using a sensitivity analysis, the essential interconnections between the measured end results and the input parameters should be identified. Using evolutional optimization algorithm in optiSLang® the best fit design with corresponding parameter set for calovo oxfordian claystone was identified.

3D Coupled THM-Simulation of a Heater Test

In Fig. 1 the Finite Element Model of the Heater Test is shown. Figure 2 shows the evolution of the three heating periods. Dynardo developed a 3D THM simulator by coupling ANSYS parametric modeling and implicit FE simulation environment with multiPlas (DYNARDO 2010).

An anisotropic material model containing the coupling of the isotropic Mohr-Coulomb model (rock matrix) and the anisotropic Mohr-Coulomb model (bedding plane) was generated with multiPlas and ANSYS®. This model was used for the continuum mechanical modeling of the claystone. The material model considers different behavior of the claystone in the pre and post fracture zone. The anisotropic behavour is caused by the layered bedding plane stucture of the claystone.

A. Ferrari and L. Laloui (eds.), *Advances in Laboratory Testing and Modelling of Soils and Shales (ATMSS)*, Springer Series in Geomechanics and Geoengineering,
DOI 10.1007/978-3-319-52773-4_55

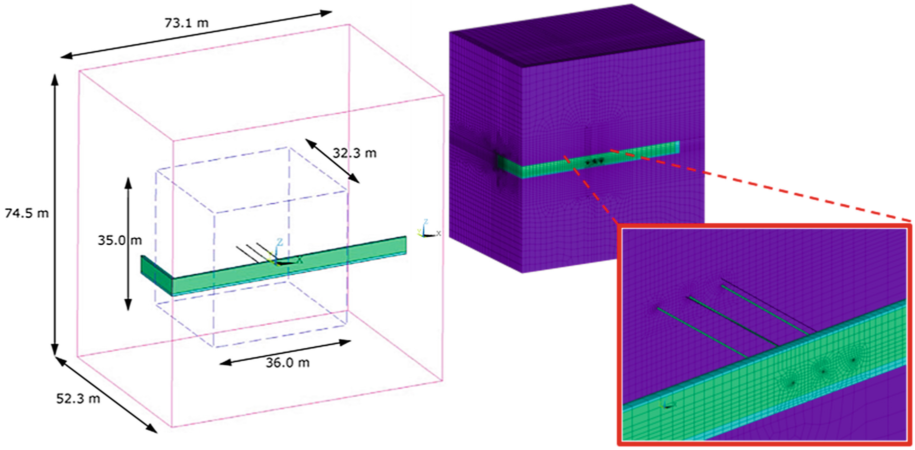

Fig. 1. Finite element model.

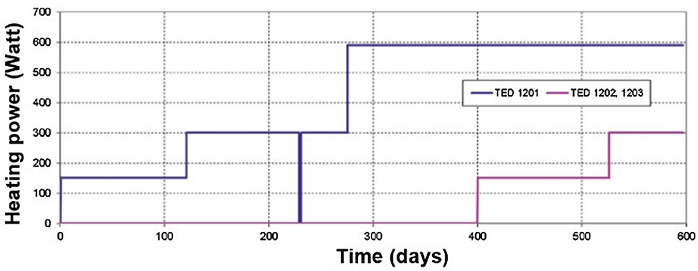

Fig. 2. Periods of heating.

The simulation of the construction process (tunneling) was conducted in the mechanical analysis by deactivation and activation the corresponding element areas. After deactivation of the claystone elements within the considered section, in a further step, the cladding elements of the tunnel were activated using the parameters of the shotcrete. The elements in the air and heater areas remained deactivated. The fracture sections were adapted to the FE mesh. For the thermal and hydraulic analyses, the construction process was considered analogously. Instead of activating and deactivating, the material properties of the respective elements of claystone to air and then air to shotcrete or heater were modified.

For the thermal-hydraulic-mechanical simulation, the following non-linear interactions between anisotropic thermal, hydraulic and mechanical material properties were considered:

- T-H coupling: the updating of the pore water pressure due to temperature changes and the temperature dependence of the hydraulic conductivity,
- T-M coupling: the influence of mechanical stress and deformation state by thermal expansion,

- H-M coupling: updating the effective stress due to pore water pressure changes and
- M-H coupling: the dependence of the hydraulic conductivity in comparison to the stress state and the vector of plastic strains as well as the updating of the pore water pressures due to stress changes

The change of the pore water pressure P is due to the changes of fluid volume ζ, volumetric expansion ε_v and temperature T (see Eq. 1).

$$\frac{1}{M}\frac{\partial P}{\partial t} = \frac{\partial \zeta}{\partial t} - \alpha\frac{\partial \varepsilon_v}{\partial t} + \beta\frac{\partial T}{\partial t} \tag{1}$$

with: M – Biot modulus, α – Biot-coefficient, β – thermal coefficient

The hydraulic conductivity of the claystone is formulated as a function of temperature and the stress-strain state. Here, the anisotropic permeability is dependent on the stress state, the vector of the plastic strain and the orientation of the bedding plane.

Sensitivity Analysis

Using optiSLang® (DYNARDO 2016), the FE model was parameterized. In the sensitivity analysis, the material parameters (including the parameters of the coupling dependencies) were varied within physically possible parameter limits. It should be investigated which of the material parameters have a relevant and physically understandable context for a comparison with the experimental results. For the analyzes, data of temperature and pore water pressure from a total of 17 measurement points were available. Due to the many uncertainties of the Tunnel excavation and the installation of the instruments, model calibration and parameter identification were limited to the

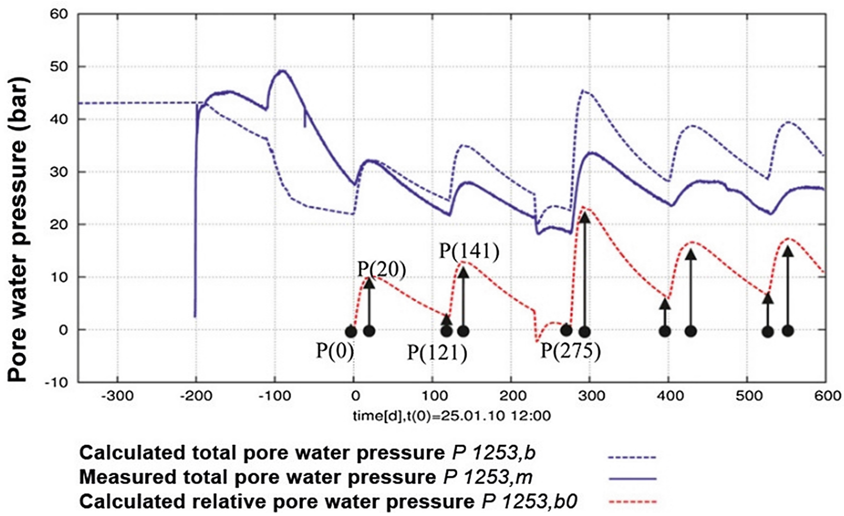

Fig. 3. Relative pore water pressures for parameter identification.

heating experiment. Here, not the total pore water pressure but the pressure differentials and gradients as results of the heating and applied to the beginning of the heating periods were considered (see Fig. 3).

For the sensitivities evaluation of the relative pore water pressures, discrete values at certain times were used. The selection of these response variables made an evaluation of the sensitivity at the beginning and the end of the respective heating phases as well as at the time of reaching the maximum pore water pressure possible. Important results of the sensitivity analysis could be derived from the CoP values (Coefficients of Prognosis), which show the significance of the input parameters. In order to determine the CoP values, the MOP (Metamodel of Optimal Prognosis) is generated by optiSLang showing the best correlation between the variation of response variables and input variables (Most and Will, 2011). OptiSLang® filters out automatically unimportant input parameters. This strategy allows optiSLang, with a minimal number of designs, to identify efficiently the significant input parameters even in large parameter spaces. Thereby, also non-linear correlations are detected.

Figures 4, 5 and 6 are examples of the measurement point 1251 showing the CoP values of the input variables for the relative pore pressures at the times t = 0 (start of heating), t = 20 days (reaching the maximum pore water pressure) and t = 121 days (end of the heating phase 1).

Evaluating the CoP values at all measuring points, it can be stated that at time t = 0 (before start of heating), especially the following input variables influence the pore water pressure:

- Perm_N_p, Perm_K_0_p - the permeability function of H-M coupling constants
- CG and phig - strength parameters (cohesion and friction angle) of the claystone
- M – Biot modulus

During the heating phases of the experiment especially the following input variables influence the pore water pressure:

- Alpha_f_fact - factor of the temperature-dependent volumetric expansion of the pore fluid (T-H coupling)

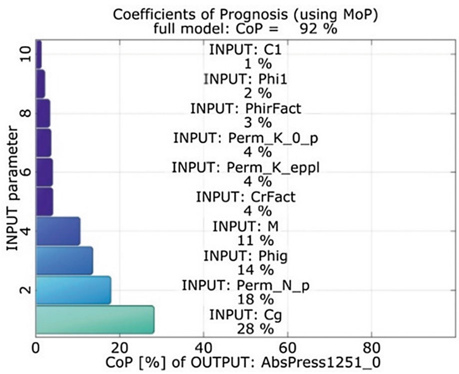

Fig. 4. CoP relative pore pressure at time t = 0, the measuring point in 1251.

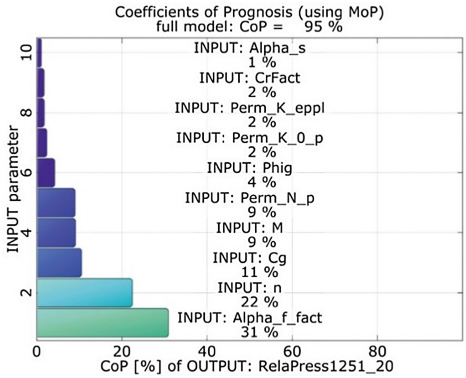

Fig. 5. CoP relative pore pressure at time t = 20 days, measurement point 1251.

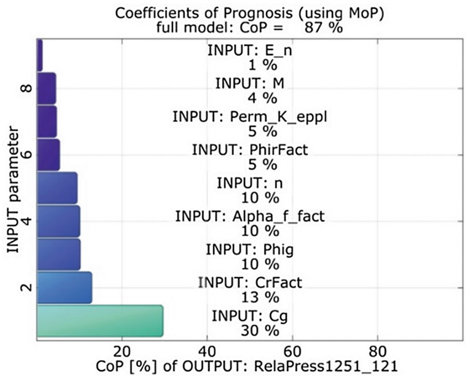

Fig. 6. CoP relative pore pressure at time t = 121 days, measurement point 1251.

- n - porosity (T-H coupling)
- Perm_N_p, Perm_K_0_p, Perm_N_n, Perm_K_0_n - permeability function of the H-M coupling constants,
- CG and phig - strength parameters (cohesion ans friction angle) of the claystone and
- M – Biot modulus

It can be seen that the pore water pressure increase at the beginning of each heating phase, is in particular influenced by the value Alpha_f_fact and n (values of the TH-coupling). The subsequent decrease of pore water pressure values, however, shows a significant correlation to the strength characteristics of the claystone (cg and Phig). This is an indication for the pore water pressure decline being particularly caused by stress redistribution, change of permeability and drainage effects. The high total CoP values of the individual response variables of >85% emphasize the high plausibility of the main physical phenomena by the identified correlation.

Furthermore, by comparing the scattering ranges of the calculated values with the time variations of the measurement results (see Fig. 7), evaluations about the model

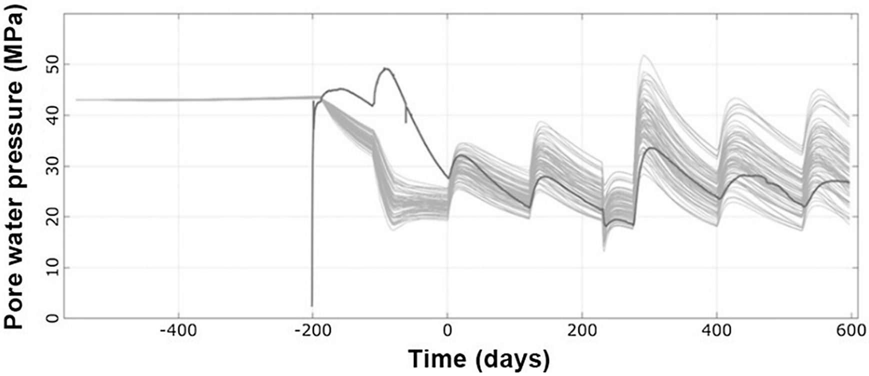

Fig. 7. pore water pressure at the measurement point 1253 with a scattering range of the simulation model.

quality and adjustability of the numerical model with the experimental results could be made. If the scattering range of the simulation model includes the measured evolution of parameters, a successful comparison within the selected parameter limits is possible. Figure 7 shows the correctness of this evaluation starting from the beginning of the experiment (t = 0).

Parameter Identification

Within the parameter identification, a set of input parameters is determined which simulates decently the time evolution of the measured and calculated temperatures and pore water pressures. Parameters not affecting the response variables in the sensitivity analysis were excluded from the parameter identification. They were taken into account with their reference values. Because the effects of initial disturbances (e.g. from tunnel excavation and installation of heating devices) decline in the course of the test, prognosis quality rises with each heating period. Therefore, the objective function for each heating periods were chosen with different priority factors (0.6 for heating period 1, 0.8 for heating period 2 and 1.0 for heating period 3). For the calibration of measurement and simulation, besides discrete values of the sensitivity analysis (see Fig. 3), also the integral differences between the measured and calculated ranges were considered.

For optimization, the adaptive response surface method being available in optiSLang was used. The comparison of the measured and calculated time signals of the temperatures and the relative pore water pressures (see Fig. 8) shows the very accurate simulation of the used model concerning the observed physical phenomena (thermal-hydraulic and thermo-mechanical as well as thermo-plastic effects) in the heating experiment.

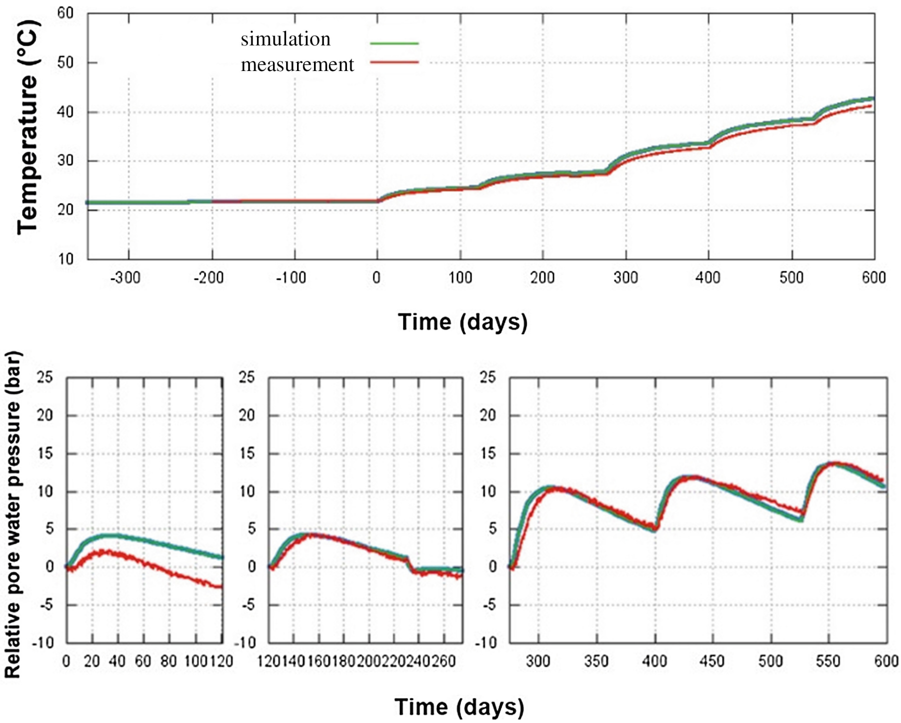

Fig. 8. Comparison of simulation vs. measurement at point 1252 after the parameter identification. Top: Temperature curve, Bottom: Relative pore water pressure of the three heating periods

Conclusions

Using powerful sensitivity and optimization algorithms in optiSLang, the most important parameters for THM coupled simulations in claystone (Callovo-Oxfordian) could be successfully identified. The precise simulation results of the measured and calculated differences of pressures illustrated the accurate evaluation of both the rising of the heating gradient of the pore water pressure due to the start of each heating phases and the subsequent declining gradient. The used simulation model and the THM coupling proved to be capable to explain the important thermal hydraulic effects (rising pore water pressure due to temperature increase) and thermo-mechanical effects (decrease of pore pressure due to changes of stress, drainage effects and plastic activities as well as related changes in the permeability). There are plans to continue using the developed THM simulator for future calculations or other identifications in the field of disposal sites research for hazardous waste in underground laboratories.

References

Dynardo 2010: multiPlas – elastoplastic material models for ANSYSn version 6.0. DYNARDO GmbH, Weimar, 2010, user's manual

Dynardo 2016: OPTISLANG - the optimizing Structural Language version 5.1.1, DYNARDO GmbH, Weimar, user's manual

Most T, Will J (2011) Sensitivity analysis using the Metamodel of Optimal Prognosis. In: Weimar Optimization and Stochastic Days 2011, Conference Proceedings

Gens A, Vaunat J, Garitte B, Wileveau Y (2006) Response of a saturated mudstone under excavation and thermal loading. In: Proceedings of Eurock 2006, multiphysics coupling and long term behaviour in rock mechanics, Liège, Belgium, pp. 35–44

A Thermodynamic Model for Rate-Dependent Geomaterials

Hao Wang and Xiaohui Cheng(✉)

Department of Civil Engineering, Tsinghua University, Beijing 100084, China
chengxh@tsinghua.edu.cn

Abstract. Geomaterials exhibit complicated rate-dependent behaviors. A deeper understanding and interpretation of these rate-dependent behaviors possess important theoretical and practical values. From the development of the rate-dependent constitutive model point of view, the paper deeply investigates the rate-dependent physical mechanisms and the mathematical models of soils. Based on the classical elasto-plastic models, traditional elasto-viscoplastic models apply viscous dissipations, similar to what has been used in fluid mechanics, for the description of rate-dependent dissipations. Traditional thermodynamic models are rate-independent. Starting from the theory of non-equilibrium thermodynamics and by introducing the matrix of migration coefficients, a thermodynamic rate-dependent model for soil is established, which is able to represent both the viscous dissipations and the non-viscous dissipations concerning rate dependency. The paper explores to which degree non-viscous dissipation, which is not familiar for the researchers of rock and soil mechanics, is able to describe the rate-dependent behaviors of soil, and carries out the constitutive modeling of one-dimensional compressional and three-dimensional shear behaviors of soil. The simulations are compared with those using elasto-viscoplastic models and the experimental results.

Introduction

The rate dependency of soft clays has long been viewed as an important topic of geotechnical engineering. Studies of the rate dependency of unbounded geomaterials such as sands, although quite limited compared with soft clays, shows that they also exhibit significant creep deformation in drained triaxial compression (TC) tests, plane strain compression tests and direct shear tests (e.g. Enomoto et al. 2006; Duttine et al. 2008). According to Ezaoui et al. (2011), the rate-dependent behaviors of soil can generally be divided into three categories, as shown in Fig. 1. Isotach is the typical behavior of bounded geomaterials with high packing density. Upon a sudden increase of strain rate, the shear stress increases accordingly and maintains above the loading curve of the original strain rate. For the cases where the bonding becomes weaker or the packing becomes looser, the behavior of geomaterials tends to be non-isotach. During constant-rate loading of different strain rates, TESRA (temporary effect of strain rate and acceleration) materials show rate independency, while P&N (positive and negative) materials exhibit negative correlation between stresses and strain rates. Upon a sudden change of strain rate, the stress of TESRA materials jumps and falls back onto the

A. Ferrari and L. Laloui (eds.), *Advances in Laboratory Testing and Modelling of Soils and Shales (ATMSS)*, Springer Series in Geomechanics and Geoengineering,
DOI 10.1007/978-3-319-52773-4_56

loading curve of the original strain rate, while that of P&N materials also jumps but falls below the loading curve of the original strain rate. “Combined” is a type of behavior between Isotach and TESRA.

Traditional soil mechanics usually apply elasto-viscoplastic models for the description of rate dependency. Early works can be traced back to the Isotach theory by Suklje and the time lines theory by Bjerrum. The subsequent developments include the one-dimensional abc model by Den Haan (1996) and the three-dimensional SSC model by Vermeer and Neher (1999). These models are generally developed for Isotach materials, but are able to be mathematically modified to include the TESRA or P&N behaviors (e.g. Enomoto et al. 2006; Ezaoui et al. 2011). It is necessary to point out that from the energy point of view, many of the elasto-viscoplastic models can violate the first or the second law of thermodynamics, and the physical mechanisms of rate dependency have not been explicitly explained.

In order to avoid producing thermodynamically unreasonable results, Houlsby and Puzrin (2000) established a thermomechanical framework for constitutive models of dissipative materials. Because of the selection of internal variables and dissipative functions, the framework is rate-independent.

Another thermodynamic approach starts from non-equilibrium thermodynamics. Based on the theory, Jiang and Liu (2003) established the framework of Granular Solid Hydrodynamics (GSH) for granular materials, in which rate dependency is naturally included. The GSH framework highlights two features. The first feature is the granular transient elasticity. GSH assumes that a granular system at rest can be described by its elastic energy. When external stimulation occurs, the former elastic state immediately breaks and the system rearranges during which both the elastic energy change (reversible deformation) and the energy dissipation (irreversible deformation) takes place simultaneously. The second feature is the “double entropy” theory. GSH assumes the energy dissipation occurs both macroscopically, into real entropy, and mesoscopically, through inter-particle colliding, rolling and sliding, into granular entropy. The granular entropy is ultimately transformed into real entropy, but not otherwise.

By applying GSH framework, Zhang and Cheng (2015a,b) proposed the Tsinghua Thermodynamic Soil (TTS) model for geomaterials. The model is able to simulate the complicated rate-dependent behaviors of geomaterials. Thermodynamic concepts such as dissipative force, dissipative flow and migration coefficients are used for the unified description of energy dissipation, instead of yield function or flow rule commonly used in soil mechanics. The model treats the total energy dissipation as the combination of viscous dissipation and non-viscous dissipation. In order to try to explore the specific rate-dependent physical mechanisms of geomaterials, the paper neglects the viscous dissipation part of TTS and focuses only on the part of non-viscous dissipation, to investigate to which extent non-viscous dissipation is able to simulate the rate-dependent behaviors observed in soil mechanics laboratory.

Formulations of the TTS Model for Rate Dependency

The paper takes the dry density ρ_d, the elastic strain tensor ε_{ij}^{e}, the temperature T and the granular temperature T_g as independent state variables. Wang et al. (2015) and

Zhang and Cheng (2015a) gives detailed explanations of the formulations. Here, due to the limitation of space, the equations are introduced briefly.

According to the theory of thermodynamics, under the framework of small-strain continuous mechanics, the free energy function can be expressed in four ways, namely the internal energy $u = u(\varepsilon_{ij}^e, s)$, the Helmholtz free energy $f = f(\varepsilon_{ij}^e, T)$, the enthalpy $h = h(\sigma_{ij}, s)$, and the Gibbs free energy $g = g(\sigma_{ij}, T)$. Where ε_{ij}^e and stress tensor σ_{ij}, T and entropy s are thermodynamic conjugates. The four expressions of energy are related through Legendre transformations. The paper takes the form of Helmholtz free energy and defines the elastic potential energy function of the granular system as:

$$\begin{cases} \omega_e = B(\varepsilon_{kk}^e + c)^{1.5}[(\varepsilon_{kk}^e)^2 + \xi(\varepsilon_s^e)^2] \\ B = B_0 \exp(B_1 \rho_d) \end{cases} \tag{1}$$

Where ε_{kk}^e is the elastic volumetric strain; $\varepsilon_s^e = \sqrt{e_{ij}^e e_{ij}^e}$ is the second elastic strain invariant; e_{ij}^e is the deviatoric elastic strain; B_0, B_1, c, ξ are material constants. The effective stress can then be expressed as the derivative of the elastic potential energy function:

$$\pi_{ij} = \frac{\partial \omega_e}{\partial \varepsilon_{ij}^e} = 1.5B\left(\varepsilon_{kk}^e + c\right)^{0.5}\left[\left(\varepsilon_{kk}^e\right)^2 + \xi\left(\varepsilon_s^e\right)^2\right]\delta_{ij} + 2B\left(\varepsilon_{kk}^e + c\right)^{1.5}\left(\varepsilon_{kk}^e \delta_{ij} + \xi e_{ij}^e\right) \tag{2}$$

According to non-equilibrium thermodynamics, the energy dissipation is expressed as the product of dissipative forces and dissipative flows. Under isothermal conditions, the dissipative forces of a granular system are the total strain rate $\dot{\varepsilon}_{ij}$, the effective stress π_{ij} and the granular temperature T_g (which is the thermodynamic conjugate of granular entropy S_g), and their corresponding dissipative flows are expressed as σ_{ij}^{vs}, Y_{ij} and I. Based on classical Onsager theory (Onsager 1931), at or near the thermodynamic equilibrium state, there is a linear relationship between the dissipative forces and the dissipative flows:

$$\begin{bmatrix} \sigma_{ij}^{vs} \\ Y_{ij} \\ I \end{bmatrix} = \begin{bmatrix} \chi_{ijkl} & \alpha_{ijkl} & 0 \\ -\alpha_{ijkl} & \lambda_{ijkl} & 0 \\ 0 & 0 & \gamma \end{bmatrix} \begin{bmatrix} \dot{\varepsilon}_{ij} \\ \pi_{ij} \\ T_g \end{bmatrix} \tag{3}$$

Where χ_{ijkl}, α_{ijkl}, λ_{ijkl} and γ are coefficients of migration. For simplicity, the coefficients are treated as scalars. The first term on the diagonal of Eq. 3 represents the viscous dissipation. The second term on the diagonal represents the energy change from elastic energy to granular entropy through inter-particle movements, or so called "non-viscous dissipation". The third term on the diagonal represents the transformation from granular entropy to real entropy, according to the "double entropy" theory. The off-diagonal term α_{ijkl} represents the coupling between viscous dissipations and non-viscous dissipations. Therefore, TTS model is able to account for both the viscous dissipation and the non-viscous dissipation. Here, in order to investigate only the non-viscous dissipation, χ_{ijkl} and α_{ijkl} are set to be 0.

Because of the assumption of granular transient elasticity, the total strain rate is decomposed into the sum of elastic strain rate and irrecoverable strain rate:

$$\frac{d}{dt}\varepsilon_{ij}^{e} = \dot{\varepsilon}_{ij} - Y_{ij} \tag{4}$$

According to the relaxation time concept (Jiang and Liu 2009), the irrecoverable strain rate is closely related to the elastic strain and the granular entropy:

$$Y_{ij} = \lambda_s T_g^a e_{ij}^e + \lambda_v T_g^a \varepsilon_{kk}^e \delta_{ij} \tag{5}$$

Where λ_s and λ_v are migration coefficients. a is a rate-dependent material constant.

Finally, the evolution of granular temperature is related to the dry density and the strain rates through a series of migration coefficients:

$$\frac{d}{dt}\tilde{T}_g + \frac{\tilde{T}_g}{m_3\rho_d} = \frac{m_1\dot{\varepsilon}_d^2 + m_2\dot{\varepsilon}_v^2}{m_3\rho_d}, \tilde{T}_g = \lambda_v^{1/a} T_g \tag{6}$$

Where m_1, m_2 and m_3 are migration coefficients. For simplicity, set $m_4 = \lambda_s/\lambda_v$. The TTS model with only non-viscous dissipation is then complete with 5 material constants (B_0, B_1, c, ξ, a) and 4 migration coefficients (m_1, m_2, m_3, m_4). The detailed calibration of the parameters can be found in Zhang and Cheng (2015a).

Analyses of Rate-Dependent Parameters and Simulations

Due to the reasonable dissipation mechanism, the TTS model is able to simulate the Isotach, TESRA and P&N behaviors without additional constructors. Particularly, the rate-dependent mechanism can be explicitly described when at the critical state defined by the critical state soil mechanics. From Eqs. 2∼6, in triaxial space, the state variables and stresses at the critical state are as follows:

$$\begin{cases} (\rho_d)_{cs} = const. & (\tilde{T}_g)_{cs} = m_1(\dot{\varepsilon}_d)_{cs}^2 \\ (\varepsilon_{kk}^e)_{cs} = 0 & (\varepsilon_d^e)_{cs} = (\dot{\varepsilon}_d)_{cs}^{1-2a}/(m_1^a m_4) \\ p'_{cs} = 1.5B\xi c^{0.5}(\dot{\varepsilon}_d)_{cs}^{2(1-2a)}/(m_1^{2a}m_4^2) & q_{cs} = \sqrt{6}B\xi c^{1.5}(\dot{\varepsilon}_d)_{cs}^{1-2a}/(m_1^a m_4) \end{cases} \tag{7}$$

Where subscript cs means critical state; p' and q are effective mean stress and shear stress. Detailed discussions of the equation, the vanishing elastic volumetric strain at the critical state, in particular can be found in Zhang and Cheng (2015b). Equation 7 indicates that both p' and q are proportional to the shear strain rate with a power of $1-2a$. Therefore at critical state, if $a<0.5$, the material shows the Isotach behavior with a positive correlation between stress and strain; if $a = 0.5$, the material shows the rate-independent TESRA behavior; if $a > 0.5$, the material shows the P&N behavior.

For the whole stress-strain curve, the rate dependency depends not only on a but also on m_3, as m_3 influences the production rate of granular entropy and the dissipation

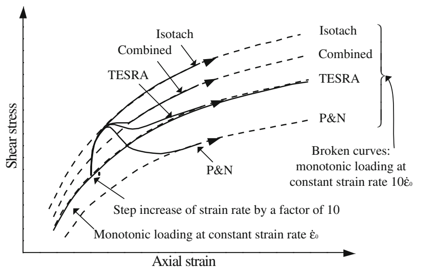

Fig. 1. Three basic types of geomaterials in TC tests (after Ezaoui et al. 2011).

Table 1. Parameters of the TTS model for different types of soil

Parameters	Haney clay	Silica No. 8 sand	Albany silica sand	Kaolin clay	Bangkok clay
B_0	300.0	500.0	135.5	800.0	195
B_1	0.0018	0.0034	0.0041	0.0026	0.0058
c	0.59	0.3	0.26	0.03	0.01
ξ	7.0	1.7	0.08	1.2	12.2
m_1	5.0	0.9	0.044	1.0	1900.0
m_2	5.0	10.1	8.5	5.0	1900.0
m_3	0.0004	0.005	0.0005	0.0001	0.005
m_4	50.2	30.5	2.6	3.3	0.4
a	0.485	0.5	0.54	0.45	0.485

rate from granular entropy to real entropy (Eq. 4). Normally, the model is rate-independent only if $a = 0.5$ and m_3 is very small. Figures 2, 3, 4 and 5 shows the simulation of TC tests of Isotach, TESRA and P&N behaviors. Figure 6 illustrates the simulation of sustained loading tests at various stages during otherwise CRS loading for Bangkok clay. The parameters for each type of soil are listed in Table 1.

Figure 2 presents the simulation of undrained TC tests of normally consolidated Haney clay carried out by Vaid and Campanella (1977). The samples were first isotropically consolidated to 525 kPa, then let stand in undrained condition for 12 h before the triaxial shear. The axial strain rates are 0.000094%/min, 0.15%/min and 1.10%/min. Both the TTS model and the SSC model give good simulation of the whole stress-strain curve. Here, parameter a of the TTS model is taken as 0.485.

Figure 3 illustrates the simulation of drained TC tests of normally consolidated Silica No. 8 sand by Kiyota and Tatsuoka (2006), where the effective principle stress ratio is defined as the ratio between the axial effective stress and the confining pressure. The samples were first isotropically consolidated to 400 kPa, then let creep for 180 min before the constant strain rate loading. Although the axial strain rates were different by a factor of up to 200, both the test data and the simulation curves indicate the TESRA behavior of the material. Here a is 0.5 and m_3 is quite small. The slight difference in the curves is caused by the difference of initial density.

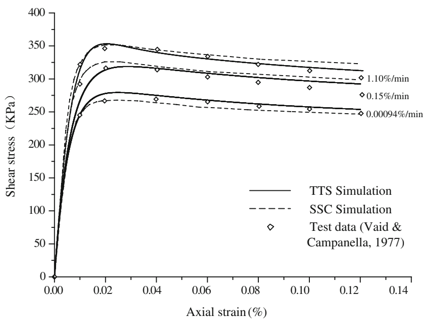

Fig. 2. Simulation of the Isotach behavior of Haney clay under undrained TC tests.

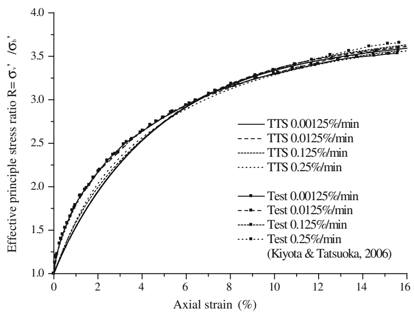

Fig. 3. Simulation of the TESRA behavior of Silica No. 8 sand under drained TC tests.

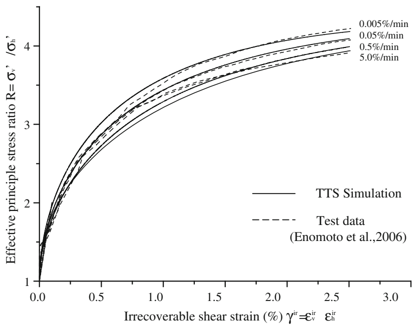

Fig. 4. Simulation of the P&N behavior of Albany silica sand under drained TC tests.

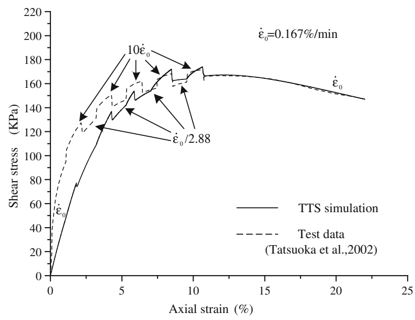

Fig. 5. Simulation of the undrained TC tests of kaolin clay with step changes of the axial strain rate.

Figure 4 shows the simulation of drained TC tests of poorly graded, non-viscous, round Albany silica sand carried out by Enomoto et al. (2006). The samples were first isotropically consolidated to 400 kPa, then let creep for 30 min before the triaxial shear. The irrecoverable shear strain is the difference between the axial and the radial irrecoverable strain. The test data of irrecoverable strains were obtained from two drained TC tests, while the irrecoverable strain in the TTS model is the difference between the total strain and the elastic strain. The model can well simulate the four constant rate loading curves of the P&N behavior. Here a is 0.54.

How to estimate the stress-strain curves with step changes of strain rates (as shown in Fig. 1) is often a problem for rate-dependent modeling. The elasto-viscoplastic models usually use fitting formulas. For example, Enomoto et al. (2006) added constructors such as ΔR and ΔR_r to represent the magnitudes of "jumps" and "falls" of the shear stress. While for the TTS model, the behaviors when change of rates totally depend on the rates of energy dissipation. Figure 5 presents the simulation of undrained TC tests of normally consolidated Kaolin clay by Tatsuoka et al. (2002). The samples were first isotropically consolidated to 350 kPa, then let stand for 20 h before triaxial shear. The initial axial strain rate was $\dot{\varepsilon}_0 = 0.167\%/\text{min}$. Through several times of stepwise change of strain rates to $10\dot{\varepsilon}_0$ and $\dot{\varepsilon}_0/2.88$, the shear stress reached its peak and the strain rate turned back to $\dot{\varepsilon}_0$. The difference between the test data and the simulation is quite obvious before the peak. The model is able to estimate the positive stress-strain correlation, but not the sudden "jumps" and "falls" of shear stress. The authors believe the physical mechanism of the "jumps" of stress lies in the viscous effect (the first term on the diagonal of Eq. 3) or the inter-particle locking effect (the off-diagonal term of Eq. 3), which is not considered in this non-viscous model.

The ability of the non-viscous TTS model is also investigated in CRS tests. In the test by Kongkitkul et al. (2011), the Bangkok clay sample was firstpre-consolidated to 100 kPa of axial stress for a day and then unloaded to 5 kPa, at which the sample was allowed to swell for another day. Finally, the CRS test began with the speed of $\pm 0.01\%/\text{min}$. During the test, three-hour sustained loading tests were performed at various stages, with the arrows in Fig. 6 showing the direction of creep. Figure 6

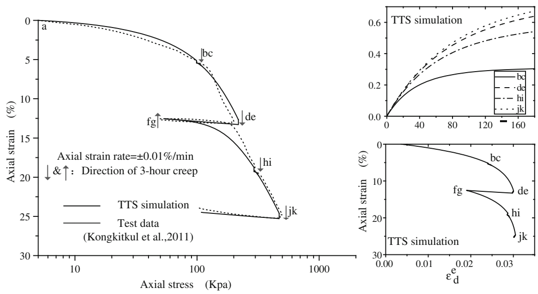

Fig. 6. Sustained loading tests at various stages during otherwise CRS loading for Bangkok clay.

indicates that the model can well simulate the loading-unloading behaviors and the creep performances. But without the consideration of viscous effects, the hysteresis loop of unloading-reloading is unsatisfactory. Here according to the theory of the TTS model, the physical mechanisms regarding the relative magnitudes and the directions of the creep stages are quite clear. From Eqs. 4 ~ 5, the 1D creep rate can be expressed as:

$$\dot{\varepsilon}_v = \sqrt{1.5}[\dot{\varepsilon}_d^e + m_4(\tilde{T}_g)^a \varepsilon_d^e] \tag{8}$$

For the normally consolidated loading stage, the production rate of granular entropy is the same as its dissipation rate, which indicates that T_g remains constant. Since the difference of $\dot{\varepsilon}_d^e$ through time is not obvious, according to Eq. 8, the creep rate mainly depends on ε_d^e. As shown in Fig. 6, the creep rates and the three-hour creep strains of sustained loading tests bc, de, hi and jk are positively correlated with ε_d^e. While for the test fg, ε_d^e and T_g decreases significantly during the unloading which makes $\dot{\varepsilon}_d^e$ the decisive term. Since $\dot{\varepsilon}_d^e$ is negative, the creep strain of test fg is negative, as is usually called "creep recovery" (e.g. Tatsuoka et al. 2002). The creep simulation is in accordance with the test results.

Conclusions

The Tsinghua Thermodynamic Soil (TTS) model presents a novel approach for simulating the complicated rate dependency of geomaterials. The paper provides a brief illustration of the constitutive equations to show how rate-dependent parameters and dissipation mechanisms affect the model performance. By only considering non-viscous dissipation, the model is able to simulate the monotonic loading of Isotach, TESRA and P&N type of geomaterials and the creep in one-dimensional sustained loading tests, but unable to accurately present the sudden change of stress due to stepwise change of strain rates in triaxial compression tests or the unloading-reloading hysteresis loops in CRS tests.

References

Den Haan EJ (1996) A compression model for non-brittle soft clays and peat. Géotechnique 46 (1):1–16

Duttine A, Tatsuoka F, Kongkitkul W, Hirakawa D (2008) Viscous behavior of unbound granular materials in direct shear. Soils Found 48(3):297–318

Enomoto T, Tatsuoka F, Shishime M, Kawabe S, Benedetto HD (2006) Viscous property of granular material in drained triaxial compression. In: Soil stress-strain behavior: measurement, modeling and analysis, pp. 383–397

Ezaoui A, Tatsuoka F, Duttine A, Benedetto HD (2011) Creep failure of geomaterials and its numerical simulation. Géotech Lett 1(3):41–45

Houlsby GT, Puzrin AM (2000) A thermomechanical framework for constitutive models for rate-independent dissipative materials. Int J Plast 16(9):1017–1047

Jiang Y, Liu M (2003) Granular elasticity without the Coulomb condition. Phys Rev Lett 91 (14):144301

Jiang Y, Liu M (2009) Granular solid hydrodynamics. Granular Matter 11(3):139–156

Kiyota T, Tatsuoka F (2006) Viscous property of loose sand in triaxial compression, extension and cyclic loading. Soils Found 46(5):665–684

Kongkitkul W, Kawabe S, Tatsuoka F, Hirakawa D (2011) A simple pneumatic loading system controlling stress and strain rates for one-dimensional compression of clay. Soils Found 51 (1):11–30

Onsager L (1931) Reciprocal relations in irreversible processes. I. Phys Rev 37(4):405–426

Tatsuoka F, Ishihara M, Benedetto HD, Kuwano R (2002) Time-dependent shear deformation characteristics of geomaterials and their simulation. Soils Found 42(2):103–129

Vaid YP, Campanella RG (1977) Time-dependent behavior of undisturbed clay. J Geotech Eng Div 103(7):693–709

Vermeer PA, Neher HP (1999) A soft soil model that accounts for creep. In: Proceedings of the International Symposium “Beyond 2000 in Computational Geotechnics”, pp. 249–261

Wang H, Chen Z, Cheng X (2015) A quasi-static and hysteretic constitutive model for sand based on granular solid hydrodynamics: a triaxial compression example. Geomechanics from Micro to Macro, IS Cambridge, pp. 639–644

Zhang Z, Cheng X (2015a) A thermodynamic constitutive model for undrained monotonic and cyclic shear behavior of saturated soils. Acta Geotech. doi:10.1007/s11440-015-0389-5

Zhang Z, Cheng X (2015b) Critical state and ultimate state surface of soils: a granular solid hydrodynamic perspective. Granular Matter 17(2):253–263

Thermo-Viscoplastic Subloading Soil Model for Isotropic Stress and Strain Conditions

J.R. Maranha(✉), C. Pereira, and A. Vieira

Geotechnics Department, National Laboratory for Civil Engineering (LNEC), Lisbon, Portugal
jmaranha@lnec.pt

Abstract. This paper presents a thermo-viscoplastic subloading soil model with a mobile centre of homothety. The model is formulated to describe the influence of non-isothermal conditions on the stress-strain-time behaviour of soils and is restricted to isotropic stress and strain conditions. Numerical simulations of three isotropic drained heating tests at constant isotropic effective stress for different overconsolidation ratios were performed. The model was able to accurately reproduce the experimental results.

Introduction

Experimental tests carried out by Cekerevac and Laloui (2004) in Kaolin clay samples showed, for overconsolidated soils, significant values of dilatant volumetric strains at the start of isotropic drained heating tests. These values appear significantly larger than the volumetric strains due to thermal expansion considering the values of the thermal expansion coefficients of the constituents (solid grain minerals and water).

In Vieira and Maranha (2016), numerical analysis with an inviscid thermo-elastoplastic model revealed significant shortcomings in describing the thermal response of overconsolidated soils. The model was not able to reproduce the large values of dilatant volumetric strains at the beginning of test. The computed values were limited by a realistic value for the elastic (reversible) thermal expansion.

Maranha et al. (2016) recently proposed a viscoplastic subloading model which has the capability of simulating the main aspects of rate-dependent soil behaviour. The model has a mobile centre of homothety, enabling the occurrence of viscoplastic strains inside the yield surface and avoiding the abrupt change in stiffness of the traditional overstress viscoplastic models, i.e. the elastoplastic soil hardening models (e.g. Cam Clay) extended into rate-dependent range using the formulation proposed by Perzyna (1966). The model showed the ability to reproduce the main observed aspects of time-dependent behaviour under complex loading paths.

To evaluate the possibility that rate dependent behaviour may influence the observed thermo-mechanical response, an extension of the viscoplastic model presented by Maranha et al. (2016), restricted to one-dimensional isotropic stress and strain, to non-isothermal conditions is presented. The mathematical formulation of the model is described and three drained heating tests at constant isotropic effective stress and different overconsolidation ratios are simulated.

A. Ferrari and L. Laloui (eds.), *Advances in Laboratory Testing and Modelling of Soils and Shales (ATMSS)*, Springer Series in Geomechanics and Geoengineering,
DOI 10.1007/978-3-319-52773-4_57

Thermo-Viscoplastic Subloading Soil Model

In this section, the mathematical formulation of a thermo-viscoplastic subloading soil model is presented. The constitutive model is formulated to represent the non-isothermal behaviour of soils for isotropic stress and strain conditions. This model is an extension to non-isothermal behaviour of the viscoplastic subloading soil model presented by Maranha et al. (2016), at this stage restricted to isotropic stress and strain conditions. Therefore, the capability of reproducing relevant soil behaviour's characteristics, under isotropic stress and strain conditions, such as elastic to viscoplastic smooth transition, loading reversals, rate-dependency as well as the occurrence of viscoplastic strains inside the yield surface is preserved.

Figure 1 schematically represents, in the isotropic effective stress space, p, the different homothetic surfaces of the model with a mobile centre of homothety, p_{a}. In one-dimensional isotropic effective stress space, the surfaces are represented as points. Considering that

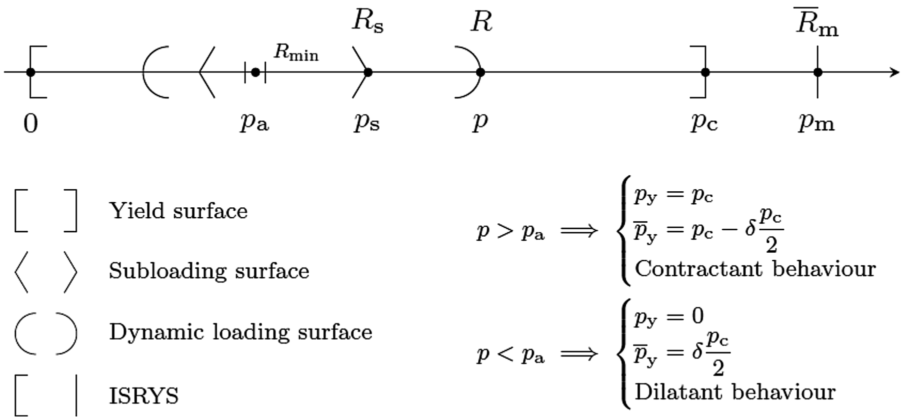

Fig. 1. Schematic representation, in the isotropic stress space, of the homothetic surfaces which define the thermal-viscoplastic subloading model with a mobile centre of homothety p_{a}.

$$p_y = p_a + \frac{1}{R}(p - p_a) \quad \text{and} \quad p_y = p_a + \frac{1}{R_s}(p_s - p_a)$$

is the homothetic image of both p and p_{s} on the yield surface relative to p_{a}, R and R_{s} are the homothetic ratios of the dynamic loading and subloading surfaces relative to the yield surface, respectively. The stress state is always on the dynamic loading surface. Additionally, it is assumed that $p_m = \bar{R}_m p_y$ is the homothetic image of p_{y} on the Infinite Strain Rate Yield Surface (ISRYS), with the centre of homothety at the origin of the stress space, where $\bar{R}_m$ is the respective homothety ratio relative to the yield surface. The ISRYS defines a limit to the evolution of the stress for very high volumetric strain-rates.

Subloading, Dynamic Loading and Yield Surfaces

f,$\hat{f}$ and $\bar{f}$ designate the yield, dynamic loading and subloading functions, respectively. The subloading and dynamic loading surfaces are determined from the yield surface as

$$\bar{f}(p) = f(p_y)\big|_{p_y = p_a + \frac{1}{R_s}(p-p_a)} = 0 \quad \text{and} \quad \hat{f}(p) = f(p_y)\big|_{p_y = p_a + \frac{1}{R}(p-p_a)} = 0,$$

respectively. The yield surface is given by

$$f(p) = p(p - p_c) = 0$$

where p_c is the size of the yield surface. R is given by

$$R = \begin{cases} 1 - \frac{p}{p_a} & \textit{if } p \leq p_a \ \wedge \ p_a \neq 0 \\ \frac{p_a - p}{p_a - p_c} & \textit{if } p > p_a \ \wedge \ p_a \neq p_c \end{cases}.$$

As described in Maranha et al. (2016), the constant $\bar{R}_m$ defines the scaling factor of the ISRYS and a variable R_m must be computed in order to obtain the viscoplastic strain rate by solving the equation

$$f(p_y)\big|_{p_y = \frac{1}{R_m}\left[p_a + \frac{R_m}{R}(p-p_a)\right]} = 0.$$

Viscoplastic Strain

Considering a dynamic plastic potential function $\hat{g}(p) = \hat{f}(p)$, the viscoplastic strain rate is defined as

$$\dot{\varepsilon}_v^{vp} = \begin{cases} 0 & \textit{if } \ R \leq R_{\min} \\ C\frac{\partial \hat{g}(p)}{\partial p} & \textit{if } \ R > R_{\min} \end{cases} \text{ with } \ C = \frac{1}{\mu}\frac{\exp[n(R - R_s)] - 1}{R_m - R}$$

where $R_{\min}$ defines a small elastic region in order to avoid numerical problems associated with $p = p_a$ (Fig. 1), μ the viscosity at absolute temperature T and n a material constant. $R - R_s$ is a measure of the distance of the isotropic effective stress to the subloading surface i.e., the overstress. Therefore, volumetric viscoplastic strain-rate occurs when p is outside the subloading surface, even when still inside the yield surface.

Hardening Laws

The subloading hardening law, represented by the evolution of R_s, is defined by

$$\dot{R}_s = \begin{cases} \dot{R}^e & \text{if } R = R_s \ \wedge \ \dot{R}^e \leq 0 \ \vee \ R \leq R_{\min} \\ -c_R \ln\left(\frac{R_s - R_{\min}}{1 - R_{\min}}\right) \left|\dot{\varepsilon}_v^{vp}\right| & \text{if } \textit{otherwise} \end{cases}$$

where always $R \geq R_s$. c_{R} is a material constant and $\dot{R}^e$ the rate of R assuming elastic behaviour, where the internal variables p_a and p_c can change due to T but not due to viscoplastic strains.

The movement of the centre of homothety is given by

$$\dot{p}_a = c_a \left|\dot{\varepsilon}_v^{vp}\right| \left(\bar{p}_y - p_a\right) + \frac{\dot{p}_c}{p_c} p_a \ \text{ with } \ \bar{p}_y = \delta \frac{p_c}{2} + (1 - \delta) p_y$$

where c_{a} is a material constant. The movement of p_{a} is directed towards $\bar{p}_y$, controlled by the constant δ, avoiding p_{a} being on the yield surface.

Extension to Non-isothermal Conditions

The extension of the viscoplastic subloading soil model to non-isothermal conditions (restricted to isotropic stress and strain) incorporates the reversible thermal expansion, thermal isotropic hardening and the evolution of the viscosity with temperature. Three additional material model constants are needed for thermal response.

The rate of the isotropic effective stress, $\dot{p}$, is given by

$$\dot{p} = K\left(\dot{\varepsilon}_v^e - \dot{\varepsilon}_v^T\right) = K\left(\dot{\varepsilon}_v - \dot{\varepsilon}_v^{vp} - \dot{\varepsilon}_v^T\right) \ \text{ with } \ K = \frac{p + p_e}{\bar{\kappa}} \ \text{ and } \ \dot{\varepsilon}_v^T = -\beta \dot{T}$$

where p_{e} is a material constant defined as the mean effective stress for which specific volume v become infinite, $\bar{\kappa}$ the slope of the unloading compression line in (ln p, ln v) plane, $\dot{\varepsilon}_v^T$ the volumetric strain due to thermal expansion and β the volumetric free drained thermal expansion coefficient. In this model β is not temperature dependent.

Following Vieira and Maranha (2016), the isotropic hardening rate $\dot{p}_c$ was defined as

$$\dot{p}_c = (p_c + p_e)\left[\frac{\dot{\varepsilon}_v^{vp}}{\bar{\lambda} - \bar{\kappa}} - d_T \dot{T}\right]$$

where $\bar{\lambda}$ is the slope of the normal compression line in (ln p, ln v) plane and d_{T} a constant that determines the rate at which the yield surface evolves with temperature.

Viscosity as a function of absolute temperature is given by

$$\mu = \mu_0 \left(\frac{T_0}{T}\right)^{\beta_\mu}$$

where μ_0 is the viscosity at $T = T_0$ and β_μ a constant of the model. The following properties are verified: $\mu = \infty$ when $T \to 0$ °K, $\mu = 0$ when $T \to \infty$ and $\mu(T_0) = \mu_0$.

Heating Tests for Different OCR Values

Cekerevac and Laloui (2004) presented an experimental study, where several samples of saturated Kaolin clay were isotropically consolidated to 600 kPa, followed by, in some cases, isotropic unloading to achieve different OCR values. Then, the samples were heated in drained conditions from 22 to 90 °C, with a heating rate of 10 °C per 3 h under constant mean effective stress. In this type of test the thermally induced volume change of a soil sample under constant mean effective stress is measured. As represented in Fig. 2, three isotropic drained heating tests were selected for comparison with the model's response: HT-T21 (OCR = 1), ISO-T1 (OCR = 6) and HT-T17 (OCR = 12).

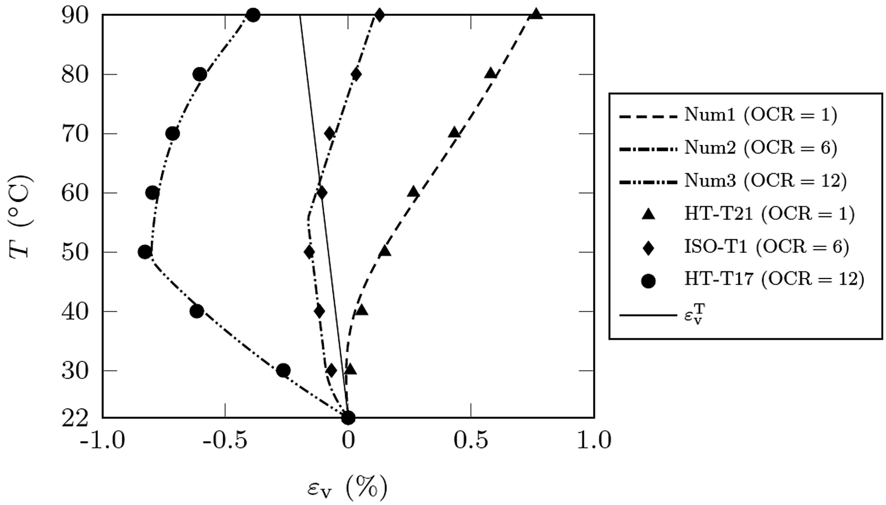

Fig. 2. Volumetric deformations of Kaolin clay under isotropic drained heating from 22 to 90 °C for three different OCR values: laboratory results obtained by Cekerevac and Laloui (2004) are represented by marks, numerical simulation results are represented by discontinuous lines and the volumetric strain due to reversible thermal expansion is represented by a continuous line.

The numerical simulation results of the three isotropic drained heating tests are represented in Fig. 2. Regarding the model's calibration, it was assumed that $\beta = 2.9 \times 10^{-5}$ °C^{-1} (Vieira and Maranha 2016), $T_0 = 20$ °C, $p_e = 0$ kPa, $R_{\min} = 10^{-10}$, $\delta = 0.01$ and $p_c(\text{OCR} = 1) = 600$ kPa. The remaining constants and initial values of internal variables were obtained by the application of a genetic algorithm (Pereira et al. 2014): $\bar{\kappa} = 0.0078$, $\bar{\lambda} = 0.024$, $c_R = 0.13$, $c_a = 4.1$, $\bar{R}_m = 3.1$, $\mu_0 = 5.1 \times 10^9$ kPa.s, $\beta_\mu = 16.9$, $n = 2.28$, $d_T = 0.0082$, p_s(OCR = 12) = 100.07 kPa, p_c(OCR = 12) = 184.7 kPa, p_a(OCR = 12) = 100.08 kPa, p_s(OCR = 6) = 112.1 kPa, p_c(OCR = 6) = 571.6 kPa, p_a(OCR = 6) = 137.6 kPa, p_s(OCR = 1) = 578.3 kPa, p_a(OCR = 1) = 495.5 kPa.

As can be seen, a good adjustment was obtained. The main aspects of soil response are correctly reproduced by the constitutive model.

For normally consolidated conditions (HT-T21 test) contractant inelastic volumetric strains take place from the beginning of heating in addition to the reversible thermal elastic strains, ε_v^T. For overconsolidated soils (OCR = 6 and 12), significant values of dilatant volumetric strains are observed at the beginning of the test (mainly for OCR = 12), with greater magnitude than the value of ε_v^T that is also represented in Fig. 2. The assumed value of the coefficient of thermal expansion, β, was based on the corresponding values of the minerals composing the solid phase (kaolin and quartz) and their respective fractions (Vieira and Maranha 2016). The viscous (rate-dependent) properties of the model were responsible for the adjustment by means of the assumption that the unloading stage, which precedes the thermal loading, was not slow enough to extinguish the viscoplastic dilatant volumetric strains associated with unloading. As a consequence, these viscoplastic strains will take place at the beginning of the thermal loading.

Figure 3 shows the evolution of p and the internal variables p_a, p_s and p_c during the three heating tests (with OCR = 1, 6 and 12). In both overconsolidated tests, the initial relative position of p, p_a and p_s (reflected in the values of R and R_s), results in dilatant volumetric viscous strains as $p < p_a$ and $p < p_s$. During the increase in temperature, p_s approaches p extinguishing the dilatant viscous strains, followed by p_a and p_s becoming smaller than p causing contractant viscoplastic strains. The movement of p_a, from the right to the left of p induces the transition from dilatant to contractant behaviour. In the normally consolidated case, p_c starts by decreasing, because the thermal softening is greater than the viscoplastic strain hardening, followed by an increase where the relative contribution of each factor is reversed.

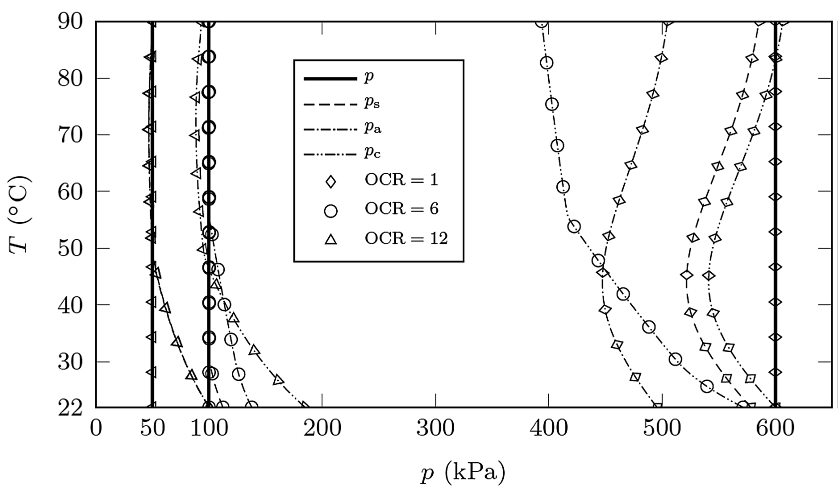

Fig. 3. Evolution of the isotropic effective stress, p, the subloading surface boundary point, p_s, the homothetic centre, p_a, and size of the yield surface, p_c, during the three drained heating tests.

Due to its rate dependent nature and the capability to simulate inelastic behaviour inside the yield surface, the model was capable of accurately reproducing the volumetric response to an increase in temperature of Kaolin clay samples with different stress consolidation histories.

Final Remarks

This paper presents an extension of a viscoplastic subloading soil model (Maranha et al. 2016), restricted to isotropic stress and strain, to non-isothermal behaviour with only three additional constants.

Results from isotropic drained heating tests were used to evaluate the capability of the model to simulate this type of behaviour. The model was shown to accurately reproduce the measured strains. Key aspects responsible for the model's performance were rate dependency as well as being able to reproduce inelastic behaviour inside the yield surface, including loading reversals.

Acknowledgements. The authors acknowledge the support provided by the Portuguese Foundation for Science and Technology, under the Project Success (Sustainability of shallow geothermal systems. Applied studies to southern Europe climates PTDC/ECM-GEO/0728/2014).

References

Cekerevac C, Laloui L (2004) Experimental study of the thermal effects on the mechanical behaviour of a clay. Int J Numer Anal Meth Geomech 28(3):209–228

Maranha JR, Pereira C, Vieira A (2016) A viscoplastic subloading soil model for rate dependent cyclic anisotropic structured behaviour. Int J Numer Anal Meth Geomech 40(11):1531–1555

Pereira C, Maranha JR, Brito A (2014) Advanced constitutive model calibration using genetic algorithms: some aspects. In: Proceedings of the 8th european conference on numerical methods in geotechnical engineering, Delft, The Netherlands. CRC Press, Boca Raton, pp 485–490

Perzina P (1966) Fundamental problems in viscoplasticity. Adv Appl Mech 9(2):244–368

Vieira A, Maranha JR (2016) Thermoplastic analysis of a thermoactive pile in a normally consolidated clay. Int J Geomech. doi:10.1061/(ASCE)GM.1943-5622.0000666

Numerical Simulation of Multi-phase Flow in CO_2 Geological Sequestration

X.W. Wang[1], B. Ye[1(✉)], Y.L. Xiong[1], F. Zhang[1,2], K.Y. Li[1], and W.M. Ye[1]

[1] Tongji University, Shanghai, China
yebin@tongji.edu.cn
[2] Nagoya Institute of Technology, Nagoya, Japan

Abstract. Global warming is an important environmental issue today, and the increasing concentration of carbon dioxide (CO_2) in the atmosphere is considered to be the main causative factor. CO_2 sequestration in geological formations is regarded as one of the most promising approaches for reducing the emission of anthropogenic CO_2. Predicting the migration and evaluating the long-term stability of CO_2 injected into geological formations is a major concern in CO_2 sequestration projects. A numerical method is an effective and economical approach to achieve this goal. In this paper, a numerical method based on the three-phase (rock-water-CO_2) theory and energy conservation law was established. To verify this numerical method, the Norwegian Sleipner CO_2 geological sequestration project in Utsira formation was simulated to obtain the distribution of CO_2 after a certain time of continuous injection.

Introduction

Global warming is an important environmental issue today. In the past century, the average global temperature has risen 0.6 ± 0.2 °C (Metz et al. 2005, Houghton et al. 1992). And it resulted in polar ice melting as well as sea level rise. In all kinds of greenhouse gases that cause the climate change, CO_2 emission from human activities accounts for 65% of the total (Mccarthy 2001). From 1959 to 2009, the average annual change of carbon dioxide concentration in the atmosphere and temperature outliers of land surface, both of which show an increasing trend, consists of each other. Reducing the CO_2 content in the atmosphere is vitally necessary to alleviate environmental degradation.

Carbon capture and storage (CCS) (or carbon capture and sequestration) is the process of capturing waste carbon dioxide (CO_2) from large point sources, such as fossil fuel power plants, transporting it to a storage site and depositing it where it will not enter the atmosphere, normally an underground geological formation. CCS is regarded as one of the most promising approaches for reducing the emission of anthropogenic CO_2.

It is important to study and understand how CO_2 migrates and distributes in the aquifer. It helps us to choose a right site and decide how to inject. There are two main methods to study the CO_2 migration in an aquifer: in-situ experiment and simulation. Some countries have conducted in-situ experiments. Basically, seismic wave and

A. Ferrari and L. Laloui (eds.), *Advances in Laboratory Testing and Modelling of Soils and Shales (ATMSS)*, Springer Series in Geomechanics and Geoengineering,
DOI 10.1007/978-3-319-52773-4_58

drilling are the most common methods to monitor the migration and distribution of CO_2 after the injection. But it is quite expensive and time-consuming due to the fact that migration of CO_2 in the aquifer is very slow. As such, simulation is considered to be a very important and economical approach to study the migration and distribution of CO_2 in an aquifer. Quite a lot of researchers have conducted various studies on the numerical approach to understand the behaviour of CO_2 in deep aquifer. For example, two-dimensional model was built and applied to study the migration of injected CO_2 in Utsira underground layers at Sleipner site (Audigane et al. 2007).

In this paper, a THM coupled numerical method based on three-phase (rock-water-CO_2) theory and energy conservation law was established. The following content mainly focuses on the verification of the numerical method.

Governing Equations for CCS Numerical Simulation

The proposed numerical method for CCS numerical simulation mainly adopts the following governing equations:

(1) Equilibrium equation

$$\frac{\partial \sigma_{ij}}{\partial x_j} + \rho b_i = 0$$

where σ_{ij} is the stress tensor, ρ is the density of the mixture of the three phrases, b_i is the body force.

(2) Continuum equation of water phase

$$\frac{\dot{\varepsilon}^s_{ii}}{n} - \frac{k^w}{\gamma^w}\frac{\partial^2 p^w_d}{\partial x_i \partial x_i} - \frac{1}{K^w}\dot{p}^w_d - 3\alpha^w_T \dot{T} + \frac{1}{S_r}\dot{S}_r = 0$$

where ε^s_{ij} is the strain tensor, n is the porosity, γ is the bulk density, k is the coefficient of permeability, p_d is the excessive pore pressure, K is the volume compressibility coefficient, α_T is the thermal expansion coefficient, T is the temperature, S_r is the saturation degree for water phase. In all the above and the following equations, the superscripts s, w, c indicate the variables for solid phase, water phase and CO_2 phase, respectively.

(3) Continuum equation of CO_2 phase

$$\frac{\dot{\varepsilon}^s_{ii}}{n} - \frac{k^c}{\gamma^c}\frac{\partial^2 p^c_d}{\partial x_i \partial x_i} - \frac{1}{K^c}\dot{p}^c_d - 3\alpha^c_T \dot{T} - \frac{1}{1 - S_r}\dot{S}_r = 0$$

(4) Equation of energy conservation

$$\rho c \frac{\partial T}{\partial t} + nS_r(\rho c)^w v_i^w \frac{\partial T}{\partial x_i} + n(1 - S_r)(\rho c)^c v_i^c \frac{\partial T}{\partial x_i} = k_t \frac{\partial^2 T}{\partial x_i \partial x_i} + Q$$

where c is the specific heat, v is the velocity, k_t is the heat conductivity, Q is the energy produced by heat source per unit volume.

Based on these governing equations, a program code was developed for CCS numerical simulation.

Verification of the Numerical Method

To verify this numerical method, two models of the Norwegian Sleipner CO_2 geological sequestration project in Utsira formation was simulated to obtain the distribution of CO_2 after a certain time of continuous injection.

Setup of Model A

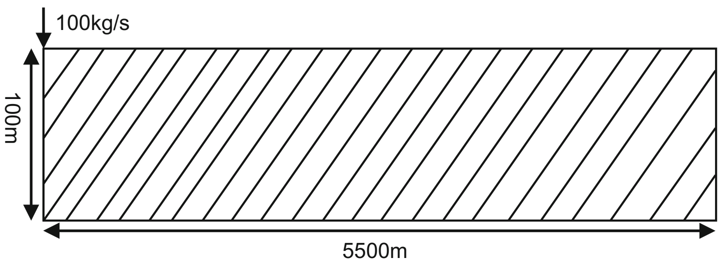

Fig. 1. Model A.

Model A (Fig. 1) is the simplest model to simulate the two-phase flow in deep aquifer. The effect of gravity and temperature change is ignored in this model. It is a half cross profile of a cylinder. CO_2 will be injected into isotropic and horizontally infinite aquifer through the centre of the cylinder which is the top-left corner of model A. The thickness is set to 100 m and the radius is set to 5500 m. The radius of the injection well is 0.3 m and the injection rate is 100 kg/s which is the same as the CO_2 emission speed of a 288 million Watt thermal power plant. The whole finite element area is divided into 10 $\times$ 550 cells. The top and bottom are no-flow boundaries. In the aquifer, CO_2 horizontally diffuses away from the injection well.

The migration and distribution of CO_2 over 10000 days (27.38 years) is simulated. Key parameters for this simulation are listed in Table 1.

Table 1. Key parameters.

Permeability (m^2)	10^{-13}
Porosity	0.12
Thickness (m)	100
Coefficient of compressibility (Pa^{-1})	4.5×10^{-10}
Uniform Pressure Field (MPa)	12
Uniform Temperature Field (°C)	45
CO_2 injection rate (kg/s)	100

Result of Model A

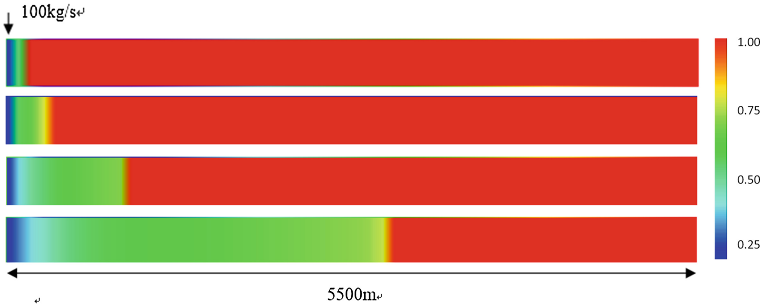

Fig. 2. CO_2 saturation contour after continuous injection at 30, 100, 1000 and 10000 days.

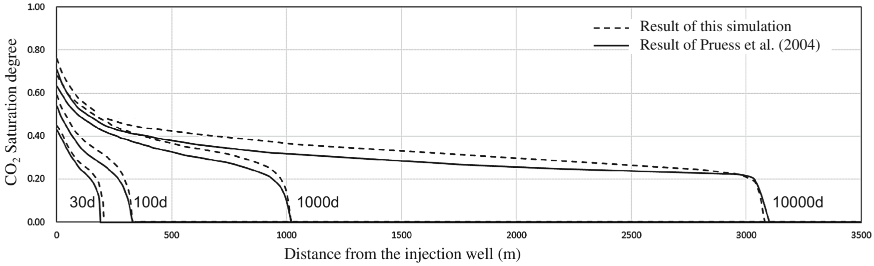

Fig. 3. Relationship of CO_2 saturation and horizontal distance to the injection well.

In Fig. 2, the simulated distribution of CO_2 after continuous injection of 30, 100, 1000 and 10000 days are shown from top to bottom. It is obvious that in the figure the area with high CO_2 saturation increases with time.

In Fig. 3, the dash line shows the result of this simulation and the solid line shows the result of Pruess et al. (2004). The four groups of lines from left to right are the results at different injection duration which are respectively 30, 100, 1000 and 10000 days. In comparison, for simulation results of all time duration, the dash line and solid line match each other.

Setup of Model B

A multi-layer model, which is a simplification of Utsira formation at Sleipner site (Pruess et al. 2004), is established to simulate the distribution of CO_2 after it is continuously injected into a reservoir that consists of homogeneous, isotropic and horizontally infinite layers. As shown in Fig. 4, the benchmark model has 9 layers of the porous rock and shale next to each other. The porous rock which is sandstone which has higher permeability and the shale, which can be called cap rock, has low permeability. CO_2 will be injected into porous rock which contains water (Fig. 5). The upper and lower shale are impermeable. The van Genuchten's theory (1980) is applied to the relative coefficient of permeability. Simulation duration is 1000 days. Key parameters for this simulation are listed in Table 2.

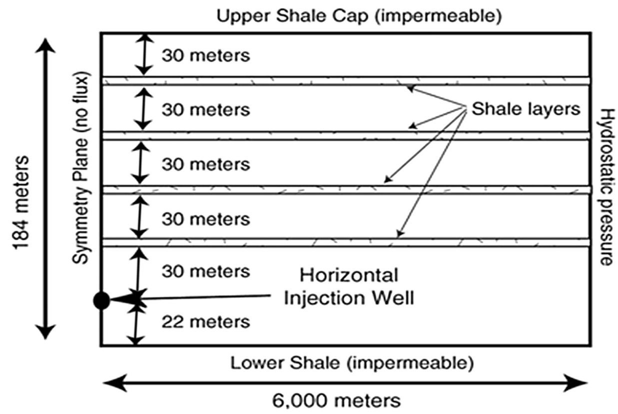

Fig. 4. Benchmark model of Sleipner (Pruess et al. 2004) for Model B.

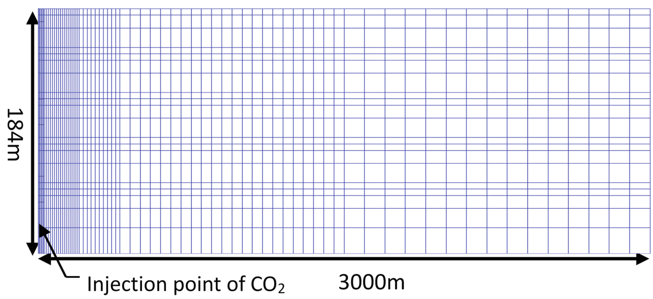

Fig. 5. Mesh setup.

Table 2. Parameter for model B.

	Sandstone	Shale
Permeability (m^2)	3×10^{-12}	1×10^{-14}
Porosity	0.35	0.1025

Result of Model B

Fig. 6. Saturation of water in the aquifer model after 30, 150 and 700 days (top to bottom).

The injection duration is 1000 days. The contour map of water saturation in the aquifer is shown in Fig. 6. From top to bottom, the three figures illustrate the situation of 30, 150 and 700 days after the CO_2 injection. As shown in the figure, CO_2 concentrates below each layer of the cap rock. And the saturation of CO_2 decreases from top to bottom in each porous rock layer.

Figure 7 shows the CO_2 saturation along the depth at the position where $x = 500$ m. The diagram on the left is the result of Pruess et al. (2004) and the right one is the simulation of this paper. The result indicates that in a same porous rock layer, CO_2 saturation increase vertically from bottom to top. And the area right below every layer of cap rock has the highest CO_2 saturation. The result is quite close to Pruess et al.'s (2004) work.

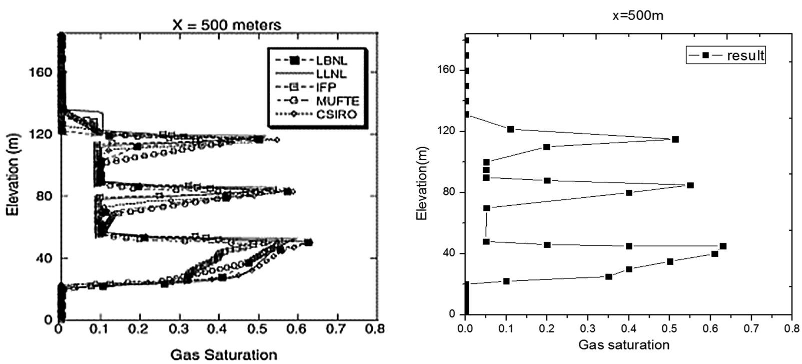

Fig. 7. CO_2 saturation along the depth (The result of Pruess et al. (2004) is on the left).

Conclusion

After the verification through two different models and comparison made with other benchmarks, it is confirmed that the method is qualified to simulate the CO_2 migration and distribution in porous rock. Two brief conclusions can be made based on the simulation of this paper:

If the effect of gravity is ignored, CO_2 saturation will decrease as the distance to the injection point increases. The CO_2 saturation-distance line can be divided into three parts according to the slope. From $x = 0$, the saturation of CO_2 decreases sharply as x increases and then enters a zone where it decreases very slowly. After this, CO_2 saturation again decreases sharply to zero.

If the effect of gravity is considered, CO_2 moves upwards and is able to permeate the low permeability cap rock. Inside an aquifer layer, the upper part has the highest CO_2 saturation because of cap rock. The horizontal distribution of CO_2 is basically the same as the case in which the effect of gravity was not considered.

References

Metz B, Davidson O, Coninck H, Loos M, Meyer L (2005) IPCC special report on carbon dioxide capture and storage: intergovernmental panel on climate change, Geneva, Switzerland

Houghton JT, Callander BA, Varney SK (1992) Climate change 1992: the supplementary report to the IPCC scientific assessment. Cambridge University Press

McCarthy JJ (2001) Climate change 2001: impacts, adaptation, and vulnerability: contribution of working group II to the third assessment report of the intergovernmental panel on climate change. Cambridge University Press

Audigane P, Gaus I, Czernichowski LI, Pruess K, Xu T (2007) Two-dimensional reactive transport modeling of CO_2 injection in a saline aquifer at the Sleipner site. North Sea Am J Sci 307(7):974–1008

Pruess K, García J, Kovscek T, Oldenburg C, Rutqvist J, Steefel C, Xu T (2004) Code intercomparison builds confidence in numerical simulation models for geologic disposal of CO_2. Energy 29(9):1431–1444

van Genuchten MT (1980) A closed-form equation for predicting the hydraulic conductivity of unsaturated soils. Soil Sci Soc Am J 44(5):892–898

Mechanics and Modeling of Cohesive Frictional Granular Materials

S. Singh(✉), R.K. Kandasami, and T.G. Murthy

Department of Civil Engineering,
Indian Institute of Science, Bangalore 560012, India
saurabh@civil.iisc.ernet.in

Abstract. In nature, weakly cemented granular materials are encountered in the form of soft rocks such as limestone, sandstone, mudstone, shale, etc. The mechanical behaviour of these materials is quite different from the purely frictional granular materials. The presence of cementation between the grains causes a significant variation in mechanical response under complex boundary conditions. In order to understand the manifestation of this interparticle cohesion at the ensemble level, we have used a hollow cylinder torsional testing apparatus which is capable of independently controlling the magnitude and the direction of the three principal stresses. From this experimental programme, the small strain response, peak strength and post peak behaviour with changing intermediate principle stress ratio (*b*) and initial mean effective stress (I_1) is studied. In addition to the analysis of stress strain behaviour at different *b* and I_1, stress-dilatancy characteristics of these cohesive frictional material are also discussed. This experimental study is followed by calibration and validation of a single hardening constitutive model which considers cementation as additional confinement. Observations from validation exercises suggest that this consideration works well for stress-strain response whereas it fails to predict the volumetric behaviour.

Introduction

Natural sands subjected to saline environment over a long period of time develop cementatious bonds between the grains due to precipitation of organic and inorganic matter (Clough et al. 1981; O'Rourke and Crespo 1988; Santamarina et al. 2001; Mitchell and Soga 1976). Other instances of cohesive-frictional materials are seen in many other geo-engineering applications, for example, geomaterials are stabilized using cement in high way application for strengthening subgrade, for canal lining, in earthen dams and for other earthen fills. Cement is also used to improve the liquefaction resistance of contractive sands. Presence of these cohesive bonds changes the mechanical behaviour of sands under different loading conditions. When sheared, these cemented sands shows a more rigid and contractant behaviour in comparison with reconstituted uncemented sands under similar test conditions. At small strain, these cemented sands show a pseudo-equilibrium state or metastable state (since at larger strains, inter particulate cohesive bonds are destroyed and a reduction in the ensemble stress is seen with further shearing).

A. Ferrari and L. Laloui (eds.), *Advances in Laboratory Testing and Modelling of Soils and Shales (ATMSS)*, Springer Series in Geomechanics and Geoengineering,
DOI 10.1007/978-3-319-52773-4_59

Obtaining undisturbed cemented sand specimens for testing in the laboratory is extremely challenging, because of which most laboratory studies of soft rocks and cohesive frictional materials have involved artificially reconstituted “weakly cemented” sands (Clough et al. 1981; Coop and Atkinson 1993; Huang and Airey Airey 1993). To study the mechanical behaviour of these weakly cemented sands, direct shear, triaxial and simple shear test were carried out with varying initial density, confining pressure, amount and type of cementation etc. (Coop and Atkinson 1993; Leroueil and Vaughan 1990; Huang and Airey 1998; Lade and Overton 1989; Airey 1993; Cuccovillo and Coop 1997; Menendez et al. 1996; Abdulla and Kiousis 1997; Ismail et al. 2002; Schnaid et al. 2001). These studies suggest that the presence of cement or cohesion between particles enhances elastic stiffness and peak strength with reduction in ductility. The volumetric response shows more dilative behaviour in comparison to pure sand under similar conditions. With further increase in the cementation, it is observed that the peak strength increases and the strain required to mobilize this peak strength decreases. In the post peak behaviour a transition from brittle to ductile mode of failure is observed with increasing confining pressure and decreasing density.

We present results of conventional triaxial compression tests and hollow cylinder tests performed on a reconstituted weakly cemented sand ensemble at different confining pressures and intermediate principal stress ratios, respectively. The stress-dilatancy plots obtained from these experiment is discussed next which is followed by a study on the performance of a single hardening elasto-plastic constitutive model to predict the stress strain and volumetric response of these weakly cemented materials.

Experimental

A series of HCT experiments on reconstituted weakly cemented sand specimens are performed in this programme. These specimens are prepared by mixing sand with 4% of ordinary Portland cement (53-grade) at optimum moisture content of 18% to a density of 1.5 g/cc (through static compaction). A hollow cylinder mould (inner diameter - 60 mm, outer diameter - 100 mm, height - 200 mm) was used to cast the specimens. After preparation, specimens were cured under moist condition for 14 days.

This experimental study is performed using hollow cylinder torsional shear apparatus (GDS, UK) shown in the Fig. 1. Unlike conventional triaxial shear apparatus, hollow cylinder apparatus is capable of performing tests along different stress paths, not only on the triaxial plane but also on the octahedral plane, identified by intermediate principal stress ratio $\left(b = \frac{\sigma_2 - \sigma_3}{\sigma_1 - \sigma_3}\right)$. This study comprises of conventional triaxial experiments (with constant confining pressure of 50, 300, 450 kPa) and test performed at constant mean effective stress of 300 kPa with b ranging from 0.0 to 1.0 at an interval of 0.2. In all the experiments, specimens were saturated with an effective stress of 20 kPa and isotropically consolidated to desired effective stress before shearing under drained condition at a strain rate of 0.5% per min.

The peak stress state and the critical state were identified in all the tests. The results are analysed in the critical state soil mechanics framework. We further utilize these experimental results for calibrating a third generation constitutive model, details of which are present in the ensuing.

Fig. 1. An image of HCT apparatus with specimen inside HCT cell.

Description of Constitutive Model

In this study, Lade's single hardening constitutive model (Kim and Lade 1988; Lade and Kim 1988a; Lade and Kim 1988b) is calibrated with the results of conventional triaxial experiments and further validated with tests performed at a constant mean effective stress of 300 kPa with *b* ranging from 0.0 to 1.0 at an interval of 0.2. The details about the model and extraction of model parameters are provided in Kim and Lade 1988; Lade and Kim 1988a; Lade and Kim 1988b. Model parameters for artificially weakly cemented sand used in this study are provided in Table 1.

Table 1. Lade's model parameters for artificially weakly cemented sand.

Elastic Parameters			Failure Parameters			Plastic Potential Parameters			Hardening Parameters		Yield Parameters	
υ	M	λ	a	m	η	ψ_1	ψ_2	μ	C	p	h	α
0.23	456	0.27	1.14	0.19	27	0.013	-3.3	2.59	8.9E-5	2.24	0.069	1.42

Results and Discussion

In this study, two sets of tests were performed as discussed in experimental section. A series of conventional triaxial compression tests with varying confining pressures are performed. The mechanical behaviour of these cohesive frictional granular materials obtained from these experiments is presented in Fig. 2 with deviatoric effective stress (q) vs. deviatoric effective strain (ε_q) and volumetric strain (ε_v) vs. deviatoric effective strain plots. Deviatoric effective stress (q), deviatoric effective strain (ε_q), volumetric strain (ε_v) and mean effective stress (p) are defined as follows:

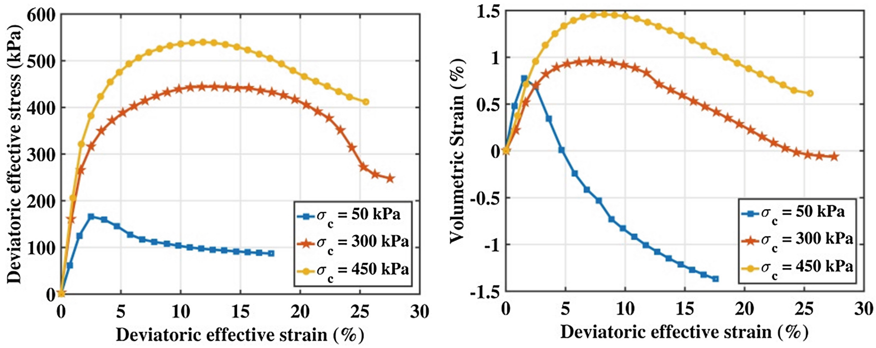

Fig. 2. Stress strain and volumetric strain plots for confining pressure ($\boldsymbol{\sigma_c}$) of 50 kPa, 300 kPa, and 450 kPa.

$$q = \sqrt{3J_{2\sigma}}, \varepsilon_q = \frac{2}{\sqrt{3}}\sqrt{J_{2\varepsilon}}, \varepsilon_v = I_{1\varepsilon}, p = \frac{I_{1\sigma}}{3}$$

Where $I_{1\sigma}$, $I_{1\varepsilon}$ are first invariants of stress and strain tensor, respectively. $J_{2\sigma}$, $J_{2\varepsilon}$ are second invariants of the deviatoric stress and strain tensor.

From Fig. 2, it is observed that elastic stiffness along with peak strength of cemented sand specimen increases with increase in confining pressure whereas volumetric response becomes increasingly contractive. Ductility of the specimen also increases with increasing confining pressure.

Second set consists of experiments performed at a constant mean effective stress of 300 kPa with b of 0.2, 0.4, 0.6, and 0.8. The results of stress strain and volumetric response are plotted in Fig. 3. For test preformed at constant mean effective stress, elastic stiffness is independent of b, which implies that specimen is isotropic, although peak strength varies with changing b. With change in 'b' from the compression zone

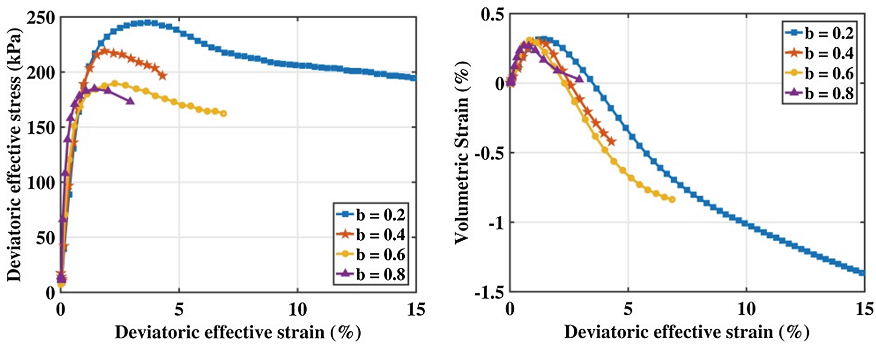

Fig. 3. Stress strain and volumetric strain plots for intermediate principal stress ratio (b) of 0.2, 0.4, 0.6, 0.8 at a constant mean effective stress of 300 kPa (mean effective stress of 300 kPa was kept constant throughout the test.).

(b = 0 – 0.2) to tension side (b = 0.8 – 1.0), peak strength decreases and material response changes from ductile to brittle behaviour. However, the volumetric response is not significantly affected with intermediate principal stress ratio. As a general trend, the specimen initially contracts following which it dilates with progress of shear.

Figure 4 shows stress ratio $\left(\eta = \frac{q}{p}\right)$ vs. plastic dilatancy $\left(D_p = \frac{\Delta\varepsilon_v^p}{\Delta\varepsilon_q^p}\right)$ plots for constant mean effective stress tests with different intermediate principal stress ratio and varying confining pressure. Typically, for granular materials, the point of maximum dilatancy coincides with point of peak stress ratio. However, in case of weakly cemented granular material there is a lag between these two states. It is apparent that material initially contracts and then dilates before reaching a brittle failure or zero dilatancy state (critical state). Maximum plastic dilatancy remains unaffected with changing intermediate principal stress ratio whereas peak stress ratio decreases with increasing b. Mode of failure for specimen tested at lower b and higher confining pressure is ductile since final plastic dilatancy reaches a near zero value. However for higher b and lower confining pressure failure mode is brittle, in which, failure is accompanied with strain localization or shear banding.

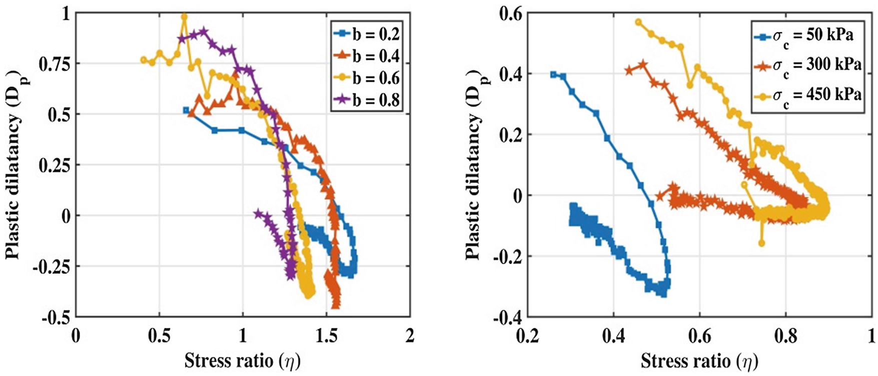

Fig. 4. Stress dilatancy plots for b of 0.2, 0.4, 0.6, 0.8 and confining pressure ($\boldsymbol{\sigma_c}$) of 50 kPa, 300 kPa, and 450 kPa.

The behaviour of weakly cemented sand is intriguing as it has facets of behaviour that resemble both a cohesive material such as concrete/rock and a typical frictional ensemble such as sand. At low strains the network of soil and cementatious bonds resist the load with initial mobilization of strain occurring due to the breakage/damage in the bonds since the sand grains are significantly stiffer and stronger than cohesive/ cementatious bonds. For traditional cohesive materials like soft rocks or concrete wherein the cohesive matrix dominates the behaviour (Moavenzadeh and Kuguel 1969; Van Mier 1984), the fractures lead to a drastic brittle failure, while in case of weakly cemented sands resistance beyond the peak brittle failure is provided from particle rearrangement (dilation). With further shearing material reaches a state where resistance comes from pure friction.

The volumetric response at low strain level remains contractive till the start of bond breakage, following which the sample dilates (and records a drop in strength). Further increase in strain level brings forth dilation due to particle rearrarrangement (and increase in the strength). When these cemented sand samples are sheared, at the microscale, a slight densification of bonds, breakage of bonds, particle rearrangement, and eventually localization mobilized only through friction occur simultaneously, in that no clear demarcation of strain magnitudes or threshold stress values can be obtained here. This simultaneous occurrence of bond breakage and dilation at the interparticle level manifests itself as a peak in stress-strain response as has been observed through some post deformation studies through microscopy and tomography (Kandasami et al. 2016).

These experimental results are used to benchmark Lade's model for weakly cemented sand. This constitutive model was originally suggested for purely frictional granular materials, which was subsequently extended to cohesive frictional granular materials by translating the stress space along the hydrostatic axis to provide extra confinement offered by the cohesive bonds. In this study we have used single point integration to validate the model for elemental test response rendered by hollow cylinder testing. Results from the validation exercise are plotted in Fig. 5 for different intermediate principal stress ratio. It can be seen that the model prediction response matches well with the experimental results for stress-strain behaviour whereas prediction of volumetric response is not so satisfactory. We believe that the reason for this mismatch is because of addition of extra confinement for weakly cemented granular materials in the elasto-plastic constitutive model. This addition of confinement to a purely frictional material shows higher peak strength while at the same time becomes more contractive. In the suite of experiments conducted, the weakly cemented granular material shows higher peak strength but relatively dilative response due to presence of cementation bonds.

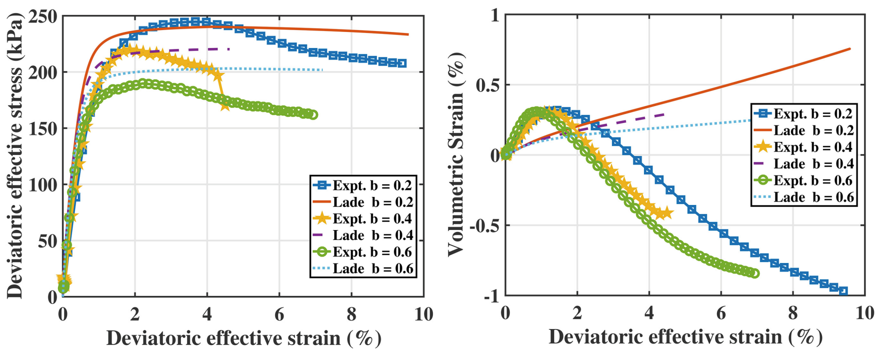

Fig. 5. Comparison of experimental and model response at intermediate principal stress ratio of 0.2, 0.4, and 0.6.

Conclusions

The mechanical behaviour of weakly cemented sand is studied using conventional triaxial compression test at different confining pressure. Further a set of experiments were performed on octahedral plane of stress space by keeping the mean effective stress constant and with changing intermediate principal stress ratio to traverse the behaviour along different stress paths other than just compression or tension. For this purpose a hollow cylinder torsional shear apparatus was used which is capable of independently controlling the 4 components of stress tensor $(\sigma_r, \sigma_\theta, \sigma_z, \sigma_{z\theta})$. The results of these experiments are presented on stress-strain and volumetric strain plots. The initial stiffness of the weakly cemented sand was found to be invariant of intermediate principal stress ratio. The peak strength decreases from compression (b = 0) to tension (b = 1) path zone which mobilizes at lower strain levels. A transition of ductile to brittle failure mode is observed with increase in b. Further these results are analyzed using stress-dilatancy plots.

Next, an advanced single hardening constitutive model is calibrated using conventional triaxial compression tests. Further, this is used for model validation exercise using experiments performed on octahedral plane. Lade's model, used in this study, was originally suggested for purely frictional granular materials. For cemented granular materials, a translation of stress space is performed to allow extra confinement offered by cemented sand in modeling. The result of this validation exercise shows that model is capable of predicting stress response satisfactorily but does not perform well in capturing the volumetric behaviour.

References

Abdulla AA, Kiousis PD (1997) Behavior of cemented sands—I. Testing. Int J Numer Anal Meth Geomech 21(8):533–547

Airey DW (1993) Triaxial testing of naturally cemented carbonate soil. J Geotech Eng 119 (9):1379–1398

Clough GW, Sitar N, Bachus RC, Rad NS (June 1981) Cemented sands under static loading. Journal of Geotechnical and Geoenvironmental Engineering 107(ASCE 16319 Proceeding)

Coop MR, Atkinson JH (1993) The mechanics of cemented carbonate sands. Geotechnique 43 (1):53–67

Cuccovillo T, Coop MR (1997) The measurement of local axial strains in triaxial tests using LVDTs. Géotechnique 47(1):167–171

Huang JT, Airey DW (1998) Properties of artificially cemented carbonate sand. J Geotech Geoenviron Eng 124(6):492–499

Ismail MA, Joer HA, Sim WH, Randolph MF (2002) Effect of cement type on shear behavior of cemented calcareous soil. J Geotech Geoenviron Eng 128(6):520–529

Kandasami R, Singh S, Murthy TG (July 2016) Mechanical behaviour of cemented granular materials: experimental and model calibration. Submitted Int J Solids Struct

Kim MK, Lade PV (1988) Single hardening constitutive model for frictional materials: I. plastic potential function. Comput Geotech 5(4):307–324

Lade PV, Kim MK (1988a) Single hardening constitutive model for frictional materials II. yield criterion and plastic work contours. Comput Geotech 6(1):13–29

Lade PV, Kim MK (1988b) Single hardening constitutive model for frictional materials III. comparisons with experimental data. Comput Geotech 6(1):31–47

Lade PV, Overton DD (1989) Cementation effects in frictional materials. J Geotech Eng 115 (10):1373–1387

Leroueil S, Vaughan PR (1990) The general and congruent effects of structure in natural soils and weak rocks. Géotechnique 40(3):467–488

Menéndez B, Zhu W, Wong TF (1996) Micromechanics of brittle faulting and cataclastic flow in berea sandstone. J Struct Geol 18(1):1–6

Mitchell JK, Soga K (1976) Fundamentals of soil behavior. Wiley, New York

Moavenzadeh F, Kuguel R (September 1969) Fracture of concrete. J Mater

O'Rourke TD, Crespo E (1988) Geotechnical properties of cemented volcanic soil. J Geotech Eng 114(10):1126–1147

Santamarina JC, Klein A, Fam MA (2001) Soils and waves: particulate materials behavior, characterization and process monitoring. J Soils Sediments 1(2):130

Schnaid F, Prietto PD, Consoli NC (2001) Characterization of cemented sand in triaxial compression. J Geotech Geoenviron Eng 127(10):857–868

Van Mier JG (1984) Strain-softening of concrete under multiaxial loading conditions. Technische Hogeschool, Eindhoven

Numerical Modelling of Liquefaction Tests of Partially Saturated Sands in CSSLB

Seyed Mohsen Seyedi Viand(✉) and E.E. Eseller-Bayat

Department of Civil Engineering, Istanbul Technical University, Maslak, Turkey
seyediviand@itu.edu.tr

Abstract. The undrained behavior of partially saturated sands under repetitive loading has been investigated by many researchers experimentally. The research to date demonstrate that partially saturated sands do not liquefy however, significant amount of excess pore water pressures may develop especially in loose sand specimens with degrees of saturation above 80%. Cyclic Simple Shear Liquefaction Box (CSSLB) was developed by Eseller-Bayat et al. to perform cyclic simple shear tests on large specimens using a shaking table. In this study, based on the experimental results, the behavior of loose to dense partially saturated sand specimens to cyclic simple shear strains under drained and undrained conditions was modelled numerically in finite difference software program FLAC^{3D} (Itasca Consulting Group). The CSSLB was first modelled and the sand specimen was numerically tested under drained conditions. Then Finn and Byrne liquefaction models were used to simulate the liquefaction behavior of sands. Sand specimens with different degrees of saturation (40–83%) were tested under several cyclic simple shear strain amplitudes and the excess pore water pressures were numerically obtained. Finally, excess pore water pressure ratio (r_u) values were compared both in numerical and experimental tests. The results were also compared with the excess pore water pressures generated in fully saturated sand specimens.

Introduction

Overview of Cyclic Simple Shear Liquefaction Box (CSSLB)

Simple shear apparatus has been designed by number of researchers. Norwegian Geotechnical Institute Simple Shear Apparatus (NGISSA) uses cylindrical specimens. The Cambridge University Simple Shear Apparatus Mk7 (CUSSA Mk7) uses square shaped specimens with dimensions 10 cm × 10 cm × 2 cm surrounded with fixed platens. Based on the idea of both shear apparatus stated above, Cyclic Simple Shear Liquefaction Box (CSSLB) was designed and manufactured at Northeastern University, that allows testing large size fully and partially saturated test specimens under controlled drainage conditions (Fig. 1) (Eseller-Bayat et al. (2013b)).

Figure 2 demonstrates the mechanism through which shear strain was applied to the sand specimen. The tops of Plexiglas rotating walls were fixed against translation through a metal bar support located next to the table. The bottoms of the two rotating walls rested on a flexible sealant and hinges, which were used to connect them to the base plate of the box. The rotating walls were connected to the rigid walls using the

A. Ferrari and L. Laloui (eds.), *Advances in Laboratory Testing and Modelling of Soils and Shales (ATMSS)*, Springer Series in Geomechanics and Geoengineering,
DOI 10.1007/978-3-319-52773-4_60

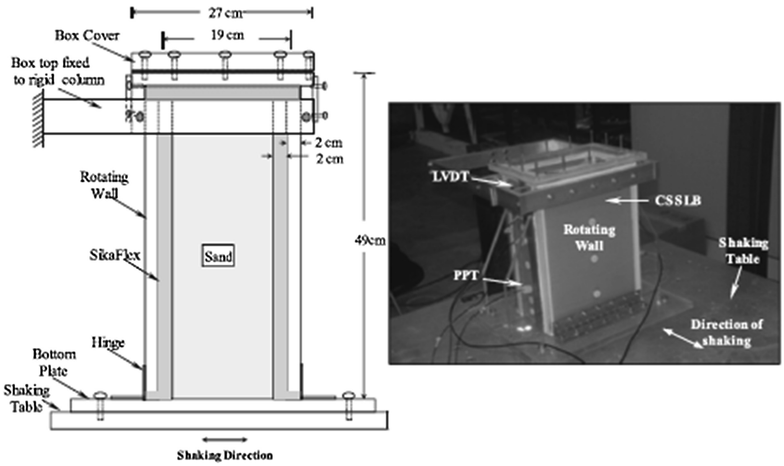

Fig. 1. Side view of CSSLB (left), experimental setup (right). (Eseller-Bayat et al. (2013b), with permission from ASCE).

flexible sealant, which allowed relative translations between the rotating and rigid walls. When the shaking table was displaced by an amount d to the left (as shown in Fig. 2), the base plate and the two rigid walls translated by the same amount. The two rotating walls rotated, and thus the sand specimen experienced an average shear strain of $\gamma = d/H$ as shown in Fig. 2. “H” is height of the box and “d” is displacement amplitude.

Numerical Model of CSSLB Test Set-up on Shaking Table

Numerical Model of CSSLB

CSSLB was modeled in FLAC^{3D} using elastic materials for the walls and the sealant. The elastic models are characterized by reversible deformation after unloading. Parameters which were assigned to material in elastic model are shear modulus (G), bulk modulus (K) and Poisson ratio (ν). Behavior of the side walls of the CSSLB, bottom of the box and flexible sealant material (rubber) are considered elastic and their properties are presented in Table 1.

Numerical model of CSSLB in FLAC^{3D} is shown in Fig. 3. Numerical model parameters of sand tested in FLAC^{3D} was presented in a paper published by the authors (Eseller-Bayat et al. (2016)).

For liquefaction modelling, the Finn model (Finn et al. (1976)) was selected that relates the variation of volumetric strain in drained condition to the increase of excess pore pressure in undrained condition. Martin et al. (1975) considered that the volumetric strain increment depends on volumetric strain and cyclic shear strain amplitude.

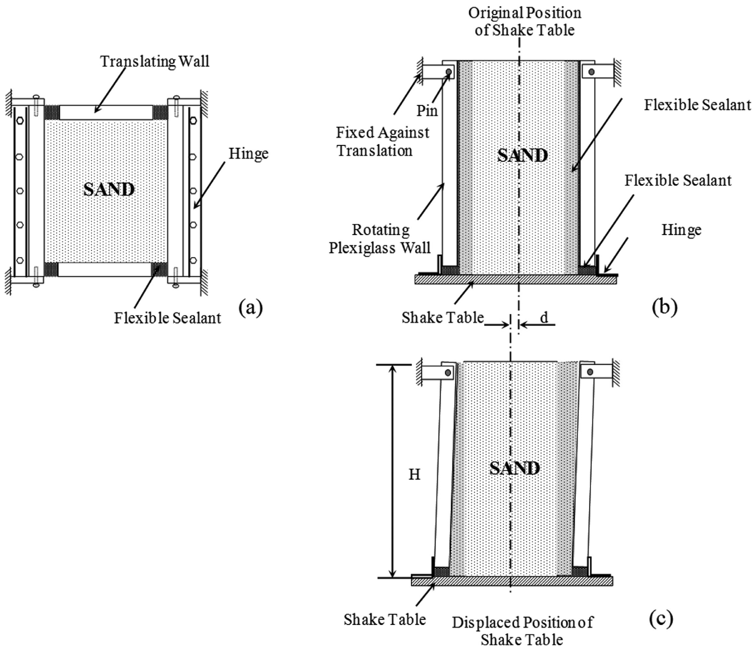

Fig. 2. Simple shear mechanism for the CSSLB, plan section before shearing (left) elevation section before shearing (right top) & elevation section after shearing by displacing shaking table (right bottom) (Eseller-Bayat et al. (2013a), with permission from ASCE).

Table 1. Material properties used in CSSLB model.

Material	K (Pa)	G (Pa)	Poisson ratio
Plexi-glass	2.00E + 11	1.00E + 11	0.3
Flexible sealant	8.333E + 5	8.62E + 4	0.45

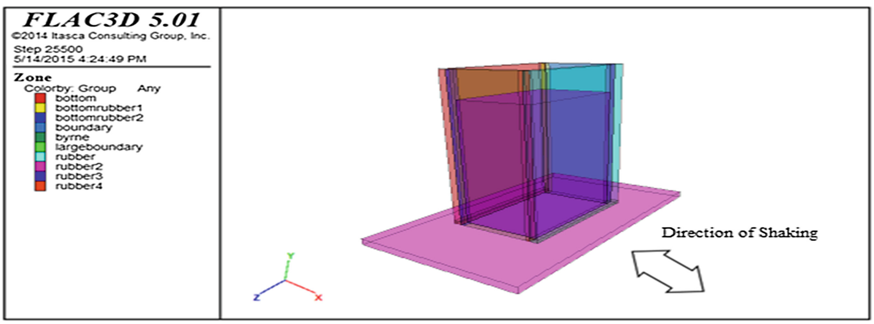

Fig. 3. The numerical model of CSSLB in FLAC^{3D}.

Byrne (1991) introduced a modified and simple volume change model with two calibration parameters as shown in Eq. 1:

$$\Delta\varepsilon_{vd} = \gamma C_1 e^{\left(-C_2\left(\frac{\varepsilon_{vd}}{\gamma}\right)\right)} \tag{1}$$

in which, C_1 is defined as:

$$C_1 = 3800(D_r)^{-2.5} \tag{2}$$

where D_r is relative density of the soil, γ is cyclic shear strain amplitude and in many cases, $C_2 = 0.4/C_1$. $\Delta\varepsilon_{vd}$ is the increment of volumetric strain per cycle and ε_{vd} is the accumulated volumetric strain from previous cycles. FLAC^{3D} contains a built-in constitutive model (Finn model) that incorporates Eq. 1 into the standard Mohr-Coulomb plasticity model and it can be modified by the user as required.

Excess pore water pressures were correlated to the volumetric strain increment using Eq. (3) to predict pore pressure build-up of the liquefiable soil:

$$\Delta u = \frac{\Delta\varepsilon_{vd}}{\frac{1}{E_r} + \frac{n}{K_w}} \tag{3}$$

Where, K_w is bulk modulus of water, n is porosity of sample, E_r is rebound modulus of one dimensional unloading curve. The bulk modulus of fluid in the pores, which is water in fully saturated case, is entered in the program as 2.2×10^9 Pa.

Partially Saturated Sand Analysis

In FLAC^{3D}, pore pressure is considered zero if degree of saturation at any point is less than 1. The effect of dissolved and trapped air may be allowed by reducing the fluid modulus while keeping the saturation at 1. It should be noticed that the compressibility of the fluid (C) is the reciprocal of bulk modulus (K).

Fluid compressibility is defined in two ways in FLAC^{3D} (1) Biot coefficient and Biot modulus are specified (2) Fluid bulk modulus and porosity are specified. The first case considers the compressibility of the solid grains. In the second case, solid grains are assumed to be incompressible. When the grain compressibility is neglected, the user has the choice to either use the default value of Biot coefficient which is equal to one or assign a value equal to bulk modulus over porosity (K_n) to Biot modulus, or give the fluid bulk modulus K as input. The numerical modeling of fully and partially saturated sand difference is in the high compressibility of air and water mixture. The increment of compressibility is assigned to the numerical model by fluid bulk modulus.

The compressibility of air and water mixture is calculated in different ways by the researchers. Some of the calculations take into account the surface tension between water and air while others ignored it by considering the same air and water pressures in the mixture. Boyle's and Henry's law are mostly used in these calculations. It takes into account the surface tension between water and air.

Bishop, Alan W, 1950 and Skempton (1954) and Bishop (1954) did their calculation based on Boyle's and Henry's laws. The surface tension and differences between air and water tension were disregarded by them. Koning (1963) calculated the compressibility of air water mixture by using Boyle's law. His formula is sufficient for practical proposes where pressure changes are small. Koning 1963 did not take into account the influence of surface tension. His final equation is presented as below:

$$\frac{1}{K_{wa}} = \frac{S}{K_w} + \frac{1-S}{u_w} \tag{4}$$

where S is the degree of saturation, K_w is water bulk modulus, K_{wa} is air and water mixture bulk modulus and u_w is absolute pore water pressure. In this paper, for numerical modelling of partially saturated sand, compressibility of the air and water mixture is defined by Koning equation. In this due, the effect of dissolved air is allowed by reducing the fluid modulus in FLAC^{3D} codes.

Numerical Modelling of Cyclic Simple Shear Tests

Dynamic Model (Drained Conditions)

Cyclic simple shear tests on sand specimens in CSSLB were simulated by applying uniform velocity time history at all the grid points from the base to the surface. Equation 5 is used for applying the velocity uniform shear strain to all the zones. As the height of CSSLB is 0.49 m, Eq. 5 is introduced for velocity wave as below:

$$\text{Local V} = \text{V} \times \frac{0.49 - gp}{0.49} \tag{5}$$

where Local V is the velocity of each grid point and gp shows the height of the position of each grid point.

In this study, the frequency of the wave is used as 10 Hz. In dynamic model, the constitutive model was selected as Mohr-Coulomb and the fluid command was set as "on", which represents the drained conditions. Uniform shear strains exerted on the specimen in CSSLB were confirmed throughout the height of the specimen at the center as demonstrated in Fig. 4.

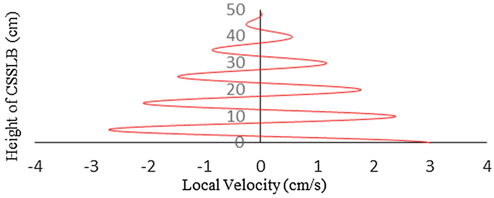

Fig. 4. Applied shear wave velocity at the specimen.

Liquefaction Model (Undrained Conditions). For liquefaction modeling of sand specimens tested under cyclic simple shear tests in CSSLB, Finn model was entered as the constitutive model and the fluid command was set as "off" which represents the undrained conditions. Excess pore water pressures and effective stresses were obtained. Initial liquefaction, which is defined as the point where the increment of pore pressure becomes equal to initial effective stress ($r_u = \Delta u/\sigma'_v = 1$). Furthermore, maximum excess pore water pressure ratios (r_{umax}) were also obtained and compared with experimental results.

Comparison of Numerical Model Results with Experimental Results. A series of cyclic simple shear tests were performed in specimens prepared in CSSLB by Eseller-Bayat (2009). Loose to very dense sand specimens were tested under shear strain levels ranging from 0.01% to 0.2%. Numerical analysis was performed at the same conditions and compared with experimental results. Excess pore water pressure ratio (r_u) generation plots obtained from numerical analysis performed on the sand specimens at degree of saturation S = 62%. Then, this result was compared with experimental result. According to Fig. 5, numerical and experimental results are in good agreement and it confirms that the numerical model is constructed properly.

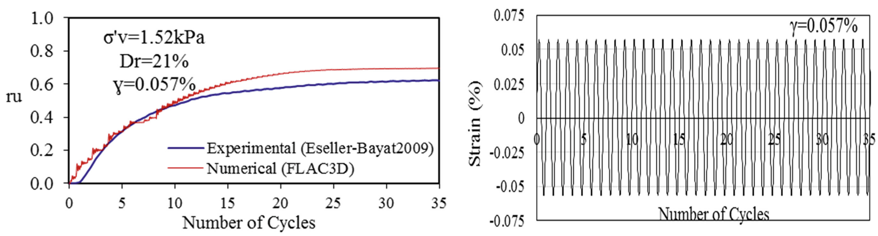

Fig. 5. Excess Pore Water Pressure Generations obtained from numerical model and experimental tests for S = 62% (left), Shear strain induced in the specimen (right).

Numerical Analysis Results

Excess pore water pressures in fully and partially saturated sand models were obtained at depth 32 cm from the top during the numerical liquefaction model tests. Some results of numerical analysis are presented graphically in Figs. 6 and 7. It is noticeable that numerical results for r_{umax} are in good agreement with the experimental findings (Table 2).

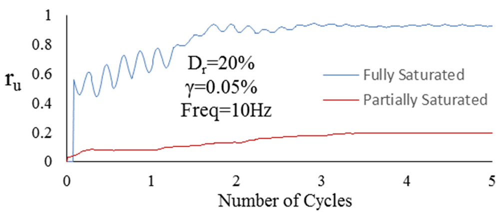

Fig. 6. Excess pore water pressure for Loose Sand (S = 48%).

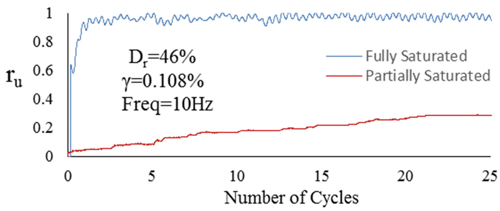

Fig. 7. Excess pore water pressure for Medium-Dense Sand (S = 70%).

Table 2. Comparison of numerical and experimental results.

Test	$\sigma'_0 v$ (kPa)	D_r (%)	S (%)	Kwa (MPa)	γ (%)	r_{umax} (Experimental)	r_{umax} (Numerical)
1	2.81	31	84	0.65	0.06	0.85	0.82
2	2.24	20	48	0.20	0.05	0.25	0.21
3	2.27	29	45	0.19	0.015	0.13	0.13
4	2.30	33	45	0.19	0.20	0.28	0.24
5	2.44	21	62	0.27	0.057	0.64	0.63
6	2.50	31	61	0.26	0.053	0.44	0.40
7	2.51	35	60	0.26	0.10	0.49	0.53
8	2.53	44	56	0.23	0.10	0.31	0.36

Conclusion

Numerical modelling of cyclic simple shear tests on sand specimens using CSSLB on a shaking table was presented. CSSLB and the sand specimens were modeled in $FLAC^{3D}$ (provided by Itasca Consulting Group, Inc.). Dynamic (drained) and liquefaction (undrained) tests analysis were numerically performed. Uniform shear strains were confirmed to be generated everywhere in the specimen modeled in CSSLB. Maximum excess pore water pressure ratio (r_{umax}) was obtained in fully and partially saturated sand models. The maximum excess pore water pressure ratio values achieved at different relative densities & degrees of saturation and shear strain amplitudes are in good agreement with the experimental shaking table test results in partially saturated sand specimens.

Acknowledgement. This research was funded by The Scientific and Technological Research Council of Turkey (TÜBİTAK) under grant No. 213M367. The valuable comments and suggestions in using $FLAC^{3D}$ software made by Professor Michael H. Beaty (Beaty Engineering LLC) are very much appreciated.

References

Byrne PM (1991) A cyclic shear volume coupling and pore-pressure model for sand. In: Second International Conference on Recent Advances in Geotechnical Engineering and Soil Dynamics, pp. 47–55

Eseller-Bayat E (2009) Seismic response and prevention of liquefaction failure of sands partially saturated through introduction of gas bubbles, Ph.D. dissertation, Northeastern University, Boston

Eseller-Bayat E, Gokyer S, Yegian MK, Ortakci E, Alshawabkeh A, (2013a) Design and application of simple shear liquefaction Box. Geotech Test J 36(3):1–9. doi:10.1520/GTJ20120025. ISSN 0149-6115

Eseller-Bayat E, Yegian MK, Alshawabkeh A, Gokyer S (2013b) Liquefaction response of partially saturated sands. I: experimental results. J Geotech Geoenviron Eng 139(6):863–871

Eseller-Bayat E, Nateghi A, Viand, AS, Jadidoleslam M (2016) Numerical modelling of liquefaction tests of fully saturated sands in CSSLB. In: 4th International Conference on New Developments in Soil Mechanics and Geotechnical Engineering, Near East University, Nicosia, North Cyprus

Finn WDL, Byrne PM, Martin GR (1976) Seismic response and liquefaction of sands. J Geotech Eng Div 102(8):841–856

Martin GR, Seed HB, Finn WDL (1975) Fundamentals of liquefaction under cyclic loading. J Geotech Eng Div 101(5):423–438

Bishop AW (1954) The Use of Pore-Pressure Coefficient in Practice. Geotechnique, 4:4:148

Skempton AW (1954) The Pore Pressure Coefficients A and B, Geotechnique 4(4), pp. 143–147

Koning H (1963) Some Observation on the Modulus of Compressibity of Water. In Settelement and Compressibilty of Soil. Wisbaden

Aspects of Thermal Fracturing of Clays with Electromagnetic Excitation

Morteza Mohamadi(✉) and Richard G. Wan

Department of Civil Engineering, University of Calgary, Calgary, AB, Canada
{mmohamad, wan}@ucalgary.ca

Abstract. The study explores the feasibility of fracturing clays during fast electromagnetic (EM) heating. An oedometer setup customized with an EM wave source is simulated numerically at the continuum level. Solid matrix equilibrium, fluid flow and heat transfer equations are solved together with the laws of electromagnetism, i.e. Maxwell's equations, using the COMSOL multiphysics code. Numerical simulations involve EM excitation in a fluid-saturated isotropic, homogeneous, linear thermo-poro-elastic and lossy (EM wave loses power as it propagates in a lossy material.) medium at both 50 MHz and 2.45 GHz frequencies. It is found that the thermal expansion contrast between the fluid and solid phase results into a local buildup of fluid pressure that cannot dissipate due to the very low permeability of the medium, hence promoting fracturing.

Introduction

Understanding the interaction of electromagnetic (EM) excitations with geomaterials is of interest in many industrial and research applications such as geophysical subsurface imaging and explorations, geotechnical site characterization, and detection of contaminants in deep soil layers. In the area of heavy oil/bitumen recovery in Canada, EM-based thermal methods offer a promising means for fracturing interbedded shales (IBS) intrusions in oilsand reservoirs (Mohamadi and Wan 2015) to enhance oil production as they deliver a fast heating rate. Therefore, knowledge of the coupled multi-physics associated with EM heating of clays/shales is of prime interest.

From the microscopic viewpoint, the interaction of an EM field with geomaterials is quite complex and depends on numerous factors such as: particle shape and mineralogy, pore fluid chemistry, charge distribution in the soil mixture, particle orientation, and frequency of the EM excitation; see Rinaldi and Francisca (1999), among others. More relevant to EM heating, the frequency of EM excitation has been reported to change the heating mechanisms. For frequencies greater than 10 MHz and less than 1 GHz, the interaction of the electromagnetic field with polar components of the soil mixture, mainly water, causes electrical energy to be transformed into heat, the so-called dielectric heating. On the other hand, EM heating at lower frequencies mostly relies on electrical and thermal conduction, the so-called Ohmic heating.

To guide a forthcoming experimental study, the present work was undertaken to elucidate the most influential macroscopic mechanisms of EM heating in low-permeability soils. One of the main purposes is to highlight coupling mechanisms

A. Ferrari and L. Laloui (eds.), *Advances in Laboratory Testing and Modelling of Soils and Shales (ATMSS)*, Springer Series in Geomechanics and Geoengineering,
DOI 10.1007/978-3-319-52773-4_61

between the thermodynamic governing equations, i.e. conservation of mass, momentum and energy, and Maxwell's equations. The collective set of these equations are solved numerically to simulate EM wave propagation, energy losses and scattering in a fluid-saturated thermo-poro-elastic medium. The basic interactions of the radiation energy with the medium are investigated in the range of MHz and GHz frequencies. The numerical results indicate the importance of local pore pressure escalation as a main contributor to the potential thermal fracturing.

Mathematical Model

The equations of EM wave propagation in a porous medium are examined next.

Electromagnetism

Maxwell's equations govern the generation and propagation of electric and magnetic fields in nature. However, for a homogeneous, isotropic, linear and charge free fluid-saturated porous medium, the volumetrically averaged Maxwell's equations in the differential form write (Pride 1994):

$$\epsilon_{eff}\nabla.\mathbf{E}=0;\quad \nabla.\mathbf{B}=0;\quad \nabla\times\mathbf{E}=-\frac{\partial\mathbf{B}}{\partial t};\ \frac{1}{\mu_{eff}}\nabla\times\mathbf{B}=\sigma_{eff}\mathbf{E}+\epsilon_{eff}\frac{\partial\mathbf{E}}{\partial t} \tag{1}$$

where $\mathbf{E}$ is the electric field intensity, $\mathbf{B}$ is the magnetic flux density, ∇ is the Del operator, and ϵ_{eff}, μ_{eff} and σ_{eff} represent effective permittivity, magnetic permeability, and electrical conductivity of the solid-fluid mixture, respectively.

In a deformable saturated porous medium, the set of Eq. (1) needs to be solved in conjunction with mass, energy and momentum conservation equations. The latter equations formulated in the context of mixture theory for an isotropic, homogeneous thermo-poro-elastic saturated medium are presented in the next subsection. The interested reader is referred to Coussy (2004) for detailed derivations of these equations.

Mass, Energy and Momentum Balance

The linear momentum balance, effective stress, constitutive, and compatibility equations for a thermo-poro-elastic saturated medium are respectively given by:

$$\nabla.\mathbf{\Sigma}+\left(n\rho_f+(1-n)\rho_s\right)\mathbf{g}+\mathbf{f}_{em}=0 \tag{2}$$

$$\mathbf{\Sigma}=\mathbf{\Sigma}'-\alpha p_f\mathbf{I};\ \ \mathbf{\Sigma}'=\mathbf{D}_e\cdot\left(\boldsymbol{\mathcal{E}}-\boldsymbol{\mathcal{E}}^T\right);\ \ \boldsymbol{\mathcal{E}}=\frac{1}{2}\left(\nabla\mathbf{u}+(\nabla\mathbf{u})^T\right) \tag{3}$$

where $\mathbf{\Sigma}$ and $\mathbf{\Sigma}'$ are the total and effective stress, respectively, $\mathbf{g}$ is the gravity vector, ρ_ξ denotes the density of phase $\xi=s,f$, $\mathbf{f}_{em}$ is the EM body force vector explained later in the paper, α is Biot's poroelastic coefficient, p_f is the fluid pressure, $\mathbf{I}$ is the identity matrix, $\boldsymbol{\mathcal{E}}$ is strain of the solid matrix, $\mathbf{D}_e$ is elastic constitutive matrix, $\mathbf{u}$ is the vector of solid displacements, and temperature-induced strain $\boldsymbol{\mathcal{E}}^T = \mathbf{I}(\beta_{eff}/3)\Delta T$ with ΔT and β_{eff} respectively representing temperature variation and effective volumetric thermal expansion coefficient, herein taken equal to that of the solid matrix. The mass balance equation of the solid-fluid mixture is:

$$\left(\frac{\alpha - n}{K_s} + \frac{n}{K_f}\right)\frac{\partial p_f}{\partial t} + \nabla^T\left(\frac{\kappa}{\mu^*}\left(-\nabla p_f + \rho_f \mathbf{g}\right)\right) - \left((\alpha - n)\beta_s + n\beta_f\right)\frac{\partial T}{\partial t} + \alpha\frac{\partial \boldsymbol{\mathcal{E}}_v}{\partial t} = 0 \quad (4)$$

where K_ξ and β_ξ are the bulk modulus and volumetric thermal expansion coefficient of phase $\xi = s, f$, respectively, κ is the permeability, μ^* is the viscosity of the fluid phase, and $\boldsymbol{\mathcal{E}}_v = \boldsymbol{\mathcal{E}} : \mathbf{I}$ is the volumetric strain. The energy balance equation of the solid-fluid mixture writes:

$$\begin{aligned} &\left((1-n)\rho_s C_s + n\rho_f C_f\right)\frac{\partial T}{\partial t} - \nabla^{tr}\left(\left(n\chi_f + (1-n)\chi_s\right)\nabla T\right) \\ &\qquad + \left(\rho_f C_f \frac{\kappa}{\mu^*}\left(-\nabla p_f + \rho_f \mathbf{g}\right)\right).\nabla T = Q \end{aligned} \quad (5)$$

where C_ξ and χ_ξ are the heat capacity and thermal conductivity of phase $\xi = s, f$ and Q is the heat source/sink term.

Equations (1)–(5) form a complete set of equations describing the propagation of EM radiation in a saturated porous medium. In these equations, the solid skeleton displacement vector $\mathbf{u}$, fluid pressure p_f, temperature of the mixture T, and the electric field intensity $\langle \mathbf{E} \rangle$ are chosen as primary unknowns. The electric field is determined by solving Maxwell's equations in the frequency domain, the results of which are then inserted into the mass, momentum and energy conservation equations to solve for $\mathbf{u}$, p_f and T.

Coupling Mechanisms

The coupling mechanisms among fluid flow, energy transport and mechanical equilibrium are due to the existence of volumetric deformations, effective stresses and thermal strains, among others. These mechanisms can be easily inferred from Eqs. (2)–(5). The thermodynamic balance laws are innately coupled with EM radiations due to the dependence of the electrical properties of the porous medium on water content and temperature. On the other hand, variations of electrical properties influence EM field distribution, and, hence, the EM energy and force delivered to the medium.

The EM force is readily derived from Lorentz law of force in conjunction with the microscopic form of Maxwell's equations and constitutive relations. For a stationary EM field, which is the case in our simulations, the electromagnetic force $\mathbf{f}_{em}$ is neglected as it is of order 10-100 N/m^3 being much smaller than the applied mechanical forces.

Based on the Poynting's theorem, the increase of the stored energy within a control volume plus the rate of losses should be equal to the flow of energy induced by propagating electromagnetic fields, Orfanidis (1999), i.e.

$$-\nabla.(\langle \mathbf{E}\rangle \times \langle \mathbf{H}\rangle) = \langle \mathbf{J}\rangle.\langle \mathbf{E}\rangle + \frac{\partial}{\partial t}\left(\frac{\epsilon_{eff}}{2}\langle \mathbf{E}\rangle.\langle \mathbf{E}\rangle + \frac{\mu_{eff}}{2}\langle \mathbf{H}\rangle.\langle \mathbf{H}\rangle\right) \tag{6}$$

It is clear from Eq. (6) that electromagnetic heating, as opposed to conventional heating methods, is a volumetric process that is governed by electrical properties of the medium. As such, the electromagnetic-induced heat is included as a source/sink term in Eq. (5) for the heat term Q.

Numerical Study

The coupled governing equations presented in the previous section were solved using the finite element package COMSOL Multiphysics 5.2a.

Physical Model and Input Parameters

A schematic of the axially symmetric physical model together with boundary conditions is illustrated in Fig. 1. The sample is 45 mm high and 37.75 mm wide. The lateral and bottom surfaces are fixed in the horizontal and vertical directions, respectively, while a surcharge of 100 kPa is applied on the top surface. All of the sample boundaries are impermeable and adiabatic, and satisfy the condition of perfect electric conductor. Initially, the sample has a uniform temperature of 20°C. The electromagnetic excitation at an input power of 400 W and impedance of 50 Ω is applied for a period of 30 s at the bottom of the antenna (electrode) which is made of copper. The computational domain is discretized into 2588 triangular elements with maximum size of 2 mm. Maxwell's equations are solved in the frequency domain with two input frequencies of 50 MHz and 2.45 GHz, hitherto referred to as low and high frequency respectively.

The selected material parameters, with regard to the thermal, hydraulic and mechanical physics are specified as follows: Young's modulus of the drained skeleton $E = 122$ MPa, Poisson's ratio $v = 0.3$, density of the solid material and pore fluid $\rho_s = 3696$ and $\rho_f = 1000\,\mathrm{kg/m^3}$ respectively, porosity $n = 0.42$, viscosity of the pore fluid $\mu^* = 0.001$ Pa.s, permeability $k = 1 \times 10^{-16}$ m^2, Biot's coefficient $\alpha = 1$, thermal conductivity of the solid material and pore fluid $X_s = 1.38$ and $X_f = 0.6$ W/m.K, respectively, specific heat of the solid material and pore fluid $C_s = 703$ and $C_w =$ 4180 J/kg.K respectively, and thermal expansion coefficient of the solid material and pore fluid $\beta_s = 1.65 \times 10^{-6}$ and $\beta_f = 2.07 \times 10^{-4}$ 1/K, respectively. The electromagnetic properties of the clay-water mixture, measured on thin disks of one-dimensionally consolidated saturated kaolinite samples, are: effective relative permittivity $\epsilon_r = 5$, effective relative magnetic permeability $\mu_r = 1$, effective conductivity $\sigma_{eff} = 0.1$ S/m.

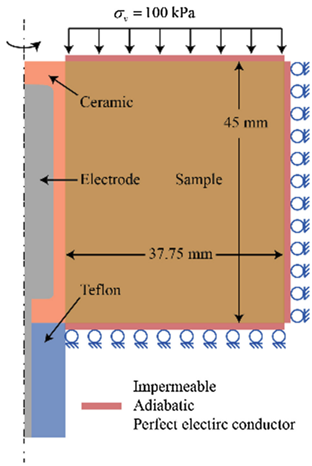

Fig. 1. A schematic of physical model together with boundary conditions.

Simulation Results

Figure 2 shows the spatial distribution of electric field norm inside the sample for the low frequency excitation along with the corresponding temperature distribution on the side wall of the antenna. It is observed that the electric field attenuates radially while being fairly uniform, see Fig. 2a. It is only near the bottom and top corners of the antenna that the electric field is more intense due to the abrupt change of the wave propagation direction. As expected, the distribution of temperature increase conforms to the EM wave intensity contour, i.e. more intense heating occurs near the two ends of the antennas shown in Fig. 2b.

Figure 3 compares the evolution of fluid pressure at point 1, mid-height of the sample on the side wall of the antenna, for three different values of fluid thermal expansion coefficient β_f. When the actual value of β_f is used in the simulations, fluid pressure increases monotonically causing radially inward migration of the fluid.

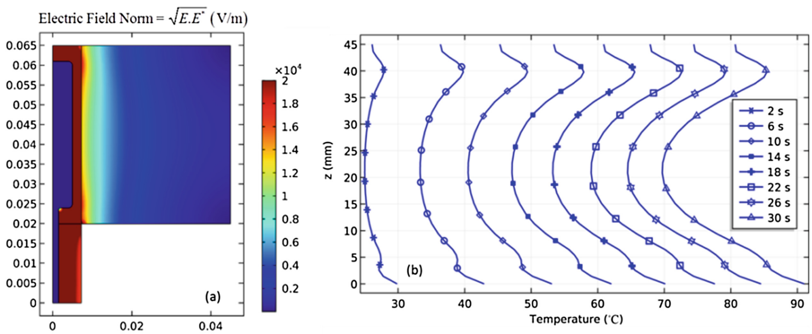

Fig. 2. (a) Spatial distribution of the norm of electric field, and (b) temperature distribution on the side wall of the antenna.

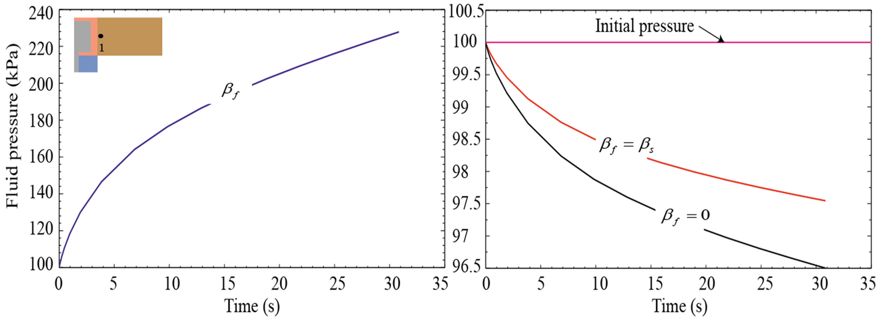

Fig. 3. Comparison of fluid pressure profiles for different values of fluid thermal expansion coefficient at point 1.

Interestingly, for the other two cases, $\beta_f = \beta_s$ and $\beta_f = 0$, the pressure decreases monotonically giving rise to an outward fluid motion. These seemingly anomalous behaviors are due to the competing effects of the rate of volume change and temperature-induced fluid pressure as suggested by the right-hand-side of Eq. (4). If the pore fluid and solid particles are assumed incompressible, the pressure gradient at a given point in a homogenized porous medium becomes positive mainly due to the larger thermal expansion of the fluid as compared to that of the solid particles. Such buildup of pore fluid pressure cannot dissipate due to the very low permeability of the clay, resulting in the reduction of mean effective stress.

Figure 4 shows the radial distribution of the mean effective stress along the mid-height of the sample for $\beta_f = \beta_s$ and $\beta_f = 0$. In the case of $\beta_f = 0$, effective stress increases due to the development of negative pore pressures, while for the actual value of β_f effective stress decreases by 73 kPa as a result of pore pressure build-up. The latter can potentially instigate tensile fracturing of the sample.

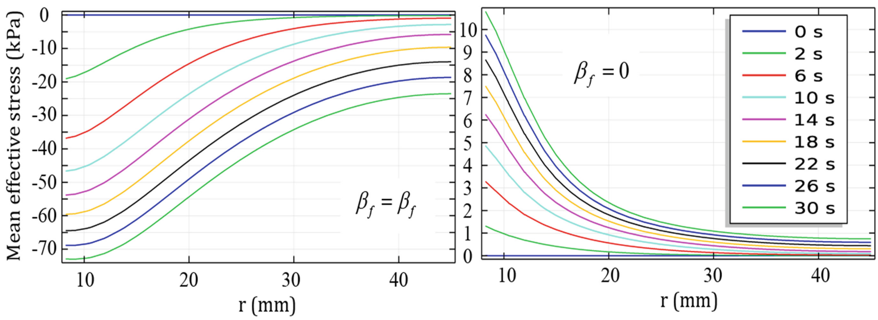

Fig. 4. Comparison of mean effective stress values for different thermal expansion coefficients of the fluid; values corresponds to the mid-height of the sample.

Figure 5 shows the spatial distribution of the electric field for the high-frequency excitation. As opposed to the low-frequency case, distribution of the electric field at high frequency is non-homogeneous inside the sample, reaching its maximum intensity near the top, bottom and mid-height of the sample. These maximum points coincide with the peaks and troughs of the electromagnetic wave whose wavelength is 1.22 times of the sample height.

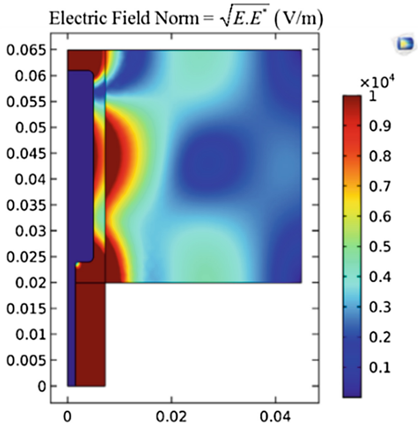

Fig. 5. Spatial distribution of the electric field norm for the high frequency excitation.

Concluding Remarks

All field variables are driven by the intensity and spatial distribution of the EM excitation. At low frequency, the EM and temperature fields are fairly homogeneous and pore pressure development is mainly due to the contrast between the fluid and solid phase thermal expansion. In simulations with actual fluid thermal expansion, the pore pressure rises and the effective mean stress drops by 73 kPa, a limit that is deemed enough for fracturing a low plasticity clay under initially small effective stresses. On the other hand, for a pore fluid whose thermal expansion is ideally zero, the effective mean stress increases as a result of negative pore pressure development. As such, the sample becomes less prone to fracturing. At high frequency the induced pore pressures attenuate both radially and vertically near the antenna, as opposed to the low frequency case where pressure attenuates only radially. The developed pore pressures at high and low frequencies are positive and is driven mainly by the contrast of fluid and solid thermal expansions.

Acknowledgements. Financial support for this research was provided by the Natural Sciences and Engineering Research Council of Canada (NSERC) and Foundation CMG.

References

Mohamadi M, Wan RG (2015) Strength and post-peak response of Colorado shale at high pressure and temperature. Int J Rock Mech Min Sci 84:34–46

Orfanidis SJ (1999) Electromagnetic Waves and Antennas. Rutgers University

Pride S (1994) Governing equations for the coupled electromagnetics and acoustics of porous media. Phys Rev B 50(21):15678–15696

Rinaldi V, Francisca F (1999) Impedance analysis of soil dielectric dispersion (1 MHz–1 GHz). J Geotech Geoenviron. Eng. 125(2):111–121

Coussy O (2004) Poromechanichs, p. 312. John Wiley & Sons

Reproduction of Discrete Element Model by 3D Printing and Its Experimental Validation on Permeability Issue

A. Kondo(✉), S. Matsumura, T. Mizutani, and E. Kohama

National Institute of Maritime, Port and Aviation Technology,
Port and Airport Research Institute, Yokosuka, Japan
kondoh-a@pari.go.jp

Abstract. The results of laboratory tests for examining the mechanical properties of a geomaterial always vary because of the changes in the microscopic structure. Same results for the tests cannot be obtained even on using the same particle aggregation owing to the influence of particle arrangement. In this study, we attempt to replicate the particle arrangement using 3D printing and examine the feasibility of evaluation of this influence experimentally. A 3D printed specimen is made from numerically simulated packing samples using discrete element method (DEM). This printed specimen shows good reproducibility as verified from the comparison of the cross-section of the specimen obtained using X-ray CT scanning. To validate the mechanical parameters, the value of the permeability coefficient of the 3D printed specimen obtained from laboratory testing is compared with that obtained from numerical simulations using DEM coupled with simplified maker and cell method and permeability-estimating equation. The permeability coefficients obtained using each method are found to be qualitatively consistent. Conclusively, we demonstrate the reproducibility of numerical simulation through experimental validation focusing on permeability.

Introduction

A geomaterial is composed by a discrete body in which macroscopic behavior results from microscopic behavior such as particle movement, slip, and rotation at contact point. Therefore, we cannot obtain the same behavior of soil even if same particle aggregation is tested as long as the particle arrangement differs. To obtain the same behavior of soil, all particle arrangements need to be replicated to those observed with the contact conditions. This influence of particle arrangements especially becomes significant during geotechnical testing. Moreover, numerical simulation such as discrete element method (DEM) (Cundall 1979) is adopted to evaluating this influence.

According to the replication techniques for geotechnical enginnering, reproduction of granular particle shape using three-dimensional (3D) printing technique has been reported by Hanaor et al. (2016). Furthermore, Matsumura et al. (2015) shows the applicability of this technique on the particle aggregation and arrangement to examine the mechanical properties of the material.

In this study, we attempt to replicate the particle arrangement obtained by DEM using 3D printing. This method suggests the possibility of evaluating this influence

A. Ferrari and L. Laloui (eds.), *Advances in Laboratory Testing and Modelling of Soils and Shales (ATMSS)*, Springer Series in Geomechanics and Geoengineering,
DOI 10.1007/978-3-319-52773-4_62

experimentally which has studied in the numerical simulation. This study describes the methodology of producing 3D printed specimen using the DEM geometric model. Moreover, the applicability of 3D printing for experimental elucidation is evaluated through validation of their permeability.

Experimental modeling of numerical simulation

Research scheme

The research scheme for evaluating variations in geotechnical laboratory tests using 3D printing is categorized primarily along the three lines (Fig. 1). The first one is the red line indicating real soil material for ordinary geotechnical tests that reveal variations in basic test results. In addition, X-ray scanning is conducted before and during the test for subsequent comparison. The second one is the blue line involving numerical simulation for elucidation of mechanism through verification and validation (V&V) for real soil material. Regarding numerical simulation method, it adopts discrete element method (DEM). The third one is the green line involving duplicate samples produced using 3D printing. This line is related to the red and blue lines in the following manner. The red and green line use X-ray CT scanning data of real soil material for duplicating, as reported by Matsumura et al. (2015). The blue and green lines use controlled particle arrangement generated using DEM. The present study focuses on the blue and green lines.

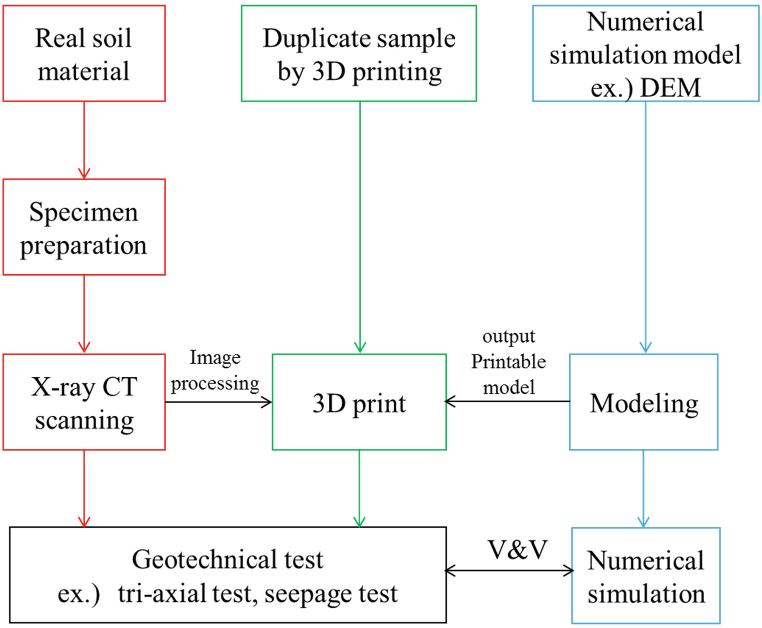

Fig. 1. Research scheme.

Numerical simulation model made by DEM

DEM is used to produce identical specimens, including their particle arrangement, for both numerical and experimental investigations. As for a making procedure of specimen, uniform-sized DEM particles are packed into cylindrical shape walls by gravitational force. This specimen size is 50 mm in diameter and 100 mm in height. The analysis parameters are summarized in Table 1.

Table 1. Analysis parameters of DEM specimen creation.

Parameter	Unit	Particle
Number of particle	–	696
Density	kg/m^3	2650
Diameter	mm	6.5
Normal spring coefficient, k_n	N/m	1.0×10^6
Shear spring coefficient, k_s	N/m	2.5×10^5
Damping	–	Critical damping
Interparticle friction angle, $\tan\phi_\mu$	–	0.25
Gravity	m/s^2	9.81

Modeling of DEM simulated specimen for 3D printing

This section describes the 3D printing procedure for DEM simulated specimen. To model the data for printable DEM particles, adopted 3D printer requires input data to follow the data type of standard triangulated language (STL), which is expressed by assembling triangles with surface identification. In this paper, DEM particle is ordinary sphere shape which expressed by the position of its center and its radius. Therefore, each DEM particle was converted to assembly of 512 triangles, as shown in Fig. 2.

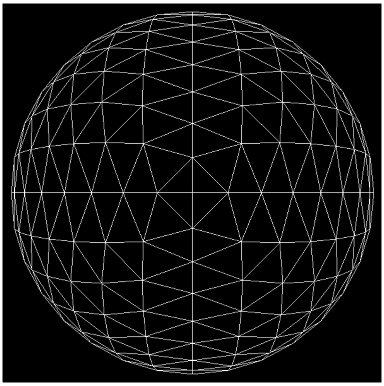

Fig. 2. Modeling of DEM particle for 3D printing.

Moreover, each DEM particle have contact points with neighboring particles. Because DEM algorism express particle contact as their particle overlapping, these contact points are expressed as bonding in the 3D printed specimen. Therefore, 3D printed particle can maintain their particle arrangement. However, it is difficult to directly reproduce each contact point because of the 3D printer resolution as layer thickness. For instance, it is possibile to disassemble the particle arrangement when overlapping area is significantly smaller than 3D printer resolution. Therefore, the diameter of each particle is increased by 1.0%, which is the smallest expansion ratio without disassembling of adopted 3D printer in this study.

3D printing of DEM simulated specimen

A UV-curing resin type 3D printer (model Agilista-3100 manufactured by Keyence Corporation) is used for this study. The maximum printable size is 297 mm wide, 210 mm deep and 200 mm high. Print resolution is 40 μm by 63.5 μm in the horizontal plane and 15 μm thick. This printer uses two types of resins: the first type constructs the main flame of the intended objects, and the second type construct the void area supporting main flame during printing. In addition, this support-type resin is water-soluble; therefore, we can achieve particle aggregation by submerging the as-printed specimen without disturbing the particle arrangement. The detail of this procedure have been reported by Matsumura et al. (2015).

Figure 3 compares three types of specimens: a DEM simulated specimen with cylindrical boundary conditions, a converted 3D model with mold, and 3D printed specimen.

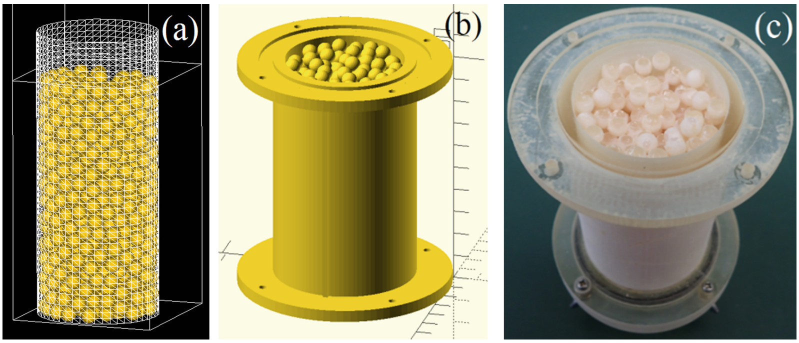

Fig. 3. Comparison of specimen appearance; (a) DEM simulated specimen, (b) DEM conversion 3D model with mold, (c) 3D printed specimen.

Reproducibility of printed DEM specimen

The reproducibility of the printed DEM simulated specimen is verified using an X-ray CT scanner (model ScanXmate-D200RSS900 manufactured by Comscantecno Co. Ltd.). As a specification of this scanner, the maximum voltage and current of the X-ray tube are 225 kV and 0.6 mA. The transmitted X-rays are detected using a 418 × 418 mm flat

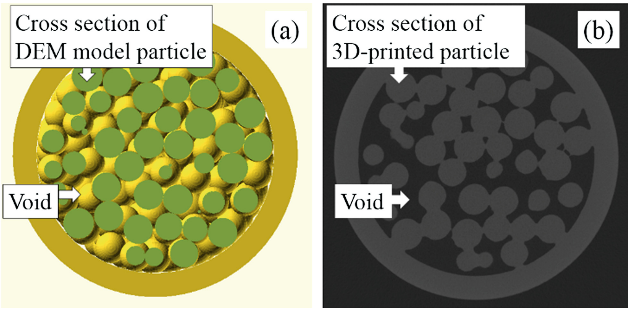

Fig. 4. Verification of 3D printing by cross section images; (a) DEM simulated specimen, (b) 3D printed specimen.

panel with a resolution of 3008 × 3008 pixels; however, a resolution of 1504 × 1504 pixels was employed in this study.

Figure 4(a) shows horizontal cross sectional image of the DEM simulated specimen taken at a height of 50 mm from bottom, in which light green indicate particle cross section. Figure 4(b) shows a cross sectional image of the 3D printed specimen taken at the same height, obtained by using CT scanning, in which the gray area indicates 3D printed particles and the black area indicates void areas. A comparison of these two images shows that the particle position and shape are consistent; however, the 3D printed model shows that the contact points have thick connections caused by the misallocated printing material or the remaining water-soluble support resin.

Experimental validation of numerical simulation focusing on permeability

Test conditions of numerical simulation and experiment

We adopted a constant head permeability test for experimental validation of numerical simulation. The experiment was conducted by maintaining a water head difference between upper and lower water tank. The mold was capped by an O-ring and a 3D printed cap, as shown in Fig. 5(a).

Numerical simulation was conducted by coupling simulation of DEM and simplified marker and cell method (SMAC) (Amsden and Harlow 1970). We focused on describing interaction force, which is based on a simplified equation of motion for particle in a turbulent fluid (Tchen 1947.), as shown below.

$$(\rho^s + \rho^w C_M)A_3 \frac{du_p}{dt} = \frac{1}{2} C_D \rho A_2 \left| u - u_p \right| \left(u - u_p \right) + \rho (1 + C_M) A_3 \frac{du}{dt} + (\rho^s - \rho^w) A_3 g$$

where, u_p is the particle velocity, u is the flow velocity, A_3 is the particle volume, A_2 is the projected area, C_D is the drag coefficient, C_M is the coefficient of additional mass, ρ^s

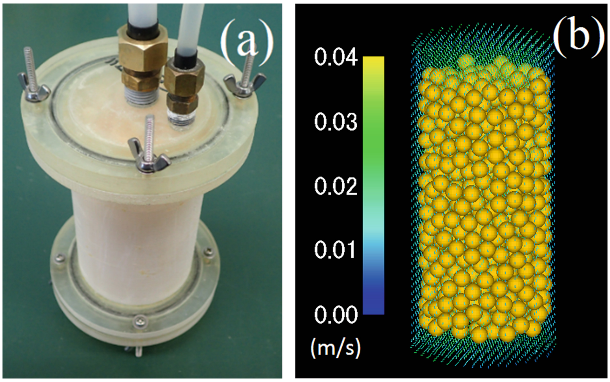

Fig. 5. Appearance of constant head permeability test; (a) 3D printed specimen, (b) DEM-SMAC simulation.

is the particle density, and ρ^{w} is the water density. The drag coefficient is expressed as function of Reynolds number. (Schiller and Naumann 1933). Moreover, flow velocity is reduced in proportion to porosity of each mesh. Figure 5(b) shows appearance of this calculation, showing the variation of flow velocity caused by variation of porosity.

Table 2 gives the parameters for numerical simulation and experiment. The difference in water density and viscosity are caused by the experimental water temperature.

Table 2. Permeability test parameters of numerical simulation and experiment.

Parameter	Unit	Value	
		Simulation	Experiment
Specimen diameter	mm	50.0	50.0
Specimen height	mm	100.0	100.0
Particle size	mm	6.5	6.5
Particle number	–	696	696
Particle density	g/cm^3	2.65	1.105
Water density	g/cm^3	1.0	0.99691
Viscosity	Pa·s	1.0×10^{-3}	8.94×10^{-4}
Void ratio	–	0.960	0.971

Comparison of permeability between numerical simulation and 3D printed material

Figure 6 shows comparison of permeability coefficient between 3D printed specimen and DEM-SMAC coupled simulation. Each permeability coefficient is converted to a permeability coefficient at 15° considering the effects of viscosity influenced by temperature. Moreover, the horizontal dashed line shows the permeability estimating

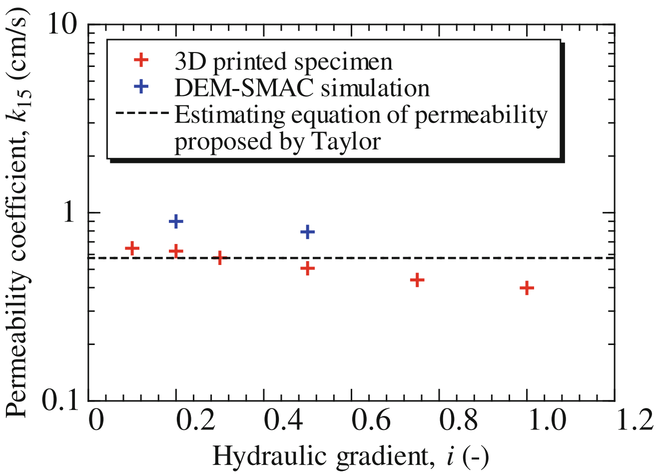

Fig. 6. Comparison of permeability between numerical simulation and 3D printed specimen.

equation proposed by Taylor (1948). According to this figure, both methods agree qualitatively.

Conclusion

In this study, in order to develop a method for evaluating the mechanical properties of a granular material while maintaining its particle arrangement in experiment and numerical simulation, we examined the permeability of the DEM packed model and its 3D printed specimen. This method of replicating particle arrangement is qualitatively reproducible, as demonstrated by the comparison of the cross-sections of a DEM simulated specimen with those of X-ray CT scanned images of a 3D printed specimen. In addition, the mechanical properties of this 3D printed specimen are validated through comparison of constant head permeability test with DEM-SMAC coupled simulation. The results of this validation showed that both methods agree qualitatively.

References

Amsden AA, Harlow FH (1970) A simplified MAC technique for incompressible fluid flow calculations. J Comp Phys 6:322–325

Cundall PA, Strack ODL (1979) A discrete model for granular assemblies. Geotechnique 29 (1):47–65

Hanaor DAH, Gan Y, Revay M, Airey DW, Einav I (2016) 3D printable geomaterials. Geotechnique 66(4):323–332

Matsumura S, Kobayashi T, Mizutani T (2015) 3D printing of granular material and its application in soil mechanics. In: Proceedings of Fifth International Conference on Geotechnique, Construction Materials and Environment, pp. 436–441

Schiller L, Naumann AZ (1933) Uber die grundlegenden berechungen bei der schwerkraftaufbereitung. Ver Deut Ing 77:318–321

Taylor DW (1948) Fundamentals of Soil Mechanics. Wiley, New York, pp. 97–123

Tchen C (1947) Mean value and correlation problems connected with the motion of small particles suspended in a turbulent fluid. D. Sc. dissertation, Techniche Hogeschool. Delft

Author Index

A. Ferrari and L. Laloui (eds.), *Advances in Laboratory Testing and Modelling of Soils and Shales (ATMSS)*, Springer Series in Geomechanics and Geoengineering,
DOI 10.1007/978-3-319-52773-4